Martin Faccinelli

Defect Complexes in Proton Implanted Silicon

DOCTORAL THESIS

For obtaining the academic degree of
Doktor der technischen Wissenschaften
Doctoral Programme of Technical Physics

Graz University of Technology
Institute of Solid State Physics

Supervisor: Univ.-Prof. Ph.D Peter Hadley

Graz, 2018

Abstract

The electrical, optical and mechanical properties of materials are often determined by the defects those materials contain. Small changes in the defect concentration, or the introduction of of a new kind of defect can cause large changes in the material properties, even though, in many cases the concentration of these defects is very low.

The implantation of high energy protons is a technique mostly relevant for power devices, where it is used to produce the field stop region. In this process, hydrogen is introduced into the material and simultaneously vacancies and silicon self-interstitials are generated due to the interaction of the high energy protons with the silicon lattice. These three defects are mobile already at moderate temperatures and undergo reactions with each other. Furthermore, reactions with different impurities such as carbon, oxygen, boron and phosphorus take place. Considering defect complexes consisting of several different point defects, hundreds of different combinations are possible. Some of these defect complexes are electrically active and lead to an increase of the electron concentration in the implanted region. Here the change of the electron concentration depends on many parameters, such as the implantation energy, the implanted proton dose and also on the temperature and duration of a subsequent anneal.

Directly measuring the concentrations of the relevant defects in these devices is often impossible. So in this thesis simulations are combined with experiments to infer the concentration of the defects. The simulations describe the generation, diffusion, and reaction of the defects. The information needed to perform accurate simulations is incomplete and the computation time needed is very long. For this reason, some simplifying assumptions about the diffusion and reactions have to be made.

Nevertheless, some conclusions can be reached. The charge carrier profiles calculated from the simulated concentration profiles of electrically active defects are in good qualitative agreement with doping profiles measured using spreading resistance profiling. Furthermore, a new model describing the change of the electrical properties of the material caused by proton implantation is deduced from these results. It is shown that the observed changes can be explained by the generation and deactivation of the double acceptor V_2 and the double donor C_iOI.

Kurzfassung

Die elektrischen, optischen und mechanischen Eigenschaften von Materialien werden oft durch die Defekte bestimmt, welche sie beinhalten. Geringe Veränderungen der Defektkonzentrationen, oder das Hinzufügen neuer Defekte, können starke Auswirkungen auf die Materialeigenschaften haben. Oft ist die Konzentration solcher Defekte sehr gering.

Die Implantation von hochenergetischen Protonen ist vor allem für die Herstelung von Leistungshalbleitern relevant, wo sie zur Erzeugung der Felstopp-Region verwendet wird. In diesem Verfahren wird Wasserstoff in den Kristall eingebracht. Zur gleichen Zeit, werden durch die Wechselwirkung der hoch-energetischen Teilchen mit dem Kristallgitter, Leerstellen und Zwischengitteratome erzeugt. Diese drei Defekte sind schon bei geringen Temperaturen beweglich und gehen chemische Reaktionen miteinander ein. Außerdem reagieren diese Defekte mit weiteren Verunreinigungen, wie Kohlenstoff, Sauerstoff, Bor oder Phosphor. Zieht man hierbei entstehende Defektkomplexe in Betracht, welche aus mehreren Punktdefekten bestehen, sind hunderte verschiedene Kombinationen möglich. Manche dieser Komplexe sind elektrisch aktiv und führen zu einer Erhöhung der Konzentration von Leitungselektronen im implantierten Bereich. Die hier beobachtete Veränderung der Elektronenkonzentration hängt von mehreren Parametern ab. Neben der Implantationsenergie und der Dosis spielen hier auch die Temperatur und die Dauer des, auf die Implantation folgenden, Ausheilschrittes eine wichtige Rolle.

Eine direkte Messung der Konzentrationen der relevanten Defekte ist meist nicht möglich. Aus diesem Grund wurden in dieser Arbeit Experimente mit Simulationen kombiniert um die Konzentrationen dieser Defekte abzuleiten. Diese Simulationen beschreiben die Erzeugung, Diffusion und Reaktionen der Defekte. Die für die Durchführung genauer Simulationen notwendigen Informationen sind jedoch unvollständig und lange Rechenzeiten werden benötigt, weshalb einige vereinfachende Annahmen im Bezug auf die Diffusion und Reaktionen gemacht werden müssen.

Nichtsdestotrotz können aus den Simulationsergebnissen Schlussfolgerungen getroffen werden. Die aus den simulierten Konzentrationen elektrisch aktiver Defekte berechneten Ladungsträgerprofile zeigen eine gute qualitative Übereinstimmung mit mittels Ausbreitungswiderstandsmessungen bestimmten Dotierprofilen. Von diesen Resultaten konnte des Weiteren, ein neues Modell, welches die durch Protonenimplantation verursachte Änderung der elektrischen Eigenschaften des Materials beschreibt, abgeleitet werden. Es wird gezeigt, dass die beobachteten Veränderungen durch die Erzeugung und Deaktivierung des Doppel-Akzeptors V_2 und des Doppel-Donators C_iOI erklärt werden können.

Eidesstattliche Erklärung

Statutory Declaration

Ich erkläre an Eides statt, dass ich die vorliegende Arbeit selbstständig verfasst, andere als die angegebenen Quellen/Hilfsmittel nicht benutzt, und die den benutzten Quellen wörtlich und inhaltlich entnommenen Stellen als solche kenntlich gemacht habe. Das Textdokument, welches ins TUGRAZonline hochgeladen wurde ist identisch zu der hier präsentierten Doktorarbeit.

I declare that I have authored this thesis independently, that I have not used other than the declared sources/resources, and that I have explicitly marked all material which has been quoted either literally or by content from the used sources. The text document uploaded to TUGRAZonline is identical to the present doctoral thesis.

Graz, am ____________________ ________________________

Datum Unterschrift

Acknowledgments

First and foremost I would like to thank my supervisor Prof. Peter Hadley for supporting me during this thesis and for keeping his door open and taking his time to answer any question and discuss any topic.

Furthermore, I would like to thank Thomas, Wübben, who, on short notice, filled in as my second supervisor and supported me in any issue concerning the collaboration with Infineon Technologies AG. I am also very grateful to thank Johannes Laven, Hans-Joachim Schulze, Werner Schustereder and Moriz Jelinek for numerous interesting discussions in our bi-weekly meetings. A big thank you also goes to Tobias Bianga and the FA-team of Infineon Technologies Austria AG for all their efforts concerning sample preparation and measurements.

I would also like to thank the people of the institute of solid state physics for welcoming me. I am very grateful to Elisabeth Stern, for being the heart of the institute and a great support at any time. Furthermore, I would like to thank Prof. Roland Resel who provided the possibility to use his lab and his equipment whenever needed. I am also very grateful to Prof. Karin Zojer who provided great advice concerning simulations. Moreover, I want to thank Christian Gspan for his support, his kindness and his advice.

I am very glad to have shared the office with many great colleagues. Amongst them I want to point out Stefan Kirnstötter - thank you for all the good times we had in the lab - and Gernot Gruber, who became good friends of mine. Furthermore I would like to thank Lukas Etzlinger and Julia Hassler for many interesting discussions during their master thesis projects.

At last I would like to thank my dear fiancée Sandra for her moral support, my parents for supporting me, also financially, throughout my studies, and I want to thank my family and friends for always being there for me.

This work has been performed in the project EPPL, co-funded by grants from Austria, Germany, The Netherlands, Italy, France, Portugal- ENIAC member States and the ENIAC Joint Undertaking. This project is co-funded within the program "Forschung, Innovation und Technologie für Informationstechnologie" by the Austrian Ministry for Transport, Innovation and Technology.

Martin Faccinelli　　　　Graz, 2018

Contents

1 Introduction

Many properties of materials, are determined by the defects they contain. Steel for example is hardened by the incorporation of defects, plastics are softened by certain additives. In semiconductor industry impurities are introduced to change the electrical properties of the material.

Often, very low concentrations of defects have a significant impact on the change of certain properties of the material. One phosphorus atom per a billion silicon atoms reduces the resistivity of the material by four orders of magnitude compared to a perfect silicon crystal. The urge of constantly developing more efficient and faster semiconductor devices requires narrowing the specifications of the properties of the used materials. Here, the problem is that apart from being introduced on purpose, impurities are also brought into the material unintentionally during the various steps in the production cycle of a semiconductor device. Often the introduced impurities are changed during the process steps and form defect complexes. To still be able to stay within the desired specifications in a reproducible way, the formation of defect complexes and their impact on the material properties have to be studied intensively.

Ion implantation is a process, where an impurity is purposely introduced into the material by accelerating ionized atoms or molecules and shooting them into the silicon crystal. A byproduct of this process is the generation of intrinsic defects (vacancies and self-interstitials) by knocking silicon atoms off their initial lattice positions. The intrinsic point defects are very mobile and tend to react with other defects forming defect complexes.

The implantation of protons into a silicon crystal leads to the formation of several kinds of defect complexes which are useful in semiconductor device engineering. If low proton doses are implanted, the formation of recombination centers is observed, which reduce the lifetime of charge carriers. At intermediate implantation doses, defect complexes are generated which act as electron donors and change the charge carrier concentration in the material. The implantation of high proton doses leads to the formation of plate-like defect complexes, used to cleave off a thin layer of a silicon wafer in the so-called “Smart-Cut” process.

The implantation process is always accompanied by a subsequent heat treatment in which the final defect complexes, which change the material properties to the desired specifications are formed. To find out the best conditions under which the implantation process and the subsequent anneal are conducted usually demands complex and extensive empirical studies.

Despite decades of research on the defects and defect complexes formed by the proton implantation process, it is still not clear which exact defects are responsible for the observed changes in the material. There are many candidates, as a large number of different defect complexes is formed when silicon is irradiated with protons. In this process, hydrogen is introduced into the material and vacancies and self-interstitials are generated. Those point-defects are mobile at the usual temperatures used during the implantation process and during the subsequent anneal. Once two defects come close to each other, they react, forming defect complexes. The mobile defects do not only react among each other but they also interact with other impurities in the material. Among these defects, the most important ones are oxygen and carbon, which are unintentionally introduced during the crystal growth. Other impurities undergoing reactions are dopants such as boron, and phosphorus. Also nitrogen and different transition metals such as iron can form complexes with the mobile defects.

Considering defect complexes which can consist of ten point-defects and more, a large number of different combinations is theoretically possible. Even though not all of these defect complexes are stable, the number of different defects which are generated in the proton implantation process is suspected to be very high, as lots of different studies on this topic agree about.

It is impossible, though, to experimentally access all these defects at once in a single measurement. Most measurements used in semiconductor industry are sensitive to a certain part of these defects. Electron paramagnetic resonance (EPR) is used to measure the overall concentrations of paramagnetic defects in the material, while deep level transient spectroscopy (DLTS) detects electrically active defects which show transitions of their ionization state at energies close to the center of the silicon band gap. The distribution of the concentrations of different chemical elements can be accessed using secondary ion mass spectrometry (SIMS) and the concentration of vacancy-complexes can be measured by positron annihilation. Transmission electron microscopy (TEM) yields the distribution of large defect complexes, but no information about their composition. Other methods such as spreading resistance profiling (SRP) or capacitance-voltage (CV) measurements yield the residual charge carrier concentration, resulting from the contributions of all electrically active defects in the material. Furthermore, ab-initio calculations such as density functional theory (DFT) are used to derive the stability of different configurations of defects in the lattice and to determine the ratio of the concentration of their different charge states.

To be able to further develop and improve semiconductor devices, a better understanding of the defects those materials contain is crucial. One way to accomplish this, is through process simulations. Existing simulation tools of the proton implantation process, such as “Stopping and Range of Ions in Matter” (SRIM), are based on Monte-Carlo approaches. Such calculations only consider the interaction of the implanted ions with the crystal lattice and do not include the diffusion of those defects and the reactions amongst them, not to mention the reactions with other impurities in the material. Hence, in the course of this project, a process simulation was developed which includes not only the generation of defects during proton implantation, but also the diffusion of mobile defects, reactions between defects and also dissociations of the formed defect complexes.

From the results of this simulation, qualitative deductions can be drawn in respect to which defect complexes are formed under certain conditions and how their concentrations influence the overall charge carrier concentration. Furthermore, calculations of the kinetics of the formation of different defect complexes are presented which investigate the influence of the Fermi energy and the doping concentration, on the temperature dependence of the rate constants of those reactions.

2 Fundamentals

This chapter provides an overview of the fundamental concepts of semiconductor physics and defects in semiconducting materials. Here, a special focus is set on defects and defect complexes generated by the implantation of protons in silicon. Some parts of this chapter, such as the sections on charge carrier recombination, junctions, raw-silicon production and crystal systems can safely be skipped by an experienced researcher.

2.1 Introduction to Semiconductor Physics

In this section fundamental concepts of the physics of semiconducting devices are explained. More detailed information about the topic can be found in references [1–4].

2.1.1 Crystal Lattice

A single crystalline solid material is characterized by a periodic arrangement of the atoms it consists of. The smallest repeating pattern of this arrangement is the unit cell. The side lengths of the unit cell along the crystal coordinates x_c, y_c and z_c are the lattice constants a_1, a_2 and a_3. Crystals are classified by their inherent symmetry. In this classification a crystal is associated with one of the seven crystal systems. Crystals of the same crystal system can differ in their translational symmetry, which means the arrangement of lattice points within the crystal structure. This leads to the 14 Bravais-lattices. Table 2.1 shows an overview of the different crystal structures and Bravais-lattices including the ratios of the lattice constants and the lattice angles α_l, β_l and γ_l. Taking into account that the basis of a crystal lattice can consist of more than one atom, further symmetry operations are possible and the crystal structures can be classified into 32 point groups and 230 space groups. A more detailed description of symmetry operations, point and space groups can be found in reference [5].

The crystal structure of silicon corresponds to the diamond structure and consists of a diatomic basis which is repeated on a fcc crystal lattice with the side length $a_{\mathrm{Si}}= 0.543\,\mathrm{nm}$. Due to sp^3-hybridization of the outer electron shells each silicon forms four similar covalent bonds to its neighboring atoms. The solid angle between two bonds is 109.5 °. Figure 2.1 shows the conventional unit cell of silicon. The eight atoms in the corners and the six atoms at the center of the faces correspond to the fcc-structure of the atom based at [0,0,0]. The other four atoms correspond to the fcc-sub-lattice of the atom based at $[\frac{a_{\mathrm{Si}}}{4},\frac{a_{\mathrm{Si}}}{4},\frac{a_{\mathrm{Si}}}{4}]$.

The conventional unit cell is not the smallest building block of a crystal. The primitive unit cell, which contains only one lattice point (basis) of a crystal is called Wigner-Seitz cell in real space, or first Brillouin zone in reciprocal, or momentum space. The first Brillouin zone is important in the description of waves, such as electrons, traveling through a crystal.

Table 2.1: List of crystal systems and Bravais lattices

Crystal System	Bravais Lattices	Lattice Constants	Lattice Angles
triclinic	simple	$a_1 \neq a_2 \neq a_3$	$\alpha_l \neq \beta_l \neq \gamma_l$
monoclinic	simple, body-centered	$a_1 \neq a_2 \neq a_3$	$\alpha_l = \beta_l = 90^\circ \neq \gamma_l$
orthorhombic	simple, body-centered, base-centered, face-centered	$a_1 \neq a_2 \neq a_3$	$\alpha_l = \beta_l = \gamma_l = 90^\circ$
tetragonal	simple, body-centered	$a_1 = a_2 \neq a_3$	$\alpha_l = \beta_l = \gamma_l = 90^\circ$
rhombohedral	centered	$a_1 = a_2 = a_3$	$\alpha_l = \beta_l = \gamma_l < 120^\circ, \neq 90^\circ$
hexagonal	simple	$a_1 = a_2 \neq a_3$	$\alpha_l = \beta_l = 90^\circ$, $\gamma_l = 120^\circ$
cubic	simple, body-centered, face-centered	$a_1 = a_2 = a_3$	$\alpha_l = \beta_l = \gamma_l = 90^\circ$

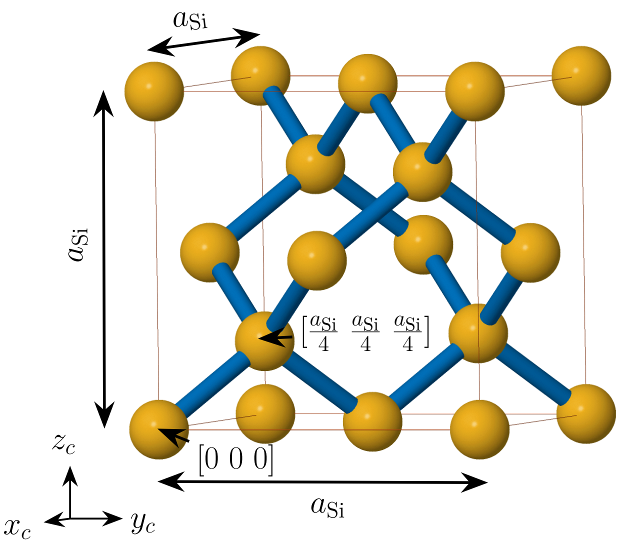

Figure 2.1: Conventional unit cell of fcc-silicon. Silicon atoms are colored in yellow, bonds between silicon atoms are colored in blue. The crystallographic coordinates x_c, y_c and z_c are shown in the corner. The two atoms of the diatomic base are indicated.

2.1.2 Band Structure and Density of States

Electrons can occupy certain states at certain energies E in an atom, which are determined by the Schrödinger equation

$$\frac{-\hbar}{2m_e}\nabla^2\Psi + V\Psi = E\Psi, \tag{2.1}$$

where $\hbar = \frac{h}{2\pi}$ is Planck's reduced constant, m_e is the electron mass, V is the potential energy and Ψ is the wave function. In a crystal, electrons travel like waves and are associated with a certain wavelength $\lambda = \frac{2\pi}{|\vec{k}|}$. Here $\vec{k}$ is the electron wave-vector which points in the direction the electron wave is traveling. When calculating the energy states of electrons in a crystal the periodic potential of the crystal lattice has to be taken into account. Here, Ψ has the form

$$\Psi = \exp(i\vec{k}x)\mu_k(x), \tag{2.2}$$

where μ_k is this periodic part of the wave-function. The result of such a calculation are energy states as a function of the electron wave-vector. The energy states merge to continuous energy bands. There are bands of different excited states of the electron, forming the band structure $E(\vec{k})$ of the crystal. To know the band structure of the whole crystal, it is sufficient to calculate just the band structure in the first Brillouin zone. The band structure of a crystal can be calculated using different methods, such as tight binding [6], pseudo-potentials [7], or density functional theory (DFT) [8].

Figure 2.2 shows the band structure of silicon calculated using the localized atomic orbital method (LAOM)[9]. There is a range of energies in the band structure of silicon, where no energy states appear. This region, the energy gap, is bounded by the conduction band at energies higher than the band gap and by the valence band at lower energies. The energy at the maximum of the valence band is the valence band energy E_V, the energy at the minimum of the conduction band is the conduction band energy E_C. The energy difference between E_C and E_V is the band gap energy E_G.

In an intrinsic semiconductor at 0 K, all energy states in the valence band are occupied with electrons while all energy states in the conduction band are empty. At elevated temperatures electrons are excited into the conduction band. This generates empty states in the valence band, which are referred to as holes and can be treated a quasi-particles. Before we calculate the concentration of charge carriers, namely electrons n and holes p we take a closer look on the conduction band and the valence band of silicon.

Counting all energy states at a certain energy in the band structure $E(\vec{k})$ yields the density of states $D(E)$. For a parabolic energy band $D(E)$ is

$$D(E) = \frac{2N_{\text{band}}}{\sqrt{\pi}}\left(\frac{1}{k_BT}\right)^{\frac{3}{2}}\sqrt{E-E_0}, \tag{2.3}$$

where N_{band} is the effective density of states in the band, $E - E_0$ is the energy range of the band and k_B is the Boltzmann constant. N_{band} is calculated from the effective mass

m^* of the charge carrier in the band

$$N_{\text{band}} = \frac{1}{\sqrt{2}} \left(\frac{m^* k_B T}{\pi \hbar^2} \right)^{\frac{3}{2}} . \tag{2.4}$$

The effective mass m^* of a charge carrier reflects its apparent mass, relative to the electron rest mass m_e when responding to an electric field. It can be calculated from the curvature of the band structure

$$\frac{d^2 E(\vec{k})}{d\vec{k}^2} = \frac{\hbar^2}{m^*}. \tag{2.5}$$

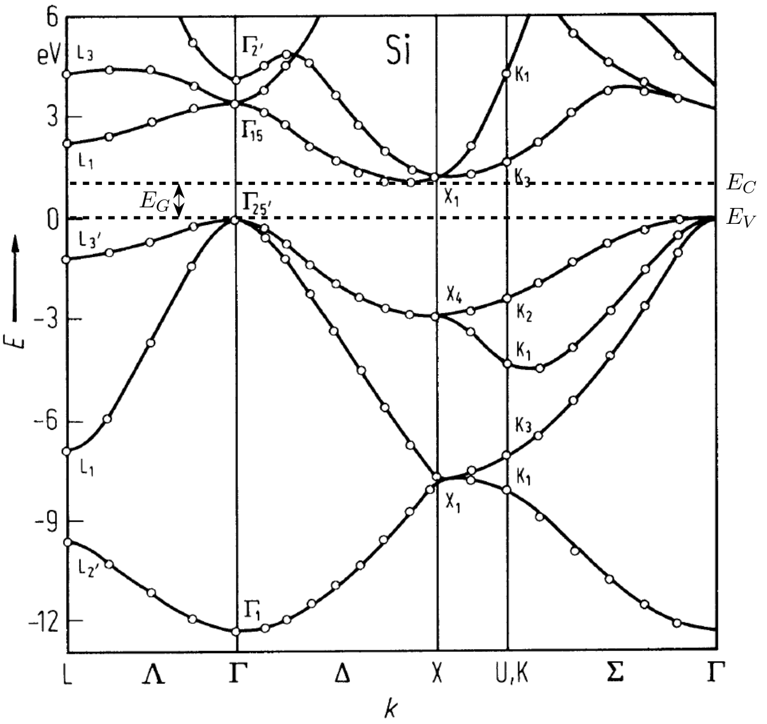

Figure 2.2: Band structure $E(\vec{k})$ of silicon along different crystal directions in the first Brillouin zone calculated using LAOM. High symmetry points are indicated. The band gap E_G and the conduction band and valence band energies E_C and E_V are highlighted. Taken from reference [10] and modified.

The band structure of silicon displays more than just one conduction band minimum and several valence band maxima. The minimum of the conduction band actually consists of six minima which can be approximated by the six paraboloids

$$\begin{aligned}
E_{C100} &= E_G + \frac{\hbar^2}{2m_l^*}\left(k_x - \frac{1.7\pi}{a_{\mathrm{Si}}}\right)^2 + \frac{\hbar^2}{2m_t^*}{k_y}^2 + \frac{\hbar^2}{2m_t^*}{k_z}^2, \\
E_{C\bar{1}00} &= E_G + \frac{\hbar^2}{2m_l^*}\left(k_x + \frac{1.7\pi}{a_{\mathrm{Si}}}\right)^2 + \frac{\hbar^2}{2m_t^*}{k_y}^2 + \frac{\hbar^2}{2m_t^*}{k_z}^2, \\
E_{C010} &= E_G + \frac{\hbar^2}{2m_t^*}{k_x}^2 + \frac{\hbar^2}{2m_l^*}\left(k_y - \frac{1.7\pi}{a_{\mathrm{Si}}}\right)^2 + \frac{\hbar^2}{2m_t^*}{k_z}^2, \\
E_{C0\bar{1}0} &= E_G + \frac{\hbar^2}{2m_t^*}{k_x}^2 + \frac{\hbar^2}{2m_l^*}\left(k_y + \frac{1.7\pi}{a_{\mathrm{Si}}}\right)^2 + \frac{\hbar^2}{2m_t^*}{k_z}^2, \\
E_{C001} &= E_G + \frac{\hbar^2}{2m_t^*}{k_x}^2 + \frac{\hbar^2}{2m_t^*}{k_y}^2 + \frac{\hbar^2}{2m_l^*}\left(k_z - \frac{1.7\pi}{a_{\mathrm{Si}}}\right)^2, \\
E_{C00\bar{1}} &= E_G + \frac{\hbar^2}{2m_t^*}{k_x}^2 + \frac{\hbar^2}{2m_t^*}{k_y}^2 + \frac{\hbar^2}{2m_l^*}\left(k_z + \frac{1.7\pi}{a_{\mathrm{Si}}}\right)^2.
\end{aligned} \tag{2.6}$$

The electron effective mass in the conduction band is anisotropic. m_l^* is the longitudinal electron effective mass and m_t^* is the transverse electron effective mass.

The effective density of states at the bottom of the conduction band of silicon N_C is the sum over all six conduction electron (ce) energy minima

$$N_C = \frac{6}{\sqrt{2}}\left(\frac{\sqrt[3]{m_l^* m_t^* m_t^*}\,k_B T}{\pi\hbar^2}\right)^{\frac{3}{2}} = N_C(300\,\mathrm{K}) * \left(\frac{T}{300}\right)^{\frac{3}{2}}. \tag{2.7}$$

Here $N_C(300\,\mathrm{K})$ is the effective density of states in the conduction band at 300 K. Sometimes in literature the effective mass $m_{ed}^* = 6^{\frac{2}{3}}\sqrt[3]{m_l^* m_t^* m_t^*}$ can be found which is the density of states effective mass of electrons for the calculation of the density of states in the conduction band.

The valence band of silicon is divided into three bands. While the energy maxima E_V of the light hole (lh) and heavy hole (hh) band fall on each other, there is a split-off (so) band with its maximum E_{SO}. Like electrons, holes are associated with an effective mass. The effective masses of holes in the valence band are m_{lh}^* for the light-hole-band, m_{hh}^* for the heavy-hole-band and m_{so}^* for the split-off band. The effective density of states in the valence band N_{lh}, N_{hh}, N_{so} are

$$\begin{aligned}
N_{lh} &= \frac{1}{\sqrt{2}}\left(\frac{m_{lh}^* k_B T}{\pi\hbar^2}\right)^{\frac{3}{2}}, \\
N_{hh} &= \frac{1}{\sqrt{2}}\left(\frac{m_{hh}^* k_B T}{\pi\hbar^2}\right)^{\frac{3}{2}}, \\
N_{so} &= \frac{1}{\sqrt{2}}\left(\frac{m_{so}^* k_B T}{\pi\hbar^2}\right)^{\frac{3}{2}} = N_{SO}(300\,\mathrm{K}) * \left(\frac{T}{300}\right)^{\frac{3}{2}}.
\end{aligned} \tag{2.8}$$

Here, $N_{SO}(300\,\mathrm{K})$ is the effective density of states in the split-off band at 300 K.As the energy maximum of both, the light-hole and the heavy-hole band are at the same energy, their effective density of states are added to N_V

$$N_V = N_{lh} + N_{hh} = N_V(300\,\mathrm{K}) * \left(\frac{T}{300}\right)^{\frac{3}{2}}, \tag{2.9}$$

with the effective density of states $N_V(300\,\mathrm{K})$ in the light- and heavy-hole bands at 300 K.

As the shape of the top of the valence band an the bottom of the conduction band are parabolic, knowing the number of states in the bands and using equation 2.3 the density of states $D(E)$ can be calculated. The density of states for energies below and above the band gap is

$$D(E) = \begin{cases} \frac{2N_V}{\sqrt{\pi}}\left(\frac{1}{k_BT}\right)^{\frac{3}{2}}\sqrt{E_V - E} + \frac{N_{so}}{\sqrt{\pi}}\left(\frac{1}{k_BT}\right)^{\frac{3}{2}}\sqrt{E_{SO} - E}, & \text{for } E < E_{SO} \\ \frac{2N_V}{\sqrt{\pi}}\left(\frac{1}{k_BT}\right)^{\frac{3}{2}}\sqrt{E_V - E}, & \text{for } E_{SO} < E < E_V \\ 0, & \text{for } E_V < E < E_C \\ \frac{2N_C}{\sqrt{\pi}}\left(\frac{1}{k_BT}\right)^{\frac{3}{2}}\sqrt{E - E_C}, & \text{for } E_C < E \end{cases} \tag{2.10}$$

The parameters used for the calculation of the density of states are listed in table 2.2.

Table 2.2: Parameters for the calculation of the density of states in silicon found in references [1, 4, 11].

Parameter	Value	Unit
m_l^*	$0.98m_e$	kg
m_t^*	$0.19m_e$	kg
m_{ed}^*	$1.08m_e$	kg
m_{lh}^*	$0.16m_e$	kg
m_{hh}^*	$0.49m_e$	kg
m_{so}^*	$0.24m_e$	kg
$N_C(300\,\mathrm{K})$	2.78×10^{19}	cm^{-3}
$N_V(300\,\mathrm{K})$	9.84×10^{18}	cm^{-3}
$N_{SO}(300\,\mathrm{K})$	2.98×10^{18}	cm^{-3}

Figure 2.3 shows the density of states in silicon. The solid line shows the actual density of states, extracted from a simulation of the band diagram as shown in figure 2.2 by counting the number of energy states per energy. The dashed line represents the analytic density of states, calculated as the sum of the density of states in the sub-bands at the bottom of the conduction band and at the top of the valence band, using equations 2.10 and the parameters listed in table 2.2.

Despite the strong deviation of the analytic calculation from the simulation, in the region close to the band edges, the two overlap. Figure 2.4 offers a close look on the interesting energy region. The contributions of the sub-bands of the silicon band structure are also plotted. The figure reveals that the analytic calculation and the simulation coincide right at the band edges. This small overlap is enough for the calculation of the free charge carriers in the bands.

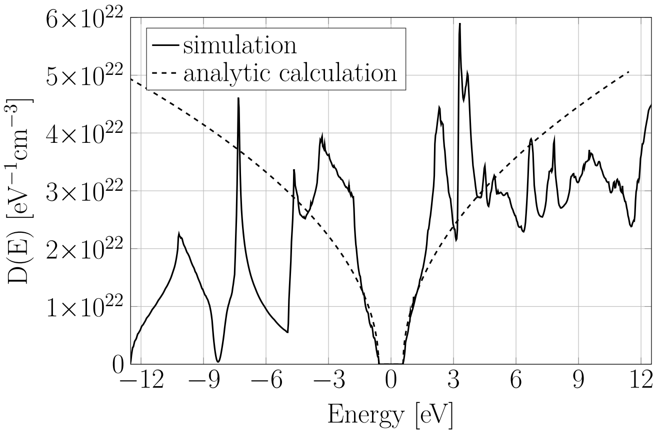

Figure 2.3: Density of states in silicon. The solid line represents the density of states in silicon extracted from a simulation of the band structure as shown in figure 2.2. The dashed line is the density of states in silicon calculated using equations 2.10 and the parameters listed in table 2.2.

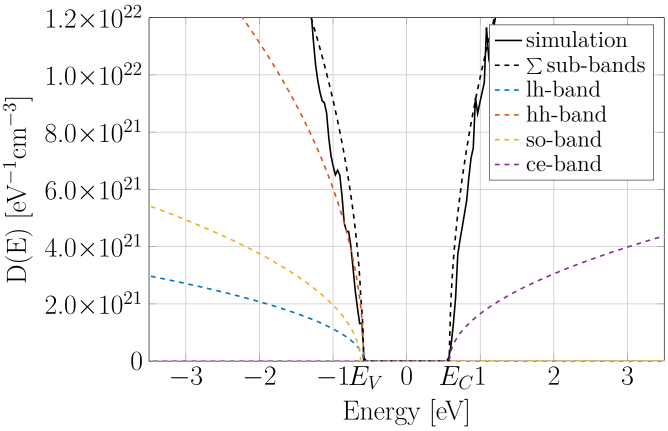

Figure 2.4: Density of states close to the band gap in silicon. The solid line represents the density of states in silicon extracted from a simulation of the band structure as shown in figure 2.2. The density of states in the sub-bands was calculated using equations 2.10 and the parameters listed in table 2.2.

2.1.3 Free Charge Carriers in a Semiconductor

As we now have an analytic formulation for the density of states close to the band edges we can calculate the concentration of charge carriers. The density of electrons in the conduction band n of a semiconductor at thermal equilibrium is calculated from the density of states in the conduction band and the Fermi function $f(E)$

$$n = \int_{E_C}^{\infty} D(E) f(E) dE. \tag{2.11}$$

The Fermi function describes the probability that a certain energy state is occupied at a certain temperature

$$f(E) = \frac{1}{1 + \exp\left(\frac{E - E_F}{k_B T}\right)}, \tag{2.12}$$

where E_F is the Fermi energy. At 0 K, all energy states below E_F are occupied with electrons, and all states above E_F are empty. In an intrinsic semiconductor, E_F is in the middle of the band gap. The occupation probability of energy states around the Fermi energy is shown in figure 2.5 for different temperatures. The higher the temperature, the more the Fermi function gets smeared out. The inset in figure 2.5 shows a zoom into the Fermi function at energy states close to the conduction band energy.

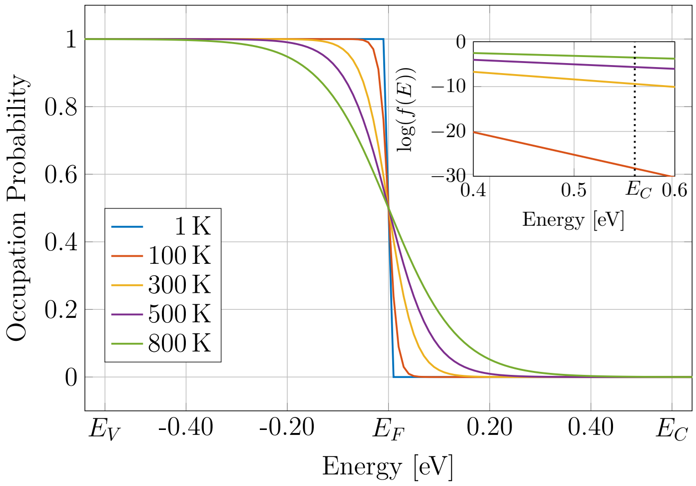

Figure 2.5: Occupation probability of energy states around E_F at different temperatures. The inset shows the Fermi function for energies around E_C on a logarithmic scale.

At 0 K the probability that an energy state at E_C is occupied by an electron is zero. At elevated temperatures this probability increases to $6{\times}10^{-29}$ at 100 K, $4{\times}10^{-10}$ at 300 K, $2{\times}10^{-6}$ at 500 K and $3{\times}10^{-4}$ at 800 K.

Close to the conduction band the occupation probability of states in the conduction band can be approximated by the exponential function $f(E)_e$

$$f(E) \approx f(E)_e = \exp\left(\frac{E_F - E}{k_B T}\right). \tag{2.13}$$

The probability of an energy state in the valence band being empty, and hence, occupied by a hole is $1-f(E)$. For energy states close to the valence band this can be approximated using the exponential function $f(E)_h$:

$$1-f(E)=1-\frac{1}{\exp\left(\frac{E-E_F}{k_BT}\right)+1}\approx f(E)_h=\exp\left(\frac{E-E_F}{k_BT}\right). \tag{2.14}$$

In figure 2.6 the occupation probability calculated using $f(E)$ and the approximations $f(E)_h$ and $f(E)_e$ are compared. There is an overlap of $f(E)_e$ and $f(E)_h$ with the Fermi function $f(E)$ for energies more than $3k_BT$ higher or lower than E_F.

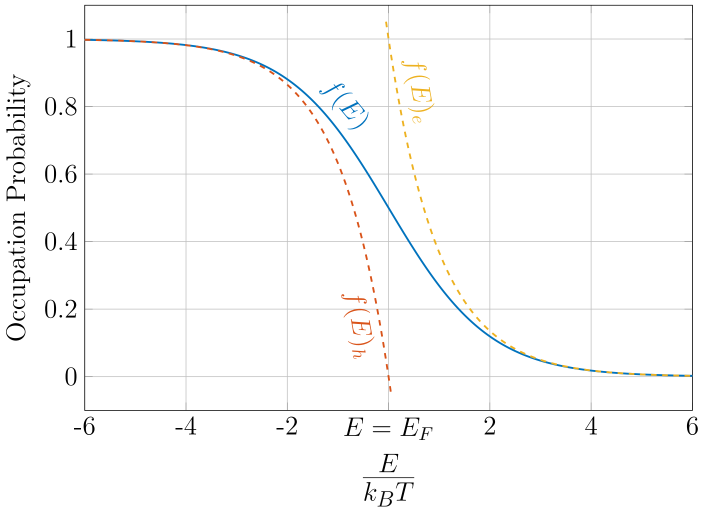

Figure 2.6: Occupation probability of energy states close to the Fermi energy including approximations of $f(E)$ for the valence band edge $f(E)_h$ and the conduction band edge $f(E)_e$.

The concentration of electrons in the conduction band is calculated by inserting the density of states $D(E)$ in the conduction band from equation 2.10 and $f(E)_e$ into equation 2.11

$$n\approx\int_{E_C}^{\infty}\frac{2N_C}{\sqrt{\pi}}\left(\frac{1}{k_BT}\right)^{\frac{3}{2}}\sqrt{E-E_C}\,\exp\left(\frac{E_F-E}{k_BT}\right). \tag{2.15}$$

After integrating over the energy states above E_C the electron density in the conduction band is

$$n=N_C\exp\left(\frac{E_F-E_C}{k_BT}\right). \tag{2.16}$$

The concentration of holes in the valence band is then calculated using the density of states in the valence band (see equation 2.10) and $f(E)_h$

$$\begin{aligned}
p = &\int_{-\infty}^{E_V} D(E)f(E)_h dE \approx \\
&\int_{-\infty}^{E_V} \frac{2N_V}{\sqrt{\pi}} \left(\frac{1}{k_BT}\right)^{\frac{3}{2}} \sqrt{E_V - E}\, \exp\left(\frac{E-E_F}{k_BT}\right) dE + \\
&\int_{-\infty}^{E_{SO}} \frac{N_{so}}{\sqrt{\pi}} \left(\frac{1}{k_BT}\right)^{\frac{3}{2}} \sqrt{E_{SO} - E}\, \exp\left(\frac{E-E_F}{k_BT}\right) dE.
\end{aligned} \tag{2.17}$$

After the integration over the energy states below E_V and E_{SO}, the hole concentration p in the valence band is

$$p = N_V \exp\left(\frac{E_V - E_F}{k_BT}\right) + N_{so} \exp\left(\frac{E_{SO} - E_F}{k_BT}\right). \tag{2.18}$$

At thermal equilibrium the product of n and p is constant. This is described by the law of mass action:

$$\begin{aligned}
np = {n_i}^2 = N_C \exp\left(\frac{E_F - E_C}{k_BT}\right) \times \left[N_V \exp\left(\frac{E_V - E_F}{k_BT}\right) + N_{so} \exp\left(\frac{E_{SO} - E_F}{k_BT}\right)\right] = \\
= N_C N_V \exp\left(\frac{-E_G}{k_BT}\right) + N_C N_{so} \exp\left(\frac{-E_G}{k_BT}\right) \exp\left(\frac{E_{SO} - E_V}{k_BT}\right).
\end{aligned} \tag{2.19}$$

Here, n_i is the intrinsic carrier concentration. As described by Varshni et al. [12], the temperature dependence of the band gap is described by

$$E_G(T) = E_G(0\,\mathrm{K}) - \frac{\alpha_{E_G} T^2}{T + \beta_{E_G}}, \tag{2.20}$$

where $E_G(0\,\mathrm{K})$ is the energy gap at (K 0). α_{E_G} and β_{E_G} are material dependent parameters. The temperature dependence of E_G and n_i in silicon is plotted in figure 2.7 The necessary parameters for this calculation are listed in tables 2.2 and 2.3.

Table 2.3: Parameters for the calculation of the band gap energy E_G silicon (from reference [13]).

Parameter	Value	Unit
$E_G(0\,\mathrm{K})$	1.169	eV
α_{E_G}	4.9×10^{-4}	eVK^{-1}
β_{E_G}	655	K

While the band gap energy decreases with increasing temperature, the intrinsic charge carrier concentration is increased. At room temperature n_i is only $6.8\times10^{9}\,\mathrm{cm}^{-3}$ but it is increased to concentrations higher than $10^{14}\,\mathrm{cm}^{-3}$ at temperatures above 200 °C. Electronic devices should be operable in a wide temperature range. This implies that in this temperature range the electrical properties must not change. The charge carrier concentration in a semiconductor can be fixed to a certain value by doping.

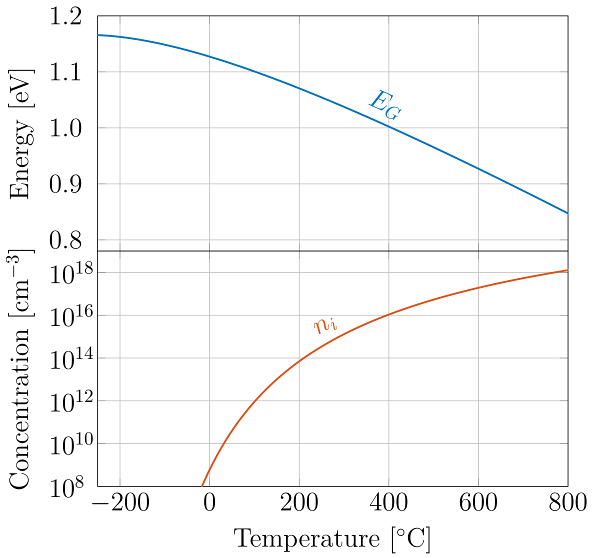

Figure 2.7: Temperature dependence of the band gap energy E_G and the intrinsic charge carrier concentration n_i in silicon.

2.1.4 Doping

The electrical properties of semiconductors can be changed by a controlled doping of the material with impurities. There are different doping techniques reaching from adding impurities to the silicon melt during crystal growth, to implanting high energy ions. The introduction of impurities can result in the formation of new energy levels in the band gap. Dopants creating energy states close to the bottom of the conduction band (E_d) are called donors. Donors increase the concentration of electrons in the conduction band. At the same time the concentration of holes in the valence band is decreased, as $p = \frac{{n_i}^2}{n}$. This kind of doping is referred to as n-type doping. If introducing dopants results in the formation of energy states in the band gap close to the top of the valence band (E_a), the dopants are acceptors and cause p-type doping by increasing the concentration of holes in the valence band. The predominant charge carriers in a doped, or extrinsic semiconductor are called majority carriers (electrons in n-type and holes in p-type material), while charge carriers of the other type are the minority carriers.

In a solid crystal, the law of charge conservation has to be observed. At thermal equilibrium the sum of all positive charges has to equal the sum of all negative charges

$$p + N_d^+ = n + N_a^- . \tag{2.21}$$

Here, N_d^+ is the concentration of ionized donors and N_a^- is the concentration of ionized acceptors, which depend on the total concentrations of donors N_d and acceptors N_a and on the energy states E_d and E_a which are formed in the band gap. Furthermore, the concentration of ionized donors depends on the extrinsic Fermi energy $E_{F,\text{ext}}$ of the system

($E_{F,n}$ in n-type and $E_{F,p}$ in p-type material).The concentration of ionized dopants is

$$\begin{aligned} N_d^+ &= \frac{N_d}{1+g_d\exp\left(\frac{E_{F,n}-E_d}{k_BT}\right)} \\ N_a^- &= \frac{N_a}{1+g_a\exp\left(\frac{E_a-E_{F,p}}{k_BT}\right)}. \end{aligned} \tag{2.22}$$

g_d and g_a are the degeneracies of the of the conduction and valence band. In silicon g_d is 2 and g_a is 4, as the valence band of silicon includes the light- and heavy-hole band.

In figure 2.8 the concentration of charge carriers and ionized dopants is plotted as a function of the Fermi energy in n- and p-type silicon at room temperature. In the n-type silicon the acceptor concentration N_a is $10^{12}\,\mathrm{cm}^{-3}$ and the donor concentration N_d is $10^{14}\,\mathrm{cm}^{-3}$. In the plot of the p-type material these concentrations are exchanged. The energy level of the donors E_d is 0.045 eV below the conduction band edge and the level of acceptors E_a is 0.045 eV above the valence band. The concentrations of electrons n and holes p are calculated according to equations 2.16 and 2.18.

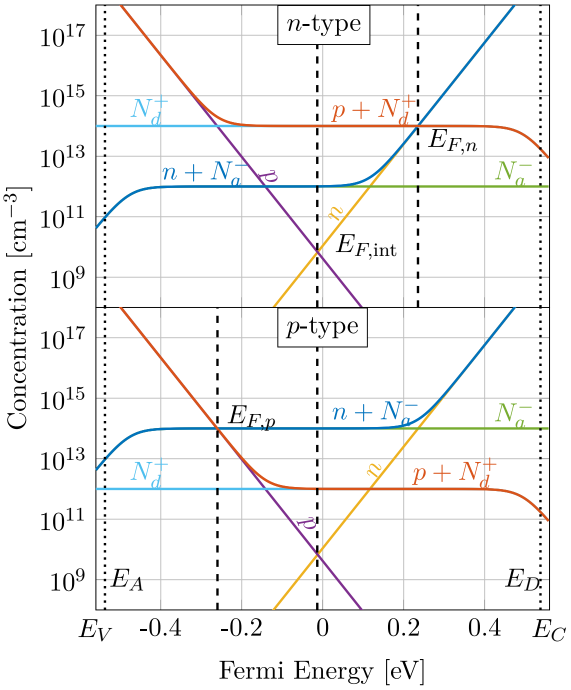

Figure 2.8: Concentration of charge carriers n and p and ionized dopants N_d^+ and N_a^- as a function of the Fermi energy in n- and p-type silicon at room temperature (300 K). The Fermi energy is shifted from the Fermi energy in intrinsic silicon $E_{F,\mathrm{int}}$ to the point of charge neutrality at $E{=}E_{F,n}$ in n-type silicon and at $E{=}E_{F,p}$ in p-type silicon.

The Fermi energy, $E_{F,n}$ in n-type and $E_{F,p}$ in p-type material, is at the energy where the concentration of positive charges $p{+}N_d^+$ is the same as the concentration of negative charges $n{+}N_a^-$. This energy differs from the intrinsic Fermi energy $E_{F,\mathrm{int}}$ in an undoped semiconductor, at which the concentrations of holes and electrons are the same. In p-type material the Fermi energy is shifted towards the valence band and in n-type material it shifts towards the conduction band. The charge carrier concentrations at thermodynamic equilibrium correspond to the concentrations of electrons and holes at the extrinsic Fermi energy.

$E_{F,\mathrm{ext}}$ is a function of the dopant concentrations and the temperature. This dependence is illustrated in figure 2.9. In silicon under intrinsic conditions ($N_d = N_a$) the Fermi energy is shifted to slightly negative values as the temperature is increased, because N_C is higher than N_V. In n-type material the Fermi energy is above the intrinsic-level, in p-type material it is below. At temperatures lower than -250 °C, the $E_{F,\mathrm{ext}}$ is between E_d and E_C, if $N_d > N_a$, or between E_a and E_V if $N_a > N_d$. With increasing temperature the Fermi energy is shifted towards the middle of the bandgap. This shift is retained if the doping concentration is increased. While at a dopant concentration of $10^{14}\,\mathrm{cm}^{-3}$ $E_{F,\mathrm{ext}}$ reaches the intrinsic level around 200 °C, at a dopant concentration of $10^{18}\,\mathrm{cm}^{-3}$ extrinsic conditions are still retained at temperatures around 800 °C. Figure 2.9 also illustrates the temperature dependence of E_C and E_V. Due to the decrease of the band gap energy (see figure 2.7), the conduction band energy decreases and the valence band energy increases with increasing temperature.

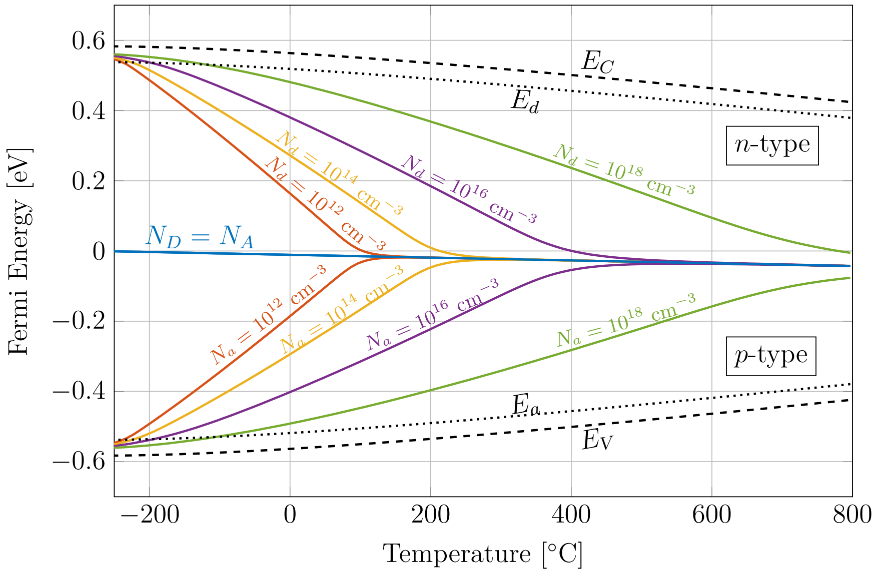

Figure 2.9: Fermi Energy as a function of the temperature for different concentrations of donors (N_d) and acceptors (N_a). Additionally the energies of the bottom of the conduction band E_C and the top of the valence band E_V, as well as the energy states of the donors ($E_d = E_C - 0.045\,\mathrm{eV}$) and acceptors ($E_a = E_V + 0.045\,\mathrm{eV}$) are included.

The temperature dependence of the charge carrier concentration for different dopant concentrations in n- and p-type silicon is illustrated in figure 2.10. In n-type silicon in figure 2.10 the donor concentration is varied between $10^{12}\,\mathrm{cm}^{-3}$ and $10^{18}\,\mathrm{cm}^{-3}$, while the acceptor concentration is constant at $10^{12}\,\mathrm{cm}^{-3}$. The dopant concentrations in the p-type material are exchanged. E_d and E_a are 0.045 eV away from the conduction and valence band energy.

At low temperatures the charge carrier concentrations are low. This is called the "freeze out" regime, because at low temperatures most of the dopant states are still occupied with electrons. As the temperature is increased, the dopants are ionized and the concentration of majority carriers is increased until it reaches the effective dopant concentration ($|N_d$-$N_a|$). The majority carrier concentration is almost constant at this value over a broad temperature range, the extrinsic regime. The extrinsic range increases with increasing dopant concentration and can last up to more than 700 °C at a dopant concentration of $10^{18}\,\mathrm{cm}^{-3}$. At higher temperatures, the electron and hole concentration equal the intrinsic charge carrier concentration n_i ($N_d = N_a$).

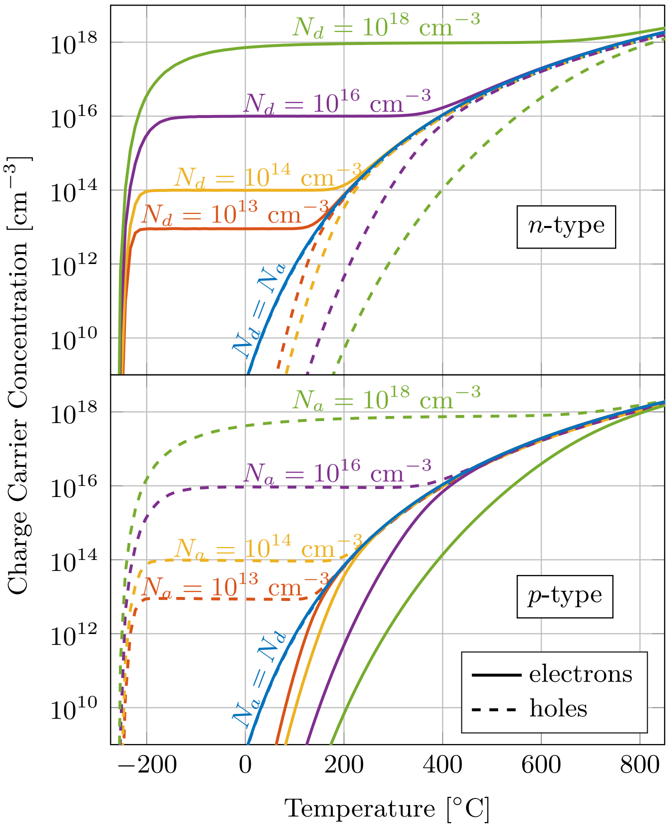

Figure 2.10: Charge carrier concentration as a function of the temperature for different dopant concentrations in n- and p-type silicon. Electron concentrations are plotted as sold lines, hole concentrations as dashed lines.

2.1.5 Electron and Hole Mobility and Resistivity

The resistivity ρ of a material is a measure of how good it can conduct an electrical current. Resistivities of solids at room temperature range from $10^{-10}\,\Omega$cm in some metals to more than $10^{22}\,\Omega$cm in insulating materials [1]. In a semiconductor the resistivity is a function of the concentration of both, electrons and holes

$$\rho = \frac{1}{e(n\mu_e + p\mu_h)}. \tag{2.23}$$

Here, e is the elementary charge, μ_e is the electron mobility and μ_h is the hole mobility. The mobility μ of a charge carrier relates its drift velocity v_d through a material to an applied electric field $\vec{E}$

$$v_d = \mu \vec{E}. \tag{2.24}$$

In an intrinsic, defect-free semiconductor the mobility of a charge carrier corresponds to its lattice mobility μ_L which is defined by the charge carrier's effective mass and the average lattice scattering time τ_{sc}

$$\mu_L = \frac{e\tau_{sc}}{m^*}. \tag{2.25}$$

As lattice vibrations increase with temperature, also the scattering increases, which leads to a reduction of the mobility. The mobility of charge carriers is also decreased by the introduction of impurities, including dopants. A further influence on the mobility is also the presence of excess charge carriers. The dependence of the mobility of charge carriers in silicon on different influences has been studied intensively [14–19]. In silicon μ_e is higher than μ_h, as the effective mass of electrons in the conduction band is smaller than that of holes in the valence band. The temperature dependence of the mobility is semi-empirically described by

$$\mu_L = \mu_L(300\,\mathrm{K}) \left(\frac{T}{300}\right)^{-\alpha_\mu}, \tag{2.26}$$

where $\mu_L(300\,\mathrm{K})$ and α_μ are material and charge carrier dependent [15]. In figure 2.11 the electron and hole mobility, as well as the resistivity of intrinsic silicon are plotted as a function of temperature (using parameters from table 2.4).

As described by equation 2.26 the mobility decreases with increasing temperature. The resitivity also decreases as a function of temperature, due to the temperature dependent increase of the intrinsic charge carrier concentration n_i (see figure 2.7). While at room temperature the resistivity of silicon is around $3\times10^5\,\Omega$cm, it decreases to less than $0.1\,\Omega$cm at temperatures above 700 °C (see figure 2.11). As described by Dorkel and Leturcq in reference [15], several influences have to be taken into account to describe the dependence of the mobility on the doping concentration and on the excess charge carrier concentration in silicon. Interactions of the charge carriers with ionized dopants are described by the impurity mobility μ_I

$$\mu_I = \frac{A_{\mu_I} T^{\frac{3}{2}}}{N^{\pm}} \left[\ln\left(1 + \frac{B_{\mu_I} T^2}{N^{\pm}}\right) - \frac{B_{\mu_I} T^2}{N^{\pm} + B_{\mu_I} T^2}\right]^{-1}. \tag{2.27}$$

Here, A_{μ_I} and B_{μ_I} are parameters depending on the type of charge carrier and $N^{\pm}$ is the concentration of ionized impurities. The contribution of carrier-carrier scattering is included in the mobility μ_{ccs}

$$\mu_{ccs} = \frac{A_{\mu_{ccs}} T^{\frac{3}{2}}}{\sqrt{np}} \left[\ln\left(1 + B_{\mu_{ccs}} T^2 (np)^{-\frac{1}{3}}\right)\right]^{-1}. \tag{2.28}$$

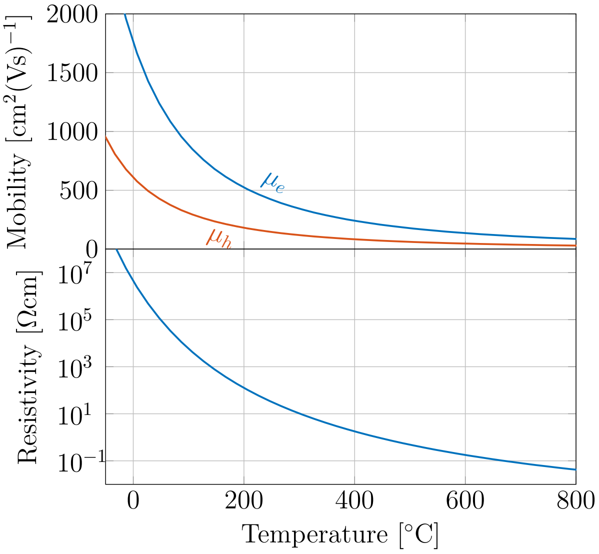

Figure 2.11: Temperature dependence of the mobility of electrons μ_e and holes μ_h and temperature dependence of the resistivity ρ in silicon.

μ_{ccs} becomes significant at high injection levels ($np >> {n_i}^2$). At such conditions the concentration of electrons is $n = n_0 + \Delta n$ and the concentration of holes is $p = p_0 + \Delta p$, where n_0 and p_0 are the charge carrier concentrations at thermodynamic equilibrium and Δn and Δp are the excess charge carrier concentrations. μ_I and μ_{ccs} are combined with the lattice mobility μ_L to calculate μ using

$$\mu = \mu_L \left[\frac{1.025}{1 + (X_\mu/1.68)^{1.43}} - 0.025 \right], \tag{2.29}$$

with

$$X_\mu = \sqrt{\left(\frac{6\mu_L(\mu_I + \mu_{ccs})}{\mu_I \mu_{ccs}} \right)}. \tag{2.30}$$

Using equations 2.26-2.30 and the parameters listed in table 2.4 the mobility of charge carriers in silicon can be calculated for different temperatures and doping concentrations. Figure 2.12 shows the mobility of majority and minority carriers as a function of the temperature in n-type and p-type silicon doped at different concentrations. Furthermore the resistivity of the material is shown. Both, an increase in temperature, as well as an increase in dopant concentration reduce the charge carrier mobility in silicon. Yet, the mobility is more sensitive to changes in temperature than it is to changes in the concentration of ionized dopants. Nevertheless, the characteristic of the resistivity as a function of temperature is strongly influenced by the doping concentration. As long as the majority carrier concentration is higher than n_i, the resistivity is smaller than the intrinsic resistivity and increases with temperature. As the semiconductor enters the intrinsic regime, the resistivity shows a decrease with temperature.

In figure 2.13 the mobility of charge carriers in n- and p-type silicon and the resistivity of the material are plotted as a function of the dopant concentration at different temperatures.

Table 2.4: Parameters used for the calculation of the mobility of charge carriers in silicon from reference [15].

Parameter	electrons	holes	unit
$\mu_L(300\,\mathrm{K})$	1430	495	$\mathrm{cm}^2(\mathrm{Vs})^{-1}$
α_μ	2.20	2.20	
A_{μ_I}	4.61×10^{17}	1.00×10^{17}	$(\mathrm{cmVs})^{-1}\mathrm{K}^{-\frac{3}{2}}$
B_{μ_I}	1.52×10^{15}	6.25×10^{14}	$\mathrm{cm}^{-3}\mathrm{K}^{-2}$
$A_{\mu_{ccs}}$	2×10^{17}		$(\mathrm{cmVs})^{-1}\mathrm{K}^{-\frac{3}{2}}$
$B_{\mu_{ccs}}$	8.28×10^{8}		$\mathrm{cm}^{-3}\mathrm{K}^{-2}$

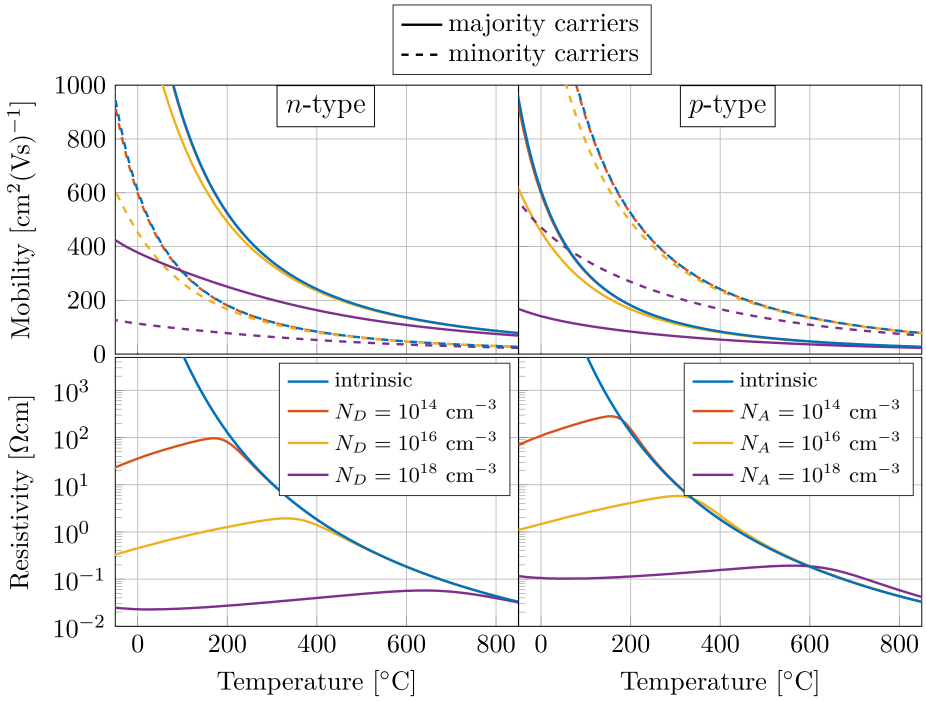

Figure 2.12: Majority and minority carrier mobility and resistivity as a function of temperature in n- and p-type silicon doped at different concentrations.

The plot shows that the mobilitiy of both, majority and minority carriers is constant at low doping concentrations and decreases at higher dopant concentration. The critical concentration at which the decrease of the mobility begins is shifted towards higher values as the temperature is increased. While in the extrinsic regime the resistivity decreases with increasing dopant concentration, it is constant in the intrinsic regime.

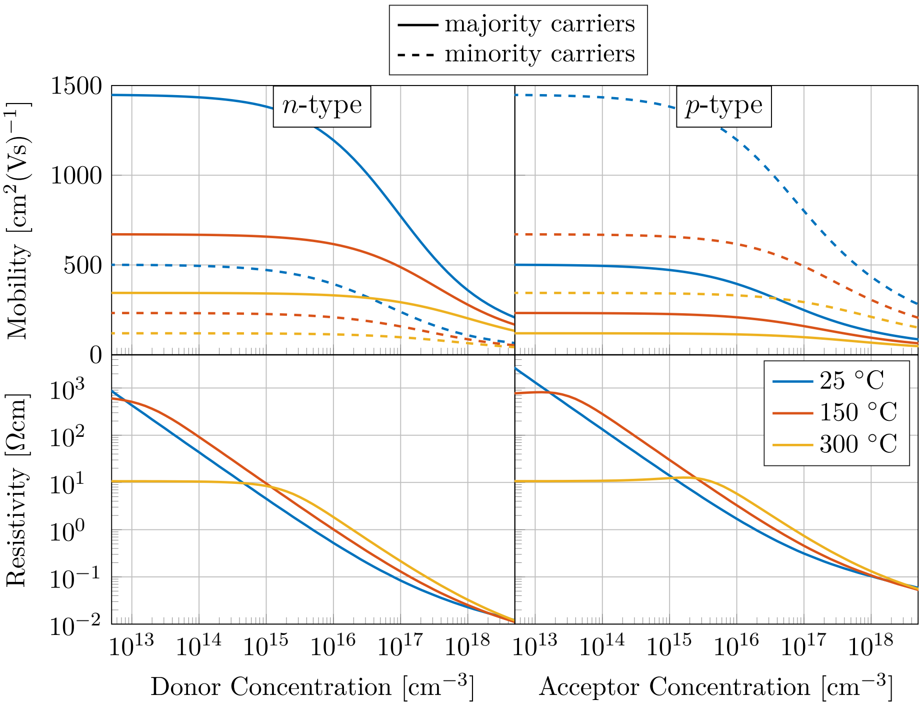

Figure 2.13: Majority and minority carrier mobility and resistivity as a function of dopant concentration in n- and p-type silicon at different temperatures.

2.1.6 Diffusion of Free Charge Carriers

By shining light on a semiconductor or by irradiating a semiconductor with electrons or ions, excess charge carriers can be generated. The change of the charge carrier concentration over time depends on the generation rate G_{cc} and recombination rate R_{cc} of electron-hole pairs:

$$\frac{\delta n_{\text{cc}}}{\delta t} = G_{\text{cc}} - R_{\text{cc}}. \tag{2.31}$$

In thermal equilibrium the generation and the recombination are the same. Hence, $\frac{\delta n_{\text{cc}}}{\delta t}$ is zero and the concentration of electrons is n_0 and the concentration of holes is p_0. Local differences in the charge carrier concentration cause a movement of the charge carriers away from regions of higher concentration to regions of lower concentration. This migration along a concentration gradient is the diffusion current j_{diff}

$$j_{\text{diff}} = j_n + j_p = eD_n\nabla n - eD_p\nabla p, \tag{2.32}$$

where j_n and j_p are the diffusion currents of electrons and holes and D_n and D_p are the diffusion constants of electrons and holes. The diffusion constant D_{cc} of a charge carrier is related to its mobility μ_{cc} as described by the Einstein relation

$$D_{\mathrm{cc}} = \frac{k_B T}{e} \cdot \mu_{\mathrm{cc}}. \tag{2.33}$$

Hence, the diffusion constant shows the same dependence to doping as shown for the mobility in figures 2.11, 2.13 and 2.12.

2.1.7 Charge Carrier Recombination

If there is an excess concentration of eh-pairs, there are different recombination paths for the generated charge carriers. One way for charge carriers to recombine is via direct band to band recombination. This process is associated with the emission of a photon. As the crystal momentum has to be conserved, this process is more probable in direct semiconductors, where the top of the valence band and the bottom of the conduction band are at the same wave-vector. In an indirect semiconductor, this process works by absorbing or emitting a phonon to account for the change in momentum, and hence, happens less frequently. The rate of direct band to band recombination R_{direct} is

$$R_{\mathrm{direct}} = \frac{np - n_0 p_0}{\tau_{\mathrm{direct}}} = \frac{n_0 \Delta p + p_0 \Delta n + \Delta n \Delta p}{\tau_{\mathrm{direct}}}, \tag{2.34}$$

where τ_{direct} is the recombination time constant for the direct recombination, n and p are the electron and hole concentrations, n_0 and p_0 are the equilibrium electron and hole concentrations and Δn and Δp are the excessive concentrations of electrons and holes ($\Delta n = n - n_0, \Delta p = p - p_0$). When the concentration of electrons is far higher than the concentration of holes ($n_0 >> p_0$) and Δn is far smaller than n_0, as it is the case in an n-type semiconductor and low generation, R_{direct} can be simplified to

$$R_{\mathrm{direct}} = \frac{(n_0 + \Delta n)\Delta p}{\tau_{\mathrm{direct}}} = \frac{n_0 \Delta p}{\tau_{\mathrm{direct}}} = \frac{\Delta p}{\tau_{h,\mathrm{direct}}}, \tag{2.35}$$

where $\tau_{h,\mathrm{direct}}$ is the minority carrier lifetime (in this case holes) associated with the direct band to band recombination. Another recombination path, which is the dominant recombination path in indirect semiconductors, such as silicon, is the recombination at traps or recombination centers. These recombination centers are defects with energy levels close to the center of the band gap. The rate of the so-called Shockley-Read-Hall [20] recombination R_{SRH} is

$$R_{\mathrm{SRH}} = \frac{np - {n_i}^2}{\tau_{\mathrm{SRH},p}(T)(n + n_{\mathrm{SRH}}(T)) + \tau_{\mathrm{SRH},n}(T)(p + p_{\mathrm{SRH}}(T))}. \tag{2.36}$$

Here, n_{SRH} and p_{SRH} are the concentration of charge carriers occupying states between the energy state of the recombination centers E_T and the band edges

$$\begin{aligned} n_{\mathrm{SRH}}(T) &= N_C(T) \exp\left(\frac{E_T - E_C}{k_B T}\right) \\ p_{\mathrm{SRH}}(T) &= N_V(T) \exp\left(\frac{E_V - E_T}{k_B T}\right). \end{aligned} \tag{2.37}$$

R_{SRH} increases the closer E_T is to the center of the band gap. $\tau_{\mathrm{SRH},p}$ and $\tau_{\mathrm{SRH},n}$ are the recombination lifetimes of electrons and holes, associated with the trap concentration N_T and the capture cross sections $\sigma_{T,n}$ for electrons and $\sigma_{T,p}$ for holes.

$$\begin{aligned} \tau_{\mathrm{SRH},n}(T) &= \frac{1}{\sigma_{T,n} N_T v_{th,n}(T)} \\ \tau_{\mathrm{SRH},p}(T) &= \frac{1}{\sigma_{T,p} N_T v_{th,p}(T)} \end{aligned} \tag{2.38}$$

The recombination lifetime of charge carriers depends on the thermal velocity v_{th}

$$v_{th} = \sqrt{\frac{3k_B T}{m^*}}. \tag{2.39}$$

The recombination process of charge carriers at surfaces and interfaces is also described by the Shockley-Read-Hall process [21]. The contribution of the surface to the overall recombination is described by an additional surface recombination velocity s_0, which decays with the distance d_s from the surface. The charge carrier lifetimes, $\tau_{\mathrm{sur},n}$ for electrons and $\tau_{\mathrm{sur},p}$ for holes, at the surface are then

$$\begin{aligned} \tau_{\mathrm{sur},n}(T, d_s) &= \frac{1}{\sigma_{T,n} N_T v_{th,n}(T) + s_n/d_s} \\ \tau_{\mathrm{sur},p}(T, d_s) &= \frac{1}{\sigma_{T,p} N_T v_{th,p}(T) + s_p/d_s}. \end{aligned} \tag{2.40}$$

The third recombination path of charge carriers in semiconductors is the Auger recombination. In this process, the recombination energy is used to excite another electron in the conduction band. This excited electron then dissipates its energy to the lattice by generating heat. An Auger-process always includes three charge carriers hence, the recombination rate R_{Auger} shows a cubic dependence on the charge carrier concentration

$$R_{\mathrm{Auger}} = (c_{\mathrm{Au},n} n + c_{\mathrm{Au},p} p) \cdot (np - {n_i}^2), \tag{2.41}$$

where $c_{\mathrm{Au},n}$ and $c_{\mathrm{Au},p}$ are the Auger capture coefficients. The charge carrier lifetime τ_{Au} associated with this process is

$$\tau_{\mathrm{Au}} = \frac{n - n_0}{R_{\mathrm{Auger}}}. \tag{2.42}$$

The effective lifetime τ_{eff} of charge carriers in a semiconductor depends on all recombination processes. τ_{eff} is described by Matthiessen's rule

$$\frac{1}{\tau_{\text{eff}}} = \frac{1}{\tau_{\text{direct}}} + \frac{1}{\tau_{\text{SRH}}} + \frac{1}{\tau_{\text{sur}}} + \frac{1}{\tau_{\text{Au}}}. \tag{2.43}$$

When eh-pairs are generated at moderate concentrations ($\Delta n + \Delta p < n_0 + p_0$), the change in the concentration is higher for minority carriers than it is for majority carriers. Hence, the minority carrier lifetime is much smaller than the lifetime of majority carriers. When charge carriers are generated, minority carriers diffuse away from the generation point until they recombine. The average distance between the points of generation and recombination is the minority carrier diffusion length $L_{D,\text{cc}}$

$$L_{D,\text{cc}} = \sqrt{D_{\text{cc}}\tau_{\text{eff}}}. \tag{2.44}$$

In a crystalline semiconductor this length can vary from a few µm to several hundred µm.

2.1.8 *pn*-Junction

When two adjacent regions of a semiconductor show different majority doping, a *pn*-junction is formed. Figure 2.14 displays a *pn*-junction and shows the distributions of the charge Q, the electric field $\vec{E}$ and the potential V across this structure. Furthermore the conduction and valence band energies, relative to the Fermi energy along a *pn*-junction are illustrated.

Due to their concentration gradient, electrons diffuse from the n-type region into the p-type region, where they recombine with holes. At the same time holes diffuse into the other direction and recombine with electrons in the n-type material. The diffusing charge carriers leave back ionized donors and acceptors forming a space charged region. To conserve charge neutrality, the charge concentration in the space charge region on both sides of the *pn*-junction has to be the same

$$N_a x_p = N_d x_n. \tag{2.45}$$

Here, N_a and N_d are the acceptor and donor concentrations and x_p and x_n are the widths, describing how far the space charge region extends into the p-type and n-type region. Due to the depleted dopants in the space charge region, an electric field is formed, pointing from the n-side to the p-side of the junction. This field pushes holes back into the p-type region and electrons into the n-type region. At an abrupt *pn*-junction, the electric field $\vec{E}$ has a triangular shape. While $\vec{E}$ is zero at a distance of x_n and x_p from the junction, the maximum electric field E_{max} is directly at the junction. Its absolute value is

$$|E_{\text{max}}| = -\frac{eN_a x_p}{\epsilon} = \frac{eN_d x_n}{\epsilon}, \tag{2.46}$$

where e is the elementary charge, ϵ is the dielectric constant, which is the product of the vacuum permittivity ϵ_0 and the material specific relative permittivity ϵ_r.

As there is an electric field across the *pn*-junction, there is also a potential difference between the p-type and the n-type region. Without any external bias voltage, the difference between the potentials on both sides of the junction V_p and V_n is the built-in potential

V_{bi}.

$$V_{bi} = V_n - V_p = \frac{eN_d}{2\epsilon}{x_n}^2 + \frac{eN_a}{2\epsilon}{x_p}^2. \tag{2.47}$$

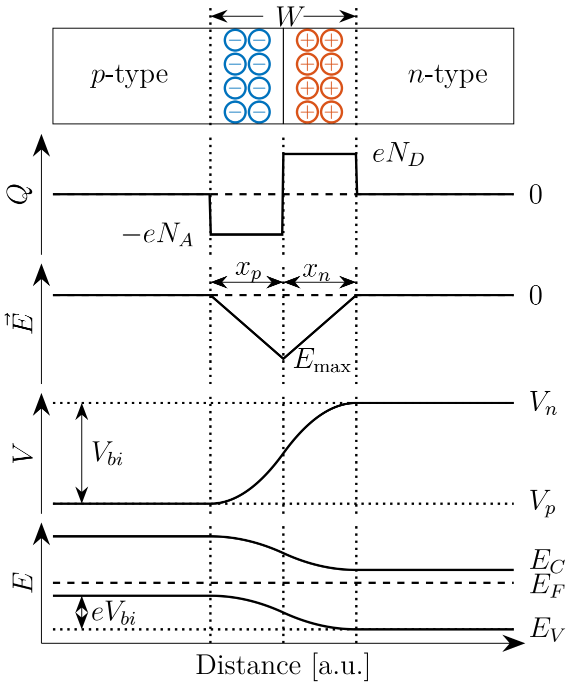

Figure 2.14: Schematic representation of a pn-junction including the distribution of charges Q, the electric field $\vec{E}$, the potential V and the band diagram as a function of the distance from the junction. Important parameters such as the widths x_p, x_n and W, the charges $-eN_a$ and eN_d, the maximum electric field $E_{\max}$ and the built-in potential V_{bi} are indicated.

The Fermi energy is constant throughout the material. As E_F is close to the valence band in p-type material and close to the conduction band in n-type material (see section 2.1.4), the valence band and the conduction band have to bend at the pn-junction. The difference of the valence and conduction band energies on both sides of the pn-junction corresponds to eV_{bi}.

Taking into account, that the width W of the space charge region is the sum of x_p and x_n, V_{bi} can be expressed as

$$V_{bi} = \frac{eN_dN_a}{2\epsilon\,(N_d + N_a)}W^2. \tag{2.48}$$

The depletion width of W at a pn-junction is then

$$W = \sqrt{\frac{2\epsilon\,(N_d + N_a)\,(V_{bi} - V_b)}{eN_dN_a}}, \tag{2.49}$$

where V_b stands for an additional external bias voltage. If there is a positive bias voltage, the depletion width is decreased and a current flows across the pn-junction. If V_b is negative, the *pn*-junction blocks current from flowing and at the same time the depletion width is increased. The current over a *pn*-junction is limited by carrier diffusion to the junction and is

$$I_{pn} = eA\left(\frac{p_{n0}D_p}{L_{D,p}} + \frac{n_{p0}D_n}{L_{D,n}}\right)\left[\exp\left(\frac{e(V_b - V_{bi})}{k_BT}\right) - 1\right] = I_{S,pn}\left[\exp\left(\frac{e(V_b - V_{bi})}{k_BT}\right) - 1\right], \tag{2.50}$$

where $I_{S,pn}$ is the saturation, or reverse bias current. $I_{S,pn}$ depends on the area of the junction A, the minority carrier concentrations of holes in n-type material (p_{n0}) and electrons in p-type material (n_{p0}), as well as on their diffusion properties. D_p and D_n are the diffusion constants of holes and electrons and $L_{D,p}$ and $L_{D,n}$ are the diffusion lengths of the charge carriers (see equation 2.44).

2.1.9 Schottky-Junction

A Schottky-junction is formed, when a semiconductor is brought in contact with a metal. In theory the Fermi energies of the materials align and the conduction and valence bands in the semiconductor bend in the region close to the junction, depending on the difference in work-function of the both materials. The current across a Schottky-junction is

$$I_{\text{Schottky}} = I_{S,\text{Schottky}}\left[\exp\left(\frac{e(V_b - V_{bi})}{k_BT}\right) - 1\right]. \tag{2.51}$$

The built-in potential V_{bi} at a Schottky junction is similar to V_{bi} at a one-sided *pn*-junction (when e.g. $N_d >> N_a$ in equation 2.48). For an n-type semiconductor V_{bi} is

$$V_{bi} = \frac{eN_d}{2\epsilon}W^2. \tag{2.52}$$

The saturation current $I_{S,\text{Schottky}}$ of a Schottky-junction is dominated by thermionic emission, which is strongly temperature dependent.

$$I_{S,\text{Schottky}} = R^*AT^2\exp\left(-\frac{e\phi_b}{k_BT}\right). \tag{2.53}$$

Here, R^* is the Richardson constant, A is the area of the junction and $e\phi_b$ is the barrier height of the Schottky-junction. The interface between a metal and a semiconductor is not perfect but contains a high concentration of interface defects. In silicon, these defects form energy states close to the center of the band gap E_I [22–24]. The barrier height $e\phi_b$ of the Schottky junction depends on the interface states E_I and the energy gap E_G of the semiconducting material:

$$e\phi_b = E_G - E_I. \tag{2.54}$$

Table 2.5 lists barrier heights at the interfaces between silicon and different metals.

Figure 2.15 illustrates a Schottky junction between a metal and an n-type semiconductor including the distribution of charge, electric field and potential across the junction.

Similar to a *pn*-junction, also at a Schottky-junction a space charge region is formed. In contrast to the situation at a *pn*-junction, the depleted region extends only into the semiconducting material while at the interface a very thin region containing the counter

Table 2.5: Energy states $e\phi_b$ at the interface between different metals and silicon in [eV].

Metal	n-type silicon	p-type silicon	Reference
Au	0.8	0.25	[23]
Al	0.68	0.48	[23]
Ag	0.67	0.47	[23]
Cu	0.61	0.50	[23]
Sn	0.58	0.57	[23]
W	0.66	0.55	[24]

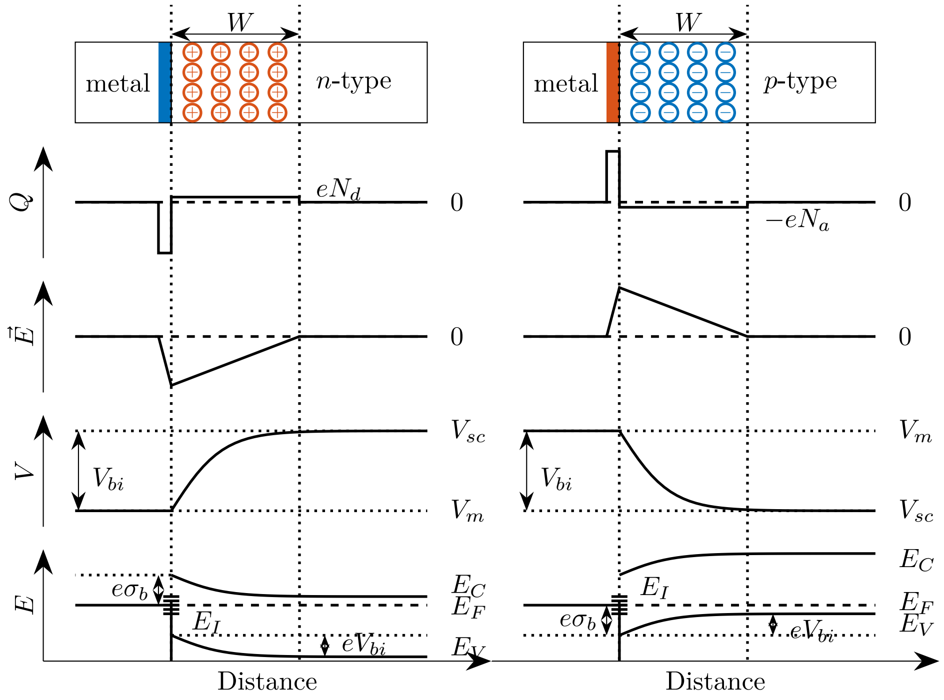

Figure 2.15: Schematic representation of a Schottky-junction between a metal and an n- and p-type semiconductor, including the distribution of charges Q, the electric field $\vec{E}$, the potential V and the band diagram as a function of the distance from the junction. Important parameters such as the widths x_p, x_n and W, the charges $-eN_a$ and eN_d, the maximum electric field $E_{\max}$, the built-in potential V_{bi} the Schottky barrier height ϕ_b and the energy states at the interface E_I are indicated.

charge is formed. As the Fermi energy is pinned to the center of the band gap, the direction of the electric field at a Schottky junction is solely dependent on the position of the Fermi energy in the semiconductor. In an n-type semiconductor E_F is above the mid-gap energy, hence the energy bands bend up and an electric field pointing from the metal to the semiconductor is established. If the semiconducting material is p-type, the bands band down and the electric field points from the metal to the semiconductor.

Electronic devices have the need of electrical contacting. To avoid large contact resistances, ohmic contacts are desired. To produce an ohmic contact between a metal and a semiconductor the semiconductor is highly doped at the surface. If the doping concentration is higher than $10^{18}\,\mathrm{cm}^{-3}$, the space charge region at the junction becomes small enough for charge carriers to tunnel through it, establishing a low resistance path for the current.

2.2 Properties of Defects in Crystalline Silicon

The vast majority of semiconducting devices are made of silicon [4]. The following section provides an overview of the production methods of silicon and on the properties of defects, intentionally and unintentionally introduced into the material, in regard of their charge states, diffusion and reactions. If the reader is interested in more detailed information about defects in silicon, Peter Pichler's compressive book "Intrinsic point defects, impurities and their diffusion in silicon" [5] is recommended.

2.2.1 Production Cycle

Even though silicon is the second most abundant element on the Earth's crust (after oxygen), the production of semiconductor grade material is a complex and expensive process. The purity of semiconductor grade silicon has to be higher than 99.9999999 %, or 9N. In figure 2.16 the production cycle of mono-crystalline semiconductor-grade silicon is illustrated. A more detailed description of the processes can be found in references 2 and 4.

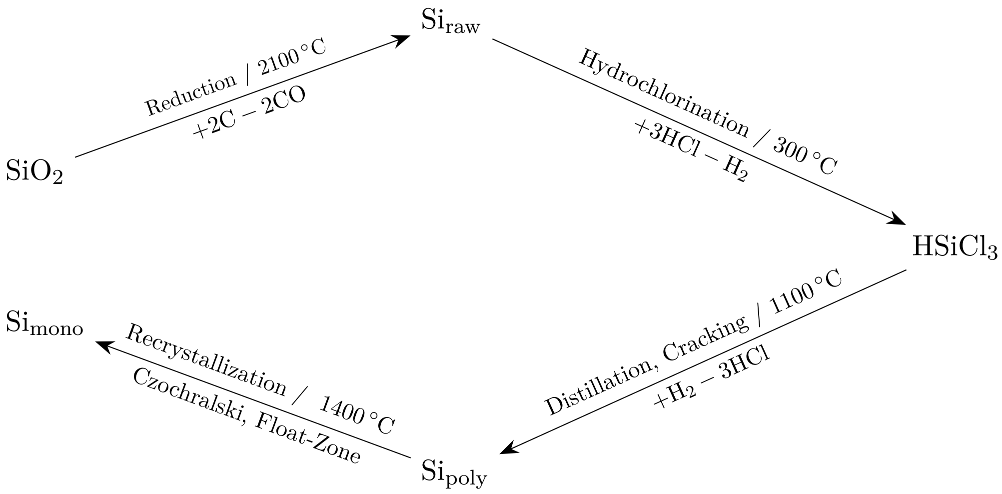

Figure 2.16: Production cycle of semiconductor-grade silicon.

In the first step of this production cycle, quartz is reduced to raw, poly-crystalline silicon in an electric arc furnace.

$$SiO_2 + 2\,C \xrightarrow{2100\,°C} Si_{raw} + 2\,CO \tag{2.55}$$

This raw silicon Si_{raw} has a purity of about 98 %. To achieve further purification, the raw silicon is transferred into a volatile form by hydrochlorination.

$$Si_{raw} + 3\,HCl \xrightarrow{300\,°C} HSiCl_3{}^{+}H_2 \tag{2.56}$$

As Trichlorosilane $HSiCl_3$ has a boiling temperature of 31.8 °C the further purification can be done in the gas phase. In a fractional distillation process impurities such as phosphorus trichloride (PCl_3) and boron trichloride (BCl_3), which condense at higher temperatures than $HSiCl_3$, are removed. After the distillation the trichlorosilane is transferred back to crystalline silicon in a process called cracking at 1100 °C.

$$HSiCl_3{+}H_2 \xrightarrow{1100\,^\circ C} Si_{poly} + 3\,HCl \tag{2.57}$$

The product of the cracking process is poly-crystalline silicon (Si_{poly}). Most silicon devices, except for solar cells require mono-crystalline silicon (Si_{mono}). Hence, re-crystallization is necessary. This is the crucial step in the production cycle of semiconductor-grade silicon as it defines the final impurity concentrations in the material. There are two major re-crystallization techniques which are used to produce high quantities of high quality semiconductor-grade silicon, the Czochralski-process and the float-zone method. A very good review explaining both techniques in detail can be found in reference 25.

2.2.1.1 Czochralski-Process

The Czochralski (Cz) process was developed in 1918 by Jan Czochralski [26]. In this technique, silicon is melted in a quartz crucible. This melt is brought in contact with a seed crystal. The seed crystal is slowly pulled upwards while growing layer by layer. During this process, both the crystal and the crucible are rotated. Using the Cz-process, silicon ingots with a diameter of more than 300 mm and several meters in length can be produced. Dopants, such as boron or phosphorus can be directly added to the silicon melt and are then incorporated into the growing crystal. When compared to other crystallization processes, the Cz-process is cheap and fast but a big drawback of the method is the unintentional introduction of impurities from the crucible through the silicon melt into the silicon single crystal. The concentrations of oxygen and carbon can be as high as $10^{18}\,\mathrm{cm}^{-3}$. The Cz-method has been improved by applying a vertical magnetic field (m:Cz) during the crystal growth. This field reduces thermal convections in the melt which results in a decrease of the gradients in the impurity concentration [27].

2.2.1.2 Float-Zone Method

An alternative to the Czochralski-process for growing single-crystalline silicon is the float-zone (FZ) method. In this method a poly-crystalline silicon ingot is re-crystallized using vertical zone melting. The re-crystallization takes place at the interface of the ingot and a seed crystal. Radio-frequency (RF) coils are used to melt a thin layer of the poly-crystalline material, which then re-crystallizes on the seed crystal. By moving the RF-coil from top to bottom, the whole poly-crystalline ingot is recrystallized. The surface tension of the silicon melt is high enough to enable the production of silicon ingots with a diameter up to 200 mm. The impurity concentration in the material is strongly reduced, as impurities are better soluble in the silicon melt than in the crystal. If the process is repeated several times, impurity concentrations of less than $5{\times}10^{10}\,\mathrm{cm}^{-3}$ can be achieved [4]. Dopants can be added during the process as gaseous substances such as PH_3 (Phosphine) or B_2H_6 (diborane). The most popular method for doping FZ-silicon is neutron-transmutation doping [28]. In this method, silicon ingots grown using the float-zone method are placed close to a nuclear reactor where they are bombarded with neutrons. Silicon is found in three stable isotopes ${}^{28}_{14}Si$ (~92 %), ${}^{30}_{14}Si$ (~5 %) and ${}^{30}_{14}Si$ (~3 %). The neutrons only affect the isotope $^{30}_{14}$Si, which is first transmuted to the unstable $^{31}_{14}$Si

$$^{30}_{14}\mathrm{Si} + \mathrm{n} \longrightarrow {}^{31}_{14}\mathrm{Si} + \gamma, \tag{2.58}$$

under the release of a γ-particle. $^{31}_{14}$Si has a half life of 2.6 h before it decays to $^{31}_{15}$P

$$^{31}_{14}\mathrm{Si} \xrightarrow{2.6\,\mathrm{h}} {}^{31}_{15}\mathrm{P} + \beta^-, \tag{2.59}$$

releasing a high energy electron (β^-). Using neutron-transmutation doping, very uniform doping concentrations can be obtained [29].

2.2.2 Defects in Crystals

According to Nernst's theorem, a perfect, defect-free crystal can only exist at 0 K. Hence, at finite temperature it is the nature of crystalline materials to contain defects as it lowers the total free energy of the system. These defects are classified into different groups. While intrinsic defects involve only defects which are inherent to the crystal, other chemical impurities are considered as extrinsic defects. Another classification is the geometry of defects.

The simplest form of defects are "point-defects". Figure 2.17 gives an overview of different kinds of point defects. If an atom is removed from a lattice position which is usually occupied, a vacancy V is generated (see figure 2.17a). When a lattice atom is located at a position in-between the usual lattice sites, it is called a "self-interstitial" I (figure 2.17b). Often self-interstitials and vacancies are generated at the same time, when a lattice atom is removed from its initial position in the lattice and shifted to an interstitial site. This process is also known as Frenkel pair generation. Impurity atoms X can reside on interstitial X_i or substitutional lattice sites X_s (figure 2.17c and d).

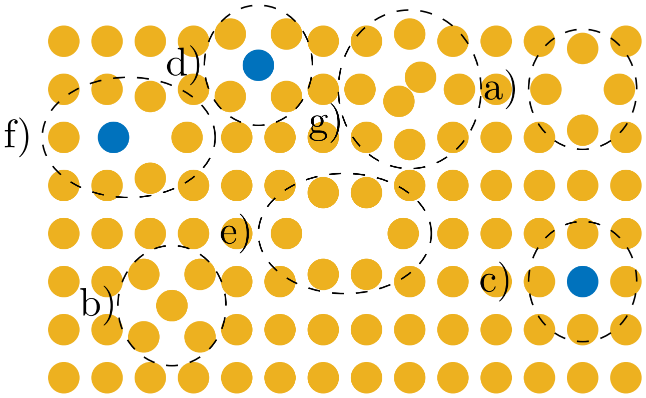

Figure 2.17: Schematic representation of different kinds of of point defects in a crystal adopted from reference [5]: a) vacancy, b) self-interstitial, c) substitutional impurity, d) interstitial impurity, e) di-vacancy, f) vacancy-impurity complex, g) split-self-interstitial (interstitialcy).

Some point-defects can migrate through the lattice and react with other defects, forming complexes (see section 2.2.3). Intrinsic defect complexes, as the divacancy V_2 (figure 2.17e) are clusters of either vacancies or interstitials. Extrinsic defect complexes, on the other hand, can consist of all kinds of different point defects. An example for an extrinsic defect complex is a vacancy-impurity complex VX_s of a vacancy and a substitutional impurity (figure 2.17f). Another geometrical configuration of a self-interstitial is the split-state, also called the interstitialcy (figure 2.17g). Here, two atoms “share” a substitutional lattice site. One of these wo atoms can also be an impurity atom. As more and more point-defects react, extended defect complexes are formed. Such defects can be one-dimensional "line-defects" such as screw- or edge dislocations, two-dimensional defects such as grain-boundaries and three-dimensional defects which include clusters and voids. The point defects forming these extended defects do not necessarily share chemical bonds. Often the total energy of the system is the lowest, if the point-defects are not in immediate vicinity but rather reside at a constant distance from each other at defined lattice sites [30–32].

2.2.3 Diffusion of Point Defects

Defects can move in a crystal such as solvents do in a solution. In the following subsection this movement, called diffusion is explained. More detailed information about the diffusion of defects can be found in references [5] and [33]. Defects occupy those lattice sites in a crystal which lead to a minimization of the system’s total energy. To move from one local minimum X^0 to another, the defects must pass through an activated state X^*. The energy difference between the ground state and the activated state is the activation energy $E_{A,X}$ of the migration process. The energy minima X^0 and the activation energy are different for every excited state of every charge state of a defect. The energy state of an excited state of a charge state of a defect is illustrated in figure 2.18 as a function of the lattice vector.

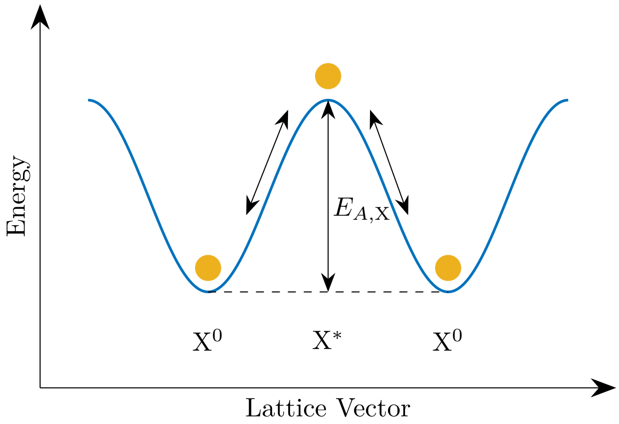

Figure 2.18: Energy states of an impurity as a function of the lattice vector. X^0 is the ground state and X^* is the activated state of the impurity X. The energy difference between the two states is the activation energy $E_{A,X}$.

From an atomic perspective the motion of point-defects in a crystal is not directed. If there is a difference in the defect concentration c_X, though, more atoms will migrate from regions of high concentration to regions of low concentration than vice versa. This results in a particle flux J_X which is described by Fick's first law of diffusion as

$$J_\mathrm{X} = -D_\mathrm{X} \nabla c_\mathrm{X}, \tag{2.60}$$

where D_X is the diffusion constant of the impurity X. The change of the impurity concentration over time is described by Fick's second law

$$\frac{\delta c_\mathrm{X}}{\delta t} = D_\mathrm{X} \nabla^2 c_\mathrm{X}. \tag{2.61}$$

The diffusion constant increases with temperature, as described by Arrhenius' law

$$D = D_0 \exp\left(-\frac{E_A}{k_B T}\right). \tag{2.62}$$

Here, E_A is the activation energy, which is needed, to overcome the energy barrier between two lattice sites, as illustrated in figure 2.18. D_0 is the diffusion pre-factor. The Arrhenius parameters are individual for each excited state of each charge state of each defect. Combining the contributions of the different charge states of one defect results in an effective diffusivity of the defect (see section 2.2.5).

In the random walk model the diffusion constant is calculated from the jump-rate Γ_i and jump-distance δl_i of different types i of jumps of an impurity in the crystal [34]

$$D = \frac{1}{6} \sum_i \Gamma_i {\delta l_i}^2. \tag{2.63}$$

The jump-rate Γ_i can be expressed as a function of the change in the Gibbs free energy between the ground state and the activated state

$$\Delta G = \Delta H + T \Delta S. \tag{2.64}$$

Here, ΔH is the change in enthalpy and ΔS is the change in entropy. Γ_i is then

$$\Gamma_i = f_v \exp\left(-\frac{\Delta G}{k_B T}\right) = f_v \exp\left(\frac{\Delta S}{k_B}\right) \exp\left(-\frac{\Delta H}{k_B T}\right), \tag{2.65}$$

where f_v is the vibrational frequency of an impurity at its lattice site. The jump-distance δl_i can be expressed as

$$\frac{1}{6} \sum_i {\delta l_i}^2 = \gamma_{D_0} {a_L}^2, \tag{2.66}$$

where γ_{D_0} is a geometrical factor which is mostly 1 and a_L is the lattice constant. By inserting equations 2.65 and 2.66 equation 2.63 becomes

$$D = \gamma_{D_0} {a_L}^2 f_v \exp\left(\frac{\Delta S}{k_B}\right) \exp\left(-\frac{\Delta H}{k_B T}\right). \tag{2.67}$$

Following Zener [34], who assumes ΔH to be the same as E_A, the equations 2.62 and 2.67

are combined and the pre-factor D_0 can be expressed as

$$D_0 = \gamma_{D_0} {a_L}^2 f_v \exp\left(\frac{\Delta S}{k_B}\right). \tag{2.68}$$

When an impurity is introduced into a crystal from the gas phase, the concentration of the impurity at the surface c_{X_0} depends on the solubility of impurity X in the crystal and on the partial pressure of X in the gas phase. While the number of impurity atoms in the crystal increases over time, c_{X_0} is constant and can be seen as a constant source. In this case, the solution to equation 2.61 is

$$c_{\mathrm{X}}(t) = c_{\mathrm{X}_0} \mathrm{erfc}\left(\frac{x}{\sqrt{4 D_{\mathrm{X}} t}}\right), \tag{2.69}$$

where erfc(x) stands for the complementary error function

$$\mathrm{erfc}(x) = \frac{2}{\sqrt{\pi}} \int_x^\infty \exp(-\xi^2) d\xi. \tag{2.70}$$

When the impurity distribution at $t = 0$ is approximated by a δ-function at the depth $(x = x_0)$, the impurity concentration over time is

$$c_{\mathrm{X}}(t) = \frac{N_{\mathrm{X}}}{\sqrt{4\pi D_{\mathrm{X}} t}} \exp\left(-\frac{(x - x_0)^2}{4 D_{\mathrm{X}} t}\right), \tag{2.71}$$

where N_{X} is the implanted dose of X. In this case the source of impurities is limited, as the total number of impurities in the crystal stays constant. Neglecting the effusion of the impurity at the surfaces of the material, its distribution after ion-implantation can be approximated by a sum of delta distributions and the resulting defect concentration over time is then

$$c_{\mathrm{X}}(t) = \sum_i \frac{N_{\mathrm{X},i}}{\sqrt{4\pi D_{\mathrm{X}} t}} \exp\left(-\frac{(x - x_{0,i})^2}{4 D_{\mathrm{X}} t}\right). \tag{2.72}$$

Here, $x_{0,i}$ is the depth of the i^{th} delta-function and $N_{\mathrm{X},i}$ is the number of defects.

The progress of the diffusion process can be described using the diffusion length $L_{D_{\mathrm{X}}}$ of the impurity which is

$$L_{D_{\mathrm{X}}}(t) = \sqrt{4 D_{\mathrm{X}} t}. \tag{2.73}$$

Figure 2.19 shows the depth profiles of the impurity for different values of $L_{D_{\mathrm{X}}}$ when it diffuses from a constant source. The concentration c_{X} is scaled to the impurity concentration at the surface c_{X_0}. In figure 2.20 the impurity diffusion from a limited source is plotted for different diffusion lengths $L_{D_{\mathrm{X}}}$. The implantation depth x_0 is 2 µm and the concentration c_{X} is scaled to the implantation dose N_{X}.

The discussion of the evolution of the impurity concentration profiles presented here is valid if the reactions between the impurities (see section 2.2.7) are neglected. This is often the case for donors and acceptors in semiconductors. If other kinds of defects are present in the material, the defect diffusivity might be changed, as the diffusing defects might be slowed down by reactions with other defects, or accelerated by forming fast diffusing defect complexes.

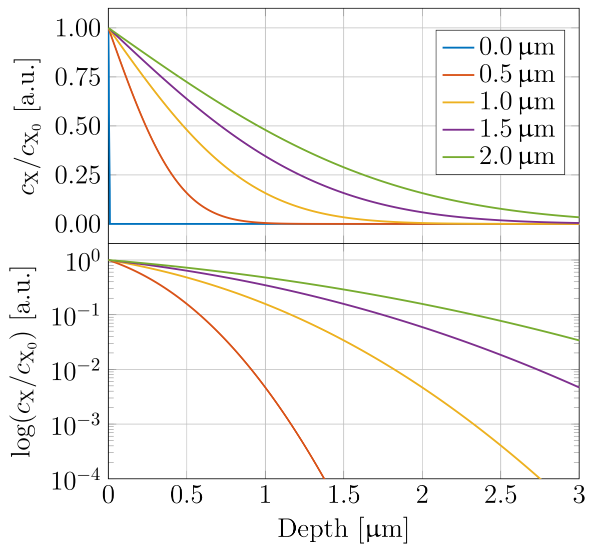

Figure 2.19: Constant source diffusion profiles of impurity X for different L_{D_X}.

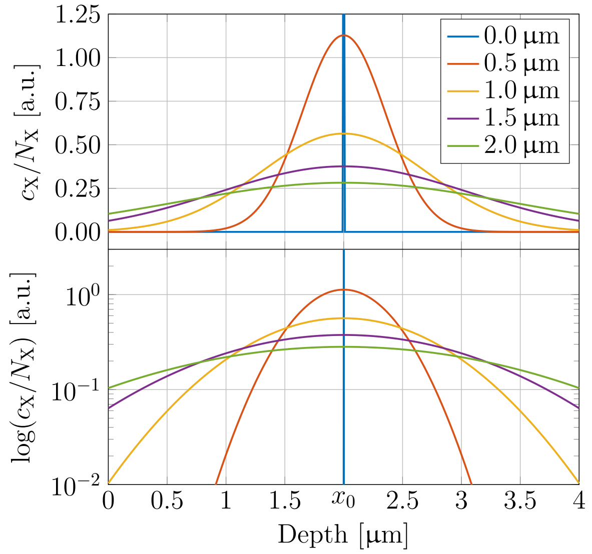

Figure 2.20: Limited source diffusion profiles of impurity X for different L_{D_X}.

2.2.4 Charge States of Point Defects

A defect X can be present at different energy states E_X in a crystal. If charge carriers are captured or released, the ionization state q of the defect is changed. Furthermore, each ionization, or charge state E_{X^q} has a spectrum of excited states $E_{\mathrm{X}_j^q}$. The spectrum of excited states can be measured using photoabsorption spectroscopy (PAS) [35] or photothermal ionization spectroscopy (PTIS) [36]. As described by Landsberg in reference [37], the probability $P_{\mathrm{X}_j^q}$ that a certain energy state $E_{\mathrm{X}_j^q}$ is populated, in a simplified form, is

$$P_{\mathrm{X}_j^q} = \frac{1}{Z_\mathrm{gr}} \exp\left(-\frac{qE_F}{k_BT}\right) \exp\left(-\frac{E_{\mathrm{X}_j^q}}{k_BT}\right). \tag{2.74}$$

Here, Z_gr is the grand canonical partition function which is the sum over all charge states and excited states of a defect

$$Z_\mathrm{gr} = \sum_q \exp\left(-\frac{qE_F}{k_BT}\right) \sum_j \exp\left(-\frac{E_{\mathrm{X}_j^q}}{k_BT}\right) \tag{2.75}$$

By summing over all excited states one can further calculate the probability P_{X^q}, that a certain charge state of a defect P_{X^q} is populated

$$P_{\mathrm{X}^q} = \frac{1}{Z_\mathrm{gr}} \exp\left(-\frac{qE_F}{k_BT}\right) \sum_j \exp\left(-\frac{E_{\mathrm{X}_j^q}}{k_BT}\right). \tag{2.76}$$

In a lot of cases it is sufficient to know the ground state energies $E_{\mathrm{X}_0^q}$ of the charge states to calculate the occupation probability

$$P_{\mathrm{X}^q} = \frac{1}{Z_\mathrm{gr}} \exp\left(-\frac{qE_F}{k_BT}\right) \exp\left(-\frac{E_{\mathrm{X}_0^q}}{k_BT}\right) = \frac{1}{Z_\mathrm{gr}} \exp\left(-\frac{E_\mathrm{form}^{\mathrm{X}^q}}{k_BT}\right), \tag{2.77}$$

where $E_\mathrm{form}^{\mathrm{X}^q}$ is the Fermi energy dependent formation energy of the charge state q of the defect X. The formation energy is the energy change of the system due to the introduction of a defect X into a perfect crystal and can be calculated using density functional theory DFT (see below). The concentration c_{X^q} of a certain charge state X^q is

$$c_{\mathrm{X}^q} = c_\mathrm{X} P_{\mathrm{X}^q}, \tag{2.78}$$

where c_X is the sum of the concentrations of all charge states of the defect.

Taking the occupation probabilities of all charge states into account, the effective charge state of a defect $q_\mathrm{X}^\mathrm{eff}$ is be defined as

$$q_\mathrm{X}^\mathrm{eff} = \sum_q q P_{\mathrm{X}^q}. \tag{2.79}$$

The effective charge state of a defect can be used to estimate the affinity of the defect to react with another defect, associated with another effective charge state.

In figure 2.21, the formation energies of different charge states of a defect are plotted as a function of the position of the Fermi energy within the band gap. The formation energy of the neutral charge state X^0 is set to zero and the formation energies of all other charge states are plotted relative to the neutral state. The figure also includes the relative concentrations c_{X^q}/c_X of the different charge states of the defect. The formation energies of X have been chosen arbitrarily, in a way that each charge state from X^{2-} to X^{2+} appears at a certain energy range in the silicon band gap. Table 2.6 lists the formation energies $E_{X_0^q}$ at the middle of the band gap ($E_F = 0\,\text{eV}$). If the Fermi energy is close to the valence band, the formation energy of X^{2-} is lower than the formation energies of the other charge states, and hence its concentration is the highest. With increasing Fermi energy, the concentrations of other charge states dominate.

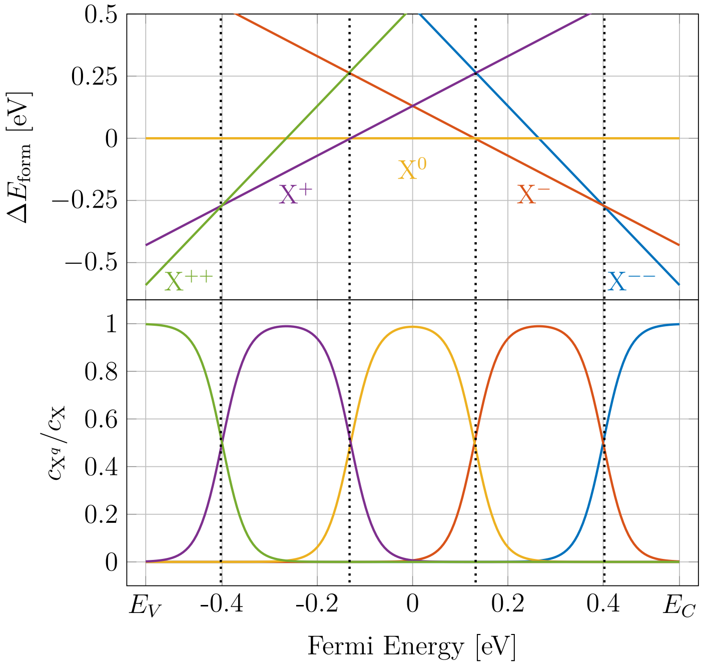

Figure 2.21: Formation energies and relative concentrations of different charge states of a defect as a function of the position of the Fermi energy within the band gap. The ground state energies relative to the ground state energy of the neutral charge state of the defect (ΔE_{form}) are listed in table 2.6. The vertical dashed lines indicate points, where the the Fermi energy matches an ionization energy of the defect.

The change of the charge state of a defect goes along with an ionization energy $E_{q/q+1}$ which is needed to remove an electron from the defect

$$X^q \xrightarrow{E_{q/q+1}} X^{q+1} + e^-. \tag{2.80}$$

The ionization energies of defects in semiconductors can be experimentally measured using techniques such as deep level transient spectroscopy (DLTS) [38]. At the point in the band gap, where the energy difference of the Fermi energy to the valence band energy at 0 K $E_F - E_V(0\,\text{K})$ and the ionization energy $E_{q/q+1}$ coincide, the formation energies, and hence, the occupation probabilities and the concentrations of both charge states of

Table 2.6: Ground state energies $E_{\mathrm{X}_0^q}$ of different charge states of impurity X at the center of the band gap, relative to the formation energy of the neutral state of the defect X^0.

	ΔE_{form} [eV]
X^{2-}	0.53
X^{-}	0.13
X^{0}	0.00
X^{+}	0.13
X^{2+}	0.53

the defect, X^q and X^{q+1} are the same

$$E_{\mathrm{X}_0^q} + q(E_V(0\,\mathrm{K}) + E_{q/q+1}) = E_{\mathrm{X}_0^{q+1}} + (q+1)(E_V(0\,\mathrm{K}) + E_{q/q+1}). \tag{2.81}$$

If $E_F < E_{q/q+1} + E_V(0\,\mathrm{K})$, most of the defects occupy the charge state q. If, on the other hand, E_F is shifted to values above $E_{q/q+1} + E_V(0\,\mathrm{K})$, the charge state $q+1$ will be more populated than the charge state q. In figure 2.21 the conditions $E_F = E_{q/q+1} + E_V(0\,\mathrm{K})$ can be observed as intersections between the formation energies of different charge states and are indicated by vertical, dashed lines. In this thesis the mid gap energy is set to zero. Hence, the valence band energy is $-E_G/2$. Following equation 2.20, describing the temperature dependence of the silicon band gap, at 0 K this energy is -0.585 eV. Figure 2.22 shows a schematic representation of the ionization energies of the defect X in the silicon band.

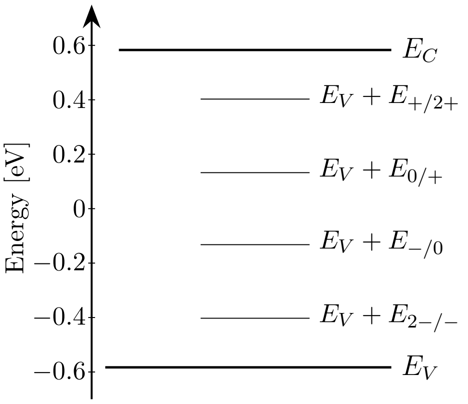

Figure 2.22: Schematic representation of the ionization energies of the defect X in the silicon band gap at 0 K.

If the ionization energy of a defect lies in the center of the band gap, the defect is considered a recombination center, as such levels show the highest Shockley-Read-Hall recombination rate R_{SRH} of excess charge carriers (see section 2.1.7). If an ionization energy is close to the valence band, the defect has an acceptor state and if an ionization energy is close to the conduction band, a donor state is present.

A method to directly calculate the ground state energies of different charge states is by applying ab-initio calculations such as DFT. Here, the energy change of the system due to the introduction of a defect X into a perfect crystal is calculated. The change in energy is the formation energy $E_{\text{form}}^{\text{X}^q}$ of the defect [39, 40]

$$E_{\text{form}}^{\text{X}^q} = E_{\text{tot}}(\text{X}^q) - E_{\text{tot}}(\text{bulk}) - \sum_i N_i \mu_i + qE_F = E_{\text{X}_0^q} + qE_F. \tag{2.82}$$

Here, $E_{\text{tot}}(\text{X}^q)$ is the total energy of the system including the defect X at the charge state q. $E_{\text{tot}}(\text{bulk})$ is the total energy of the perfect crystal. Formation energies are calculated using large supercells [41]. N_i is the number of atoms of type i, which can be either bulk, or impurity atoms and μ_i is the chemical potential corresponding to those atoms. If the defect is charged ($q_{\text{X}} \neq 0$) the formation energy also depends on the position of the Fermi energy E_F in the band gap (see figure 2.21). The slope of the formation energy corresponds to the charge state of the defect. The formation energy of X^+ has a slope of $+1$, while the slope of the charge state X^{2-} is -2. One drawback of most DFT-calculations is that only the formation energies of the ground states of different charge states are calculated while excited states are mostly neglected.

As mentioned before in section 2.1.4, the charge neutrality in a crystal has to be conserved. As impurities are charged, the charge neutrality condition (see equation 2.21) has to be be extended to

$$p + \sum_{i,q>0} q\, c_{\text{X}_i^q} = n + \sum_{i,q<0} q\, c_{\text{X}_i^q}. \tag{2.83}$$

Using the effective charge state,$q_{\text{X}}^{\text{eff}}$, this equation can be stated in terms of absolute concentration of the defects, c_{X_i}, instead of the concentration of the charged states $c_{\text{X}_i^q}$

$$p - n = \sum_i q_{\text{X}}^{\text{eff}}\, c_{\text{X}_i}. \tag{2.84}$$

All charged defects and impurities in the crystal contribute to the electrical properties of the material.

2.2.5 Effective Diffusivity of Point Defects

Defects can be present at different ionized states (see section 2.2.4) at the same time and each of these ionized states is associated with an individual diffusion constant (see section 2.2.3). While the defect diffuses, it can capture or release charge carriers. As this process is much faster than the diffusion process [5], an equilibrium distribution of the different charge states of a defect is assumed at any time. The diffusion of the defect therefore follows an effective diffusivity D^{eff}. $D_{\text{X}}^{\text{eff}}$ of the impurity X is calculated using the concentration ratio P_{X^q} of the charge state X^q (see equation 2.78)

$$D_{\text{X}}^{\text{eff}} = \sum_q P_{\text{X}^q} D_{\text{X}^q}. \tag{2.85}$$

The effective diffusivity is experimentally more accessible than the theoretical diffusivities of the separate charge states of the defect and it still follows Arrhenius law (see equation

2.62). In most experiments, the effective diffusivity furthermore includes reactions and dissociations, which slow down the migration of point-defects. A study on the effects of different influences on the effective diffusivity of hydrogen will be discussed in section 3.

2.2.6 Ionic Drift of Point Defects

Diffusion is not the only migration path of defects in solids. In the presence of an electric field, charged defects will experience a displacement called ionic drift. The evoked particle flux J_{X} depends on the ion mobility μ_{X} and on the electric filed $\vec{E}$.

$$J_{\mathrm{X}} = \mu_{\mathrm{X}} \vec{E} c_{\mathrm{X}}. \tag{2.86}$$

The mobility of a charged defect is related to its diffusion coefficient following the Einstein relation

$$\mu_{\mathrm{X}} = \frac{q_X D_{\mathrm{X}}}{k_B T}. \tag{2.87}$$

As described in sections 2.1.8 and 2.1.9, internal electric fields are generated at *pn*- and at Schottky-junctions. Furthermore, gradients in the overall concentration of charged defects induce an electric field. Another way to generate an electric field is by applying an external potential difference to both sides of the material. The displacement Δx of an ion due to the ionic drift after the time t is

$$\Delta x = \mu_{\mathrm{X}} \vec{E} t. \tag{2.88}$$

2.2.7 Reaction and Dissociation of Point Defects

Different forms of impurities can be present in a crystal. The simplest form are point-defects but under certain conditions point defects can react with other point-defects to form defect complexes. All reactions in a crystal can be summarized in a chemical reaction equation

$$v_{\mathrm{e1}}\,\mathrm{X_{e1}} + v_{\mathrm{e2}}\,\mathrm{X_{e2}} + \ldots {}^{+} v_{\mathrm{ei}}\,\mathrm{X_{ei}} \underset{r_{\leftarrow}}{\overset{r_{\rightarrow}}{\rightleftharpoons}} v_{\mathrm{p1}}\,\mathrm{X_{p1}} + v_{\mathrm{p2}}\,\mathrm{X_{p2}} + \ldots {}^{+} v_{\mathrm{pi}}\,\mathrm{X_{pi}}\,. \tag{2.89}$$

Here, v_{e} and v_{p} are the stoichiometric numbers for educts ($\mathrm{X_e}$) and products ($\mathrm{X_p}$). $r_{\rightarrow}$ stands for the reaction rate in forward direction and $r_{\leftarrow}$ is the rate of the backward reaction [5]. The system always tries to reach the thermodynamical equilibrium, where the Gibbs free energy G is at its minimum and the change in the Gibbs free energy ΔG is zero. In thermodynamic equilibrium the rates of the forward and backward reaction are the same and the concentrations of all impurities stay constant. A real crystal, though, is mostly far away from the thermodynamical equilibrium.

The reaction equation 2.89 can be divided into sub-reactions, like second-order reactions, where two educts react to one product in the forward reaction and the product dissociates to the educts in the backward reaction

$$\mathrm{X_A} + \mathrm{X_B} \underset{r_d^{\mathrm{AB}}}{\overset{r_r^{\mathrm{AB}}}{\rightleftharpoons}} \mathrm{X_{AB}} \tag{2.90}$$

Here, X_A and X_B are the educts and X_{AB} is the product. r_r^{AB} is the second-order reaction rate and r_d^{AB} is the dissociation rate. These rates are calculated from the reaction constant k_r^{AB} and the diffusion constant k_d^{AB}

$$\begin{aligned} r_r^{AB} &= k_r^{AB} c_{X_A} c_{X_B}, \\ r_d^{AB} &= k_d^{AB} c_{X_{AB}}. \end{aligned} \tag{2.91}$$

While the reaction rate depends on the concentrations of both educts, the dissociation rate is solely dependent on the concentration of the product. Figure 2.23 shows the potential energy of the crystal as a function of the reaction coordinate of the reaction of X_A and X_B to X_{AB}. Here, the potential energy of the defect complex is lower than the potential energy of the separate defects X_A and X_B. This energy difference $\Delta H_{X_{AB}}$ signalizes, whether the single defect, or the defect pair is more stable. According to the transition-state theory [5, 42] the reactants have to overcome a transition state X_{AB^*} in order to form the defect complex X_{AB}. This activation process is characterized by the energy difference ΔE_{AB} between the initial state and the transition state. The energy difference between the final state and the transition state is the binding energy $E_{b,X_{AB}}$ of the defect complex.

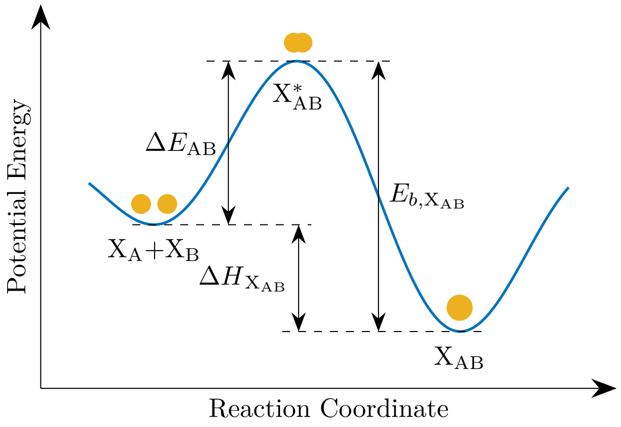

Figure 2.23: Potential energy as a function of the reaction coordinate for the reaction of X_A and X_B to X_{AB}, including the transition state X_{AB^*}. ΔE_{AB} is the activation energy of the reaction, $E_{b,X_{AB}}$ is the binding energy of the complex X_{AB} and $\Delta H_{X_{AB}}$ is the difference in potential energy between $X_A + X_B$ and X_{AB}.

As the impurity concentrations in silicon are very small, the distances between the point defects are rather large. At a defect concentration of $10^{20}\,\mathrm{cm}^{-3}$, the average distance between two defects is only about 2.2 nm but it increases to 215 nm if the concentration is $10^{14}\,\mathrm{cm}^{-3}$. As the distances are so high, the driving force of such reactions is not necessarily the change in the free energy ΔG but the diffusion properties of the educts. Diffusion limited reactions were first described by von Smoluchowski in 1916 [43, 44]. The rate constant of a second-order diffusion limited reaction is

$$k_{r,S}^{AB} = 4\pi \left(D_{X_A} + D_{X_B} \right) r_c^{AB}, \tag{2.92}$$

where r_c^{AB} the capture radius of the reaction, which is the critical distance between the two reactants and $D_{\mathrm{X_A}}$ and $D_{\mathrm{X_B}}$ are the respective diffusivities of the reactants. This model assumes, that once the defects reach the critical distance, they immediately react to the defect complex $\mathrm{X_{AB}}$. Waite extended this formalism in reference 45, by adding a term describing the probability of the reaction to take place

$$k_{r,\mathrm{W}}^{\mathrm{AB}} = k_{r,\mathrm{S}}^{\mathrm{AB}} \frac{r_c^{\mathrm{AB}}\ \beta_p}{r_c^{\mathrm{AB}}\ \beta_p + 1}, \tag{2.93}$$

with

$$\beta_p = \frac{2\Delta r f_{\mathrm{AB}}^{\mathrm{r}}\ p_{\mathrm{AB}}^{o}\ \exp\left(\frac{\Delta E_{\mathrm{AB}}}{k_B T}\right)}{D_{\mathrm{X_A}} + D_{\mathrm{X_B}}}. \tag{2.94}$$

Here Δr is a distance in the order of r_c^{AB} and $f_{\mathrm{AB}}^{\mathrm{r}}$ is the attempt frequency with which the reactants are driven against each other. p_{AB}^{o} is derived from the kinetic theory of gases and describes the probability that $\mathrm{X_A}$ and $\mathrm{X_B}$ are oriented in the right way and ΔE_{AB} is the minimum energy needed for the reaction to occur [45].

The influence of the charge state of the defects on the reaction constant was elaborated by Debye in reference 46:

$$k_{r,\mathrm{D}}^{\mathrm{AB}} = k_{r,\mathrm{S}}^{\mathrm{AB}} f_C, \tag{2.95}$$

where f_C is

$$f_C = \frac{\beta_C}{\exp(\beta_C) - 1}, \tag{2.96}$$

and β_C is

$$\beta_C = \frac{q_1 q_2 e^2}{4\pi\epsilon_0\epsilon_r k_B T r_c^{\mathrm{AB}}}. \tag{2.97}$$

Here, $q_1 q_2$ is the product of the charge states of the two defects. The effect of the charge states of the reacting defects on the reaction rate is shown in figure 2.24. In this figure the relative reaction rate ($f_C = k_{r,\mathrm{D}}^{\mathrm{AB}}/k_{r,\mathrm{S}}^{\mathrm{AB}}$) of defects in silicon ($\epsilon_r = 11.7$) is plotted for a temperature of 25 °C and a capture radius r_c^{AB} of 0.2 nm.

When one of the reactants is neutral, β_C goes to zero and f_C is one. Hence, there is no influence on the reaction rate and $k_{r,\mathrm{D}}^{\mathrm{AB}} = k_{r,\mathrm{S}}^{\mathrm{AB}}$. If the two educts are of opposite charge ($q_1 \cdot q_2 < 0$), β_C is negative and the numerator of f_C is higher than the denominator, leading to an increase of the reaction rate constant. This increase is linearly dependent on the product of the charges of the reacting defects. If, on the other hand, the educts are of the same charge, β_C is positive and f_C goes to zero. This behavior is explained by the nature of the Coulomb interaction of charged particles which attract each other if they are of opposite charge but repel each other if their charge is the same.

In figure 2.25 the temperature dependence of f_C is investigated. In this figure, a capture radius r_c^{AB} of 0.2 nm was used for the calculation of the relative reaction rate of two educts with a charge product $q_1 \cdot q_2$ of -1.

The relative reaction rate constant f_C is strongly temperature dependent. At low temperatures f_C is high but it decreases with increasing temperature. The factor f_C also decreases, as the capture radius of the reaction of neutral defects is increased. This dependence is illustrated in figure 2.26.

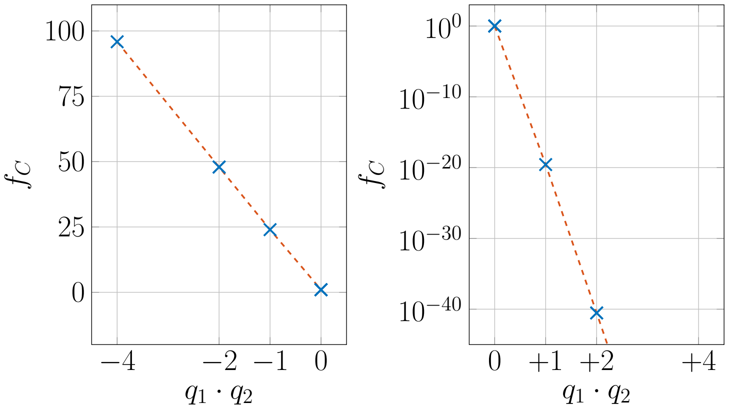

Figure 2.24: Relative reaction rate constant f_C as a function the product of the charge states of the reacting educts. On the left side, f_C is plotted for the case when both reactants are of opposite charges. On the right side f_C is plotted for defects of the same charge

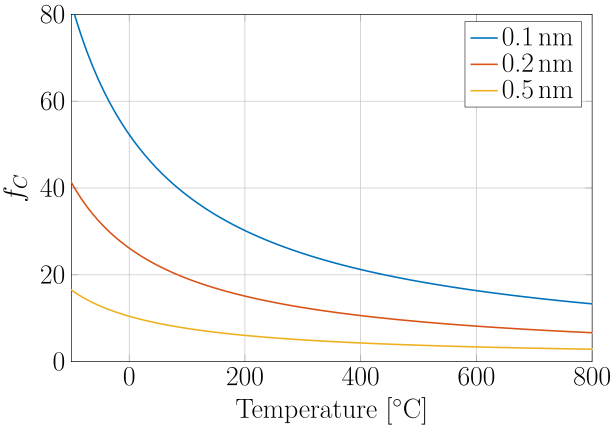

Figure 2.25: Temperature dependence of the relative reaction rate constant f_C for different values of the capture radius of the neutral reactants.

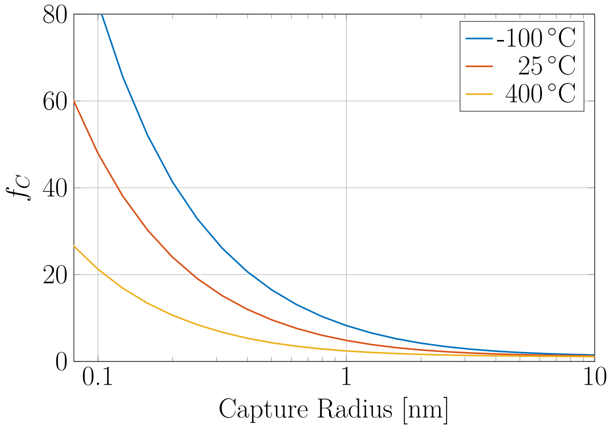

Figure 2.26: Relative reaction rate constant f_C as a function of the capture radius of neutral defects at different temperatures.

The smaller r_c^{AB}, the higher becomes f_C. This effect is further increased when the temperature is lowered.

Once a defect complex is formed it can undergo further reactions and grow in size. At the same time, though, it can dissociate back into the educts from which it was formed. As described in equation 2.91, the dissociation of a defect complex happens at a dissociation rate r_d^{AB}, which depends on the rate constant of the dissociation k_d^{AB} [47, 48]

$$k_d^{\mathrm{AB}} = f_{\mathrm{d}}^{\mathrm{AB}} \exp\left(-\frac{E_{b,\mathrm{X_{AB}}}}{k_B T}\right), \tag{2.98}$$

where $f_{\mathrm{d}}^{\mathrm{AB}}$ is the attempt frequency of the dissociation and $E_{b,\mathrm{X_{AB}}}$ is the binding energy of the defect complex $\mathrm{X_{AB}}$.

The change of the concentration of a defect complex over time is

$$\frac{\delta c_{\mathrm{X_{AB}}}}{\delta t} = r_r^{\mathrm{AB}} - r_d^{\mathrm{AB}} = k_r^{\mathrm{AB}} c_{\mathrm{X_A}} c_{\mathrm{X_B}} - k_d^{\mathrm{AB}} c_{\mathrm{X_{AB}}}. \tag{2.99}$$

Both, the reaction rate and the dissociation rate depend on the concentrations of either the defect complex $c_{\mathrm{X_{AB}}}$ or the educts $c_{\mathrm{X_A}}$ and $c_{\mathrm{X_B}}$. At thermal equilibrium, $\frac{dc_{\mathrm{X_{AB}}}}{dt}$ goes to zero and the concentrations of all defects are constant. Substituting $c_{\mathrm{X_A}}$ by $c_{\mathrm{X_A},0} - c_{\mathrm{X_{AB}}}$ and $c_{\mathrm{X_B}}$ by $c_{\mathrm{X_B},0} - c_{\mathrm{X_{AB}}}$, $c_{\mathrm{X_{AB}}}$ can be calculated from the quadratic equation

$${c_{\mathrm{X_{AB}}}}^2 - \left(\frac{k_d^{\mathrm{AB}}}{k_r^{\mathrm{AB}}} + c_{\mathrm{X_A},0} + c_{\mathrm{X_B},0}\right) c_{\mathrm{X_{AB}}} + c_{\mathrm{X_A},0} c_{\mathrm{X_B},0} = 0. \tag{2.100}$$

Figure 2.27 illustrates the temperature dependence of the concentrations of the defect complex and the reactants at thermal equilibrium, using the reaction of H and $\mathrm{B_i}$, forming $\mathrm{B_iH}$. Different reaction rates were used according to the different models described above.

The figure shows that at the thermodynamic equilibrium at low temperatures, the concentration of the defect complex $\mathrm{B_iH}$ predominates. Hence, at such temperature, the reaction forming the defect complex dominates its dissociation. Both, the reaction and the dissociation rate, increase with increasing temperature. The binding energy of $\mathrm{B_iH}$ is higher than the activation energies of the diffusion of the point-defects H and $\mathrm{B_i}$, which determine the rate of the reaction of the two defects. Hence, the temperature dependent increase of the dissociation is higher than that of the reaction. This leads to a decrease of the equilibrium concentration of $\mathrm{B_iH}$ at a certain temperature. At an intermediate temperature range, the defect complex and the reactants are present at significant equilibrium concentrations, until, at high temperatures, the $\mathrm{B_iH}$ concentration goes to zero, as the dissociation process dominates the reaction process. Assuming that $c_{\mathrm{H},0} = c_{\mathrm{B_i},0}$, at the transition temperature T_t the equilibrium concentrations of $\mathrm{B_iH}$ and H are the same. Allowing for Coulomb interaction (marked as Debye in figure 2.27), shifts the equilibrium towards the reaction and increases T_t to a higher temperature. The consideration of the reaction probability (Waite) causes a shift of the equilibrium towards the dissociation of $\mathrm{B_iH}$ and lowers the transition temperature. It has to be emphasized that the concentration ratios plotted in figure 2.27 do not necessarily correspond to the real equilibrium concentrations but are calculated from the parameters listed in table 2.7. Unfortunately some parameters needed for this calculation are not available as they have not yet been measured or calculated. So the capture radius and the energy difference $\Delta E_{\mathrm{B_iH}}$, used for the calculation of the reaction probability, have been estimated by the author. Furthermore the temperature dependence of the charge states of $\mathrm{B_i}$ and H has not been accounted for.

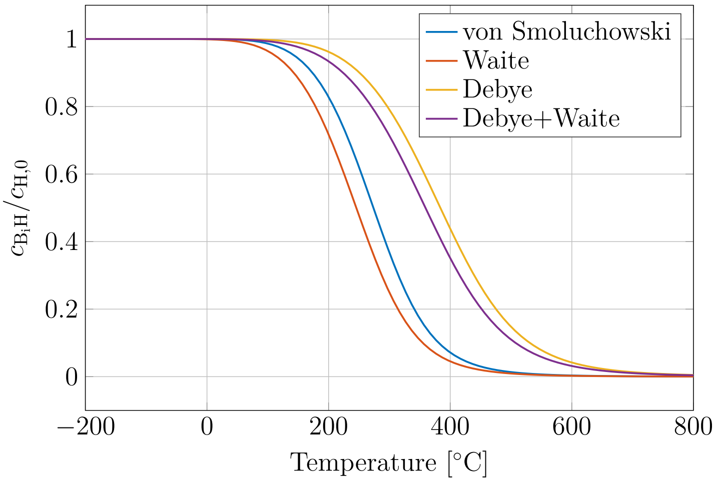

Figure 2.27: Temperature dependence of the thermal equilibrium concentrations of products and educts in the formation of a defect complex. The reaction rate was calculated using the different models described above.

Table 2.7: Parameters used for the calculation of the defect concentrations of the reaction of H and B_i to B_iH at thermal equilibrium.

Parameter	Value	Reference
$D_{0,\mathrm{H}}$ [$\mathrm{cm^2s^{-1}}$]	9.41×10^{-7}	[49]
$D_{0,\mathrm{B_i}}$ [$\mathrm{cm^2s^{-1}}$]	4×10^{-8}	[5]
$E_{A,\mathrm{H}}$ [J]	0.48	[49]
$E_{A,\mathrm{B_i}}$ [J]	0.6	[5]
$r_{c,\mathrm{B_iH}}$ [m]	2×10^{-10}	
$c_{\mathrm{H},0}$ [$\mathrm{cm^{-3}}$]	10^{22}	
$c_{\mathrm{B_i},0}$ [$\mathrm{cm^{-3}}$]	10^{22}	
$c_{\mathrm{B_iH},0}$ [$\mathrm{cm^{-3}}$]	0	
q_H	$+1$	
$q_{\mathrm{B_i}}$	-1	
$E_{b\mathrm{B_iH}}$ [J]	1.28	[48]
$f_{\mathrm{d,B_iH}}$ [$\mathrm{s^{-1}}$]	2×10^{14}	[48]
$\Delta E_{\mathrm{B_iH}}$ [J]	0.64	

2.3 Defects in Silicon

This section focuses on common point defects in silicon. In the first part, the point defects intrinsic to silicon are presented and discussed. The second part concentrates on the impurities carbon and oxygen, which are introduced during the production of silicon crystals. The last part of this section deals with the most important dopants in silicon semiconductor industry, boron and phosphorus. A short summary of the charge states of each defect and of the diffusivity of mobile defects discussed in this section can be found in the catalog on defects in appendix C. There is a reference to the respective page in the appendix on the beginning of each section.

2.3.1 Intrinsic Defects

As described in section 2.2.2 there are different kinds of point-defects in a crystal. Among these, vacancies and interstitials are inherent to each crystal. Therefore, these point-defects are also called "intrinsic" point-defects. The presence of intrinsic defects is explained by the entropy term S in the Gibbs free energy G of a system

$$G = H + TS. \tag{2.101}$$

At 0 K the energy of the system is minimized if the defect concentration goes to zero. At finite temperatures, though, the defect concentration is increased due to entropy. Hence, the higher the temperature, the higher is the concentration of intrinsic defects at thermodynamic equilibrium.

As silicon is made up of only one element, its intrinsic defects are the silicon vacancy V and the silicon self-interstitial I. The measurement of the equilibrium concentration of the intrinsic defects is quite demanding and there is a large variation between different studies found in literature. For more detailed information reference [5] is recommended. Figure 2.28 shows the concentration of vacancies and interstitials as a function of temperature, computed by Sinno et al. from crystal-growth experiments [50].

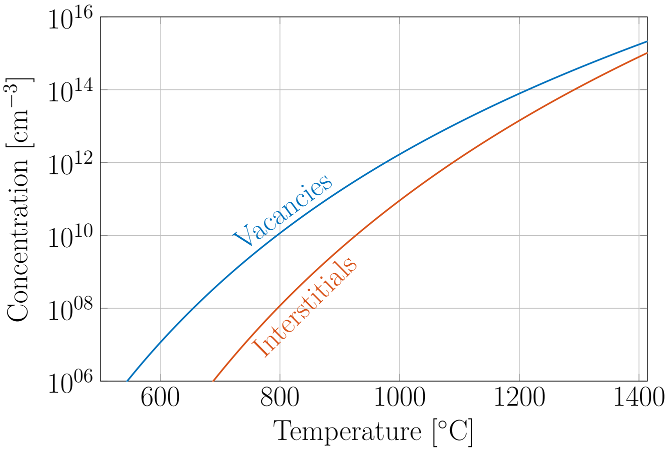

Figure 2.28: Equilibrium concentrations of intrinsic point defects as a function of the temperature computed from crystal-growth experiments [50].

According to this study, the equilibrium concentrations of the intrinsic point defects become significant only at temperatures above 800 °C. Here, the vacancy concentration is always higher than the concentration of self-interstitials.

Apart from thermal generation, intrinsic defects can also be generated by processes such as electron irradiation or ion-implantation. Here, the impinging particles dissipate a fraction of their energy by knocking silicon atoms off their lattice positions and create Frenkel pairs (see section 2.4.1).

Due to their high diffusivity, intrinsic defects almost instantly react with other point-defects or defect complexes. Silicon self-interstitials can react with substitutional impurities $\mathrm{X_s}$ in an exchange reaction to create interstitial impurities $\mathrm{X_i}$. Vacancies, on the other hand, form vacancy-impurity-complexes $\mathrm{VX_s}$ with substitutional impurities.

$$\begin{aligned} \mathrm{I} + \mathrm{X_s} &\rightleftharpoons \mathrm{X_i} \\ \mathrm{V} + \mathrm{X_s} &\rightleftharpoons \mathrm{VX_s} \end{aligned} \tag{2.102}$$

Furthermore, vacancies and interstitials can annihilate in a process called "direct recombination".

$$\mathrm{V} + \mathrm{I} \rightleftharpoons 0 \tag{2.103}$$

There is also the possibility of "indirect recombination" when intrinsic point defect first react with impurities and then annihilate.

$$\begin{aligned} \mathrm{VX_s} + \mathrm{I} &\rightleftharpoons \mathrm{X_s} \\ \mathrm{X_i} + \mathrm{V} &\rightleftharpoons \mathrm{X_s} \end{aligned} \tag{2.104}$$

As described in equation 2.91, the rate of the direct recombination depends on the rate constant of the reaction and on the concentrations of the intrinsic point defects. The reaction rate constant depends on the diffusivities of the reactants and on the capture radius. Most point-defects are found in several different charge states, hence, the Coulomb interaction between the charged defects has to be accounted for. In the following sections the charge states and diffusivities of vacancies and interstitials are discussed. The calculation of the reaction rate constants of some selected reactions are found in appendix D.

2.3.1.1 Silicon Vacancy

The silicon vacancy V (see appendix C.1) was first measured in its positively charged state $\mathrm{V^+}$ by Watkins et al. using low temperature electron paramagnetic resonance spectroscopy (EPR) [51]. Later studies also showed evidence of other charge states of the vacancy in the silicon band gap [52, 53]. Silicon vacancies can take charge states from -2 to $+2$, depending on the temperature and on the position of the Fermi energy in the band gap [5, 54, 55]. Figure 2.29 shows the relative formation energy of each charge states of the silicon vacancy and its corresponding concentration ratio as a function of the position of the Fermi energy at 25 °C. In this figure the results of two different simulations are compared. Both studies [54, 55] used different variants of DFT-simulations to calculate the ionization energies of the silicon vacancy, which correspond to the crossing points of the relative formation energies of the charge states. The relative formation energies used to generate this plot are listed in table 2.8 and were calculated from the ionization energies published in the references 54 and 55. The relative formation energies were calculated using the band gap of silicon at 0 K (1.166 eV). The ionization energies which are observable using experimental techniques such as deep level transient spectroscopy (DLTS) are indicated as dashed lines. The ionization energy closest to the valence band energy in both plots is $E_{(0/+2)}$, which indicates the transition of the doubly positive state V^{2+} to the neutral state V^0 of the silicon vacancy. This transition is called a “negative-U”-transition [56]. Even though the relative formation energies calculated from the studies of Mueller and Puska differ only slightly, the results of Mueller predict an energy range in the band gap where V^- is stable, while Puska’s results show a second negative-U transition. Further calculations in this thesis involving the charge states of the silicon vacancy, will use Mueller’s results as input data.

Street and Mott were the first to propose the existence of negative-U defects [56]. A usual defect occurs at subsequent charge states, as the Fermi energy is shifted through the band gap, as it is shown for the random impurity X in figure 2.21. A negative-U-defect exhibits metastable states and for such a defect it can be energetically favorable to directly transit from e.q. a neutral to a doubly positively charged state. Even before it was experimentally shown, that the silicon vacancy shows the negative U-effect [57], its existence was proposed by Baraff et al. [58]. For the silicon vacancy, the negative-U-system consists of the charge states V^0, V^+ and V^{2+}, which are associated with tetragonal lattice distortions [58]. Here, the ionization energy of the transition of V^0 to V^+ has an ionization energy of 0.06 eV, while the ionization energy of the transition from V^+ to V^{2+} is 0.23 eV [54]. Hence, when the Fermi energy is shifted from the mid gap to the valence band, a direct transition from V^0 to V^{2+} occurs (see figure 2.29). The V^+ state is a metastable state and decays after being photo-generated, depending on the Fermi-level, to either V^0 or V^{2+} [59]. Figure 2.29 shows that already at a temperature of 25 °C the state is present at small concentration.

Table 2.8: Ionization energies of the silicon vacancy in eV, calculated by Mueller [54] and Puska [55]. The corresponding formation energies (in eV) at $E_F = 0$, relative to the formation energy of the neutral charge state V^0 assuming a band gap of 1.166 eV are included as well.

Transition	$E_{q/q+1}$ [54]/[55]	Charge State	ΔE_{form} [54]/[55]
		V^{2-}	-0.098 /-0.20
$E_{(-2/-)}$	0.58/0.40	V^-	-0.08 /-0.01
$E_{(-/0)}$	0.50/0.57	V^0	0.00 /0.00
$E_{(0/+)}$	0.06/0.11	V^+	0.52 /0.47
$E_{(+/+2)}$	0.23/0.19	V^{2+}	0.88 /0.87

The relative concentrations of the different charge states of the silicon vacancy depend on both, the temperature and the Fermi energy (see equations 2.76 and 2.77). Figure 2.30 shows relative concentrations of the charge states of the silicon vacancy (using the relative formation energies calculated by Mueller et al. [54]) as two dimensional maps, where the x-axis is the position of the Fermi energy in the band gap and the y-axis is the temperature. In highly-doped *p*-type material, if the Fermi energy is very close to the valence band energy, the doubly positively charged state dominates. At energies closer to the middle of the band gap V^0 is the most stable state. In intrinsic silicon ($E_F \approx 0\,\mathrm{eV}$) V^- shows the highest concentration and in n-type material, V^{2-} is the dominant charge state. The concentration maps further show that at low temperatures only one or two charge states are present at the same time at significant relative concentrations ($c_{V^q}/c_V > 10^{-4}$). At low temperatures transitions between the charge states, as the Fermi energy is swept through the band gap are very abrupt. At elevated temperatures, these transitions smear out and the energy range where a specific charge state is present increases.

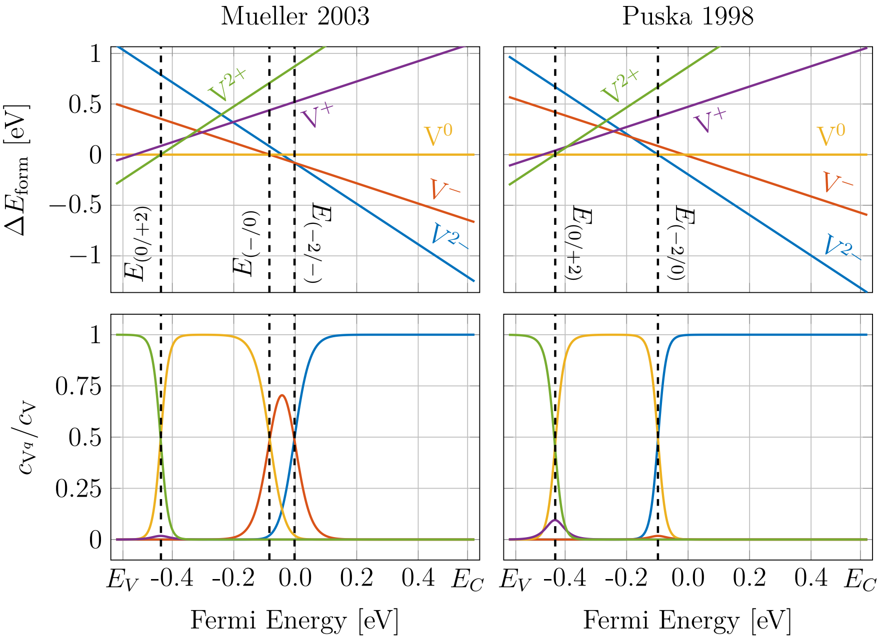

Figure 2.29: Relative formation energies and relative concentrations of the different charge states of the silicon vacancy as a function of the position of the Fermi energy in the band gap at 25 °C. The relative formation energies at $E_F = 0$ were calculated from ionization energies published in references 54 and 55. The experimentally observable ionization energies are indicated by dashed lines.

Figure 2.30 also includes a plot of the temperature dependence of the valence and conduction band energies, as well as the temperature dependence of the position of the Fermi energy $E_F(T)$ in the band gap at different doping concentrations. This plot is similar to figure 2.9 but here, the axes are switched. The relative concentration of a charge state along $E_F(T)$, is used to visualize the temperature dependence of the relative concentration of that charge state at the doping concentration used to calculated the Fermi energy. This procedure is only valid if the defect concentration is much smaller than the doping concentration. If the defect concentration is too high, all the present, charged states of the defect have to be accounted for in the calculation of the neutrality condition (see equation 2.83) which will then yield a different position of the Fermi energy.

In figure 2.31 the relative concentrations of the different charge states of the vacancy are plotted as a function of the inverse temperature for different doping concentrations. As already addressed above, the dominant species in intrinsic silicon is V^-. Nevertheless,

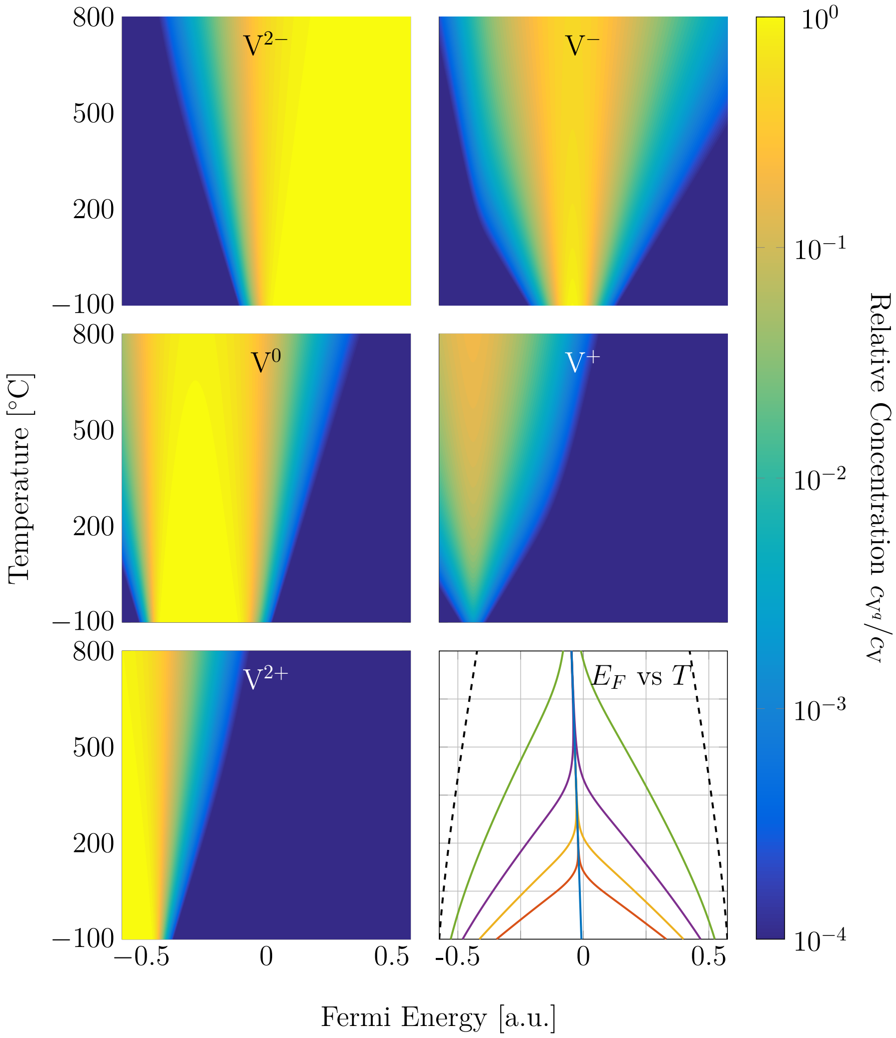

Figure 2.30: Relative concentrations of the charge states of the silicon vacancy as a function of the temperature and of the position of the Fermi energy in the band gap. The temperature dependence of the conduction and valence band energies, as well as the temperature dependence of the Fermi energy for different doping concentrations are included. A color coding, similar to figure 2.9 was used. blue: intrinsic silicon; red: doping = $10^{12}\,\mathrm{cm}^{-3}$; yellow: doping = $10^{14}\,\mathrm{cm}^{-3}$; violet: doping = $10^{16}\,\mathrm{cm}^{-3}$; green: doping = $10^{18}\,\mathrm{cm}^{-3}$; dashed lines: E_V and E_C

at the same time V^{2-} and V^0 are present at significant concentrations. For increasing temperature, the relative concentration of V^0 increases as the Fermi energy slightly shifts towards the valence band. In n-type material at low temperatures the dominant vacancy charge state is V^{2-}. With increasing temperature, the relative concentrations approach the distribution of the charge states in intrinsic material. At a certain temperature, the dominant charge species changes from V^{2-} to V^-. As the doping concentration is increased, this temperature is shifted towards higher (smaller inverse) values. In p-type material at doping concentrations up to $10^{16}\,\mathrm{cm}^{-3}$, the neutral charge state shows the highest concentration at low temperatures and the concentrations of the different charge states converge to their ratio observed in intrinsic silicon. In p-type material at high doping concentrations and low temperatures though, also the positive charge states are present. While V^{2+} is the dominant species at low temperatures, the relative concentration of V^+ ($c_{\mathrm{V}^+}/c_{\mathrm{V}}$) is always below 0.05.

Figure 2.32 shows a map of the effective charge state of the silicon vacancy $q_{\mathrm{V}}^{\mathrm{eff}}$ as a function of the temperature and the Fermi energy, calculated according to equation 2.79. The figure includes the temperature dependence of the energies of the valence band and the conduction band. Furthermore, the temperature dependence of the position of the Fermi energy in the band gap at different doping concentrations is included.

The effective charge state of the silicon vacancy as a function of the inverse temperature for different doping concentrations is plotted in figure 2.33.

In intrinsic silicon, the effective charge state is about -1.4 at -100 °C and increases slightly to -1 at 800 °C as the concentration of V^0 increases. In p-type silicon $q_{\mathrm{V}}^{\mathrm{eff}}$ is above than the intrinsic level, while it is lower in n-type material. At acceptor concentrations below $10^{16}\,\mathrm{cm}^{-3}$, the effective charge state of the vacancy at low temperatures is 0. At a certain temperature, which depends on the acceptor concentration, the effective charge state decreases until it converges to the intrinsic level. The positive charge states of the silicon vacancy are only present at acceptor concentrations higher than $10^{16}\,\mathrm{cm}^{-3}$. Hence only at such acceptor concentrations positive values for $q_{\mathrm{V}}^{\mathrm{eff}}$ are observed. At an acceptor concentration of $10^{18}\,\mathrm{cm}^{-3}$, the effective charge state at -100 °C is $+2$. Here, with increasing temperature, the effective charge state first shows the transition from $+2$ to 0 at temperatures between 0 °C and 250 °C, followed by another transition from 0 to -1 between 450 °C and 850 °C. In n-type material $q_{\mathrm{V}}^{\mathrm{eff}}$ is -2 at low temperatures and approaches the intrinsic level at higher temperatures. The temperature at which this transition takes place increases with increasing doping concentration.

The experimental determination of the diffusion coefficient of the silicon vacancy is very difficult, as it immediately reacts with other point defects after being generated. Different studies, measuring the migration of the silicon vacancy resulted in values for the effective vacancy diffusivity spreading over ten orders of magnitude (see the section on the diffusion of the silicon vacancy in reference [5]). As each of the different states of the vacancy is associated with a different diffusion constant, the effective vacancy diffusivity strongly depends on the concentration ratio of its charge states. The Arrhenius coefficients describing the diffusion of each charge state of the vacancy have been determined by Watkins et al. [51, 59–61] using (EPR) at low temperatures and are listed in table 2.9.

Figure 2.34 shows the temperature dependence of the diffusivity of each charge state of the silicon vacancy, calculated from the Arrhenius coefficients listed in table 2.9. While the Arrhenius coefficients describing the diffusion coefficient of the neutral vacancy V^0

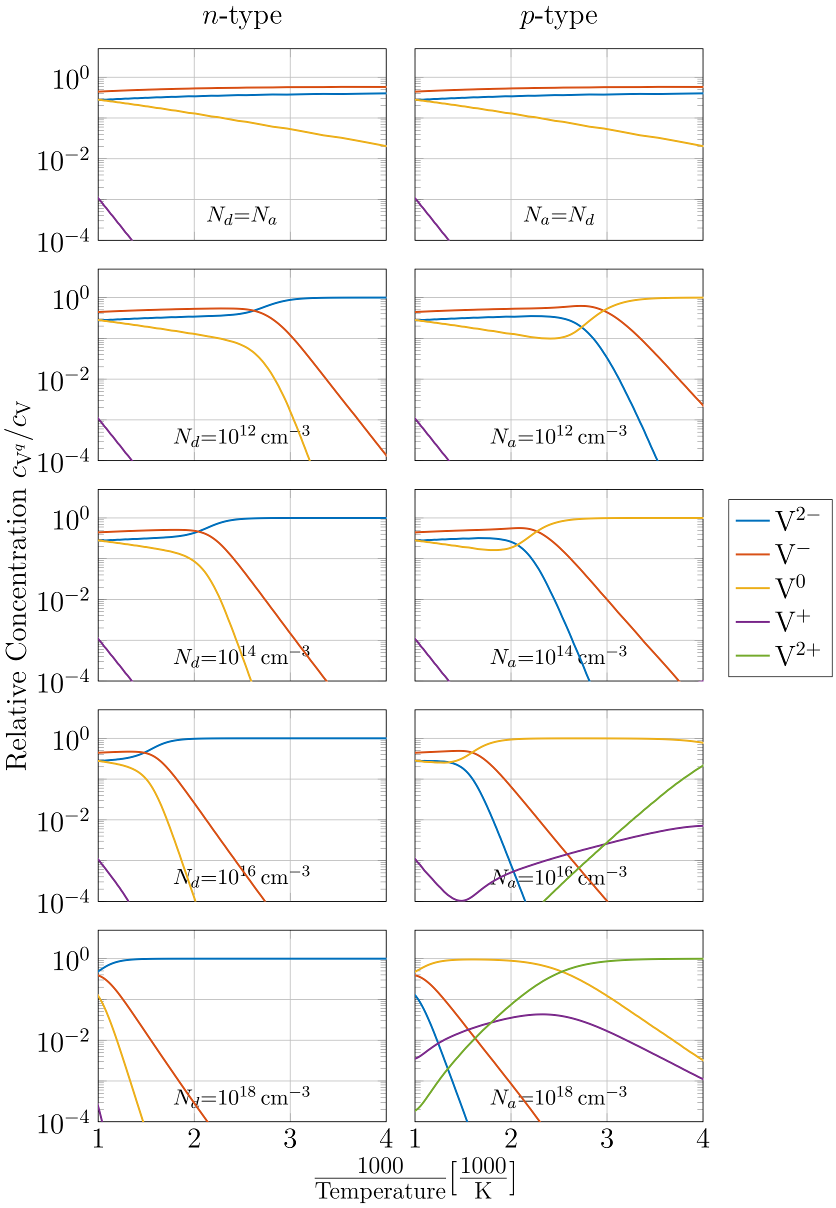

Figure 2.31: Temperature dependence of the relative concentrations of the different charge states of the silicon vacancy at different doping concentrations in *n*-type and *p*-type silicon.

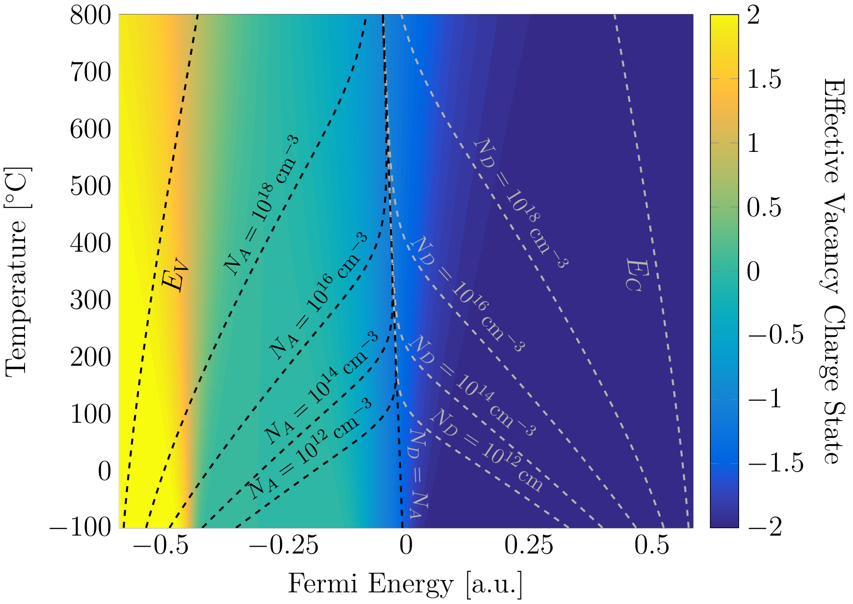

Figure 2.32: Map of the effective charge state of the silicon vacancy $q_{\mathrm{V}}^{\mathrm{eff}}$ as a function of temperature and Fermi energy. The temperature dependence of the valence and conduction band energies and of the Fermi energy at different doping concentrations are included.

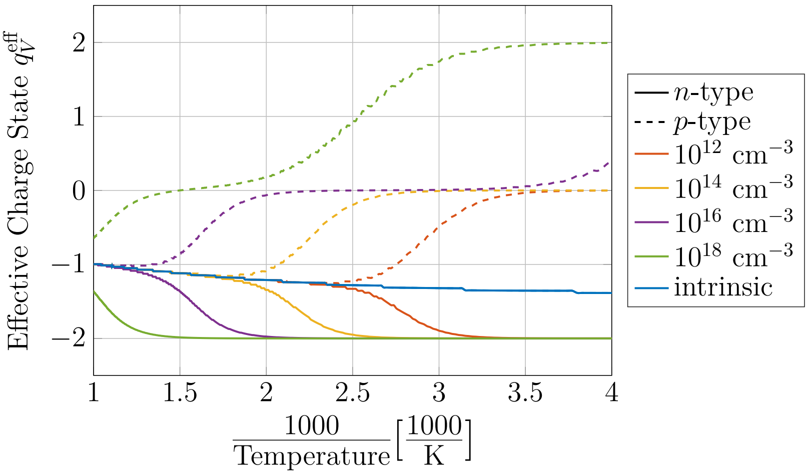

Figure 2.33: Temperature dependence of the effective charge state of the silicon vacancy $q_{\mathrm{V}}^{\mathrm{eff}}$ at constant doping concentrations.

and the doubly charged states V^{2-} and V^{2+}, as well as the activation energy of V^{-} are published values [5], the parameters for V^{+} and the pre-factor of V^{-} have been estimated by the author of this thesis in a way, so that the diffusion coefficient of the singly charged vacancy lies between the diffusion coefficients of the neutral and the doubly charged states. Here, the Arrhenius coefficients determined at cryogenic temperatures have been used to extrapolate the vacancy diffusivity also for higher temperatures. This estimation presumes, that the activation energies stay constant over the whole temperature range.

Table 2.9: Arrhenius coefficients describing the temperature dependence of the diffusion of each charge states of the silicon vacancy as reported in reference [5]. *: Coefficients estimated by the author in a way to fit between the diffusion coefficients of the neutral and the double charged vacancy.

Species	E_A [eV]	D_0 [cm^{2}s^{-1}]
V^{2-}	0.18	1.5×10^{-2}
V^{-}	0.25	3.0×10^{-3}*
V^{0}	0.45	1.3×10^{-3}
V^{+}	0.38 *	3.0×10^{-4}*
V^{2+}	0.32	9.6×10^{-5}

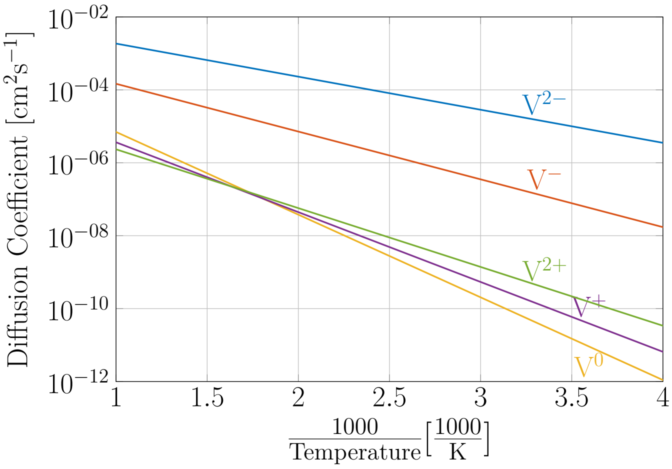

Figure 2.34: Diffusion coefficients of the silicon vacancy at different charge states as a function of the inverse temperature, calculated from the Arrhenius parameters published in reference [5] and listed in table 2.9.

Over the whole temperature range from -100 °C to 800 °C V^{2-} shows the highest diffusion coefficient. At temperatures below 300 °C, the neutral vacancy is the slowest diffusing species. Above 300 °C V^{2+} state has the smallest diffusion coefficient of all charge states.

Taking the concentration ratio of the charge states of the silicon vacancy into account, the effective diffusivity D_V^{eff} is calculated following equation 2.85. Figure 2.35 shows a two dimensional map of D_V^{eff}, where one axis is the position of the Fermi energy in the band gap and the other axis is the temperature. The figure furthermore includes the temperature dependence of the valence and conduction band energies and the temperature dependence of the Fermi energy at different doping concentrations.

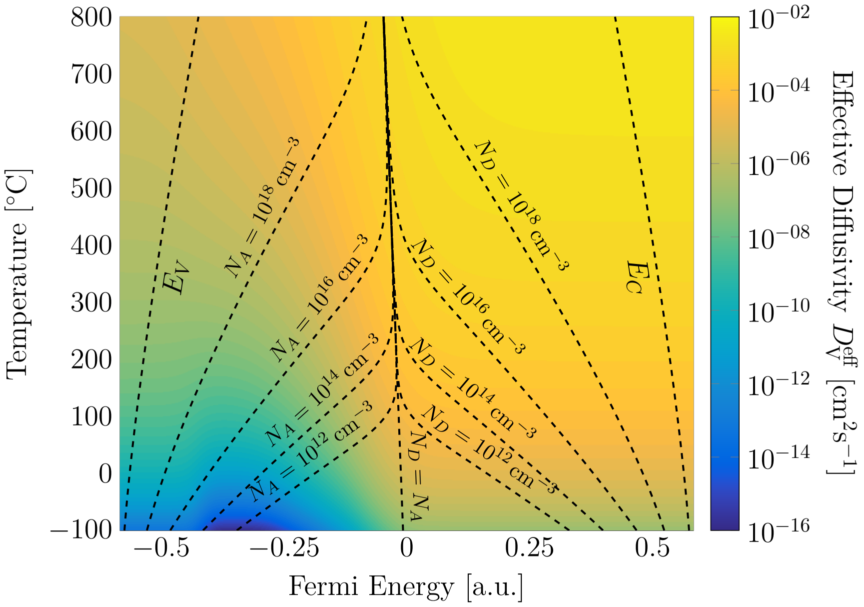

Figure 2.35: Map of the effective diffusivity of the silicon vacancy as a function of the temperature and the Fermi energy. The temperature dependence of the valence and conduction band energies and the temperature dependence of the position of the Fermi energy in the band gap at different doping concentrations are included.

The Arrhenius law (see equation 2.62) implicitly states that for positive activation energies, the diffusion coefficient increases with temperature. As a consequence, also the effective diffusivity D_V^{eff} increases with temperature. Nevertheless, the difference of D_V^{eff} at the same temperature but for different positions of the Fermi energy can be as high as six orders of magnitude. As the doubly negatively charged species V^{2-} shows the highest diffusivity, D_V^{eff} is large when the Fermi energy is close to the conduction band. At temperatures below 300 °C, the lowest values of D_V^{eff} are found at Fermi energies between -0.45 eV and -0.15 eV, where V^0 is the dominant charge state. Assuming a vacancy concentration much smaller than the doping concentration, the temperature dependence of D_V^{eff} can be plotted for different doping concentrations, as shown in figure 2.36.

In intrinsic silicon there is a linear relationship between the inverse temperature $1/T$ and the natural logarithm of D_V^{eff}, which follows the Arrhenius law and is described by an activation energy E_A of 0.17 eV and a pre-factor D_0 of 4.7×10^{-3} cm^{2}s^{-1}. In p-type silicon D_V^{eff} is lower than in the intrinsic material, as here the less mobile species V^0, V^+ and V^{2+} are present. With increasing temperature D_V^{eff} approaches the intrinsic level. The apparent activation energy of D_V^{eff} before the transition is higher than the intrinsic activation energy and gets close to 1 eV, which is more than twice as high than the highest activation energy of each individual charge state of the vacancy. The temperature at which this transition occurs, increases with the acceptor concentration.

In n-type material D_V^{eff} is higher than in the intrinsic material until a transition to the

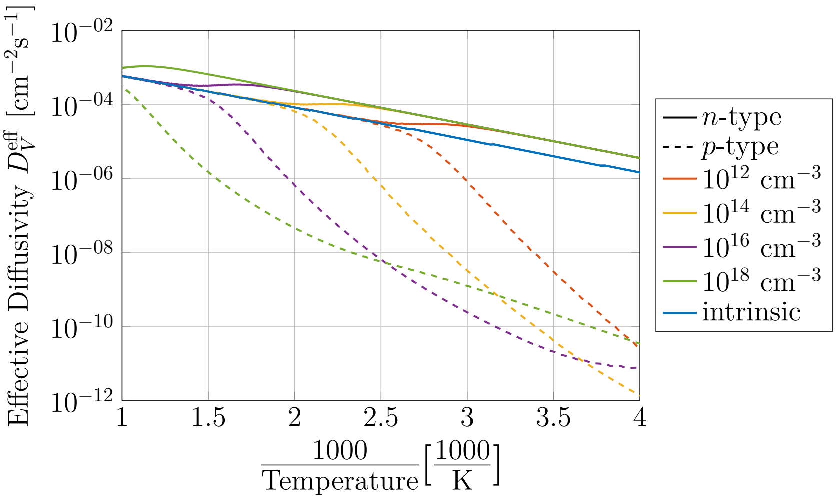

Figure 2.36: Temperature dependence of the effective diffusivity of the silicon vacancy $D_{\mathrm{V}}^{\mathrm{eff}}$ at different doping concentrations.

intrinsic level is observed. The apparent activation energy before the transition is 0.18 eV, which is close to the intrinsic activation energy. At doping concentrations above $10^{16}\,\mathrm{cm}^{-3}$ the effective vacancy diffusivity decreases in the transition region. In this temperature range the activation energy of the effective diffusivity is negative.

2.3.1.2 Silicon Divacancy V_2

Whenever intrinsic point-defects are present at a significant concentration in a silicon crystal and the temperature is high enough for them to be mobile, they will react with other defects to form defect complexes or annihilate (in the case of the reaction of vacancies with interstitials). One of these reaction paths includes two vacancies reacting to form a divacancy V_2 (see appendix C.2). The divacancy was first identified by Corbett and Watkins from EPR measurements of electron-irradiated silicon [62] and has been studied intensively. While most of the early studies used EPR [63–66], others applied DLTS [67–71] or infra-red- (IR-) spectroscopy [72]. Furthermore, ab-initio calculations of the formation energies of the different charge states, using pseudo-potentials [73] and DFT [54] have been made. The ionization energies calculated by Mueller et al. were used to calculate the relative formation energies of each charge states of the divacancy in the center of the band gap. These energies are listed in the table in figure C.2.1a. Figure 2.37 shows the formation energies of the different charge states of the silicon divacancy, relative to the formation energy of its neutral chagre state, as a function of the position of the Fermi energy in the band gap. The figure also includes the relative concentrations of the charge states ($c_{\mathrm{V}_2^q}/c_{\mathrm{V}_2}$) at 25 °C.

According to Mueller et al. [54], in contrast to the single vacancy, the divacancy does not show a negative-U-system. There are only transitions between different ionization states involving the release or capture of a single charge carrier. For more than half of the band gap, V_2^{2-} is the dominant charge state. Only in p-type silicon are the other charge states present at significant concentrations. Figure C.2.1(b) shows the relative

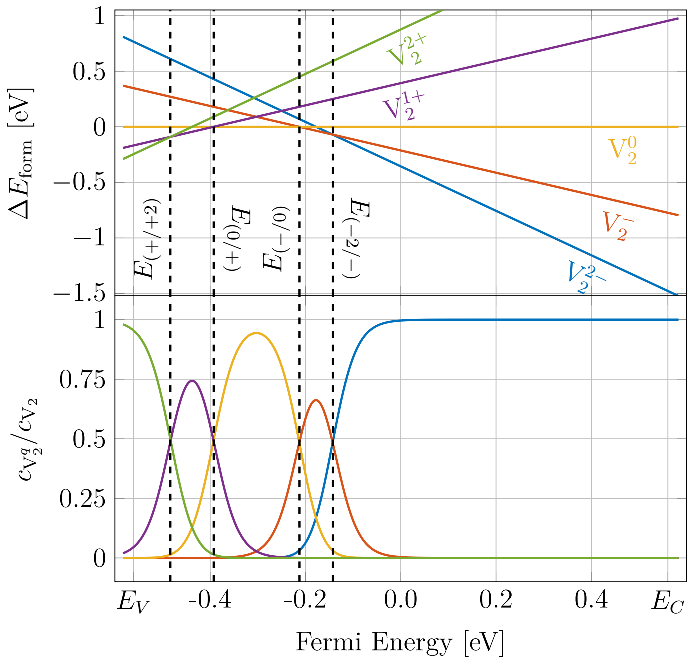

Figure 2.37: Relative formation energy and relative concentration of each charge state of the silicon divacancy as a function of the position of the Fermi energy in the band gap at 25 °C. The formation energies at $E_F = 0$ were calculated from DFT simulations [54].

concentration of each charge state of the divacancy as a function of the position of the Fermi energy in the band gap and of the temperature. In *n*-type material, over the whole temperature range from -100 °C to 800 °C, V_2^{2-} is the dominant charge state. V_2^{-} is the most stable configuration of the divacancy at a Fermi energy between -0.21 eV and -0.15 eV. At Fermi energies between -0.39 eV and -0.21 eV V_2^{0} shows the highest concentration and if the Fermi energy is between -0.48 eV an -0.39 eV V_2^{+} is present. At Fermi energies even closer to the valence band, V_2^{2+} is the dominant charge state.

Figure C.2.2a shows the temperature dependence of the relative concentration of each charge state of the divacancy at different doping concentrations. In intrinsic silicon, V_2^{2-} is the dominant charge state over the whole investigated temperature range. At room temperature the relative concentration of V_2^{-} is in the percent-range and increases to approximately 20 % at 800 °C. The concentration of the neutral charge state increases as well with temperature but it never exceeds 5 %. The dominant charge state of the divacancy in *n*-type material is always V_2^{2-}. In *p*-type silicon the distribution of the different charge states is more diverse. At an acceptor concentration of $10^{12}\,\mathrm{cm}^{-3}$ and at a temperature below -15 °C, the neutral charge state of the divacancy shows the highest concentration. Between -15 °C and room temperature, V_2^{-} is the dominant charge state and at temperatures above room temperature the doubly negative charge state shows the highest concentration. At higher acceptor concentrations the transitions between the charge states are shifted towards higher temperatures and at an acceptor concentration of $10^{16}\,\mathrm{cm}^{-3}$ also the positive charge states appear at significant concentrations. If the acceptor concentration is above $10^{18}\,\mathrm{cm}^{-3}$, each charge state is dominant at a certain temperature range between -100 °C and 800 °C.

In a similar way as for the single vacancy, the effective charge state of the divacancy $q_{\mathrm{V}_2}^{\mathrm{eff}}$ was calculated and is plotted in figure 2.38.

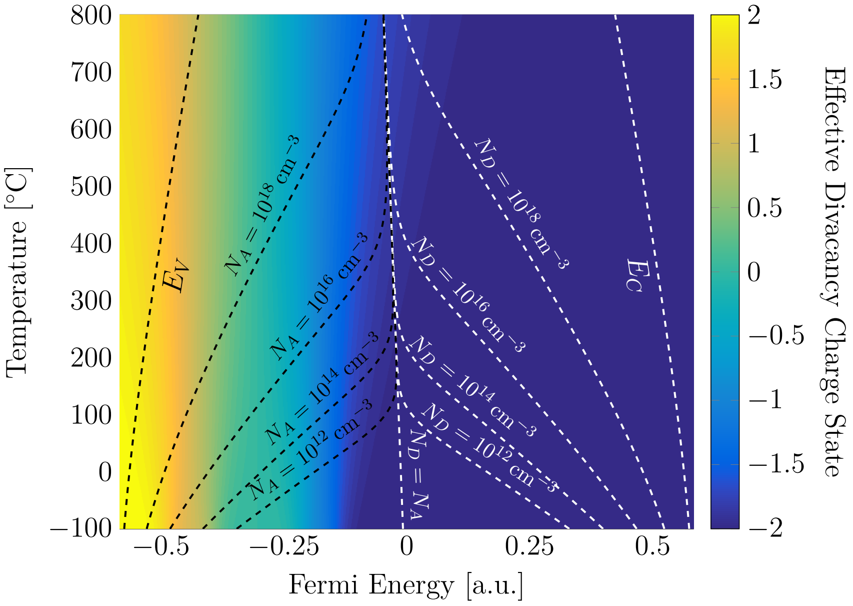

Figure 2.38: Map of the effective charge state of the divacancy in silicon as a function of the temperature and the position of the Fermi energy in the band gap. The temperature dependence of E_V, E_C and E_F at different doping concentrations is included.

In n-type silicon $q_{\mathrm{V}_2}^{\mathrm{eff}}$ is close to -2 over the whole temperature range between -100 °C and 800 °C. The closer the Fermi energy is shifted towards the valence band, the higher becomes $q_{\mathrm{V}_2}^{\mathrm{eff}}$. Figure 2.39 shows the effective charge state of the silicon divacancy as a function of the inverse temperature for different donor and acceptor concentrations. This representation assumes that the divacancy concentration is much smaller than the doping concentration, and hence, does not influence the position of the Fermi energy in the band gap.

In intrinsic silicon $q_{\mathrm{V}_2}^{\mathrm{eff}}$ is -2 at low temperatures and slightly increases to about -1.7 at 800 °C. In n-type silicon, the effective charge state is similar to the intrinsic level. Only at higher donor concentrations ($10^{16}\,\mathrm{cm}^{-3}$), the temperature range at which the effective charge state is retained at -2 is increased. In p-type material at an acceptor concentration of $10^{12}\,\mathrm{cm}^{-3}$ $q_{\mathrm{V}_2}^{\mathrm{eff}}$ is slightly negative at very low temperatures and decreases with increasing temperature until it converges to the intrinsic level at around 90 °C. The effective charge state at low temperature increases with the acceptor concentration. At the same time, the point at which $q_{\mathrm{V}_2}^{\mathrm{eff}}$ approaches the intrinsic level shifts towards higher temperatures.

The Arrhenius parameters of the diffusivity of the silicon divacancy were determined from the reaction kinetics of the reaction $\mathrm{V}_2 + \mathrm{O} \rightarrow \mathrm{V}_2\mathrm{O}$ in n-type silicon [69, 74]. Both, Pellegrino et al. and Mikelsen et al. report an activation energy of the diffusion of the divacancy of 1.3 eV, which agrees with the molecular dynamics simulations by Prasad and

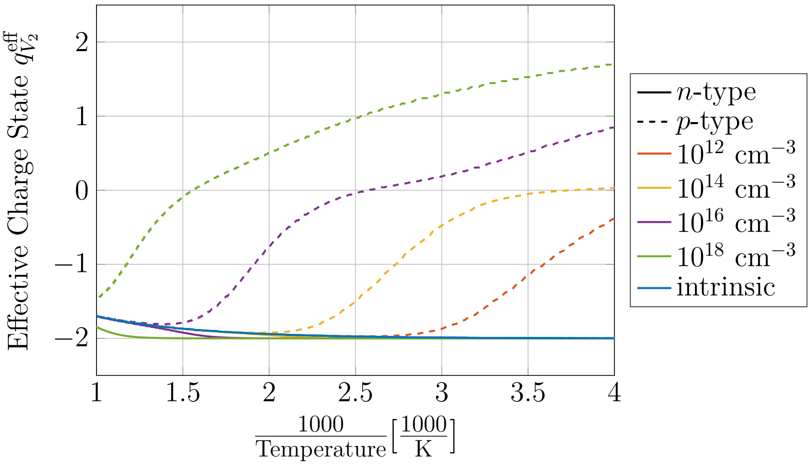

Figure 2.39: Temperature dependence of the effective charge state of the divacancy in silicon at different doping concentrations.

Sinno [75]. Furthermore Mikelsen et al. found a pre-factor of $3{\times}10^{-3}\,\text{cm}^2\text{s}^{-1}$. As the measurement of the divacancy diffusivity was carried out in n-type silicon, the diffusing species is most probably V_2^{2-}. Ganagona et al. calculated the diffusivity of the divacancy in p-type material, also using the reaction of V_2 and O to V_2O. They found similar Arrhenius parameters as Mikelsen et al. ($E_A = 1.31\,\text{eV}$ and $D_0 = 1.5{\times}10^{-3}\,\text{cm}^2\text{s}^{-1}$) [71]. The resistivity of the material investigated in their study was 6 Ωcm which corresponds to an acceptor concentration of approximately $2{\times}10^{15}\,\text{cm}^{-3}$. At the temperatures they used for the anneals (200 °C-300 °C) the charge state of the divacancy is either neutral or negative (see figure C.2.2a). Unfortunately, the diffusivity of the positive charge states of the divacancy still remains unknown. The temperature dependence of the diffusivity of V_2 is shown in figure 2.44. Compared to the diffusivities of the single vacancy and the self-interstitial it is rather small.

2.3.1.3 Silicon Tri-vacancy V_3 and Vacancy Clusters

A divacancy can react with a further vacancy and produce a trivacancy V_3 (see appendix C.3). This type of intrinsic defect was first used for interpreting EPR measurements by Lee and Corbet [76]. Markevich et at. measured the trivacancy using Laplace-DLTS and correlated their findings to pseudopotential DFT calculations [77]. In a subsequent calculation, Coutinho et al. found the ionization energies of the charge state transitions of V_3 and the corresponding relative formation energies [78]. The temperature dependence of the relative formation energies and the ionization energies are plotted in figure 2.40 and are listed in the table in figure C.3.1a.

The trivacancy shows two negative-U systems as there are direct transitions from V_3^{+2} to V_3^0 and from V_3^0 to V_3^{2-}. In figure C.3.1 the relative concentration of each charge state is plotted as a function of the Fermi energy and the temperature. Throughout most of the silicon band gap and the temperature range from -100 °C to 800 °C, the neutral state of the trivacancy is the dominant charge state. Only if the Fermi energy is close to the valence or conduction band, the doubly charged states show the highest relative concentrations.

In both, intrinsic and silicon doped below $10^{16}\,\mathrm{cm}^{-3}$, only the neutral charge state of the trivacancy is present. Only if the doping concentration is rather high ($10^{16}\,\mathrm{cm}^{-3}$ in n-type and $10^{18}\,\mathrm{cm}^{-3}$ in p-type material), the doubly charged states are dominant. As a consequence, also the effective charge state of the trivacancy only differs from zero if the doping concentrations are high.

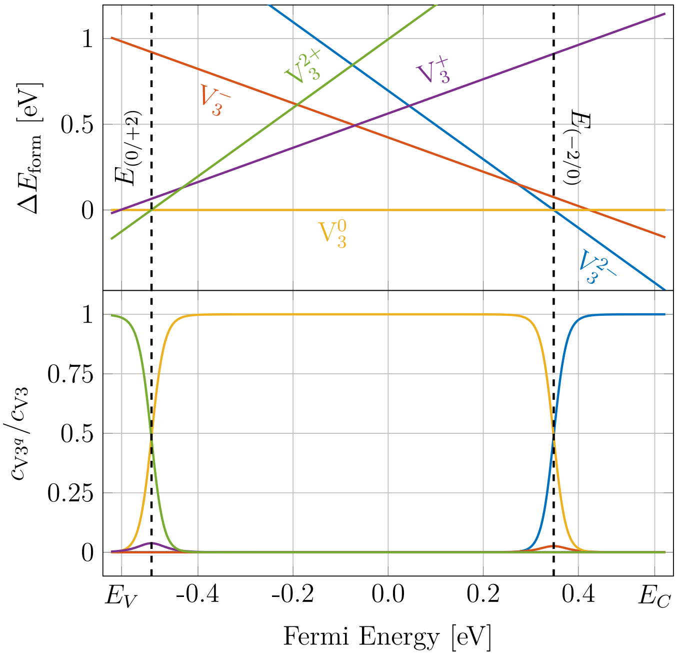

Figure 2.40: Relative formation energies and relative concentrations of the different charge states of the trivacancy in silicon as a function of the Fermi energy at 25 °C. The relative formation energies at $E_F = 0$ were calculated from ionization energies published in reference 78. The experimentally observable ionization energies are indicated by dashed lines.

As it has been pointed out by Prasad et al. the trivacancy is a mobile defect [75]. Using molecular-dynamics simulations, a diffusivity of $2.2\times10^{-6}\,\mathrm{cm}^2\mathrm{s}^{-1}$ was calculated for a temperature of 1600 K. Markevich et al. determined an activation energy for the trivacancy diffusion of 1.47 eV interpreting DLTS measurements and using DFT simulations [79]. The combination of both findings, yields an Arrhenius pre-factor for the trivacancy diffusion of $1.0\,\mathrm{cm}^2\mathrm{s}^{-1}$. The temperature dependence of the diffusivity of V_3 is included in figure 2.44. At temperatures higher than 100 °C, the diffusion of V_3 is faster than that of the divacancy.

If high vacancy concentrations are present, larger vacancy complexes, such as the tetravacancy V_4, pentavacancy V_5 and hexavacancy V_6 are formed [5]. Many of these open volume defect complexes were measured in positron annihilation experiments [80–82]. Different simulation methods have been used to calculate the energy reduction of the system due to the formation of vacancy agglomerates [75, 83, 84]. Especially the hexagonal ring structure of the hexavacancy shows a very high stability [85]. Prasad et al. also argue that vacancy cluster with up to ten vacancies are mobile. They calculated diffusion coefficients between $10^{-7}\,\mathrm{cm}^2\mathrm{s}^{-1}$ and $10^{-5}\,\mathrm{cm}^2\mathrm{s}^{-1}$ for different vacancy clusters at a temperature of 1600 K using molecular-dynamics simulations [75]. Unfortunately the temperature dependence of the diffusivity of these clusters has not been determined, so their diffusivity at lower temperatures remains unknown and those defects are treated as immobile species in further calculations.

2.3.1.4 Silicon Self-Interstitial

The self-interstitial I (see appendix C.4) is the second intrinsic point-defect in crystalline silicon. Due to the nature of the self-interstitial, which is already mobile at temperatures below 5 K [86, 87], it tends to quickly react with other defects. Hence, it is extremely difficult to directly observe the silicon self-interstitial experimentally. While vacancies can be measured directly using EPR, interstitials are rather observed indirectly through interstitial impurities such as interstitial carbon C_i, which is formed by the reaction of substitutional carbon C_s with silicon self-interstitials [88].

There are several different sites which the self-interstitial can occupy in the silicon lattice. As described by Watkins et al. the interstitial can be found at tetrahedral (T-site) or hexagonal sites (H-site), as well as at bond-centered positions or at split sites (X-site), where two interstitial atoms “share” one substitutional site [86]. Several ab-initio calculations of the formation energies of each charge state of the self-interstitial have been performed [89, 90], which come to different conclusions. In figure 2.41 the results of the two studies performed by Lee et al.[89] and by Lopez et al.[90] are compared. The formation and ionization energies used to generate the figure are listed in table in figure C.4.1a. While Lee applied pseudopotential calculations, Lopez used DFT for the calculation of the relative formation energies. In both studies, the relative formation energies of the charge states I^{2-} to I^{2+} were calculated for three different lattice sites (H-site, T-site and X-site). While Lee found a negative-U system between I^{2+} and I^{-}, Lopez calculations predict stable configurations of all charge state from I^{2+} to I^{-} at different energy ranges in the silicon band gap. As the calculations by Lopez et al. are more recent, than the work of Lee et al., further calculations in this thesis involving the charge state of the silicon self-interstitial will use the results published by Lopez as input data.

At Fermi energies close to E_V, I^{2+} at the tetrahedral lattice site is the dominant state of the silicon interstitial. If the Fermi energy is between -0.22 eV and 0.1 eV, the most stable state is I^{-} at the tetrahedral position. The neutral state showing the lowest formation energy is the one at the [110]-split site and it is the dominant state of the interstitial defect at Fermi energies between 0.1 eV and 0.45 eV. If the Fermi energy is even closer to the conduction band edge, I^{+} at the split site is the most stable configuration of the silicon self-interstitial.

In figure 2.41 the relative concentration of each charge state of the interstitial is plotted as a function of the Fermi energy and the temperature. Applying the simulation results by Lopez et al.[90], there is an energy range within the band gap, where each charge state, from I^{-} to I^{2+}, is the dominant state of the self-interstitial. I^{2-}, on the other side, never shows the highest relative concentration.

If the interstitial concentration is assumed to be much lower than the doping concentration, the temperature dependence of the relative concentration of each charge state of the interstitial at a certain doping concentration can be calculated. This is shown in figure C.4.2a. In intrinsic silicon, I^{+} shows the highest concentration. At low temperatures, the concentrations of all other charge states are below 1 %. With increasing temperature, the concentration of both, I^0 and I^{2+} increases in such a way that at 800 °C, the concentrations of both are above 10 %. In n-type silicon at low doping concentration, I^0 overtakes the concentration of I^+ at low temperatures, before the concentrations approach the intrinsic ratio. This transition is shifted towards higher temperatures by increasing the donor concentrations. At high donor concentrations ($10^{18}\,\mathrm{cm}^{-3}$) and temperatures below 0 °C, I^- appears as the dominant charge state. In p-type silicon the concentration of I^{2+} overtakes that of I^+ and is the dominant charge state of the interstitial at low temperatures. The transition back to the intrinsic ratio is also shifted towards higher temperatures by increasing the acceptor concentration.

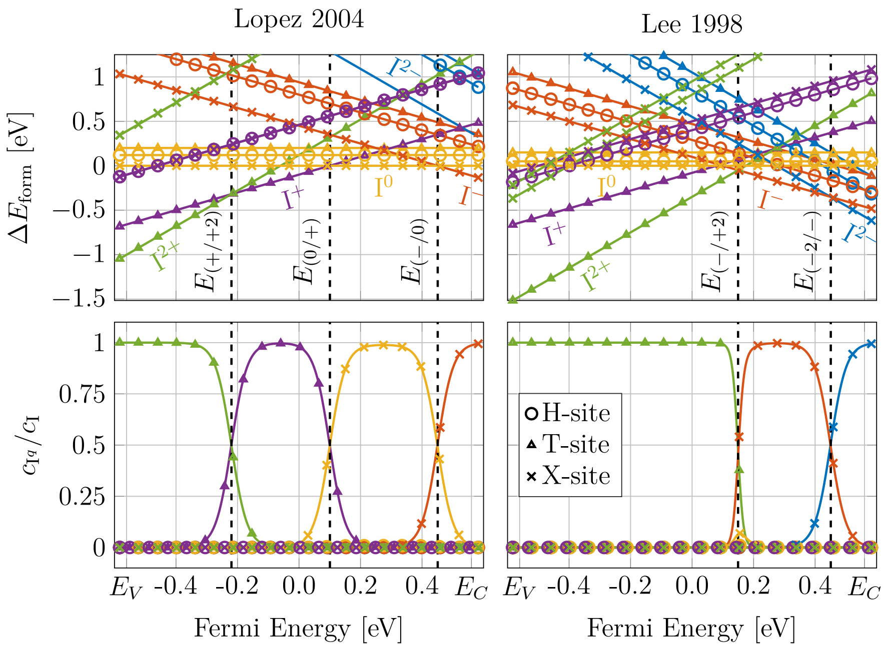

Figure 2.41: Relative formation energies and relative concentrations of the different charge states of the silicon interstitial at different lattice sites as a function of the position of the Fermi energy in the band gap at 25 °C as calculated by Lopez [90] and Lee [89]. The formation energies at $E_F = 0$ are plotted relative to the formation energy of I^0 at the [110]-split site. H: hexagonal site, T: tetrahedral site, X: [110]-split site.

Figure 2.42 shows a map of the effective charge state of the silicon self-interstitial calculated using equation 2.79. The figure also includes the temperature dependence of E_V, E_C and the Fermi energy at different doping concentrations.

At Fermi energies close to E_V the effective charge state is +2. At the center of the band gap $q_{\mathrm{I}}^{\mathrm{eff}}$ is +1 and close to the conduction band energy it converges to −1. In figure 2.43 the temperature dependence of the effective charge state of the interstitial is shown in silicon at different doping levels.

In intrinsic silicon the effective charge state of the self-interstitial is almost temperature independent and is close to −1 over a wide temperature range from -100 °C to 800 °C. In p-type material $q_{\mathrm{I}}^{\mathrm{eff}}$ starts out at +2 at low temperatures and converges to the intrinsic

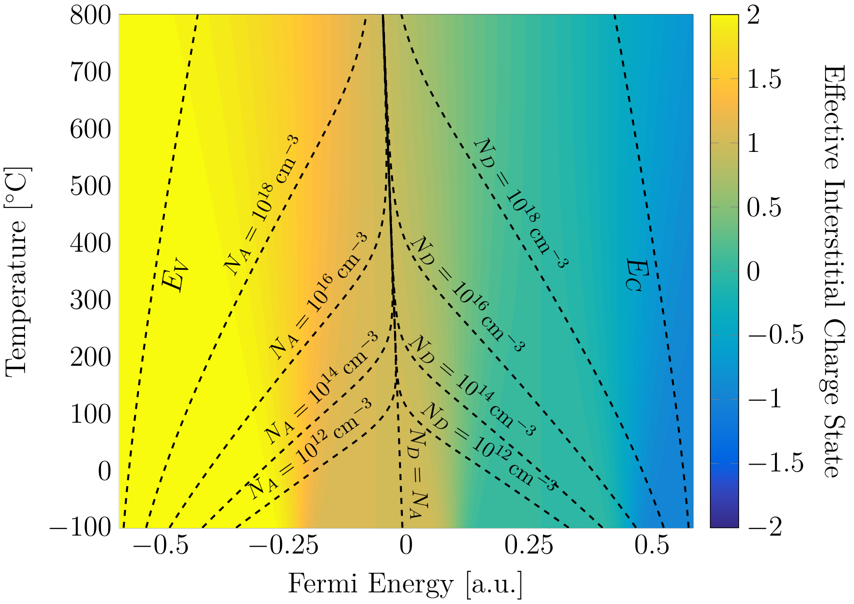

Figure 2.42: Map of the effective charge state of the silicon self-interstitial $q_{\mathrm{I}}^{\mathrm{eff}}$ as a function of the temperature and the position of the Fermi energy in the band gap. The temperature dependence of the valence and conduction band energies and of the Fermi energy at different doping concentrations are included.

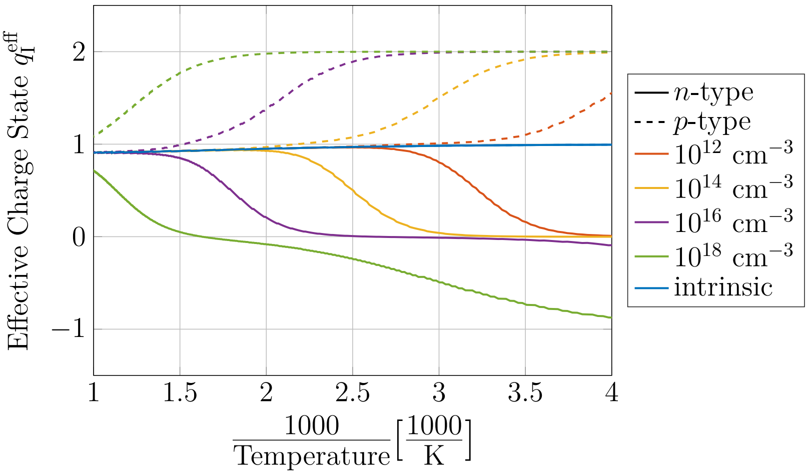

Figure 2.43: Temperature dependence of the effective charge state of the silicon self-interstitial $q_{\mathrm{I}}^{\mathrm{eff}}$ at different doping concentrations.

level of -1 for increasing temperatures. In n-type silicon at donor concentrations below $10^{16}\,\mathrm{cm}^{-3}$, $q_{\mathrm{I}}^{\mathrm{eff}}$ is 0 at low temperatures, before it approaches the intrinsic effective charge state as the temperature is increased. At higher donor concentrations the effective charge states also takes negative values before it first converges to 0 and afterwards to the intrinsic $q_{\mathrm{I}}^{\mathrm{eff}}$. All the transitions of $q_{\mathrm{I}}^{\mathrm{eff}}$ can be shifted towards higher temperatures by increasing the doping concentration.

Due to the high mobility and reactivity of the silicon self-interstitial, it is almost impossible to determine the diffusivities of its charge states separately. A large number of studies have been carried out to investigate the migration of interstitials and an excellent review of many of those studies is found in reference [5].

Panteleev et al. presented an experimental study [91] where they generated intrinsic point defects on one side of a sample by ion implantation and investigated their arrival on the other side of the material by photo-stimulated electron emission. In contrast to most other studies measuring the diffusivity of the self-interstitial, their investigation was carried out at lower temperatures (100-350 °C). They calculated an activation energy E_A of 0.12 eV and a pre-factor D_0 of $1.1\times10^{-6}\,\mathrm{cm}^2\mathrm{s}^{-1}$ describing the temperature dependence of the interstitial diffusivity. The study neglects the slowdown of the defect diffusivity due to reactions and it does not look at the separate charge states of the interstitial individually. Nevertheless, due to the lack of better data, the interstitial diffusivity, as published by Panteleev et al. is used to describe the diffusivity of all charge states of the self-interstitial in further calculations in this thesis.

Figure 2.44 shows a plot of the temperature dependence of the interstitial diffusivity using the Arrhenius parameters calculated by Panteleev at al. [91]. The figure also includes the diffusivity of the di-interstitial I_2 with an activation energy of 1.52 eV and a pre-factor of $0.38\,\mathrm{cm}^2\mathrm{s}^{-1}$) [92], the tri-interstitial I_3 with an activation energy of 0.49 eV and a pre-factor of $4\times10^{-5}\,\mathrm{cm}^2\mathrm{s}^{-1}$ [93] the divacancy (E_A: 1.3 eV and D_0: $4\times10^{-3}\,\mathrm{cm}^2\mathrm{s}^{-1}$) [69] and the trivacancy (E_A: 1.47 eV and D_0: $1.0\,\mathrm{cm}^2\mathrm{s}^{-1}$) [75, 79].

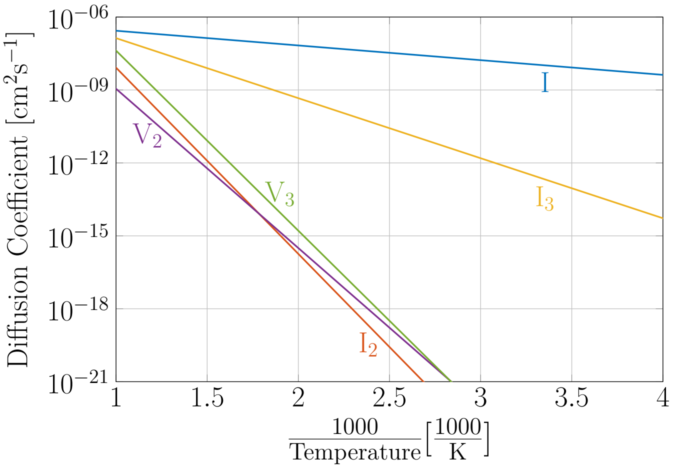

Figure 2.44: Diffusion coefficients of the silicon self-interstitial [91], the di-interstitial [92], the tri-interstitial [93], the divacancy [69] and the tri-vacancy [75, 79] as a function of the inverse temperature.

Table 2.10: Arrhenius coefficients describing the temperature dependence of the diffusion of different self-interstitial and vacancy complexes in silicon as reported in references [69, 75, 79, 91–93].

Species	E_A [eV]	D_0 [cm^{2}s^{-1}]	Reference
I	0.12	1.1×10^{-6}	[91]
I_2	1.52	3.8×10^{-1}	[92]
I_3	0.49	4.0×10^{-5}	[93]
V_2	1.3	4.0×10^{-3}	[69]
V_3	1.47	1.0×10^{0}	[75, 79]

As there is no data available, describing the diffusivity of each separate charge state, it is assumed in further calculations that all charge states of the self-interstitial share the same diffusion coefficient. It has to be emphasized, that this assumption is flawed. As Lopez et al. show, the activation energy of each charge state can in principle be calculated by evaluating the maximal difference in the formation energy of the defect along the migration path[90]. There is also a large number of other theoretical studies, calculating the activation energy of the diffusivity of the self-interstitial [94–96]. Unfortunately the results spread over a wide range and often the estimated errors of the calculations are large. Furthermore most studies lack the calculation of the pre-factor D_0.

2.3.1.5 Di-interstitial I_2, Tri-interstitial I_3 and Interstitial Clusters

Due to their high mobility, silicon self-interstitials tend to quickly react to form defect complexes already at low temperatures. Among these complexes are the di-interstitial I_2 (see appendix C.5) and the tri-interstitial I_3 (see appendix C.6). Different configurations of the di-interstitial have been experimentally determined using EPR [97–99]. Several theoretical investigations of these structures have been carried out using various methods [100–103]. The tri-interstitial is considered very stable, as molecular dynamics studies revealed a high binding energy of the interstitials in this complex [104]. Furthermore, I_3 was associated as the origin of a photoluminescence band measured by Giri et al. [105]. Several structures for the tri-interstitial have been proposed and their formation energies have been calculated [90, 106–109]. The results of the DFT simulations by Lopez et al. [90] were used to plot the temperature dependence of the relative formation energy of each charge state of the di-interstitial I_2 and the tri-interstitial I_3 and the corresponding relative concentrations (see figure 2.45). The corresponding formation- and ionization energies are listed in the tables in figures C.5.1a and C.6.1a.

According to the results of Lopez et al. I_2 belongs to the group of negative-U-defects, as it shows a direct transition from I_2^{2+} to I_2^0. In the case of I_3 no negative U-system has been reported and the defect shows usual transitions from I_3^{2+} to I_3^+ and I_3^+ to I_3^0. For both, the di-interstitial and the tri-interstitial, no negative charge states are stable for Fermi energies within the band gap of silicon.

The neutral state is the most stable charge state in both, the di- and tri-interstitial throughout most of the band gap. In intrinsic silicon, as well as in *n*-type and in *p*-type material the neutral states are the only charge states present at significant concentrations.

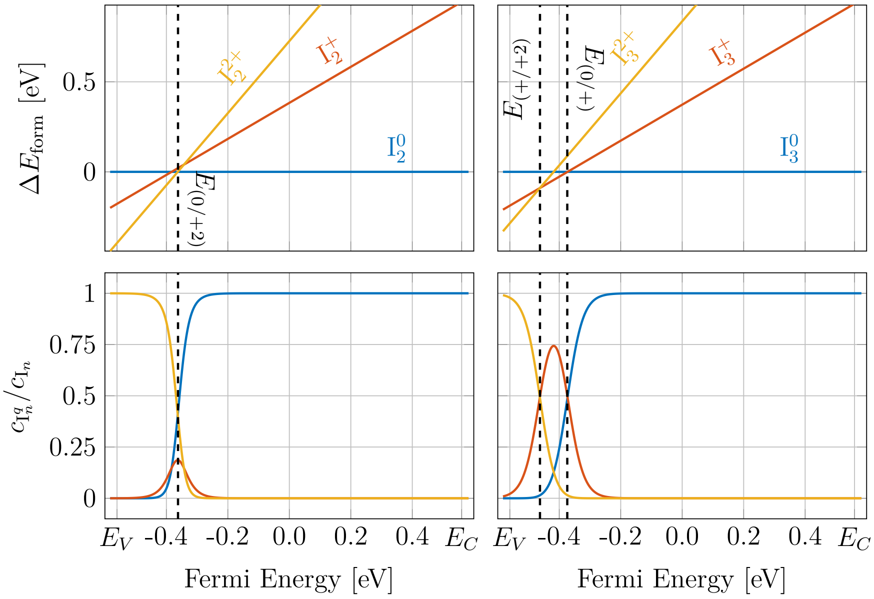

Figure 2.45: Relative formation energy and relative concentration of the each charge state of the di-interstitial and the tri-interstitial in silicon as a function of of the position of the Fermi energy in the band gap at 25 °C. The relative formation energies at $E_F = 0$ were calculated using DFT simulations [90].

Only at acceptor concentrations above $10^{15}\,\mathrm{cm}^{-3}$ the positive charge states of both defect complexes appear.

Several theoretical investigations indicated that the di-interstitial [100, 102] and the tri-interstitial [93, 107, 108, 110] are mobile defects. The Arrhenius coefficients produced by these studies vary a lot. In further calculations in this thesis involving I_2, the Arrhenius coefficients, calculated by Hane et al. [92] and will be used. Their tight-binding molecular dynamics simulations yielded an activation energy of 1.52 eV and a pre-factor of $0.38\,\mathrm{cm}^2\mathrm{s}^{-1}$. Further calculations involving the diffusivity of I_3 will make use of the Arrhenius coefficients computed by Du et al. using tight-binding molecular dynamics paired with DFT simulations. Their calculations resulted in an activation energy of 0.49 eV and a pre-factor of $4\times10^{-5}\,\mathrm{cm}^2\mathrm{s}^{-1}$ [93]. The temperature dependent diffusivities of I_2 and I_3 are shown in figure 2.44. While the diffusivity of I_2 is comparable to that of the divacancy, I_3 is a much faster diffusing species.

Interstitials also form larger clusters such as tetra-, penta-, hexa- and octo-interstitials (I_4,I_5,I_6,I_8) [5], as well as larger defects such as rod-like {311}-defects [111, 112] or planar {111}-defects [113]. The stability and diffusivity of I_2 and I_3 might be one of the driving forces in the formation of extended interstitial clusters [93, 102].

2.3.2 Extrinsic Defects

Extrinsic point-defects are elements which are not part of the composition of a material. Many of these defects form energy states close to the valence or the conduction band and hence, can be used as dopants or recombination centers. Especially atoms belonging to group III and VI in the periodic table, such as boron, aluminum, phosphorus or antimony are used to change the electrical properties of silicon to a desired level. Other defects, such as oxygen or carbon, are unintentionally introduced into the material during the crystal growth (see section 2.2.1). Extrinsic point defects occupy substitutional or interstitial lattice sites (see figure 2.17) and react with other point defects to form defect complexes. While substitutional defects tend to be rather immobile, interstitial impurities can show high mobilities. Furthermore, in the presence of intrinsic point-defects, some immobile impurities form defect pairs with vacancies or interstitials which can then be mobile [5].

2.3.3 Oxygen

Silicon always contains traces of oxygen (see appendix C.7). The temperature dependence of the solubility of oxygen in silicon, as determined by Mikkelsen [114] is

$$[\mathrm{O}]_{\mathrm{sol}} = 9\times10^{22}\,\mathrm{cm}^{-3}\exp\left(-\frac{1.52\,\mathrm{eV}}{k_B T}\right) \tag{2.105}$$

In Czochralski-grown material, the oxygen is introduced from the silicon melt. Close to the melting temperature (1414 °C) the oxygen solubility is $2.5\times10^{18}\,\mathrm{cm}^{-3}$. As the material is cooled down rapidly, the solubility decreases which leads to an oxygen supersaturation. At room temperature oxygen is immobile but at elevated temperatures the oxygen atoms precipitate to agglomerates [115–117]. While in Czochralski grown material the oxygen concentration is usually higher than $10^{17}\,\mathrm{cm}^{-3}$, in FZ-material the oxygen content can be decreased to levels around $10^{15}\,\mathrm{cm}^{-3}$ [118].

In the silicon lattice oxygen atoms occupy interstitial positions [5] and throughout the whole band gap, O^0 is the most stable charge state. Figure 2.46 shows the formation energies of the charge states of the oxygen interstitial in the silicon band gap, as calculated by Wang et al. using DFT simulations [119]. The formation energies used to create the figure are listed in the tables in figures C.7.1a and C.8.1a. Figure 2.46 also includes the formation energies of the charge states of the oxygen dimer O_2 (see appendix C.8), calculated from DFT simulations by Du et al. [120].

Not even if the Fermi energy is very close to E_V or E_C, other charge states than O^0 are present at significant concentrations. So, independent of the temperature and dopant concentration, the effective charge state of the oxygen interstitial $q_{\mathrm{O}}^{\mathrm{eff}}$ is 0. The oxygen dimer, on the other hand, shows a negative-U system. Du et al. found a direct transition from the 2+ state to the neutral state, which goes along with a change from a square to a staggered configuration [120].

The diffusion of oxygen in silicon has been an intensively studied topic for decades. For temperatures below 400 °C and above 700 °C, the Arrhenius coefficients have been determined with very good precision [5, 114, 121]. In these temperature regions, the activation energy for oxygen diffusion is 2.53 eV and the pre-factor is $0.16\,\mathrm{cm}^2\mathrm{s}^{-1}$. Figure 2.47 shows the temperature dependence of the oxygen diffusivity in silicon. The figure also includes the diffusivities of the oxygen dimer (E_A: 1.3 eV, D_0: $3\times10^{-4}\,\mathrm{cm}^2\mathrm{s}^{-1}$) [122], the vacancy oxygen complex VO (E_A: 1.8 eV, $D_0 = 6\,\mathrm{cm}^2\mathrm{s}^{-1}$) [74] and the diffusivity of the OH-complex (E_A: 2.0 eV, D_0: $7.1\times10^{-4}\,\mathrm{cm}^2\mathrm{s}^{-1}$) [123].

At temperatures between 400 °C and 700 °C, though, the oxygen diffusivity does not follow the Arrhenius law but shows a very strange temperature dependence [124, 125]. This

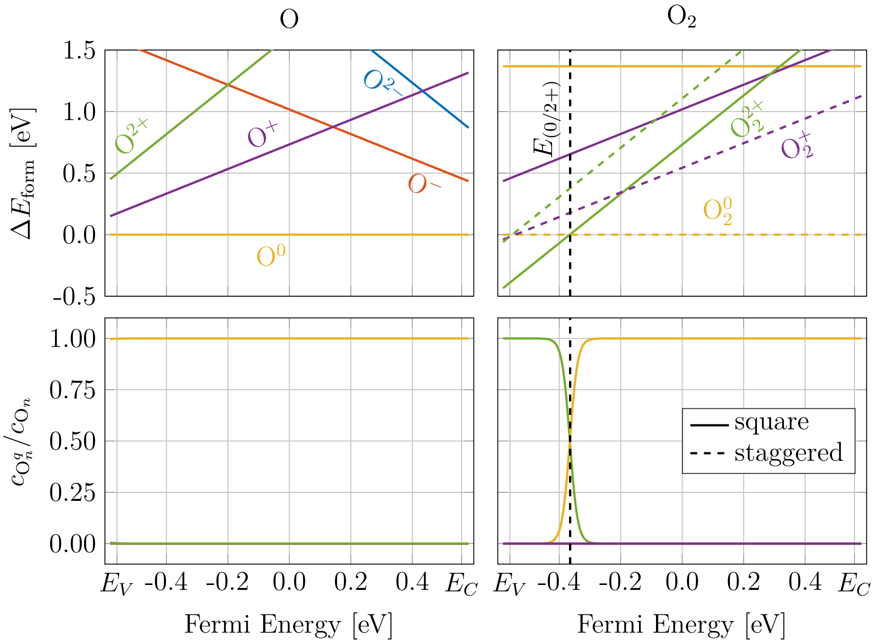

Figure 2.46: Formation energies and relative concentrations of the different charge states of the oxygen interstitial and the oxygen dimer in silicon as a function of the Fermi energy at 25 °C. The formation energies at $E_F = 0$ were calculated from formation energies published in reference 119 and 120.

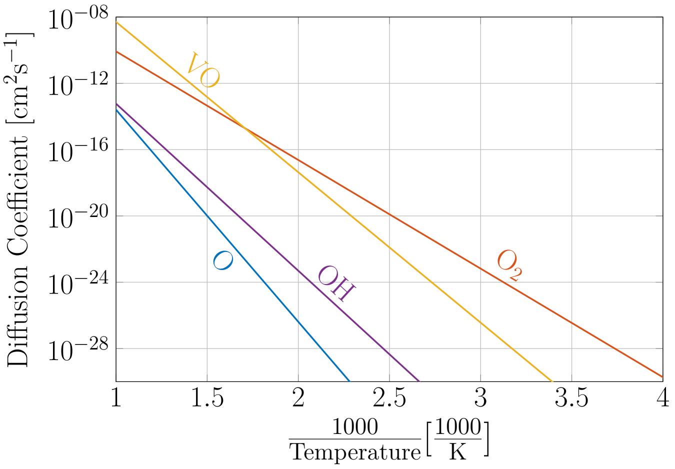

Figure 2.47: Diffusion coefficients of the oxygen interstitial [5], the oxygen dimer [122], the vacancy oxygen complex VO [74] and the OH-complex [123] in silicon as a function of the inverse temperature.

Table 2.11: Arrhenius coefficients describing the temperature dependence of the diffusion of different oxygen containing complexes in silicon as reported in references [5, 69, 74, 122, 123].

Species	E_A [eV]	D_0 [cm^{2}s^{-1}]	Reference
O	2.53	1.6×10^{-1}	[5]
O_2	1.3	3.0×10^{-4}	[122]
VO	1.8	6.0×10^{0}	[74]
OH	2.0	7.1×10^{-4}	[123]

temperature range also coincides with the appearance of the oxygen-related thermal-donors. Gösele at al. suggested an involvement of the fast diffusing oxygen dimer O_2 to explain experimental observations [126]. Åberg et al. estimated the diffusivity of the dimer to be about six orders of magnitude higher than that of atomic oxygen at 400 °C. Other fast diffusing defects containing oxygen, which could explain the high diffusivity in this temperature region are the vacancy oxygen complex VO [74] or the self-interstitial oxygen complex IO [30]. Furthermore, the presence of hydrogen leads to an enhanced diffusivity of oxygen, presumably through the formation of the faster diffusing OH complex [123, 127]. Straight oxygen chains are also mobile. Not only “short” chains containing two to nine oxygen atoms show low migration energies (0.4 eV-1.6 eV), but also longer oxygen chains might have a smaller migration energy than interstitial oxygen [128].

2.3.3.1 Thermal Donors

Already in the 1950’s Fuller et al. observed, that the resistivity of silicon can be changed by heat treatments at temperatures between 300 °C and 700 °C [129, 130]. While anneals around 450 °C lead to an increase of the electron concentration, a subsequent heat treatment caused a decrease. This effect was immediately attributed to the formation and dissociation of impurity defect complexes and there was broad agreement that oxygen had to play a crucial part in this effect [130, 131]. After annealing at temperatures between 600 °C and 900 °C, the formation of further, “new” thermal donors (NTDs) was observed [132, 133]. Until today the structure of these oxygen related thermal donors (OTD) is not completely resolved. Most certainly there is not only one type of thermal donor but there are several different defect complexes, consisting of different point defects. While some studies propose complexes containing self-interstitials alongside oxygen ($\mathrm{I_nO_m}$) [30, 134–136], others studied defects containing nitrogen or carbon and oxygen [137–141]. Other thermal donors consist solely of oxygen [31, 72, 131, 142, 143]

Electron nuclear double resonance (ENDOR) measurements by Meilwes et al. supported the concept that OTDs contain only oxygen. They also showed that the thermal donors observed in oxygen rich Czochralski-grown silicon are the same as in float zone material, where the oxygen content was increased by in-diffusion [144]. A pathway for the formation of oxygen agglomerates, acting as thermal donors was proposed by Ourmazd [145] and elaborated by Voronkov [146]. He proposed a process, where oxygen agglomerates grew by one oxygen monomer at a time, along with the emission of self-interstitials. The resulting agglomerate $\mathrm{O_nV_m}$ consists of n oxygen atoms, while m self-interstitials were generated in the process. As the diffusivity of interstitial oxygen is low, experimentally observed formation rates can only be explained by this process, if the agglomerates themselves are mobile [146]. Over time, it has been accepted, that most OTDs are chains of oxygen atoms [147] and there are at least 16 different species [32, 148]. This view has been strongly supported by theoretical calculations by Lee et al. which did not only show that straight oxygen chains are the most stable configuration of oxygen complexes, but also confirmed the mobility of these chains [128, 149].

Most oxygen related thermal donors are double donors. This means they posses a negative U-system, as there is a direct ionization from the neutral to the 2+ state. The observed ionization energies of OTDs lie between 30 meV and 250 meV [142, 150–154]. DFT simulations of the formation energies of the charge states of different OTDs by Pesola et al. also show negative U-systems for all investigated oxygen chains [155]. Investigations of the generation of thermal donors in high resistivity p-type material ($\rho > 10^3\,\Omega\mathrm{cm} \approx N_a < 1.5{\times}10^{13}\,\mathrm{cm}^{-3}$) even showed an overcompensation of the initial acceptor concentration and a conversion from p- to n-type doping after heat treatment [156–158].

2.3.3.2 Vacancy-Oxygen Complexes

Vacancy-oxygen defects are primarily generated by electron or ion irradiation. The VO-defect (see appendix C.9) was first identified using EPR [159, 160] and is referred to as the Si-A-center [161], or the Si-$B1$-center [162]. This defect can grow by consuming oxygen and/or vacancy atoms. A variety of different $\mathrm{V_mO_n}$ defects have been reported. Figure 2.48 shows the formation energies of each charge state of VO, $\mathrm{V_2O}$ (see also appendix C.10) and $\mathrm{V_3O}$ (see also appendix C.11) as a function of the Fermi energy. The formation energies of the VO-states were calculated from ionization energies published by Ferreira-Resende, computed by DFT [163] and the formation energies of $\mathrm{V_3O}$ were derived from ionization energies published by Markevich et al. [164]. The formation energies of $\mathrm{V_2O}$ were plotted from ionization energies calculated by Ferreira-Resende [163] and measured by Ganagona et al. [70].

All three defects show acceptor levels close to the conduction band. The VO defect levels agree very well with the studies of Bemski and Watkins. Both found an ionization energy for VO of about $E_C - 0.15\,\mathrm{eV}$ [159, 160] which corresponds to an ionization energy of 1 eV relative to E_V. The computed value (0.69 eV) of the ionization energy of $\mathrm{V_2O}$ agrees very well with the ionization energy of the Si-$A14$- center ($E_C - 0.5\,\mathrm{eV}$) which Lee at al. attributed to the $\mathrm{V_2O}$ complex [165]. Furthermore, Ganagona et al. found a donor level of $\mathrm{V_2O}$ at an energy of 0.23 eV. Various other computational studies have been performed to find the most stable configurations of VO and $\mathrm{V_2O}$. Both, Pesola et al. [166] and Wang et al. [119] found stable configurations of $\mathrm{VO^{2-}}$, but the ionization energies they calculated strongly deviate from experimental findings. Markevich et al. identified several ionization energies of $\mathrm{V_3O}$ which they confirmed with pseudo-potential DFT calculations. Using photo-induced EPR, Lee et al. identified also $\mathrm{V_3O_2}$ (0.4 eV and 0.77 eV) and $\mathrm{V_2O_2}$ (0.4 eV and 0.77 eV) as electrically active defects [165].

Experimental [167] and theoretical studies [168] show that $\mathrm{VO_2}$ is an electrically inactive complex, as its neutral state is the most stable charge state throughout the silicon band gap. Also $\mathrm{VO_3}$ is considered electrically inactive [167].

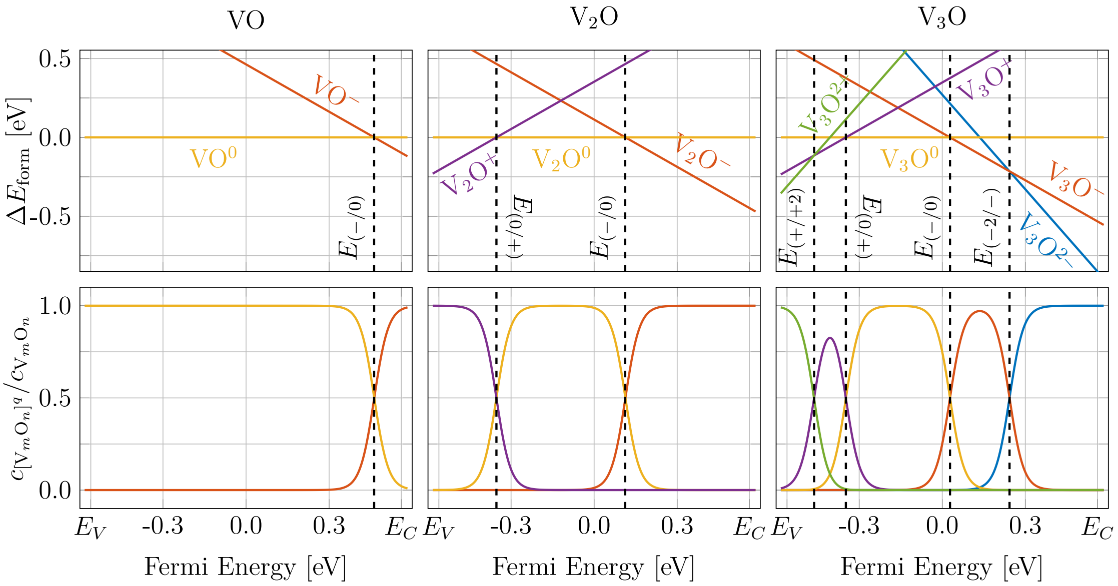

Figure 2.48: Formation energies and relative concentrations of the different charge states of VO, V_2O and V_3O in silicon as a function of the position of the Fermi energy in the band gap at 25 °C. The formation energies at $E_F = 0$ were calculated from ionization energies published in references 163, 164 and 70.

Vacancy-oxygen complexes can be a location of indirect recombination of intrinsic point defects, leading to the generation of e.g. oxygen dimers [169] in the reaction

$$VO_2 + I \rightarrow O_2. \tag{2.106}$$

Some V_mO_n-complexes might be mobile. Pellegrino et al. proposed a pre-factor of $6\,\mathrm{cm^2 s^{-1}}$ and an activation energy of 1.8 eV for the diffusivity of VO [74]. A similar activation energy (1.84 eV) was calculated by Grönberg et al. using molecular dynamics simulations [170]. Other studies also suggest that V_2O could be mobile [171].

2.3.3.3 Self-Interstitial-Oxygen Complexes

At the same time as vacancy-oxygen complexes form, also self-interstitial-oxygen defects are generated. Compared to the V_mO_n defects, though, I_nO_m-complexes have been studied less intensively. Interstitial oxygen defects were thought of as a candidate for OTDs [30, 135, 136]. Investigating IO and IO_2, Deak et al. found a $(0/+2)$ transition close to the conduction band using semi-empirical calculations [30, 172]. Markevich et al., on the other hand, attributed a donor level closer to the valence band ($E_V + 0.255\,\mathrm{eV}$) to the $(0/+2)$-transition of IO_2 [173]. Additionally they found an acceptor level at $E_C - 0.11\,\mathrm{eV}$ which they first interpreted as the $(-/0)$ transition of IO_2. Later, using DLTS experiments and DFT simulations, Markevich et al. attributed a similar donor level (0.11-0.13 eV) to the ionization of I_2O [174]. Further I_nO_m-complexes discussed in literature are IO_3, I_2O_3 [135] and I_2O_2 [175].

There has not yet been a lot of research on the diffusivity of I_nO_m-complexes, though some studies argue that the IO-complex might be very mobile [30, 176, 177].

2.3.4 Carbon

Another important impurity which is always present in silicon is carbon. While the carbon concentration in epitaxially grown silicon can be as low as $10^{14}\,\mathrm{cm^{-3}}$ [178] concentrations in Cz- and FZ-material lie between $10^{16}\,\mathrm{cm^{-3}}$ and $5{\times}10^{17}\,\mathrm{cm^{-3}}$ and usually originate from the polycrystalline starting material [5, 179, 180]. In silicon, carbon resides on substitutional lattice sites $\mathrm{C_s}$ (see appendix C.12), but it can be converted to mobile interstitial carbon $\mathrm{C_i}$ (see appendix C.13) by exchange reactions with self-interstitials [181, 182]. Substitutional carbon is electrically inactive. DFT simulations by Windl et al. showed an acceptor level close to, or even above the conduction band edge [183]. Interstitial carbon, on the other hand, shows an acceptor and a donor transition within the band gap [163, 184, 185]. Figure 2.49 shows the relative formation energy of each charge state of $\mathrm{C_s}$ and $\mathrm{C_i}$ as a function of the Fermi level including the relative concentration of each charge state at 25 °C. The ionization and formation energies used to create the plots are listed in the tables in figure C.12.1a and C.13.1a.

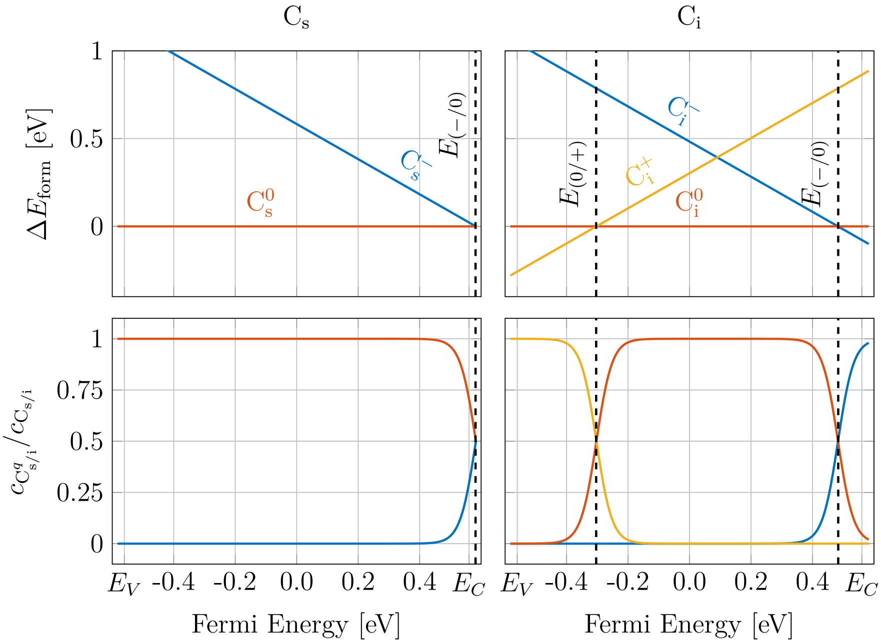

Figure 2.49: Formation energies and relative concentrations of the different charge states of substitutional ($\mathrm{C_s}$) and interstitial carbon ($\mathrm{C_i}$) in silicon as a function of the Fermi energy at 25 °C. The formation energies at $E_F = 0$ were calculated from ionization energies published in reference 183, 184 and 163.

The temperature dependence of the diffusion of substitutional carbon in silicon is described by an activation energy of 3.29 eV and a pre-factor of $6.11\,\mathrm{cm^2s^{-1}}$. This is an effective diffusivity, as $\mathrm{C_s}$ itself is assumed to be immobile. It rather reacts with silicon self-interstitials forming $\mathrm{C_i}$ which then diffuses, until it is captured by a vacancy and falls back on a substitutional lattice position [5, 181, 182]. In different studies the diffusivity of the neutral charge state of $\mathrm{C_i}$ was investigated [186–189]. Combining these studies yields an activation energy of 0.84 eV and a pre-factor of $0.17\,\mathrm{cm^2s^{-1}}$ for the temperature dependent diffusivity of $\mathrm{C_i^0}$. In reference 5 Pichler calculated the diffusivities of $\mathrm{C_i^+}$ and $\mathrm{C_i^-}$ from measurements by Song et al. [190]. The Arrhenius coefficients calculated from those diffusivities are listed in table 2.12. The temperature dependence of the diffusivity of each charge state of $\mathrm{C_i}$ and of the effective diffusivity of $\mathrm{C_s}$ is shown in figure 2.50.

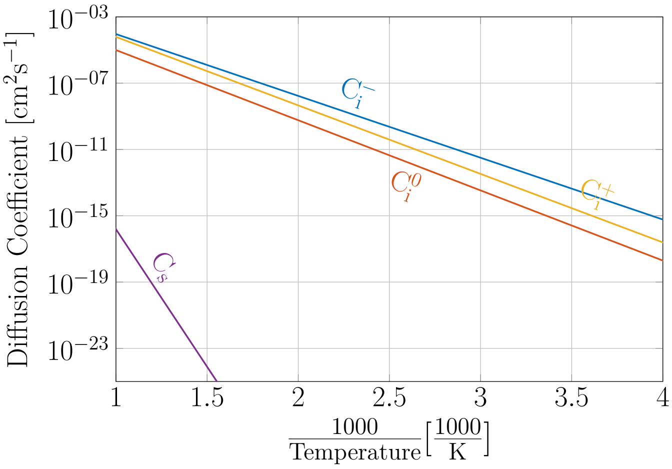

Figure 2.50: Diffusion coefficients of each charge state of the carbon interstitial $\mathrm{C_i}$ in silicon as a function of the inverse temperature [5, 186–190].

Table 2.12: Arrhenius coefficients describing the temperature dependence of the diffusion of interstitial carbon $\mathrm{C_i}$ [186–190] and the effective diffusivity of substitutional carbon $\mathrm{C_s}$ [5].

	E_A [eV]	D_0 $[\mathrm{cm^2s^{-1}}]$
$\mathrm{C_i^-}$	0.74	0.49
$\mathrm{C_i^0}$	0.84	0.17
$\mathrm{C_i^+}$	0.82	0.84
$\mathrm{C_s}$	3.29	6.11

The plot shows, that the diffusion coefficients of $\mathrm{C_i}$ are more than ten orders of magnitude faster than the effective diffusivity of $\mathrm{C_s}$. Furthermore, it can be observed, that the neutral state of the carbon interstitial is a slower diffuser than the charged states.

As interstitial carbon is present at different charge states and each charge state has its own diffusivity, an effective diffusivity $D_{\mathrm{C_i}}^{\mathrm{eff}}$ depending on the doping concentration can be calculated. This calculation is only valid, if the concentrations of the charged states of the carbon interstitial are much lower than the doping concentration. Otherwise, the charged states of $\mathrm{C_i}$ have to be included in the calculation of the Fermi energy (see equation 2.83). Figure 2.51 shows the relative diffusivity of $\mathrm{C_i}$ for different doping concentrations.

In intrinsic silicon, only the neutral charge state of $\mathrm{C_i}$ is populated. As soon as charged states get occupied, $D_{\mathrm{C_i}}^{\mathrm{eff}}$ increases. The higher the doping concentration the higher is the effective diffusivity of $\mathrm{C_i}$. For the same doping concentration at low temperatures, $D_{\mathrm{C_i}}^{\mathrm{eff}}$ is

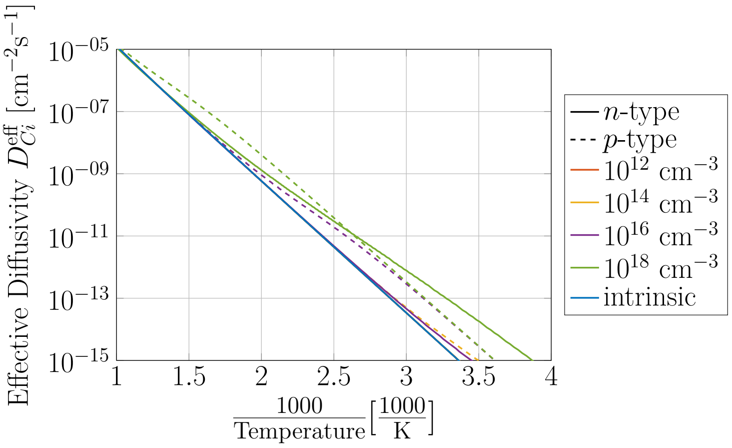

Figure 2.51: Temperature dependence of the effective diffusivity of interstitial carbon C_i at different doping concentrations.

higher in n-type than in p-type material. At higher temperatures, on the other hand, the effective diffusivity of C_i is higher in p-type silicon.

2.3.4.1 Carbon-Oxygen Complexes

As oxygen and carbon usually show the highest concentrations of all impurities in the active regions of power devices, the formation of defect complexes consisting of those two constituents is very obvious. Early investigations of carbon-oxygen complexes were made by Bean and Newman using IR-spectroscopy [191, 192]. Using DLTS, the donor state of C_iO (see appendix C.14) was measured to be between 0.32 eV and 0.4 eV above the valence band energy [189, 193–198]. This level coincides with theoretical calculations by Coutinho et al. [199] and Backlund [185], who found the transition from C_iO^+ to C_iO^0 at an energy of 0.364 eV and 0.37 eV, respectively, above E_V. Wang et al. found in a more recent study that also the double positive charge state of C_iO might be stable at Fermi energies slightly below the valence band [200]. Figure 2.52 shows the relative formation energy of each charge state of C_iO as a function of the Fermi energy and the corresponding relative concentrations of the charge states. The figure also includes the defect complexes C_iOH (see appendix C.15) and C_iO_2H (see appendix C.16) which are formed by the reaction of C_iO with hydrogen in proton-implanted material [141, 199] and are discussed in the section on proton implantation 2.4. The formation and ionization energies used to create figure 2.52 are listed in the tables in figures C.14.1a, C.15.1a and C.16.1a.

The donor level of C_iO lies between the mid gap and the valence band (0.36 eV) and, hence, compensates ionized acceptors. Both, C_iOH and C_iO_2H show negative-U systems and their donor transitions are much closer to the conduction band. These two defect complexes belong to the group of the "shallow thermal donors" STD [141]. Another candidate for being a member of this group is C_iOH_2, which was believed to have a donor transition at an energy of 0.075 eV from the conduction band [201]. Theoretical studies of this defect, though only showed the occupation of the neutral charge state throughout the whole band gap [199].

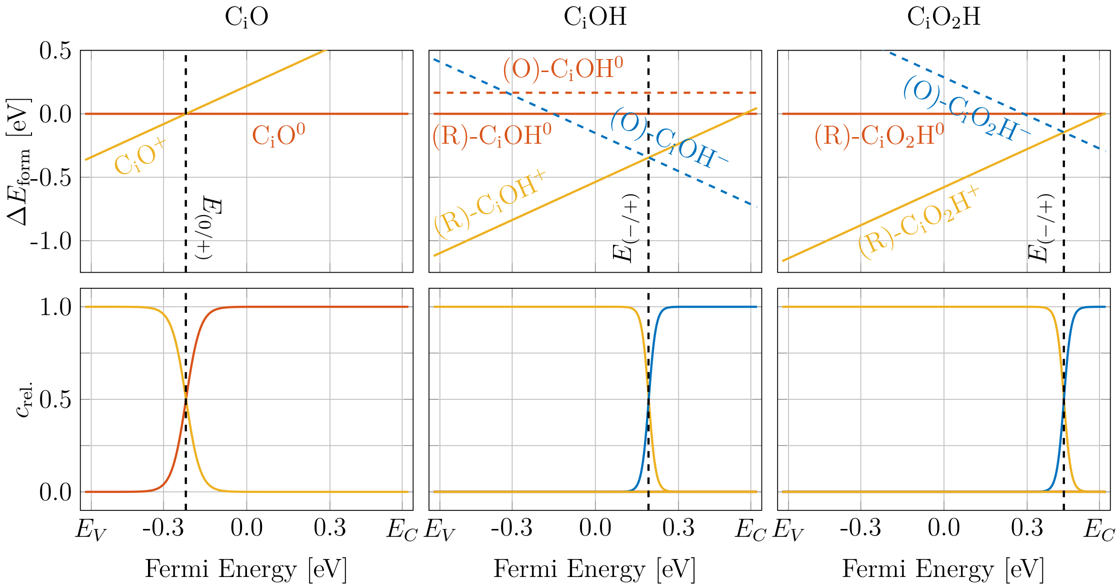

Figure 2.52: Formation energies and relative concentrations of each charge state of C_iO, C_iOH and C_iO_2H in silicon as a function of the position of the Fermi energy in the band gap at 25 °C. The formation energies at $E_F = 0$ were calculated from ionization energies published in reference 199. (R): ring structure and (O): open structure of C_iOH and C_iO_2H.

Different studies [169, 202, 203] also proposed the formation of defect complexes of substitutional carbon and oxygen formed by the following reactions:

$$\begin{aligned} C_i + VO &\rightarrow C_sO \\ C_i + VO_2 &\rightarrow C_sO_2 \\ C_iO + VO &\rightarrow C_sO_2 \\ C_i + VO_3 &\rightarrow C_sO_3 \end{aligned} \tag{2.107}$$

Intrinsic point defects can indirectly recombine by the reaction of C_s and I forming C_i which then can react with vacancies forming C_s again. In the same way, vacancies might react with complexes including interstitial carbon such as C_iO, yielding C_sO.

Some studies furthermore suggest that C_iO might be mobile [204, 205], but up to now, no theoretical calculations or experiments have been performed to prove this claim and, hence, no Arrhenius parameters describing the temperature dependence of the diffusivity of C_iO have been calculated yet.

2.3.4.2 Carbon-Carbon and Carbon-Silicon Complexes

Apart from oxygen, carbon also forms defect complexes with silicon self-interstitials. Here, an interstitial carbon C_i can capture either another silicon self-interstitials I to form C_iI_n [185, 200, 202, 206], or a substitutional carbon atom C_s resulting in the C_iC_s (see appendix C.19) complex [184, 187, 188, 197, 207]. A further growth of different defect complexes by adding silicon self-interstitials is also possible, resulting in defect complexes such as $\mathrm{C_iOI}$ (see appendix C.18) [185, 200, 202, 203, 208, 209], or $\mathrm{C_iC_sI}$ [185, 202, 206, 210] and even larger defect complexes [206, 210].

Using hybrid-DFT simulations, Wang et al. calculated the formation energies of each charge state from −2 to +2 of $\mathrm{C_iI}$ (see appendix C.17) and of different configurations of $\mathrm{C_iOI}$ and $\mathrm{C_iC_s}$ [200]. The resulting charge state distributions, including the formation energies of the different states as a function of the Fermi energy are shown in figure 2.53. The formation and ionization energies used to create the plots are listed in the tables in figures C.17.1a, C.18.1a and C.19.1a.

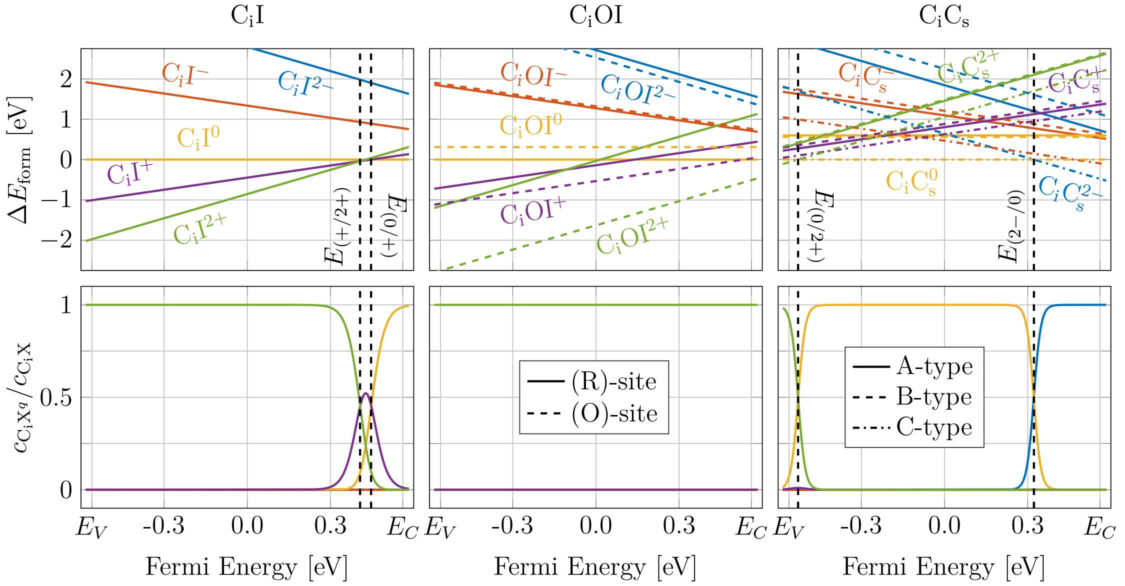

Figure 2.53: Formation energies and relative concentrations of each charge state of $\mathrm{C_iI}$, $\mathrm{C_iOI}$ and $\mathrm{C_iC_s}$ in silicon as a function of the position of the Fermi energy in the band gap at 25 °C. The formation energies at $E_F = 0$ were calculated from ionization energies published in reference 200.

According to the simulations by Wang et al. [200] $\mathrm{C_iI}$ shows two donor transitions close to the conduction band (0.99 eV and 1.04 eV, respectively). Hence, for most energies within the band gap, only the positive charge states of $\mathrm{C_iI}$ are present. Only if the Fermi energy is close to E_C, is the neutral state populated, while the negatively charged states are never stable.

Theoretical studies on the $\mathrm{C_iOI}$ defect, or "C4"-center by Backlund et al. predict three possible structures of the defect and predict a deep donor transition, around 0.1 eV from the valence band and an acceptor transition about 0.1 eV below E_C [185, 211]. Wang et al., on the other hand, found that the +2 state of the open-ring configuration (O)-$\mathrm{C_iOI}$ is the most stable state throughout the band gap [200] (see middle plot in figure 2.53).

The $\mathrm{C_iC_s}$-complex can be stable in several different configurations in the silicon crystal [212, 213]. Wang et al. labeled those configurations A-, B- and C-type $\mathrm{C_iC_s}$ and found that the C-type is energetically the most favorable configuration [200]. According to their simulations, $\mathrm{C_iC_s}$ has two negative-U systems, as they found direct transitions from the double positive to the neutral state and from the neutral to the double negative charge state.

Further carbon containing defect complexes are discussed in the next sections.

2.3.5 Boron

In the semiconductor industry, boron is one of the most commonly used impurities in silicon to establish p-type doping [5]. Boron usually resides on substitutional lattice sites B_s (see appendix C.20) [214, 215] and shows a donor transition which lies about 45 meV above E_V [216–221]. B_s tends to react with silicon self interstitials I which results in the formation of boron interstitials B_i (see appendix C.21) [5, 222, 223]. Contrary to boron at a substitutional lattice site, the boron interstitial acts as an acceptor in n-type material and as a donor in p-type material [223], showing a negative-U system [224]. The actual configuration of B_i has been under discussion for decades. The reaction of B_s and I can either yield a boron interstitial via the so-called “kick-out”-mechanism, or it can produce a defect complex consisting of a substitutional boron atom and a silicon self-interstitial (B_sI) [225, 226]. For simplification, B_sI is treated as just another configuration of B_i and not as a separate defect complex. Hakala et al. calculated the formation energies of the charge states of the boron interstitial at different lattice points (hexagonal, tetrahedral, split-configuration and bond-centered), including the relative formation energy of the charge states of B_sI using DFT-simulations [225]. According to their calculations, the interstitialcy-configuration (see figure 2.17g) shows the lowest formation energy for all charge states. Furthermore they found a direct transition from the positive to the negative state of B_sI. In figure 2.54 the formation energies of each charge state of B_s and B_i are plotted as a function of the Fermi energy within the band gap of silicon. Additionally the relative concentrations of the charge states at 25 °C are shown. In the tables in figures C.20.1a and C.21.1a, the formation and ionization energies are listed which were used to create the figure.

Apart from being added directly to the silicon melt during crystal growth (see section 2.2.1), boron can be introduced into the material by ion-implantation, by in-diffusion from a doped oxide or from the gas phase. If silicon layers are grown in an epitaxy process, boron can be directly added during the growth process [5]. Either way, to end up with the desired doping concentration profile, the diffusion of boron has to be considered. Including several different studies on the effective diffusion of boron in silicon at temperatures between 950 °C and the melting temperature of silicon, an activation energy of 3.645 eV and a pre-factor of $3.79\,\mathrm{cm^2 s^{-1}}$ were calculated [5].

An enhancement of the diffusion of boron can be observed, if the concentration of silicon self-interstitials is increased [227–229]. From this it can be deduced, that the major diffusing boron species is the boron interstitial. Using photo-induced EPR-measurements, Watkins measured an activation energy of 0.6 eV for the temperature dependence of the reorientation time of B_i [230]. He argued that the activation energy of the diffusion of B_i should be approximately the same. Later studies confirmed an activation energy in the range between 0.3 eV and 0.7 eV [231–235]. While some studies only consider the diffusion of a single charge state of B_i [226, 231, 232], Martin-Bragado et al. published Arrhenius parameters for each charge state of B_i [236], which they used to reproduce the effective boron diffusivity measured by Haddara et al. [237].

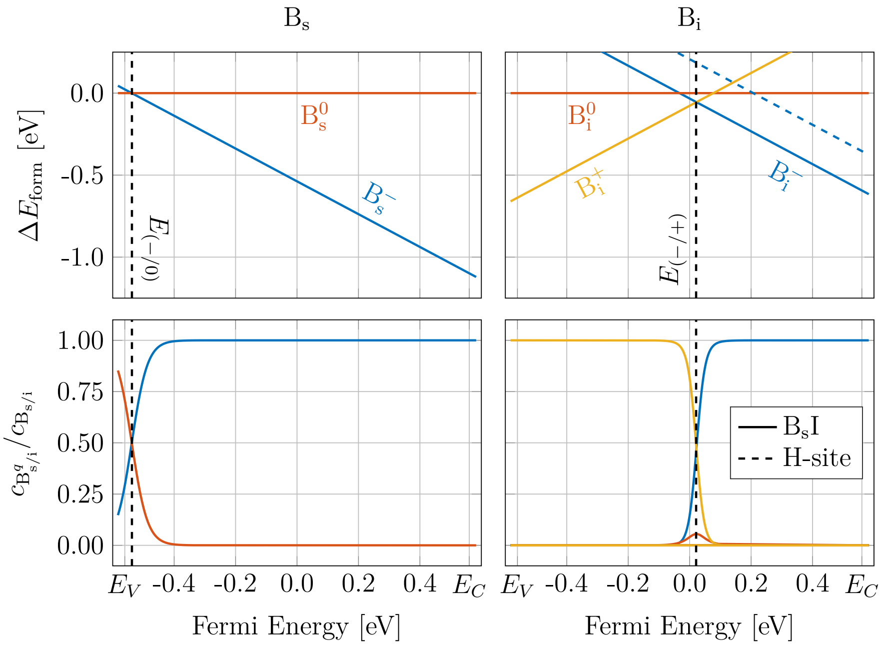

Figure 2.54: Formation energies and relative concentrations of the different charge states of substitutional (B_s) and interstitial boron (B_i) in silicon as a function of the Fermi energy at 25 °C. The formation energies of the charge states of B_s were calculated using an ionization energy $E_{(-/0)}$ of 45 meV. The formation energies of the different configurations and charge states of B_i were published in reference 225. Only the lowest energy configurations ($\Delta E_{form} < 0.2$ eV) are shown. H-site: B_i at a hexagonal lattice site.

Figure 2.55 shows the temperature dependence of the diffusivity of boron containing defects at different charge states. Apart from B_i, also B_sV [238] and B_iB_s [239] are considered to be mobile. Another presumably mobile boron containing defect complex is B_iH [240], though, no information on Arrhenius parameters describing the temperature dependence of its diffusion have been published yet. Figure 2.55 also includes the temperature dependence of the effective boron diffusivity under intrinsic conditions. The Arrhenius parameters used to create this figure are listed in table 2.13. The diffusivity of B_i is orders of magnitude higher than that of B_sV. Here, the neutral and negative charge states of B_i, according to Martin-Bragado et al. show higher diffusion constants than the positive charge state, in the temperature range below 1000 °C. In the depiction shown in figure 2.55, the diffusivity of the neutral charge state of B_sV is higher than that of the positive complex. As no report on a pre-factor of the Arrhenius equation describing the temperature dependence of the diffusion of B_sV^+ have been found, the same pre-factor as for B_sV^0 was assumed. As B_sV is only stable at low temperatures [241], its contribution to the overall boron diffusion is considered to be relatively small [242]. The diffusivity of B_iB_s at temperatures below 750 °C is lower than that of B_sV.

In comparison to the diffusivities of the different charge states of B_i, B_sV and B_iB_s the effective diffusivity of all boron compounds combined is orders of magnitude smaller. The migration of boron is primarily slowed down by reactions of the mobile species with intrinsic point defects (indirect recombination) [243, 244].

$$\begin{aligned} B_s + I &\leftrightarrow B_i \\ B_i + V &\leftrightarrow B_s \\ B_s + V &\leftrightarrow B_sV \\ B_sV + I &\leftrightarrow B_s \end{aligned} \tag{2.108}$$

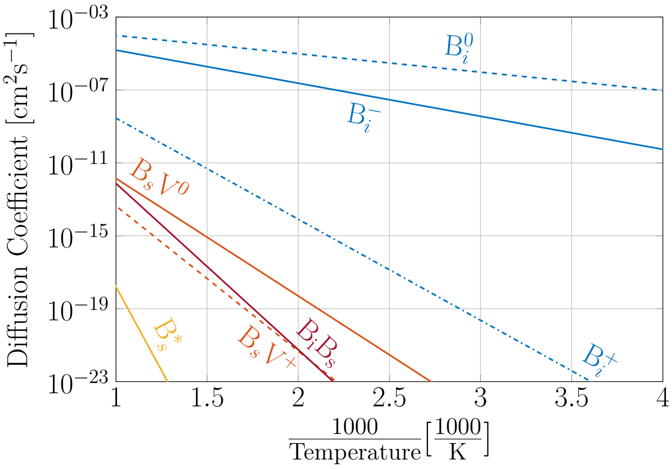

Figure 2.55: Diffusion coefficients of the charge states of different defect complexes containing boron in silicon as a function of the inverse temperature [236, 238]. The effective diffusivity of boron ($B_s{}^*$) as found in reference 5 is included.

Table 2.13: Arrhenius coefficients describing the temperature dependence of the diffusion of the charge states of different defect complexes containing boron, including the effective diffusivity of boron ($B_s{}^*$). **: values chosen by the author (no experimental, theoretical evidence).

	E_A [eV]	D_0 [cm^{2}s^{-1}]
B_i^-	0.36 [236]	1.0×10^{-3} [236]
B_i^0	0.20 [236]	1.0×10^{-3} [236]
B_i^+	1.10 [236]	1.0×10^{-3} [236]
B_sV^0	1.26 [238]	4.0×10^{-6} [238]
B_sV^+	1.58 [238]	$4.0\times10^{-6**}$
B_iB_s	1.81 [239]	1.0×10^{-3} [239]
B_s^*	3.645 [5]	3.79 [5]

Taking into account the concentration ratios of the different charge states of B_i and their corresponding diffusivities, the temperature dependence of the effective diffusivity of B_i can be calculated. In the same way as shown before (see figure 2.36), the effective diffusivity can further be calculated for different doping concentrations. This representation is only valid, if the concentration of B_i is much smaller than the doping concentration. If the

B_i concentration was on the same order of magnitude as the doping concentration it has to be taken into account in the calculation of the Fermi energy (see equation 2.83). The effective diffusivity of the boron interstitial $D_{B_i}^{eff}$ is shown in figure 2.56.

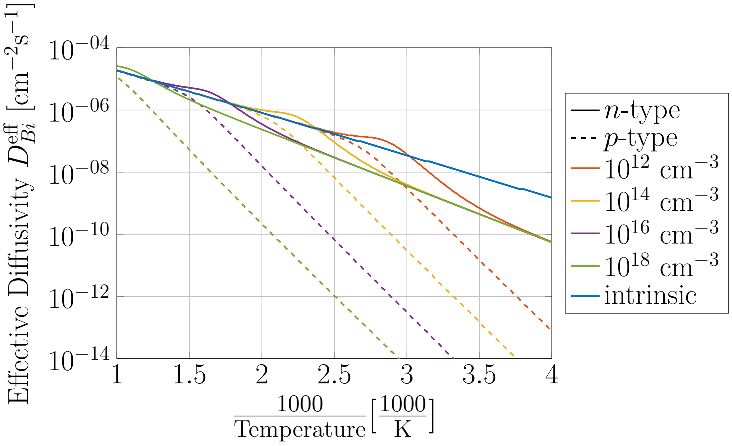

Figure 2.56: Temperature dependence of the effective diffusivity of interstitial boron $D_{B_i}^{eff}$ at different doping concentrations.

In intrinsic silicon, throughout the temperature range from -150 °C to 800 °C, the effective diffusivity of B_i can be described by an activation energy of 0.27 eV and a pre-factor of 4×10^{-4} cm^{2}s^{-1}. In n-type material, at low temperatures, the diffusivity of interstitial boron is smaller than its intrinsic diffusivity. Here, an activation energy of 0.36 eV and a pre-factor of 10^{-3} cm^{2}s^{-1} can be observed, which corresponds to the diffusivity of the negative charge state (which is the only one present under these conditions). At a certain temperature range, the the effective diffusivity approaches the intrinsic level. Within a small range of temperatures, $D_{B_i}^{eff}$ even overcomes the intrinsic level, as the population of the neutral charge state, which shows the highest diffusivity, becomes slightly more populated. The temperature range, where the transition from extrinsic to intrinsic conditions takes place, is shifted towards higher values by increasing the donor concentration. In p-type silicon $D_{B_i}^{eff}$ is always smaller than in n-type and in intrinsic material. Before the effective diffusivity of the boron interstitial reaches the intrinsic level, its temperature dependence is described by an activation energy of 0.91 eV.

2.3.5.1 Complexes Containing Boron and Intrinsic Defects

Substitutional boron impurities can interact with intrinsic point defects, forming the above mentioned, mobile defects B_i (see appendix C.21) and B_sV (see appendix C.22). B_sV is stable up to a temperature of around -15 °C [223, 245]. By either B_sV capturing another vacancy or, by the reaction of B_s with a divacancy V_2, the B_sV_2-complex (see appendix C.23) is formed. This defect complex is predicted to be stable up to temperatures around 300 °C [245]. Figure 2.57 shows the formation energies of the different charge states of B_sV and B_sV_2, calculated from ionization energies published by Adey et al. [245]. The figure includes the relative concentrations of each charge state of the defects, as well as, the relative concentrations of each configuration of the corresponding charge states.

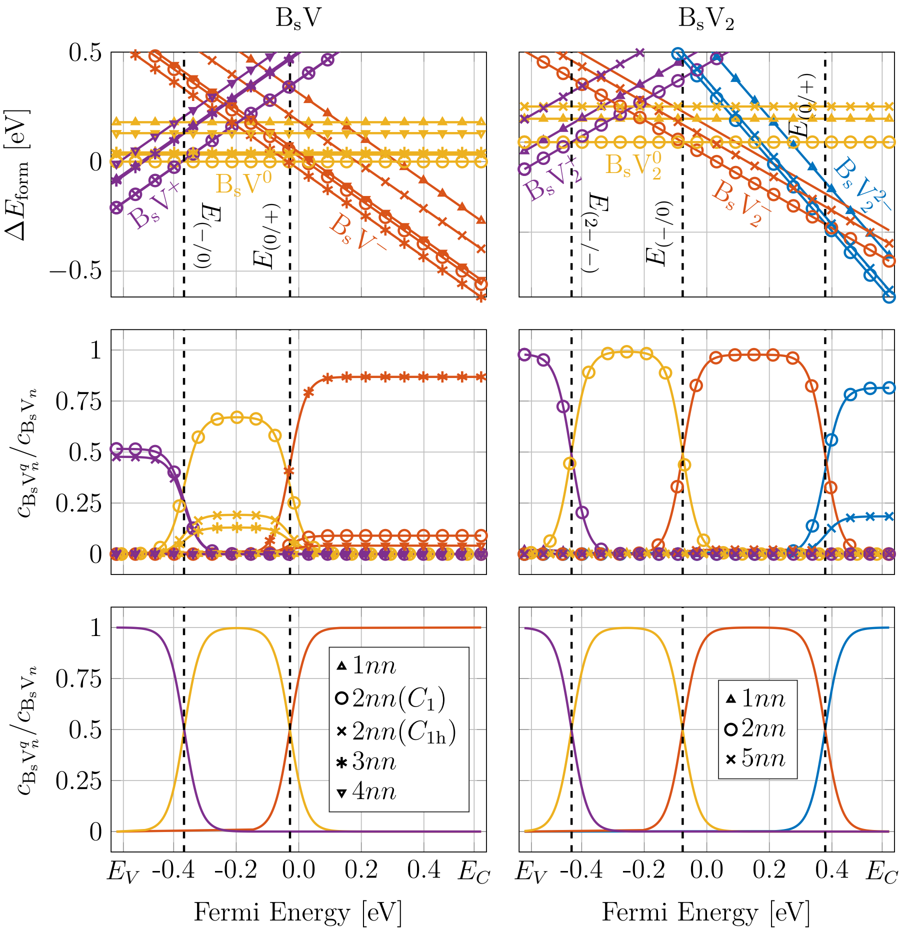

Figure 2.57: Formation energies and relative concentrations of B_sV and B_sV_2 in silicon as a function of the position of the Fermi energy in the band gap at 25 °C. The formation energies were calculated from ionization energies published by Adey et al. [245]. The legend entries represent different configurations of the defects described in reference 245.

In Adey's study [245], the energies of five different configurations of B_sV were calculated. In the positive charge state, the configurations $2nn(C_1)$ and $2nn(C_{1h})$ are the most stable ones. If B_sV is in its neutral state, three different configurations of the defect are populated. Here, the $2nn(C_1)$-configuration shows the highest concentration, followed by $2nn(C_{1h})$ and $3nn$. In the negative charge state mostly the $3nn$-configuration is populated, but some defect complexes are also found in the $2nn(C_1)$- and in the $4nn$-configuration.

The B_sV_2-complex is stable at charge states from −2 to +1 and in three different configurations at different levels of the Fermi energy within the band gap of silicon [245]. Here, the stablest configuration in all charge states is the $2nn$-configuration. If the defect complex is positively charged, a small fraction also occupies the $1nn$ configuration. The negatively charged B_sV_2 also appears in the $5nn$-configuration.

As already mentioned above, substitutional boron pairs with silicon self-interstitials and forms mobile B_i. This defect can then capture further silicon self-interstitials to form the defect group B_iI_n [246–248]. Furthermore, substitutional boron atoms can capture mobile boron interstitials to form the complex $\mathrm{B_iB_s}$ [242, 246]. By capturing more boron interstitials and vacancies $\mathrm{B_{i_m}B_{s_n}}$ are formed [246–250]

$$\begin{aligned}
\mathrm{B_s} + \mathrm{B_i} &\leftrightarrow \mathrm{B_iB_s} \\
\mathrm{B_iB_s} + \mathrm{B_i} &\leftrightarrow \mathrm{B_{i_2}B_s} \\
\mathrm{B_iB_s} + \mathrm{V} &\leftrightarrow \mathrm{B_{s_2}} \\
\mathrm{B_{s_2}} + \mathrm{B_i} &\leftrightarrow \mathrm{B_iB_{s_2}} \\
\mathrm{B_i} + \mathrm{I} &\leftrightarrow \mathrm{B_iI} \\
\mathrm{B_iI}_n + \mathrm{I} &\leftrightarrow \mathrm{B_iI}_{n+1}
\end{aligned} \tag{2.109}$$

There are different notations of boron clusters [250]. In this thesis, a defect complex consisting of a substitutional boron and a silicon self-interstitial is considered to be equal to a boron interstitial $\mathrm{B_i}$. Hence, the notation of a defect complex consisting of three boron atoms and three silicon self-interstitials ($\mathrm{B_3I_3}$) is similar to three boron interstitials ($\mathrm{B_{i_3}}$) and a defect complex such as $\mathrm{B_3I_2}$ is similar to $\mathrm{B_{i_2}B_s}$. As $\mathrm{B_s}$ is considered to be immobile, clusters of substitutional boron atoms can only grow in the presence of intrinsic defects according to

$$\begin{aligned}
\mathrm{B_{i_m}B_{s_n}} + \mathrm{B_i} &\leftrightarrow \mathrm{B_{i_{m+1}}B_{s_n}} \\
\mathrm{B_{i_m}B_{s_n}} + \mathrm{I} &\leftrightarrow \mathrm{B_{i_{m+1}}B_{s_{n-1}}} \\
\mathrm{B_{i_m}B_{s_n}} + \mathrm{V} &\leftrightarrow \mathrm{B_{i_{m-1}}B_{s_{n+1}}}
\end{aligned} \tag{2.110}$$

Boron clusters consisting of up to twelve boron atoms have been studied theoretically [247, 251].

In several studies the stability of different charge states of boron clusters were simulated [247–250, 252, 253]. In figure 2.58 the formation energies of the different charge states of a selection of $\mathrm{B_{i_m}B_{s_n}}$-defect complexes consisting of two ($\mathrm{B_iB_s}$, see also appendix C.24), three ($\mathrm{B_{s_3}}$, see also appendix C.25) and four boron atoms ($\mathrm{B_{i_2}B_{s_2}}$, see also appendix C.26) are plotted as a function of the Fermi energy in the band gap of silicon. The formation energies at $E_F = 0\,\mathrm{eV}$ stem from DFT simulations by Lenosky et al. [248] and are listed in the tables in figures C.24.1a, C.25.1a and C.26.1a.

According to the calculations by Lenosky et al., the most stable state of $\mathrm{B_iB_s}$ throughout most of the band gap is the neutral one. Only very close to the conduction band, the negative charge state becomes populated. Experimental investigations of the $\mathrm{B_iB_s}$-defect additionally showed a donor transition at about $E_V + 0.3\,\mathrm{eV}$ [254, 255].

The $\mathrm{B_iB_s}$-complex is considered to be mobile [239, 256]. Using DFT simulations, Hwang et al. calculated an activation energy of $1.81\,\mathrm{eV}$ and a pre-factor of $10^{-3}\,\mathrm{cm^2s^{-1}}$ [239]. The temperature dependence of the diffusion constant of $\mathrm{B_iB_s}$ is plotted in figure 2.55 and is orders of magnitude smaller than the diffusivity of $\mathrm{B_i}$, similar to the that of $\mathrm{B_sV}$, and much faster than the effective boron diffusivity.

Figure 2.58 also shows the formation energies of the charge charge states of two larger boron complexes, $\mathrm{B_{s_3}}$ and $\mathrm{B_{i_2}B_{s_2}}$. Consisting of three boron atoms at substitutional lattice sites, $\mathrm{B_{s_3}}$ is stable at charge states from neutral to -3 in the silicon band gap. Two of the three acceptor ionizations lie between the mid gap and the valence band. $\mathrm{B_{i_2}B_{s_2}}$, on the other hand shows only one, deep acceptor level, close to the center of the band gap.

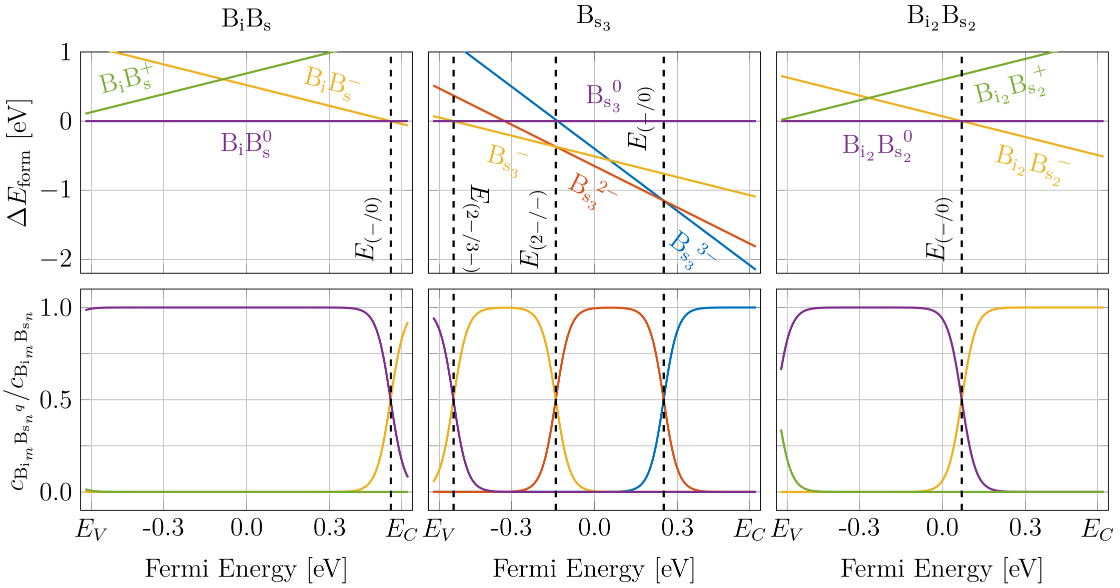

Figure 2.58: Formation energies and relative concentrations of each charge state of B_iB_s, B_{s_3} and $B_{i_2}B_{s_2}$ in silicon as a function of the Fermi energy at 25 °C. The formation energies at $E_F = 0$ were calculated and published in reference 248.

2.3.5.2 Boron Complexes Containing Oxygen or Carbon

The mobile interstitial boron defect (B_i) can be trapped by oxygen or carbon. The resulting defect complexes are considered as the main reason for the degradation of Cz-grown silicon solar cells [255, 257–260]. The most prominent defect complex consisting of boron and carbon is B_iC_s [254, 257, 261] (see appendix C.29). This defect includes the configurational isomers B_sC_i [255] and BCI [262]. Boron-oxygen defects can be formed by reactions of the mobile oxygen dimer with immobile, substitutional boron atoms [93, 259, 263], and by reactions of mobile boron interstitials B_i with interstitial oxygen [255, 257, 261, 264] or with vacancy-oxygen defects (VO or VO_2). An overview of possible reactions of different defects forming boron-oxygen and boron-carbon defect complexes is listed in equation 2.111.

$$\begin{aligned} B_i + C_s &\leftrightarrow B_iC_s \\ B_s + C_i &\leftrightarrow B_sC_i \\ B_i + C_i &\leftrightarrow B_iC_i \\ B_s + O_2 &\leftrightarrow B_sO_2 \\ B_i + O &\leftrightarrow B_iO \\ B_i + VO &\leftrightarrow B_sO \\ B_i + VO_2 &\leftrightarrow B_sO_2 \end{aligned} \tag{2.111}$$

In figure 2.59 the formation energies of the charge states of different defect complexes of boron with oxygen (B_iO, see also appendix C.27, and B_sO_2, see also appendix C.28) and with carbon (B_iC_s) are plotted as a function of the Fermi energy in the band gap of silicon.

Ionization energies for the transitions between different charge states, computed by Adey et al. using DFT-simulations [261] were used to calculate the formation energies of the charge states of B_iO and B_iC_s. The formation energies of the charge states of B_sO_2 were published by Du et al. in reference [120]. The ionization energies and the corresponding formation energies of the charge states of B_iO, B_sO_2 and B_iC_s at 0 K and $E_F = 0$ are listed in the in the tables in figures C.27.1a, C.28.1a and C.29.1a.

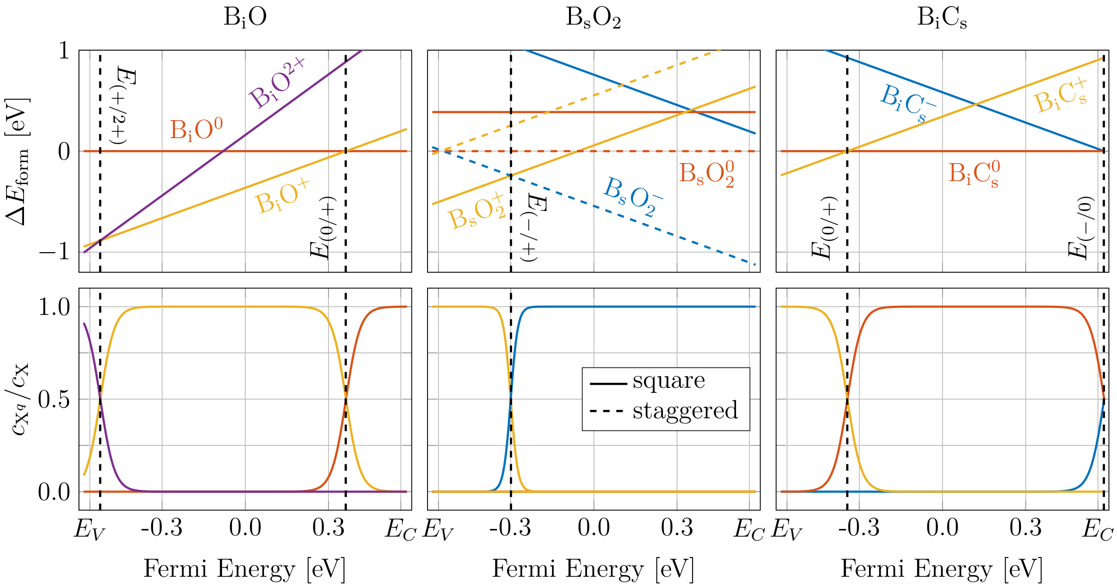

Figure 2.59: Formation energies and relative concentrations of each charge state of B_iO, B_sO_2 and B_iC_s in silicon as a function of the Fermi energy at 25 °C. The formation energies of the charge states of B_iO and B_iC_s at $E_F = 0$ were calculated from ionization energies published in reference 261. The formation energies of B_sO_2 at $E_F = 0$ were published in reference 120.

2.3.6 Phosphorus

Another widely used impurity in the silicon semiconductor industry is phosphorus, which is used to establish *n*-type doping. In a similar way to boron impurities, phosphorus atoms tend to reside on substitutional lattice positions (P_s, see appendix C.30) in the silicon crystal [214]. At a substitutional lattice site phosphorus atoms, which have five valence electrons, only form bonds to four silicon atoms at neighboring lattice sites. The remaining valence electron is “donated” to the conduction band with an ionization energy of about 45 meV [214]. In other studies, similar ionization energies between 39 meV and 50 meV using experimental [265–268] and theoretical approaches [269] were found.

In the presence of silicon self-interstitials, P_s is kicked-out of the substitutional lattice site, resulting in an interstitial phosphorus impurity P_i [270–272] (see appendix C.31). Similarly, the VP_s-defect complex (see appendix C.32), also called the “E-center” is formed by the reaction of a substitutional phosphorus with a vacancy [160, 163, 273]. Figure 2.60 depicts the formation energies of each charge state of P_s, P_i and VP_s. While the formation energies of the two charge states of P_s were calculated using an ionization energy of E_C-0.045 eV, the formation energies of the different configurations and charge states of P_i were calculated by Liu et al. [262, 274] and the formation energies of the charge states of VP_s were calculated by Ferreira-Resende [163]. The tables in figures C.30.1a, C.31.1a and C.32.1a list all the formation and ionization energies used to create the plots in figure 2.60.

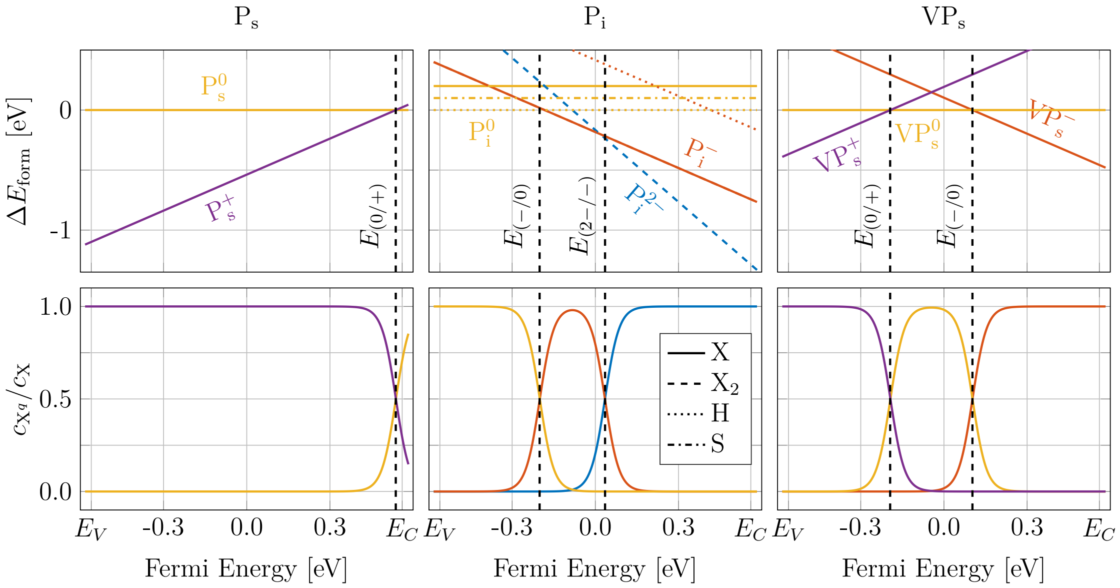

Figure 2.60: Formation energies and relative concentrations of each charge state of P_s, P_i and VP_s in silicon as a function of the Fermi energy at 25 °C. The formation energies of the charge states of P_s were calculated using an ionization energy of 45 meV. The formation energies of P_i were published in references 262, 274 and the formation energies of the charge states of VP_s were calculated from ionization energies computed in reference [163]. X: [110]-dumbbell structure, X_2: X-configuration including distortion, H: hexagonal site, S: [100]-dumbbell structure

As already mentioned before, P_s shows one transition very close to the conduction band and its most stable charge state throughout the band gap of silicon is P_s^+. The phosphorus interstitial P_i, on the other hand, according to the calculations of Liu et al. [262], acts as an acceptor in silicon. There is an acceptor transition 0.39 eV above E_V and another transition at an energy of 0.61 eV above the valence band edge. At Fermi energies close to E_V, P_i populates the neutral charge state in the hexagonal configuration (H). Nevertheless at elevated temperatures, a significant fraction of P_i is found in the [100]- and [110]-dumbbell structures (X, X_2 and S), which show a slightly higher formation energy. If the phosphorus interstitial is negatively charged it exclusively forms the [110]-dumbbell structures (X and X_2) [262]. The acceptor level at $E_C - 0.43$ eV of the VP_s complex was already reported by Watkins et al. in 1959 [160], but it took more than forty years until also the donor transition of the defect was revealed by Larsen et al. [275, 276], 0.27 eV above E_V. Ferreira-Resende predicted this donor transition already earlier using first principles local-density formalism cluster theory [163, 277].

Phosphorus is thought of as the fastest diffusing group V donor in silicon [5]. The effective diffusivity of $\mathrm{P_s}$ is on the same order as that of substitutional boron and is described by an activation energy of 3.507 eV and a pre-factor of $1.03\,\mathrm{cm^2s^{-1}}$ [5]. The actual diffusion process of phosphorus is, in a similar way to the diffusion process of boron, quite complex [270, 278]. The diffusing, phosphorus-containing species are $\mathrm{P_i}$ and $\mathrm{VP_s}$[5, 270, 274]. As described in reference [270], the following reactions determine the effective diffusivity of phosphorus:

$$\begin{aligned} \mathrm{P_s + I} &\leftrightarrow \mathrm{P_i} \\ \mathrm{P_i + V} &\leftrightarrow \mathrm{P_s} \\ \mathrm{P_s + V} &\leftrightarrow \mathrm{VP_s} \\ \mathrm{VP_s + I} &\leftrightarrow \mathrm{P_s} \end{aligned} \tag{2.112}$$

Another diffusing, phosphorus-containing defect is $\mathrm{P_iH}$ which shows an activation energy between 1.81 eV and 2.04 eV [279].

The diffusivities of the negative and neutral charge states of the $\mathrm{VP_s}$-complex are described by Arrhenius equations published in reference [5] and are listed in table 2.14. The diffusivity of the positive charge state of $\mathrm{VP_s}$ is yet to be determined. The diffusivity of $\mathrm{P_i}$ was studied by Liu et al. using DFT simulations [262, 274]. They calculated activation energies of 1.4 eV and 0.6 eV for the diffusion of $\mathrm{P_i^-}$ and of the neutral charge state of $\mathrm{P_i}$. For the calculation of diffusion coefficients, the pre-factors of $\mathrm{P_i^-}$ and $\mathrm{P_i^0}$ were estimated. The temperature dependence of the diffusivity of the mobile phosphorus defects is shown in figure 2.61 and the corresponding Arrhenius parameters are listed in table 2.14.

As several Arrhenius parameters describing the diffusivities of mobile phosphorus containing defect complexes are estimated, it is difficult to discuss the effective diffusivity of these defects. It can be stated, though, that these defects show diffusivities which are several orders of magnitude higher than the effective diffusivity of phosphorus.

Table 2.14: Arrhenius coefficients describing the temperature dependence of the diffusion of the charge states of different defect complexes containing phosphorus, including the effective diffusivity phosphorus ($\mathrm{P_s}$*). **: estimated values.

	E_A [eV]	D_0 [$\mathrm{cm^2s^{-1}}$]
$\mathrm{P_i^-}$	1.4 [274]	10^{-2**}
$\mathrm{P_i^0}$	0.6 [274]	10^{-6**}
$\mathrm{VP_s^-}$	1.25 [5]	9.6×10^{-2} [5]
$\mathrm{VP_s^0}$	0.93 [5]	9.7×10^{-4} [5]
$\mathrm{P_s^*}$	3.507 [5]	1.03 [5]

2.3.6.1 Phosphorus Complexes

Phosphorus can form various complexes with other point defects in silicon. One of these defect complexes is $\mathrm{P_iC_s}$ (or $\mathrm{P_sC_i}$, or PCI, depending on the notation) [277, 280–284]. Zhan et al. found five different configurations (IA, IB, IIA, IIB and III) of the defect complex using EPR [283]. They also measured the electronic transition of each charge

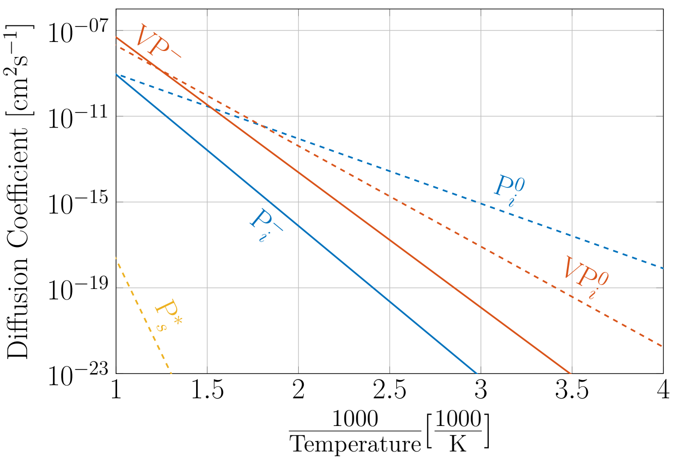

Figure 2.61: Diffusion coefficients of the charge states of different defect complexes containing phosphorus in silicon as a function of the inverse temperature [5, 274]. The effective diffusivity of phosphorus (P_s*) as found in reference 5 is included.

state using DLTS. Unfortunately the relative stabilities of the different configurations have not been determined yet. Resende er al. calculated the ionization energies of P_iC_s using DFT [277], though they did not mention the configuration of the defect complex they used in their simulations. Most studies agree, that P_iC_s has an acceptor level in vicinity of the bottom of the conduction band and an acceptor level closer to the valence band [277, 282, 283].

Lindström et al. reported on a defect complex containing phosphorus and oxygen (P_2VO) which might be formed by some reaction of VP_s and VO [285]. The defect should show a transition between charge states 0.27 eV below E_C.

Apart from VP_s further defect complexes containing phosphorus and vacancies have been proposed. Chadi et al. proposed the formation of donor pairs consisting of several phosphorus atoms and a vacancy (P_nV) [286]. Larsen et al. found a donor transition 0.15 eV below E_C which they assigned to the VP_{s_2}-complex [287]. Suezawa et al. proposed a complex consisting of two vacancies and a phosphorus substitutional V_2P_s to account for a transition 0.276 eV below E_C [288]. To explain concentration profiles of phosphorus after transient enhanced diffusion, Schroer and Uematsu considered the formation of P_iI as a major influence [289, 290]. Furthermore, the generation of larger phosphorus-self-interstitial clusters was suggested as well [291, 292].

2.4 Proton Implantation

The implantation of protons is a widely used process in the silicon semiconductor industry. This section is mainly based on the work by Kozlovskii et al. [293] and by Laven [294]. Proton implantation in silicon can have several purposes: Low implantation doses (below $5{\times}10^{12}\,\mathrm{H^+cm^{-2}}$) are used to locally control the lifetime of charge carriers by generating recombination centers [295, 296]. The implantation of proton doses around $10^{13}\,\mathrm{H^+cm^{-2}}$ to $10^{15}\,\mathrm{H^+cm^{-2}}$ leads to the formation of hydrogen related donors [297, 298]. If proton doses above $10^{16}\,\mathrm{H^+cm^{-2}}$ are implanted, the formation of platelet defects [299] is initiated, which are used to produce thin layers of silicon in the "Smart-Cut"-process [300, 301]. The following section shortly presents the fundamentals of implantation physics and the simulation tool "Stopping and Range of Ions in Matter" (SRIM), which is used to simulate damage profiles created by proton bombardment. Furthermore, defect complexes generated during the implantation process and in a subsequent anneal are discussed. A short summary of the charge states of each defect and of the diffusivities of mobile defects discussed in this section can be found in the catalog on defects in appendix C. There is a reference to the respective section in the appendix at the beginning of the section about each defect.

2.4.1 Shooting High Energy Protons Into a Silicon Crystal

When ions are implanted into a material, they are accelerated to high kinetic energies. If the energy is high enough, these particles even reach velocities, close to the speed of light c_l. The speed of light c_l in a material can be calculated from its relative permeability ϵ_r and its relative permittivity μ_r

$$c_\mathrm{l} = \frac{1}{\sqrt{\epsilon\epsilon_r\mu\mu_r}}. \tag{2.113}$$

In vacuum, ϵ_r and μ_r are 1, hence the speed of light is $c_{\mathrm{l},0}$, $2.9979{\times}10^8\,\mathrm{ms^{-1}}$. The relative permeability ϵ_r of silicon is 11.7 [1] and, as the magnetic susceptibility ξ_m of silicon is smaller than 10^{-5} [302] and $\mu_r = 1{+}\xi_m$ the relative permeability of the material is almost 1. This results in a speed of light of $8.8{\times}10^7\,\mathrm{ms^{-1}}$ or $0.29\ c_{\mathrm{l},0}$. In classical mechanics, the relation between the kinetic energy E and the velocity v of a particle is

$$E = \frac{mv^2}{2}, \tag{2.114}$$

where m is the rest mass of the particle. If the particle is accelerated to a velocity, which is a significant fraction of the speed of light, relativistic effects have to be taken into account and the relation of energy and velocity becomes

$$E = \frac{m{c_\mathrm{l}}^2}{\sqrt{1-\frac{v^2}{{c_\mathrm{l}}^2}}} - m{c_\mathrm{l}}^2. \tag{2.115}$$

Considering protons, which have a rest mass of $m_{\mathrm{H}^+} = 1.673{\times}10^{-27}\,\mathrm{kg}$, particles with kinetic energies below about 100 MeV can be treated using classical mechanics, while the description of interactions of particles at higher kinetic energies require the application of relativistic mechanics. Figure 2.62a shows the velocity of protons in silicon as a function of the kinetic energy of the protons, calculated using the relativistic and classical model. Furthermore, the speed of light in vacuum and in silicon are indicated.

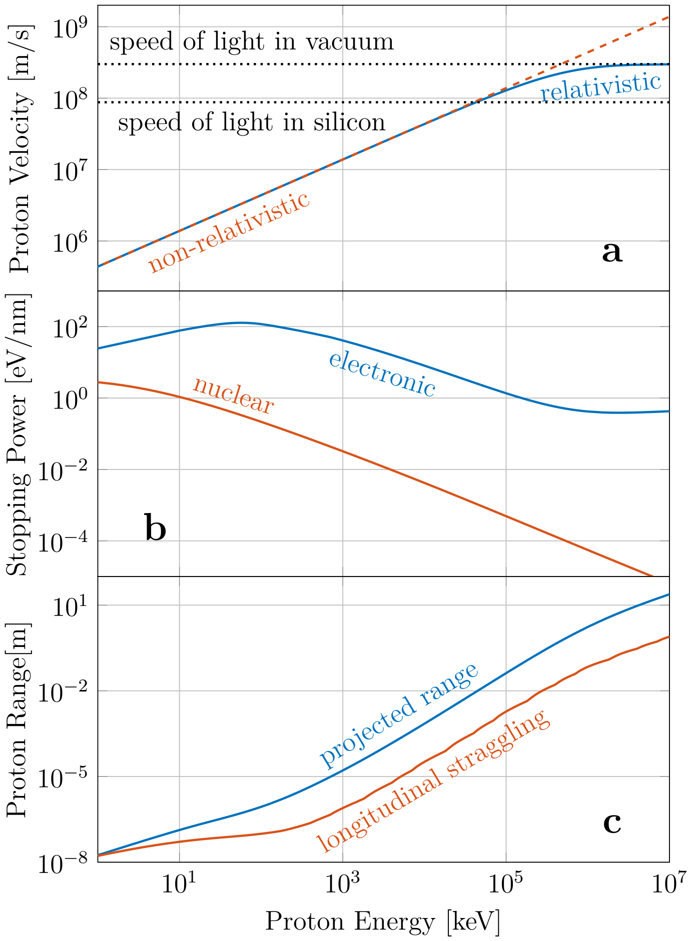

Figure 2.62: Stopping power, velocity and range of protons in silicon as a function of their kinetic energy. The stopping power was calculated using the PSTAR [303]. The projected range and the longitudinal straggling were calculated using SRIM [304, 305].

As already derived by Bohr in the early 19th century, the power loss or deceleration of a fast traveling, charged particle passing through a material is divided into interactions of that particle with the electrons (electronic interaction) and with the nuclei (nuclear interaction) of the material [306, 307]. Electronic interaction goes along with the ionization of the irradiated material, while elastic and inelastic collisions of the incoming particles with lattice atoms make up the nuclear interactions. Using the software tool “PSTAR” of the National Institute of Standards and Technology [303], the electronic and nuclear contribution to the stopping power can be calculated as a function of the particle energy. This is plotted in figure 2.62b, for the case of protons in silicon.

The electronic contribution to the stopping power working on protons in silicon, as a function of the kinetic energy of the protons, peaks at an energy of about 100 keV.

Protons with lower kinetic energies “feel” less electronic stopping power. For protons at higher energies, the electronic stopping power scales with the speed of the protons. Hence, it saturates at as the speed of the protons approaches the speed of light. The nuclear contribution to the stopping power is several orders of magnitude smaller than the electronic contribution. Nevertheless this power loss is responsible for the generation of intrinsic defect pairs, as the impinging protons knock silicon atoms off their lattice positions. High energy protons can also undergo nuclear fusion reactions with substrate atoms, converting $^{30}_{14}\mathrm{Si}$ to $^{31}_{15}\mathrm{P}$ in a reaction similar to the reaction 2.59. Protons moving faster than the speed of light in silicon will also lose energy due to the emission of Ĉerenkov radiation [308, 309]. The energies used to implant protons in this thesis, though, with the highest energy being 4 MeV, are too low to observe either of the last two effects.

After loosing all their kinetic energy, the implanted protons capture an electron and come to rest as atomic hydrogen. The generation of radiation damage in the material due to the interactions of impinging particles with lattice atoms and the distribution of the implanted particles after having lost all their kinetic energy can be simulated using Monte-Carlo simulations such as the software package “Stopping and Range of Ions in Matter” or SRIM [304, 305]. From such simulations, which will be discussed in the next section 2.4.2, the range, and also the distribution of the implanted protons can be calculated. This, so-called “projected range” r_p, which corresponds to the mean implantation depth, and the “longitudinal straggling” σ_{r_p}, describing the standard deviation of the projected range of the generated hydrogen concentration profile, are plotted in figure 2.62c as a function of the implantation energy, the kinetic energy of the protons before they enter the material.

Both, the projected range and the straggling of the spreading of the implanted protons increase with increasing proton implantation energy. Values of the projected range and the longitudinal straggling for selected implantation energies are listed in table 2.15.

Table 2.15: Projected range r_p and longitudinal straggling σ_{r_p} for selected proton implantation energies calculated with SRIM.

H^+ Energy [keV]	r_p [µm]	σ_{r_p} [µm]
100	0.9	0.1
400	4.4	0.2
1000	16	0.8
2500	68	3.1
4000	148	6.1

When particles are implanted into a crystalline material, there is a certain chance that they will travel along a high symmetry direction, inside a channel between the lattice atoms. Due to the positive charges of the lattice atoms, the moving particle is held inside the channel. This leads to an increase of the projected range, as the electron density inside the channel is lower than outside and, hence, the electronic stopping power per unit length along this path is decreased [310]. Depending on the particle velocity and the temperature, there is a critical implantation angle, relative to each high symmetry surface plane of a crystal [311]. If the implantation angle is higher than the critical angle, channeling effects can be neglected. Samples investigated in this thesis were all implanted at an angle of 7 ° to avoid channeling.

2.4.2 Calculation of Damage Profiles Generated by Proton Implantation Using SRIM

“Stopping Range of Ions In Matter”, or short SRIM [304] is a software package based on Monte-Carlo simulations of the deceleration and scattering of ions in a solid material [312]. This software package includes a tool for the calculation of the “Transport of Ions in Matter” (TRIM).

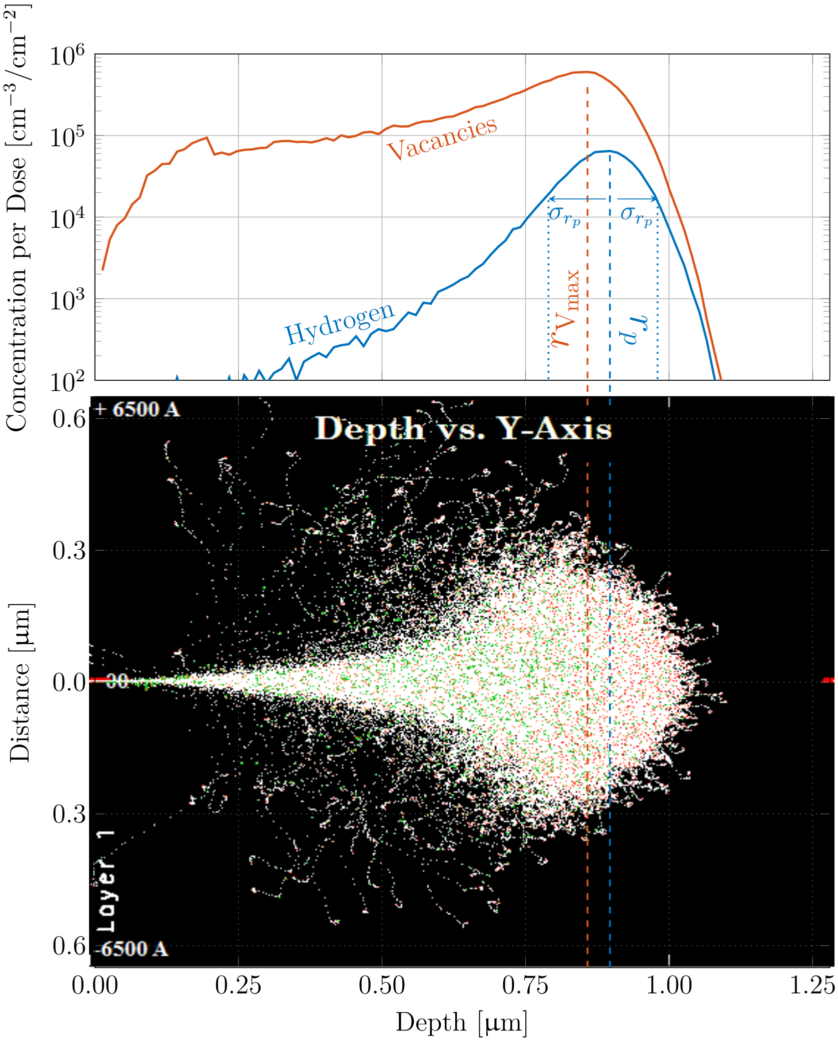

Figure 2.63: TRIM simulation of the scatter paths of 10000 100 keV-protons in silicon. Red dots show the rest place of the implanted protons, white dots show scattering events and green dots show collision cascades. Additionally concentration depth profiles of protons and vacancies are shown including an indication of the projected range r_p, the “lateral straggling” and the position of the maximum vacancy concentration $r_{V_{max}}$.

Figure 2.63 shows the interactions of 100 keV protons with a silicon substrate calculated using the “Detailed Calculation with Full Damage Cascades”-option of TRIM. For this calculation, the scattering paths of 10000 protons have been simulated. While the final rest places of the implanted protons are shown as red dots in the figure, white points indicate locations at which scattering events took place and green points signalize damage cascades. Such damage cascades are initiated, when protons transfer an amount of kinetic energy to a lattice atom, that is several times the binding energy of that atom to the lattice. This triggers a cascade of further scattering events of that atom, generating a number of vacancies and interstitials. Additionally, the concentration profiles of the hydrogen atoms, after coming to rest and the concentration profile of the vacancies generated by those atoms during the implantation are shown. The concentrations are normalized to the implanted proton dose, the number of implanted protons per unit area. While the position of the maximum of the hydrogen concentration defines the projected range r_p, the vacancy concentration peaks at $r_{\mathrm{V_{max}}}$, which is closer to the surface than r_p. After being knocked off its lattice position by an impinging proton, the created interstitial usually resides close to the generated vacancy (within a few nm). Hence, similar profiles for the concentration of vacancies and interstitials are considered.

As already indicated in figure 2.62c and table 2.15, the projected range and the longitudinal straggling scale with the implantation energy of the protons. At the same time r_p is increased, the maximum concentration of both, the hydrogen and the intrinsic defects decreases. This effect is shown in figure 2.64, were concentration profiles of hydrogen and vacancies, generated by proton implantation at different implantation energies are plotted.

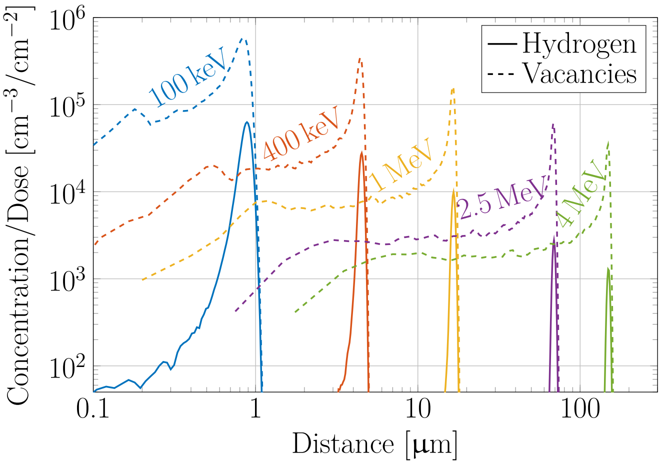

Figure 2.64: Concentration profiles of hydrogen and vacancies generated by proton implantation at different implantation energies, calculated using SRIM [304].

The normalized hydrogen concentration at r_p is $6\times10^4\,\mathrm{cm}^{-1}$ if the protons are implanted with 100 keV and decreases with increasing implantation energy to about $10^3\,\mathrm{cm}^{-1}$ at an implantation energy of 4 MeV. If the implantation energy is above several hundred eV, each implanted proton generates more than one lattice vacancy on average. Hence, the concentration of vacancies generated by the impinging protons at an implantation energy in the keV-range and above, is always higher than the concentration of the implanted hydrogen. At an implantation energy of 100 keV the vacancy concentration (normalized to the implanted dose) at $r_{\mathrm{V_{max}}}$ is $6\times10^5\,\mathrm{cm}^{-1}$ and it decreases to $3\times10^4\,\mathrm{cm}^{-1}$ at an implantation energy of 4 MeV. Figure 2.65 shows the number of vacancies generated per implanted proton as a function of the implantation energy. Furthermore, the ratio of the maximum vacancy concentration at $r_{\mathrm{V}_{\max}}$ and the maximum hydrogen concentration at r_p are plotted as a function of the implantation energy.

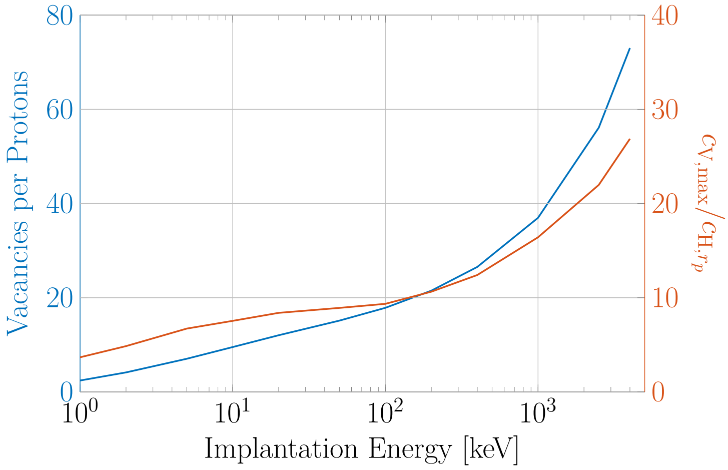

Figure 2.65: Number of vacancies generated per implanted proton and ratio of the concentration maxima of vacancies and hydrogen as a function of the implantation energy.

At an implantation energy of 1 keV, about 2.4 vacancies are generated on average per proton. This value increases to 37 vacancies per 1 MeV-proton and to more than 70 vacancies per proton if the implantation energy is 4 MeV.

The damage distributions, and the hydrogen concentration profiles after proton implantation calculated with SRIM deviate from the real conditions. To account for the diffusion of the generated point defects and reactions with each other and with extrinsic defects, a process simulation will be presented and discussed in chapter 4. As one of the results of this simulation it will be shown that about 90 % of the generated intrinsic defects already recombine during the implantation process.

2.4.3 Hydrogen in Silicon

Apart from the implanting protons [297, 313], hydrogen can be introduced using a radio frequency (RF-) plasma [314–316] or it can be diffused in from the gas phase (permeation) [49]. Other methods include the electrochemical introduction of hydrogen by boiling the material in water [317] or in oxidizing acids such as HF and HNO_3 [318]. A good review about hydrogenation methods of crystalline silicon is found in reference [319].

The solubility of hydrogen in silicon was first determined by van Wieringen et al. in 1956 using in-diffusion of hydrogen into silicon from the gas-phase [49]

$$[\mathrm{H}]_{\mathrm{sol}} = 2.4\times10^{21}\,\mathrm{cm}^{-3}\exp\left(-\frac{1.87\,\mathrm{eV}}{k_B T}\right) \tag{2.116}$$

Due to their much smaller size compared to silicon lattice atoms, hydrogen atoms do not reside on substitutional lattice positions but rather prefer interstitial sites. There are several possible sites in the silicon unit cell, where hydrogen would fit in. These different configurations were investigated theoretically by several studies [320–325]. Most of these investigations concluded that the lowest energy lattice sites for the hydrogen atom are the bond-centered (BC-) and the tetragonal (T-) sites. Building on previous work by Van de Walle et al. [323] and Deák et al [326], Herring et al. used DFT-simulations to calculate the most stable configurations of different charge states of the hydrogen interstitial as a function of the position of the Fermi energy in the band gap of silicon [327]. They found that if hydrogen is neutral or positively charged, it resides on BC-sites, while it prefers T-sites when its charge is negative. In figure 2.66 the formation energy of each charge state of atomic hydrogen, relative to the formation energy of the neutral charge state is plotted as a function of the Fermi energy within the band-gap of silicon. Additionally the relative concentrations of the charge states at a temperature of 25 °C are shown. The formation energies at the middle of the band-gap ($E_F = 0$) and the ionization energies for the direct transitions between the charge states are listed in the table in figure C.33.1.

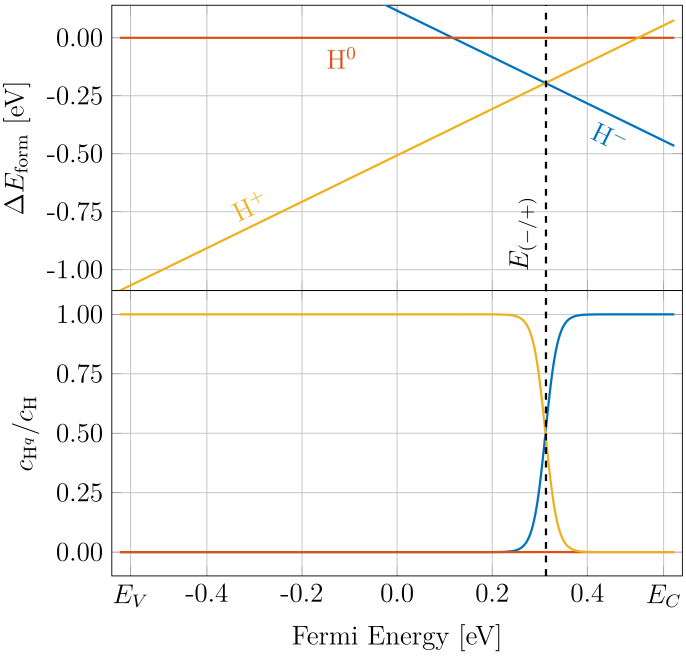

Figure 2.66: Formation energies and relative concentrations of the charge states of atomic hydrogen in silicon as a function of the Fermi energy at 25 °C. The formation energies at $E_F = 0$ were calculated from ionization energies published in reference 327. The experimentally observable ionization energy is indicated by a dashed line.

Atomic hydrogen H (see appendix C.33) shows a negative-U system, as there is a direct transition from the negatively charged to the positively charged state. The positive charge state is the most stable configuration of hydrogen for most energies in the band-gap. Only at high donor concentrations (10^{16} cm^{-3} and higher), the negative charge state is populated and becomes the dominant state. If the system is in thermodynamic equilibrium, the relative concentration of the neutral charge state of atomic hydrogen never exceeds 0.01.

2.4.4 Diffusion of Hydrogen in Crystalline Silicon

Even though the migration of hydrogen has been studied over decades, there is still no strong agreement on the diffusion process. A variety of studies measured and calculated Arrhenius coefficients describing the temperature dependence of the hydrogen diffusivity. These coefficients, though, spread over several orders of magnitude. The materials used in those studies differ in various parameters. There are variations in the crystal growing technique and in the doping type of the materials. Furthermore, different types of hydrogen isotopes (^{1}H, ^{2}H and ^{3}H) were used in the experiments and also the method of introducing the hydrogen and measuring its diffusion differ between different investigations. This section gives a small overview of selected studies, which are compared to a new set of measurements in section 3. In figure 2.67 the effective hydrogen diffusivities $D_{\mathrm{H}}^{\mathrm{eff}}$ measured in these studies are plotted as a function of the inverse temperature and table 2.16 gives an overview of the details of each study regarding the Arrhenius parameters, the investigated temperature range, the diffusing species, the studied material and the applied methods for introducing the hydrogen and detecting its diffusion.

The first investigation of the diffusion of hydrogen in silicon was carried out by van Wieringen et al. in 1956 [49]. In their experiments they measured the permeation of hydrogen gas through a Czochralski-grown (Cz), silicon sample in a diffusion cell at different temperatures from 1092 °C to 1200 °C. The amount of the hydrogen gas diffusing out of the silicon sample, was measured using a mass spectrometer (OD-MS) allowing the simultaneous determination of both, the solubility of hydrogen (see equation 2.116) and its diffusivity. They found an activation energy of 0.48 eV and a pre-factor of $9.7\times10^{-3}\,\mathrm{cm^2s^{-1}}$ describing the temperature dependence of $D_{\mathrm{H}}^{\mathrm{eff}}$. Ichimiya et al. studied the diffusivity and solubility of tritium (^{3}H) in *p*-type Cz-grown material [328]. Similar to van Wieringen et al., they introduced the tritium gas by permeation. The out-diffusion was measured by ionizing the gas and measuring the arising ion current (OD-GI). Their experiments yielded an activation energy of 0.54 eV and a pre-factor of $3.2\times10^{-3}\,\mathrm{cm^2s^{-1}}$ in a temperature range from 400 °C to 500 °C.

Using a H_2O-plasma, Hansen et al. introduced hydrogen and oxygen into *p*-type FZ material [329]. The material had previously been saturated with gold and the hydrogen diffusion was calculated by measuring the deactivation of Au-donors using DLTS. In a temperature range between 84 °C and 110 °C an activation energy of 0.69 eV and a pre-factor of $4.3\times10^{-2}\,\mathrm{cm^2s^{-1}}$ were found. Mogro-Campero et al. measured the change of spreading resistance profiles (SRP) of gold diffused *n*-type, Cz-grown silicon samples caused by hydrogen [330]. They introduced H using a radio-frequency (RF-) plasma at temperatures from 130 °C to 450 °C and calculated $D_{\mathrm{H}}^{\mathrm{eff}}$ from the penetration depth measured after different durations of the treatment. According to their study, the temperature dependence of $D_{\mathrm{H}}^{\mathrm{eff}}$ is described by an activation energy of 0.43 eV and a D_0 of $7.2\times10^{-7}\,\mathrm{cm^2s^{-1}}$. Pearton et al. also used a plasma to introduce hydrogen into silicon samples. They then inferred the penetration depth of the hydrogen from the deactivation of gold donors which they measured using DLTS [331]. As there is a kink, separating two linear regions in the temperature dependence of $D_{\mathrm{H}}^{\mathrm{eff}}$ calculated by this group, their data was separated into a high (Pea$^{\mathrm{b}}$: 350 °C-650 °C, $E_A = 1.20\,\mathrm{eV}$, $D_0 = 7.8\times10^{-2}\,\mathrm{cm^2s^{-1}}$) and a low temperature (Pea$^{\mathrm{a}}$: 95 °C-350 °C, $E_A = 0.31\,\mathrm{eV}$, $D_0 = 9.6\times10^{-9}\,\mathrm{cm^2s^{-1}}$) region. In another study, conducted by Herrero et al. *p*-type silicon was treated with a hydrogen plasma at temperatures between 90 °C and 200 °C [332]. This group used infra-red-reflectance spectra (IRR) to measure the thickness of a passivated layer containing boron-hydrogen defect complexes, which corresponds to the hydrogen diffusion length. These measurements yielded an activation energy of 0.66 eV and a pre-factor of $6.9\times10^{-5}\,\text{cm}^2\text{s}^{-1}$. Rizk et al. investigated the diffusivity of deuterium (^{2}H) in FZ silicon, which they introduced into the material from a plasma at temperatures from 120 °C to 185 °C [333]. They studied the expansion of the hydrogen concentration profile in n- and p- type material using secondary ion mass spectroscopy (SIMS) and capacitance-voltage (CV-) measurements. From the resulting data they derived separate Arrhenius coefficients for $^2\text{H}^+$ (Riz$^\text{b}$: $E_A = 0.59\,\text{eV}$, $D_0 = 8.4\times10^{-5}\,\text{cm}^2\text{s}^{-1}$), $^2\text{H}^-$ (Riz$^\text{c}$: $E_A = 0.80\,\text{eV}$, $D_0 = 1.4\times10^{-2}\,\text{cm}^2\text{s}^{-1}$) and $^2\text{H}^0$ (Riz$^\text{a}$: $E_A = 1.09\,\text{eV}$, $D_0 = 3.7\,\text{cm}^2\text{s}^{-1}$). In another study, Newman et al. studied the diffusivity of hydrogen introduced into p-type Cz-grown silicon from a plasma at temperatures from 225 °C to 350 °C [123]. This group measured the relaxation of previously stressed material. This relaxation lead to a change in the ratio of the reflection of infra-red light polarized perpendicular and parallel to the stress axis. The driving force of the relaxation is the diffusion of oxygen, which was found to be enhanced in the presence of hydrogen. From this enhancement the group derived D_H^eff. From their published diffusivities an activation energy of 1.26 eV and a pre-factor of $620\,\text{cm}^2\text{s}^{-1}$ were calculated. Johnson et al. investigated the diffusivity of negatively charged deuterium in n-type Cz-grown silicon and in n-type FZ-material [334]. They introduced deuterium from a plasma source and measured its concentration profiles using SIMS. In a temperature range from 125 °C to 200 °C they found an activation energy of 1.10 eV and a D_0 of $1.9\,\text{cm}^2\text{s}^{-1}$ for the diffusion of $^2\text{H}^-$ in FZ-material (Joh91$^\text{a}$) and an activation energy of 0.82 eV and a D_0 of $1.1\times10^{-3}\,\text{cm}^2\text{s}^{-1}$ for the diffusion of $^2\text{H}^-$ in Cz-material (Joh91$^\text{b}$). In a similar study, Sopori et al. investigated the diffusion of deuterium in FZ and in Cz silicon using a plasma treatment and SIMS at temperatures between 150 °C and 235 °C [335]. Their measurements resulted in an activation energy of 0.66 eV and a pre-factor of $8.5\times10^{-3}\,\text{cm}^2\text{s}^{-1}$ describing the temperature dependence of the diffusivity of ^{2}H in FZ (Sop92$^\text{a}$) and an activation energy of 0.67 eV and a pre-factor of $3.6\times10^{-3}\,\text{cm}^2\text{s}^{-1}$ in Cz material. Huang et al. chose another approach to measure the diffusion of hydrogen in p-type Cz-grown silicon. They introduced the hydrogen from a plasma at temperatures from 270 °C to 450 °C and measured the expansion of the donor-rich region formed by the diffusing hydrogen using SRP [336]. From the measured values of D_H^eff in this study, an activation energy of 1.50 eV and a pre-factor of $10^3\,\text{cm}^2\text{s}^{-1}$ were calculated.

Kazmerski et al. applied low energy proton implantation (low E) to introduce hydrogen into p-type, polycrystalline material at temperatures from 127 °C to 225 °C [337]. From the broadening of the hydrogen concentration profile in the grains measured with SIMS, they determined the effective diffusivity of hydrogen in the bulk material associated with an activation energy of 0.51 eV and a pre-factor of $2.1\times10^{-5}\,\text{cm}^2\text{s}^{-1}$. Seager et al. introduced hydrogen using low energy proton implantation at low temperatures (0 °C-57 °C). In their experiments, the diffusion of hydrogen lead to an increase of the capacitance of a (p-type-) Schottky diode, due to the formation of boron-hydrogen defect complexes [338]. From this increase they deduced D_H^eff and found a temperature dependence described by an activation energy of 0.3 eV and a pre-factor of $1.7\times10^{-5}\,\text{cm}^2\text{s}^{-1}$. Using high energy proton implantation (high E), Laven et al. generated a region of high donor concentration deep inside an n-type FZ-wafer [339]. In subsequent annealing treatments at temperatures between 320 °C and 370 °C, the expansion of the donor rich region towards the surface of the material was measured using SRP. From this expansion $D_{\mathrm{H}}^{\mathrm{eff}}$ was extracted. The temperature dependence of the hydrogen diffusivities measured in this study is described by an activation energy of 1.19 eV and a pre-factor of $6.1\times10^{-2}\,\mathrm{cm^2s^{-1}}$.

A special kind of technique to determine the diffusivity of hydrogen and deuterium at different charge states was developed by Johnson and Herring [340]. In this technique an *n*-type Cz-grown silicon sample is first treated with hydrogen or deuterium plasma. In a subsequent step, a Schottky-junction is formed at the surface of the material by Pd evaporation. The subsequent injection of minority carriers by pulsed illumination from the backside lead to the dissociation of hydrogen-defect complexes (mostly PH) and to a change of the capacitance at the Schottky junction due to the diffusion of hydrogen and the re-formation of these defect complexes, which was then measured. Performing this measurement at temperatures from 27 °C to 47 °C yielded an activation energy of 0.69 eV and a pre-factor of $1.2\,\mathrm{cm^2s^{-1}}$ for negatively charged deuterium [340]. Herring et al. used the same technique to investigate the diffusivity of positively charged hydrogen and deuterium. They found an activation energy of 0.49 eV and a pre-factor of $1.3\times10^{-3}\,\mathrm{cm^2s^{-1}}$ for $^1\mathrm{H}^+$ (Her01$^{\mathrm{a}}$) and an activation energy of 0.51 eV and a pre-factor of $1.1\times10^{-3}\,\mathrm{cm^2s^{-1}}$ for $^2\mathrm{H}^+$ (Her01$^{\mathrm{b}}$).

Hara measured the enhanced formation of thermal double donors due to the presence of grown-in hydrogen in Cz-material [341]. From resistance profiles of samples annealed at temperatures between 425 °C and 760 °C measured with SRP, the hydrogen diffusivity was determined and an activation energy of 0.51 eV and a pre-factor of $5.6\times10^{-3}\,\mathrm{cm^2s^{-1}}$ were calculated from their results.

Based on the assumption, that two distinct hydrogen species (H^0 and H^+) contribute to the effective hydrogen diffusivity, Capizzi et al. derived a fit for experimental data using a simulation including the diffusion and reactions of defects (DR-sim) [342]. From their calculations in the temperature region from 120 °C to 250 °C they derived the Arrhenius coefficients describing the temperature dependence of the diffusivity of H^0 (Cap87$^{\mathrm{a}}$: E_A: 1.19 eV, D_0: $1.3\,\mathrm{cm^2s^{-1}}$) and H^+ (Cap87$^{\mathrm{b}}$: E_A: 0.82 eV, D_0: $6.2\times10^{-4}\,\mathrm{cm^2s^{-1}}$). Buda et al. used ab-initio molecular-dynamics simulations (MD-sim) to calculate the diffusivity of H^+ at temperatures above 915 °C [343]. Their calculations yielded an E_A of 0.33 eV and a D_0 of $10^{-2}\,\mathrm{cm^2s^{-1}}$. Using tight binding molecular-dynamics simulations, Panzarini et al. calculated the diffusivity of hydrogen at temperatures above 527 °C [344]. They found an activation energy of 0.70 eV and a pre-factor of $2.4\times10^{-2}\,\mathrm{cm^2s^{-1}}$.

This section only includes studies, which published values of $D_{\mathrm{H}}^{\mathrm{eff}}$ measured or simulated at different temperatures. Those values were either found in tables or extracted from published figures. The Arrhenius parameters plotted in figure 2.67b (D_0 as a function of E_A) and listed in table 2.16 were calculated from these values and might differ slightly from the parameters published within the studies.

The effective hydrogen diffusivities published in the studies presented above are plotted in figure 2.67a as a function of the inverse temperature. The published values of $D_{\mathrm{H}}^{\mathrm{eff}}$ are scattered over several orders of magnitude. Especially in the temperature range from 50 °C to 150 °C ($0.003\,\mathrm{K^{-1}}$-$0.0025\,\mathrm{K^{-1}}$), $D_{\mathrm{H}}^{\mathrm{eff}}$ spreads over six orders of magnitude.

Plotting the logarithm of the pre-factor as a function of the activation energy, as shown in figure 2.67b, reveals a correlation of the two parameters. Such a correlation between Arrhenius parameters was first observed by Meyer and Neldel in 1937, who investigated

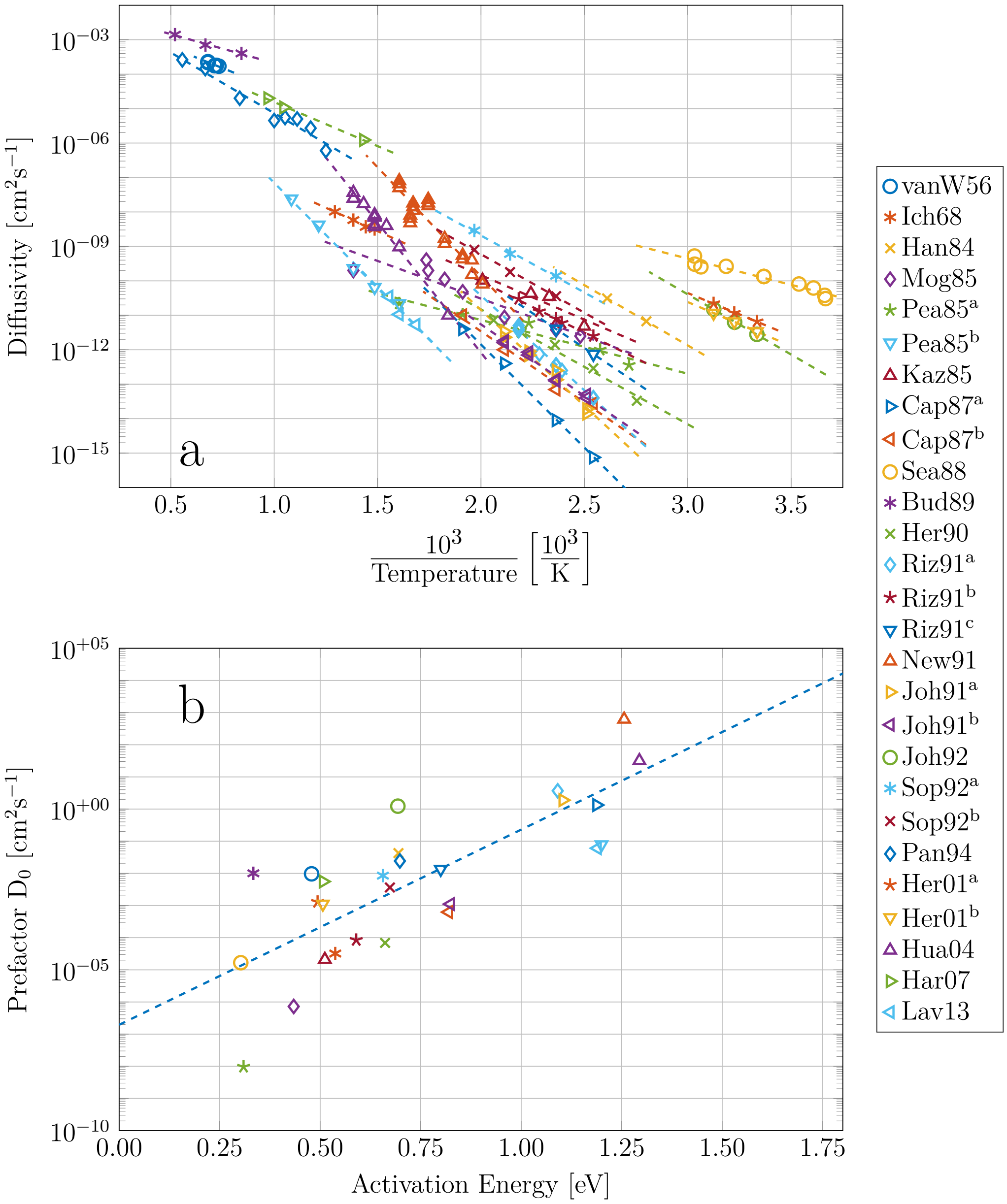

Figure 2.67: Temperature dependence of the effective hydrogen diffusivity and corresponding Arrhenius parameters derived from references 49, 123, 328, 330–339, 342–344.

Table 2.16: Arrhenius parameters describing the effective diffusivity of hydrogen calculated from data published in references 49, 123, 328, 330–339, 342–344. Temp: investigated temperature range; Spec.: diffusing species; H-Intro.: applied method for the hydrogen introduction; Det.: detection method

Study	E_A [eV]	D_0 [cm^{2}s^{-1}]	Temp. [°C]	Spec.	Material	H-Intro.	Det.	Ref.
vanW56	0.48	9.7×10^{-3}	1092–1200	$^{1}\mathrm{H}^{0}$	Cz	perm	OD-MS	[49]
Ich68	0.54	3.2×10^{-5}	400–500	$^{3}\mathrm{H}^{0}$	p-FZ	perm	OD-GI	[328]
Han84	0.69	4.3×10^{-2}	84–110	$^{1}\mathrm{H}^{0}$	p-FZ	plasma	DLTS	[329]
Mog85	0.43	7.2×10^{-7}	130–450	$^{1}\mathrm{H}^{0}$	n-Cz	plasma	SRP	[330]
Pea85^{a}	0.31	9.6×10^{-9}	95–350	$^{1}\mathrm{H}^{0}$		plasma	DLTS	[331]
Pea85^{b}	1.20	7.8×10^{-2}	350–650	$^{1}\mathrm{H}^{0}$		plasma	DLTS	[331]
Kaz85	0.51	2.1×10^{-5}	127–225	$^{1}\mathrm{H}^{0}$	p-type	low E	SIMS	[337]
Cap87^{a}	1.19	1.3×10^{0}	120–250	$^{1}\mathrm{H}^{0}$		DR-sim	DR-sim	[342]
Cap87^{b}	0.82	6.2×10^{-4}	120–250	$^{1}\mathrm{H}^{+}$		DR-sim	DR-sim	[342]
Sea88	0.30	1.7×10^{-5}	0–57	$^{1}\mathrm{H}^{+}$	p-type	low E	CV	[338]
Bud89	0.33	1.0×10^{-2}	> 915	$^{1}\mathrm{H}^{+}$		MD-sim	MD-sim	[343]
Her90	0.66	6.9×10^{-5}	90–212	$^{1}\mathrm{H}^{0}$	p-type	plasma	IRR	[332]
Riz91^{a}	1.09	3.7×10^{0}	120–185	$^{2}\mathrm{H}^{0}$	FZ	plasma	SIMS/CV	[333]
Riz91^{b}	0.59	8.4×10^{-5}	120–185	$^{2}\mathrm{H}^{+}$	p-FZ	plasma	SIMS/CV	[333]
Riz91^{c}	0.80	1.4×10^{-2}	120–150	$^{2}\mathrm{H}^{-}$	n-FZ	plasma	SIMS/CV	[333]
New91	1.26	6.2×10^{2}	225–350	$^{1}\mathrm{H}^{0}$	p-Cz	plasma	IR	[123]
Joh91^{a}	1.10	1.9×10^{0}	125–200	$^{2}\mathrm{H}^{-}$	n-FZ	plasma	SIMS	[334]
Joh91^{b}	0.82	1.1×10^{-3}	125–200	$^{2}\mathrm{H}^{-}$	n-Cz	plasma	SIMS	[334]
Joh92	0.69	1.2×10^{0}	27–47	$^{2}\mathrm{H}^{-}$	n-Cz	plasma	mc-CV	[340]
Sop92^{a}	0.66	8.5×10^{-3}	150–235	$^{2}\mathrm{H}^{0}$	FZ	plasma	SIMS	[335]
Sop92^{b}	0.67	3.6×10^{-3}	150–235	$^{2}\mathrm{H}^{0}$	Cz	plasma	SIMS	[335]
Pan94	0.70	2.4×10^{-2}	> 527	$^{1}\mathrm{H}^{0}$		MD-sim	MD-sim	[344]
Her01^{a}	0.49	1.3×10^{-3}	27–47	$^{1}\mathrm{H}^{+}$	n-Cz	plasma	mc-CV	[327]
Her01^{b}	0.51	1.1×10^{-3}	27–47	$^{2}\mathrm{H}^{+}$	n-Cz	plasma	mc-CV	[327]
Hua04	1.29	3.2×10^{0}	270–450	$^{1}\mathrm{H}^{0}$	p-Cz	plasma	SRP	[336]
Har07	0.51	5.6×10^{-3}	425–760	$^{1}\mathrm{H}^{0}$	Cz	in-grown	SRP	[341]
Lav13	1.19	6.1×10^{-2}	320–370	$^{1}\mathrm{H}^{0}$	n-FZ	high E	SRP	[339]

conduction processes in disordered materials [345]. The correlation is expressed by the Meyer-Neldel rule (MNR)

$$\ln D_0 = \ln D_{\mathrm{MN}} + \frac{E_A}{k_B T_{\mathrm{MN}}}, \tag{2.117}$$

where D_{MN} is the Meyer-Neldel pre-factor and T_{MN} is the Meyer-Neldel temperature. According to the MNR, at the temperature T_{MN}, the diffusivity is D_{MN}, for all activation energies. Substituting for D_0 in the Arrhenius equation (see equation 2.62) yields

$$D = D_{\mathrm{MN}} \exp\left(-\frac{E_A}{k_B\left(T - T_{\mathrm{MN}}\right)}\right). \tag{2.118}$$

The correlation of the Arrhenius coefficients plotted in figure 2.67b is described by a D_{MN} of $2.0\times10^{-7}\,\mathrm{cm^2s^{-1}}$ and a T_{MN} of $560\,^{\circ}\mathrm{C}$ ($0.0013\,\mathrm{K}^{-1}$).

The MNR is also known as the compensation law [346] or the isokinetic relationship [347]. It has been found in various instances, such as reaction kinetics [346], conduction processes [348–351] and also in diffusion processes in metals [352, 353] and semiconductors [354–356]. MNR is an empirical rule and has been broadly discussed in the recent decades. While some researchers argue that this correlation might originate from the co-contribution of intrinsic and extrinsic mechanisms [357] or from assisted processes, in which a number of low energy excitations is necessary to provide the energy for the whole process [353, 358, 359], other studies link its origin to impurity concentrations [350, 355]. There is also decline of the relevance and significance of the correlation described by the MNR. Kirchheim et al. showed that T_{MN} was very often close to the average of the temperature range in which experiments had been conducted. They argue that the information on physical reasons leading to the MNR might be lost due to the mathematical treatment of the problem [352]. A comprehensive review on the Meyer-Neldel rule is given in reference 360.

Beyer et al. investigated the diffusion of hydrogen in micro-crystalline and in crystalline silicon [355]. They found a dependence of the diffusion coefficient of hydrogen on the hydrogen concentration. They observed an increase of $D_{\mathrm{H}}^{\mathrm{eff}}$ with increasing hydrogen concentration which they contributed to the change in the chemical potential of hydrogen μ_{H} in micro-crystalline silicon. At the same time a decrease of the hydrogen diffusivity with increasing hydrogen concentration was observed in crystalline material. A study conducted within this thesis and presented in chapter 3 contradicts these results.

For the calculation of the doping concentration dependent diffusivity of hydrogen the Arrhenius coefficients derived by Johnson et al. ($^{2}\mathrm{H}^{-}$ (Joh92) [340]) and by Herring et al. ($^{1}\mathrm{H}^{+}$ (Her01$^{\mathrm{a}}$) [327]) are used for the respective charge states of hydrogen. The temperature dependence of the hydrogen diffusivity at different doping concentrations is plotted in figure 2.68.

As the dominant charge state throughout most of the band gap is H^{+} (see figure 2.66), the effective diffusivity of hydrogen is the same in intrinsic, and also in p-type silicon. Only in n-type material doped at donor concentrations higher than $10^{14}\,\mathrm{cm}^{-3}$ the effective diffusivity differs from the intrinsic conditions. In slightly doped n-type silicon at low temperatures, hydrogen diffuses more slowly than under intrinsic conditions. Only at high donor concentrations, the hydrogen diffusivity is also changed at increased temperature.

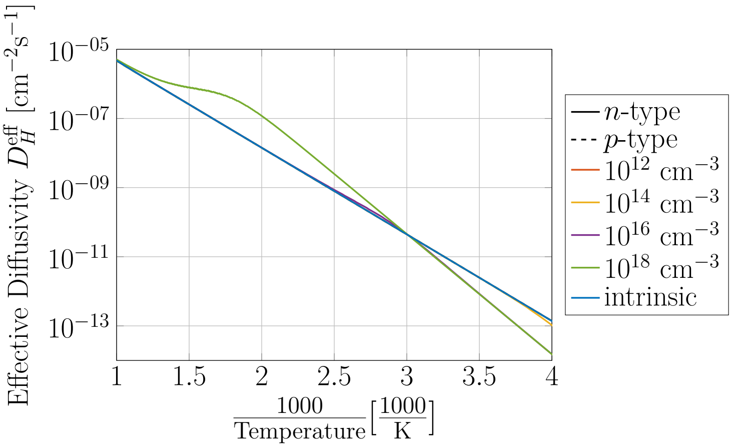

Figure 2.68: Temperature dependence of the effective diffusivity of atomic hydrogen at different doping concentrations.

Here it even overtakes the intrinsic diffusivity.

As mentioned in the introduction to this chapter, one of the applications of proton implantation in silicon, is the formation of donor rich layers [297, 313]. Figure 2.66 shows that atomic hydrogen itself is a donor. Furthermore, defect complexes formed by the implantation of protons (or in a subsequent annealing treatment) are also responsible for the changes of the electrical properties of the material. The next sections will discuss such defect complexes.

2.4.5 Hydrogen Dimer H_2

As soon as the temperature is high enough for atomic hydrogen to diffuse, it will form molecular hydrogen H_2. Various theoretical studies had already predicted the existence of the hydrogen dimer in silicon [320, 361] before it was detected using Rutherford backscattering [362], EPR [363], Raman spectroscopy [364–366] and infra-red spectroscopy [367]. In the silicon lattice H_2 either resides at a tetrahedral position (H_2^T), or at a “bond-centered-anti-bonding” position (H_2^*) [334, 368]. As shown by Estreicher et al., the only stable charge state of both configurations is the neutral one [325].

The hydrogen dimer is a mobile defect [369]. Experimental determinations of the diffusivity by Johnson et al. using SIMS measurements yielded an activation energy of 0.81 eV and a pre-factor of $1.1\times10^{-3}\,\mathrm{cm^2s^{-1}}$ [334]. These results were later reproduced experimentally [370] and theoretically [371] in different studies. The temperature dependence of the diffusivity of the hydrogen dimer is plotted in figure 2.71 alongside other mobile, hydrogen containing defects.

2.4.6 Defect Complexes of Hydrogen with Intrinsic Point Defects

Atomic hydrogen can react with intrinsic defects to form a variety of different defect complexes. Early work on such defects was done by Stein, who investigated proton implanted silicon using IR-spectroscopy [372, 373]. Changes in the IR absorption due to different annealing parameters were contributed to the formation and dissociation of defect complexes containing hydrogen and intrinsic point-defects. This defect family is labeled $\mathrm{V_mH}_n$ and $\mathrm{I_mH}_n$ (sometimes also $\{\mathrm{V}_m,\mathrm{H}_n\}$ and $\{\mathrm{I}_m,\mathrm{H}_n\}$) for defect complexes consisting of m vacancies or interstitials and n hydrogen atoms. Usually m is either 1 or 2 and n is an integer from 1 to 6 [374–385]. Also larger structures such as $\mathrm{V_6H_{12}}$ have been assigned to measured defect signals [386].

Ferreire-Resende used DFT simulations to calculate the ionization energies of VH (see appendix C.34), $\mathrm{VH_2}$ (see appendix C.35), $\mathrm{VH_3}$ (see appendix C.36) and $\mathrm{VH_4}$ in the silicon band gap [163]. Figure 2.69 shows the formation energy of each charge state of VH, $\mathrm{VH_2}$ and $\mathrm{VH_3}$, relative to E_form of the corresponding neutral state, as a function of the position of the Fermi energy in the band gap of silicon. Additionally the relative concentration of each charge state is plotted. The corresponding ionization energies and the formation energies at $E_F = 0$ and 0 K are listed in the tables in figure C.34.1a, C.35.1a and C.36.1a. According to Ferreira-Resende's calculations, $\mathrm{VH_4}$ is electrically inactive and its most stable configuration is the neutral charge state.

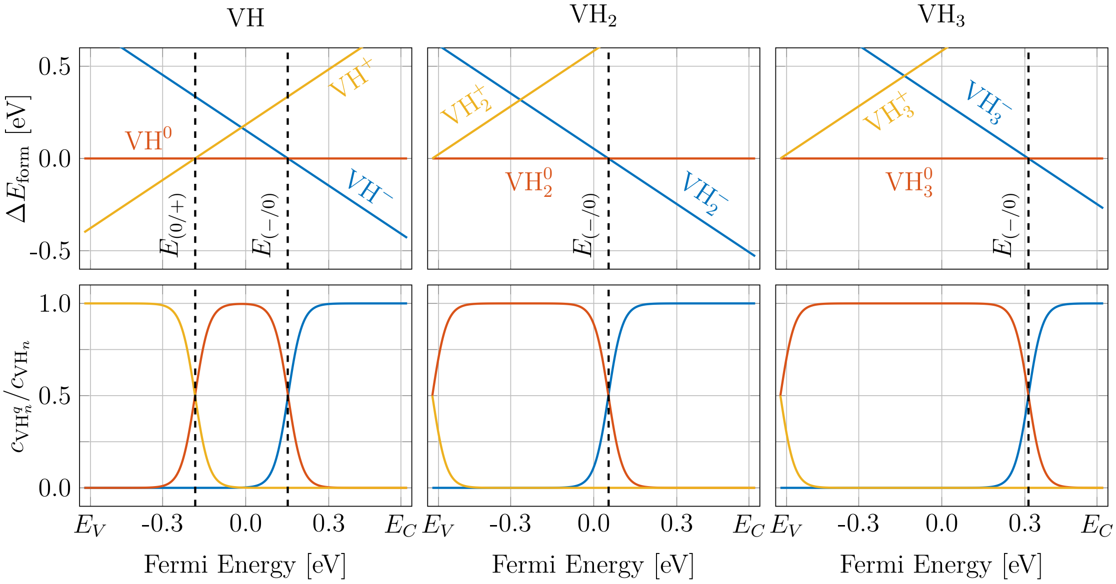

Figure 2.69: Formation energies and relative concentrations of each charge state of VH, $\mathrm{VH_2}$ and $\mathrm{VH_3}$, relative to E_form of the corresponding neutral state, in silicon as a function of the Fermi energy at 25 °C. The formation energies at $E_F = 0$ were calculated from ionization energies published in reference 163.

VH, on the other hand shows two charge state transitions within the band gap. Close to the middle of the band gap and for low doping concentrations, $\mathrm{VH^0}$ is the most stable state. In p-type material the positive charge state is dominant and in n-type material $\mathrm{VH^-}$ shows the highest relative concentration. According to the calculations of Ferreira-Resende, both defect complexes, $\mathrm{VH_2}$ and $\mathrm{VH_3}$, show an acceptor transition within the band gap and a donor transition at E_V. While the acceptor ionization level is close to the middle of the band gap for $\mathrm{VH_2}$, it appears closer to E_C for $\mathrm{VH_3}$.

Defect complexes of hydrogen and intrinsic defects often act as centers for indirect recombination:

$$\begin{aligned} \mathrm{V_m}\mathrm{H}_n + I &\leftrightarrow \mathrm{V}_{m-1}\mathrm{H}_n \\ \mathrm{I_m}\mathrm{H}_n + V &\leftrightarrow \mathrm{I}_{m-1}\mathrm{H}_n \end{aligned} \tag{2.119}$$

Furthermore, the dissociation of large defect complexes into smaller, more stable ones has been proposed [387]:

$$\begin{aligned} \mathrm{V}_m\mathrm{H}_{2m+2} + 2\mathrm{H} &\leftrightarrow \mathrm{V}_m\mathrm{H}_{2m+4} \\ \mathrm{V}_m\mathrm{H}_{2m+4} &\leftrightarrow \mathrm{V}_{m-1}\mathrm{H}_{2m} + \mathrm{VH}_4 \end{aligned} \tag{2.120}$$

Vacancy hydrogen defects and especially VH_4 act as nucleation centers for the formation of platelet defect, which are discussed in section 2.4.8.

According to several studies, the VH defect complex is considered to be mobile [373, 375, 388], though no Arrhenius coefficients describing its mobility have been published.

2.4.7 Hydrogen Defect Complexes Containing Extrinsic Point Defects

Most of the extrinsic defects in silicon form defect complexes with hydrogen. In this section only a selection of those defect complexes is discussed. Early studies already showed the inactivation of shallow dopants due to the pairing with hydrogen [389–394]. The dissociation of the neutral dopant-hydrogen pairs was investigated by Bergman et al. [47] and Zundel et al. [48]. The Arrhenius parameter describing the temperature dependence of the dissociation rate (see equation 2.98) of boron-hydrogen (BH) complexes were determined to be 1.32 eV for the binding energy and $10^{13}\,\mathrm{s}^{-1}$ for the attempt frequency [47]. The dissociation of phosphorus-hydrogen (PH) complexes is described by a E_b of 1.28 eV and an f_d of $2.8\times10^{14}\,\mathrm{s}^{-1}$ [48]. Furthermore, hydrogen can saturate defects such as $\mathrm{B_iB_s}$, forming electrically active $\mathrm{B_iB_sH}$ [261] (see appendix C.38). The relative formation energy of each charge state of $\mathrm{B_iB_sH}$, calculated from DFT-simulations by Adey et al. [261] is plotted as a function of the Fermi energy within the silicon band gap in figure 2.70. In intrinsic silicon, both charge states, the neutral and the negative state are populated, as the acceptor ionization lies in the middle of the band gap. Only for small acceptor concentrations is $\mathrm{B_iB_sH^0}$ the dominant charge state. Closer to E_V, the positive state shows the highest relative concentration. In n-type material the prevailing state is $\mathrm{B_iB_sH^-}$.

Both, PH and BH are considered to be mobile [240, 279]. The Arrhenius coefficients describing the diffusivity of the two complexes are, though, still to be measured and/or calculated.

The reaction of hydrogen with oxygen forms OH, OH_2 and O_2H_2-defect complexes [367, 370, 395–397]. Here, the notation OH_2 is used to not confuse this defect with crystal water H_2O, which often appears in ionic crystals. In the case of OH_2, the point defects making up the defect complex don't necessarily share the same chemical bonds. Several studies reported on an enhancement of the effective oxygen diffusivity [123, 127, 398], or the enhancement of the formation of oxygen related thermal donors in the presence of hydrogen [399–403]. The observed phenomena can be explained by the formation a of mobile defect. An obvious candidate for such a defect is OH. Hence, the determined enhanced oxygen diffusivity has been attributed to this defect. The temperature dependence of its diffusivity (D_OH), as determined by Newman et al. is described by an activation energy of 2.0 eV and a pre-factor of $7.1\times10^{-4}\,\mathrm{cm^2s^{-1}}$ [123] and is plotted in figures 2.47 and 2.71. At temperatures below 750 °C D_{OH} is higher than the diffusion constant of interstitial oxygen, but much lower than the diffusivity of VO, O_2, H_2 and atomic hydrogen. VOH (see appendix C.37) and VOH_2 are formed from the reaction of hydrogen with VO [404, 405], and V_2OH is formed from the reaction of V_2H with O [406]. Some possible reaction paths forming oxygen and vacancy containing defects are:

$$\begin{aligned} \mathrm{O + H} &\leftrightarrow \mathrm{OH} \\ \mathrm{OH + H} &\leftrightarrow \mathrm{OH_2} \\ \mathrm{O + H_2} &\leftrightarrow \mathrm{OH_2} \\ \mathrm{VO + H} &\leftrightarrow \mathrm{VOH} \\ \mathrm{VOH + H} &\leftrightarrow \mathrm{VOH_2} \\ \mathrm{VH + O} &\leftrightarrow \mathrm{VOH} \\ \mathrm{V + OH} &\leftrightarrow \mathrm{VOH} \\ \mathrm{VO + H_2} &\leftrightarrow \mathrm{VOH_2} \\ \mathrm{VH_2 + O} &\leftrightarrow \mathrm{VOH_2} \\ \mathrm{V_2H + O} &\leftrightarrow \mathrm{V_2OH} \\ \mathrm{VH + VO} &\leftrightarrow \mathrm{V_2OH} \end{aligned} \tag{2.121}$$

While VOH_2 is electrically inactive [405], VOH shows an acceptor transition between the mid band gap and E_C [163]. From DFT-simulations by Ferreira-Resende, the formation energies of the two charge states of VOH were calculated and are plotted in figure 2.70. For most of the energies within the silicon band gap, the neutral charge state of VOH is dominant. Only close to E_C is VOH^- the strongest populated state.

Another kind of defect complexes is formed when hydrogen reacts with carbon containing defects. This way CH [407, 408] and complexes containing carbon, oxygen and hydrogen, such as C_iOH [199] (see appendix C.15), C_iO_2H [141, 199] (see appendix C.16) and C_iOH_2 [199, 201] are formed. While C_iOH_2 is electrically inactive [199], DFT-calculations by Coutinho et al. show that both, C_iOH and C_iO_2H act as donors [199]. The relative formation energy of each of their charge states is plotted in figure 2.52 as a function of E_F. These defect complexes are of current interest, as they are candidates to explain the formation of the “shoulder”-peak in the spreading resistance profile of proton implanted silicon, which only appears in Cz-material and is not observed in FZ-silicon [409]. Another carbon-hydrogen defect complex, discussed in the literature is C_iC_sH (see appendix C.39). This complex is also electrically active, as calculations by Ferreira-Resende at al. show [163, 277]. Figure 2.70 shows the formation energies of C_iC_sH as a function of the Fermi energy. The formation energies at $E_F = 0$ at 0 K, used to create figure 2.70, including the ionization energies of the direct charge state transitions, measured from E_V are listed in the tables in figures C.37.1a, C.38.1a and C.39.1a. C_iC_sH is in its neutral state when the Fermi energy is close to the middle of the band gap. Only at high doping concentrations, the defect complex is charged. If the Fermi energy is close to the valence band, $C_iC_sH^+$ is dominant and if E_F approaches E_C, $C_iC_sH^-$ is the prevailing charge state.

Figure 2.71 shows the diffusivities of different hydrogen defect complexes. The Arrhenius parameters describing the temperature dependence of these diffusivities are listed in

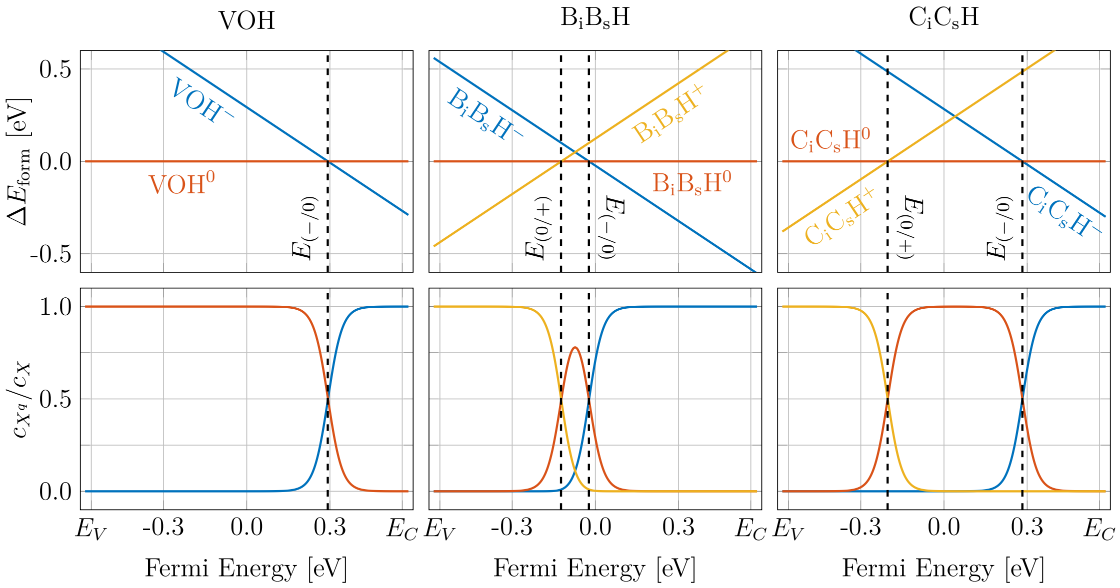

Figure 2.70: Formation energies and relative concentrations of each charge state of VOH, B_iB_sH and C_iC_sH in silicon as a function of the Fermi energy at 25 °C. The formation energies at $E_F = 0$ were calculated from ionization energies published in references 163 and 261.

table 2.17. Unfortunately this list is incomplete, as no Arrhenius parameters could be found for BH and PH and also other hydrogen containing defect complexes, such as VH might be mobile [373, 375, 388].

Table 2.17: Arrhenius coefficients describing the temperature dependence of the diffusion different hydrogen containing complexes in silicon as reported in references [123, 327, 334, 340].

Species	E_A [eV]	D_0 [cm^{2}s^{-1}]	Reference
H^-	0.69	1.2×10^0	[340]
H^+	0.49	1.3×10^{-3}	[327]
H_2	0.81	1.1×10^{-3}	[334]
OH	2.0	7.1×10^{-4}	[123]

Atomic hydrogen is the fastest hydrogen containing species. While at low temperature the diffusivity of the positive charge state is higher, at high temperature H^- is the fastest defect. The diffusivity of molecular hydrogen is about two orders of magnitude below the diffusion coefficient of atomic hydrogen and the smallest diffusivities were found for OH.

2.4.8 Platelet Defects

The implantation of high doses of protons into silicon leads to the generation of extended defects which can be visualized using transmission electron microscopy (TEM). The distribution, size and orientation of these microscopic defects depends on the material,

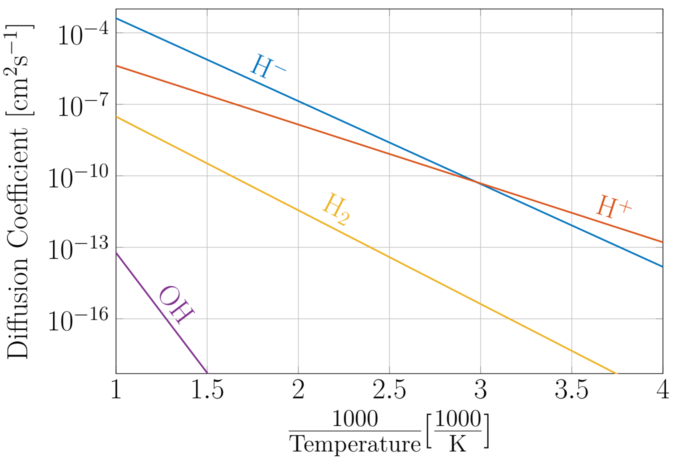

Figure 2.71: Diffusion coefficients of different hydrogen defect complexes, as reported in references [123, 327, 334, 340] in silicon as a function of the inverse temperature.

the implantation flux, the implanted dose and the temperature [410, 411]. One type of extended defects which are formed, are micro-cracks, oriented along {001} and {111}-lattice planes, which are called "platelets" [299, 412]. The diameter of these planar defects varies, depending on implantation and annealing conditions between a few Ångstroms up to several nanometers [413]. The implantation energy defines the depth in which the platelets are formed. Energies between 15 keV [414] up to several MeV [415] and implantation doses from $8\times10^{15}\,\mathrm{H^+cm^{-2}}$ to $10^{17}\,\mathrm{H^+cm^{-2}}$ were used to generate defects in different studies [416–421]. Other studies introduced the hydrogen into a shallow region in the material from a plasma source to form similar defects [412, 422, 423].

Van de Walle et al. proposed a mechanism describing the formation of platelets. If the hydrogen concentration is high, the generation of a Frenkel pair, which usually needs an input of about 8 eV goes along with the saturation of the four created dangling bonds at the vacancy by four hydrogen atoms [323]. The energy release of the formation of a silicon-hydrogen bond was calculated to be 2.2 eV, making the overall process exothermic. Once such a VH_4-complex is formed, it is energetically favorable to eject another silicon atom, neighboring the created defect, which is only three-fold coordinated and, thus, forming a V_2H_6-defect and releasing another self-interstitial. This process goes on inside a lattice plane until the hydrogen concentration becomes too small [323]. Deák et al. proposed another model for the formation and structure of the platelet. Their calculations showed, that "a strain driven alignment of pairs of hydrogen atoms, breaking and saturating the bonds between adjacent (111) silicon planes" shows the lowest formation energy for platelet structures [424]. A very comprehensive model of the formation process was derived by Reboredo et al. describing both, nucleation and growth of the platelets [383]. In a similar way as in the model of Van de Walle, the nucleation center is VH_4. One growth path is described by the following reactions:

$$\begin{aligned} \mathrm{VH_4} + \mathrm{H_2} + 2.5\,\mathrm{eV} &\rightarrow \mathrm{V_2H_6} + \mathrm{I} \\ \mathrm{V_2H_6} + \mathrm{H_2} + 2.5\,\mathrm{eV} &\rightarrow \mathrm{V_3H_8} + \mathrm{I} \qquad (2.122) \\ \mathrm{V}_m\mathrm{H}_{2m+2} + 2\mathrm{H} + 2.5\,\mathrm{eV} &\leftrightarrow \mathrm{V}_m\mathrm{H}_{2m+4} + \mathrm{I} \end{aligned}$$

This way, voids are formed in the material. Another reaction path, including the dissociation of a larger defect leads to the formation of platelets

$$V_2H_6 + H_2 \leftrightarrow [VH_4]_2 + 0.1\,\mathrm{eV}. \tag{2.123}$$

Here, $[VH_4]_2$ stands for a pair of second neighbor VH_4-complexes. The platelet formation goes on by adding two other hydrogen molecules:

$$\begin{aligned}[VH_4]_2 + H_2 + 2.4\,\mathrm{eV} &\rightarrow [VH_4V_2H_6 + I]\\ [VH_4V_2H_6] + H_2 + 2.4\,\mathrm{eV} &\leftrightarrow [VH_4]_3\,.\end{aligned} \tag{2.124}$$

Adding further hydrogen molecules increases the number of second neighboring VH_4-complexes. At a certain size, the platelet surface then undergoes a reconstruction and releases half of the bound hydrogen [383]. This hydrogen then forms H_2 which is trapped within the platelet which was also observed in experiments [425].

The generation of platelet defects can be of technological use, as shown in the “Smart Cut”-process developed by Bruel et al. [301], where hydrogen is implanted into a silicon wafer (wafer A). Then this wafer A is bonded to another wafer B. During a thermal treatment platelets are formed at the implantation depth which leads to the split-off of a thin layer of wafer A which remains bonded to wafer B. After polishing, wafer B can be used as a substrate for the productions of silicon on insulator devices and wafer A can be recycled e.g. as a new wafer B [300, 301, 426, 427].

3 Determination of the Kinetics of Different Processes in Proton Implanted Silicon Using Spreading Resistance Profiling

When silicon is implanted with protons and subsequently annealed, many different defect complexes are formed. Some of these complexes are electrically active. Due to the distribution of these defects during the implantation, a profile of the charge carrier concentration (c_{CC}) is generated, which shows a region of low c_{CC}, in the irradiated region, accompanied by a peak in the c_{CC}-profile at the implantation depth. Below the implantation depth, the charge carrier concentration converges to that of the substrate material.

During a subsequent anneal, the c_{CC}-profile is changed, as mobile defects diffuse and electrically active defect complexes are formed, and/or deactivated. From these changes, the effective diffusivity of hydrogen is extracted. Furthermore, the kinetics of the formation of thermal donors and the formation of the “shoulder” in the c_{CC}-profile are investigated.

In the first section of this chapter spreading resistance profiling (SRP), a method used to measure the charge carrier concentration profile, is explained. The next section investigates the influence of the maximum hydrogen concentration of the effective diffusivity of hydrogen $D_{\mathrm{H}}^{\mathrm{eff}}$. Here, $D_{\mathrm{H}}^{\mathrm{eff}}$ is is calculated from the change in the diffusion length, $L_{D_{\mathrm{H}}}$ of hydrogen as a function of the annealing time. $L_{D_{\mathrm{H}}}$ is determined from the extend of a region of increased charge carrier concentration. In a further section, the effective diffusivity of hydrogen is extracted from the decay of c_{CC} at the implantation depth and the kinetics of the formation of thermal donors in different parts of the proton implanted material is investigated.

3.1 Spreading Resistance Profiling

Spreading resistance profiling, or SRP, is a widely used measurement technique in semiconductor analysis. In this method, the resistance between two tungsten tips, is measured as a function of the position on a silicon sample [428, 429]. The resulting profile of the resistance is then converted to a resistivity-profile using a calibration function. This calibration function is derived from the measurement of calibration samples of known resistivity. As shown in figure 2.13, the donor, or acceptor concentration can be calculated from the resistivity.

The measurement requires the knowledge of the doping type of the analyzed material, as both, the calibration and the calculation of the dopant or charge carrier concentration differs for n-type and for p-type material. Figure 3.1 shows the calibration curve for the conversion of the resistance into the resistivity for n-type and p-type <100>silicon.

In this method it is crucial that the quality of the contacts between the tips and the sample is reproducible. Hence, the surface of the specimen, as well as the calibration samples has to be conditioned in the same way by grinding and polishing the materials. Furthermore, a constant temperature is important. To ensure a constant quality of the technique, a reference sample is measured on a regular basis. As soon as the measured resistance profile of the reference sample leaves certain boundaries, the measurement tips are re-conditioned and new sets of calibration curves are recorded until the resistance of the reference sample returns to values within the boundaries.

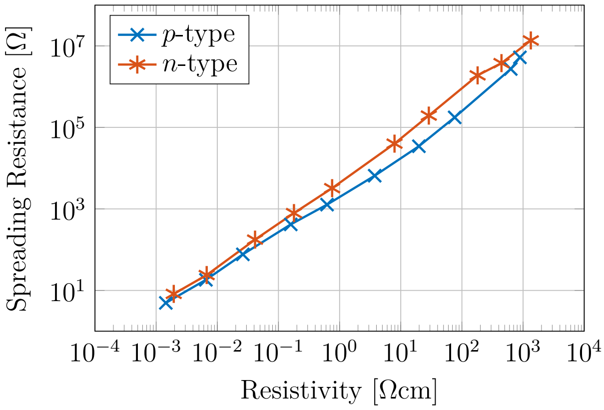

Figure 3.1: Calibration curves for n-type and p-type silicon, as used in SRP.

The usual spacing between the measurement tips is around 40 µm-50 µm and the distance between the measurement points (step width) is on the order of 5 µm. To be able to achieve a measurement resolution better than 5 µm, the specimen is beveled. This is done by grinding the material at the desired bevel angle. In this study, angels around 5 ° 44 ' and 11 ° 32 ' have been used. The samples were ground using silicon carbide grinding paper and afterwards polished using a suspension of 0.1 µm diamond powder in sawing oil. The bevel angle was then measured using a profilometer.

All SRP-measurements presented in this thesis were performed in a SSM2000-SRP tool and the post processing was done using the software NANOSRP Analysis.

3.1.1 Sample Preparation and Measurements

As indicated above, in this study, different samples have been implanted with protons at different energies and doses. Table 3.1 lists the eight samples investigated in this study. The samples S5 and S8 were already the subject of a prior investigation by Kirnstötter et al. published in reference 430.

An 8-inch wafer of each specimen was proton implanted at Infineon Technologies AG in Villach. The wafers were cut to pieces of 1 cm×1 cm using a diamond pen. To diffuse the hydrogen, pieces of each sample were annealed at temperatures from 400 °C to 500 °C for 0 h to 75 h in nitrogen atmosphere using an Anton Paar DHS 1100 heating stage. The annealing time was measured from the point, where the annealing temperature was reached to the point where the cooling was initiated. An annealing time of 0 h means that

Table 3.1: List of investigated samples including material and doping type, oxygen concentration, implantation parameters and nominal doping concentration.

	Material	c_O [cm^{-3}]	Energy [MeV]	Dose [H$^+$cm^{-2}]	Doping [cm^{-3}]
S1	p-m:Cz	$< 4{\times}10^{17}$	2.5	$5{\times}10^{14}$	$< 10^{13}$
S2	p-m:Cz	$< 4{\times}10^{17}$	2.5	$1{\times}10^{15}$	$< 10^{13}$
S3	p-m:Cz	$< 4{\times}10^{17}$	2.5	$5{\times}10^{15}$	$< 10^{13}$
S4	p-m:Cz	$< 4{\times}10^{17}$	2.5	$1{\times}10^{16}$	$< 10^{13}$
S5	p-m:Cz	$< 4{\times}10^{17}$	4.0	$1{\times}10^{14}$	$< 10^{13}$
S6	p-m:Cz	$< 4{\times}10^{17}$	4.0	$1{\times}10^{15}$	$< 10^{13}$
S7	p-m:Cz	$< 2{\times}10^{17}$	2.5	$1{\times}10^{14}$	$< 6 \times 10^{12}$
S8	n-FZ	$< 1{\times}10^{17}$	4.0	$1{\times}10^{14}$	3×10^{13}

those samples where heated to the annealing temperature and immediately cooled down again. The heating and cooling rate were around 1 Ks^{-1}. After the annealing the samples were cut to pieces of 1 cm×0.2 cm, beveled, polished and measured at 25 °C using SRP.

Figure 3.2 shows the charge carrier concentration profile, measured on a piece of sample S1 after an anneal for 1 h at 450 °C.

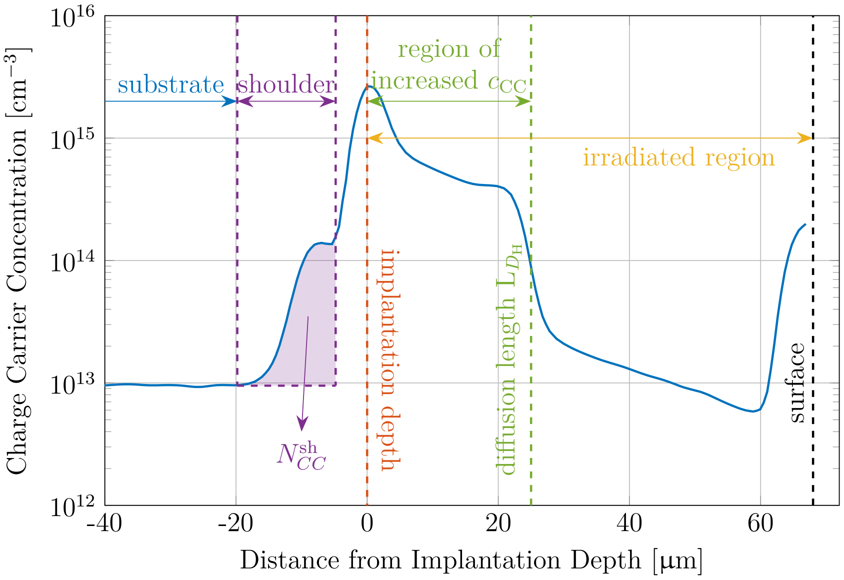

Figure 3.2: SRP-measurement of a piece of sample S1 annealed at 450 °C for 1 h.

In this figure, the important regions in the material are indicated. The implantation depth is marked by a red, dashed line. Here, the maximum charge carrier concentration is found. The region of constant c_{CC} more than 20 µm deeper than the implantation depth is called the substrate. At a depth from -20 µm to -5 µm, a shoulder in the c_{CC}-profile is observed. The integral over the charge carrier concentration in this region yields the number of charge carriers in the shoulder, N_{CC}^{sh} (see section 3.3.4). The surface of the material is at a distance of 68 µm from the implantation depth. The region between the surface and the implantation depth is called the irradiated region. Inside the irradiated region, a section with increased c_{CC} is observed. As explained in the next section, the diffusion length of hydrogen is extracted from the position of the edge of this region. Figure 3.3 shows the SRP-measurements on pieces of sample S1 after different anneals.

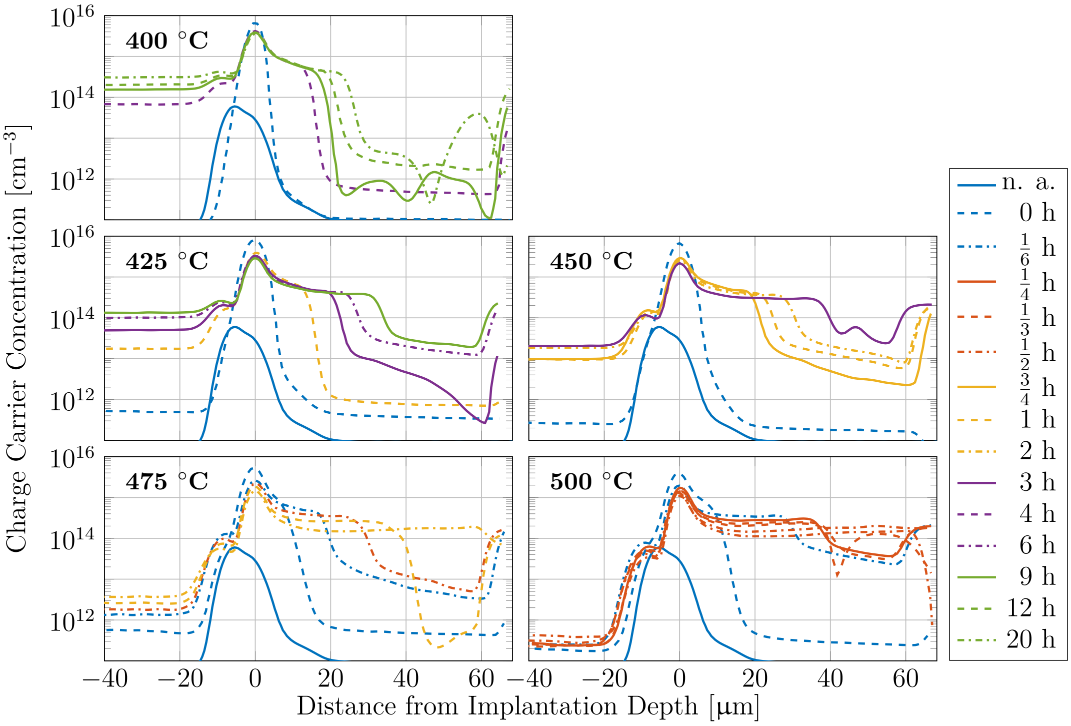

Figure 3.3: SRP-measurements of pieces of sample S1 annealed under different conditions.

Each sub-figure shows a set of c_{CC}-profiles after anneals at a certain temperature for different durations. The c_{CC} is plotted as a function of the distance from the implantation depth. In these plots, the surface of the material is in the positive direction of the distance and the substrate material is at negative distances. The solid blue line in each sub-figure signalizes the c_{CC}-profile of the sample directly after the proton implantation, without annealing (“n.a.” means not annealed).

Figures including the c_{CC}-profiles measured on pieces of samples S2-S8 are shown in appendix B.

3.2 Influence of the Maximum Hydrogen Concentration on Its Effective Diffusivity

In this section the effective diffusivity of hydrogen $D_{\mathrm{H}}^{\mathrm{eff}}$ is extracted from the expansion of a region of increased charge carrier concentration after anneals of proton implanted silicon samples at different annealing temperatures. From the temperature dependence of $D_{\mathrm{H}}^{\mathrm{eff}}$, the Arrhenius parameters describing this process are extracted and a correlation of these parameters and the maximum hydrogen concentration in the material is found.

3.2.1 SRP Measurements and Calculation of Effective Diffusivity of Hydrogen from the Expansion of a Donor Rich Region

As shown by Huang et al. [336] in material treated with a hydrogen plasma, and, by Laven et al. [339] and by Kirnstötter et al. [430] in proton implanted silicon, SRP can be used to extract the diffusion length of hydrogen, L_{D_H}. In these studies, the diffusion of hydrogen leads to the formation of a *pn*-junction, which is shifted towards the surface of the material with increasing annealing time. The c_{CC}-profiles measured in this study, except for those of the low-dose samples S5, S7, and S8, do not show such a junction. Nevertheless, the diffusion of hydrogen is observed, as a region of increased charge carrier concentration expands towards the surface of the material with increasing annealing time. Here, the diffusion length of hydrogen is approximated as the position of the steepest decay in the logarithmic c_{CC}-profile, at the edge of this expanding region. Figure 3.3 shows the propagation of this region towards the surface of the material with increasing annealing time. As it is explained later, the change in the carrier concentration does not happen due to the formation of hydrogen related donor complexes but as a consequence of the deactivation of acceptors by the diffusing hydrogen.

In figure 3.4 the L_{D_H}, extracted from pieces of sample S1 after different anneals, is plotted as a function of the square root of the annealing time.

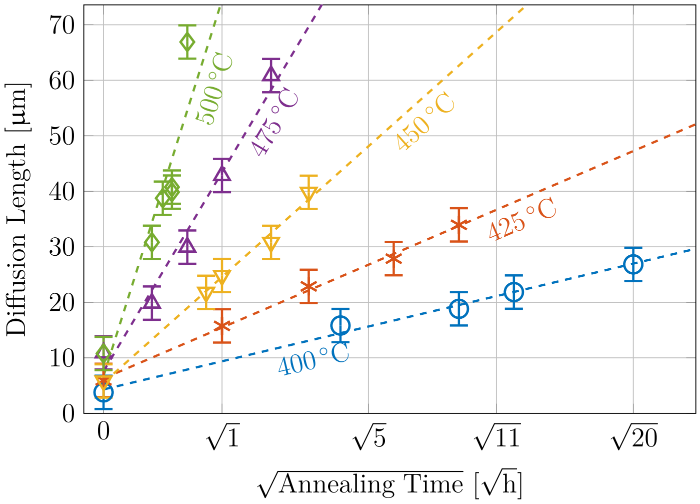

Figure 3.4: Diffusion length of hydrogen in sample S1 as a function of the square root of the annealing time at different temperatures.

As described in equation 2.73, there is a linear correlation between L_{D_H} and the square root of the annealing time. The error-bars used in figure 3.4 indicate the uncertainty in the extraction of L_{D_H} which is estimated to be $\pm 3\,\mu\mathrm{m}$. The dashed lines represent linear fit functions through the experimental data. The values of the effective diffusivity of hydrogen $D_\mathrm{H}^\mathrm{eff}$ at the corresponding annealing temperatures are extracted from the slopes of these fit functions.

The temperature dependence of $D_\mathrm{H}^\mathrm{eff}$ is described by the Arrhenius law. Figure 3.5 shows a plot of $D_\mathrm{H}^\mathrm{eff}$ in sample S1 as a function of the inverse annealing temperature.

This dashed line represents a linear fit using an activation energy of 2.35 eV and a

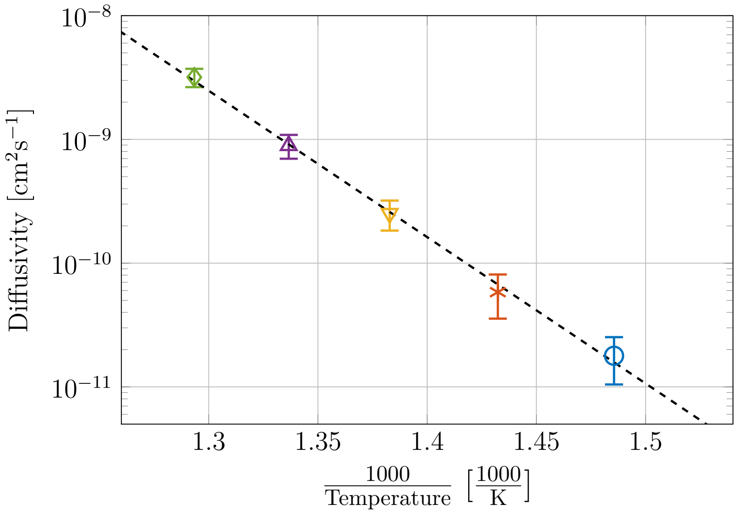

Figure 3.5: Effective diffusivity of hydrogen in sample S1 at different temperatures.

pre-factor of $5.9\times10^{6}\,\mathrm{cm^2s^{-1}}$. The error-bars shown in this figure are calculated from the uncertainty in the measurement of the diffusion length and from an error in the annealing time of ±60 s.

Similar figures of the diffusion length and the diffusivity of hydrogen in the other samples (S2-S8) are shown in appendix B. Table 3.2 lists all values of the effective hydrogen diffusivity, extracted from the SRP-measurements on all samples at different annealing temperatures.

Table 3.2: Effective diffusivity of hydrogen in samples S1-S8 at different annealing temperatures in $\mathrm{cm^2s^{-1}}$.

	400 °C	425 °C	450 °C	475 °C	500 °C
S1	$1.8\times10^{-11}\pm41\,\%$	$5.8\times10^{-11}\pm39\,\%$	$2.5\times10^{-10}\pm27\,\%$	$8.9\times10^{-10}\pm22\,\%$	$3.2\times10^{-09}\pm17\,\%$
S2	$2.1\times10^{-11}\pm37\,\%$	$5.1\times10^{-11}\pm42\,\%$	$1.3\times10^{-10}\pm36\,\%$	$8.0\times10^{-10}\pm23\,\%$	$1.9\times10^{-09}\pm24\,\%$
S3	$1.1\times10^{-10}\pm19\,\%$	$2.7\times10^{-10}\pm22\,\%$	$9.1\times10^{-10}\pm23\,\%$	$2.4\times10^{-09}\pm21\,\%$	$3.9\times10^{-09}\pm25\,\%$
S4	$5.4\times10^{-11}\pm27\,\%$	$1.4\times10^{-10}\pm28\,\%$	$1.6\times10^{-10}\pm22\,\%$	$4.3\times10^{-10}\pm40\,\%$	$7.7\times10^{-10}\pm27\,\%$
S5	$2.5\times10^{-11}\pm48\,\%$		$4.7\times10^{-10}\pm18\,\%$		
S6	$1.7\times10^{-11}\pm41\,\%$		$2.4\times10^{-10}\pm14\,\%$		$3.3\times10^{-09}\pm13\,\%$
S7	$2.4\times10^{-11}\pm36\,\%$	$9.0\times10^{-11}\pm30\,\%$	$2.7\times10^{-10}\pm27\,\%$	$1.1\times10^{-09}\pm21\,\%$	$4.3\times10^{-09}\pm19\,\%$
S8	$8.4\times10^{-11}\pm40\,\%$		$8.2\times10^{-10}\pm18\,\%$		

The Arrhenius parameters describing the temperature dependence of $D_{\mathrm{H}}^{\mathrm{eff}}$ in each sample are listed in table 3.3. Here, the uncertainties of the calculated Arrhenius coefficients include the error in the temperature measurement of the annealing stage which is estimated as ±2 K.

Table 3.3: Activation energy E_A and pre-factor D_0 extracted from samples S1-S8.

Sample	E_A [eV]	D_0 [cm^{2}s^{-1}]
S1	2.35±1 %	$5.9\times10^{+6}\pm40\,\%$
S2	2.10±1 %	$8.1\times10^{+4}\pm42\,\%$
S3	1.67±1 %	$3.8\times10^{+2}\pm30\,\%$
S4	1.15±1 %	$2.1\times10^{-2}\pm35\,\%$
S5	2.45±1 %	$6.0\times10^{+7}\pm30\,\%$
S6	2.34±1 %	$5.6\times10^{+6}\pm34\,\%$
S7	2.31±1 %	$4.2\times10^{+6}\pm37\,\%$
S8	1.91±1 %	$1.7\times10^{+4}\pm38\,\%$

3.2.2 Correlations of the Arrhenius Parameters

Similar to the previous observation, when comparing data from literature (see section 2.4.4), also the Arrhenius parameters calculated in this study are scattered over a wide range. While the activation energies range from 1.15 eV to 2.45 eV, the pre-factors are spread over almost ten orders of magnitude. The extracted parameters also show a very strong Meyer-Neldel correlation [345]. This correlation, shown in figure 3.6, is described by a Meyer-Neldel-temperature T_{MN} of 453 °C and by a Meyer-Neldel pre-factor D_{MN} of $4.2 \times 10^{-10}\,\mathrm{cm^2s^{-1}}$.

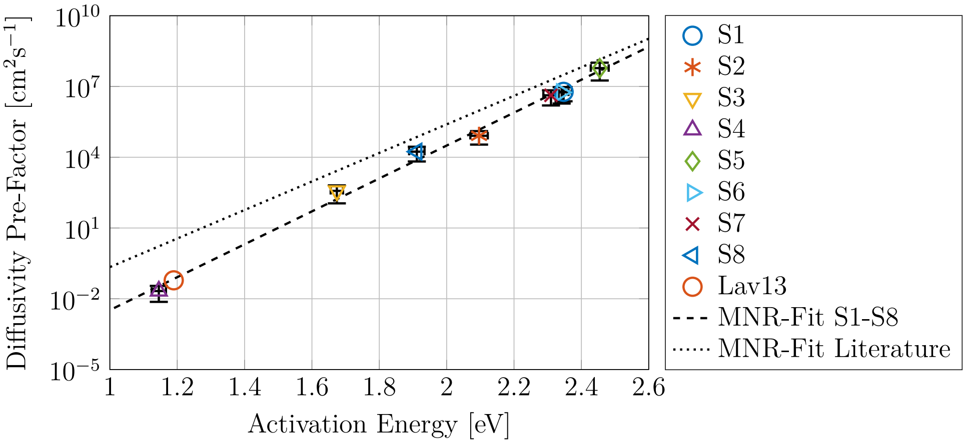

Figure 3.6: Correlation of the pre-factors of samples S1-S8 with the corresponding activation energies. The Arrhenius parameters calculated from data published by Laven et al. (Lav13) in reference [339] are included. The dashed line represents a fit through the Arrhenius parameters of S1-S8, the dotted line represents the fit through the Arrhenius parameters from other studies as shown in figure 2.67, according to the Meyer-Neldel-Rule.

As shown in figure 3.6, the Meyer-Neldel parameters differ from those, extracted from the correlation of the Arrhenius parameters found in literature (see figure 2.67). Though, the parameters calculated from $D_{\mathrm{H}}^{\mathrm{eff}}$, published by Laven et al. (see reference 339), fall exactly on the same MNR-fit, as the Arrhenius coefficients determined in this work. In

Laven's study, an n-type FZ-silicon wafer, similar to the substrate material of sample S8, was implanted with a dose of $4 \times 10^{14}\,\mathrm{H^+cm^{-2}}$ at an energy of 2.5 MeV.

In figure 3.7, the activation energies and the pre-factors of the samples S1-S8, including the Arrhenius parameters, calculated by Laven et al. are plotted as a function of the maximum hydrogen concentration. This concentration is calculated from the maximum of the dose-normalized hydrogen concentration profile, computed with SRIM (see figure 2.64), multiplied by the corresponding proton dose. The maximum hydrogen concentration is a theoretical value before the anneal. The maximum concentration of radiation induced defects in the material is supposed to scale with the maximum hydrogen concentration. The higher the implanted dose and the lower the implantation energy are, the higher is the maximum hydrogen concentration.

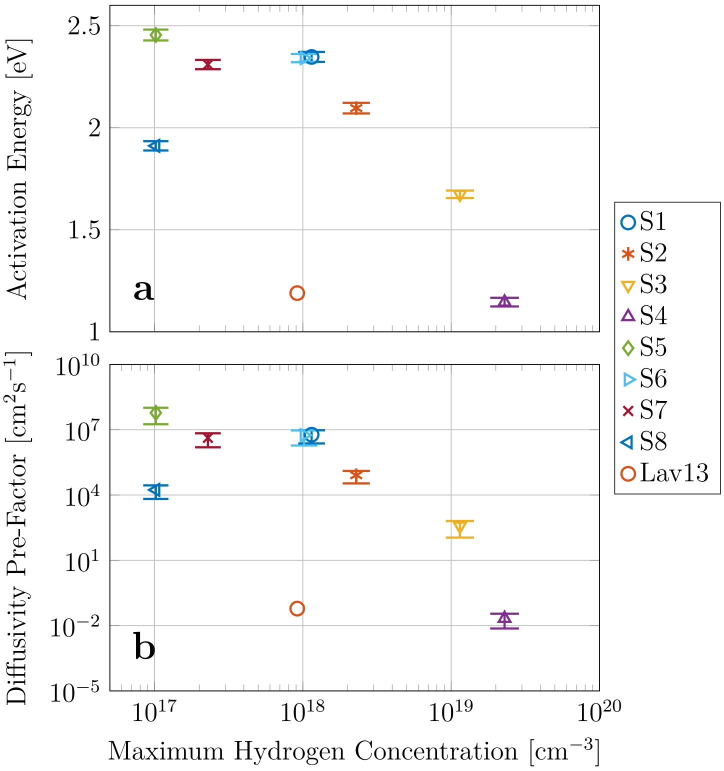

Figure 3.7: Correlation of **a**: the activation energy and **b**: the pre-factor of the effective diffusivity of hydrogen in samples S1-S8 with the theoretical maximum of the hydrogen concentration calculated from SRIM-simulations.

Figure 3.7 shows, that both, the activation energy and the pre-factor decrease with increasing hydrogen concentration. Especially for the Arrhenius parameters determined for samples S1-S6, which were all produced from the same substrate material, this trend is very distinct. The samples S8 and Lav13, which were prepared from low-impurity FZ-material, show lower Arrhenius parameters at the same maximum hydrogen concentration. The E_a and D_0, calculated from the measurements on the low oxygen m:Cz-specimen S7 also seem slightly reduced compared to the Arrhenius parameters found in the other m:Cz-samples.

3.3 Kinetics of Different Processes Determined From the Change of the Charge Carrier Concentration in Other Regions of the Material

Parallel to the expansion of the charge carrier rich region in proton implanted silicon, also the charge carrier concentration (c_{CC}) at and around the peak, and in the substrate material is changed. These changes appear due to the formation and dissociation of electrically active defects and defect complexes in the material. Even though the net doping of most of the samples after the anneals is n-type, also acceptor complexes are formed. This is indicated by the formation of p-type regions in the irradiated regions of some samples. In this section different aspects regarding the formation of electrically active defects are investigated. First, the change of the residual number of charge carriers in the region of the material directly influenced by the proton implantation is studied for different annealing conditions. Then the change of the doping concentration in the substrate material and at the implantation depth are investigated. The last part of this section takes a look at the change of the number of charge carriers in the shoulder peak after different anneals.

3.3.1 Evaluation of the Change in the Number of Residual Charge Carriers

By evaluating the integral over the c_{CC}-profile (see figure 3.2) in the region from the surface of the to the interface to the substrate material, the number of residual charge carriers per unit area, N_{CC}, is calculated. This number represents the sum over all ionized defects in this region, where each defect is multiplied by its effective charge.

The change of N_{CC} over time is described by

$$N_{CC}(t) = N_{CC}^0 - r_{N_{CC}} t, \tag{3.1}$$

where $r_{N_{CC}}$ is the rate of the change in the number of charge carriers and N_{CC}^0 is the number of charge carriers at $t = 0\,\mathrm{s}$. Figure 3.8 shows N_{CC} in pieces of sample S1 after different anneals. Figures showing the change of the number of residual charge carriers in the other samples are found in appendix B.

The number of residual charge carriers per area in sample S1 at the beginning of the anneal (at t=0) is more than two orders of magnitude lower than the number of implanted hydrogen atoms ($5 \times 10^{14}\,\mathrm{H}^+\mathrm{cm}^{-2}$). Hydrogen itself is a donor (see figure 2.66), so the lower number of residual charge carriers suggests, that either the electrons donated by hydrogen are compensated by acceptors, or that a large fraction of the hydrogen donors are deactivated due to the formation of defect complexes.

Most of sample S1 is n-type after all applied annealing conditions, hence, N_{CC} corresponds to the residual electron concentration. An increase in N_{CC} can mean either the generation of new donors, or the deactivation of acceptors. At low temperatures (400 °C and 425 °C) N_{CC} grows with increasing annealing time, indicating that the formation of donors or deactivation of acceptors is happening faster than the deactivation of donors or the formation of acceptors. Starting at an annealing temperature of 450 °C, N_{CC} gets smaller the longer the sample is annealed. Here, more acceptors are formed, or more

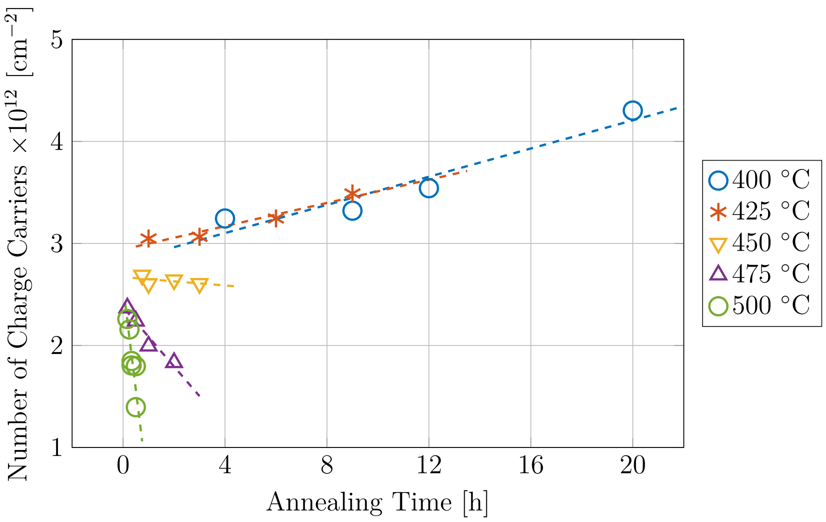

Figure 3.8: Number of charge carriers per unit area in the proton implanted region of sample S1 after different anneals.

donors are deactivated, compared to the formation of donors and the deactivation of acceptors.

Table 3.4 lists the rates $r_{N_{CC}}$ in each sample at every applied annealing temperature. Only in sample S3, $r_{N_{CC}}$ is positive at all annealing temperatures. All other samples show an increase in N_{CC} at low temperatures and a decrease of N_{CC} at higher temperatures.

Table 3.4: Rate of the change in the number of charge carriers, $r_{N_{CC}}$, in the region directly influenced by proton implantation in samples S1-S8 at different annealing temperatures in $\text{cm}^{-2}\text{s}^{-1}$. The range of the calculated number of charge carriers before the anneal, N^0_{CC}, is also given for each sample.

	400 °C	425 °C	450 °C	475 °C	500 °C	N^0_{CC} [cm^{-2}]
S1	1.9×10^7	1.5×10^7	-5.7×10^6	-8.1×10^7	-5.6×10^8	2.4×10^{12}-2.9×10^{12}
S2	2.5×10^7	-8.8×10^6	-8.4×10^6	-9.3×10^7	-2.0×10^8	2.9×10^{12}-4.2×10^{12}
S3	3.8×10^7	3.0×10^7	4.2×10^7	9.4×10^7	8.1×10^7	3.5×10^{12}-4.8×10^{12}
S4	9.8×10^7	1.2×10^8	1.5×10^8	4.1×10^8	-3.3×10^7	5.2×10^{12}-7.8×10^{12}
S5	3.5×10^6		-1.6×10^7			1.9×10^{12}-2.1×10^{12}
S6	3.1×10^6		6.9×10^6		-8.3×10^7	3.2×10^{12}-4.6×10^{12}
S7	1.6×10^6	2.7×10^6	-3.0×10^6	-2.2×10^7	-5.9×10^7	6.8×10^{11}-7.7×10^{11}
S8	-9.4×10^6		-1.7×10^7			2.4×10^{12}-3.8×10^{12}

One explanation for the observations is the change of the ratio of the rates of the formation of donors and of their dissociations. At low temperatures, reaction rates are higher than dissociation rates, if the activation energy of the diffusivity of the mobile reactants is lower than the binding energy of the formed defect complex. As a consequence of that low activation energy, the increase of the reaction rate with increasing temperature is low. The binding energy of defect complexes is usually higher than the activation energies of the mobile reactants. A high binding energy is associated with a strong temperature dependence of the dissociation rate. Hence, at low temperatures, reactions between defects are favored over dissociations. At increased temperatures, though, the dissociation rates overtake the reaction rates. This leads to a positive $r_{N_{CC}}$ at low temperatures and to a negative $r_{N_{CC}}$ at high temperatures.

3.3.2 Evaluation of the Change in the Charge Carrier Concentration in the Substrate Material

The change in the charge carrier concentration in the substrate material is predominantly caused by the formation of thermal donors (see section 2.3.3.1). The doping type of the substrate materials of the samples S1-S7, which is p-type without anneal, is converted to n-type at the investigated annealing temperatures. In a sequence of isochronal anneals, the lowest temperature where the conversion from p-type to n-type occurs was determined to lie between 350 °C and 400 °C. A conversion of the doping type was observed until an annealing temperature of 510 °C [431].

The dependence of the charge carrier concentration in the substrate material,c_{CC}^{sub}, on the annealing time, is described by

$$c_{CC}^{\text{sub}}(t) = c_{CC}^{\text{sub},0} - r_{c_{CC}}^{\text{sub}} t, \tag{3.2}$$

where $c_{CC}^{\text{sub},0}$ is the charge carrier concentration in the substrate material before the anneal and $r_{c_{CC}}^{\text{sub}}$ is the formation rate of the thermal donors. Figure 3.9 shows c_{CC}^{sub} in sample S1 on a logarithmic scale after anneals under different conditions. At all investigated temperatures, the charge carrier concentration in the substrate material grows with increasing annealing time. The higher the annealing temperature is, though, the smaller is the time dependent increase of c_{CC}^{sub}.

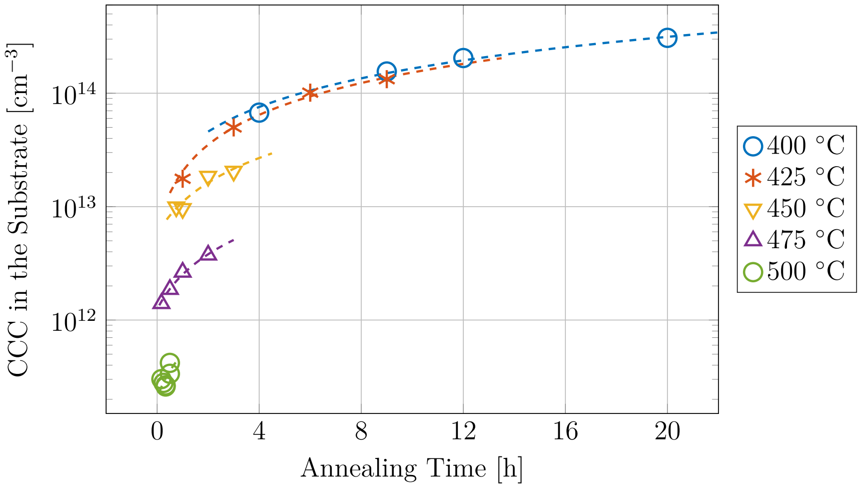

Figure 3.9: Evolution of the charge carrier concentration in the substrate material of sample S1 at different annealing temperatures.

In the tables 3.5 and 3.7 the formation rate of thermal donors in the substrate, $r_{c_{CC}}^{\text{sub}}$

and the charge carrier concentration before the anneal $c_{CC}^{\mathrm{sub},0}$ are listed for the samples S1 to S8 at different annealing temperatures.

Table 3.5: Formation rate of thermal donors in the substrate materials of samples S1-S8 at different annealing temperatures in $\mathrm{cm^{-3}s^{-1}}$.

	400 °C	425 °C	450 °C	475 °C	500 °C
S1	4.1×10^{9}	4.1×10^{9}	1.5×10^{9}	3.6×10^{9}	8.3×10^{7}
S2	6.6×10^{9}	4.5×10^{9}	2.1×10^{9}	1.9×10^{8}	-1.8×10^{8}
S3	5.1×10^{9}	3.5×10^{9}	2.5×10^{9}	2.6×10^{9}	5.4×10^{7}
S4	1.8×10^{10}	8.4×10^{9}	4.3×10^{9}	1.7×10^{9}	-1.3×10^{9}
S5	1.9×10^{8}		2.9×10^{7}		
S6	2.4×10^{9}		1.3×10^{7}		5.8×10^{7}
S7	2.7×10^{8}	1.7×10^{8}	4.9×10^{7}	6.6×10^{6}	1.1×10^{7}
S8	1.4×10^{6}		9.8×10^{6}		

In figure 3.10 the rate of the formation of thermal donors in sample S1 is plotted as a function of the inverse temperature.

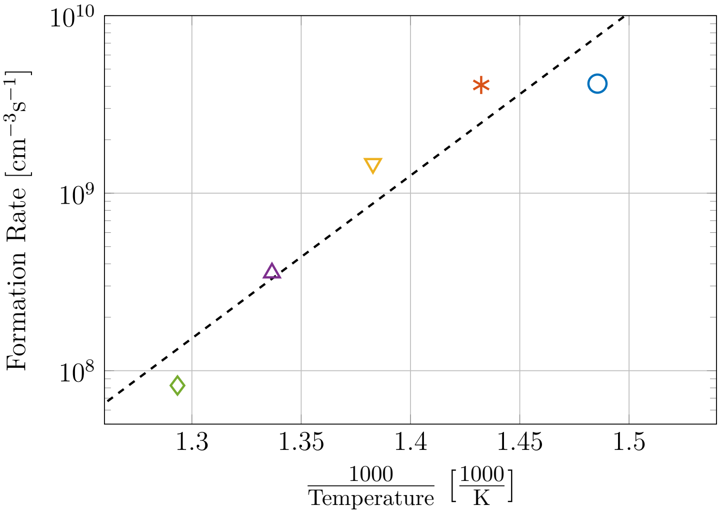

Figure 3.10: Formation rate of thermal donors in the substrate material of sample S1 as a function of the inverse temperature.

The Arrhenius fit through the data yields a negative activation energy of -1.8 eV. All m:Cz samples (S1-S7) show a monotonic decrease of r_{CCC}^{sub} with increasing temperature. The Arrhenius coefficients describing this temperature correlation, according to

$$r_{CCC}^{\mathrm{sub}} = r_{CCC}^{\mathrm{sub},0} \exp\left(-\frac{E_{CCC}^{\mathrm{sub}}}{k_B T}\right) \tag{3.3}$$

are listed in table 3.6. Here, $r_{CCC}^{\mathrm{sub},0}$ is the pre-factor and E_{CCC}^{sub} is the activation energy of the temperature correlation of r_{CCC}^{sub}.

Table 3.6: Arrhenius parameters describing the temperature dependence of the formation of thermal donors in the substrate material of samples S1-S8.

Sample	E_{cCC}^{sub} [eV]	$r_{cCC}^{\text{sub},0}$ [cm^{-3}s^{-1}]
S1	-1.8	1.8×10^{-4}
S2	-1.9	2.9×10^{-5}
S3	-1.6	5.4×10^{-3}
S4	-1.3	2.1×10^{0}
S5	-1.6	3.7×10^{-4}
S6	-1.7	9.3×10^{-5}
S7	-1.8	2.6×10^{-5}
S8	1.6	1.4×10^{18}

Also in this case, a correlation between the Arrhenius parameters, following the Meyer-Neldel-Rule (see equation 2.117), is observed. This correlation is shown in figure 3.11 and is described by a T_{MN} of 499 °C and by a Meyer-Neldel pre-factor of 6.1×10^7 cm^{-3}s^{-1}.

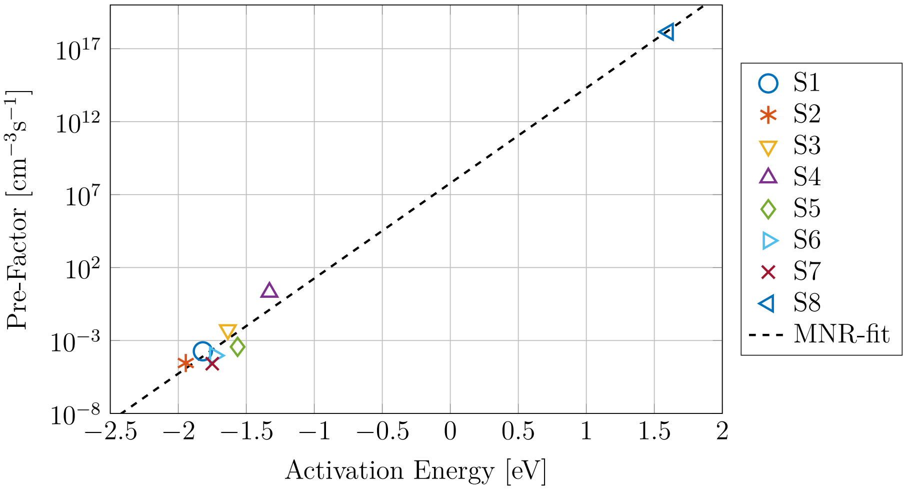

Figure 3.11: Correlation of $r_{cCC}^{\text{sub},0}$ and E_{cCC}^{sub}, describing the temperature dependence of r_{cCC}^{sub}. The dotted line represents the fit according to the Meyer Neldel-Rule.

In figure 3.12, $c_{CC}^{\text{sub},0}$, the charge carrier concentration in the substrate material of each sample before the annealing, is plotted as a function of the inverse temperature. This concentrations stem from the fits through the measured charge carrier concentrations in the substrate material at different annealing times.

For most samples, $c_{CC}^{\text{sub},0}$ decreases with increasing temperature. This observation suggests that the formation of the thermal donors might deviate from its linear behavior during the heat-up phase and at the beginning of the anneal. The samples implanted with the highest proton doses (S3 and S4) show the largest values of $c_{CC}^{\text{sub},0}$. Here, the initial charge carrier concentration in the substrate material is strongly increased compared to its nominal doping concentration ($< 10^{13}$ cm^{-3}, see table 3.1). An explanation for this circumstance might be a different temperature during the proton implantation process,

Table 3.7: Charge carrier concentration in the substrate material before the anneal ($c_{CC}^{\mathrm{sub},0}$) of samples S1-S8 at different temperatures in cm^{-3}, calculated from linear fits through the measured data.

	400 °C	425 °C	450 °C	475 °C	500 °C
S1	1.6×10^{13}	5.9×10^{12}	5.7×10^{12}	1.2×10^{12}	2.1×10^{11}
S2	1.7×10^{13}	2.6×10^{13}	6.4×10^{12}	2.9×10^{12}	6.3×10^{11}
S3	1.1×10^{14}	2.5×10^{13}	8.4×10^{12}	3.1×10^{12}	7.5×10^{12}
S4	2.2×10^{14}	7.0×10^{13}	5.1×10^{13}	3.0×10^{13}	2.9×10^{13}
S5	1.7×10^{13}		4.0×10^{11}		
S6	9.7×10^{12}		8.9×10^{12}		1.6×10^{11}
S7	-6.0×10^{11}	6.2×10^{11}	9.4×10^{11}	8.9×10^{11}	7.7×10^{11}
S8	9.9×10^{12}		1.0×10^{13}		

which could lead to an increased formation of thermal donors. Unfortunately, detailed information on the implantation conditions, except for the implantation energy and the implanted dose, is not available.

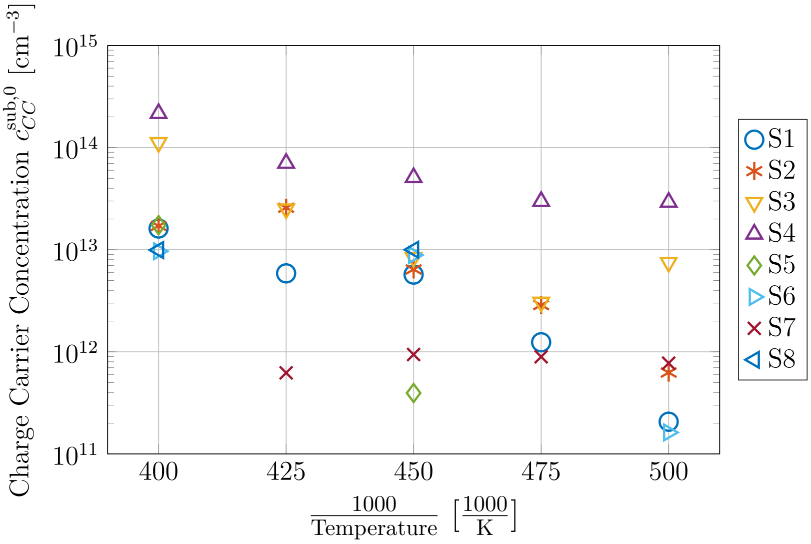

Figure 3.12: Calculated charge carrier concentration $c_{CC}^{\mathrm{sub},0}$ in the substrate material of sample S1 before the anneal as a function of the inverse temperature.

3.3.3 Diffusion of Hydrogen Away from the Implantation Depth

The maximum in the charge carrier concentration profile is found at the implantation depth and, hence, coincides with the position of the maximum hydrogen concentration. Even though hydrogen itself is a donor (see figure 2.66), as shown in sub-section 3.3.1, the number of residual charge carriers per area is several orders of magnitude smaller than the implanted proton dose. That makes it very certain, that also other electrically active defects are present in the material. Nevertheless, in many cases, a decrease of the maximum charge carrier concentration with increasing annealing time is observed. This decrease is attributed to hydrogen diffusing away from this position. The change of the maximum hydrogen concentration $c_{CC\mathrm{max}}$ over time is described by

$$\left(c_{CC\mathrm{max}}(t) - c_{CC\mathrm{max}}^{\mathrm{eq}}\right)\frac{\sigma_{\mathrm{d}}}{d} = \left(4\pi D_{\mathrm{H}}^{\mathrm{peak}}t\right)^{-\frac{1}{2}}, \tag{3.4}$$

where $c_{CC\mathrm{max}}^{\mathrm{eq}}$ is the equilibrium concentration to which $c_{CC\mathrm{max}}$ converges at long annealing times and which depends on the annealing temperature. d is the implanted proton dose and σ_{d} is the donor formation efficiency, which relates the hydrogen concentration to the charge carrier concentration. Usually σ_{d} is far smaller than 1, as the effective donor concentration is lower than that of hydrogen due to the formation of donor and acceptor complexes. $D_{\mathrm{H}}^{\mathrm{peak}}$ is the effective diffusivity of hydrogen at the implantation peak.

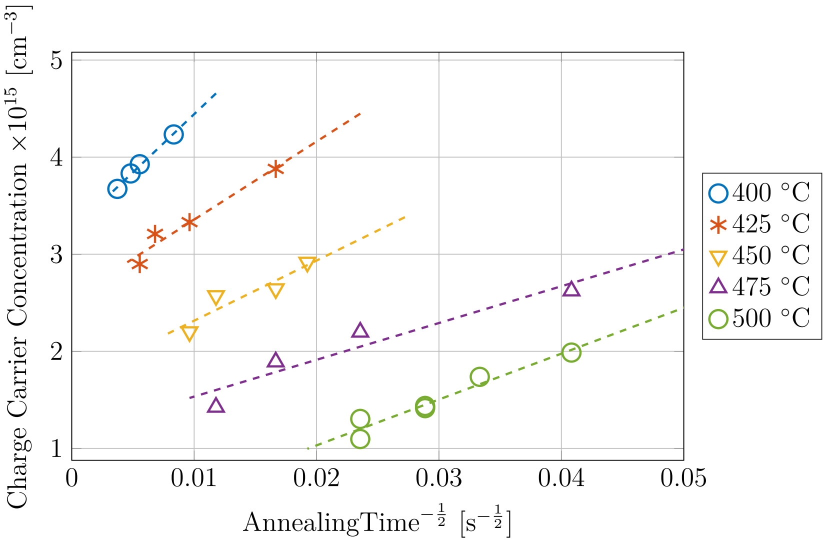

Figure 3.13: Charge carrier concentration at the implantation depth of sample S1 as a function of the annealing temperature.

Figure 3.13 shows $c_{CC\mathrm{max}}$ at the implantation depth in sample S1 as a function of the inverse square root of the annealing time. The maximum carrier concentration in sample S1 shows a decrease with increasing annealing time at all temperatures between 400 °C and 500 °C. From the decrease of $c_{CC\mathrm{max}}$, the effective hydrogen diffusivity at the peak in sample S1 is extracted at each annealing temperature. This data is plotted in figure 3.14, as a function of the inverse temperature. From the decay of the effective hydrogen diffusivity with the inverse temperature, an activation energy of 1.0 eV is found. Table 3.8 lists the effective diffusivities calculated from the decay of $c_{CC\mathrm{max}}$ in the samples S1-S8 at different annealing conditions. Figures of the change of $c_{CC\mathrm{max}}$ with the annealing time and of the temperature dependence of the extracted hydrogen diffusivity for the samples S2-S8 are shown in appendix B.

The two samples, S3 and S4, which were implanted with the highest proton doses ($5 \times 10^{15}\,\mathrm{H^+cm^{-2}}$ and $10^{16}\,\mathrm{H^+cm^{-2}}$, respectively) show a different evolution of $c_{CC\mathrm{max}}$ than the samples implanted at lower doses. Here, for sample S4 at some and for sample

S3 at all annealing temperatures, the maximum charge carrier concentration grows with increasing annealing time.

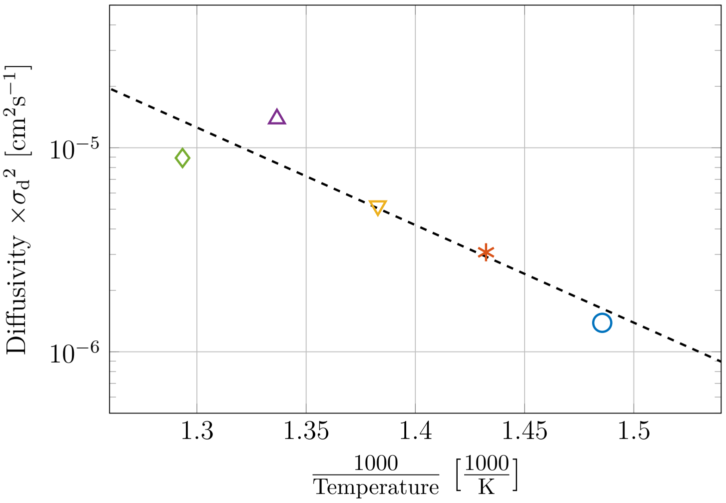

Figure 3.14: Effective diffusivity of hydrogen multiplied by the donor formation efficiency at the implantation depth of sample S1 as a function of the inverse annealing temperature.

Table 3.8: Effective diffusivity of hydrogen calculated from the decrease of the charge carrier concentration at the implantation depth in samples S1-S8 at different annealing temperatures in cm^{2}s^{-1}. The values are not corrected for the donor formation efficiency.

	400 °C	425 °C	450 °C	475 °C	500 °C
S1	1.4×10^{-6}	3.1×10^{-6}	5.2×10^{-6}	1.4×10^{-5}	8.9×10^{-6}
S2	9.4×10^{-7}	2.5×10^{-6}	2.2×10^{-5}	5.0×10^{-5}	2.5×10^{-4}
S3	-4.0×10^{-3}	-2.2×10^{-4}	-2.7×10^{-4}	-1.3×10^{-3}	-4.2×10^{-4}
S4	1.4×10^{-5}	-2.9×10^{-4}	-1.2×10^{-4}	-1.3×10^{-3}	1.2×10^{-2}
S5	2.7×10^{-7}		2.7×10^{-7}		
S6	1.5×10^{-6}		4.5×10^{-5}		2.7×10^{-4}
S7	4.5×10^{-5}	1.8×10^{-5}	3.8×10^{-6}	4.9×10^{-6}	5.1×10^{-6}
S8	7.4×10^{-8}		3.5×10^{-7}		

In table 3.9 the activation energy of the effective diffusivity of hydrogen in the samples S1 to S8 are listed. For the calculation of the activation energy, only positive values of the diffusivity, and hence only annealing temperatures, where $c_{CC\text{max}}$ grows with the annealing time, are accounted for. As a consequence, no activation energy of the effective hydrogen diffusivity at the implantation depth is found for sample S3. The activation energies calculated for the other samples spread from -1.0 eV to 3.0 eV.

Similar to previous observations, the Arrhenius parameters describing the temperature dependence of the effective hydrogen diffusivity, extracted from the decay of the charge carrier concentration at the implantation depth, show a correlation following the Meyer-Neldel-Rule (see equation 2.117). Here, the correlation is described by a Meyer-Neldel Temperature of 405 °C and by a pre-factor of 1.8×10^{-6} cm^{2}s^{-1}.

Table 3.9: Arrhenius parameters describing the temperature dependence of the effective hydrogen diffusion at the implantation depth in samples S1-S8.

Sample	E_A [eV]	$D_0 \times \sigma_\mathrm{d}$ [cm^{2}s^{-1}]
S1	1.0	2×10^1
S2	2.5	8×10^{12}
S3		
S4	3.0	6×10^{17}
S5	0.0	2×10^{-7}
S6	2.4	8×10^{11}
S7	-1.0	6×10^{-13}
S8	1.3	4×10^2

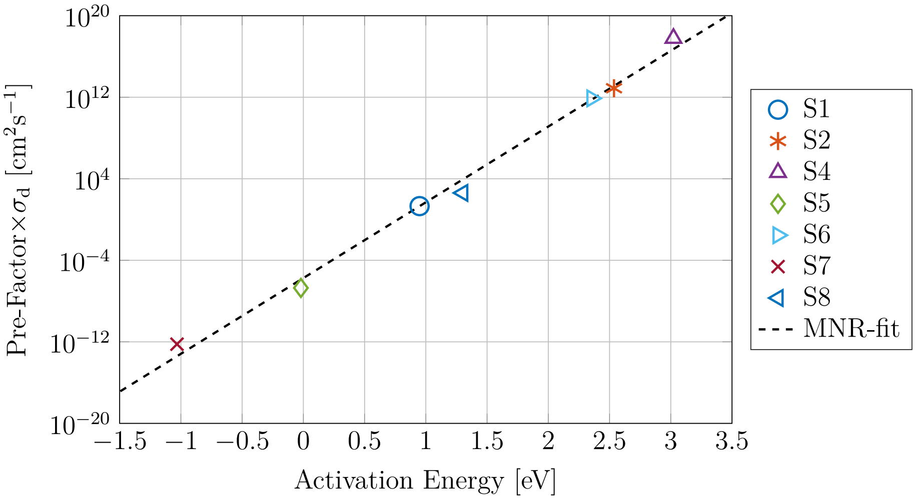

Figure 3.15: Correlation of the pre-factors and the activation energies describing the temperature dependence of $D_\mathrm{H}^\mathrm{eff}$ at the peak. The dotted line represents the fit according to the Meyer Neldel-Rule.

The activation energies of the samples implanted with low proton doses (S5 and S7) show strange activation energies. While the activation energy of sample S5 is 0 eV, that of sample S7 is negative, meaning that the effective hydrogen diffusivity decreases with increasing temperature. It is assumed, that the lower the implantation dose is, the higher becomes the influence of other electrically active defects on the residual charge carrier concentration at the implantation depth. This most certainly has an influence on the effective hydrogen diffusivity extracted from the decay of c_{CC} at this position.

Figure 3.16 shows the activation energies of all samples, except for sample S3, as a function of the maximum hydrogen concentration, in a similar way, as the data is plotted in figure 3.7.

The activation energy extracted from the effective hydrogen diffusivity at the implantation depth shows a quite different correlation with the maximum hydrogen concentration as does the activation energy extracted from the expansion of the region with increased charge carrier concentration. Here, the activation energy grows with increasing hydrogen concentration.

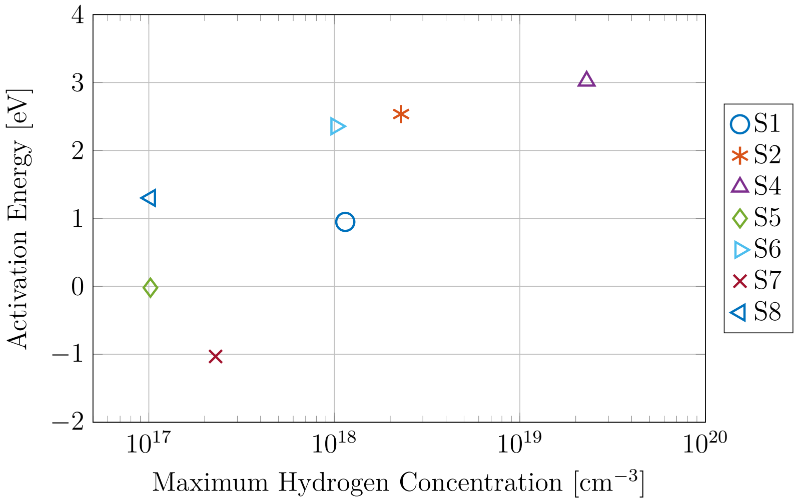

Figure 3.16: Correlation of the activation energy describing the temperature dependence of the effective diffusivity of hydrogen at the implantation depth and the maximum hydrogen concentration.

At the same time, as $D_{\mathrm{H}}^{\mathrm{eff}}$ at the implantation depth increases with temperature, the equilibrium charge carrier concentration at this position, $c_{CC}{}_{\mathrm{max}}^{\mathrm{eq}}$, changes as well. This concentration is not necessarily defined by the equilibrium concentration of hydrogen after the end of the diffusion process when the hydrogen is evenly spread in the material. The increased c_{CC}, observed here, rather stems from immobile donor complexes which are formed at the implantation depth. The influence of the annealing temperature on the equilibrium charge carrier concentration at the implantation depth after long anneals is shown in figure 3.17 and the corresponding values are listed in table 3.10.

The equilibrium charge carrier concentration at the implantation depth of the different samples spreads over more than an order of magnitude. While $c_{CC}{}_{\mathrm{max}}^{\mathrm{eq}}$ decreases in samples implanted at low doses, it shows a slight increase in the high dose samples (S3 and S4). A decrease of $c_{CC}{}_{\mathrm{max}}^{\mathrm{eq}}$ with temperature, signalizes a shift of the equilibrium between formation and dissociation of donor complexes towards the dissociation, while an increase of $c_{CC}{}_{\mathrm{max}}^{\mathrm{eq}}$ is caused by the formation of other kinds of donor complexes, whose formation requires high defect concentrations. Figure 3.18 shows $c_{CC}{}_{\mathrm{max}}^{\mathrm{eq}}$ as a function of the maximum hydrogen concentration, which also stands for the concentration of defects generated during the proton implantation process, at different annealing temperatures.

An increase of the equilibrium charge carrier concentration at the implantation depth with increasing maximum hydrogen concentration is observed. The increase is enhanced the higher the annealing temperature is. This effect favors the assumption that at least one other kind of donor complex is generated at higher defect concentrations, whose formation requires higher annealing temperatures.

The change of the equilibrium charge carrier concentration, and of the formation and dissociation of immobile defect complexes which go along with it, imply, that the effective

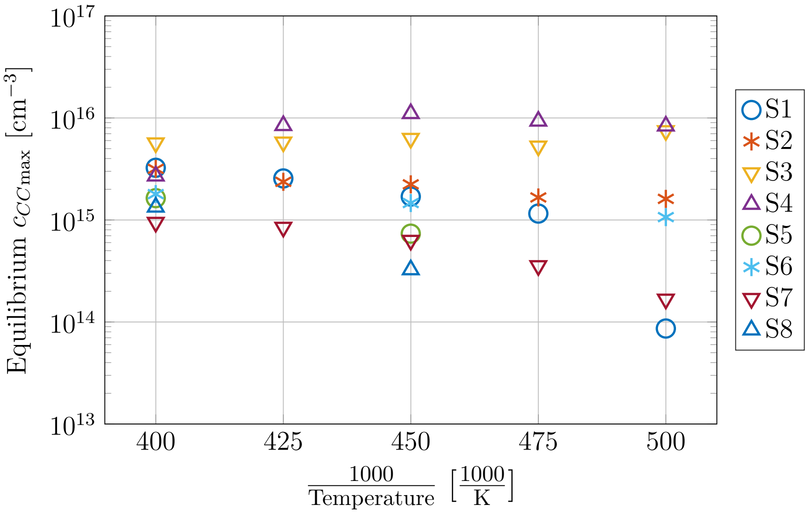

Figure 3.17: Equilibrium charge carrier concentration at the implantation depth after long anneals as a function of the annealing temperature.

Table 3.10: Equilibrium charge carrier concentration at the implantation depth after long annealing times calculated from the decay of $c_{CC\max}$ in [cm^{-3}].

	400 °C	425 °C	450 °C	475 °C	500 °C
S1	3.2×10^{15}	2.6×10^{15}	1.7×10^{15}	1.2×10^{15}	8.6×10^{13}
S2	3.2×10^{15}	2.4×10^{15}	2.2×10^{15}	1.7×10^{15}	1.6×10^{15}
S3	5.7×10^{15}	5.8×10^{15}	6.3×10^{15}	5.3×10^{15}	7.5×10^{15}
S4	2.7×10^{15}	8.4×10^{15}	1.1×10^{16}	9.3×10^{15}	8.3×10^{15}
S5	1.6×10^{15}		7.3×10^{14}		
S6	1.8×10^{15}		1.5×10^{15}		1.1×10^{15}
S7	9.5×10^{14}	8.5×10^{14}	6.3×10^{14}	3.6×10^{14}	1.7×10^{14}
S8	1.3×10^{15}		3.3×10^{14}		

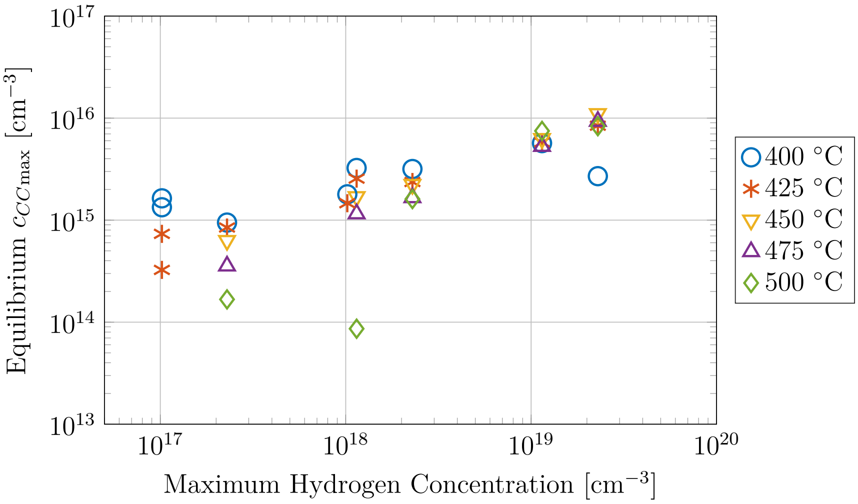

Figure 3.18: Equilibrium charge carrier concentration at the implantation depth after long anneals as a function of the maximum hydrogen concentration.

hydrogen diffusivity extracted from the decay of $c_{CC\mathrm{max}}$ might be flawed and that this method is not suited for measuring $D_{\mathrm{H}}^{\mathrm{eff}}$.

3.3.4 Evaluation of the Change of the Residual Number of Charge Carriers in the Shoulder of the Charge Carrier Concentration Profile

A feature of interest in the charge carrier profiles of m:Cz-silicon (samples S1-S7) is the shoulder in the profile which forms next to the peak at the implantation depth in the substrate material at the applied annealing conditions (see figure 3.2). Once hydrogen diffuses away from the implantation depth and into this region, it reacts with precursor defects which had already been generated during the proton implantation process. This leads to a change in the concentrations of electrically active defects and an increase of the charge carrier concentration is observed. During longer anneals, c_{CC} decreases again.

The number of charge carriers per area in the shoulder, N_{CC}^{sh} is calculated according to

$$N_{CC}^{\mathrm{sh}} = \int_{x_1}^{x_2} c_{CC} \, dx - c_{CC}^{\mathrm{sub}} \left(x_2 - x_1\right), \tag{3.5}$$

where x_1 and x_2 are the depths of the beginning and the end of the shoulder. $c_{CC}^{\mathrm{sub}} \left(x_2 - x_1\right)$ is the number of thermal donors, formed in the same region.

Figure 3.19 shows the number of charge carriers per area in the shoulder of the c_{CC}-profile of sample S1 after anneals under different conditions. At all investigated annealing temperatures N_{CC}^{sh} decays with increasing annealing time. The change of the number of charge carriers in the shoulder, N_{CC}^{sh} depends on the rate $r_{N_{CC}^{\mathrm{sh}}}$.

$$N_{CC}^{\mathrm{sh}}(t) = N_{CC}^{\mathrm{sh},0} + r_{N_{CC}^{\mathrm{sh}}} t. \tag{3.6}$$

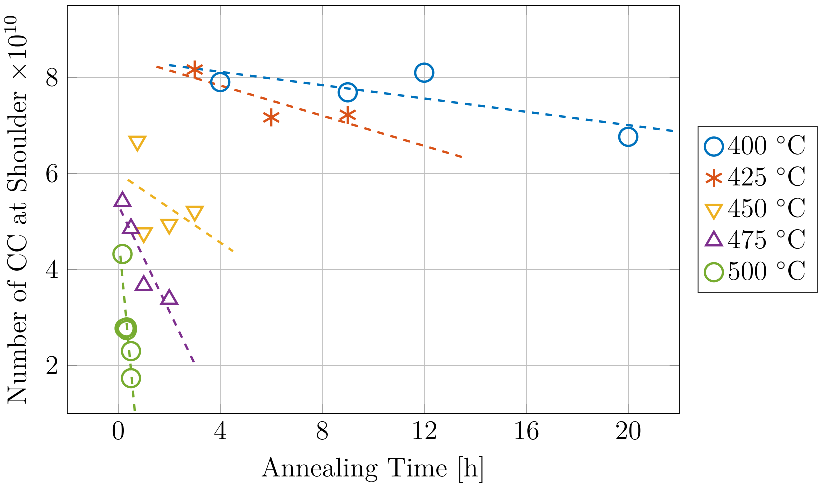

Figure 3.19: Number of charge carriers per unit area in the shoulder of the c_{CC}-profile of sample S1 after different anneals.

Here, $N_{CC}^{\text{sh},0}$ reflects the concentration of precursor defects which are activated by the reaction with hydrogen. The rates extracted from the change in N_{CC}^{sh}, in all samples at different annealing temperatures, are listed in table 3.11. Not all of these rates are negative, hence in some cases, the number of charge carriers in the shoulder grows with increasing annealing time. This is especially the case for the samples S3 and S4 which were implanted with high proton doses. Also in sample S2, $r_{N_{CC}^{\text{sh}}}$ increases with annealing time at low temperature.

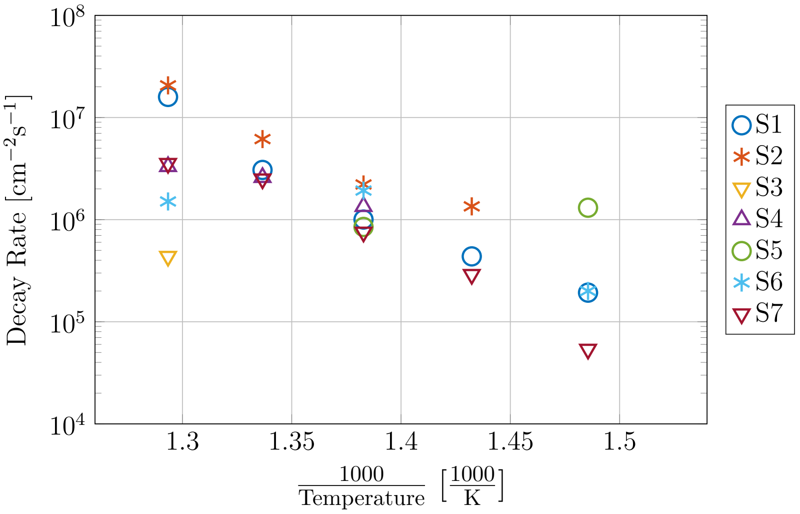

Figure 3.20: Effective decay rate of charge carriers in the shoulder of the c_{CC}-profiles of samples S1-S7 as a function of the inverse temperature.

Considering the change in the number of charge carriers in the shoulder as the effective decay rate of N_{CC}^{sh}, which is -$r_{N_{CC}^{\text{sh}}}$, an increase with increasing temperature is observed. In figure 3.20 the effective decay rates extracted from samples S1-S7 are plotted as a function of the inverse temperature.

From the correlation of the effective decay rate with the inverse temperature, the activation energies of the decay are extracted and listed in table 3.12. The extracted values range from -0.4 eV to 1.9 eV. The activation energies found for the temperature dependence of the samples S5 (-0.4 eV) and S6 (0.9 eV) have to be taken with care as only two data points could be used to calculate the decay rates at low temperature (see figures B.5.2c and B.6.2c). The activation energies found in samples S1, S2, S4 and S7 (0.9 eV-1.9 eV) are in the same range as the activation energies of $D_{\mathrm{H}}^{\mathrm{eff}}$ extracted from the expansion of the donor rich region ($1.1\,\mathrm{eV} - 2.4\,\mathrm{eV}$), presented in section 3.2.2.

Table 3.11: Rates of the change in the number of charge carriers in the shoulder of the c_{CC}-profile in samples S1-S8 at different annealing temperatures in cm^{-2}s^{-1}. A range of the initial number of charge carriers, $N_{CC}^{\mathrm{sh},0}$, is included for each sample.

	400 °C	425 °C	450 °C	475 °C	500 °C	N_{CC}^{0} [cm^{-2}]
S1	-1.9×10^{5}	-4.4×10^{5}	-1.0×10^{6}	-3.1×10^{6}	-1.6×10^{7}	5×10^{10}-8×10^{10}
S2	3.1×10^{5}	-1.3×10^{6}	-2.2×10^{6}	-6.2×10^{6}	-2.1×10^{7}	6×10^{10}-1×10^{11}
S3	1.2×10^{6}	1.7×10^{6}	1.0×10^{6}	9.1×10^{5}	-4.4×10^{4}	8×10^{9}-2×10^{10}
S4	7.9×10^{5}	3.2×10^{5}	-1.3×10^{6}	-2.6×10^{6}	-3.3×10^{6}	2×10^{10}-8×10^{10}
S5	-1.3×10^{6}		-8.5×10^{5}			6×10^{10}-1×10^{11}
S6	-2.0×10^{5}		-1.9×10^{6}		-1.5×10^{6}	4×10^{10}-2×10^{11}
S7	-5.4×10^{4}	-2.9×10^{5}	-7.5×10^{5}	-2.5×10^{6}	-3.5×10^{6}	2×10^{10}-4×10^{10}

Table 3.12: Arrhenius parameters describing the temperature dependence of the deactivation of donors in the shoulder of the c_{CC}-profile of samples S1-S7.

Sample	E_A [eV]	$r_{N_{CC}^{\mathrm{sh},0}}$
S1	1.9	3×10^{19}
S2	1.7	2×10^{18}
S3		
S4	0.9	2×10^{12}
S5	-0.4	2×10^{3}
S6	0.9	3×10^{12}
S7	1.9	1×10^{19}

The Arrhenius parameters show, as observed before, a correlation following the Meyer-Neldel-Rule (see equation 2.117). In this case the correlation is described by a T_{MN} of 442 °C and by a pre-factor of $9.6\times10^{5}\,\mathrm{cm}^{-2}\mathrm{s}^{-1}$.

Figure 3.22 shows the correlation of the activation energies describing the temperature dependence of the decay rate $r_{N_{CC}^{\mathrm{sh}}}$ and the maximum hydrogen concentration. Here only the activation energies of samples S1, S2, S4 and S7 are plotted, which are considered to be the least flawed data. A similar correlation of the activation energy with the maximum hydrogen concentration is found, as for the activation energy of $D_{\mathrm{H}}^{\mathrm{eff}}$, extracted from the expansion of the charge carrier rich region (see figure 3.7).

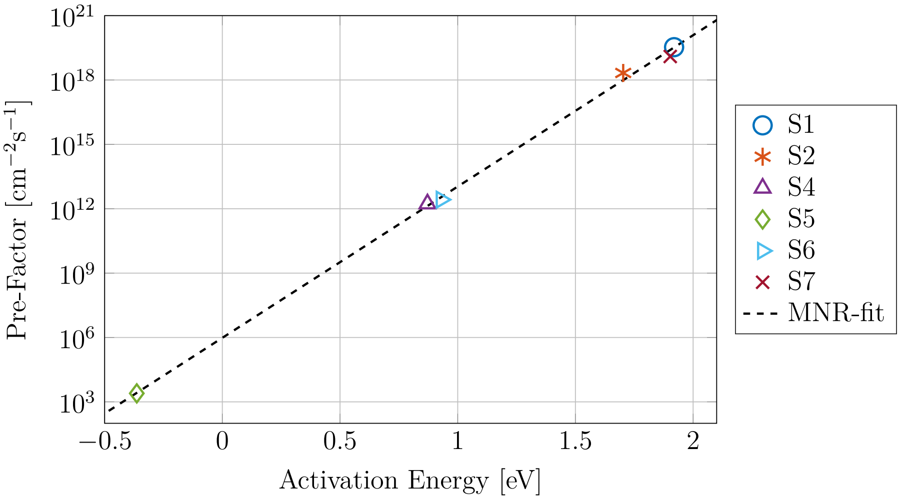

Figure 3.21: Correlation of the Arrhenius parameters describing the temperature dependence of $r_{N^{\text{sh}}_{CC}}$. The dotted line represents the fit according to the Meyer Neldel-Rule.

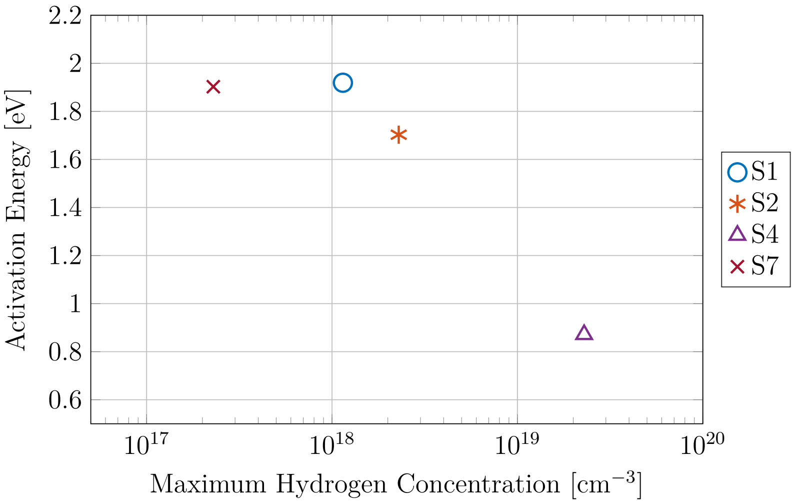

Figure 3.22: Correlation of the activation energy describing the temperature dependence of the decay rate $r_{N^{\text{sh}}_{CC}}$ and the maximum hydrogen concentration.

3.4 Discussion of the Kinetics of Different Processes in Proton Implanted Silicon Determined from Spreading Resistance Measurements

The interpretation of the results presented in the last two sections is difficult, as the data is very limited. Nevertheless, it fits to a model of the migration of hydrogen which is based on the interaction of hydrogen with other impurities and defects in the material. As explained in section 2.4, hydrogen forms defect complexes with a number of different impurities. Each of these impurities can be seen as a trap on the migration path of the hydrogen atom. Here, the deepest traps are those defects which result in the lowest energy after forming a complex with hydrogen. Trapped hydrogen can further be released again from these traps by a dissociation processes. If the concentration of hydrogen is lower than the concentration of the traps, the diffusion of hydrogen is limited to the speed of the reactions and dissociations. In this case, the activation energy of the diffusion process is related to the binding energy of hydrogen to the traps, which reaches from 0.5 eV to more than 2.5 eV [47, 48, 432–434]. If the hydrogen concentration overcomes a certain threshold ratio compared to the trap concentration, it starts to saturate the traps. This results in a lower average E_A, as the activation energy of the diffusion process itself is assumed to be much lower than the binding energy to the traps. The higher the hydrogen concentration is, the lower becomes the average activation energy, until it converges to E_A of the diffusion process. The lowering of the impurity concentration at the same hydrogen concentration, according to this model, should lead to a decrease of the activation energy. This is observed in figure 3.7, as the activation energies found for the FZ-samples, which contain lower impurity concentrations, are significantly lower than those found in m:Cz-material at the same maximum hydrogen concentration. The introduction of hydrogen by gas permeation or from a plasma leads to higher hydrogen concentrations, compared to those in proton implantation, while at the same time, less intrinsic defects are generated in this process. Hence, the literature data presented in section 2.4.4 also fits to this model, as much lower activation energies were found there.

The effective hydrogen diffusivity extracted from the decrease of the charge carrier concentration at the implantation depth cannot be directly compared to the diffusivity calculated from the expansion of the region of increased c_{CC}, as it contains the donor formation efficiency σ_d. Assuming that σ_d does not depend on the annealing temperature and does not change over time, the kinetics of $D_\mathrm{H}^\mathrm{eff}$ at the implantation depth can be calculated. The activation energies of $D_\mathrm{H}^\mathrm{eff}$, obtained this way, are quite different to those calculated before. Here, the activation energy shows an increase with increasing hydrogen concentration, which contradicts the model of the hydrogen diffusion in defect rich material, discussed above. It is very probable, though, that σ_d is not constant, as different electrically active defect complexes might be formed at different annealing temperatures. This would then also change the residual charge carrier concentration at the implantation depth. This assumption is supported by the observed changes in the equilibrium charge carrier concentration at the implantation depth, ${c_{CC}}_\mathrm{max}^\mathrm{eq}$, which is reached after long anneals. If the concentration of immobile electrically active defects in this region of the material would be the same for different annealing temperatures, ${c_{CC}}_\mathrm{max}^\mathrm{eq}$ should be constant. As this is not the case, this method is considered to be not suitable for the identification of

$D_{\mathrm{H}}^{\mathrm{eff}}$. From the correlation of ${c_{CC}}_{\mathrm{max}}^{\mathrm{eq}}$ with the annealing temperature and with the damage concentration (represented by the maximum hydrogen concentration), the presence of several different immobile and electrically active defect complexes at the implantation depth is deduced.

The change in the charge carrier concentration in the substrate material is assumed to be primarily caused by the formation of thermal donors. Here, in all m:Cz samples, investigated in this study, negative activation energies, describing the temperature dependence of this process were found. Usually negative activation energies occur in processes, where mobile reactants are trapped in a potential well before they react. This is quite different to diffusion limited reactions which are described in section 2.2.7, where the reactants immediately react once their distance falls below the capture radius. In a trap-assisted reaction process, the reactants do not immediately react once they have overcome the capture radius. The faster the reactants diffuse, the slower the reaction rate becomes, as the probability of the reactants leaving the potential well before the reaction takes place, is increased. Another explanation for this observations might include the change of the equilibrium between the formation and the dissociation or deactivation of the thermal donors [435]. It has been shown, though, that the formation of oxygen chains, which are the most likely thermal donor complexes, follows the Arrhenius law [128, 149]. Also several further studies found positive activation energies in the range from 1.0 eV to 2.8 eV [401, 436–439], describing the temperature dependence of the thermal donor formation rate.

The c_{CC}-profiles of m:Cz-material show a shoulder below the implantation depth, which sometimes is already present before the anneal, when most of the hydrogen is still at the implantation depth. Investigating the change in the number of charge carriers per area in this shoulder, N_{CC}^{sh}, in most cases a decay of N_{CC}^{sh} with increasing annealing time was observed. Only in samples implanted at high doses, under some conditions N_{CC}^{sh} showed an increase over time. The observed decay, $r_{N_{CC}^{\mathrm{sh}}}$, resembles an activated process. Fitting the correlation of $r_{N_{CC}^{\mathrm{sh}}}$ with the inverse temperature yielded activation energies, which showed a similar correlation with the maximum hydrogen concentration as the activation energies of $D_{\mathrm{H}}^{\mathrm{eff}}$, extracted from the expansion of the region of increased charge carrier concentration. Assuming that the observed decay is caused by a diffusion limited reaction of second order (see section 2.2.7), the similarity of the activation energies and their similar dependence on the hydrogen concentration, suggests the involvement of mobile hydrogen in this process. This is either the deactivation of an initial donor complex by its reaction with hydrogen or the formation of a hydrogen related acceptor complex which compensates for the initial donors in the shoulder. The structure and composition of the initial donor complex in the shoulder remains unknown. The absence of the shoulder in FZ-material, as already indicated in reference [409], suggests that this complex involves either oxygen, carbon, or both, as the concentration of these defects is much lower in FZ-silicon, compared to m:Cz material. At the same time as the charge carrier concentration in the shoulder is decreased, also that in the high-c_{CC}-region towards the surface of the material is decreased, suggesting that similar defects are present on both sides of the implantation depth.

IN the next chapter it will be shown that the double donor $\mathrm{C_iOI}$ is present in both region of the implanted material. The observed decrease in the charge carrier concentrations in the shoulder and in the irradiated region resemble the deactivation of this donor complex by its reaction with hydrogen. At the applied annealing temperatures the dominant charge state of hydrogen is H^+. Hence, the reaction of hydrogen with donor complexes (which are also negatively charged) is a slow process, such as the one observed here.

All investigations of the kinetics of different processes presented in this chapter yielded Arrhenius parameters which showed almost perfect correlation with each other, following the Meyer-Neldel-Rule. The calculated Meyer-Neldel temperatures, though, are not the same and reach from 405 °C to 499 °C. As the calculations base on the same experimental data, and hence on the same annealing conditions, this observation contradicts the findings by Kirchheim et al. [352], who state that T_{MN} is always close to the mean annealing temperature. Nevertheless, there is still no physical explanation for this correlation.

4 Simulation of the Proton Implantation Process

In this chapter, a computer simulation of the proton implantation process, developed during this thesis, is discussed. This simulation is based on the generation of defects by implanting protons, on the diffusion of these point defects and on diffusion limited second order reactions between those defects and impurities. Furthermore, the dissociation of defect complexes is included. The first section discusses in detail how this simulation is set up. A second section will look at simulated defect concentration profiles and discuss the effects of changes of certain input parameters to the simulated profiles. Preliminary results have been published in reference [440].

4.1 Theoretical Simulation Method and Input Data

A variety of different simulations of the generation of defects by particle irradiation and ion implantation have been published so far. Monte-Carlo based simulation tools such as SRIM [304, 305] focus on the generation of defects and on the introduction of impurities by ion implantation. Such simulations, though, neglect the reactions between the created point-defects. Other works look at the formation of defect complexes by the reactions of point defects [441–443]. Here the spatial distribution of those defects is not taken into account. The simulation method presented in this chapter combines the information on the spatial distribution of defects being generated and on the formation of defect complexes. Furthermore, the migration of defects inside the material and dissociations of the generated defect complexes during proton implantation are taken into account to calculate the change of the concentration profiles of different defects.

This section describes the theoretical model of this process simulation. Not all features and procedures discussed here are already implemented in the code of the current version of the simulation program. At this stage of development of the simulation, only neutral defects are taken into account. Nevertheless, it is tried to describe the simulation model in a form which is also applicable if the charge states of the defects are considered.

The first part of this section shows the differential rate equation used to calculate the changes in defect concentrations. In the subsequent part of the section, the different terms of this equation are explained in more detail, before the simulation cycle is discussed.

4.1.1 Differential Rate Equation

The proton implantation process is considered to be uniform along the cross section of the substrate material. Hence, only one-dimensional concentration profiles of the defects are considered. Here, $c_{\mathrm{X_A}}(x,t)$ is the concentration of the defect $\mathrm{X_A}$, which is also associated with a charge state q at the depth x and at the time t. The change of the concentration

$c_{\mathrm{X_A}}$ during the time interval between t_1 and t_2 is described by

$$c_{\mathrm{X_A}}(x, t_2) = c_{\mathrm{X_A}}(x, t_1) + dc_{\mathrm{X_A}}(x, dt). \tag{4.1}$$

The differential rate equation of the simulation, used to determine the change of $c_{\mathrm{X_A}}$ in the time interval $t_2 - t_1 = dt$ is shown below.

$$\frac{dc_{\mathrm{X_A}}(x,t)}{dt} = \begin{cases} \quad D_{\mathrm{X_A}}(T,x)\nabla^2 c_{\mathrm{X_A}}(x,t) \\ + \quad e\mu_{\mathrm{X}}(T,x)\nabla E_V(x)\nabla c_{\mathrm{X_A}}(x,t) \\ + \quad \sum\limits_{B,C} k_r^{\mathrm{BC,A}}(T,x)c_{\mathrm{X_B}}(x,t)c_{\mathrm{X_C}}(x,t) - \sum\limits_{B} k_r^{\mathrm{AB,X}}(T,x)c_{\mathrm{X_A}}(x,t)c_{\mathrm{X_B}}(x,t) \\ + \quad \sum\limits_{B} k_d^{\mathrm{B,AX}}(T,x)c_{\mathrm{X_B}}(x,t) - k_d^{\mathrm{A,XX}}(T,x)c_{\mathrm{X_A}}(x,t) \\ + \quad c_{\mathrm{X_A}}^{G}(x,t,\Phi,f_{\mathrm{scan}}) \end{cases} \tag{4.2}$$

To calculate $dc_{\mathrm{X_A}}$ in the time interval dt, different contributions to the changes of the defect concentration have to be taken into account. If the defect is mobile, its diffusion is considered using Fick's second law of diffusion (see section 2.2.3). Here, $D_{\mathrm{X_A}}(T,x)$ is the diffusion coefficient of the defect at the temperature T and the depth x.

In the next row the ionic drift of charged defects (see section 2.2.6) is treated. Here, a gradient in the effective concentration of charged defects can be described by a gradient in the valence band energy, ∇E_V, which resembles an internal electric field in the material. Mobile, charged defects drift along this field depending on their mobility μ_{X}, which is related to the diffusion coefficient, as described by the Einstein relation (see equation 2.87). At the current state of development of the simulation, only neutral defects are regarded, and hence, the ionic drift is not accounted for.

The third row of the master equation treats second order reactions between defects. Here, the first term includes all second order reactions (see section 2.2.7) between defects $\mathrm{X_B}$ and $\mathrm{X_C}$, forming defect $\mathrm{X_A}$. The rate of each reaction results from the product of the rate constant $k_r^{\mathrm{BC,A}}$ and the concentrations of the reacting defects, $c_{\mathrm{X_B}}$ and $c_{\mathrm{X_C}}$. The second sum takes into account all reactions, were defect $\mathrm{X_A}$ is consumed as an educt in the reaction with a defect $\mathrm{X_B}$ forming some other defect X. These reaction rates are calculated from the products of the rate constants $k_r^{\mathrm{AB,X}}$ and the concentrations of the reacting defects. As such reactions reduce the concentration of the defect $\mathrm{X_A}$, this term is subtracted in equation 4.2.

Another contribution to the change of the defect concentration regarded in the third row of equation 4.2 are dissociations of defect-complexes (see section 2.2.7). The sum of the dissociations of defects $\mathrm{X_B}$ to defect $\mathrm{X_A}$ and another defect X is added to the balance, while the fraction of the defect $\mathrm{X_A}$ dissociating to the defects $\mathrm{X_1}$ and $\mathrm{X_2}$ is subtracted. The dissociation rates are calculated from the rate constants $k_d^{\mathrm{B,AX}}$ and $k_d^{\mathrm{A,XX}}$ and the concentration of the dissociating defect.

The last term in equation 4.2, $c_{\mathrm{X_A}}^{G}$ represents the direct generation of the defect $\mathrm{X_A}$ during the implantation process. $c_{\mathrm{X_A}}^{G}$ depends on the ion flux Φ and on the frequency f_{scan}, that is used to scan the ion beam over the substrate material.

4.1.2 Numerical Treatment of the Diffusion of Mobile Defects

Due to the instability of the numerical solution to the explicit Forward Euler method, implicit methods for the numerical calculation of the concentration change due to diffusion are preferred. Using the Backward Euler method, the change of the concentration Δc_{X^q}, where X^q represents a defect at charge state q, in the time interval Δt is,

$$\frac{\Delta c_{\mathrm{X}^q}}{\Delta t} = \frac{{c_{\mathrm{X}^q}}^n_{j+1} - {c_{\mathrm{X}^q}}^n_j}{\Delta t} = D_{\mathrm{X}^q,j}\frac{{c_{\mathrm{X}^q}}^{n+1}_{j+1} - 2{c_{\mathrm{X}^q}}^n_{j+1} + {c_{\mathrm{X}^q}}^{n-1}_{j+1}}{\Delta x^2}, \tag{4.3}$$

where n indicates the position in space, j stands for the point in time and $D_{\mathrm{X}^q,j}$ is the diffusivity of the defect X^q at the time j. Only ${c_{\mathrm{X}^q}}^n_j$ is known and the concentrations at $t = j + 1$ have to be calculated in a set of N_x ordinary differential equations (ODE), where N_x is the number of uniformly distributed increments in space.

$$\begin{aligned} {c_{\mathrm{X}^q}}^1_j =& 0 \\ {c_{\mathrm{X}^q}}^2_j =& {c_{\mathrm{X}^q}}^2_{j+1} - \alpha\left({c_{\mathrm{X}^q}}^3_{j+1} - 2{c_{\mathrm{X}^q}}^2_{j+1} + {c_{\mathrm{X}^q}}^1_{j+1}\right) \\ {c_{\mathrm{X}^q}}^{N_x-1}_j =& {c_{\mathrm{X}^q}}^{N_x-1}_{j+1} - \alpha\left({c_{\mathrm{X}^q}}^{N_x}_{j+1} - 2{c_{\mathrm{X}^q}}^{N_x-1}_{j+1} + {c_{\mathrm{X}^q}}^{N_x-2}_{j+1}\right) \\ {c_{\mathrm{X}^q}}^{N_x}_j =& 0 \end{aligned} \tag{4.4}$$

Here, α stands for $D_{\mathrm{X}^q,j}\Delta t/\Delta x^2$. In general, the defect concentrations at the boundaries (at x=1 and x=N_x) should be set to the solubility level of the defect in crystalline silicon which depends on the temperature and on the partial pressure of the defect in the atmosphere outside of the material. As these values are usually lower than the defect concentration in the bulk material, they are set to zero.

The generalized form of these equations is

$${c_{\mathrm{X}^q}}^n_j = -\alpha {c_{\mathrm{X}^q}}^{n+1}_{j+1} + (1+2\alpha){c_{\mathrm{X}^q}}^n_{j+1} + \alpha {c_{\mathrm{X}^q}}^{n-1}_{j+1} \tag{4.5}$$

Written in matrix form, equation 4.5 becomes

$$A_{n,n}C^n_{j+1} = C^n_j. \tag{4.6}$$

Here, C^n_{j+1} is a vector of the concentration profile at time $j + 1$

$$C^n_{j+1} = \left({c_{\mathrm{X}^q}}^1_{j+1}, {c_{\mathrm{X}^q}}^2_{j+1}, \cdots, {c_{\mathrm{X}^q}}^{N_x}_{j+1}\right) \tag{4.7}$$

and C^n_j is the concentration profile at $t = j$

$$C^n_j = \left({c_{\mathrm{X}^q}}^1_j, {c_{\mathrm{X}^q}}^2_j, \cdots, {c_{\mathrm{X}^q}}^{N_x}_j\right). \tag{4.8}$$

$A_{n,n}$ is a tri-diagonal matrix with the elements

$$A_{n,n} = \begin{pmatrix} A_{1,1} & A_{2,1} & 0 & 0 & 0 & 0 & 0 & 0 \\ A_{1,2} & A_{2,2} & A_{2,3} & 0 & 0 & 0 & 0 & 0 \\ 0 & A_{2,3} & A_{3,3} & A_{3,4} & 0 & 0 & 0 & 0 \\ 0 & 0 & \ddots & \ddots & \ddots & 0 & 0 & 0 \\ 0 & 0 & 0 & A_{n-1,n} & A_{n,n} & A_{n+1,n} & 0 & 0 \\ 0 & 0 & 0 & 0 & \ddots & \ddots & \ddots & 0 \\ 0 & 0 & 0 & 0 & 0 & A_{N_x-2,N_x-1} & A_{N_x-1,N_x-1} & A_{N_x,N_x-1} \\ 0 & 0 & 0 & 0 & 0 & 0 & A_{N_x-1,N_x} & A_{N_x,N_x} \end{pmatrix} \tag{4.9}$$

The non-zero elements along the diagonals take the values

$$\begin{aligned} A_{n-1,n} &= -\alpha \\ A_{n,n} &= 1 + 2\alpha \\ A_{n+1,n} &= -\alpha \end{aligned} \tag{4.10}$$

At the boundaries, the concentrations ${c_{\mathrm{X}^q}}_j^1$ and ${c_{\mathrm{X}^q}}_j^{N_x}$, as well as, the elements $A_{1,1}$, $A_{1,2}$, A_{N_x,N_x-1} and A_{N_x,N_x} of matrix $A_{n,n}$ are set to zero.

Instead of treating each charge state of each defect independently the charge states of a defect can be combined in the effective charge state (see section 2.2.4). If this concept is applied, an effective diffusivity (see section 2.2.5) for each defect, combining the diffusivities of the different charge states, has to be used. As the distribution of the charge states depends on the position of the Fermi level in the band gap, also the effective diffusivity depends of the Fermi energy. The position of E_F, on the other hand depends on the concentration profiles of all charged defects. These profiles are not uniform, thus the position of E_F in the band gap is a function of the depth x and so is the effective diffusivity. In this case, equation 4.3 changes to

$$\frac{\Delta c_{\mathrm{X}}}{\Delta t} = \frac{1}{2\Delta x^2}\left[({D_{\mathrm{X}}}_{j+1}^{n+1} + {D_{\mathrm{X}}}_{j+1}^{n})({c_{\mathrm{X}}}_{j+1}^{n+1} - {c_{\mathrm{X}}}_{j+1}^{n}) + ({D_{\mathrm{X}}}_{j+1}^{n} + {D_{\mathrm{X}}}_{j+1}^{n-1})({c_{\mathrm{X}}}_{j+1}^{n-1} - {c_{\mathrm{X}}}_{j+1}^{n})\right], \tag{4.11}$$

and equation 4.4 becomes

$$\begin{aligned} {c_{\mathrm{X}}}_j^1 =& 0 \\ {c_{\mathrm{X}}}_j^2 =& {c_{\mathrm{X}}}_{j+1}^2 - \alpha_j^{2/3}({c_{\mathrm{X}}}_{j+1}^3 - {c_{\mathrm{X}}}_{j+1}^2) - \alpha_j^{1/2}({c_{\mathrm{X}}}_{j+1}^1 - {c_{\mathrm{X}}}_{j+1}^2) \\ {c_{\mathrm{X}}}_j^{N_x-1} =& {c_{\mathrm{X}}}_{j+1}^2 - \alpha_j^{N_x-1/N_x}({c_{\mathrm{X}}}_{N_x-1}^{N_x} - {c_{\mathrm{X}}}_{j+1}^{N_x-1}) - \alpha_j^{N_x-1/N_x-2}({c_{\mathrm{X}}}_{j+1}^{N_x-2} - {c_{\mathrm{X}}}_{j+1}^{N_x-1}) \\ {c_{\mathrm{X}}}_j^{N_x} =& 0 \end{aligned} \tag{4.12}$$

Here, $\alpha_j^{x1/x2}$ is

$$\alpha_j^{x1/x2} = \frac{({D_{\mathrm{X}}}_j^{x1} + {D_{\mathrm{X}}}_j^{x2})\Delta t}{2\Delta x^2}. \tag{4.13}$$

Two-dimensional maps, of the effective charge state, as well as of the effective diffusivity of several defects and defect complexes generated in proton implanted silicon can be found in section 2.3 and in the defects catalog (see appendix C). This data can be used as input in the simulation.

4.1.3 Numerical Treatment of the Reactions Between Defects and the Dissociation of Defect Complexes

In this simulation method, the reactions between defects are approximated as diffusion limited reactions of second order (see section 2.2.7). The change of the concentration c_X is calculated from the product of the rate constant of the reaction and the concentrations of the reactants $c_{\mathrm{X}_\mathrm{A}}$ and $c_{\mathrm{X}_\mathrm{B}}$

$$\frac{\Delta c_\mathrm{X}(x)}{\Delta t} = k_r^\mathrm{AB}(T,x) c_{\mathrm{X}_\mathrm{A}}(x) c_{\mathrm{X}_\mathrm{B}}(x). \tag{4.14}$$

Here, k_r^AB is the rate constant of this reaction, which is calculated following von Smoluchowski and Debye (see section 2.2.7 and equations 2.92, 2.95, 2.96 and 2.97). As the diffusion coefficients of the reactants are temperature dependent, the same is true for the rate constant. Another important parameter in the calculation of the rate constant is the capture radius, which depends on the charge states of the reactants.

If the charge states of each defect are combined to an effective charge state, also the reaction rate constants can be combined to an effective reaction rate constant, which is a function of the temperature and of the position of the Fermi energy in the band gap:

$$k_r^\mathrm{AB}\left(T,E_F\right) = \sum_{q_1,q_2} 4\pi r_c^0 \left(D_{\mathrm{X}_\mathrm{A}^{q_1}}\left(T\right) + D_{\mathrm{X}_\mathrm{B}^{q_2}}\left(T\right)\right) \frac{f_C^{q_1,q_2} c_{\mathrm{X}_\mathrm{A}^{q_1}}\left(T,E_F\right) c_{\mathrm{X}_\mathrm{B}^{q_2}}\left(T,E_F\right)}{c_{\mathrm{X}_\mathrm{A}} c_{\mathrm{X}_\mathrm{B}}}. \tag{4.15}$$

This effective reaction rate constant is the sum over the reactions between all charge states. Appendix D shows two dimensional maps of the reaction rate constants of several reactions, as a function of the position of the Fermi energy in the band gap and of the temperature, which can be used as an input for the simulation.

A chemical reaction is usually associated with a backward reaction and at thermodynamic equilibrium, the ratio of products to educts corresponds to the ratio of the rates of the forward and the backward reactions. In this simulation, backward reactions are approximated as dissociation processes, where a defect complex dissociates into two smaller compounds. Here, the rate of this process is calculated as the product of the rate constant of the dissociation process and the concentration of the dissociating defect

$$\frac{\Delta c_\mathrm{X}(x)}{\Delta t} = -k_d^\mathrm{X}(T,x) c_\mathrm{X}(x). \tag{4.16}$$

The dissociation rate constant, as explained in section 2.2.7, is calculated from the attempt frequency f_d and the binding energy E_b of the dissociating bond. Also k_d^X is a function of E_F, as it depends on the charge states of the dissociation products. If both products are of the same charge, the dissociation rate constant is increased, while it decreases, if the charges of the products are of opposite sign.

The change in the defect concentration Δc_X due to both, reactions and dissociations is evaluated using the concentration values at the time $t = j$. This scheme is not A-stable and can lead to oscillations in the defect concentrations if large time-steps are used. As a single type of defect can be part in many reactions, though, it is very difficult to use other schemes for the numeric treatment of these processes.

4.1.4 Generation of New Point-Defects During the Simulation Process

In proton implantation, new point-defects are generated during the implantation process. Hydrogen (see section 2.4.3) is directly introduced by the beam, as the impinging protons come to rest and capture an electron. Furthermore, due to interactions of the beam with the crystal lattice, self-interstitials (section 2.3.1.4) and vacancies (section 2.3.1.1) are generated. SRIM is used to calculate the defect concentration profiles, relative to the implanted dose d, which are generated during the implantation process (see section 2.4.2 and figure 2.64). The shape of these profiles is strongly dependent on the implantation energy. In a proton implanter, the beam is usually scanned over the material to implant a larger area. Hence, the generation is not continuous but time dependent. In this process simulation, this time dependence is modeled by a delta pulse which repeats the defect generation at the scan frequency f_{scan}. The integral over this delta pulse yields the concentration of introduced defects c_{pulse}, which is a function of the proton flux Φ, of the scan frequency f_{scan} and of the normalized concentration $\left(\frac{c}{d}\right)_{\text{SRIM}}$

$$c_{\text{pulse}} = \frac{\Phi}{f_{\text{scan}}} \left(\frac{c}{d}\right)_{\text{SRIM}} . \tag{4.17}$$

The proton flux corresponds to the ratio of the implantation current I and the implanted area A.

$$\Phi = \frac{I}{eA}, \tag{4.18}$$

where e is the elementary charge. The defect profiles of dopants, such as B_s and P_s and other impurities, like oxygen and carbon are introduced at the start of the simulation.

4.1.5 Input Parameters of the Process Simulation

Depending on the input data, the simulation works on different levels of sophistication. A variety of properties, such as the configuration, the charge state and their composition can be used to separate distinct defects. Each defect is associated with a unique set of parameters, describing the temperature dependence of its diffusion and dissociation (see section 2.2.3), as well as, the ratio of different charge states and configurations (see section 2.2.4). The more defects there are, though, the more computational effort is necessary to simulate the same process conditions. Hence, some properties have to be combined to reduce the number of different defects in the simulation. At the same time, the parameters of these defects have to be joined to “effective” parameters (see e.g. effective diffusivity - section 2.2.3, or effective reaction rate constants - appendix D). A lower level of sophistication would be to combine the different charge states of an impurity and use the configuration (substitutional or interstitial lattice position) as the only distinctive feature between defects of the same composition (or chemical element). A further approximation step would be to also combine the charge states and use the effective charge states (see section 2.2.4) of the defects.

A simulation is always limited by the quality of its input data. For this simulation to work, the following inputs are essential:

- defects (E_{form}, q^{eff})
- diffusivity (E_A and D_0, or 2D-map)
- reaction paths and rates (2D-maps of k_r^{eff})
- dissociation rates (f_{d} and E_b)
- implantation parameters (H^+-energy, Φ, f_{scan}, d_{fin}, T)
- impurity concentrations (doping, impurity and SRIM-profiles)

The level of sophistication at which the simulation operates is determined by the choice of defects and defect complexes. Each defect that should be regarded by the simulation has to be defined. V^{2-}, C_{i}^{+} and B_{s}^{-} are three examples of defects. In this notation, a distinction between different charge states and lattice position is made. Every one of these defects is associated with a formation energy, E_{form}, which is a function of the position of E_F in the band gap and defines the concentration of the charge state relative to the other charge states of the impurity (e.g. there are five stable charge states of the vacancy). If the charge states are combined, the defects mentioned before would belong to V, C_{i} and B_{s}. The charge of these defects is included in their effective charge state, q^{eff} (a 2D-map of q^{eff} of the vacancy is shown in figure 2.32) and is a function of the Fermi energy, and of the temperature.

Every defect is associated with a diffusion coefficient, or with an effective diffusivity. The temperature dependence of the diffusion coefficient is defined by its Arrhenius parameters (E_A and D_0). In some cases, also the temperature dependence of the effective diffusivity can be described by a single pair of Arrhenius parameters. In other cases, though, it depends on both, the temperature and the Fermi energy. In such a case, pre-calculated two-dimensional maps (as in figure 2.35) can be used as input. Immobile defects are associated with a diffusion constant/ effective diffusivity of $0\,\text{cm}^2\text{s}^{-1}$.

Another crucial input to the simulation is the information on the different reaction paths of the defects. In general, each reaction between two defects could be possible, though, not every one makes sense. The products of some reactions might not necessarily be elements of the defects which are pre-defined. Furthermore, no reaction happens, if both reactants are immobile. To calculate the reaction rate between two defects, the rate constant of the reaction has to be known. If the simulation distinguishes between different charge states, the rate constant is calculated, as described in section 2.2.7. If another level of sophistication is chosen, the effective reaction rate constant, k_r^{eff} (see equation 4.15) is used. Similar to the effective diffusivity, pre-calculated, two-dimensional maps of k_r^{eff} (see appendix D) can be used as input.

To calculate the dissociation rates, the attempt frequency f_{d} and the binding energy E_b of the dissociating defect are required. If a defect does not dissociate, f_{d} is set to zero.

The parameters describing the implantation conditions are also an important input. The implantation energy (H^+-energy) defines which normalized SRIM-concentration profiles are used for the defects generated by the ion beam. From the proton flux Φ and the scan frequency f_{scan}, the concentrations of these defects and the time interval at which they are added are calculated. The final dose d_{fin} defines the end point of the simulation. Once the simulated time t reaches d_{fin}/Φ, the simulation is cut off. The process temperature is another important input, as it defines the diffusion constants and the rates of the reactions and the dissociations.

Before the simulation can be started, the starting conditions of the defect concentration profiles have to be defined. Usually the material contains impurities such as oxygen and carbon and intentionally introduced dopants such as phosphorus and boron.

4.1.6 Simulation Cycle

Once all input data is provided, the simulation can be started. In a first step, an array $C_{\text{X}}^{\text{all}}$ of the size $(N_{\text{def}} \times N_x)$ is created. Here, N_{def} is the number of different defects and N_x is the number of spacial increments (points in depth). In this array, the initial defect concentrations are set. If a defect is not yet present at the start of the simulation, its concentration along the whole profile is set to zero. For each point in depth from 1 to N_x, E_F is determined from the defect concentrations in $C_{\text{X}}^{\text{all}}$. To find the correct position of the Fermi level, the band-gap has to be searched for the energy, where the condition

$$n(T, E_F) + \sum_{i,q<0} q c_{\text{X}_i^q}(T, E_F) - p(T, E_F) - \sum_{i,q>0} q c_{\text{X}_i^q}(T, E_F) = 0 \tag{4.19}$$

for defects at different charge states or

$$n(T, E_F) - p(T, E_F) - \sum_i q_{\text{X}}^{\text{eff}}(T, E_F) c_{\text{X}_i} = 0 \tag{4.20}$$

using the effective charge state $q_{\text{X}}^{\text{eff}}$ of each defect, is fulfilled.

Then, the diffusion constants of the mobile defects, the drift mobilities and the rate constants of the reactions and dissociations are calculated at the process temperature and at the corresponding position of the Fermi energy in the band gap for each point in depth. The array, C_{impl} is initiated, containing the pulse concentrations c_{pulse} of the defects which are directly generated by the beam. Once all initiation processes are finished, the simulation loop, as illustrated in figure 4.1, is entered and the count of the simulated time, t_{sim} is initiated.

At the start of each loop, the simulated time t_{sim} is compared to the implantation counter. As this counter is set to zero at the beginning of the simulation, the implantation is executed the first time the loop is entered. This is done by adding C_{impl} to $C_{\text{X}}^{\text{all}}$. The implantation counter is then increased by $1/f_{\text{scan}}$. As long as t_{sim} is smaller than the simulation counter, this step is skipped. In the next step of the cycle, the simulation proceeds to the main-loop, which includes the calculations of the change in defect concentrations due to diffusion, ionic drift, reactions and dissociations. These calculations are performed separately for the time interval dt, which is set to a low value (10^{-10} s) at the start of the simulation. Each of the four segments of the main loop results in a set of concentration profiles, ΔC_{diff}, ΔC_{drift}, ΔC_{reac} and ΔC_{diss}, containing the changes in the defect concentration Δc_{X}.

As a first check, each set of Δc_{X} is separately added to $C_{\text{X}}^{\text{all}}$. The resulting concentration profiles, $C_{\text{X}}^{\text{all}*}$ are then checked for negative concentrations. If negative data points are

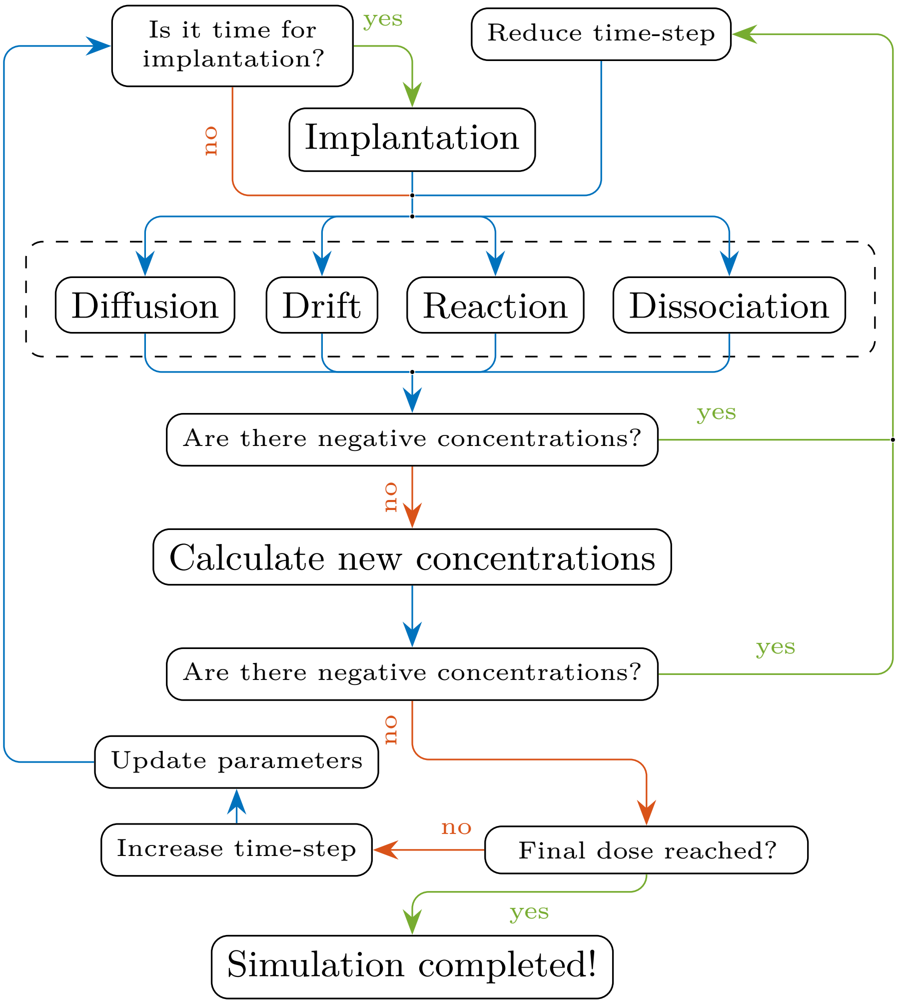

Figure 4.1: Flow-chart of the process simulation. The separate steps are explained in the text

found, the defect concentrations are reset to C_X^{all}, the time-step dt is decreased and the main-loop is re-executed. If no negative concentrations are found, ΔC_{diff}, $\Delta C_{\mathrm{drift}}$, ΔC_{reac} and ΔC_{diss} are added to C_X^{all}. As a back-up, the new concentration profiles are checked another time for negative values. If this test is passed, the program will compare t_{sim} to the time d_{fin}/Φ, when the final implantation dose is reached. As long as t_{sim} is smaller than d_{fin}/Φ, the simulation is continued and in the next step, the time-step dt is slightly increased. Before re-starting the loop, the position of the Fermi energy is recalculated and so are the diffusivities and the rates of the reactions and dissociations. The simulation cycle is complete, once the final dose is reached.

4.2 Simulation Results

In this section, the inputs for and the results of simulations using the current version of the code of the simulation of the proton implantation process are presented. At the current stage of development, the charge states of the defects, and hence, the dependence of the different parameters on the Fermi energy are not included. As a consequence, the migration of charged defects due to ionic drift as well as the influence of the Coulomb interaction on the reactions of charged particles are neglected.

The constants of the diffusion, and of the rates of reactions and dissociations are calculated at the process temperature once, and are used throughout the whole simulation run. Furthermore, the same constants are used at each point in depth. This version of the process simulation was written in FORTRAN95 by Lukas Etzlinger. More details about the simulation will be given in his master's thesis.

4.2.1 Simulation Inputs

To enable a more intuitive interpretation of the resulting defect profiles, the defects used in this simulation are combined to defect families. The classification here is mostly arbitrary and follows the objective to lower the number of concentration profiles in the overview figure. The concentration profiles of the members of each defect family are then plotted in separate figures. Table 4.1 lists these defects and includes a reference to the sections, where those defects are discussed.

Only some of these defects are mobile and diffuse if the temperature is high enough. In table 4.2 these mobile defects are listed, including the corresponding Arrhenius parameters describing the temperature dependence of the diffusion constants. The dissociation of defect complexes is also included for only some defects. The parameters describing the temperature dependence of the rate constant of the dissociation of these defects are listed in table 4.3. Due to the lack of published values, the dissociation of hydrogen containing defects is approximated using the same parameters, as for $\mathrm{P_sH}$ (f_d=$1.0\times10^{13}\,\mathrm{s}^{-1}$ and E_b=$1.32\,\mathrm{eV}$).

As, at the current stage of the process simulation, all defects are considered to be neutral, the calculation of the reaction rate constants requires, apart from the diffusivities of the reactants, only the neutral capture radius of the reactions (see equation 2.92). Here, estimations of the capture radii of some reactions, published in reference [446], are used and are listed in table 4.4. The capture radii of all other reactions are considered as 2 Å. The capture radius describes how close two defects must be before they react. Even though we somewhat arbitrarily set the capture radius to 2 Å for all reactions where it is unknown, it is clear that the capture radius cannot be much larger or much smaller than a few Angstroms.

Different sets of implantation parameters are applied in the process simulation. The process temperature, the proton flux and the implanted dose are varied, as well as the initial concentrations of oxygen and of carbon. Other parameters, such as the proton energy, the incidence angle and the concentrations of boron and phosphorus are the same in all simulation runs. All important parameters are listed in table 4.5.

The next sections show different defect concentration profiles in proton implanted silicon calculated using the process simulation.

Table 4.1: Defects and defect families used as input in the simulation of the proton implantation process.

Family	Defects	Section
B_i-complexes	B_i, B_iB_s, $B_{i2}B_s$, B_iC_s, B_iH, B_iH_2, B_iH_3, B_iO	2.3.5, 2.3.5.1, 2.3.5.2, 2.4.7
B_s-complexes	B_s B_iB_s, $B_{i2}B_s$ B_sH, B_sO	2.3.5, 2.3.5.1, 2.3.5.2, 2.4.7
C_i-complexes	C_i, C_iC_s, C_iC_sI, $C_iC_sI_2$, C_iOI, C_iOI_2, C_iP_s	2.3.4, 2.3.4.2, 2.3.6.1
C_iOH-complexes	C_iH, C_iO, C_iOH	2.3.4.1, 2.4.7
C_s-complexes	C_s, B_iC_s, C_iC_s, C_iC_sI, $C_iC_sI_2$, C_sH, C_sO, C_sOH	2.3.5.1, 2.3.4, 2.3.4.1, 2.3.4.2, 2.4.7
Hydrogen	H, H_2	2.4.3, 2.4.5
I-cluster	I, I_2, I_3, I_4, I_5, I_6, I_7, I_8	2.3.1.4, 2.3.1.5
IH-complexes	IH, IH_2, IH_3, I_2H, I_2H_2, I_2H_3	2.4.6
IO-complexes	IO, I_2O	2.3.3.3
Oxygen	O, O_2	2.3.3
OH-complexes	OH, OH_2	2.4.7
P_i-complexes	P_i, P_iI	2.3.6, 2.3.6.1
P_s-complexes	P_s, C_iP_s, P_sH, P_sO, VP_s, V_2P_s	2.3.6, 2.3.6.1
V-cluster	V, V_2, V_3, V_4, V_5, V_6	2.3.1.1, 2.3.1.2, 2.3.1.3
VH-complexes	VH, VH_2, VH_3, VH_4, VH_5, VH_6, V_2H, V_2H_2, V_2H_3, V_2H_4, V_2H_5, V_2H_6	2.4.6
VO-complexes	VO, VO_2, VO_3, V_2O, V_2O_2, V_2O_3, V_3O, V_3O_2, V_3O_3	2.3.3.2
VOH-complexes	VOH, VOH_2, V_2OH	2.4.7

Table 4.2: Mobile defects and Arrhenius parameters for the calculation of the corresponding diffusion constants used in the simulation of the proton implantation process. All other defects are considered as immobile. *: In this simulation the effective diffusivity of P_s was used. A better choice would have been to use the diffusivities of P_i and of VP_s.

Defect	E_A [eV]	D_0 [cm^{2}s^{-1}]	Reference
B_i	0.60	4.0×10^{-4}	[5]
C_i	0.88	4.4×10^{0}	[5]
H	1.22	3.3×10^{0}	[342]
H_2	0.81	7.4×10^{-4}	[444]
I	0.10	1.1×10^{-6}	[91]
I_2	1.52	3.8×10^{-1}	[92]
O	2.59	3.3×10^{-1}	[444]
O_2	2.05	2.3×10^{-2}	[444]
P_s*	3.5	1.03×10^{0}	[5]
V	0.30	3.9×10^{-4}	[445]
V_2	1.30	3.0×10^{-3}	[69]

Table 4.3: Dissociating defects and Arrhenius parameters for the calculation of the corresponding dissociation rate constants used in the simulation of the proton implantation process. All other defects are considered as non dissociating.

Defect	E_b [eV]	f_d [s^{-1}]	Reference
B_iH	1.28	2.8×10^{14}	[48]
B_sH	1.28	2.8×10^{14}	[48]
P_sH	1.32	1.0×10^{13}	[47]
I_2O	1.00	2.2×10^{10}	[174]
H-defects	1.32	1.0×10^{13}	

Table 4.4: Capture radii of selected reactions as published in reference [446].

Defect Reaction	r_c^0 [Å]	Defect Reaction	r_c^0 [Å]
$I+V\rightarrow0$	2	$B_s+I\rightarrow B_i$	2
$B_i+B_s\rightarrow B_iB_s$	20	$C_s+I\rightarrow C_i$	2
$B_i+O\rightarrow B_iO$	2	$V+V\rightarrow V_2$	2
$C_i+C_s\rightarrow C_iC_s$	4	$C_i+O\rightarrow C_iO$	4
$B_i+C_s\rightarrow B_iC_s$	40	$V+B_i\rightarrow B_s$	2
$B_i+B_iB_s\rightarrow B_{i2}B_s$	3	$V+O\rightarrow VO$	2
$V+C_i\rightarrow C_s$	2		

Table 4.5: Input parameters used in different runs of the process simulation.

Parameter	Inputs	Unit
H^+-energy	400	keV
Incidence angle	7	°
Dose	5×10^{13} - 1×10^{15}	H^+cm^{-2}
Scan frequency	5	Hz
Temperature	50 - 150	°C
Proton flux	2×10^{11} - 8×10^{11}	$H^+cm^{-2}s^{-1}$
B_s concentration	1×10^{13}	cm^{-3}
P_s concentration	1×10^{13}	cm^{-3}
C_s concentration	5×10^{15} - 2×10^{16}	cm^{-3}
O concentration	5×10^{16} - 2×10^{17}	cm^{-3}

4.2.2 Simulated Defect Profiles

Before the influence of different implantation parameters on the formation of defects is investigated, the distribution of the concentration of defect families and defects is studied, using a single set of parameters in the process simulation. Figure 4.2 shows the concentration profiles of the families of different defects listed in table 4.1. In this simulation run, a process temperature of 100 °C and a proton flux of $4\times10^{11}\,H^+cm^{-2}s^{-1}$ are applied and the simulated data is extracted after the implantation of $5\times10^{14}\,H^+cm^{-2}$. The initial oxygen concentration (c_O) is $10^{17}\,cm^{-3}$ and the concentration of carbon (c_C) is $10^{16}\,cm^{-3}$. All other input parameters are listed in table 4.5.

4.2.2.1 Defect Families

The resulting data of this process simulation are concentration profiles of 84 different defect complexes. To facilitate the interpretation of the results, the defects are, as mentioned above (see table 4.1), combined to defect families. The sum of the concentration profiles of the members of the defect families yields the concentration profile of the defect family. Figure 4.2 shows these concentration profiles.

Using the set of input parameters listed above, each defect family shows a unique concentration profile. The highest concentrations are found for the IH- and the VH-complexes whose concentration profiles are almost identical. The maximum of these concentration profiles is close to $10^{19}\,cm^{-3}$ and lies at the projected range of the implanted protons (around 4.5 µm). The same is true for the maximum of the hydrogen concentration, which is around half of the maximum concentration of the other two defect families. In the radiation damaged region, between the projected range and the surface of the material, high concentrations of VO and IO complexes (between $3\times10^{16}\,cm^{-3}$ and $5\times10^{16}\,cm^{-3}$) are found. Here, the oxygen concentration is reduced by almost an order of magnitude. Also, most of the substitutional carbon is converted to interstitial carbon defects. Here, the concentration of C_s-complexes is decreased by a factor of 30 compared to the substrate material. The concentration of interstitial clusters is slightly higher than that of vacancy clusters, with both lying around $10^{16}\,cm^{-3}$ in the irradiated region and peaking at the projected range. At this depth (approximately 4.5 µm), there are also significant concentrations of C_iOH-,

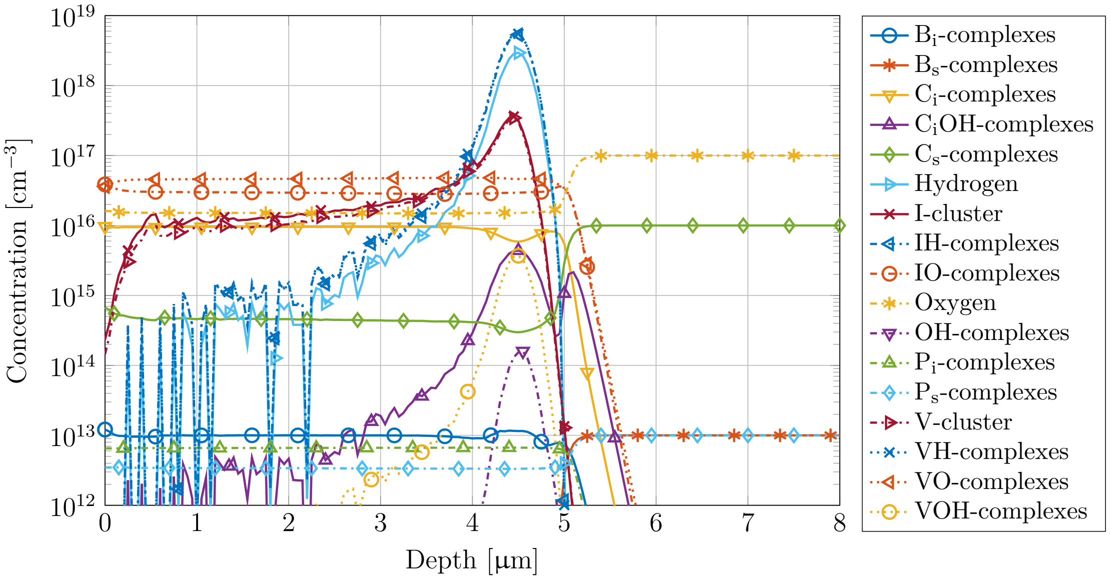

Figure 4.2: Simulated concentration profiles of the different defect families.

VOH- and OH-complexes. Here, the concentration profile of the C_iOH-complexes shows a second peak at a depth around 5 µm. The initial concentration of substitutional boron complexes is reduced in the shallow regions of the material by three orders of magnitude, as it is converted to B_i-complexes. In the case of phosphorus, the ratio between P_i- and P_s-complexes is about 2:1.

The distribution of the total concentrations of the different chemical elements (including the intrinsic point defects) is shown in figure 4.3. Additionally, the concentration profiles of hydrogen and of intrinsic defects, as simulated with SRIM and multiplied with a dose of $5\times10^{14}\,\mathrm{H^+cm^{-2}}$ are shown.

The total concentration profile of oxygen is constant at its initial level of $10^{17}\,\mathrm{cm^{-3}}$ throughout the material. Also the total concentration profiles of carbon, boron and phosphorus are almost constant. Only around the implantation depth, these concentrations deviate from their initial values. This phenomenon is discussed in section 4.2.3. The total concentration profile of hydrogen coincides very well with the hydrogen concentration profile calculated directly from the SRIM-simulation. This is the case, because hydrogen is not very mobile at the process temperature used in this simulation run. Otherwise, the total concentration profile would be broadened. The total concentration profiles of vacancies and self-interstitials are very similar. But they strongly differ from the concentration profile of intrinsic defects calculated from the SRIM-simulation. The total concentration of the profiles computed using the process simulation are more than one order of magnitude smaller than the SRIM-profile at the implantation depth and almost two orders of magnitude smaller in the irradiated region. This difference is explained by direct and indirect recombination of the intrinsic defects and it shows the importance of simulating the diffusion, reactions and dissociations of defects during the implantation process. Considering only the SRIM-profiles one would assume significantly higher concentrations of V_2 and other intrinsic defect complexes.

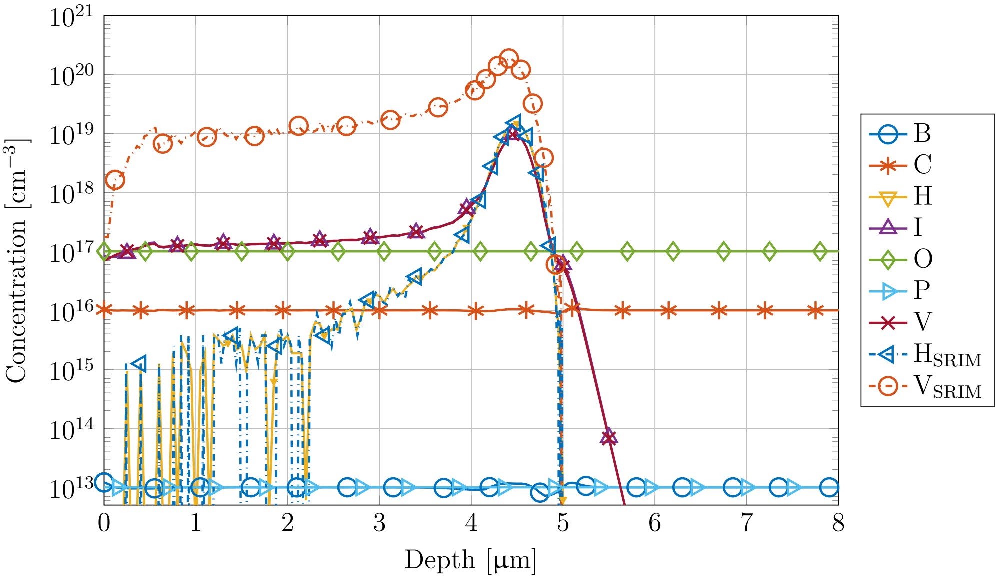

Figure 4.3: Simulated concentration profiles of the total concentration of point defects, including profiles calculated with SRIM and multiplied by a dose of $5{\times}10^{14}\,H^{+}cm^{-2}$.

In the next sections, the concentration profiles adding up to the profile of each defect family are shown separately.

4.2.2.2 B_i- and B_s-Complexes

The first two defect families investigated in more detail are the groups of boron containing defects. The concentration profiles of the members of these two families are shown in figures 4.4 and 4.5.

B_i-complexes are formed, when I reacts with B_s. Interstitials are only generated in the irradiated part of the material, up to the implantation depth (4.5 µm). So this is also the region in the material, where B_i-complexes are expected to form. Close to the surface of the material, almost all boron is present in the form of B_iO. Only at the implantation depth, the concentration of B_iH overtakes that of the interstitial boron-oxygen pair. B_iC_s is also formed in the irradiated region, though, its concentration is more than an order of magnitude below that of B_iO. At the implantation depth, where the hydrogen concentration is high, apart from B_iH, also B_iH_2 and B_iH_3 are produced. Furthermore, there are also traces of unbound B_i and B_iB_s. The maximum concentration of $B_{i2}B_s$ calculated using this set of input parameters, is only around $10^6\,cm^{-3}$.

In the irradiated region, B_s is only contained in the B_iB_s-complex, whose concentration is rather low. The highest concentration of the family of B_s-complexes is found in the non-irradiated substrate material and is attributed to B_s itself. The position, where the concentration of substitutional boron reaches its initial level, corresponding to its concentration before the proton implantation, is shifted to a depth of more than 5 µm. While, at the implantation depth, B_sH is formed at least at low concentrations, the maximum concentration of B_sO, calculated using the process simulation, is below $1\,cm^{-3}$.

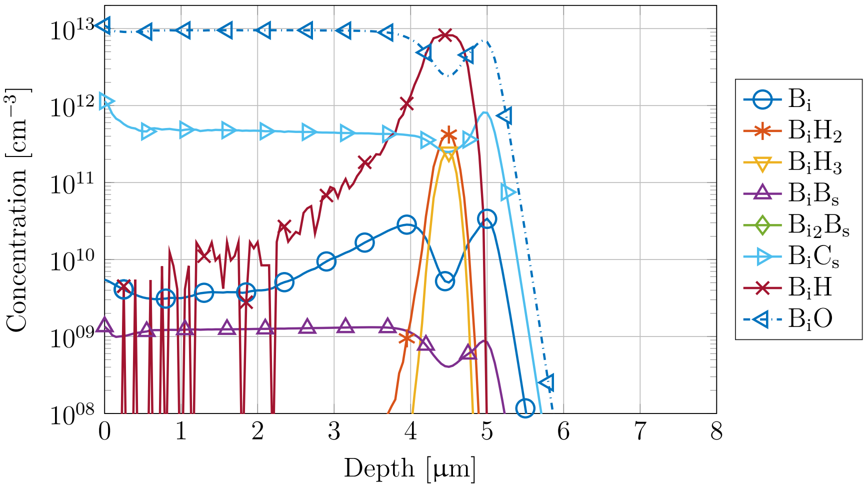

Figure 4.4: Simulated concentration profiles of the B_i-complexes. In this plot, the maximum concentration of $B_{i2}B_s$ is below $10^8\,\mathrm{cm}^{-3}$.

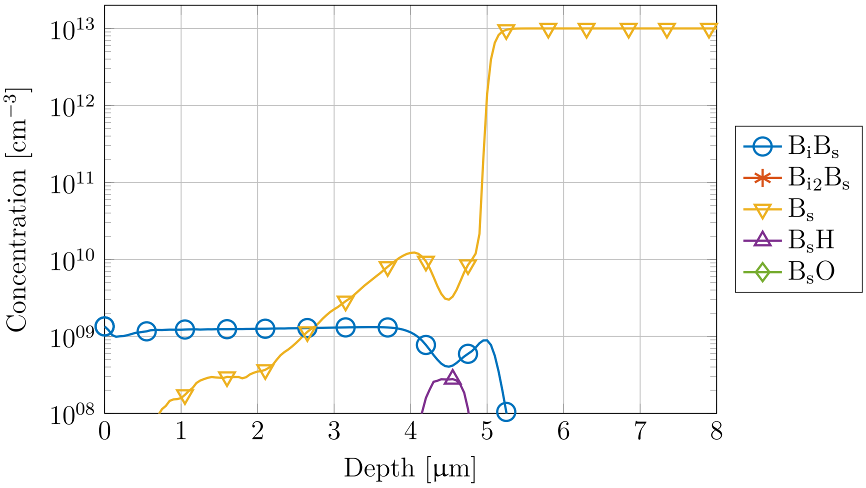

Figure 4.5: Simulated concentration profiles of the B_s-complexes. In this plot, the maximum concentrations of $B_{i2}B_s$ and B_sO are below $10^8\,\mathrm{cm}^{-3}$.

At the current stage of the process simulation, the only reaction path forming B_sH is by the reaction of substitutional boron with hydrogen and the only reaction yielding B_sO is that of B_s with O. If the indirect recombination of vacancies at B_iH and at B_iO is factored in, the concentration of the resulting B_sH and B_sO might be higher, than in the present results.

4.2.2.3 P_i- and P_s-Complexes

The concentration profiles of the defects forming the families of P_i- and of P_s-complexes are shown in figure 4.6 and 4.7. The only members of the P_i-complexes taken into account in this simulation run are P_i and P_iI. Throughout the whole irradiated region, about two thirds of the phosphorus content occurs as P_iI. Only at a depth of 5 µm some P_i is present, which immediately reacts with self-interstitials to form more P_iI.

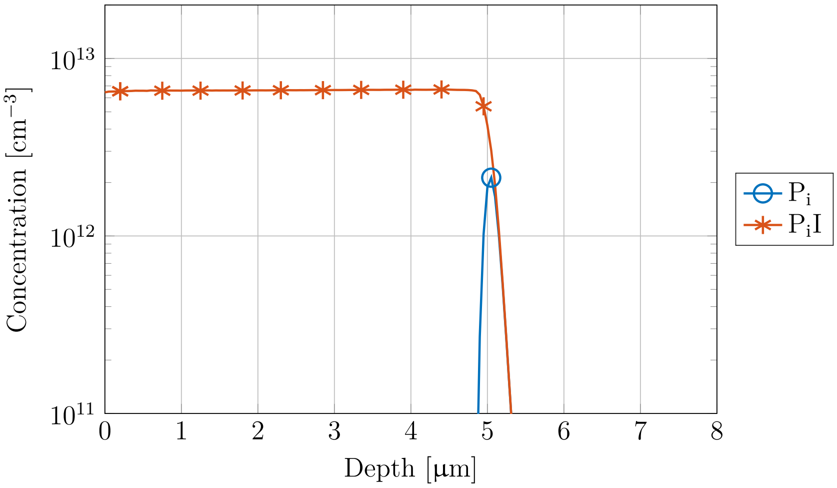

Figure 4.6: Simulated concentration profiles of the P_i-complexes.

In the substrate material, phosphorus occupies substitutional lattice sites (P_s). In the irradiated region, the concentration of unbound P_s is strongly decreased. About one third reacts with vacancies to form V_2P_s. VP_s is only present at a depth around 5 µm, where vacancies, which have diffused from the implantation depth deeper into the material, react with P_s. A small fraction of phosphorus appears in the carbon containing complex C_iP_s. Under the simulated conditions, almost none of the defects P_sH and P_sO are formed. The maximum concentration of P_sH is below $10^8\,\mathrm{cm}^{-3}$ and the maximum concentration of P_sO is even below $1\,\mathrm{cm}^{-3}$.

In this simulation run, P_s is assumed to be mobile and its effective diffusivity is used to describe its motion. A better choice would have been to consider the diffusivities of P_i and of VP_s, which might change the resulting defect profiles significantly.

4.2.2.4 C_i-, C_s- and C_iOH-Complexes

Figure 4.8 illustrates the concentration profiles of defects belonging to the family of C_i-complexes. These defects, similar to the family of B_i defects, are only generated in

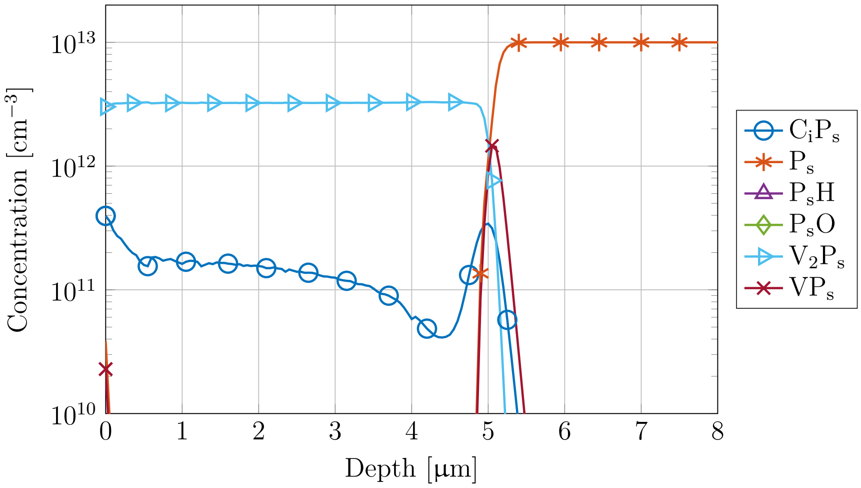

Figure 4.7: Simulated concentration profiles of the P_s-complexes.In this plot, the maximum concentrations of P_sH and P_sO are below 10^{10} cm^{-3}.

the irradiated region, where self-interstitials react with substitutional carbon. Here, the highest concentrations are found for C_iOI and for C_iOI_2, which make up about 90 % of carbon containing defects in this region. The concentration of C_iC_sI and $C_iC_sI_2$ are about an order of magnitude lower. At a depth below the projected range, at around 5 µm, low concentrations of C_iC_s are present and also traces of unbound C_i can be found. Also C_iP_s appears in the calculated profiles (see figure 4.7), though only at low concentrations, as the initial phosphorus concentration is set only to 10^{13} cm^{-3}.

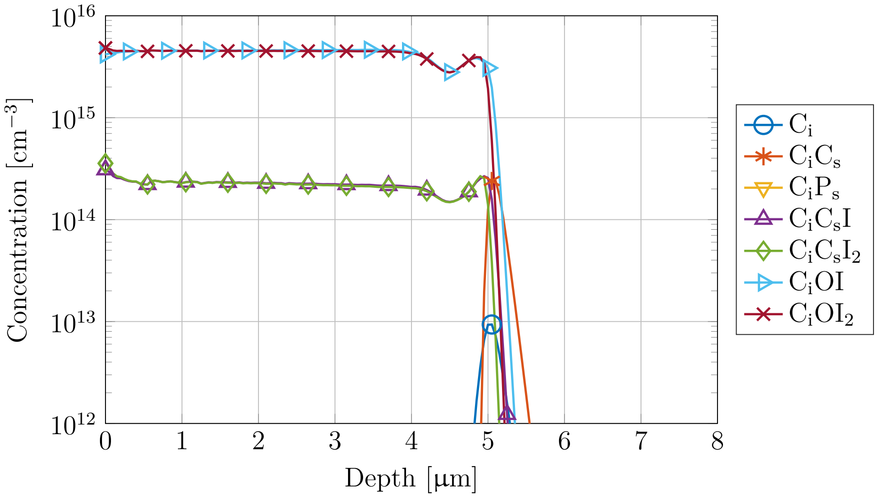

Figure 4.8: Simulated concentration profiles of the C_i-complexes. In this plot, the maximum concentration of C_iP_s is below 10^{12} cm^{-3}.

The concentration profiles of the defects making up the family of C_s-complexes are illustrated in figure 4.9.

In the substrate material, below a depth of 5 µm, C_s is the dominant carbon containing

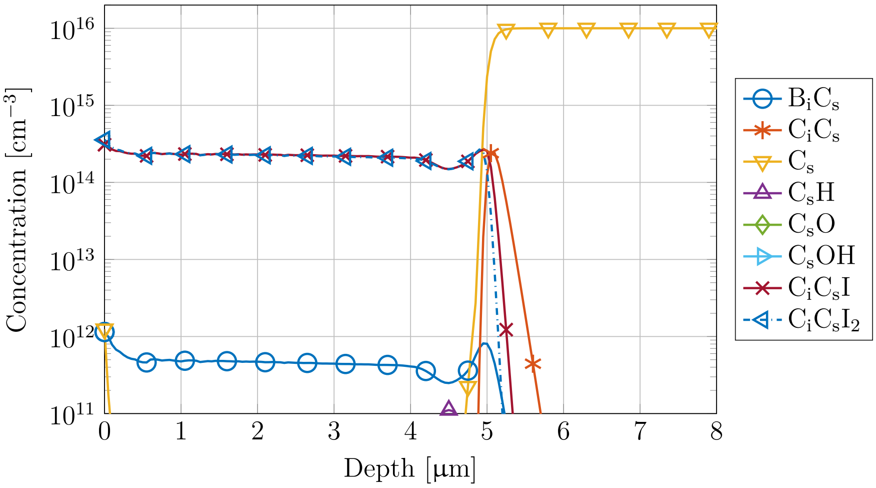

Figure 4.9: Simulated concentration profiles of the C_s-complexes. In this plot, the maximum concentrations of C_sO and C_sOH are below 10^{11} cm^{-3}

defect and hence, also the dominant defect of the family of C_s-complexes. In the irradiated region, the defects C_iC_sI and $C_iC_sI_2$ show the highest concentration of the members of this family. Furthermore, some B_iC_s is formed, whose concentration is limited to the initial boron concentration. At the implantation depth, traces of C_sH are found. The concentrations of C_sO and C_sOH are very low. Similar to B_sH and B_sO, also here, the concentrations of these defects might be orders of magnitude higher, but, the indirect recombination of vacancies at C_iH, C_iO and at C_iOH is not accounted for in the simulation inputs.

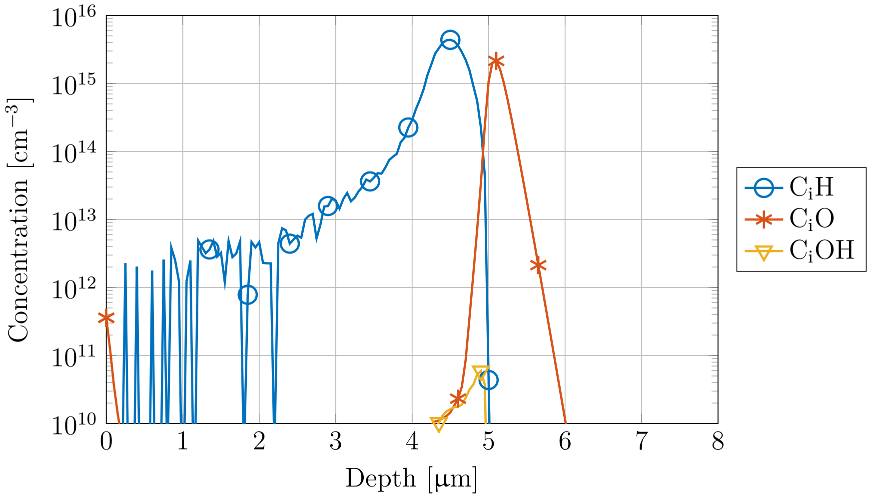

Figure 4.10: Simulated concentration profiles of the C_iOH-complexes.

A special kind of carbon containing defects are combined in the defect family of C_iOH-complexes, which are considered to cause the formation of the “shoulder” in the charge carrier concentration profiles in proton implanted Cz-silicon (see section 2.4.7). The concentration profiles of the members of this defect family are plotted in figure 4.10. Around the implantation depth, a high fraction of C_i reacts with hydrogen to C_iH. Deeper in the material, C_i reacts with oxygen forming C_iO. The peak of the C_iH-concentration is at a depth of 4.5 µm, while C_iO peaks at 5.1 µm. In between the maxima of these two defect complexes, the donor complex C_iOH is formed. At the used input condition, its concentration is still rather low (below $10^{11}\,\mathrm{cm}^{-3}$). Nevertheless, the position where it is formed, below the projected range of the protons, corresponds to the position where the shoulder-peak is observed.

4.2.2.5 Atomic and Molecular Hydrogen and Oxygen

While there is already oxygen in the material at the initial conditions, hydrogen is introduced during the simulation. Both impurities can occur as single interstitials (H, O) and as dimers (H_2, O_2). The concentration profiles of these defects are shown in figures 4.11 and 4.12.

Even though a large fraction of the introduced hydrogen immediately reacts to defect complexes, under the applied conditions, as a result of the dynamic equilibrium between reactions and dissociation processes, about 20 % of the implanted hydrogen remains in the form of atomic hydrogen. The concentration profile of hydrogen peaks at the implantation depth and its shape resembles that of the hydrogen concentration profile simulated with SRIM. The fluctuations in the irradiated region are also derived from the way the SRIM-profile is produced. Depending on the simulated temperature and on the simulated time, these fluctuations are smoothed due to diffusion. Under the conditions applied in this simulation run, the concentration of H_2, formed during the implantation, is about two orders of magnitude lower than that of atomic hydrogen.

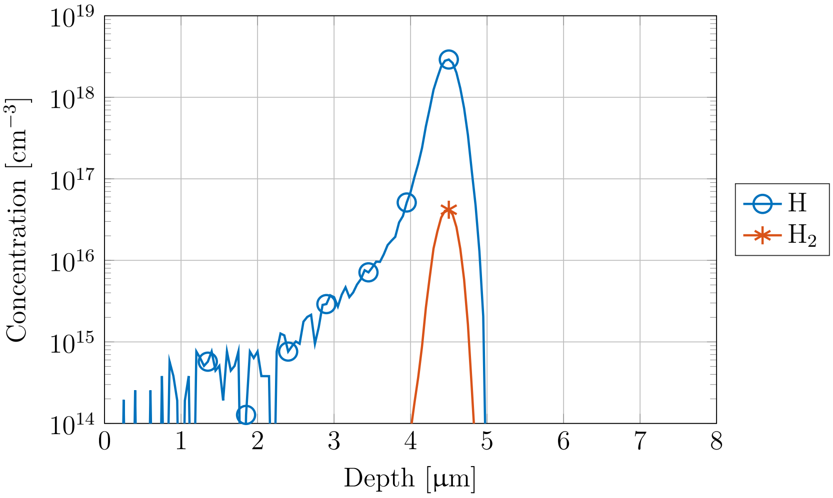

Figure 4.11: Simulated concentration profiles of atomic and molecular hydrogen.

At the simulated temperature oxygen is still immobile. Hence, it is only present as atomic oxygen O. The simulated concentration of molecular oxygen is below $1\,\mathrm{cm}^{-3}$. While in the substrate material, at a depth below 5 µm, the oxygen concentration is at its initial level, it is reduced by almost an order of magnitude in the irradiated region. The residual atomic oxygen mainly stems from the dynamic equilibrium between reactions and indirect recombinations of intrinsic defects at VO- and at IO-complexes.

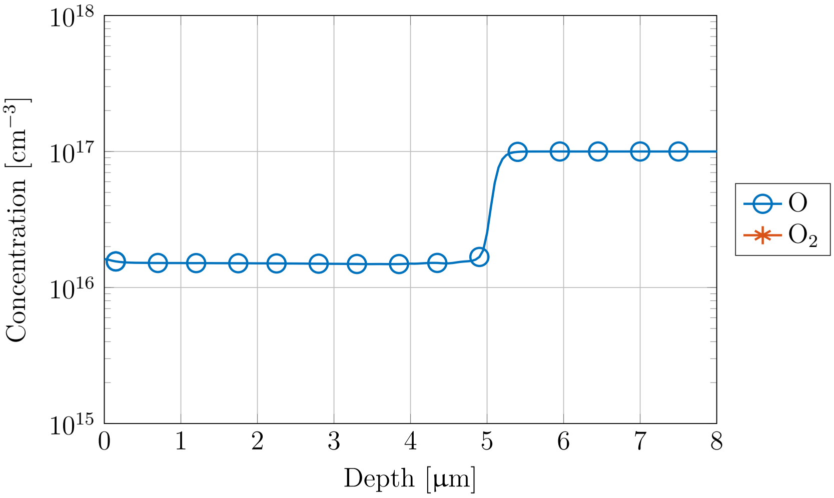

Figure 4.12: Simulated concentration profiles of atomic oxygen and of the oxygen dimer. The maximum concentration of O_2 is below 1 cm^{-3}.

4.2.2.6 Interstitial and Vacancy Clusters

If there are high concentrations of intrinsic defects, apart from other complexes, they form clusters. Figures 4.13 and 4.14 show the concentration profiles of different interstitial- and vacancy-clusters.

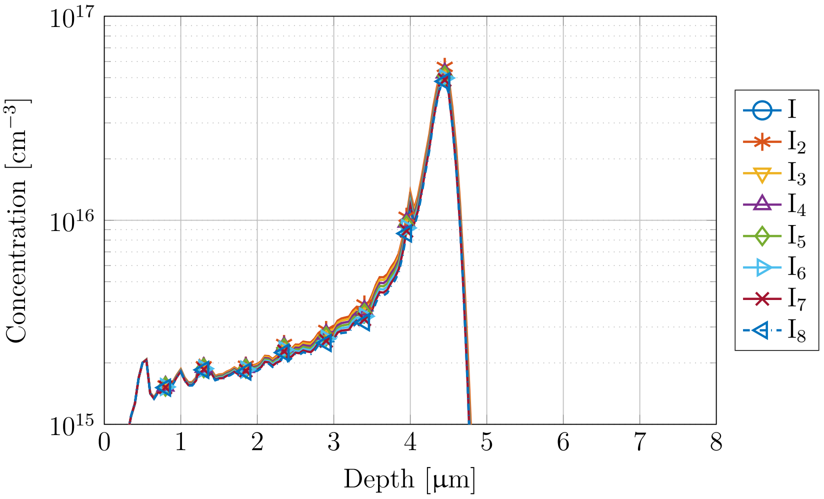

Figure 4.13: Simulated concentration profiles of I-clusters.

At the current development level of the simulation and using the input parameters listed above, the concentration profiles of the different clusters consisting of two to eight interstitials look very similar. Here, the smaller clusters show only slightly higher concentrations than the bigger ones.

Also the concentration profiles of the vacancy cluster look very similar. Other than the I-clusters, the bigger vacancy clusters are slightly higher in concentration than the small ones.

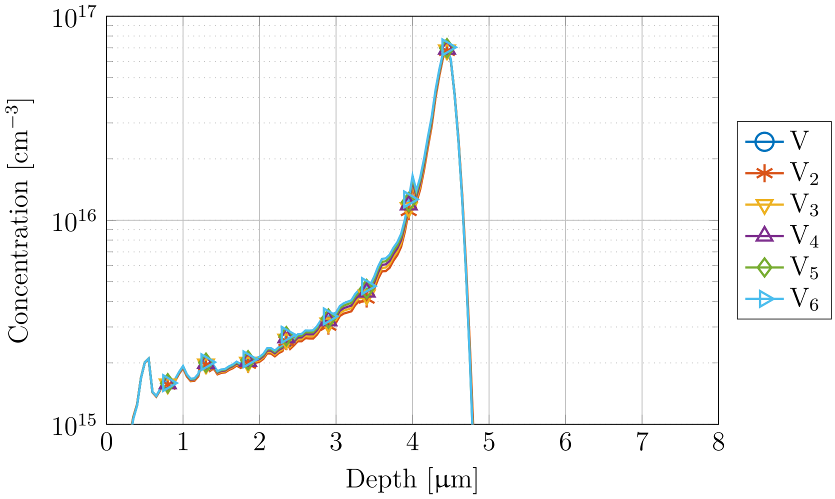

Figure 4.14: Simulated concentration profiles of vacancy cluster.

The relative concentrations of clusters might strongly change, once the dependence of the reaction rate constants on the position of the Fermi energy in the band gap (see figures D.1.1 to D.8.1 in appendix D) is factored into the process simulation.

4.2.2.7 IH- and VH-Complexes

The concentration profiles of defects belonging to the families of IH- and VH-complexes are plotted in figures 4.15 and 4.16.

In the defect family of the IH-complexes, the highest concentrations are found for IH and I_2H, whose concentration profiles look the same. The concentration of IH_2, IH_3 and I_2H_3 are lower by a factor of about 30. At even lower concentrations appears I_2H_2. This is owed to a mistake in the input data, were the reaction of IH_2 with I to I_2H_2 is not accounted for.

The highest concentrations of the members of the family of VH-complexes are found for VH and V_2H. The concentrations of VH_2, V_2H_2, VH_3 and V_2H_3 are more than an order of magnitude lower. Another two orders of magnitude below that level, are VH_4, V_2H_4, VH_5 and V_2H_5. The lowest concentrations are found for VH_6 and for V_2H_6.

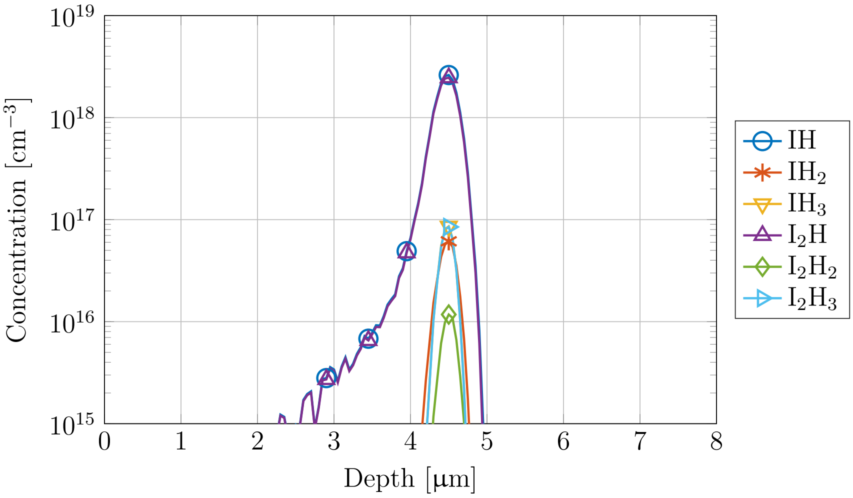

Figure 4.15: Simulated concentration profiles of the IH-complexes.

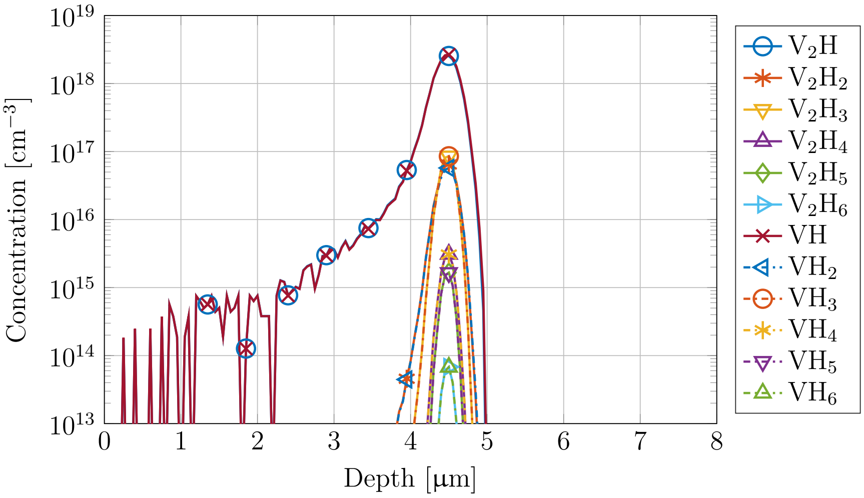

Figure 4.16: Simulated concentration profiles of the VH-complexes.

4.2.2.8 IO- and VO-Complexes

Concentration profiles of defects belonging to the IO- and to the VO-complexes are shown in figure 4.17 and 4.18.

In the irradiated region, almost a third of the oxygen concentration is converted to IO-complexes. In the irradiated region, the concentrations of IO and I_2O, the two members of this defect family, are the same. Starting at a depth below the projected range, at around 5 µm, the concentration of IO is significantly higher than that of I_2O. Self-interstitials diffuse from the projected range to this depth to react with atomic oxygen, then further self-interstitials, start converting IO to I_2O until a dynamic equilibrium is established. The region where IO is formed is shifted into the substrate material with increasing generation

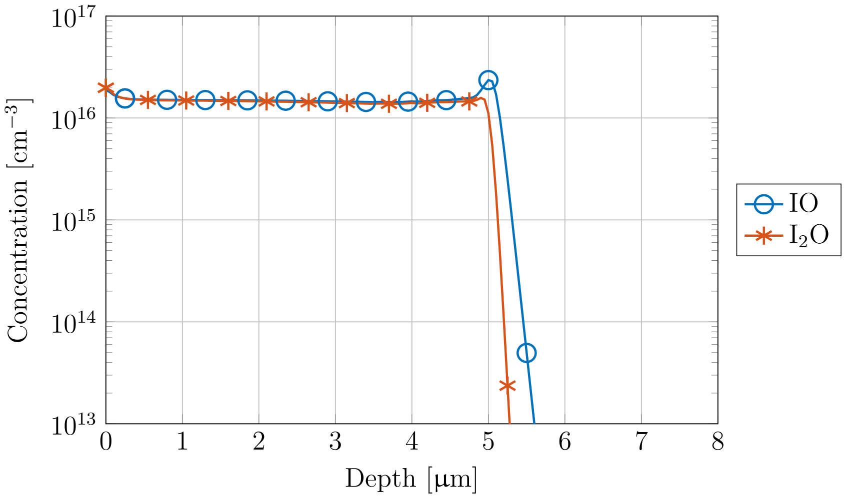

Figure 4.17: Simulated concentration profiles of the IO-complexes.

of self-interstitials. In the literature, a variety of different VO-defects are mentioned (see section 2.3.3.2). Of those defects, only the ones containing a single oxygen atom (VO, V_2O and V_3O) are formed under the applied conditions, where oxygen is immobile. The concentration profiles of these defects look very similar in the irradiated region. Only at a depth below the projected range, similar to the situation of the IO-complexes, the concentration of VO is higher than that of V_2O and V_3O.

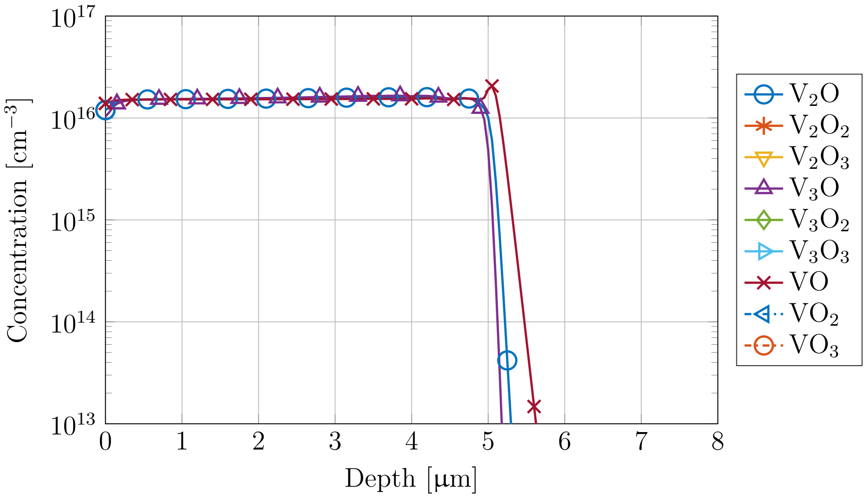

Figure 4.18: Simulated concentration profiles of the VO-complexes. In this plot, the maximum concentrations of V_2O_2, V_2O_3, V_3O_2, V_3O_3, VO_2 and VO_3 are below 1 cm^{-3}.

4.2.2.9 OH- and VOH-Complexes

The defect families containing hydrogen and oxygen are the OH-complexes and the VOH-complexes. The concentration profiles of the OH complexes are plotted in figure 4.19. Both members of this defect family show similar concentration profiles, peaking at the implantation depth (4.5 µm). The maximum concentration of both defects is close to 10^{14} cm^{-3}.

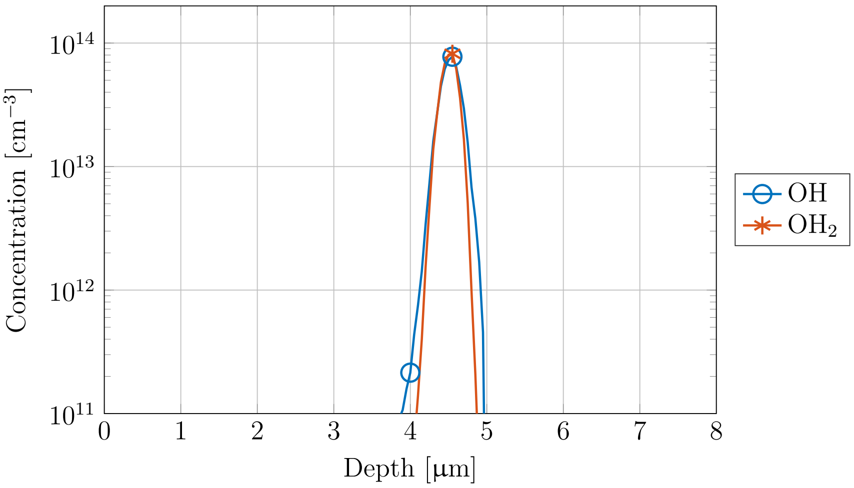

Figure 4.19: Simulated concentration profiles of the OH-complexes.

The concentration profiles of the defects belonging to the VOH-complexes are illustrated in figure 4.20. Also in this defect family, all members show similar concentration profiles, which also peak at 4.5 µm. Compared to the OH-complexes, the maximum concentrations of the VOH-complexes are higher by an order of magnitude.

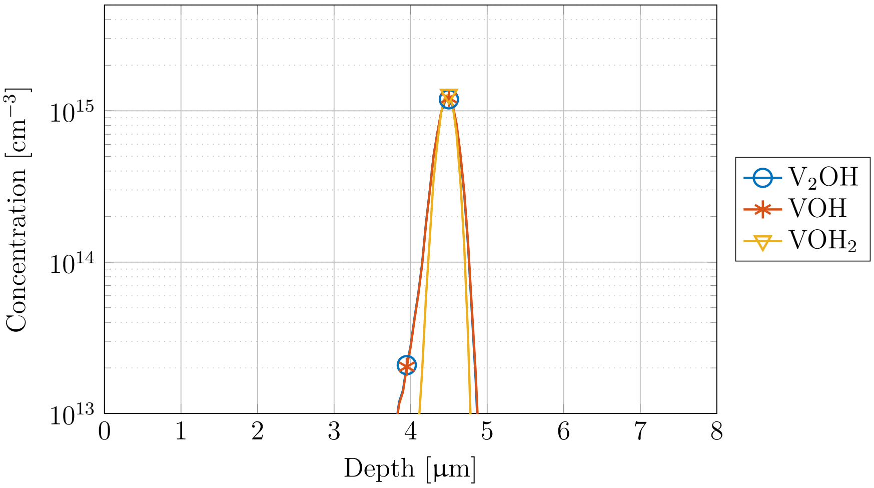

Figure 4.20: Simulated concentration profiles of the VOH-complexes.

4.2.3 Non-Uniformity of the Concentration Profiles of Different Elements

The impurities boron, carbon and phosphorous are considered to be immobile when they occupy substitutional lattice positions. If those defects reside on interstitial lattice sites, though, they start diffusing. At the projected range of the implanted protons, a high concentration of self-interstitials is formed, which react with B_s, C_s and P_s, forming interstitial defects. Due to the concentration gradient, of the interstitial species, it is suspected, that they will diffuse away from the implantation depth, creating a dip in the overall elemental concentration profiles of boron, carbon and phosphorus.

The elemental concentration profiles, computed using the set of input parameters, listed above, in the process simulation, tell a different story. Figure 4.21 shows the profiles of the overall boron concentration and of the concentrations of boron containing defects at a depth of 3.0 µm to 6.0 µm.

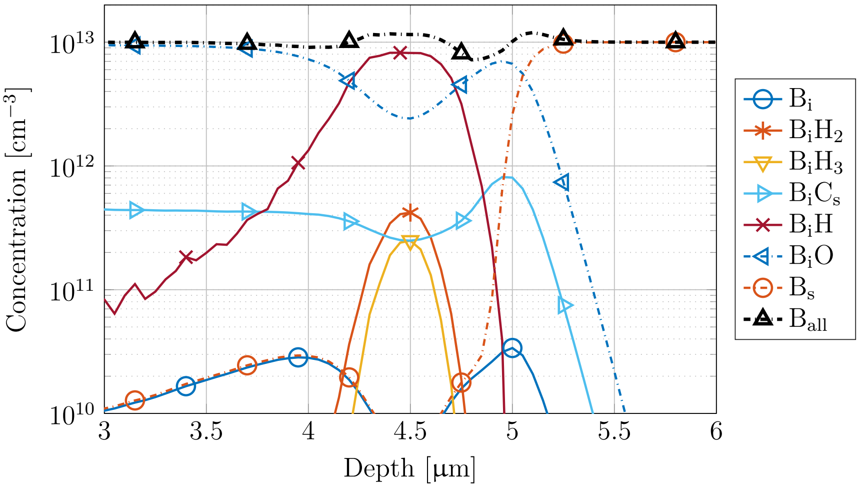

Figure 4.21: Simulated concentration profiles of boron (black dashed line) and boron containing defects (colored lines) at an implantation dose of $5{\times}10^{14}\,H^+cm^{-2}$.

Contrary to the expectation of a dip at the implantation depth, a local maximum is observed at a depth of 4.5 µm. A second maximum in the boron concentration is formed at a depth of 5.1 µm and two dips are observed at 4.0 µm and at 4.8 µm. While the boron concentration in the peaks is 15 % and 20 % higher than its initial concentration, it is reduced to 90 % and 70 % of the initial concentration in the dips. In the irradiated region, most of the boron is present in the form of B_iO. At the implantation depth, the concentration of B_iO is surpassed by that of B_iH and in the substrate material, B_s is the only boron species. Between 5 % and 8 % of the boron are found as B_iC_s, B_iH_2 and as B_iH_3. Only some traces of B_i are still present after simulating an implantation dose of $5{\times}10^{14}\,H^+cm^{-2}$. The concentration profile of B_i, though is the key in the explanation of the overall boron profile. The concentration of B_i peaks close to the dips in the B_{all}-profile. As B_i diffuses away from the peaks, the overall boron concentration at the position of these peaks is reduced.

This effect is better observed at earlier stages in the simulation. Figure 4.22 shows the profiles of the overall boron concentration and of the boron containing defects at an implantation dose of $5{\times}10^{13}\,H^+cm^{-2}$.

After an implantation of $5{\times}10^{13}\,H^+cm^{-2}$, the concentration of available B_i is still significantly high. The reason why not all B_i immediately reacts to B_iO or B_iH is its interaction with intrinsic defects. The reaction with vacancies converts B_i back to B_s

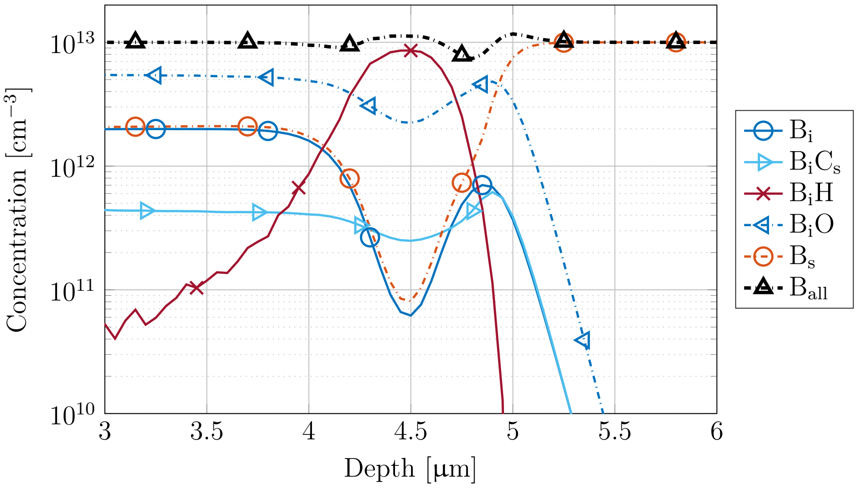

Figure 4.22: Simulated concentration profiles of boron (black dashed line) and boron containing defects (colored lines) at an implantation dose of $5\times10^{13}\,H^+cm^{-2}$.

and the reaction of B_s with self-interstitials forms new B_i. Due to the high hydrogen concentration, though, a dip in the B_i-concentration is formed which leads to the diffusion of B_i towards this dip. Furthermore, another strong gradient in the concentration profile of B_i is found deeper in the material at the transition from the implanted region to the substrate material. Due to this concentration gradient, the second peak in the profile of the overall boron concentration is formed.

A similar effect as for the concentration profile of boron, is found for that of carbon. Figure 4.23 shows the profiles of the overall carbon concentration and the concentration profiles of carbon containing defects which are present under the applied conditions.

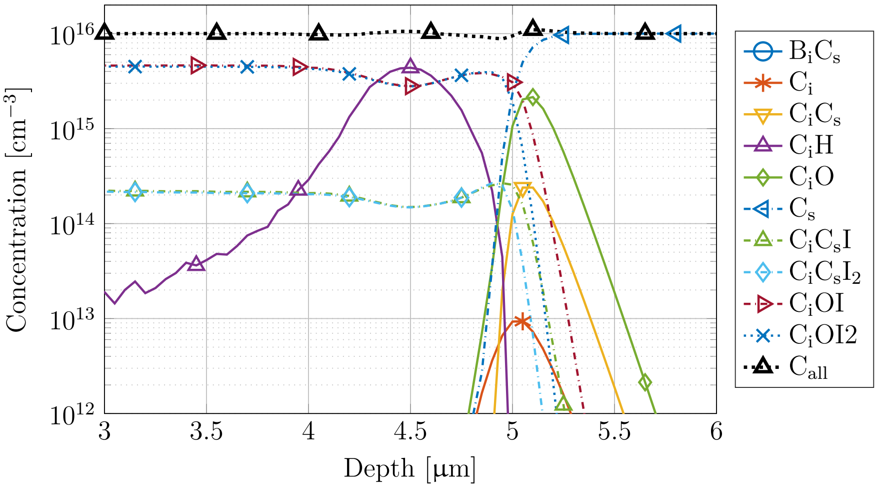

Figure 4.23: Simulated concentration profiles of carbon (black dashed line) and carbon containing defects (colored lines) at an implantation dose of $5\times10^{14}\,H^+cm^{-2}$.

Like boron, also carbon forms a defect complex with hydrogen around the implantation depth, which leads to a peak in the overall carbon concentration at this position and also a second peak at around 5.1 µm is formed. The relative change in the carbon concentration is smaller compared to boron, which might be a consequence of its higher concentration in the simulation. Still, the carbon concentration is increased by 5 % and by 10 % in the two peaks and it is reduced by 12 % and by 3.5 % in the two dips.

The situation looks different for the overall phosphorus concentration profile (see figure 4.24). Here, two peaks and one dip are formed, the change in the phosphorus concentration, though, is below 0.1 %. Furthermore, the positions of the peaks and of the dip in the concentration profile of phosphorus (peaks at 4.9 µm and at 5.2 µm; dip at 5.05 µm) differ from those in the concentration profiles of boron and carbon.

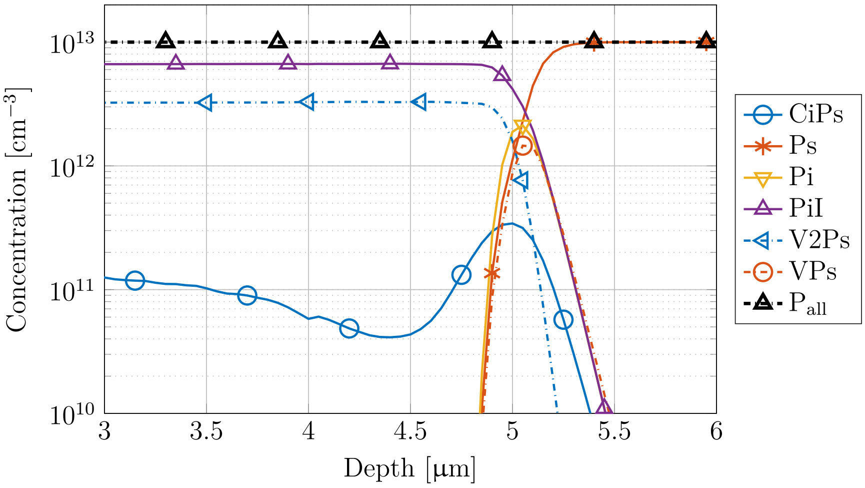

Figure 4.24: Simulated concentration profiles of phosphorus (black dashed line) and phosphorus containing defects (colored lines) at an implantation dose of $5{\times}10^{14}\,H^{+}cm^{-2}$.

There are several explanations, why the phosphorus profile looks different. First, in this simulation run, the only mobile phosphorus defect is P_s (as its effective diffusivity was used in the input data). In fact, this defect is considered to be immobile, while P_i and VP_s are mobile phosphorus species. Secondly, the formation of P_iH is not accounted for in the input data. In this simulation run, only the defect P_sH was initiated. Furthermore, the indirect recombinations of vacancies at P_iI and of self-interstitials at V_2P_s are not accounted for. Hence, the reactions of phosphorus stop, once these defect complexes are formed and the concentrations of both, P_i and P_s go to zero in the irradiated region.

The difference between the overall concentration profiles of boron and of phosphorus show the importance of high quality inputs for the process simulation. It has to be emphasized, that the current results are the product of the input data used in this simulation run and the inclusion of further defects and reaction paths might strongly change these results. Measurements of the elemental concentration profiles (e.g. using SIMS) of different impurities after proton implantation could be used to verify how genuine and accurate the simulated data is.

4.2.4 Fermi Energy and Charge Carrier Concentration Profiles

For some of the defects which are accounted for in the simulation, the data on the distribution of their charge states is available (see appendix C). Using this data, the effective charge states of the defects are calculated for different Fermi energies. Multiplying the effective charge state of each defect with its concentration yields the effective charge concentration of that defect. While the effective charge concentration of donors is positive that of acceptors is negative. At the Fermi energy, the sum of the positive charges (donors plus holes) equals the sum of the negative charges (acceptors plus electrons), as described by equation 4.20. The residual charge concentration is the difference between the concentration of positive and negative charges. Figure 4.25 shows a two dimensional map of the residual charge concentration as a function of depth in the material at Fermi energies from E_V to E_C. As a logarithmic scale is used, the absolute values of the residual charge concentration are plotted. Regions of yellow color indicate a high residual charge concentration, while blue colored regions signalize a low residual charge concentration. As the measurements which are used to evaluated the Fermi energy are usually performed at 25 °C, this temperature was also used in this calculation.

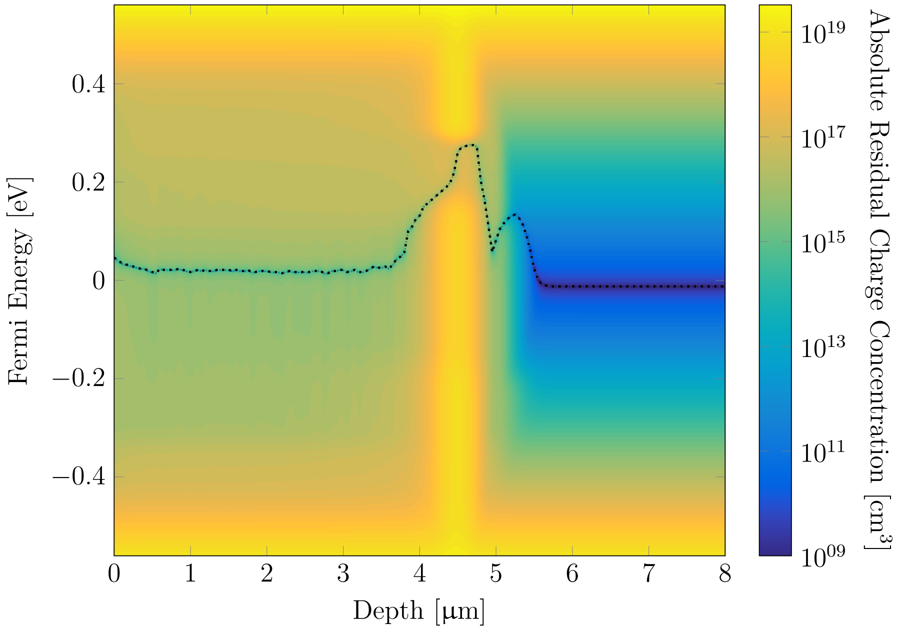

Figure 4.25: Residual charge concentration as a function of the depth and of the position of the Fermi energy relative to the middle of the band gap, calculated at a temperature of 25 °C.

The energy at each point in depth, where the lowest residual charge concentration is found, corresponds to the position of the Fermi energy in the band gap. Due to the finite energy increment, the residual charge is not always exactly 0, but it is significantly reduced. The position of the Fermi energy in the band gap is emphasized by a dotted line in figure 4.25. In figure 4.26 the valence and conduction band energies, calculated at 25 °C are plotted as a function of the depth.

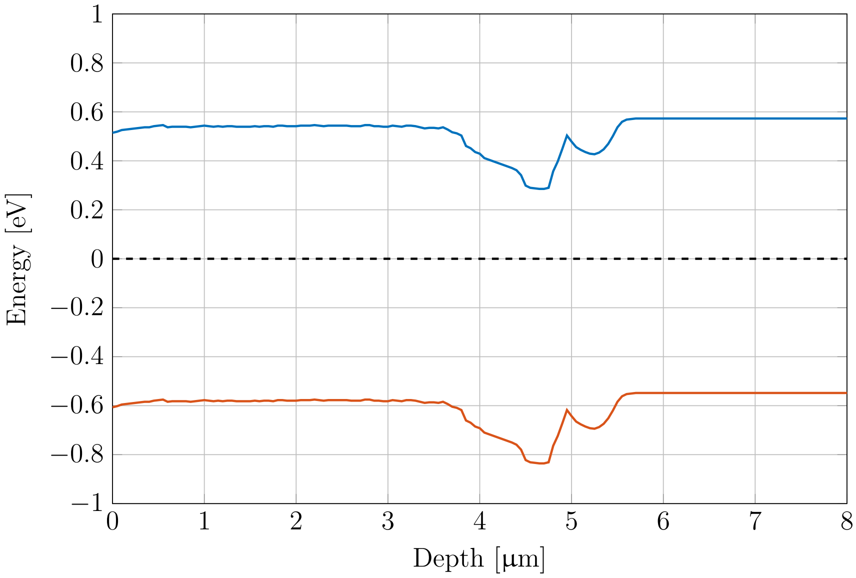

Figure 4.26: Depth-profile of the valence band(red) and conduction band (blue) energies in the simulated material calculated at a temperature of 25 °C. The dotted line represents the Fermi energy.

From the position of the Fermi energy in the band gap, the charge carrier concentrations are calculated following equation 2.16 for electrons in the conduction band and equation 2.18 for holes in the valence band. The profiles of the charge carrier concentrations are shown in figure 4.27. Even though, the charge states of the defects are not accounted for in the simulation, and the formation energies of the charge states are not known for every defect, the shape of the electron profile resembles pretty well the shape of charge carrier profiles measured with SRP (see section 3).

The electron concentration is higher than that of holes throughout the irradiated region, until a depth of 5.5 µm. Close to the implantation depth (4.5 µm-4.8 µm), there is a peak in the electron concentration, accompanied by a steep decay in the inward direction and a smoother decay towards the surface of the material. At a depth of 5.2 µm, a second peak in the electron concentration profile is observed. While the electron concentration in the main peak is $4{\times}10^{14}\,\mathrm{cm}^{-3}$, the concentration at the second peak is only slightly larger than $10^{12}\,\mathrm{cm}^{-3}$. In the irradiated region, the electron concentration is only slightly above $10^{10}\,\mathrm{cm}^{-3}$. As the same initial concentration of the dopants B_s and P_s was set at the start of the simulation, intrinsic conditions are expected in the substrate material. This is observed in figure 4.27, as the concentrations of holes and electrons are similar in this region.

To evaluate, which defects are responsible for the changes in the position of the Fermi energy in the band gap, the average charge states of the charged defects are investigated. Figure 4.28 shows the depth profile of the average charge state of each charged defect at the Fermi energy at this point (at 25 °C). Here, donors are indicated by dotted lines while dashed lines are used to mark acceptors. Only defects, whose maximum effective charge concentrations are higher than $10^{12}\,\mathrm{cm}^{-3}$ are considered in this figure.

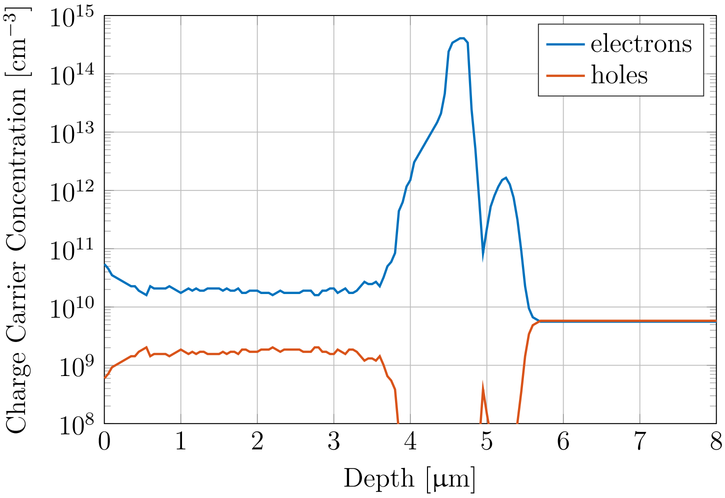

Figure 4.27: Depth-profiles of the concentrations of charge carriers in the simulated material calculated at a temperature of 25 °C.

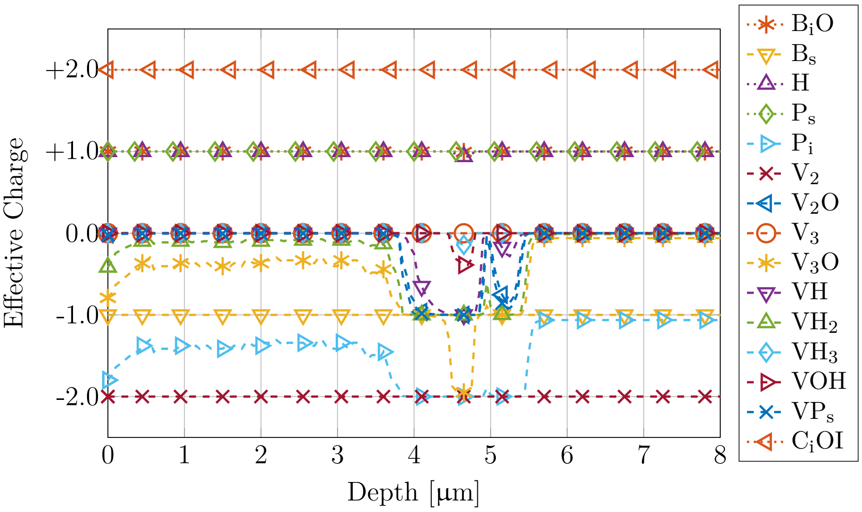

Figure 4.28: Depth-profiles of the effective charge states of ionized acceptors and donors in the simulated material calculated at a temperature of 25 °C.

Under the simulated conditions (and maybe due to the limited data on formation energies) only four donor-complexes are observed. Apart from the obvious donor P_s, also B_iO, H and C_iOI show a positive ionization throughout the simulated depth. The last of these donor complexes, C_iOI, is especially interesting, as it is a double donor.

Considering all defect complexes, which are, at least somewhere in the material, negatively ionized, eleven complexes are found under the simulated conditions. B_s is known to be a good acceptor and it is widely used in semiconductor industry. The divacancy, V_2 is a double acceptor and the effective charge state of P_i varies, depending on the Fermi energy between −1 and −2. Another interesting acceptor-like complex is V_3O. In the substrate material the charge state of this defect complex is above −0.1. In the irradiated region, it is between −0.3 and −1 and at around the projected range, the effective charge state of V_3O even gets close to −2. Other defect complexes, such as the vacancy-hydrogen defects VH, VH_2 and VH_3, the VOH- and V_2O-complexes, V_3, VP_s only accumulate negative charges in the region around the implantation depth.

As explained before, the Fermi energy is calculated from the sum of the effective charge concentrations of the defects in the material. The effective charge concentration is the product of the effective charge and the concentration of a defect. Figure 4.29**a** illustrates the concentration profiles of the defects whose effective charge states are plotted in figure 4.28. In figure 4.29**b**, the profiles of the effective charge concentrations of the same defects are plotted. Both figures include the concentration profile of electrons, which is, for better visualization, multiplied by a factor of 10^3.

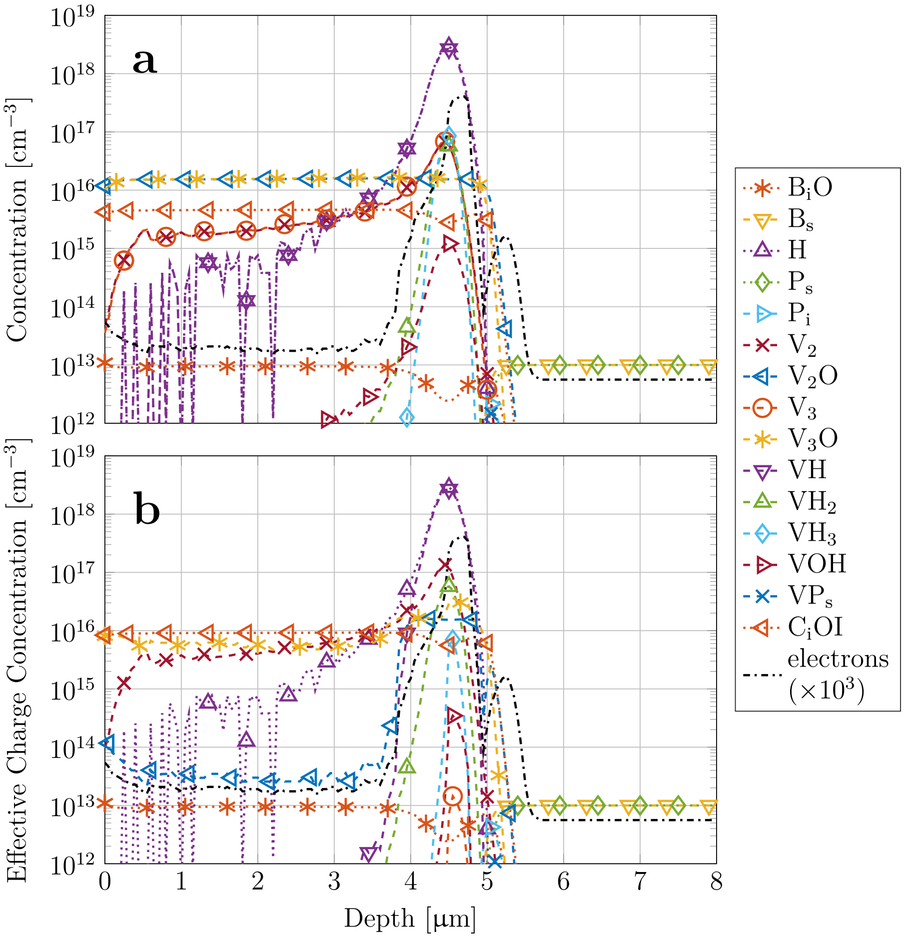

Figure 4.29: Depth-profiles of the concentration (**a**) and the effective charge concentration (**b**) of ionized acceptors and donors in the simulated material calculated at a temperature of 25 °C. The dot-dashed line indicates the concentration profile of electrons in the conduction band.

Studying this figure makes it pretty clear that not a single donor complex is responsible for the shape of the charge carrier profile of proton implanted silicon, but rather a complicated interplay of donors and acceptors. Additionally, there are defect complexes which compensate whatever charge surplus there is in the material by acquiring a state of opposite charge. In the irradiated region, the highest effective charge concentration among donors is found for C_iOI and for H, whileV_2 shows the highest effective charge concentration of the acceptors. Also most of the V_3O-complexes contribute to the charge concentration of acceptors. Furthermore, a small fraction of V_2O is ionized as well.

C_iOI and H are real electron donors. C_iOI is a double donor throughout the band gap of silicon and the transition of the positive to the negative charge state of H appears at an energy of 0.31 eV. Hence, both these donors are fully ionized in the irradiated region. Of the acceptors, which are present in this area of the material, only V_2 is a real acceptor with its ionizations lying at -0.21 eV ($-/0$) and at -0.14 eV ($-2/-$). The rest of the positive charge of the ionized donors, which is not fully balanced by V_2, is compensated by V_3O ($-/0$ at 0.03 eV and $-2/-$ at 0.24 eV) and by V_2O ($-/0$ at 0.11 eV). Hence, the Fermi energy is shifted to values between 0.01 eV and 0.04 eV.

Around the implantation depth, the concentration of hydrogen significantly increases, and with it, the donor concentration. This leads to the full ionization of V_3O and V_2O, and also other compensating defects start to accumulate negative charges. Among those, VH ($-/0$ at 0.15 eV) has the highest concentration, and also VH_2 ($-/0$ at 0.05 eV) becomes fully ionized. At the maximum Fermi energy, which is reached under the simulated conditions, 0.28 eV, the compensating defects VOH ($-/0$ at 0.29 eV) and VH_3 ($-/0$ at 0.31 eV) and even V_3 ($-/0$ at 0.43 eV) are partly ionized. This compensation explains why the electron concentration in the conduction band is “only” $3\times10^{14}\,\mathrm{cm}^{-3}$ at the implantation depth (at 4.5 µm), even though, the concentration of “real” donors (H and C_iOI) is $3\times10^{18}\,\mathrm{cm}^{-3}$ while the concentration of “real” acceptors (V_2) is only $7\times10^{16}\,\mathrm{cm}^{-3}$. As a consequence of the compensation, only one out of 10000 donors, generated during the proton implantation process under the applied conditions, really donates a conduction electron to the system.

The peak of the electron concentration does not coincide with the projected range of the protons, but is shifted deeper into the material (4.75 µm). This shift is caused by the decrease of the concentration profiles of VH and of VH_3, which occurs at a shallower depth than the decrease of the hydrogen concentration. The decline of the hydrogen concentration leads to a decrease of the electron concentration, as, at the same time, the concentrations of V_2O and of V_3O remain high, causing a shift of the Fermi energy towards the center of the band gap. Once, at a depth of 5.0 µm, also the concentrations of V_2O and of V_3O start to fall, the effective charge concentration of the double donor C_iOI becomes significant again. This leads to the formation of a second peak in the profiles of the electron concentration.

In the substrate material, at a depth deeper than 5.5 µm, the only charged defects are P_s and B_s, which compensate each other, as their initial concentrations are the same. Hence, the Fermi energy is shifted to the center of the band gap and the concentrations of electrons and holes converge to their intrinsic level.

4.2.5 Dose Dependence of Simulated Defect Profiles

One of the driving forces of the change of the defect concentrations during the proton implantation process is the implanted dose. The more protons are implanted, the more intrinsic defects are generated and the more hydrogen is introduced. Using the same inputs for the process simulation, as listed above (T=100 °C, Φ=4×10^{11} $H^+cm^{-2}s^{-1}$, c_O=10^{17} cm^{-3}, c_C=10^{16} cm^{-3}), implantation doses from 5×10^{13} H^+cm^{-2} to 1×10^{15} H^+cm^{-2} are simulated. In figure 4.30, the concentration profiles of the different defect families at a dose of 5×10^{13} H^+cm^{-2} (figure 4.30**a**), and 1×10^{15} H^+cm^{-2} (figure 4.30**b**) are compared.

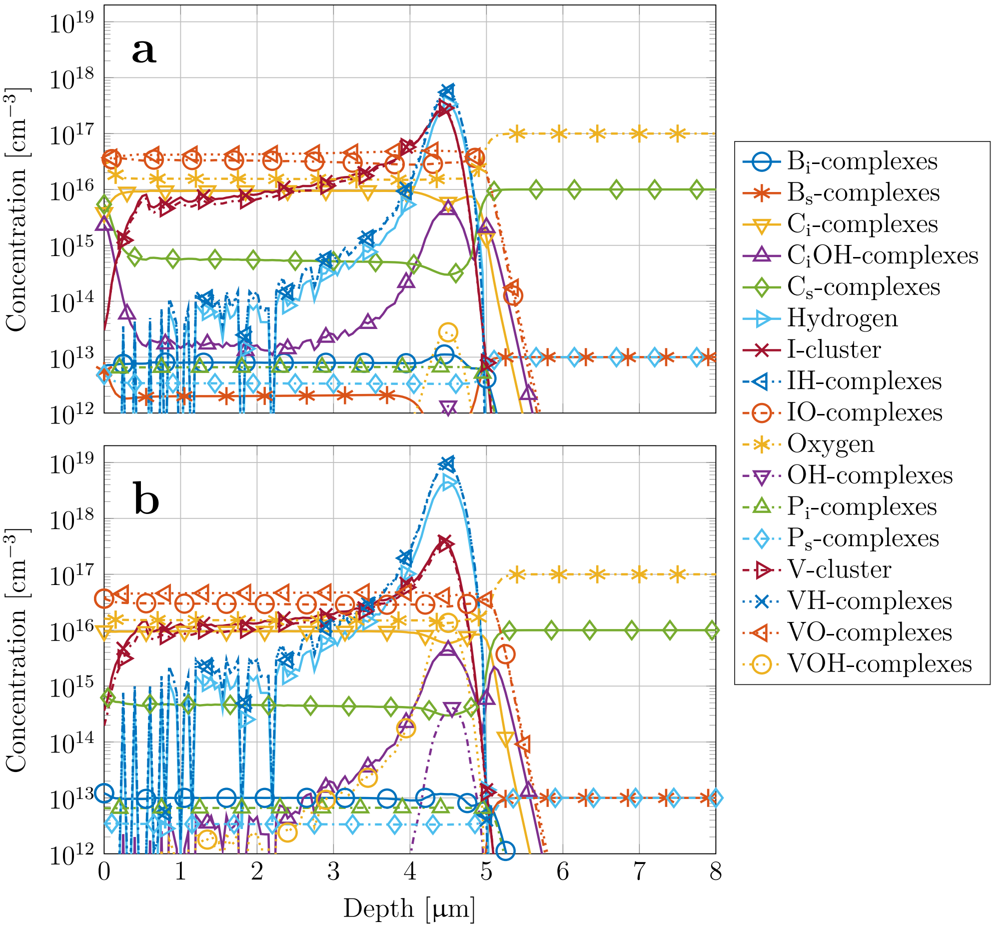

Figure 4.30: Simulated concentration profiles of the different defect families at a dose of **a**: 5×10^{13} H^+cm^{-2} and **b**: 1×10^{15} H^+cm^{-2}.

The strongest differences in the simulated concentration profiles are found for the defect families containing hydrogen (Hydrogen, IH-, VH-, VOH- and OH-complexes). Furthermore, the profiles of the IO-, VO-, C_iOH-, C_i- and B_i-complexes reach deeper into the material the higher the implantation dose is. Additionally, residual B_s-complexes which are still present in the irradiated region at an implantation dose of 5×10^{13} H^+cm^{-2} are converted to B_i-complexes at an implantation dose of 10^{15} H^+cm^{-2}.

4.2.5.1 Dose Dependence of the Absolute Number of Defects

The number of defects in the material is calculated by evaluating the integral over the defect concentration profiles in a certain depth interval. Figure 4.31 shows the overall number of defects of the different families in the first 10 µm of the simulated material, as a function of the implanted dose.

In figure 4.31**a**, the absolute numbers of the defect families are plotted on a logarithmic scale. Here, the defects containing hydrogen show an increase with increasing implantation dose, while the other defect families are, in comparison, almost constant. The difference between the number of elements of different defect families is mainly attributed to the initial impurity concentration. Hence the number of carbon containing defects is about three orders of magnitude higher than that of phosphorus and boron containing families. Another order of magnitude higher is the number of elements of the oxygen defect family. As the impurities O, C_s, B_s and P_s are also present in the substrate material, the change in the number of the elements of oxygen, C_s-complexes, B_s-complexes and P_s-complexes is strongly influenced by the length of the evaluated depth-interval. Hence the dose dependent overall change of the number of these defects is damped, as the concentration of these defects stays constant in the substrate material and does only change in the irradiated region.

To better investigate the influence of the implantation dose on the number of elements of the defect families, the values are plotted relative to their level at the lowest implantation dose ($5{\times}10^{13}\,H^{+}cm^{-2}$) in figure 4.31**b**. The relative increase is strongest for the VOH- and the OH-complexes. Also the number of IH- and VH-complexes increases by more than an order of magnitude. The relative changes of the other defect families are less distinct.

To investigate also these changes, the interval from 0.8 to 1.5 on the y-axis of figure 4.31**b** is shown in more detail in figure 4.31**c**. The data shows that the number of self-interstitial clusters increases more strongly than that of vacancy clusters. Furthermore, the number of B_i-complexes increases at the cost of B_s-complexes. While VO-, C_i- and P_i-complexes show a slight increase with the implantation dose, C_iOH-, IO-and C_s-complexes show a small decrease. The numbers of the oxygen defect family and of P_s-complexes remains more or less unchanged.

4.2.5.2 Dose Dependence of the Recombination

With increasing implantation dose, the number of hydrogen in the material, as well as that of intrinsic defects is increased. Though, at the same time as intrinsic defects are generated, a high fraction of them recombine. Integrating over the simulated elemental concentration profiles (as plotted in figure 4.3), yields the absolute number of those elements. Figure 4.32a shows the absolute number of hydrogen and of the intrinsic defects, as a function of the implantation dose. Furthermore, the number of hydrogen and of intrinsic defects, as simulated with SRIM are plotted.

The increase of the number of hydrogen atoms in the system is exactly the same as calculated from the SRIM-profile, confirming that during the simulation no hydrogen is lost and no extra hydrogen is generated (e.g. due to an increasing numerical error). At the same time, the number of intrinsic defects deviates more and more from the one calculated from the SRIM-profile. The reason for this deviation is an increase in the recombination

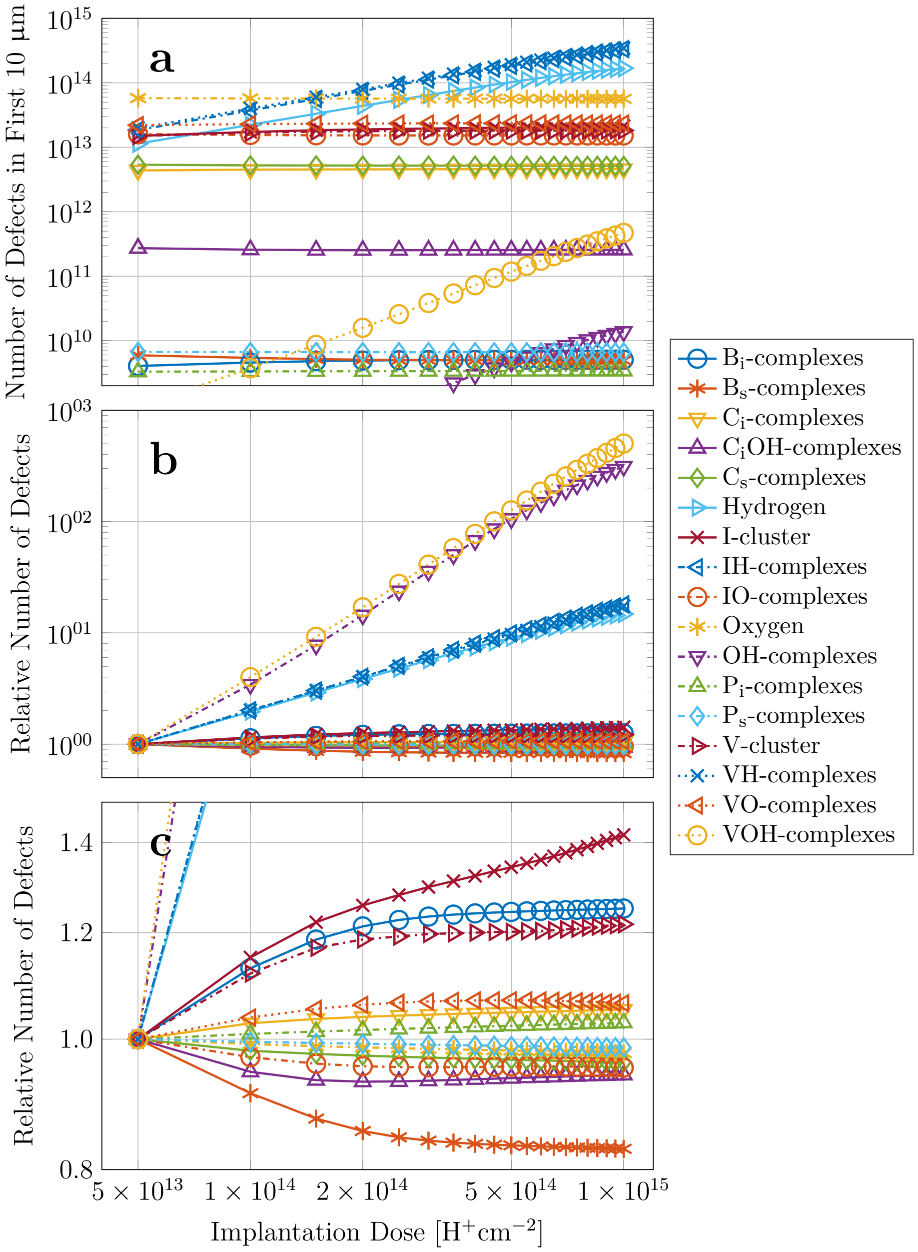

Figure 4.31: Number of elements of each defect family in the first 10 µm of the simulated material. **a**: absolute number of defects, **b**: number of defects relative to the value at a dose of 5×10^{13} H^+cm^{-2}, **c**: relative number of defects on a zoomed scale.

of intrinsic defects as their concentration is increased. Figure 4.32b shows this increase by means of the relative recombination, which is the ratio of the recombination and the generation of the intrinsic defects.

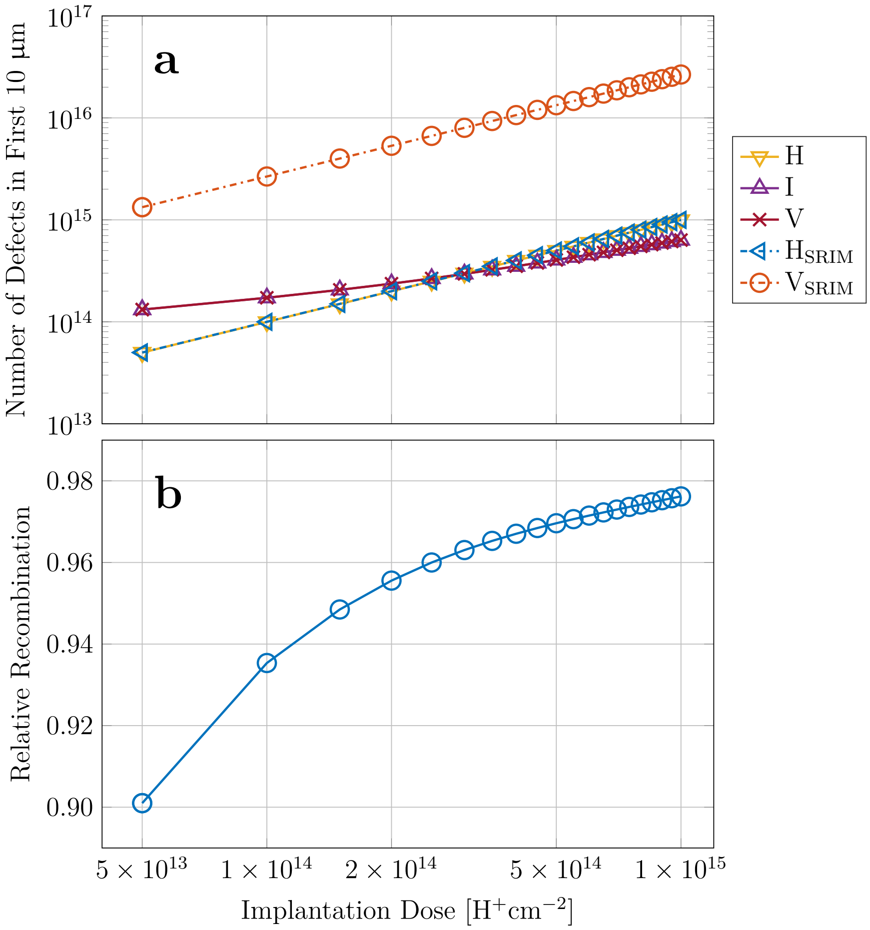

Figure 4.32: **a**: Number of vacancies self-interstitials and hydrogen atoms in the first 10 µm of the simulated material. **b**: Recombination of intrinsic defects, relative to their generation.

At a dose of $5{\times}10^{13}$ H^+cm^{-2}, nine out of ten intrinsic defects have recombined. With increasing dose, more recombination occurs and at a dose of 10^{15} H^+cm^{-2} only less than 2.5 % of the intrinsic defects are still present, while the rest is annihilated.

4.2.5.3 Dose Dependence of the Band Energies and of the Charge Carrier Concentrations

Next, the influence of the implantation dose on the depth-profiles of the valence and conduction band energy and on the concentration profiles of the of charge carriers (at a temperature of 25 °C) is investigated. Figure 4.33a shows the profile of the band energies, calculated after the simulation of different proton implantation doses using the input parameters listed above in the process simulation.

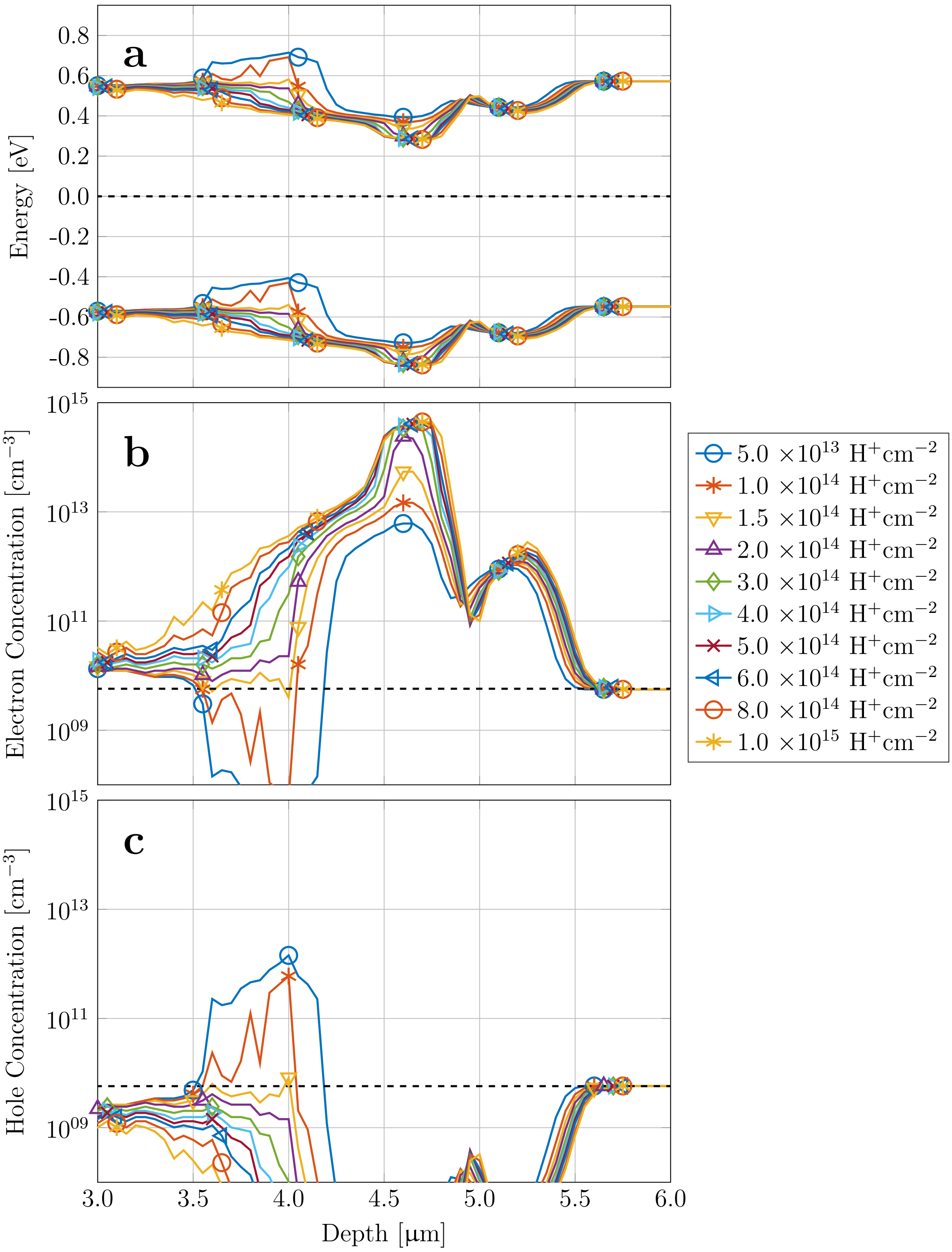

Figure 4.33: Dose dependence of **a**: the valence band and conduction band energies, **b**: the electron concentration profile and **c**: the hole concentration profile. The dashed line in **b** and in **c** indicates the intrinsic charge carrier concentration at 25 °C.

At an implantation dose of $5\times10^{13}\,\mathrm{H^+cm^{-2}}$, a *p*-type region is generated close to the implantation depth (3.5 µm to 4.2 µm). In this region, the divacancy concentration is higher than that of hydrogen and $\mathrm{C_iOI}$. Due to the high $\mathrm{V_2}$-concentration, the valence band energy in the two peaks is increased, compared to the investigation at a dose of $5\times10^{14}\,\mathrm{H^+cm^{-2}}$, shown in the last section. Also at an implantation dose of $1\times10^{14}\,\mathrm{H^+cm^{-2}}$, a *p*-type region is found, though it is narrower than at the lower dose and its peak is less pronounced. At the same time, the dips in the profiles of the valence band and the conduction band energies around the projected range become more pronounced. After the implantation of $1.5\times10^{14}\,\mathrm{H^+cm^{-2}}$, the *p*-type region has disappeared. Furthermore, the shape of the dip in the E_V- and E_C-profile begins to change and a shoulder pointing towards the surface of the material begins to form. With increasing implantation dose, this feature begins to grow, which is attributed to the growth of the peak in the hydrogen concentration profile. Moreover, with increasing implantation dose, the *n*-type region also expands into the substrate material and also the peak between dips in the E_V- and E_C-profiles is shifted away from the implantation depth.

Figures 4.33b and c show the influence of the implantation dose on the concentration profiles of electrons and holes. These figures include a dashed line which indicates the level of the intrinsic charge carrier concentration at 25 °C ($5.8\times10^{9}\,\mathrm{cm^{-3}}$). At the intersections of the charge carrier profiles with these lines, *pn*-junctions are formed. The changes in the charge carrier concentrations due to the formation of these junctions are not accounted for.

4.2.5.4 Dose Dependence of the Concentration Profiles of Different Elements

In section 4.2.3, the change of the profiles of the overall concentrations of boron, carbon and phosphorus were discussed. This section focuses on the change of these profiles, depending on the implanted proton dose. Figure 4.34 shows the profiles of the overall boron concentration after proton implantation at doses from $5\times10^{13}\,\mathrm{H^+cm^{-2}}$ to $1\times10^{15}\,\mathrm{H^+cm^{-2}}$.

While the position of the first maximum, at a depth of 4.4 µm to 4.5 µm remains unchanged, the second maximum is shifted deeper into the material (from 5.0 µm to 5.1 µm) with increasing dose. The relative boron concentration in the first maximum increases from 1.13 at an implantation dose of $5\times10^{13}\,\mathrm{H^+cm^{-2}}$ to 1.18 at an implantation dose of $1\times10^{15}\,\mathrm{H^+cm^{-2}}$. In the second peak, the increase is less pronounced (from 1.17 to 1.19).

The first minimum in the overall boron concentration profile is shifted towards the surface with increasing dose. Here, the minimal relative concentration stays around 0.9. The position of the second minimum lies at 4.8 µm and is not changed by the implanted dose. The boron concentration at this position, though, first decreases from 0.74 at an implantation dose of $5\times10^{13}\,\mathrm{H^+cm^{-2}}$ to 0.70 at an implantation dose of $1\times10^{14}\,\mathrm{H^+cm^{-2}}$, before it increases again and converges to 0.72 for doses above $3\times10^{14}\,\mathrm{H^+cm^{-2}}$.

The influence of the implanted dose on the profile of the overall carbon concentration, shown in figure 4.35, is different from that of boron. While there is still some remaining concentration of $\mathrm{B_s}$ and $\mathrm{B_i}$ in the irradiated region, in the case of carbon, these point defects are gone. Hence, there is no change of the first dip (at 4.15 µm) and of the first peak (at 4.45 µm) with increasing implantation dose, as no mobile $\mathrm{C_i}$ is present The situation is different at a depth of 4.6 µm to 5.4 µm, where new $\mathrm{C_i}$ is formed by self-interstitials

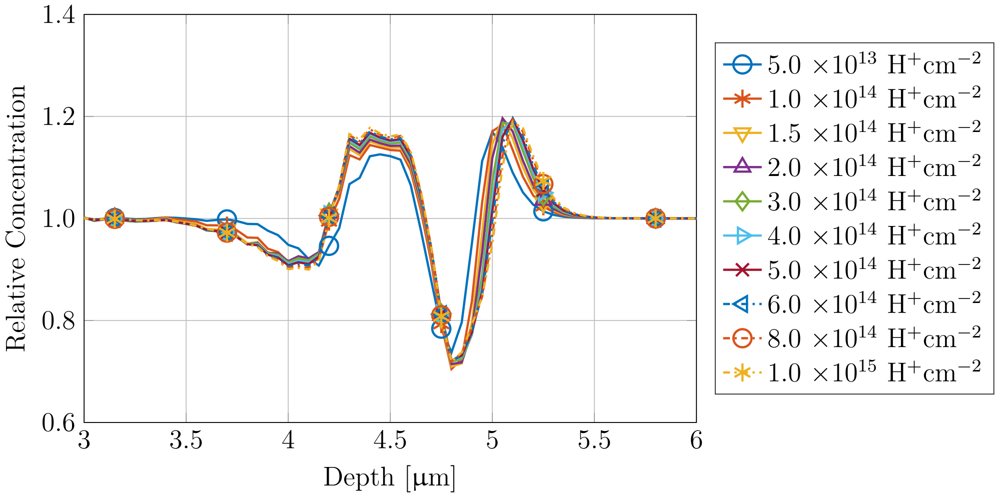

Figure 4.34: Simulated overall concentration profiles of boron at different implantation doses.

diffusing there from the implantation depth to react with C_s (see also figure 4.8). As the newly formed C_i is mobile, it diffuses away from this peak, resulting in a dip in the profiles of the overall carbon concentration at the position of the C_i-peak and two peaks in the C_{all}-profile, next to the C_i-peak. As the position of the peak of the C_i-concentration profile is shifted deeper into the material with increasing implantation dose, also the positions of the dip and the peak in the C_{all}-profile follow this shift.

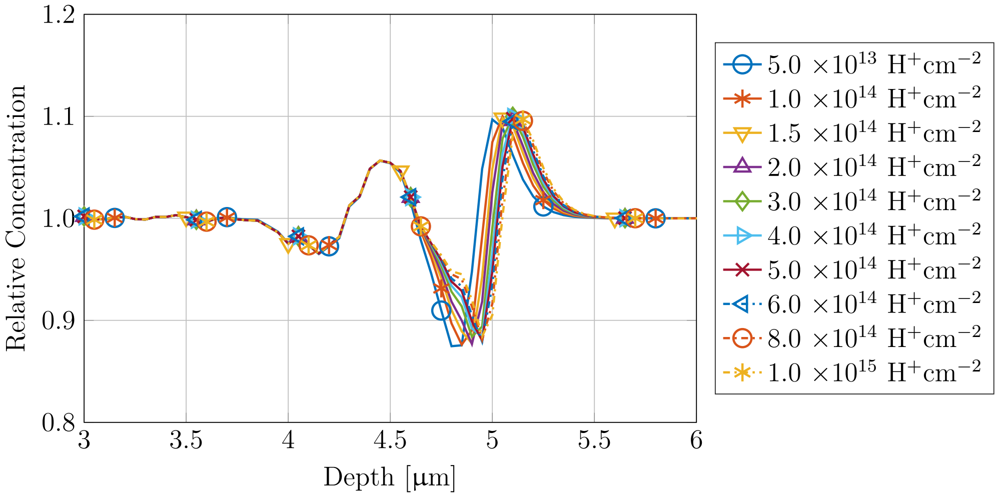

Figure 4.35: Simulated overall concentration profiles of carbon at different implantation doses.

Due to the different reasons, pointed out in section 4.2.3, the changes in the profile of the overall phosphorus concentration are only minimal. As only the effective diffusion of P_s (which itself is considered immobile) is accounted for, the changes in the profile of the overall phosphorus concentration are only caused in the region, where the concentration of P_s changes, which is at a depth around 5 µm (see figure 4.7). As P_s diffuses in the opposite direction of its concentration gradient, towards the surface, it forms a small peak and leaves back a small dip in the profile of the overall phosphorus concentration. Due to its low effective diffusivity (E_a=3.5 eV), these changes are very small. With increasing implantation dose, the observed changes increase to values around 0.1 % at an implantation dose of $1{\times}10^{15}\,\mathrm{H^+cm^{-2}}$.

SIMS-investigations of proton implanted samples could be a good way to validate the quality of the simulated elemental profiles.

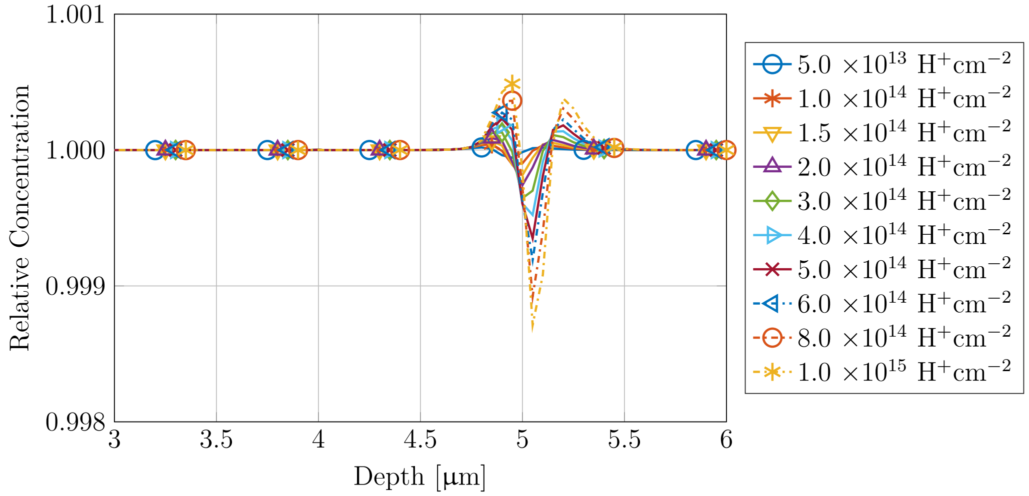

Figure 4.36: Simulated overall concentration profiles of phosphorus at different implantation doses.

4.2.6 Influence of Different Parameters on the Results of the Process Simulation

This section investigates, the influence of different parameters, such as the process temperature, the implantation flux, the oxygen concentration and the carbon concentration, on the results of the process simulation. For all the simulations discussed in this section, an implantation energy of 400 keV and an incidence angle of 7 ° were used. The initial concentrations of B_s and P_s were set to $10^{13}\,\mathrm{cm^{-3}}$ in each run. In all simulations, a scan frequency f_{scan} of 5 Hz is applied. If not mentioned explicitly, the simulations were stopped at an implantation dose of $5{\times}10^{14}\,\mathrm{H^+cm^{-2}}$. If the influence of T and Φ are investigated, the initial concentration of oxygen is set to $1{\times}10^{17}\,\mathrm{cm^{-3}}$ and that of carbon is set to $1{\times}10^{16}\,\mathrm{cm^{-3}}$. If, on the other hand, the carbon and oxygen concentrations are varied, the temperature is set to 100 °C and the proton flux is set to $4{\times}10^{11}\,\mathrm{H^+cm^{-2}s^{-1}}$.

4.2.6.1 Influence of Different Parameters on the Relative Recombination of Intrinsic Defects

In section 4.2.5.2, the relative recombination of intrinsic defects was introduced. As shown in figure 4.32b, the relative recombination increases with increasing implantation dose. Now the influences of the temperature, the proton flux and the concentrations of oxygen and carbon on the relative recombination are investigated. Figure 4.37a shows variations of T and Φ, while figure 4.37b illustrates the changes in the relative recombination due to different initial carbon and oxygen concentrations. The investigations are carried out for implantation doses from $5{\times}10^{13}\,\mathrm{H^{+}cm^{-2}}$ to $1{\times}10^{15}\,\mathrm{H^{+}cm^{-2}}$.

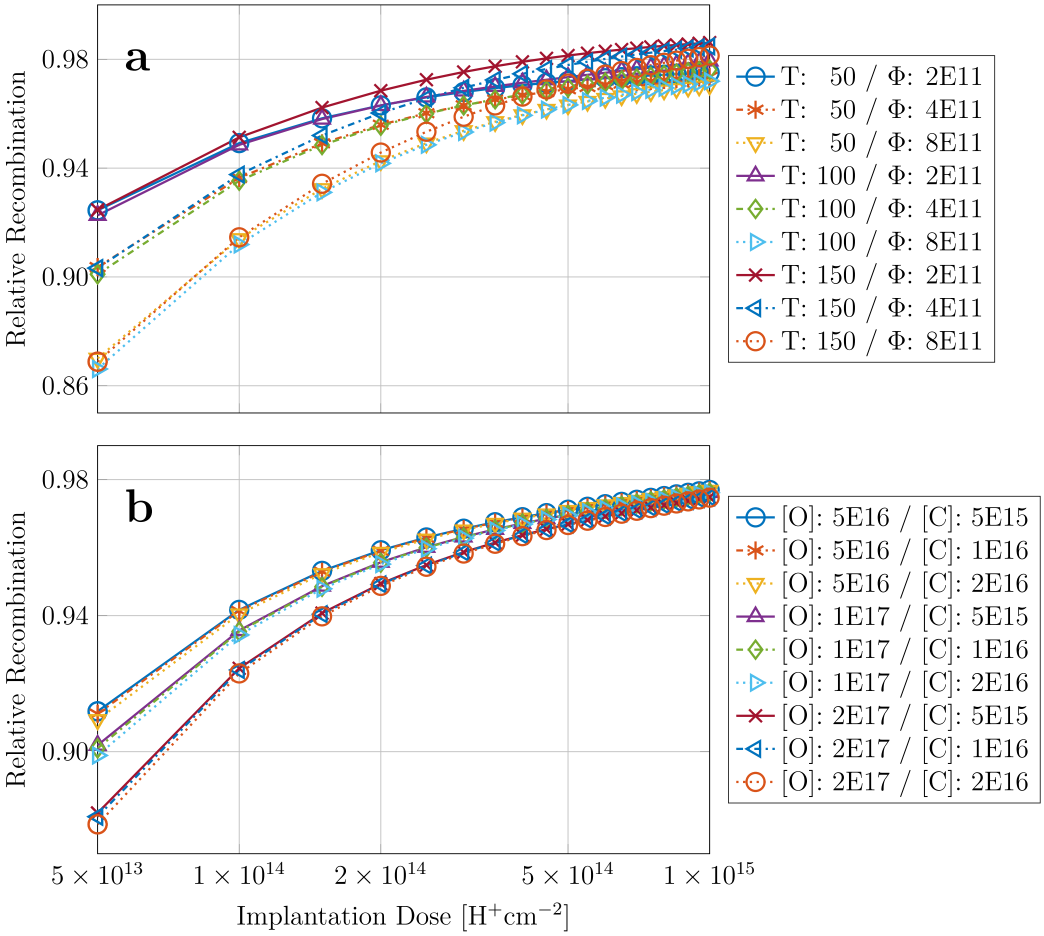

Figure 4.37: Influence of **a**: the temperature (in °C) and the proton flux (in $\mathrm{H^{+}cm^{-2}s^{-1}}$), and **b**: the oxygen and carbon concentration (in $\mathrm{cm^{-3}}$) on the relative recombination of intrinsic defects.

At low implantation doses, the relative recombination is decreased by increasing the proton flux. If Φ is $8{\times}10^{11}\,\mathrm{H^{+}cm^{-2}s^{-1}}$, the relative recombination at an implantation dose of $5{\times}10^{13}\,\mathrm{H^{+}cm^{-2}}$ is only 0.87, while it is 0.93, if a proton flux of $2{\times}10^{11}\,\mathrm{H^{+}cm^{-2}s^{-1}}$ is used. At low implantation doses, the influence of the temperature on the relative recombination of intrinsic defects is only small. If the dose is increased, though, the relative recombination rises stronger, the higher the process temperature is set. At an implantation dose of $1\times10^{15}\,\mathrm{H^{+}cm^{-2}}$, the highest value for the indirect recombination is found for the lowest proton flux ($2\times10^{11}\,\mathrm{H^{+}cm^{-2}s^{-1}}$) and the highest temperature (150 °C). Here, 99 % of the generated intrinsic defects have recombined, while at the lowest temperature (50 °C) and at highest proton flux ($8\times10^{11}\,\mathrm{H^{+}cm^{-2}s^{-1}}$), only 97 % of the intrinsic defects were annihilated.

The higher the process temperature is set, the higher are the rates of all reactions and dissociations. This leads to an increase of the fraction of generated intrinsic defects reacting to defect complexes. Due to indirect recombination, though, which is enhanced at the same time, the overall number of recombination processes is increased.

A higher proton flux leads to a higher concentration of free intrinsic defects, as more of them are generated at the same time compared to a lower proton flux. This leads to an increase of the rates of all reactions including either self-interstitials, or vacancies. As this also includes the indirect recombination reactions, one would expect an increase in the relative recombination with increasing proton flux. The opposite effect is observed, though, which is explained by the decrease of the implantation time due to the higher flux. With increasing Φ, the implantation is finished faster and the intrinsic defects have less time to recombine.

In figure 4.32b, the influence of the initial concentrations of carbon and oxygen on the relative recombination of intrinsic defects is investigated. Here, the higher the initial impurity concentration is set, the lower is the relative recombination. As the concentration of oxygen is usually set an order of magnitude higher than that of carbon, the influence of changes in the oxygen concentration show a stronger response of the relative recombination. At an implantation dose of $5\times10^{13}\,\mathrm{H^{+}cm^{-2}}$, high impurity concentrations (c_{O}: $2\times10^{17}\,\mathrm{cm^{-3}}$ and c_{O}: $2\times10^{16}\,\mathrm{cm^{-3}}$) result in the recombination of 88 % of the intrinsic defects, while 91 % recombine if the initial impurity concentrations are low (c_{O}: $5\times10^{16}\,\mathrm{cm^{-3}}$ and c_{O}: $5\times10^{15}\,\mathrm{cm^{-3}}$). This is explained by a higher fraction of intrinsic defects, trapped at impurities.

4.2.6.2 Influence of Different Parameters on the Profiles of the Valence and Conduction Band Energies and on the Charge Carrier Concentrations

Similar to the recombination of the intrinsic defects, also the formation of donors, acceptors and of compensating defects is strongly influenced by changes in the implantation parameters. Changes in the concentrations of electrically active defects are directly reflected in the energies of the valence and the conduction band and in the charge carrier concentration. In figure 4.38, the influence of the temperature and of the implantation current on the profiles of E_V, E_C and on the concentrations of electrons and holes are illustrated.

In the irradiated region, from the surface to approximately 3.5 µm, E_V and E_C slightly decrease, if the proton flux is low. Hence, the electron concentration, plotted in figure 4.38b is somewhat higher than the hole concentration, shown in figure 4.38c. At high proton flux ($8\times10^{11}\,\mathrm{H^{+}cm^{-2}s^{-1}}$), though, and especially at low temperature (50 °C), the energies of the valence band and of the conduction band are shifted towards higher energies, accompanied by an increase of the hole concentration.

E_V and E_C and the charge carrier concentration in the region from 3.5 µm to 5.5 µm

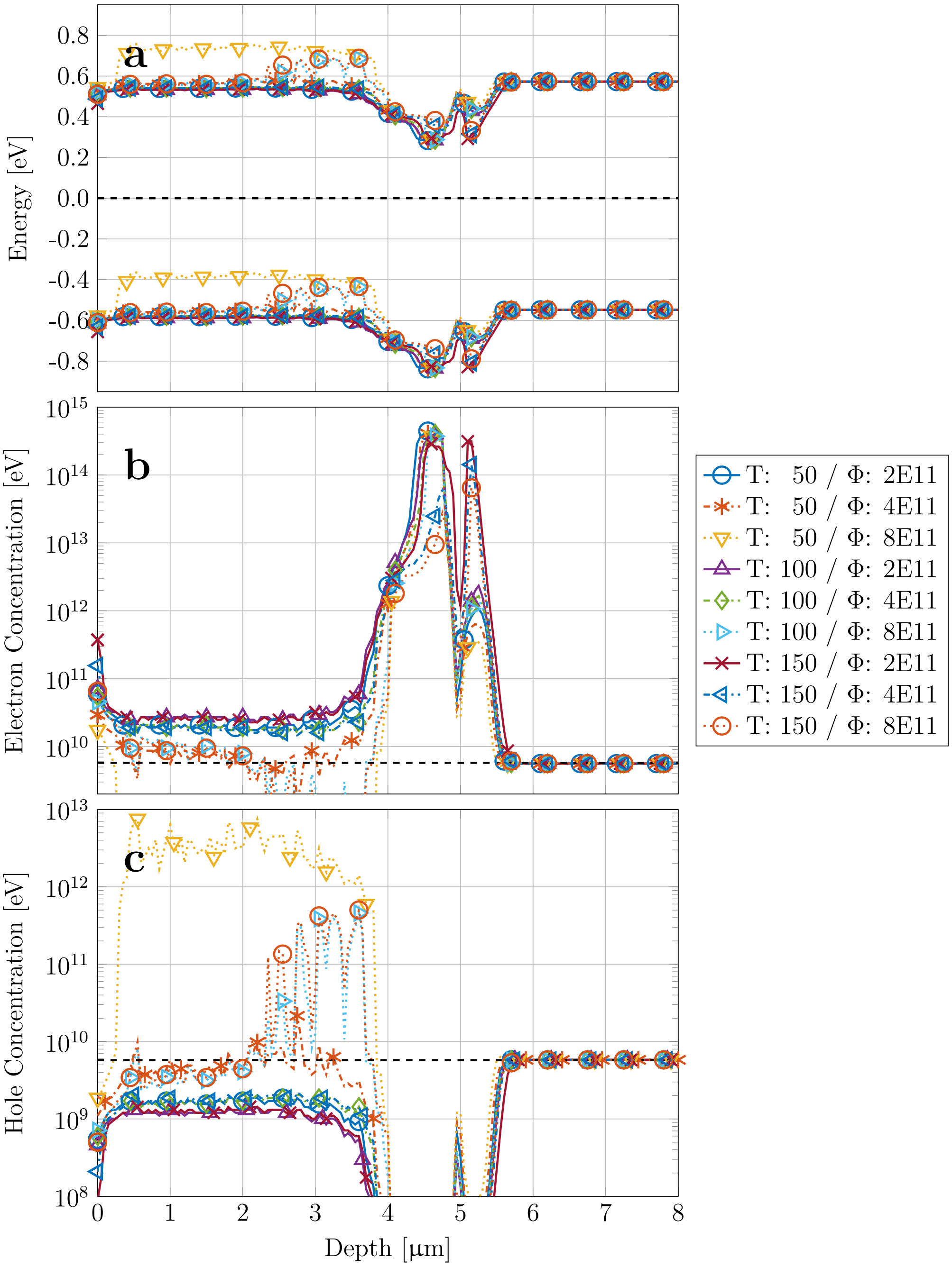

Figure 4.38: Influence of the temperature (in °C) and the proton flux (in $\mathrm{H^+cm^{-2}s^{-1}}$) on **a**: the profiles of E_V and E_C, **b**: the electron concentration profile and **c**: the hole concentration profile. The dashed line in **b** and in **c** indicates the intrinsic charge carrier concentration at 25 °C.

are also sensitive to changes in the process temperature and of the proton flux. While at lower temperatures (50 °C and 100 °C), the first peak in the electron concentration is higher than the second one, the situation is reversed at a temperature of 150 °C. This effect is even increased with increasing proton flux. At a temperature of 50 °C and a flux of $8\times10^{11}\,\mathrm{H^+cm^{-2}s^{-1}}$ the electron concentration is $4\times10^{14}\,\mathrm{cm^{-3}}$ in the first peak, and $4\ \times10^{11}\,\mathrm{cm^{-3}}$ in the second one. If the temperature is increased to 150 °C, at the same proton flux, the electron concentration in the first peak is lowered to $3\ \times10^{13}\,\mathrm{cm^{-3}}$ and in the second peak it is increased to $6\ \times10^{13}\,\mathrm{cm^{-3}}$. If the proton flux is decreased to $2\times10^{11}\,\mathrm{H^+cm^{-2}s^{-1}}$, the electron concentration in the second peak even gets as high as $3\times10^{14}\,\mathrm{cm^{-3}}$. The electron concentration at the dip between the peaks also differs by two orders of magnitude between the simulation run using low temperature and high flux, and the one, where the temperature is set high and a low proton flux is used.

The changes in the charge carrier concentration must derive from changes in the concentration profiles of donors and acceptors. Furthermore, the ionization of compensating defects can pin the Fermi energy to their ionization energy. Figure 4.39a-c shows the profiles of the donor complexes, the acceptor complexes and of the compensating defects which are present in the material. The donor complexes are $\mathrm{B_iO}$, $\mathrm{C_iOI}$, $\mathrm{C_iOH}$, H and $\mathrm{P_s}$, while the acceptors are $\mathrm{B_s}$, $\mathrm{P_i}$ and $\mathrm{V_2}$. The defects which are ionized at some place in the material and compensate partly for the excess donor concentration are $\mathrm{V_3}$, VH, $\mathrm{VH_2}$, $\mathrm{VH_3}$, $\mathrm{V_2O}$, $\mathrm{V_3O}$, VOH and $\mathrm{VP_s}$. Here, the respective defect profiles are added together.

In the irradiated region, the donor concentration increases with increasing temperature, while it is lowered when the proton flux is increased. The only donor complex in this region is $\mathrm{C_iOI}$. The acceptor profile in the same region is insensitive to changes in the process temperature. The higher the proton flux, though, the more acceptors ($\mathrm{V_2}$) are generated in this region. At high proton flux ($8\times10^{11}\,\mathrm{H^+cm^{-2}s^{-1}}$), the acceptor concentration even overtakes the concentration of donors, resulting in *p*-type doping and a strong increase in the hole concentration. This effect is even intensified at low temperature (50 °C), were less donors are formed. The effect of the compensating defects in this region is low, as their concentration in the irradiated region only slightly changes at different T and Φ.

Around the implantation depth, the concentration profiles of donors, acceptors and compensators peak. The maximum concentration of donors is more than one order of magnitude higher than that of the acceptors and the difference between the two is on the order of $10^{18}\,\mathrm{cm^{-3}}$. As the concentration of compensating defects is on the same order of magnitude as that of the donors, though, the residual electron concentration is always below $10^{15}\,\mathrm{cm^{-3}}$. While the concentrations of donors and compensators are high at low temperatures and decrease if the temperature is increased, the acceptor concentration increases with increasing temperature and proton flux. Hence, at high temperature and high proton flux, the electron concentration in the first peak is decreased.

Due to the immediate decrease of the acceptor concentration compared to the smoother decay of the donor concentration, the second peak in the profiles of the Fermi energy and the electron concentration is generated. The higher the temperature and the lower the proton flux, the deeper the donor concentration reaches into the material. Even though this shift is only on a scale of tens of nanometers, at a depth of e.g. 5.0 µm, this leads to an increase in the donor concentration by a factor of 8. As the compensator concentration is unchanged by different process temperatures or proton fluxes, the change in the donor concentration leads to an increase of the electron concentration by three

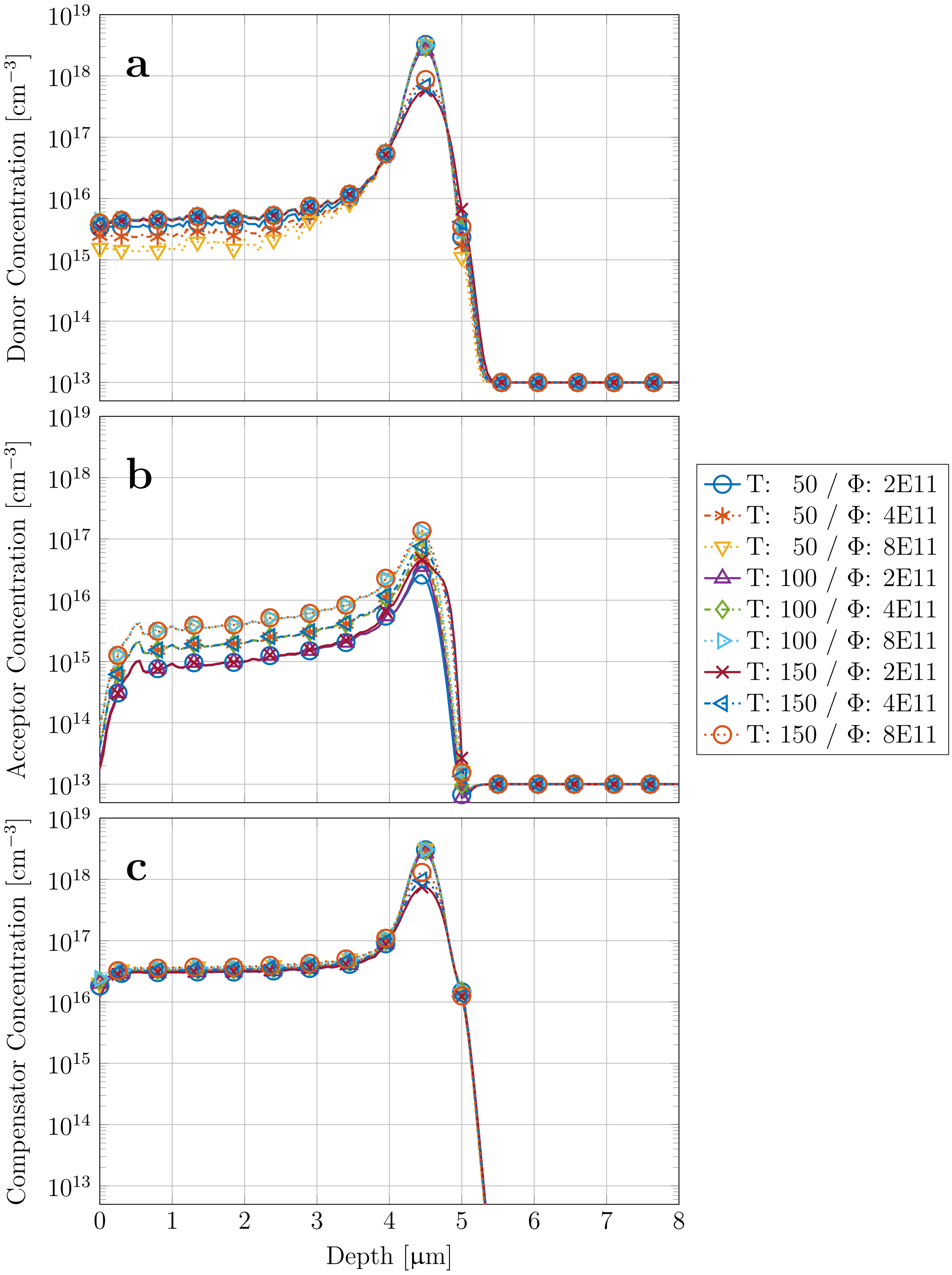

Figure 4.39: Influence of the temperature (in °C) and the proton flux (in $H^+cm^{-2}s^{-1}$) on the concentration profiles of **a**: donors, **b**: acceptors and **c**: compensating defects.

orders of magnitude.

Also changes in the initial concentrations of oxygen and carbon are reflected in the profiles of the valence band and the conduction band energy and in the charge carrier concentration profiles (see figure 4.40a and b. Here, these changes mainly affect the concentration of charge carriers in the irradiated region.

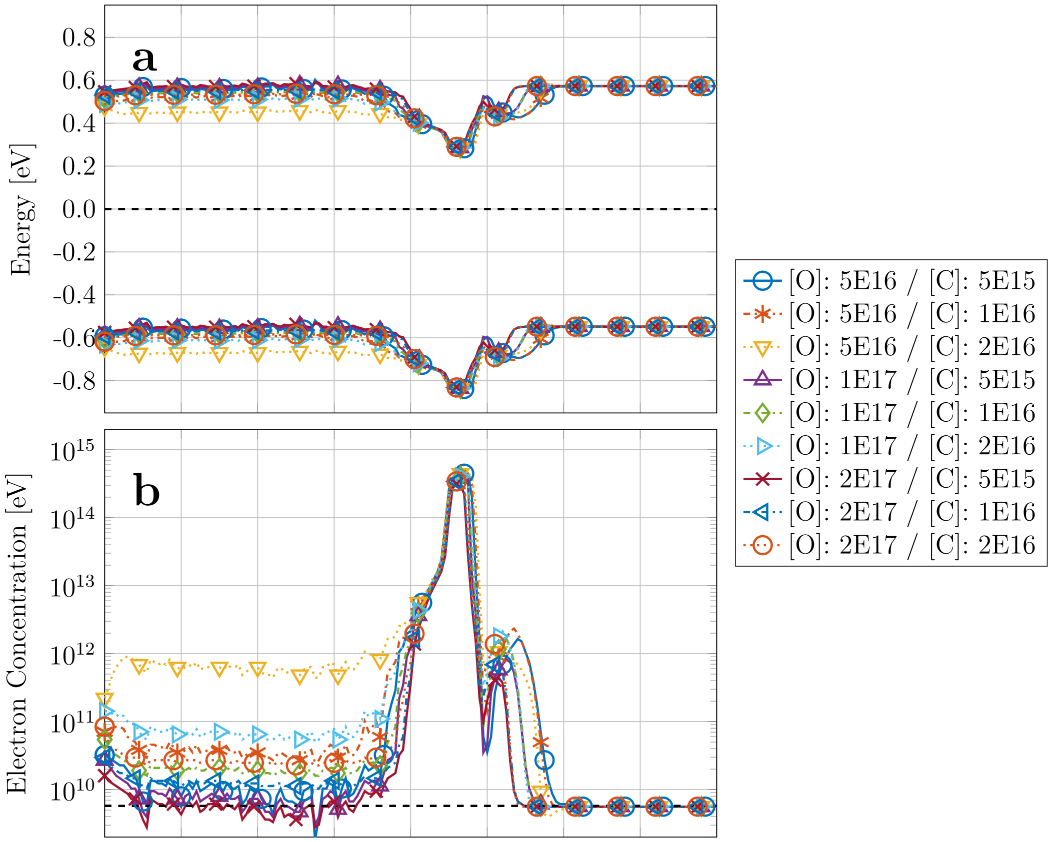

Figure 4.40: Influence of the oxygen and carbon concentration (in cm^{-3}) on **a**: the profiles of E_V and E_C, **b**: the electron concentration profile. The dashed line in **b** indicates the intrinsic charge carrier concentration at 25 °C.

The higher the carbon concentration and the lower the oxygen concentration are set, the higher gets the electron concentration in this region. If the initial carbon concentration is set to its highest value ($c_{\mathrm{C}}= 2\times10^{16}\,\mathrm{cm}^{-3}$), and if the oxygen concentration is low ($c_{\mathrm{O}}= 5\times10^{16}\,\mathrm{cm}^{-3}$), the electron concentration in the irradiated region is close to $10^{12}\,\mathrm{cm}^{-3}$, while it is two orders of magnitude lower, if the carbon concentration is low and the oxygen concentration is high.

Compared to the changes in the irradiated region, the concentration in the first peak of the electron profile is rather insensitive to changes in the concentrations of carbon and oxygen. Still, while the maximum electron concentration is $3\times10^{14}\,\mathrm{cm}^{-3}$ at high oxygen concentration, it is increased to $5\times10^{14}\,\mathrm{cm}^{-3}$ if the lowest oxygen concentration is used in the process simulation.

Both, the position and the maximum value of the second peak in the electron concentration are more sensitive to c_O and c_C. The lower the initial oxygen and carbon concentrations are set, the deeper this peak is shifted into the material. Here, the difference between its position at high and at low impurity concentrations is 0.3 µm. The maximum electron concentration in this peak is increased with increasing carbon concentration and with decreasing oxygen concentration.

As explained before, the changes in the charge carrier concentration derive from changes in the concentrations of donors and acceptors and also in the concentrations of compensating defects. As the only donor complex in the irradiated region is $\mathrm{C_iOI}$, the donor concentration in this region is strongly influenced by the initial carbon concentration. Changes in the oxygen concentration, as c_O is always higher than the c_C in the present simulation results, only show a minor influence on the donor concentration. The acceptor defect showing the highest concentration in the irradiated region is $\mathrm{V_2}$. As it neither contains oxygen, nor carbon, its concentration is not affected by changes in the initial concentrations of these defects. The concentration of compensating defects in the irradiated region strongly depends on the oxygen concentration, as the most important complexes among these defects are $\mathrm{V_2O}$ and $\mathrm{V_3O}$. Hence, if the oxygen concentration is low and the carbon concentration is high, the concentration of electrons in the conduction band is increased.

At the implantation depth, the concentrations of donors, acceptors and compensators are not affected by the initial impurity concentrations. Here, H shows the highest concentration among the donors, while divacancies are the main acceptors in this region. Among the compensating defects, the VH-complexes are the dominant species.

After the peak in the profiles, the concentration of donors, acceptors and compensating defects decays into the substrate material. The decay of the donors and of the compensators is dampened, if the oxygen concentration is decreased. Hence, at lower oxygen concentration, these defects reach deeper into the substrate material. As the concentrations of acceptors in this region is not affected by changes in the oxygen concentration, this leads to a shift of the second peak in the electron concentration.

4.2.6.3 Influence of Different Parameters on the Profiles of the Overall Concentration of Boron and Carbon

At last, the influence of different parameters on the profiles of the overall concentration of boron and carbon, calculated using the process simulation, are investigated. As shown in section 4.2.3, the overall boron concentration profile after proton implantation, is changed, compared to the initial conditions. Applying a process temperature of 100 °C, a proton flux of $4\times10^{11}\,\mathrm{H^+cm^{-2}s^{-1}}$ and initial concentrations of $1\times10^{17}\,\mathrm{cm^{-3}}$ for oxygen and $1\times10^{16}\,\mathrm{cm^{-3}}$ for carbon to the process simulation, changes in the local boron concentration of up to 30 % have been observed. Figure 4.42a shows the influence of different temperatures and proton fluxes on the distribution of boron in the material.

At low temperature (50 °C) and low proton flux ($2\times10^{11}\,\mathrm{H^+cm^{-2}s^{-1}}$) a broad peak from 4.2 µm to 4.7 µm and a second peak at 5.1 µm, next to two minima at 4.0 µm and at 4.9 µm are observed. At the first peak, the boron concentration is increased by 15 %, at the second peak, the increase is 20 %. While the drop in boron concentration at the first dip is only around 5 %, at the second dip, the boron concentration falls by 35 %. An increase of the proton flux leads to a decrease of the relative changes in the boron concentration. The location of the peaks and the dips remain the same. If the temperature

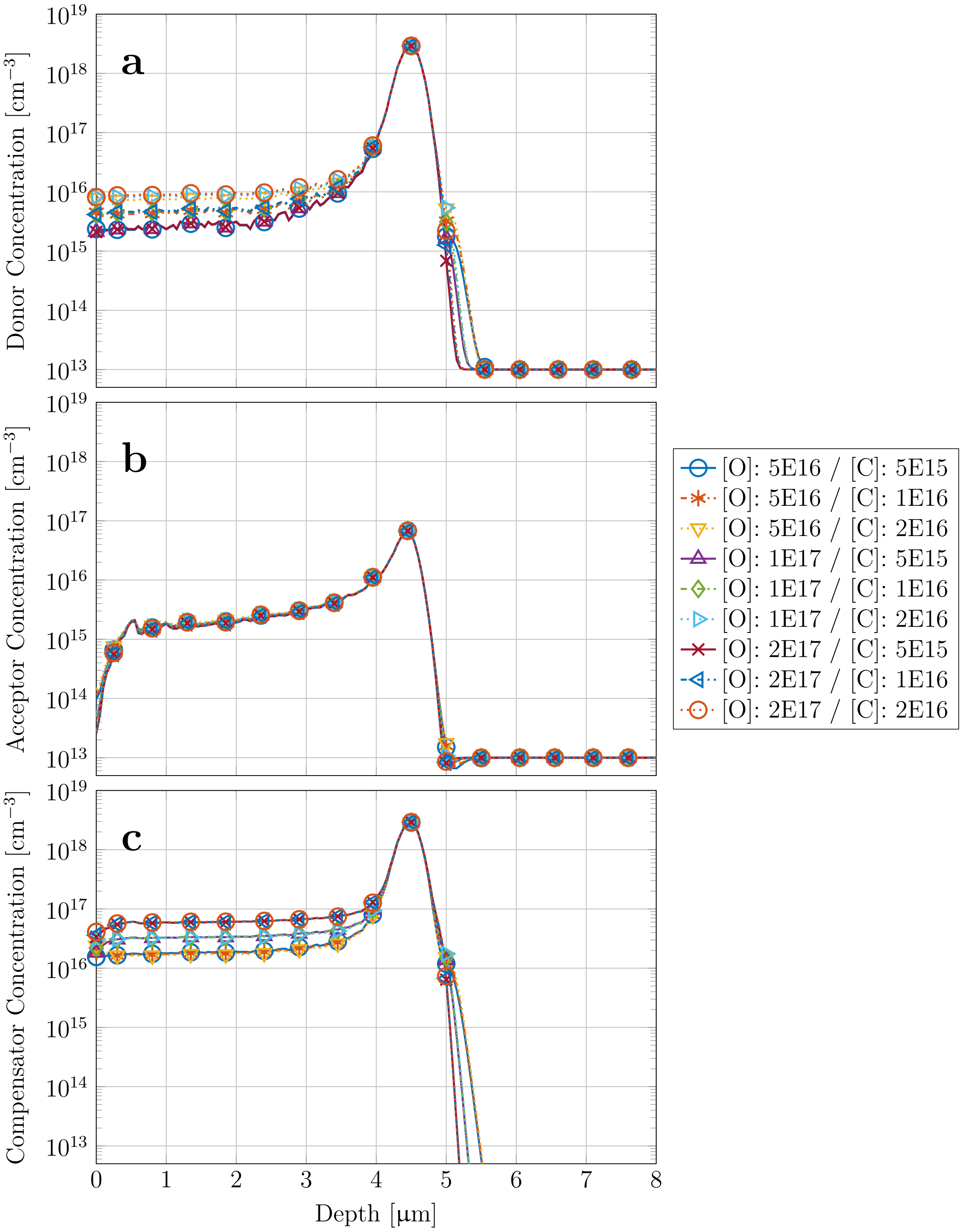

Figure 4.41: Influence of the oxygen and carbon concentration (in cm^{-3}) on the concentration profiles of **a**: donors, **b**: acceptors and **c**: compensating defects.

is increased to 100 °C, the change in concentration at the first peak and the first dip are increased, while the second dip becomes less pronounced. At the highest investigated temperature (150 °C), a different shape of the boron concentration profile is generated. Instead of a peak at the implantation depth, a dip is found at this position. At this position, the boron concentration is reduced by 10 %. At a dept of 5.1 µm, though, a similar peak as compared to lower temperatures is formed.

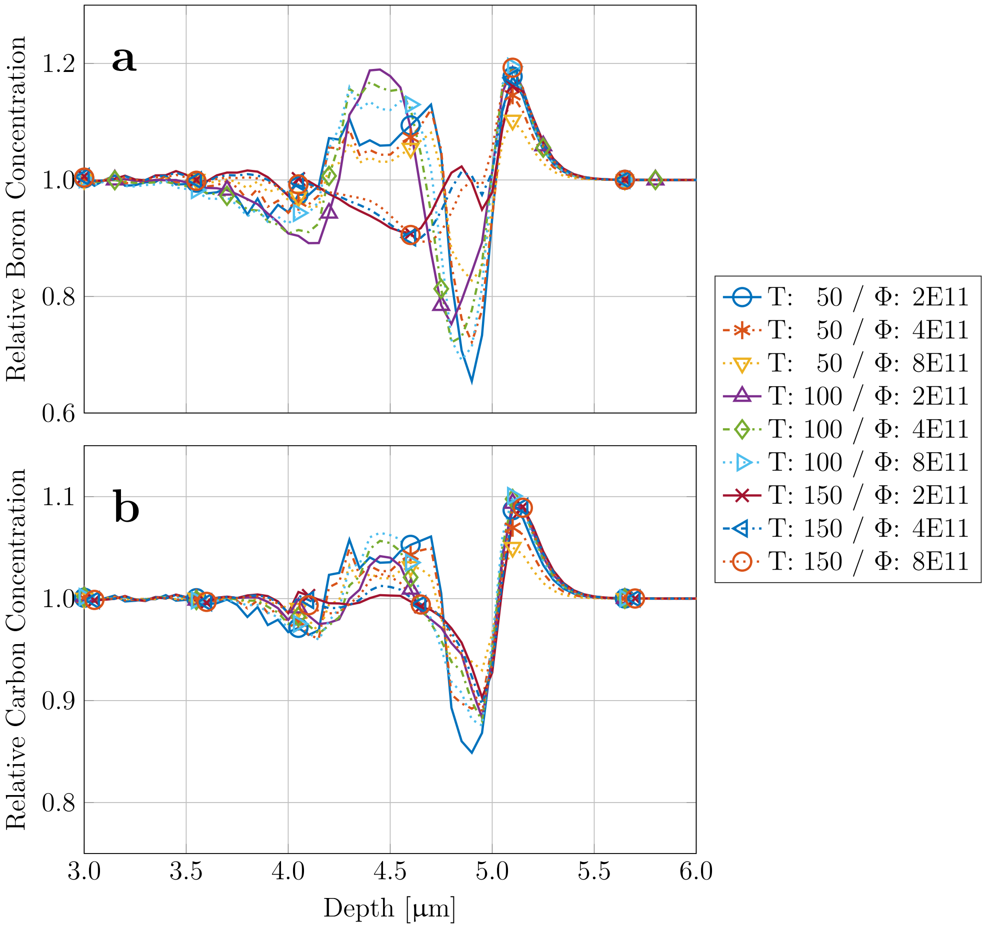

Figure 4.42: Influence of the temperature and the implantation current on the profiles of the overall concentration of **a**: boron, and **b**: carbon.

Also the profile of the overall carbon concentration (see figure 4.42b) shows two peaks and two dips at similar positions as those in the overall boron concentration profile, if the simulation is done at low temperature and low dose (T=50 °C, Φ=2×10^{11} $H^{+}cm^{-2}s^{-1}$). The relative change in the carbon concentration, though, is only half of the relative change in the boron concentration. At high temperatures (150 °C), the peak in the carbon concentration at the implantation depth vanishes, and only the dip at 4.9 µm and the peak at 5.1 µm remain.

The influence of changes in the initial oxygen and carbon concentration of the profile of the overall concentrations of boron and carbon are shown in figure 4.43a and b. The profiles of both elements are much more sensitive to changes in the oxygen concentration than they are to changes in the carbon concentration. This might be due to the higher initial concentrations of oxygen compared to carbon.

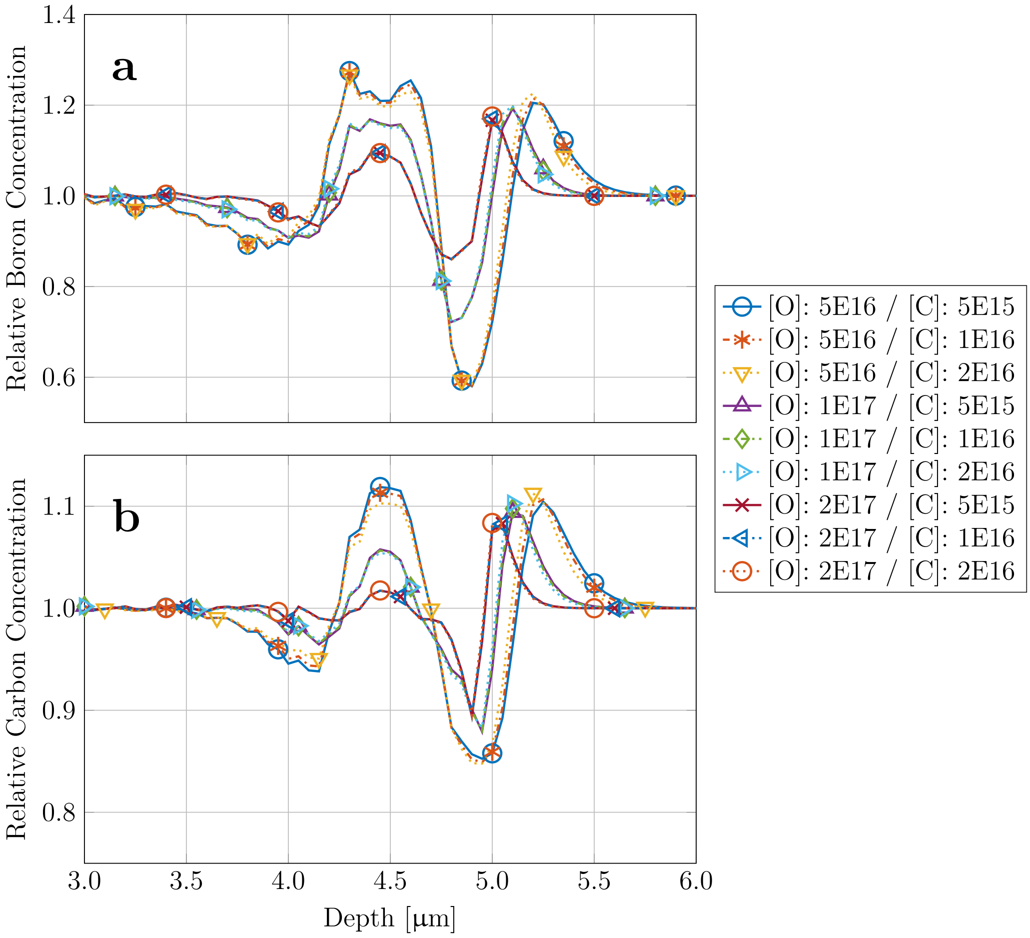

Figure 4.43: Influence of the oxygen and carbon concentration on the profiles of the overall concentration of **a**: boron, and **b**: carbon.

The lower the initial oxygen concentration is set, the stronger are the changes in the carbon and boron profiles. In the case of boron, the relative concentration at the implantation depth is changed by more than 20 % if the oxygen concentration is $5 \times 10^{16}\,\mathrm{cm}^{-3}$. at an oxygen concentration of $2 \times 10^{17}\,\mathrm{cm}^{-3}$, this change is reduced to 10 %. The relative boron concentration at the second dip is changed from 58 % at low oxygen concentration to 86 % if the initial oxygen concentration is high. Furthermore, the positions of the second dip and of the second peak are shifted deeper into the material, the lower the oxygen concentration is set. While the peak appears at a depth of 5.0 µm at high c_O, it is shifted to 5.3 µm at low oxygen concentration.

The profile of the overall carbon concentration, shows a similar response to changes in the initial oxygen and carbon concentration, as observed for boron. The changes in the relative carbon concentration, again, are smaller by a factor of two, compared to the changes in the relative boron concentration.

4.3 Discussion of the Results of the Simulation of the Proton Implantation Process

The presented simulation of the proton implantation process represents a simulation method which could be used for problem solving in many situations in semiconductor processing. Every time, mobile defects are present in a material, this kind of simulation can be applied to study the change of the distribution of those defects and the formation of defect complexes. A major drawback of this method is that it needs a large amount of input data which has to be of good quality for the simulation to yield trustworthy outputs. The results presented in section 4.2 have to be interpreted with care, as parts of the input data are assumed and approximated values. The addition or removal of defects which are accounted for, as well as changes of the parameters describing their diffusivity and the interactions between them, can have a severe impact on the resulting defect concentration profiles. Nevertheless, the qualitative aspect of the results coincides with that of measurements, suggesting that the basic concept of the simulation method is valid.

The simulation yields concentration profiles of defects and defect complexes. Due to the large number of defects, not all profiles can be viewed and interpreted at the same time. Hence, the defects are combined to defect families, which facilitates a better recognition of the distribution of different kinds of defects in the material. The distribution of chemical elements in the material is derived by combining the concentration profiles of all defects including that element. Such profiles can be compared to elemental distribution profiles measured with experimental methods such as SIMS. Furthermore, from the concentration profiles of electrically active defects and defect complexes, the profile of the position of the Fermi energy in the band gap, and hence, the charge carrier concentration profile can be calculated. c_{CC}-profiles can be compared with the output of SRP- or CV-measurements. Such comparisons can be used to improve the input data.

The profile of the electron concentration, calculated from the concentration profiles of electrically active defect complexes, consists of three regions. Around the implantation depth, two peaks are generated. In the region between the decay of the shallower peak and the surface of the material, the irradiated region, c_{CC} is changed as well, while the charge carrier concentration in the substrate material remains unchanged, compared to the initial situation before the implantation. The first peak in the electron concentration profile is formed close to the implantation depth and is caused by the high concentration of hydrogen at this position, which is a deep donor. The second, deeper peak is produced by the interplay of the double donor C_iOI, which is the major donor in the material apart from hydrogen, and the double acceptor V_2, which shows the highest concentration of the acceptors. Below the implantation depth, the concentration profile of V_2 begins to decay earlier than that of C_iOI. The difference between the defect concentration of the two defects leads to the formation of the second peak in the electron concentration profile. This peak resembles the shoulder observed in the charge carrier concentration profiles in m:Cz- silicon, which is absent in FZ-silicon. This absence is explained by the lower concentrations of oxygen and carbon introduced into the material during the FZ-process, compared to the m:Cz process. As C_iOI consists of oxygen and carbon, in FZ-material lower concentrations of this defect are expected.

The charge carrier concentration in the irradiated region also depends on the difference between the concentrations of C_iOI and of V_2. If there is more C_iOI than V_2 the residual doping is *n*-type, as observed in the irradiated region of m:Cz-silicon. At low carbon and oxygen concentrations, the concentration of V_2 is higher than that of C_iOI, resulting in *p*-type doping. This effect is observed in FZ-material, where also in initially *n*-type material, the doping in the irradiated region is changed to *p*-type. A similar situation, where the irradiated region shows residual *p*-doping is also observed, at low implantation temperatures combined with a high proton flux and low implantation doses in carbon and oxygen rich material. Such conditions, though, are unusual, as the temperature during the anneal scales with the implantation current and, hence, with the proton flux. To establish such conditions, the specimen would have to be actively cooled during the implantation.

The interplay of C_iOI and V_2 can be further transformed into a model, explaining the formation of the region of increased charge carrier concentration, which expands from the implantation depth, through the irradiated region, towards the surface of the material during anneals. The kinetics of this expansion is attributed to the diffusion of hydrogen. Instead of the formation of a hydrogen-related donor complex, the physical process behind the changes of the charge carrier concentration is the deactivation of the electrically active defects by their reaction with hydrogen. Considering, that H and V_2 are mobile while C_iOI is immobile, and assuming a similar capture radius of the reactions of hydrogen with each of the two defects, suggests that its reaction with V_2 happens on a faster scale. Furthermore, throughout the range of usual annealing temperature (above 300 °C), the charge state of hydrogen is always H^+ and the charge states of C_iOI and V_2 are always C_iOI^{2+} and V_2^{2-}, respectively. This situation favors the reaction of H with V_2 even more, as the charge states of these defects have opposite signs while those of H and C_iOI share the same sign. Hence, as the hydrogen diffuses away from the implantation depth, a larger fraction reacts with V_2 than with C_iOI, leading to an increase of the residual donor-, and hence, electron concentration.

In the appendix D the temperature dependence of the effective reaction rate constants of several reactions of point defects in proton implanted silicon are shown for different doping concentrations. This also includes the rate constants of the reactions of hydrogen with V_2 forming V_2H ($k_r^{V_2H}$ see figure D.47.1) and the reaction of hydrogen with C_iOI forming C_iOIH ($k_r^{C_iOIH}$ see figure D.48.1). In figure 4.44 the temperature dependence of the rate constants of these two reactions are compared at different doping concentrations.

Under most conditions the rate constant of the deactivation of V_2 is orders of magnitude higher than that og C_iOI. Assuming similar concentrations of V_2 and C_iOI at 400 °C in *n*-type material, $k_r^{V_2H}$ is $10^3 - 10^5$ times larger than $k_r^{C_iOIH}$. Only in *p*-type silicon at doping concentrations above $10^{15}\,\mathrm{cm}^{-3}$, the rate constant of the deactivation of C_iOI is higher than that of V_2.

If the residual doping at the implantation depth or in the irradiated region is *n*-type, the observed concentration of electrons is several orders of magnitude smaller than the difference between the concentrations of donors and acceptors. The reason for this effect lies in the presence of compensating defects, which accumulate negative charges. The ionization of such defects, pins the Fermi energy to their ionization energy, until (almost) all of them are ionized.

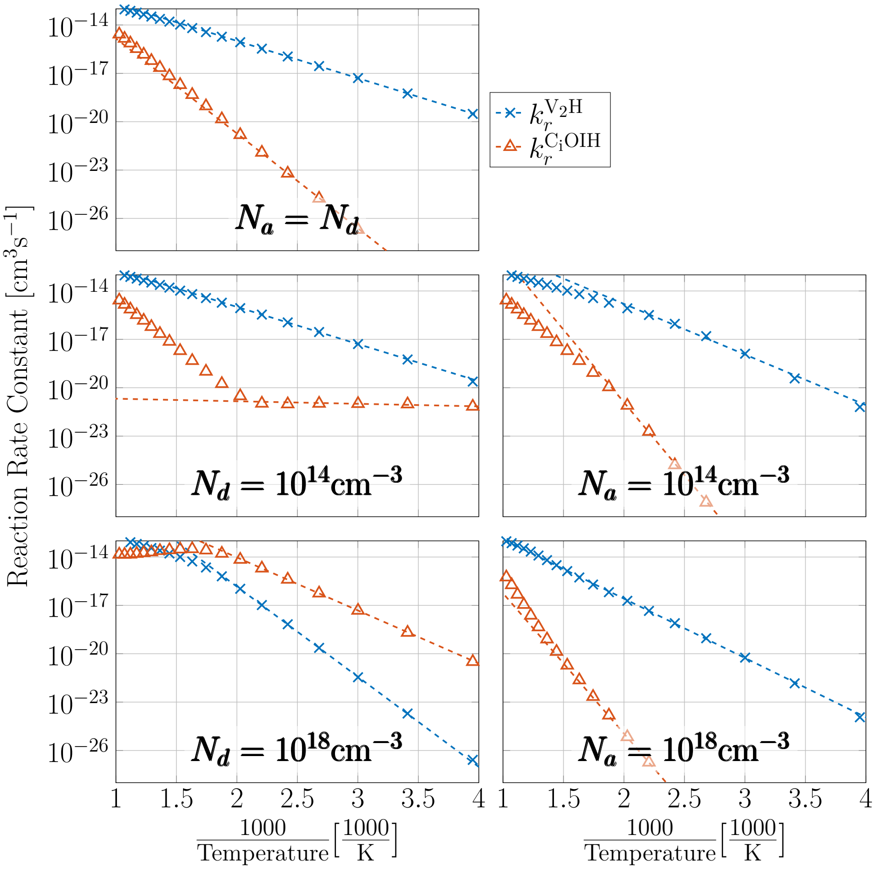

Figure 4.44: Comparison of the effective reaction rate constants of the reaction of H with V_2 forming V_2H and with C_iOI forming C_iOIH at different doping concentrations. The dashed lines indicate linear fits through the data points in the inverse temperature range from $4\,\frac{1000}{\mathrm{K}}$ to $2\,\frac{1000}{\mathrm{K}}$.

While the initial concentration profiles of carbon, oxygen, boron and phosphorus are constant, after the process simulation, the total concentration profiles of B and C (and also P, but to a lesser extent) show disturbances around the implantation depth. These changes in the overall concentrations of these impurities are evoked by the generation of mobile configurations of these defects (B_i and C_i, respectively) due to the reaction with self-interstitials. The concentration profiles of the mobile defects show two peaks, one at a shallower and the other one at a deeper position than the implantation depth. This shape is caused by the formation of immobile defects with hydrogen at the implantation depth. The diffusion of the defects away from these peaks leads to the formation of two local maxima and two local minima in the elemental concentration profiles of B and C. One of these peaks forms directly at the implantation depth and the other maximum is generated at the interface to the substrate material. In the case of phosphorus, this effect is less distinct in the output of the process simulation. The reason for this is the wrong consideration of mobile phosphorus species in the input data of the simulation. Here, instead of attributing P_i and VP_s the possibility to diffuse, the effective diffusivity of P_s was used. This observation shows the impact of using wrong, or bad input data.

The study of the influence of different implantation parameters showed, that the shape of the distortion of the elemental profiles of impurities is strongly changed by the process temperature and by the oxygen concentration. The proton flux and the carbon concentration show less influence on the elemental profiles. The maximum change in the elemental concentrations is reached already at low proton doses. An increase of the dose, though, leads to a shift of the second peak in the concentration profiles deeper into the material.

Also the portion of intrinsic defects which already recombine during the implantation process depends on the implantation parameters. The more intrinsic defects are generated by the implantation of higher doses of protons, the larger grows the fraction of them which recombine and the lower becomes the part of intrinsic defects which are trapped in defect complexes in the material. By increasing the temperature and decreasing the proton flux, the recombination of intrinsic defects is enhanced. The increase of the initial concentration of oxygen and carbon leads to a reduction of the fraction of recombined defects, as more defect complexes are formed. The fraction of recombined intrinsic defects calculated from the results of the different simulation runs ranges from 85 % to 99 %.

An important addition to the process simulation will be the consideration of the dependence of the effective diffusivities of mobile defects and the dependence of the reaction kinetics on the position of the Fermi energy in the band gap. As shown in appendices C and D, this effect can be very strong. There is also room for improvement in terms of the computing time the process simulation requires. The simulation of the implantation of a dose of $10^{15}\,\mathrm{H^+cm^{-2}}$ at an energy of 400 keV takes about 31 h if the temperature is set to 50 °C and a proton flux of $8 \times 10^{11}\,\mathrm{H^+cm^{-2}s^{-1}}$ is used. If the process temperature is set to 150 °C and a proton flux of $2 \times 10^{11}\,\mathrm{H^+cm^{-2}s^{-1}}$ is used, it takes more than 270 h for the process simulation to finish. In a real experiment these processes take only 21 min and 83 min, respectively. Here, a major issue is the process temperature. The diffusivities and the reaction rate constants grow rapidly with the process temperature. The higher these parameters are, the smaller becomes the maximum applicable time-step. Hence, it is not yet possible to simulate the annealing process which usually succeeds the implantation process. Such anneals are performed at temperatures of 400 °C and higher. The simulation of one anneal at 400 °C for one hour would currently take far more than a year in computing time. Some effort has already been put into the parallelization of the calculations, though, due to the interdependences of the concentrations of the different defects, this can only be accomplished at a very limited scale.

5 Conclusions

The change of the properties of silicon by implanting protons into the material is a very complex process. The final profile of the charge carrier concentration does not only depend on the dose and the energy of the implanted protons, but is also a function of the temperature, the implantation current and it depends on the defect and impurity concentrations in the material prior to the implantation. Another important influence on the final charge carrier concentration profile is the post implantation anneal.

The simulation of the generation of defects during proton implantation process shows, that various different defects and defect complexes are formed. Directly after the implantation process the concentration profiles of different defects are very diverse. While some defects, such as complexes containing hydrogen, are only formed around the implantation depth, other defect complexes are generated throughout the irradiated region.

By determining the position of the Fermi energy within the band gap from the concentration ratios of the charge states of each defect, the effective charge carrier concentration is determined. From a qualitative perspective, the simulated profile of the effective charge carrier concentration resembles the experimentally obtained profiles from SRP measurements of proton implanted silicon. In both, simulated and experimental results, the electron concentration shows a peak at the implantation depth and a second peak, respectively a shoulder at a deeper position in the material.

The evaluation of the charged defects determining the effective doping of the materials showed that apart from hydrogen, which is a deep donor, V_2, C_iOI are the most important dopants among the generated defect complexes. The effective charge carrier concentration in the irradiated region, as well as in the shoulder is determined by the concentration difference of V_2, which is a double acceptor and C_iOI, which is a double donor.

Immediately after the implantation process, all of the implanted hydrogen resides at the implantation depth. During the subsequent anneal it diffuses away from this position and spreads over the material. On its way it undergoes reactions with most of the point defects and defect complexes which are present in the material. The reactions of hydrogen with electrically active defects such as V_2 and C_iOI leads to their deactivation. Hydrogen itself is a donor and carries a positive charge. Hence its reactions with other donors are slow due to the Coulomb repulsion. The reactions of hydrogen with acceptors, on the other hand, happen on a much faster scale as the reactants carry opposite charges. This explains, why the diffusion of hydrogen through the irradiated regions goes along with an increase of the electron concentration. This effect is caused by the fast deactivation of V_2. Only at long anneals, a slow decrease of the electron concentration is observed, which reflects the deactivation of C_iOI by hydrogen.

The migration of hydrogen, itself, is also strongly affected by the presence of other defects and defect complexes in the material. If the ratio of the concentration of hydrogen and the concentration of defects is in favor of the defects, the effective diffusion of hydrogen is dictated by the reactions of hydrogen with the defects and by dissociations from the formed defect complexes. The the temperature dependence of this process is associated with an activation energy above 2 eV. If the hydrogen concentration exceeds the defect concentration, the influence of the reactions with these defects decreases and the activation energy of the effective diffusivity decreases.

List of References

[1] C. Kittel, *Introduction to Solid State Physics.* Wiley, 2004.

[2] J. Lutz, *Halbleiter-Leistungsbauelemente: Physik, Eigenschaften, Zuverlässigkeit.* Springer Science & Business Media, 2006.

[3] S. M. Sze and K. K. Ng, *Physics of semiconductor devices.* John wiley & sons, 2006.

[4] F. Thuselt, *Physik der Halbleiterbauelemente: Einführendes Lehrbuch für Ingenieure und Physiker.* Springer-Verlag, 2011.

[5] P. Pichler, *Intrinsic point defects, impurities, and their diffusion in silicon.* Springer Science & Business Media, 2004.

[6] R. C. Chaney, C. C. Lin, and E. E. Lafon, "Application of the method of tight binding to the calculation of the energy band structures of diamond, silicon, and sodium crystals," *Physical Review B*, vol. 3, no. 2, p. 459, 1971.

[7] P. Y. Yu and M. Cardona, "Electronic band structures," in *Fundamentals of Semiconductors*, Springer, Jan. 2010.

[8] I. Remediakis and E. Kaxiras, "Band-structure calculations for semiconductors within generalized-density-functional theory," *Physical Review B*, vol. 59, no. 8, p. 5536, 1999.

[9] K. S. Sieh and P. V. Smith, "A localized orbital description of si using non-local potentials," *physica status solidi (b)*, vol. 129, no. 1, pp. 259–269, 1985.

[10] "Silicon (si), band structure: Datasheet from landolt-börnstein - group iii condensed matter · volume 41a1β: "group iv elements, iv-iv and iii-v compounds. part b - electronic, transport, optical and other properties" in springermaterials (http://dx.doi.org/10.1007/10832182_432)." Copyright 2002 Springer-Verlag Berlin Heidelberg.

[11] A. Smakula and J. Kalnajs, "Precision determination of lattice constants with a geiger-counter x-ray diffractometer," *Phys. Rev.*, vol. 99, pp. 1737–1743, Sep 1955.

[12] Y. Varshni, "Temperature dependence of the energy gap in semiconductors," *Physica*, vol. 34, no. 1, pp. 149 – 154, 1967.

[13] V. Alex, S. Finkbeiner, and J. Weber, "Temperature dependence of the indirect energy gap in crystalline silicon," *Journal of Applied Physics*, vol. 79, no. 9, pp. 6943–6946, 1996.

[14] D. Caughey and R. Thomas, "Carrier mobilities in silicon empirically related to doping and field," *Proceedings of the IEEE*, vol. 55, no. 12, pp. 2192–2193, 1967.

[15] J. Dorkel and P. Leturcq, "Carrier mobilities in silicon semi-empirically related to temperature, doping and injection level," *Solid-State Electronics*, vol. 24, no. 9, pp. 821 – 825, 1981.

[16] N. D. Arora, J. R. Hauser, and D. J. Roulston, "Electron and hole mobilities in silicon as a function of concentration and temperature," *IEEE Transactions on Electron Devices*, vol. 29, no. 2, pp. 292–295, 1982.

[17] D. Klaassen, "A unified mobility model for device simulation—i. model equations and concentration dependence," *Solid-State Electronics*, vol. 35, no. 7, pp. 953–959, 1992.

[18] D. Klaassen, "A unified mobility model for device simulation—ii. temperature dependence of carrier mobility and lifetime," *Solid-State Electronics*, vol. 35, no. 7, pp. 961–967, 1992.

[19] F. Schindler, M. Forster, J. Broisch, J. Schön, J. Giesecke, S. Rein, W. Warta, and M. C. Schubert, "Towards a unified low-field model for carrier mobilities in crystalline silicon," *Solar Energy Materials and Solar Cells*, vol. 131, pp. 92–99, 2014.

[20] W. Shockley and W. T. Read, "Statistics of the recombinations of holes and electrons," *Phys. Rev.*, vol. 87, pp. 835–842, Sep 1952.

[21] D. Fitzgerald and A. Grove, "Surface recombination in semiconductors," in *Electron Devices Meeting, 1967 International*, vol. 13, pp. 102–104, IEEE, 1967.

[22] J. Tersoff, "Schottky barrier heights and the continuum of gap states," *Phys. Rev. Lett.*, vol. 52, no. 6, p. 465, 1984.

[23] M. Hirose, N. Altaf, and T. Arizumi, "Contact properties of metal-silicon schottky barriers," *Jap. J. Appl. Phys.*, vol. 9, no. 3, p. 260, 1970.

[24] M. Aboelfotoh, "Temperature dependence of the schottky-barrier height of tungsten on n-type and p-type silicon," *Solid-State Electronics*, vol. 34, no. 1, pp. 51 – 55, 1991.

[25] W. Zulehner, "Historical overview of silicon crystal pulling development," *Materials Science and Engineering: B*, vol. 73, no. 1–3, pp. 7 – 15, 2000.

[26] J. Czochralski, "A new method for the measurement of the crystallization rate of metals," *Zeitschrift für physikalische Chemie*, vol. 92, pp. 219–221, 1918.

[27] K. Hoshikawa, "Czochralski silicon crystal growth in the vertical magnetic field," *Japanese Journal of Applied Physics*, vol. 21, no. 9A, p. L545, 1982.

[28] M. Tanenbaum and A. Mills, "Preparation of uniform resistivity n-type silicon by nuclear transmutation," *Journal of the Electrochemical Society*, vol. 108, no. 2, pp. 171–176, 1961.

[29] H. Herrmann and H. Herzer, “Doping of silicon by neutron irradiation,” *Journal of The Electrochemical Society*, vol. 122, no. 11, pp. 1568–1569, 1975.

[30] P. Deák, L. C. Snyder, and J. W. Corbett, “Theoretical studies on the core structure of the 450 c oxygen thermal donors in silicon,” *Physical Review B*, vol. 45, no. 20, p. 11612, 1992.

[31] D. Chadi, “Core structure of thermal donors in silicon,” *Physical review letters*, vol. 77, no. 5, p. 861, 1996.

[32] S. Singh, R. Singh, and B. Yadav, “An insight in the formation of thermal double donors in cz-silicon,” *OPTOELECTRONICS AND ADVANCED MATERIALS-RAPID COMMUNICATIONS*, vol. 5, no. 11, pp. 1252–1255, 2011.

[33] S. J. Pearton, J. W. Corbett, and M. Stavola, *Hydrogen in crystalline semiconductors*, vol. 16. Springer Science & Business Media, 2013.

[34] C. Zener, “Theory of do for atomic diffusion in metals,” *Journal of Applied Physics*, vol. 22, no. 4, pp. 372–375, 1951.

[35] R. Aggarwal, P. Fisher, V. Mourzine, and A. Ramdas, “Excitation spectra of lithium donors in silicon and germanium,” *Physical Review*, vol. 138, no. 3A, p. A882, 1965.

[36] L. Darken and S. Hyder, “Photoconductive response of compensating impurities in photothermal ionization spectroscopy of high-purity silicon and germanium,” *Applied Physics Letters*, vol. 42, no. 8, pp. 731–733, 1983.

[37] P. T. Landsberg, *Basic Properties of Semiconductors.* Elsevier, 2013.

[38] D. Lang, “Deep-level transient spectroscopy: A new method to characterize traps in semiconductors,” *Journal of applied physics*, vol. 45, no. 7, pp. 3023–3032, 1974.

[39] S. Zhang and J. E. Northrup, “Chemical potential dependence of defect formation energies in gaas: Application to ga self-diffusion,” *Physical review letters*, vol. 67, no. 17, p. 2339, 1991.

[40] C. G. Van de Walle, D. Laks, G. Neumark, and S. Pantelides, “First-principles calculations of solubilities and doping limits: Li, na, and n in znse,” *Physical Review B*, vol. 47, no. 15, p. 9425, 1993.

[41] C. Freysoldt, B. Grabowski, T. Hickel, J. Neugebauer, G. Kresse, A. Janotti, and C. G. Van de Walle, “First-principles calculations for point defects in solids,” *Reviews of modern physics*, vol. 86, no. 1, p. 253, 2014.

[42] S. Glasstone, K. J. Laidler, and H. Eyring, *The theory of rate processes: the kinetics of chemical reactions, viscosity, diffusion and electrochemical phenomena.* McGraw-Hill Book Company, Incorporated, 1941.

[43] M. von Smoluchowski, “Drei Vorträge über Diffusion, brownsche Bewegung und Koagulation von Kolloidt *Z. Phys.*, vol. 17, pp. 557–585, 1916.

[44] M. von Smoluchowski, “Versuch einer mathematischen Theorie der Koagulationskinetik kolloider
Z. Phys. Chem., vol. 92, pp. 129–168, 1917.

[45] T. Waite, “General theory of bimolecular reaction rates in solids and liquids,” *The Journal of Chemical Physics*, vol. 28, no. 1, pp. 103–106, 1958.

[46] P. Debye, “Reaction rates in ionic solutions,” *Transactions of the Electrochemical Society*, vol. 82, no. 1, pp. 265–272, 1942.

[47] K. Bergman, M. Stavola, S. Pearton, and J. Lopata, “Donor-hydrogen complexes in passivated silicon,” *Phys. Rev. B*, vol. 37, no. 5, p. 2770, 1988.

[48] T. Zundel and J. Weber, “Dissociation energies of shallow-acceptor-hydrogen pairs in silicon,” *Phys. Rev. B*, vol. 39, no. 18, p. 13549, 1989.

[49] A. Van Wieringen and N. Warmoltz, “On the permeation of hydrogen and helium in single crystal silicon and germanium at elevated temperatures,” *Physica*, vol. 22, no. 6-12, pp. 849–865, 1956.

[50] T. Sinno, R. A. Brown, W. von Ammon, and E. Dornberger, “On the dynamics of the oxidation-induced stacking-fault ring in as-grown czochralski silicon crystals,” *Applied physics letters*, vol. 70, no. 17, pp. 2250–2252, 1997.

[51] G. Watkins, “An epr study of the lattice vacancy in silicon,” *J. Phys. Soc. Japan*, vol. 18, no. Suppl II, 1963.

[52] M. Sprenger, S. Muller, and C. Ammerlaan, “The negatively charged vacancy in silicon: Hyperfine interactions from endor measurements,” *Physica B+ C*, vol. 116, no. 1-3, pp. 224–229, 1983.

[53] M. Sprenger, S. Muller, E. Sieverts, and C. Ammerlaan, “Vacancy in silicon: Hyperfine interactions from electron-nuclear double resonance measurements,” *Physical Review B*, vol. 35, no. 4, p. 1566, 1987.

[54] D. C. Mueller, E. Alonso, and W. Fichtner, “Arsenic deactivation in si: Electronic structure and charge states of vacancy-impurity clusters,” *Physical Review B*, vol. 68, no. 4, p. 045208, 2003.

[55] M. J. Puska, S. Pöykkö, M. Pesola, and R. M. Nieminen, “Convergence of supercell calculations for point defects in semiconductors: Vacancy in silicon,” *Physical Review B*, vol. 58, no. 3, p. 1318, 1998.

[56] R. Street and N. Mott, “States in the gap in glassy semiconductors,” *Physical Review Letters*, vol. 35, no. 19, p. 1293, 1975.

[57] J. Newton, A. Chatterjee, R. Harris, and G. Watkins, “Negative-u properties of the lattice vacancy in silicon,” *Physica B+ C*, vol. 116, no. 1, pp. 219–223, 1983.

[58] G. Baraff, E. Kane, and M. Schlüter, “Silicon vacancy: a possible" anderson negative-u" system,” *Physical Review Letters*, vol. 43, no. 13, p. 956, 1979.

[59] G. Watkins, "Lattice defects in semiconductors 1974 (inst. phys. conf. ser. 23) ed fa huntley," *Bristol: Institute of Physics Publishing) p*, vol. 1, pp. 39–44, 1975.

[60] G. Watkins, J. Troxell, and A. Chatterjee, "Vacancies and interstitials in silicon," in *Defects and radiation effects in semiconductors, 1978*, 1979.

[61] G. Watkins, "The lattice vacancy in silicon (deep centers in semiconductors)," 1986.

[62] J. Corbett and G. Watkins, "Silicon divacancy and its direct production by electron irradiation," *Physical Review Letters*, vol. 7, no. 8, p. 314, 1961.

[63] G. Watkins and J. Corbett, "Defects in irradiated silicon: Electron paramagnetic resonance of the divacancy," *Physical Review*, vol. 138, no. 2A, p. A543, 1965.

[64] J. Corbett and G. Watkins, "Production of divacancies and vacancies by electron irradiation of silicon," *Physical Review*, vol. 138, no. 2A, p. A555, 1965.

[65] J. De Wit, E. Sieverts, and C. Ammerlaan, "Divacancy in silicon: Hyperfine interactions from electron-nuclear double resonance measurements," *Physical Review B*, vol. 14, no. 8, p. 3494, 1976.

[66] E. Sieverts, S. Muller, and C. Ammerlaan, "Divacancy in silicon: Hyperfine interactions from electron-nuclear double-resonance measurements. ii," *Physical Review B*, vol. 18, no. 12, p. 6834, 1978.

[67] A. Evwaraye and E. Sun, "Electron-irradiation-induced divacancy in lightly doped silicon," *Journal of Applied Physics*, vol. 47, no. 9, pp. 3776–3780, 1976.

[68] B. Svensson, B. Mohadjeri, A. Hallén, J. Svensson, and J. Corbett, "Divacancy acceptor levels in ion-irradiated silicon," *Physical Review B*, vol. 43, no. 3, p. 2292, 1991.

[69] M. Mikelsen, E. Monakhov, G. Alfieri, B. Avset, and B. Svensson, "Kinetics of divacancy annealing and divacancy-oxygen formation in oxygen-enriched high-purity silicon," *Phys. Rev. B*, vol. 72, no. 19, p. 195207, 2005.

[70] N. Ganagona, B. Raeissi, L. Vines, E. Monakhov, and B. Svensson, "Formation of donor and acceptor states of the divacancy–oxygen centre in p-type cz-silicon," *Journal of Physics: Condensed Matter*, vol. 24, no. 43, p. 435801, 2012.

[71] N. Ganagona, L. Vines, E. Monakhov, and B. Svensson, "Transformation of divacancies to divacancy-oxygen pairs in p-type czochralski-silicon; mechanism of divacancy diffusion," *Journal of Applied Physics*, vol. 115, no. 3, p. 034514, 2014.

[72] G. Oehrlein, J. Lindström, I. Krafcsik, A. Jaworowski, and J. Corbett, "A quantitative investigation of divacancy production enhancement by interstitial oxygen in electron-irradiated silicon," *Physica B+ C*, vol. 116, no. 1-3, pp. 230–235, 1983.

[73] M. Pesola, J. Von Boehm, S. Pöykkö, and R. M. Nieminen, "Spin-density study of the silicon divacancy," *Physical Review B*, vol. 58, no. 3, p. 1106, 1998.

[74] P. Pellegrino, P. Lévêque, J. Lalita, A. Hallén, C. Jagadish, and B. G. Svensson, “Annealing kinetics of vacancy-related defects in low-dose mev self-ion-implanted n-type silicon,” *Physical Review B*, vol. 64, no. 19, p. 195211, 2001.

[75] M. Prasad and T. Sinno, “Internally consistent approach for modeling solid-state aggregation. i. atomistic calculations of vacancy clustering in silicon,” *Physical Review B*, vol. 68, no. 4, p. 045206, 2003.

[76] Y.-H. Lee and J. W. Corbett, “Epr study of defects in neutron-irradiated silicon: Quenched-in alignment under< 110>-uniaxial stress,” *Physical Review B*, vol. 9, no. 10, p. 4351, 1974.

[77] V. Markevich, A. Peaker, S. Lastovskii, L. Murin, J. Coutinho, V. Torres, P. Briddon, L. Dobaczewski, E. Monakhov, and B. Svensson, “Trivacancy and trivacancy-oxygen complexes in silicon: Experiments and ab initio modeling,” *Physical Review B*, vol. 80, no. 23, p. 235207, 2009.

[78] J. Coutinho, V. Markevich, A. Peaker, B. Hamilton, S. Lastovskii, L. Murin, B. Svensson, M. Rayson, and P. Briddon, “Electronic and dynamical properties of the silicon trivacancy,” *Physical Review B*, vol. 86, no. 17, p. 174101, 2012.

[79] V. Markevich, A. Peaker, B. Hamilton, S. Lastovskii, L. I. Murin, J. Coutinho, A. Markevich, M. Rayson, P. Briddon, and B. Svensson, “Reconfigurations and diffusion of trivacancy in silicon,” *Physica B: Condensed Matter*, vol. 407, no. 15, pp. 2974–2977, 2012.

[80] R. Würschum, W. Bauer, K. Maier, A. Seeger, and H.-E. Schaefer, “Defects in semiconductors after electron irradiation or in high-temperature thermal equilibrium, as studied by positron annihilation,” *Journal of Physics: Condensed Matter*, vol. 1, no. SA, p. SA33, 1989.

[81] M. Kwete, D. Segers, M. Dorikens, L. Dorikens-Vanpraet, and P. Clauws, “Positron annihilation study of defects created in silicon irradiated with electrons of high energy,” *physica status solidi (a)*, vol. 122, no. 1, pp. 129–138, 1990.

[82] A. Kawasuso, M. Hasegawa, M. Suezawa, S. Yamaguchi, and K. Sumino, “Annealing processes of vacancies in silicon induced by electron irradiation: Analysis using positron lifetime measurement,” in *Materials Science Forum*, vol. 175, pp. 423–426, Trans Tech Publ, 1995.

[83] J. Hastings, S. Estreicher, and P. A. Fedders, “Vacancy aggregates in silicon,” *Physical Review B*, vol. 56, no. 16, p. 10215, 1997.

[84] A. Bongiorno, L. Colombo, and T. D. De la Rubia, “Structural and binding properties of vacancy clusters in silicon,” *EPL (Europhysics Letters)*, vol. 43, no. 6, p. 695, 1998.

[85] S. Estreicher, J. Hastings, and P. Fedders, “The ring-hexavacany in silicon: A stable and inactive defect,” *Applied physics letters*, vol. 70, no. 4, pp. 432–434, 1997.

[86] G. Watkins, R. Messmer, C. Weigel, D. Peak, and J. Corbett, “Properties of the interstitial in the diamond-type lattice,” *Physical Review Letters*, vol. 27, no. 23, p. 1573, 1971.

[87] P. Gwozdz and J. Koehler, “Changes in ac conductivity of silicon with electron irradiation at 0.5 k,” *Physical Review B*, vol. 6, no. 12, p. 4571, 1972.

[88] R. Harris, G. Watkins, L. Kimerling, and J. Parsey Jr, “Interstitial related defects in n type silicon,” in *Thirteenth International Conference on Defects in Semiconductors, edited by LC Kimerling and JM Parsey, Jr., The Metallurgical Society of AIME*, pp. 799–805, 1985.

[89] W.-C. Lee, S.-G. Lee, and K. Chang, “First-principles study of the self-interstitial diffusion mechanism in silicon,” *Journal of Physics: Condensed Matter*, vol. 10, no. 5, p. 995, 1998.

[90] G. M. Lopez and V. Fiorentini, “Structure, energetics, and extrinsic levels of small self-interstitial clusters in silicon,” *Physical Review B*, vol. 69, no. 15, p. 155206, 2004.

[91] V. Panteleev, S. Ershov, V. Chernyakhovskii, and S. Nagornykh, “Determination of the migration energy of vacancies and of intrinsic interstitial atoms in silicon in the temperature interval 400-600 K,” *JETP Lett.+*, vol. 23, no. 12, 1976.

[92] M. Hane, T. Ikezawa, and G. H. Gilmer, “Di-interstitial diffusivity and migration path calculations based on tight-binding hamiltonian molecular dynamics,” *International Conference on Simulation of Semiconductor Processes and Devices, 2000. SISPAD 2000.*, pp. 119–122, 2000.

[93] Y. A. Du, S. A. Barr, K. R. Hazzard, T. J. Lenosky, R. G. Hennig, and J. W. Wilkins, “Fast diffusion mechanism of silicon tri-interstitial defects,” *Physical Review B*, vol. 72, no. 24, p. 241306, 2005.

[94] G. Baraff and M. Schlüter, “Migration of interstitials in silicon,” *Physical Review B*, vol. 30, no. 6, p. 3460, 1984.

[95] Y. Bar-Yam and J. Joannopoulos, “Silicon self-interstitial migration: Multiple paths and charge states,” *Physical Review B*, vol. 30, no. 4, p. 2216, 1984.

[96] L. J. Munro and D. J. Wales, “Defect migration in crystalline silicon,” *Physical Review B*, vol. 59, no. 6, p. 3969, 1999.

[97] W. Jung and G. Newell, “Spin-1 centers in neutron-irradiated silicon,” *Physical Review*, vol. 132, no. 2, p. 648, 1963.

[98] D. Daly, “New epr spectra in irradiated silicon,” *Journal of Applied Physics*, vol. 42, no. 2, pp. 864–865, 1971.

[99] Y. Lee, Y. Kim, and J. Corbett, “New epr spectra in neutron-irradiated silicon,” *Radiation Effects*, vol. 15, no. 1-2, pp. 77–84, 1972.

[100] G. H. Gilmer, T. D. De La Rubia, D. Stock, and M. Jaraiz, “Diffusion and interactions of point defects in silicon: Molecular dynamics simulations,” *Nuclear Instruments and Methods in Physics Research Section B: Beam Interactions with Materials and Atoms*, vol. 102, no. 1-4, pp. 247–255, 1995.

[101] P. B. Rasband, P. Clancy, and M. O. Thompson, “Equilibrium concentrations of defects in pure and b-doped silicon,” *Journal of applied physics*, vol. 79, no. 12, pp. 8998–9011, 1996.

[102] J. Kim, F. Kirchhoff, W. G. Aulbur, J. W. Wilkins, F. S. Khan, and G. Kresse, “Thermally activated reorientation of di-interstitial defects in silicon,” *Physical review letters*, vol. 83, no. 10, p. 1990, 1999.

[103] A. Bongiorno, L. Colombo, F. Cargnoni, C. Gatti, and M. Rosati, “Evolution of energetics and bonding of compact self-interstitial clusters in si,” *EPL (Europhysics Letters)*, vol. 50, no. 5, p. 608, 2000.

[104] M. Gharaibeh, S. Estreicher, and P. Fedders, “Molecular-dynamics studies of self-interstitial aggregates in si,” *Physica B: Condensed Matter*, vol. 273, pp. 532–534, 1999.

[105] P. Giri, S. Coffa, and E. Rimini, “Evidence for small interstitial clusters as the origin of photoluminescence w band in ion-implanted silicon,” *Applied Physics Letters*, vol. 78, no. 3, pp. 291–293, 2001.

[106] M. De Souza, M. Chichkine, and E. S. Narayanan, “Self-interstitial clusters in silicon,” *MRS Online Proceedings Library Archive*, vol. 610, 2000.

[107] S. Estreicher, M. Gharaibeh, P. Fedders, and P. Ordejón, “Unexpected dynamics for self-interstitial clusters in silicon,” *Physical review letters*, vol. 86, no. 7, p. 1247, 2001.

[108] D. A. Richie, J. Kim, R. Hennig, K. Hazzard, S. Barr, and J. W. Wilkins, “Large-scale molecular dynamics simulations of interstitial defect diffusion in silicon,” in *MRS Proceedings*, vol. 731, pp. W9–10, Cambridge Univ Press, 2002.

[109] D. Richie, J. Kim, S. A. Barr, K. R. Hazzard, R. Hennig, and J. W. Wilkins, “Complexity of small silicon self-interstitial defects,” *Physical review letters*, vol. 92, no. 4, p. 045501, 2004.

[110] M. Cogoni, B. Uberuaga, A. Voter, and L. Colombo, “Diffusion of small self-interstitial clusters in silicon: temperature-accelerated tight-binding molecular dynamics simulations,” *Physical Review B*, vol. 71, no. 12, p. 121203, 2005.

[111] S. Coffa, S. Libertino, and C. Spinella, “Transition from small interstitial clusters to extended {311} defects in ion-implanted si,” *Applied Physics Letters*, vol. 76, no. 3, pp. 321–323, 2000.

[112] P. Pichler and D. Stiebel, “Current status of models for transient phenomena in dopant diffusion and activation,” *Nuclear Instruments and Methods in Physics*

Research Section B: Beam Interactions with Materials and Atoms, vol. 186, no. 1, pp. 256–264, 2002.

[113] S. S. Kapur and T. Sinno, "Detailed microscopic analysis of self-interstitial aggregation in silicon. i. direct molecular dynamics simulations of aggregation," *Physical Review B*, vol. 82, no. 4, p. 045205, 2010.

[114] J. Mikkelsen, "The diffusivity and solubility of oxygen in silicon," in *MRS Proceedings*, vol. 59, p. 19, Cambridge Univ Press, 1985.

[115] A. Hara, T. Fukuda, T. Miyabo, and I. Hirai, "Enhancement of oxygen precipitation in quenched czochralski silicon crystals," *Journal of Applied Physics*, vol. 66, no. 8, pp. 3958–3960, 1989.

[116] R. Newman, "Oxygen diffusion and precipitation in czochralski silicon," *J. Phys-Condens. Mat.*, vol. 12, no. 25, p. R335, 2000.

[117] B. C. Trzynadlowski and S. T. Dunham, "A reduced moment-based model for oxygen precipitation in silicon," *Journal of Applied Physics*, vol. 114, no. 24, p. 243508, 2013.

[118] A. Borghesi, B. Pivac, A. Sassella, and A. Stella, "Oxygen precipitation in silicon," *Journal of Applied Physics*, vol. 77, no. 9, pp. 4169–4244, 1995.

[119] H. Wang, A. Chroneos, C. Londos, E. Sgourou, and U. Schwingenschlögl, "A-centers in silicon studied with hybrid density functional theory," *Applied Physics Letters*, vol. 103, no. 5, p. 052101, 2013.

[120] M.-H. Du, H. M. Branz, R. S. Crandall, and S. Zhang, "Bistability-mediated carrier recombination at light-induced boron-oxygen complexes in silicon," *Physical review letters*, vol. 97, no. 25, p. 256602, 2006.

[121] M. Stavola, J. Patel, L. Kimerling, and P. Freeland, "Diffusivity of oxygen in silicon at the donor formation temperature," *Applied Physics Letters*, vol. 42, no. 1, pp. 73–75, 1983.

[122] D. Åberg, B. Svensson, T. Hallberg, and J. Lindström, "Kinetic study of oxygen dimer and thermal donor formation in silicon," *Physical Review B*, vol. 58, no. 19, p. 12944, 1998.

[123] R. Newman, J. Tucker, A. Brown, and S. McQuaid, "Hydrogen diffusion and the catalysis of enhanced oxygen diffusion in silicon at temperatures below 500 c," *Journal of applied physics*, vol. 70, no. 6, pp. 3061–3070, 1991.

[124] S. McQuaid, M. Binns, C. Londos, J. Tucker, A. Brown, and R. Newman, "Oxygen loss during thermal donor formation in czochralski silicon: New insights into oxygen diffusion mechanisms," *Journal of applied physics*, vol. 77, no. 4, pp. 1427–1442, 1995.

[125] H. Takeno, Y. Hayamizu, and K. Miki, "Diffusivity of oxygen in czochralski silicon at 400–750° c," *Journal of applied physics*, vol. 84, no. 6, pp. 3113–3117, 1998.

[126] U. Gösele and T. Tan, “Oxygen diffusion and thermal donor formation in silicon,” *Applied Physics A: Materials Science & Processing*, vol. 28, no. 2, pp. 79–92, 1982.

[127] L. Zhong and F. Shimura, “Hydrogen enhanced out-diffusion of oxygen in czochralski silicon,” *Journal of applied physics*, vol. 73, no. 2, pp. 707–710, 1993.

[128] Y. J. Lee, J. Von Boehm, M. Pesola, and R. M. Nieminen, “First-principles study of migration, restructuring, and dissociation energies of oxygen complexes in silicon,” *Physical Review B*, vol. 65, no. 8, p. 085205, 2002.

[129] C. Fuller, J. Ditzenberger, N. Hannay, and E. Buehler, “Resistivity changes in silicon induced by heat treatment,” in *Physical Review*, vol. 96, pp. 833–833, AMERICAN PHYSICAL SOC ONE PHYSICS ELLIPSE, COLLEGE PK, MD 20740-3844 USA, 1954.

[130] C. Fuller and R. Logan, “Effect of heat treatment upon the electrical properties of silicon crystals,” *Journal of Applied Physics*, vol. 28, no. 12, pp. 1427–1436, 1957.

[131] W. Kaiser, “Electrical and optical properties of heat-treated silicon,” *Physical Review*, vol. 105, no. 6, p. 1751, 1957.

[132] V. Cazcarra and P. Zunino, “Influence of oxygen on silicon resistivity,” *Journal of applied physics*, vol. 51, no. 8, pp. 4206–4211, 1980.

[133] G. Pensl, M. Schulz, K. Hölzlein, W. Bergholz, and J. Hutchison, “New oxygen donors in silicon,” *Applied Physics A: Materials Science & Processing*, vol. 48, no. 1, pp. 49–57, 1989.

[134] R. Newman, A. Oates, and F. Livingston, “Self-interstitials and thermal donor formation in silicon: new measurements and a model for the defects,” *Journal of Physics C: Solid State Physics*, vol. 16, no. 19, p. L667, 1983.

[135] D. Mathiot, “Thermal donor formation in silicon: A new kinetic model based on self-interstitial aggregation,” *Applied physics letters*, vol. 51, no. 12, pp. 904–906, 1987.

[136] M. Reiche, J. Reichel, and W. Nitzsche, “Correlations between thermal donor formation, rod-like defect formation, and oxygen reduction during low-temperature annealing of cz-grown silicon,” *physica status solidi (a)*, vol. 107, no. 2, pp. 851–865, 1988.

[137] M. Suezawa, K. Sumino, H. Harada, and T. Abe, “Nitrogen-oxygen complexes as shallow donors in silicon crystals,” *Japanese journal of applied physics*, vol. 25, no. 10A, p. L859, 1986.

[138] Y. Kamiura, F. Hashimoto, and M. Yoneta, “Formation of several kinds of oxygen-related donors around 500° c and effects of carbon in czochralski silicon,” *Journal of Applied Physics*, vol. 68, no. 4, pp. 1921–1923, 1990.

[139] W. Wijaranakula and J. Matlock, “A formation mechanism of the thermal donors related to carbon in silicon after an extended isochronal anneal,” *Journal of The Electrochemical Society*, vol. 137, no. 6, pp. 1964–1969, 1990.

[140] S. Hahn, H. Stein, S. Shatas, and F. Ponce, “Thermal donor formation and annihilation in oxygen-implanted float-zone silicon,” *Journal of applied physics*, vol. 72, no. 5, pp. 1758–1765, 1992.

[141] C. Ewels, R. Jones, S. Öberg, J. Miro, and P. Deák, “Shallow thermal donor defects in silicon,” *Physical review letters*, vol. 77, no. 5, p. 865, 1996.

[142] M. Suezawa and K. Sumino, “Nature of thermal donors in silicon crystals,” *physica status solidi (a)*, vol. 82, no. 1, pp. 235–242, 1984.

[143] S. McQuaid, R. Newman, E. Mun, *et al.*, “The role of rapidly diffusing dimers in oxygen loss and the association of thermal donors with small oxygen clusters,” *Materials Science and Engineering: B*, vol. 36, no. 1, pp. 171–174, 1996.

[144] N. Meilwes, J.-M. Spaeth, W. Gotz, and G. Pensl, “Thermal donors in silicon: an investigation of their structure with electron nuclear double resonance,” *Semiconductor science and technology*, vol. 9, no. 9, p. 1623, 1994.

[145] A. Ourmazd, W. Schröter, and A. Bourret, “Oxygen-related thermal donors in silicon: A new structural and kinetic model,” *Journal of Applied Physics*, vol. 56, no. 6, pp. 1670–1681, 1984.

[146] V. Voronkov, “Generation of thermal donors in silicon: oxygen aggregation controlled by self-interstitials,” *Semiconductor science and technology*, vol. 8, no. 12, p. 2037, 1993.

[147] V. Torres, J. Coutinho, R. Jones, M. Barroso, S. Öberg, and P. Briddon, “Early sio 2 precipitates in si: Vacancy-oxygen versus interstitial-oxygen clusters,” *Physica B: Condensed Matter*, vol. 376, pp. 109–112, 2006.

[148] W. Götz, G. Pensl, and W. Zulehner, “Observation of five additional thermal donor species td12 to td16 and of regrowth of thermal donors at initial stages of the new oxygen donor formation in czochralski-grown silicon,” *Physical Review B*, vol. 46, no. 7, p. 4312, 1992.

[149] Y. J. Lee, J. Von Boehm, M. Pesola, and R. M. Nieminen, “Aggregation kinetics of thermal double donors in silicon,” *Physical review letters*, vol. 86, no. 14, p. 3060, 2001.

[150] P. Gaworzewski and K. Schmalz, “On the electrical activity of oxygen in silicon,” *physica status solidi (a)*, vol. 55, no. 2, pp. 699–707, 1979.

[151] K. Schmalz and P. Gaworzewski, “On the donor activity of oxygen in silicon at temperatures from 500 to 800° c,” *physica status solidi (a)*, vol. 64, no. 1, pp. 151–158, 1981.

[152] H. Navarro, J. Griffin, J. Weber, and L. Genzel, “New oxygen related shallow thermal donor centres in czochralski-grown silicon,” *Solid state communications*, vol. 58, no. 3, pp. 151–155, 1986.

[153] Y. Kamiura, F. Hashimoto, and M. Yoneta, “A new family of thermal donors generated around 450° c in phosphorus-doped czochralski silicon,” *Journal of Applied Physics*, vol. 65, no. 2, pp. 600–605, 1989.

[154] V. Emtsev, G. Oganesyan, and K. Schmalz, “Formation of deep thermal donors in heat-treated czochralski silicon,” *Applied physics letters*, vol. 68, no. 17, pp. 2375–2377, 1996.

[155] M. Pesola, Y. J. Lee, J. Von Boehm, M. Kaukonen, and R. M. Nieminen, “Structures of thermal double donors in silicon,” *Physical review letters*, vol. 84, no. 23, p. 5343, 2000.

[156] M. Bruzzi, D. Menichelli, M. Scaringella, J. Härkönen, E. Tuovinen, and Z. Li, “Thermal donors formation via isothermal annealing in magnetic czochralski high resistivity silicon,” *Journal of applied physics*, vol. 99, no. 9, p. 093706, 2006.

[157] J. Veirman, S. Dubois, N. Enjalbert, J. Garandet, D. Heslinga, and M. Lemiti, “Hall mobility reduction in single-crystalline silicon gradually compensated by thermal donors activation,” *Solid-State Electronics*, vol. 54, no. 6, pp. 671–674, 2010.

[158] S. Kirnstötter, M. Faccinelli, P. Hadley, R. Job, W. Schustereder, J. G. Laven, and H.-J. Schulze, “Investigation of doping type conversion and diffusion length extraction of proton implanted silicon by ebic,” *ECS Transactions*, vol. 50, no. 5, pp. 115–120, 2013.

[159] G. Bemski, “Paramagnetic resonance in electron irradiated silicon,” *Journal of Applied Physics*, vol. 30, no. 8, pp. 1195–1198, 1959.

[160] G. Watkins, J. Corbett, and R. Walker, “Spin resonance in electron irradiated silicon,” *Journal of Applied Physics*, vol. 30, no. 8, pp. 1198–1203, 1959.

[161] G. Watkins and J. Corbett, “Defects in irradiated silicon. i. electron spin resonance of the si-a center,” *Phys. Rev.*, vol. 121, no. 4, p. 1001, 1961.

[162] G. Watkins, *Radiation damage in semiconductors.* Dunod, Paris, 1965.

[163] A. L. S. Ferreira-Resende, *An ab initio study of deep-level defects in silicon.* PhD thesis, University of Exeter, 2000.

[164] V. Markevich, A. Peaker, B. Hamilton, S. Lastovskii, L. Murin, J. Coutinho, V. Torres, L. Dobaczewski, and B. Svensson, “Structure and electronic properties of trivacancy and trivacancy-oxygen complexes in silicon,” *physica status solidi (a)*, vol. 208, no. 3, pp. 568–571, 2011.

[165] Y. Lee, T. Bilash, and J. Corbett, “Photo-epr experiments on defects in irradiated silicon,” *Radiation Effects*, vol. 29, no. 1, pp. 7–12, 1976.

[166] M. Pesola, J. Von Boehm, T. Mattila, and R. M. Nieminen, "Computational study of interstitial oxygen and vacancy-oxygen complexes in silicon," *Physical Review B*, vol. 60, no. 16, p. 11449, 1999.

[167] J. Svensson, B. G. Svensson, and J. L. Lindström, "Thermal donor formation in electron-irradiated czochralski silicon," *Applied physics letters*, vol. 49, no. 21, pp. 1435–1437, 1986.

[168] S.-R. Christopoulos, H. Wang, A. Chroneos, C. A. Londos, E. N. Sgourou, and U. Schwingenschlögl, "Vv and vo2 defects in silicon studied with hybrid density functional theory," *Journal of Materials Science: Materials in Electronics*, vol. 26, no. 3, pp. 1568–1571, 2015.

[169] L. Murin, V. Markevich, J. L. Lindström, M. Kleverman, J. Hermansson, T. Hallberg, and B. G. Svensson, "Carbon-oxygen-related complexes in irradiated and heat-treated silicon: Ir absorption studies," in *Solid State Phenomena*, vol. 82, pp. 57–62, Trans Tech Publ, 2002.

[170] P. Grönberg, J. von Boehm, and R. Nieminen, "Molecular dynamics study of oxygen defects in silicon," in *Early Stages of Oxygen Precipitation in Silicon*, pp. 441–446, Springer, 1996.

[171] J. Lindström, L. Murin, B. Svensson, V. Markevich, and T. Hallberg, "The vo 2* defect in silicon," *Physica B: Condensed Matter*, vol. 340, pp. 509–513, 2003.

[172] P. Deák, L. C. Snyder, and J. W. Corbett, "Silicon-interstitial–oxygen-interstitial complex as a model of the 450° c oxygen thermal donor in silicon," *Physical review letters*, vol. 66, no. 6, p. 747, 1991.

[173] V. Markevich, L. Murin, S. Lastovskii, I. Medvedeva, B. Komarov, J. Lindström, and A. Peaker, "Electrically active radiation-induced defects in czochralski-grown si with low carbon content," *Journal of Physics: Condensed Matter*, vol. 17, no. 22, p. S2331, 2005.

[174] V. P. Markevich, A. R. Peaker, B. Hamilton, V. E. Gusakov, S. B. Lastovskii, L. I. Murin, N. Ganagona, E. Monakhov, and B. G. Svensson, "Structure, electronic properties and annealing behavior of di-interstitial-oxygen center in silicon," *Solid State Phenomena*, vol. 242, p. 290, 2015.

[175] J. Lindström, T. Hallberg, J. Hermansson, L. Murin, B. Komarov, V. Markevich, M. Kleverman, and B. Svensson, "Interaction between self-interstitials and the oxygen dimer in silicon," *Physica B: Condensed Matter*, vol. 308, pp. 284–289, 2001.

[176] B. Pajot, H. Compain, J. Lerouille, and B. Clerjaud, "Spectroscopic studies of 450° c thermal donors in silicon," *Physica B+ C*, vol. 117, pp. 110–112, 1983.

[177] R. Newman, J. Tucker, and F. Livingston, "Radiation-enhanced diffusion of oxygen in silicon at room temperature," *Journal of Physics C: Solid State Physics*, vol. 16, no. 5, p. L151, 1983.

[178] S. Nakagawa and K. Kashima, “Quantitative analysis of carbon impurity concentration in silicon epitaxial layers by luminescence activation using carbon ion implantation and electron irradiation,” *physica status solidi (c)*, vol. 11, no. 11-12, pp. 1597–1600, 2014.

[179] B. Kolbesen and A. Mühlbauer, “Carbon in silicon: Properties and impact on devices,” *Solid-State Electronics*, vol. 25, no. 8, pp. 759–775, 1982.

[180] W. Skorupa and R. Yankov, “Carbon-mediated effects in silicon and in silicon-related materials,” *Materials chemistry and physics*, vol. 44, no. 2, pp. 101–143, 1996.

[181] J. Kalejs, L. Ladd, and U. Gösele, “Self-interstitial enhanced carbon diffusion in silicon,” *Applied Physics Letters*, vol. 45, no. 3, pp. 268–269, 1984.

[182] L. Ladd and J. Kalejs, “Self-interstitial injection effects on carbon diffusion in silicon at high temperatures,” in *MRS Proceedings*, vol. 59, p. 445, Cambridge Univ Press, 1985.

[183] W. Windl, O. F. Sankey, and J. Menéndez, “Theory of strain and electronic structure of si 1- y c y and si 1- x- y ge x c y alloys,” *Physical Review B*, vol. 57, no. 4, p. 2431, 1998.

[184] L. Song, X. Zhan, B. Benson, and G. Watkins, “Bistable interstitial-carbon–substitutional-carbon pair in silicon,” *Physical Review B*, vol. 42, no. 9, p. 5765, 1990.

[185] D. Backlund and S. Estreicher, “C4 defect and its precursors in si: First-principles theory,” *Physical Review B*, vol. 77, no. 20, p. 205205, 2008.

[186] A. Tipping and R. Newman, “The diffusion coefficient of interstitial carbon in silicon,” *Semiconductor science and technology*, vol. 2, no. 5, p. 315, 1987.

[187] G. Davies, E. Lightowlers, M. Thomaz, and J. Wilkes, “A metastable precursor to the production of the two-carbon-atom’g’centre in irradiated crystalline silicon,” *Semiconductor science and technology*, vol. 3, no. 6, p. 608, 1988.

[188] S. Chappell, G. Davies, E. C. Lightowlers, and R. Newman, “A metastable precursor to the di-carbon centre in crystalline silicon,” in *Materials Science Forum*, vol. 38, pp. 481–486, Trans Tech Publ, 1989.

[189] J. Lalita, N. Keskitalo, A. Hallén, C. Jagadish, and B. Svensson, “Defect evolution in mev ion-implanted silicon,” *Nuclear Instruments and Methods in Physics Research Section B: Beam Interactions with Materials and Atoms*, vol. 120, no. 1-4, pp. 27–32, 1996.

[190] L. Song and G. Watkins, “Epr identification of the single-acceptor state of interstitial carbon in silicon,” *Physical Review B*, vol. 42, no. 9, p. 5759, 1990.

[191] A. Bean, R. Newman, and R. Smith, “Electron irradiation damage in silicon containing carbon and oxygen,” *Journal of Physics and Chemistry of Solids*, vol. 31, no. 4, pp. 739–751, 1970.

[192] R. Newman and A. Bean, “Irradiation damage in carbon-doped silicon irradiated at low temperatures by 2 mev electrons,” *Radiation Effects*, vol. 8, no. 3-4, pp. 189–193, 1971.

[193] Y.-H. Lee, J. Corbett, and K. Brower, “Epr of a carbon-oxygen-divacancy complex in irradiated silicon,” *physica status solidi (a)*, vol. 41, no. 2, pp. 637–647, 1977.

[194] B. N. Mukashev, A. V. Spitsyn, N. Fukuoka, and H. Saito, “Defects in carbon-implanted silicon,” *Japanese Journal of Applied Physics*, vol. 21, no. 2R, p. 399, 1982.

[195] M. Asom, J. Benton, R. Sauer, and L. Kimerling, “Interstitial defect reactions in silicon,” *Applied physics letters*, vol. 51, no. 4, pp. 256–258, 1987.

[196] G. Ferenczi, C. Londos, T. Pavelka, M. Somogyi, and A. Mertens, “Correlation of the concentration of the carbon-associated radiation damage levels with the total carbon concentration in silicon,” *Journal of applied physics*, vol. 63, no. 1, pp. 183–189, 1988.

[197] M.-A. Trauwaert, J. Vanhellemont, H. Maes, A.-M. Van Bavel, G. Langouche, A. Stesmans, and P. Clauws, “Influence of oxygen and carbon on the generation and annihilation of radiation defects in silicon,” *Materials Science and Engineering: B*, vol. 36, no. 1-3, pp. 196–199, 1996.

[198] B. Pivac, I. Kovačević, and V. Borjanović, “Defects in carbon and oxygen implanted p-type silicon,” *Nuclear Instruments and Methods in Physics Research Section B: Beam Interactions with Materials and Atoms*, vol. 186, no. 1, pp. 355–359, 2002.

[199] J. Coutinho, R. Jones, P. Briddon, S. Öberg, L. Murin, V. Markevich, and J. Lindström, “Interstitial carbon-oxygen center and hydrogen related shallow thermal donors in si,” *Physical Review B*, vol. 65, no. 1, p. 014109, 2001.

[200] H. Wang, A. Chroneos, C. Londos, E. Sgourou, and U. Schwingenschlögl, “Carbon related defects in irradiated silicon revisited,” *Scientific reports*, vol. 4, p. 4909, 2014.

[201] V. Markevich, T. Mchedlidze, and M. Suezawa, “Silicon incorporation in a shallow donor center in hydrogenated czochralski-grown si crystals: An epr study,” *Physical Review B*, vol. 56, no. 20, p. R12695, 1997.

[202] N. Inoue, H. Ohyama, Y. Goto, and T. Sugiyama, “Quantitative analysis of complexes in electron irradiated cz silicon,” *Physica B: Condensed Matter*, vol. 401, pp. 477–482, 2007.

[203] C. Londos, E. Sgourou, A. Chroneos, and V. Emtsev, “Carbon, oxygen and intrinsic defect interactions in germanium-doped silicon,” *Semiconductor Science and Technology*, vol. 26, no. 10, p. 105024, 2011.

[204] F. Shimura, T. Higuchi, and R. Hockett, “Outdiffusion of oxygen and carbon in czochralski silicon,” *Applied physics letters*, vol. 53, no. 1, pp. 69–71, 1988.

[205] W. Wijaranakula, “Oxygen diffusion in carbon-doped silicon,” *Journal of applied physics*, vol. 68, no. 12, pp. 6538–6540, 1990.

[206] R. a. Pinacho, P. Castrillo, M. Jaraiz, I. Martin-Bragado, J. Barbolla, H.-J. Gossmann, G.-H. Gilmer, and J.-L. Benton, “Carbon in silicon: Modeling of diffusion and clustering mechanisms,” *J. Appl. Phys.*, vol. 92, no. 3, pp. 1582–1587, 2002.

[207] P. Leary, R. Jones, S. Öberg, and V. Torres, “Dynamic properties of interstitial carbon and carbon-carbon pair defects in silicon,” *Physical Review B*, vol. 55, no. 4, p. 2188, 1997.

[208] G. Davies, E. Lightowlers, R. Newman, and A. Oates, “A model for radiation damage effects in carbon-doped crystalline silicon,” *Semiconductor science and technology*, vol. 2, no. 8, p. 524, 1987.

[209] L. I. Murin, B. G. Svensson, V. P. Markevich, and A. R. Peaker, “Interactions of self-interstitials with interstitial carbon-interstitial oxygen center in irradiated silicon: an infrared absorption study,” in *Solid State Phenomena*, vol. 205, pp. 218–223, Trans Tech Publ, 2014.

[210] T. Angeletos, A. Chroneos, and C. Londos, “Infrared studies of the evolution of the cioi (sii) defect in irradiated si upon isothermal anneals,” *Journal of Applied Physics*, vol. 119, no. 12, p. 125704, 2016.

[211] D. Backlund and S. Estreicher, “Theoretical study of the c i o i and i si c i o i defects in si,” *Physica B: Condensed Matter*, vol. 401, pp. 163–166, 2007.

[212] F. Zirkelbach, B. Stritzker, K. Nordlund, J. Lindner, W. Schmidt, and E. Rauls, “Combined ab initio and classical potential simulation study on silicon carbide precipitation in silicon,” *Physical Review B*, vol. 84, no. 6, p. 064126, 2011.

[213] A. Docaj and S. Estreicher, “Three carbon pairs in si,” *Physica B: Condensed Matter*, vol. 407, no. 15, pp. 2981–2984, 2012.

[214] G. L. Pearson and J. Bardeen, “Electrical properties of pure silicon and silicon alloys containing boron and phosphorus,” *Physical Review*, vol. 75, no. 5, p. 865, 1949.

[215] F. H. Horn, “Densitometric and electrical investigation of boron in silicon,” *Physical Review*, vol. 97, no. 6, p. 1521, 1955.

[216] F. Morin and J. Maita, “Electrical properties of silicon containing arsenic and boron,” *Physical Review*, vol. 96, no. 1, p. 28, 1954.

[217] E. Burstein, E. Bell, J. Davisson, and M. Lax, “Optical investigations of impurity levels in silicon,” *The Journal of Physical Chemistry*, vol. 57, no. 8, pp. 849–852, 1953.

[218] H. Hrostowski and R. Kaiser, “Infrared spectra of group iii acceptors in silicon,” *Journal of Physics and Chemistry of Solids*, vol. 4, no. 1-2, pp. 148–153, 1958.

[219] A. Onton, P. Fisher, and A. Ramdas, “Spectroscopic investigation of group-iii acceptor states in silicon,” *Physical Review*, vol. 163, no. 3, p. 686, 1967.

[220] J. Mitchell, J. Shewchun, D. Thompson, and J. Davies, “Nitrogen- implanted silicon. ii. electrical properties,” *Journal of Applied physics*, vol. 46, no. 1, pp. 335–343, 1975.

[221] G. Samara and C. Barnes, “Pressure dependence of impurity levels in semiconductors: The deep gold acceptor level and shallow donor and acceptor levels in silicon,” *Physical Review B*, vol. 35, no. 14, p. 7575, 1987.

[222] M. Cherki and A. Kalma, “Photoconductivity studies of defects in p-type silicon: Boron interstitial and aluminum interstitial defects,” *Physical Review B*, vol. 1, no. 2, p. 647, 1970.

[223] G. Watkins, “Epr studies of the lattice vacancy and low-temperature damage processes in silicon,” in *Lattice defects in semiconductors, 1974. Invited and contributed papers from the international conference on lattice defects in semiconductors held in Freiburg, 22-25 Jul 1974*, 1975.

[224] J. Troxell and G. Watkins, “Interstitial boron in silicon: A negative-u system,” *Physical Review B*, vol. 22, no. 2, p. 921, 1980.

[225] M. Hakala, M. J. Puska, and R. M. Nieminen, “First-principles calculations of interstitial boron in silicon,” *Physical Review B*, vol. 61, no. 12, p. 8155, 2000.

[226] S. Mirabella, D. De Salvador, E. Napolitani, E. Bruno, and F. Priolo, “Mechanisms of boron diffusion in silicon and germanium,” *Journal of Applied Physics*, vol. 113, no. 3, p. 3, 2013.

[227] N. Cowern, K. Janssen, G. Van de Walle, and D. Gravesteijn, “Impurity diffusion via an intermediate species: The b-si system,” *Physical review letters*, vol. 65, no. 19, p. 2434, 1990.

[228] N. Cowern and C. Rafferty, “Enhanced diffusion in silicon processing,” *Mrs Bulletin*, vol. 25, no. 06, pp. 39–44, 2000.

[229] S. Jain, W. Schoenmaker, R. Lindsay, P. Stolk, S. Decoutere, M. Willander, and H. Maes, “Transient enhanced diffusion of boron in si,” *Journal of applied physics*, vol. 91, no. 11, pp. 8919–8941, 2002.

[230] G. Watkins, “Defects in irradiated silicon: Epr and electron-nuclear double resonance of interstitial boron,” *Physical Review B*, vol. 12, no. 12, p. 5824, 1975.

[231] A. Tipping and R. Newman, “An infrared study of the production, diffusion and complexing of interstitial boron in electron-irradiated silicon,” *Semiconductor science and technology*, vol. 2, no. 7, p. 389, 1987.

[232] B. Sadigh, T. J. Lenosky, S. K. Theiss, M.-J. Caturla, T. D. de la Rubia, and M. A. Foad, “Mechanism of boron diffusion in silicon: An ab initio and kinetic monte carlo study,” *Physical review letters*, vol. 83, no. 21, p. 4341, 1999.

[233] W. Windl, M. Bunea, R. Stumpf, S. Dunham, and M. Masquelier, “First-principles study of boron diffusion in silicon,” *Physical review letters*, vol. 83, no. 21, p. 4345, 1999.

[234] P. Alippi, L. Colombo, P. Ruggerone, A. Sieck, G. Seifert, and T. Frauenheim, “Atomic-scale characterization of boron diffusion in silicon,” *Physical Review B*, vol. 64, no. 7, p. 075207, 2001.

[235] E. Napolitani, D. De Salvador, R. Storti, A. Carnera, S. Mirabella, and F. Priolo, “Room temperature migration of boron in crystalline silicon,” *Physical review letters*, vol. 93, no. 5, p. 055901, 2004.

[236] I. Martin-Bragado, P. Castrillo, M. Jaraiz, R. Pinacho, J. Rubio, and J. Barbolla, “Physical atomistic kinetic monte carlo modeling of fermi-level effects of species diffusing in silicon,” *Physical Review B*, vol. 72, no. 3, p. 035202, 2005.

[237] Y. M. Haddara, B. T. Folmer, M. E. Law, and T. Buyuklimanli, “Accurate measurements of the intrinsic diffusivities of boron and phosphorus in silicon,” *Applied Physics Letters*, vol. 77, no. 13, pp. 1976–1978, 2000.

[238] D. Mathiot and J. Pfister, “Dopant diffusion in silicon: A consistent view involving nonequilibrium defects,” *Journal of Applied Physics*, vol. 55, no. 10, pp. 3518–3530, 1984.

[239] G. S. Hwang and W. A. Goddard III, “Diffusion of the diboron pair in silicon,” *Physical review letters*, vol. 89, no. 5, p. 055901, 2002.

[240] M. Stavola, K. Bergman, S. Pearton, and J. Lopata, “Hydrogen motion in defect complexes: reorientation kinetics of the bh complex in silicon,” *Physical review letters*, vol. 61, no. 24, p. 2786, 1988.

[241] G. Watkins, “Epr of a trapped vacancy in boron-doped silicon,” *Physical Review B*, vol. 13, no. 6, p. 2511, 1976.

[242] J. Zhu, “Ab initio pseudopotential calculations of dopant diffusion in si,” *Computational materials science*, vol. 12, no. 4, pp. 309–318, 1998.

[243] R. Fair, “On the role of self-interstitials in impurity diffusion in silicon,” *Journal of Applied Physics*, vol. 51, no. 11, pp. 5828–5832, 1980.

[244] N. Cowern, G. Van de Walle, D. Gravesteijn, and C. Vriezema, “Experiments on atomic-scale mechanisms of diffusion,” *Physical review letters*, vol. 67, no. 2, p. 212, 1991.

[245] J. Adey, R. Jones, D. Palmer, P. Briddon, and S. Öberg, “Theory of boron-vacancy complexes in silicon,” *Physical Review B*, vol. 71, no. 16, p. 165211, 2005.

[246] V. Akhmetov and V. Bolotov, “Kinetics of accumulation of radiation defects and annihilation of vacancies and interstitials in carbon-and boron-containing silicon,” *physica status solidi (a)*, vol. 72, no. 1, pp. 61–68, 1982.

[247] X.-Y. Liu, W. Windl, and M. P. Masquelier, “Ab initio modeling of boron clustering in silicon,” *Applied Physics Letters*, vol. 77, no. 13, pp. 2018–2020, 2000.

[248] T. J. Lenosky, B. Sadigh, S. K. Theiss, M.-J. Caturla, and T. D. de la Rubia, “Ab initio energetics of boron-interstitial clusters in crystalline si,” *Applied Physics Letters*, vol. 77, no. 12, pp. 1834–1836, 2000.

[249] W. Luo, P. B. Rasband, P. Clancy, and B. W. Roberts, “Tight-binding studies of the tendency for boron to cluster in c-si. ii. interaction of dopants and defects in boron-doped si,” *Journal of applied physics*, vol. 84, no. 5, pp. 2476–2486, 1998.

[250] P. Deák, A. Gali, A. Sólyom, P. Ordejón, K. Kamarás, and G. Battistig, “Studies of boron–interstitial clusters in si,” *Journal of Physics: Condensed Matter*, vol. 15, no. 29, p. 4967, 2003.

[251] J. Yamauchi, N. Aoki, and I. Mizushima, “First-principles study on b 12 clusters in si,” *Physical Review B*, vol. 55, no. 16, p. R10245, 1997.

[252] L. Pelaz, G. Gilmer, H.-J. Gossmann, C. Rafferty, M. Jaraiz, and J. Barbolla, “B cluster formation and dissolution in si: A scenario based on atomistic modeling,” *Applied physics letters*, vol. 74, no. 24, pp. 3657–3659, 1999.

[253] J. Adey, J. Goss, R. Jones, and P. Briddon, “Identification of boron clusters and boron-interstitial clusters in silicon,” *Physical Review B*, vol. 67, no. 24, p. 245325, 2003.

[254] P. Drevinsky, C. Caefer, S. Tobin, J. Mikkelsen, and L. Kimerling, “Influence of oxygen and boron on defect production in irradiated silicon,” in *MRS Proceedings*, vol. 104, p. 167, Cambridge Univ Press, 1987.

[255] A. Khan, M. Yamaguchi, Y. Ohshita, N. Dharmarasu, K. Araki, T. Abe, H. Itoh, T. Ohshima, M. Imaizumi, and S. Matsuda, “Role of the impurities in production rates of radiation-induced defects in silicon materials and solar cells,” *Journal of Applied Physics*, vol. 90, no. 3, pp. 1170–1178, 2001.

[256] E. Vandenbossche and B. Baccus, “Modeling inactive boron during predeposition processes,” *Journal of applied physics*, vol. 73, no. 11, pp. 7322–7330, 1993.

[257] J. Schmidt, A. G. Aberle, and R. Hezel, “Investigation of carrier lifetime instabilities in cz-grown silicon,” in *Photovoltaic Specialists Conference, 1997., Conference Record of the Twenty-Sixth IEEE*, pp. 13–18, IEEE, 1997.

[258] J. Schmidt and K. Bothe, “Structure and transformation of the metastable boron-and oxygen-related defect center in crystalline silicon,” *Physical review B*, vol. 69, no. 2, p. 024107, 2004.

[259] V. V. Voronkov and R. Falster, “Latent complexes of interstitial boron and oxygen dimers as a reason for degradation of silicon-based solar cells,” *Journal of Applied Physics*, vol. 107, no. 5, p. 053509, 2010.

[260] V. Voronkov, R. Falster, K. Bothe, B. Lim, and J. Schmidt, “Lifetime-degrading boron-oxygen centres in p-type and n-type compensated silicon,” *journal of applied physics*, vol. 110, no. 6, p. 063515, 2011.

[261] J. Adey, R. Jones, and P. Briddon, “Formation of B_iO_i, B_iC_s, and $B_iB_sH_i$ defects in e-irradiated or ion-implanted silicon containing boron,” *Appl. Phys. Lett.*, vol. 83, no. 4, pp. 665–667, 2003.

[262] C.-L. Liu, W. Windl, L. Borucki, S. Lu, and X.-Y. Liu, “Ab initio modeling and experimental study of c–b interactions in si,” *Applied physics letters*, vol. 80, no. 1, pp. 52–54, 2002.

[263] B. Lim, K. Bothe, and J. Schmidt, “Modeling the generation and dissociation of the boron-oxygen complex in b-doped cz-si,” in *Photovoltaic Specialists Conference, 2008. PVSC’08. 33rd IEEE*, pp. 1–4, IEEE, 2008.

[264] L. Murin, S. Lastovskii, E. Tolkacheva, V. Markevich, A. Peaker, and B. Svensson, “Local vibrational modes of interstitial boron–interstitial oxygen complex in silicon,” *physica status solidi (a)*, vol. 213, no. 11, pp. 2850–2854, 2016.

[265] G. Picus, E. Burstein, and B. Henvis, “Absorption spectra of impurities in silicon—ii: Group-v donors,” *Journal of Physics and Chemistry of Solids*, vol. 1, no. 1-2, pp. 75–81, 1956.

[266] J. Bichard and J. Giles, “Optical absorption spectra of arsenic and phosphorus in silicon,” *Canadian Journal of Physics*, vol. 40, no. 10, pp. 1480–1489, 1962.

[267] R. Aggarwal and A. Ramdas, “Optical determination of the symmetry of the ground states of group-v donors in silicon,” *Physical Review*, vol. 140, no. 4A, p. A1246, 1965.

[268] B. Pajot, J. Kauppinen, and R. Anttila, “High resolution study of the group v impurities absorption in silicon,” *Solid State Communications*, vol. 31, no. 10, pp. 759–763, 1979.

[269] D. Sasireka and E. Palaniyandi, “Effect of local relaxation on the binding energy of group-v donors in silicon,” *Physical Review B*, vol. 46, no. 4, p. 2047, 1992.

[270] S. Hu, P. Fahey, and R. Dutton, “On models of phosphorus diffusion in silicon,” *Journal of applied physics*, vol. 54, no. 12, pp. 6912–6922, 1983.

[271] A. Chelyadinskii and V. Burenkov, “Model of the pair phosphorus atom-interstitial silicon atom,” *Physics of the Solid State*, vol. 40, no. 11, pp. 1806–1808, 1998.

[272] O. Scheerer, U. Juda, and M. Höhne, “Self-interstitial shallow-donor complexes in silicon: An electron-paramagnetic-resonance study,” *Physical Review B*, vol. 57, no. 16, p. 9657, 1998.

[273] G. Watkins and J. Corbett, “Defects in irradiated silicon: Electron paramagnetic resonance and electron-nuclear double resonance of the si-e center,” *Physical Review*, vol. 134, no. 5A, p. A1359, 1964.

[274] X.-Y. Liu, W. Windl, K. M. Beardmore, and M. P. Masquelier, "First-principles study of phosphorus diffusion in silicon: Interstitial-and vacancy-mediated diffusion mechanisms," *Applied physics letters*, vol. 82, no. 12, pp. 1839–1841, 2003.

[275] A. N. Larsen, A. Mesli, K. B. Nielsen, H. K. Nielsen, L. Dobaczewski, J. Adey, R. Jones, D. Palmer, P. Briddon, and S. Öberg, "E center in silicon has a donor level in the band gap," *Physical review letters*, vol. 97, no. 10, p. 106402, 2006.

[276] A. N. Larsen and A. Mesli, "The hidden secrets of the e-center in si and ge," *Physica B: Condensed Matter*, vol. 401–402, pp. 85 – 90, 2007. Proceedings of the 24th International Conference on Defects in Semiconductors.

[277] A. Resende, R. Jones, S. Öberg, and P. Briddon, "Calculations of electrical levels of deep centers: application to au-h and ag-h defects in silicon," *Physical review letters*, vol. 82, no. 10, p. 2111, 1999.

[278] U. Gösele and H. Strunk, "High-temperature diffusion of phosphorus and boron in silicon via vacancies or via self-interstitials?," *Applied Physics A: Materials Science & Processing*, vol. 20, no. 4, pp. 265–273, 1979.

[279] L. The Anh, N. Tien Cuong, P. T. Lam, M. Manoharan, H. Mizuta, H. Matsumura, N. Otsuka, and D. Hieu Chi, "First-principles study of hydrogen-enhanced phosphorus diffusion in silicon," *Journal of Applied Physics*, vol. 119, no. 4, p. 045703, 2016.

[280] A. Chantre, J. Benton, M. Asom, and L. C. Kimerling, "New impurity-defect reactions in silicon," in *Materials Science Forum*, vol. 10, pp. 1111–1116, Trans Tech Publ, 1986.

[281] L. Song, B. Benson, and G. Watkins, "Identification of a bistable defect in silicon: The carbon interstitial-carbon substitutional pair," *Applied physics letters*, vol. 51, no. 15, pp. 1155–1157, 1987.

[282] E. Gürer, B. W. Benson, and G. D. Watkins, "Configurational metastability of carbon-phosphorus pair defects in silicon," in *Materials Science Forum*, vol. 83, pp. 339–344, Trans Tech Publ, 1992.

[283] X. Zhan and G. Watkins, "Electron paramagnetic resonance of multistable interstitial-carbon–substitutional-group-v-atom pairs in silicon," *Physical Review B*, vol. 47, no. 11, p. 6363, 1993.

[284] Y. Kamiura, T. Maeda, Y. Yamashita, and M. Nakamura, "Formation of carbon-related defects during the carbon-enhanced annihilation of thermal donors in silicon," *Japanese journal of applied physics*, vol. 37, no. 2A, p. L101, 1998.

[285] J. L. Lindström, B. G. Svensson, and W. Chen, "A new defect observed in annealed phosphorus-doped electron-irradiated silicon," in *Materials Science Forum*, vol. 83, pp. 333–338, Trans Tech Publ, 1992.

[286] D. Chadi, P. Citrin, C. Park, D. Adler, M. Marcus, and H.-J. Gossmann, “Fermi-level-pinning defects in highly n-doped silicon,” *Physical review letters*, vol. 79, no. 24, p. 4834, 1997.

[287] A. N. Larsen, C. Christensen, and J. W. Petersen, “Room-temperature vacancy migration in crystalline si from an ion-implanted surface layer,” *Journal of applied physics*, vol. 86, no. 9, pp. 4861–4864, 1999.

[288] M. Suezawa, N. Fukata, T. Mchedlidze, and A. Kasuya, “Many optical absorption peaks observed in electron-irradiated n-type si,” *Journal of applied physics*, vol. 92, no. 11, pp. 6561–6566, 2002.

[289] E. Schroer and M. Uematsu, “Simulation of clustering and pile-up during post-implantation annealing of phosphorus in silicon,” *Japanese journal of applied physics*, vol. 38, no. 1R, p. 7, 1999.

[290] M. Uematsu, “Simulation of high-concentration phosphorus diffusion in silicon taking into account phosphorus clustering and pile-up,” *Japanese journal of applied physics*, vol. 38, no. 11R, p. 6188, 1999.

[291] P. H. Keys, *Phosphorus-defect interactions during thermal annealing of ion implanted silicon.* PhD thesis, University of Florida, 2001.

[292] M. Uematsu, “Simulation of transient enhanced diffusion in silicon taking into account ostwald ripening of defects,” *MRS Online Proceedings Library Archive*, vol. 717, 2002.

[293] V. Kozlovskii, V. Kozlov, and V. Lomasov, “Modification of semiconductors with proton beams. a review,” *Semiconductors*, vol. 34, no. 2, pp. 123–140, 2000.

[294] J. G. Laven, *Protonendotierung von Silizium: Untersuchung und Modellierung protoneninduzierter Dotierungsprofile in Silizium.* Springer-Verlag, 2014.

[295] D. Sawko and J. Bartko, “Production of fast switching power thyristors by proton irradiation,” *IEEE Transactions on Nuclear Science*, vol. 30, no. 2, pp. 1756–1758, 1983.

[296] P. Hazdra, K. Brand, J. Rubeš, and J. Vobeck, “Local lifetime control by light ion irradiation: impact on blocking capability of power p–i–n diode,” *Microelectron. J.*, vol. 32, no. 5, pp. 449–456, 2001.

[297] Y. Zohta, Y. Ohmura, and M. Kanazawa, “Shallow donor state produced by proton bombardment of silicon,” *Jap. J. Appl. Phys.*, vol. 10, no. 4, p. 532, 1971.

[298] J. Hartung and J. Weber, “Defects created by hydrogen implantation into silicon,” *Materials Science and Engineering: B*, vol. 4, no. 1-4, pp. 47–50, 1989.

[299] S. Romani and J. Evans, “Platelet defects in hydrogen implanted silicon,” *Nucl. Instrum. Meth. B*, vol. 44, no. 3, pp. 313–317, 1990.

[300] M. Bruel, “Silicon on insulator material technology,” *Electronics letters*, vol. 31, no. 14, pp. 1201–1202, 1995.

[301] M. Bruel, B. Aspar, B. Charlet, C. Maleville, T. Poumeyrol, A. Soubie, A. Auberton-Herve, J. Lamure, T. Barge, F. Metral, *et al.*, “" smart cut": a promising new soi material technology,” in *SOI Conference, 1995. Proceedings., 1995 IEEE International*, pp. 178–179, IEEE, 1995.

[302] D. R. Lide, “Magnetic susceptibility of the elements and inorganic compounds,” *CRC handbook of chemistry and physics*, vol. 86, pp. 130–135, 2005.

[303] M. Berger, J. Coursey, M. Zucker, and J. Chang, “Estar, pstar, and astar: Computer programs for calculating stopping-power and range tables for electrons, protons, and helium ions (version 1.2.3). [online] available: http://physics.nist.gov/star [2017,05,10].” National Institute of Standards and Technology, Gaithersburg, MD, 1998-2005.

[304] J. Ziegler, “SRIM(Version2013.00) - http://www.srim.org,” 1984-2013.

[305] J. F. Ziegler, M. D. Ziegler, and J. P. Biersack, “Srim–the stopping and range of ions in matter (2010),” *Nucl. Instrum. Meth. B*, vol. 268, no. 11, pp. 1818–1823, 2010.

[306] N. Bohr, “Ii. on the theory of the decrease of velocity of moving electrified particles on passing through matter,” *The London, Edinburgh, and Dublin Philosophical Magazine and Journal of Science*, vol. 25, no. 145, pp. 10–31, 1913.

[307] N. Bohr, “Lx. on the decrease of velocity of swiftly moving electrified particles in passing through matter,” *The London, Edinburgh, and Dublin Philosophical Magazine and Journal of Science*, vol. 30, no. 178, pp. 581–612, 1915.

[308] P. A. Cherenkov, “Visible emission of clean liquids by action of γ radiation,” *Doklady Akademii Nauk SSSR*, vol. 2, p. 451, 1934.

[309] G. B. Collins and V. G. Reiling, “Čerenkov radiation,” *Physical Review*, vol. 54, no. 7, p. 499, 1938.

[310] J. Lindhard, “Influence of crystal lattice on motion of energetic charged particles.,” *MATEMATISK-FYSISKE MEDDELELSER KONGELIGE DANSKE VIDENSKABERNES SELSKAB*, vol. 34, no. 14, p. 64, 1965.

[311] B. Kononov and V. Struts, “Proton channeling in silicon at various temperatures,” *Russian Physics Journal*, vol. 13, no. 6, pp. 738–740, 1970.

[312] J. P. Biersack and L. Haggmark, “A monte carlo computer program for the transport of energetic ions in amorphous targets,” *Nuclear Instruments and Methods*, vol. 174, no. 1-2, pp. 257–269, 1980.

[313] Y. Ohmura, Y. Zohta, and M. Kanazawa, “Electrical properties of n-type si layers doped with proton bombardment induced shallow donors,” *Solid State Communications*, vol. 11, no. 1, pp. 263–266, 1972.

[314] C. Seager and D. Ginley, “Passivation of grain boundaries in polycrystalline silicon,” *Applied Physics Letters*, vol. 34, no. 5, pp. 337–340, 1979.

[315] S. Pearton and A. Tavendale, “Hydrogen passivation of gold-related deep levels in silicon,” *Physical review B*, vol. 26, no. 12, p. 7105, 1982.

[316] A. Tavendale and S. Pearton, “Deep level, quenched-in defects in silicon doped with gold, silver, iron, copper or nickel,” *Journal of Physics C: Solid State Physics*, vol. 16, no. 9, p. 1665, 1983.

[317] A. Tavendale, D. Alexiev, and A. Williams, “Field drift of the hydrogen-related, acceptor-neutralizing defect in diodes from hydrogenated silicon,” *Applied Physics Letters*, vol. 47, no. 3, pp. 316–318, 1985.

[318] C. Seager, R. Anderson, and J. Panitz, “The diffusion of hydrogen in silicon and mechanisms for “unintentional” hydrogenation during ion beam processing,” *Journal of Materials Research*, vol. 2, no. 01, pp. 96–106, 1987.

[319] C. H. Seager, “Hydrogenation methods,” *Semiconductors and Semimetals*, vol. 34, pp. 17–33, 1991.

[320] J. Corbett, S. Sahu, T. Shi, and L. Snyder, “Atomic and molecular hydrogen in the si lattice,” *Physics Letters A*, vol. 93, no. 6, pp. 303–304, 1983.

[321] P. Deák, L. C. Snyder, and J. W. Corbett, “State and motion of hydrogen in crystalline silicon,” *Physical Review B*, vol. 37, no. 12, p. 6887, 1988.

[322] P. Deák, L. Snyder, J. Lindström, J. Corbett, S. Pearton, and A. Tavendale, “The self-trapping of hydrogen in semiconductors,” *Physics Letters A*, vol. 126, no. 7, pp. 427–430, 1988.

[323] C. G. Van de Walle, P. Denteneer, Y. Bar-Yam, and S. Pantelides, “Theory of hydrogen diffusion and reactions in crystalline silicon,” *Physical review B*, vol. 39, no. 15, p. 10791, 1989.

[324] K. Chang and D. Chadi, “Hydrogen bonding and diffusion in crystalline silicon,” *Physical Review B*, vol. 40, no. 17, p. 11644, 1989.

[325] S. Estreicher, M. Roberson, and D. M. Maric, “Hydrogen and hydrogen dimers in c-c, si, ge, and α-sn,” *Physical Review B*, vol. 50, no. 23, p. 17018, 1994.

[326] P. Deák, L. Snyder, and J. Corbett, “Charge state of hydrogen in crystalline silicon,” *Physical Review B*, vol. 43, no. 5, p. 4545, 1991.

[327] C. Herring, N. Johnson, and C. G. Van de Walle, “Energy levels of isolated interstitial hydrogen in silicon,” *Physical Review B*, vol. 64, no. 12, p. 125209, 2001.

[328] T. Ichimiya and A. Furuichi, “On the solubility and diffusion coefficient of tritium in single crystals of silicon,” *The International Journal of Applied Radiation and Isotopes*, vol. 19, no. 7, pp. 573–578, 1968.

[329] W. Hansen, S. Pearton, and E. Haller, “Bulk acceptor compensation produced in p-type silicon at near-ambient temperatures by a h2o plasma,” *Applied Physics Letters*, vol. 44, no. 6, pp. 606–608, 1984.

[330] A. Mogro-Campero, R. Love, and R. Schubert, “Drastic changes in the electrical resistance of gold-doped silicon produced by a hydrogen plasma,” *Journal of The Electrochemical Society*, vol. 132, no. 8, pp. 2006–2009, 1985.

[331] S. Pearton, “The properties of hydrogen in crystalline si,” *J. Electron. Mater*, pp. 737–743, 1985.

[332] C. Herrero, M. Stutzmann, A. Breitschwerdt, and P. Santos, “Trap-limited hydrogen diffusion in doped silicon,” *Physical Review B*, vol. 41, no. 2, p. 1054, 1990.

[333] R. Rizk, P. De Mierry, D. Ballutaud, M. Aucouturier, and D. Mathiot, “Hydrogen diffusion and passivation processes in p-and n-type crystalline silicon,” *Physical review B*, vol. 44, no. 12, p. 6141, 1991.

[334] N. Johnson and C. Herring, “Migration of the h 2* complex and its relation to h- in n-type silicon,” *Physical Review B*, vol. 43, no. 17, p. 14297, 1991.

[335] B. L. Sopori, K. Jones, and X. J. Deng, “Observation of enhanced hydrogen diffusion in solar cell silicon,” *Applied physics letters*, vol. 61, no. 21, pp. 2560–2562, 1992.

[336] Y. Huang, Y. Ma, R. Job, and A. Ulyashin, “Hydrogen diffusion at moderate temperatures in p-type czochralski silicon,” *Journal of applied physics*, vol. 96, no. 12, pp. 7080–7086, 2004.

[337] L. L. Kazmerski, “Compositional microcharacterization of electrically active and chemically passivated silicon grain boundaries,” *Journal of Vacuum Science & Technology A*, vol. 3, no. 3, pp. 1287–1290, 1985.

[338] C. Seager and R. Anderson, “Real-time observations of hydrogen drift and diffusion in silicon,” *Applied physics letters*, vol. 53, no. 13, pp. 1181–1183, 1988.

[339] J. Laven, R. Job, H.-J. Schulze, F.-J. Niedernostheide, W. Schustereder, and L. Frey, “Activation and dissociation of proton-induced donor profiles in silicon,” *ECS Journal of Solid State Science and Technology*, vol. 2, no. 9, pp. P389–P394, 2013.

[340] N. Johnson and C. Herring, “Diffusion of negatively charged hydrogen in silicon,” *Physical Review B*, vol. 46, no. 23, p. 15554, 1992.

[341] A. Hara, “Diffusion coefficient of hydrogen in silicon at an intermediate temperature,” *Japanese journal of applied physics*, vol. 46, no. 3R, p. 962, 2007.

[342] M. Capizzi and A. Mittiga, “Hydrogen in Si: Diffusion and shallow impurity deactivation,” *Physica B & C*, vol. 146, no. 1, pp. 19–29, 1987.

[343] F. Buda, G. L. Chiarotti, R. Car, and M. Parrinello, “Proton diffusion in crystalline silicon,” *Physical review letters*, vol. 63, no. 3, p. 294, 1989.

[344] G. Panzarini and L. Colombo, “Hydrogen diffusion in silicon from tight-binding molecular dynamics,” *Physical review letters*, vol. 73, no. 12, p. 1636, 1994.

[345] W. v. Meyer and H. Neldel, “Über die beziehungen zwischen der energiekonstanten und der mengenkonstanten a in der leitwerts temperaturformel bei oxydischen halbleitern,” *Zeitschrift für technische Physik*, vol. 18, p. 588, 1937.

[346] F. Constable, “The mechanism of catalytic decomposition,” *Proceedings of the Royal Society of London. Series A, Containing Papers of a Mathematical and Physical Character*, vol. 108, no. 746, pp. 355–378, 1925.

[347] W. Linert and R. Jameson, “The isokinetic relationship,” *Chemical Society Reviews*, vol. 18, pp. 477–505, 1989.

[348] R. Metselaar and G. Oversluizen, “The meyer-neldel rule in semiconductors,” *Journal of Solid State Chemistry*, vol. 55, no. 3, pp. 320–326, 1984.

[349] R. Widenhorn, M. Fitzgibbons, and E. Bodegom, “The meyer-neldel rule for diodes in forward bias,” *Journal of applied physics*, vol. 96, no. 12, pp. 7379–7382, 2004.

[350] P. Stallinga and H. L. Gomes, “Trap states as an explanation for the meyer–neldel rule in semiconductors,” *Organic Electronics*, vol. 6, no. 3, pp. 137–141, 2005.

[351] A. Dalvi, N. P. Reddy, and S. Agarwal, “The meyer–neldel rule and hopping conduction,” *Solid State Communications*, vol. 152, no. 7, pp. 612–615, 2012.

[352] R. Kirchheim and X. Huang, “A relationship between prefactor and activation energy for diffusion,” *physica status solidi (b)*, vol. 144, no. 1, pp. 253–257, 1987.

[353] G. Boisvert, L. J. Lewis, and A. Yelon, “Many-body nature of the meyer-neldel compensation law for diffusion,” *Physical review letters*, vol. 75, no. 3, p. 469, 1995.

[354] J. Shinar, R. Shinar, X.-L. Wu, S. Mitra, and F. Girvan, “Hydrogen dynamics in a-si: H: Multiple trapping, structural relaxation, and the meyer-neldel relation,” *Physical Review B*, vol. 43, no. 2, p. 1631, 1991.

[355] W. Beyer and U. Zastrow, “Concentration dependence of hydrogen diffusion in hydrogenated silicon,” in *MRS Proceedings*, vol. 507, p. 679, Cambridge Univ Press, 1998.

[356] N. Zangenberg and A. N. Larsen, “The meyer–neldel rule for diffusion in si and sige,” *Physica B: Condensed Matter*, vol. 340, pp. 780–783, 2003.

[357] R. Widenhorn, A. Rest, and E. Bodegom, “The meyer–neldel rule for a property determined by two transport mechanisms,” *Journal of applied physics*, vol. 91, no. 10, pp. 6524–6528, 2002.

[358] A. Yelon and B. Movaghar, “Microscopic explanation of the compensation (meyer-neldel) rule,” *Physical review letters*, vol. 65, no. 5, p. 618, 1990.

[359] A. Yelon, B. Movaghar, and H. Branz, “Origin and consequences of the compensation (meyer-neldel) law,” *Physical Review B*, vol. 46, no. 19, p. 12244, 1992.

[360] A. Yelon, B. Movaghar, and R. Crandall, “Multi-excitation entropy: its role in thermodynamics and kinetics,” *Reports on Progress in Physics*, vol. 69, no. 4, p. 1145, 2006.

[361] P. Deák and L. Snyder, “Dihydrogen complexes in silicon,” *Radiation Effects and Defects in Solids*, vol. 111, no. 1-2, pp. 77–81, 1989.

[362] L. Meda, G. Cerofolini, G. Ottaviani, R. Tonini, F. Corni, R. Balboni, M. Anderle, R. Canteri, and R. Dierckx, “Evidence for molecular hydrogen in single crystal silicon,” *Physica B: Condensed Matter*, vol. 170, no. 1-4, pp. 259–264, 1991.

[363] P. Stallinga, T. Gregorkiewicz, C. Ammerlaan, and Y. V. Gorelkinskii, “Electron paramagnetic resonance of molecular hydrogen in silicon,” *Physical review letters*, vol. 71, no. 1, p. 117, 1993.

[364] K. Murakami, N. Fukata, S. Sasaki, K. Ishioka, M. Kitajima, S. Fujimura, J. Kikuchi, and H. Haneda, “Hydrogen molecules in crystalline silicon treated with atomic hydrogen,” *Physical review letters*, vol. 77, no. 15, p. 3161, 1996.

[365] N. Fukata, S. Sasaki, K. Murakami, K. Ishioka, K. Nakamura, M. Kitajima, S. Fujimura, J. Kikuchi, and H. Haneda, “Hydrogen molecules and hydrogen-related defects in crystalline silicon,” *Physical review B*, vol. 56, no. 11, p. 6642, 1997.

[366] A. Leitch, J. Weber, and V. Alex, “Formation of hydrogen molecules in crystalline silicon,” *Materials Science and Engineering: B*, vol. 58, no. 1, pp. 6–12, 1999.

[367] R. Pritchard, M. Ashwin, J. Tucker, R. Newman, E. Lightowlers, M. Binns, S. McQuaid, and R. Falster, “Interactions of hydrogen molecules with bond-centered interstitial oxygen and another defect center in silicon,” *Physical Review B*, vol. 56, no. 20, p. 13118, 1997.

[368] K. Chang and D. Chadi, “Diatomic-hydrogen-complex diffusion and self-trapping in crystalline silicon,” *Physical review letters*, vol. 62, no. 8, p. 937, 1989.

[369] B. Hourahine, R. Jones, S. Öberg, and P. Briddon, “Molecular hydrogen traps within silicon,” *Materials Science and Engineering: B*, vol. 58, no. 1, pp. 24–25, 1999.

[370] V. Markevich, M. Suezawa, and L. Murin, “Interaction of hydrogen (deuterium) molecules with interstitial oxygen atoms in silicon,” *Materials Science and Engineering: B*, vol. 58, no. 1, pp. 26–30, 1999.

[371] V. Gusakov, “Diffusion of interstitial hydrogen molecules in crystalline germanium and silicon: Quantumchemical simulation,” *Materials science in semiconductor processing*, vol. 9, no. 4, pp. 531–535, 2006.

[372] H. Stein, “Bonding and thermal stability of implanted hydrogen in silicon,” *Journal of Electronic Materials*, vol. 4, no. 1, pp. 159–174, 1975.

[373] H. Stein, “Vacancies and the chemical trapping of hydrogen in silicon,” *Physical Review Letters*, vol. 43, no. 14, p. 1030, 1979.

[374] H. Xu, "Electronic structure of hydrogen-vacancy complexes in crystalline silicon: A theoretical study," *Physical Review B*, vol. 46, no. 3, p. 1403, 1992.

[375] M. Roberson and S. Estreicher, "Vacancy and vacancy-hydrogen complexes in silicon," *Physical Review B*, vol. 49, no. 24, p. 17040, 1994.

[376] B. Bech Nielsen, L. Hoffmann, M. Budde, R. Jones, J. P. Goss, and S. Öberg, "H interacting with intrinsic defects in si," in *Materials Science Forum*, vol. 196, pp. 933–938, Trans Tech Publ, 1995.

[377] B. Sopori, X. Deng, J. Benner, A. Rohatgi, P. Sana, S. Estreicher, Y. Park, and M. Roberson, "Hydrogen in silicon: a discussion of diffusion and passivation mechanisms," *Solar Energy Materials and Solar Cells*, vol. 41, pp. 159–169, 1996.

[378] B. B. Nielsen, P. Johannesen, P. Stallinga, K. B. Nielsen, and J. Byberg, "Identification of the silicon vacancy containing a single hydrogen atom by epr," *Physical review letters*, vol. 79, no. 8, p. 1507, 1997.

[379] A. Nazarov, V. Pinchuk, T. Yanchuk, V. Lysenko, Y. N. Vovk, S. Rangan, S. Ashok, V. Kudoyarova, and E. Terukov, "Hydrogen effect on enhancement of defect reactions in semiconductors: example for silicon and vacancy defects," *International journal of hydrogen energy*, vol. 26, no. 5, pp. 521–526, 2001.

[380] M. Budde, B. B. Nielsen, J. Keay, and L. Feldman, "Vacancy–hydrogen complexes in group-iv semiconductors," *Physica B*, vol. 273, pp. 208–211, 1999.

[381] J. Hastings, M. Gharaibeh, S. K. Estreicher, and P. Fedders, "Hydrogen interactions with intrinsic defects in silicon," *Physica B: Condensed Matter*, vol. 273, pp. 216–219, 1999.

[382] S. Estreicher, J. Hastings, and P. Fedders, "Hydrogen-defect interactions in si," *Mater. Sci. Eng. B-Adv.*, vol. 58, no. 1, pp. 31–35, 1999.

[383] F. Reboredo, M. Ferconi, and S. Pantelides, "Theory of the nucleation, growth, and structure of hydrogen-induced extended defects in silicon," *Physical review letters*, vol. 82, no. 24, p. 4870, 1999.

[384] S. Z. Tokmoldin and B. Mukashev, "Defects agglomeration in the vicinity of hydrogen-related vacancy-type complexes in proton-implanted silicon," *Physica B*, vol. 308, pp. 167–170, 2001.

[385] E. Lavrov, J. Weber, L. Huang, and B. B. Nielsen, "Vacancy-hydrogen defects in silicon studied by raman spectroscopy," *Physical Review B*, vol. 64, no. 3, p. 035204, 2001.

[386] S. Z. Tokmoldin, B. Mukashev, K. A. Abdullin, and Y. V. Gorelkinskii, "Hydrogen interactions with interstitial-and vacancy-type defects in silicon," *Physica B: Condensed Matter*, vol. 273, pp. 204–207, 1999.

[387] S. Zhang and H. M. Branz, “Hydrogen above saturation at silicon vacancies: H-pair reservoirs and metastability sites,” *Physical review letters*, vol. 87, no. 10, p. 105503, 2001.

[388] J. Corbett, J. Lindström, and S. Pearton, “Hydrogen in silicon,” in *MRS Proceedings*, vol. 104, p. 229, Cambridge Univ Press, 1987.

[389] C.-T. Sah, J. Y.-C. Sun, and J. J.-T. Tzou, “Deactivation of the boron acceptor in silicon by hydrogen,” *Applied Physics Letters*, vol. 43, no. 2, pp. 204–206, 1983.

[390] J. Pankove, D. Carlson, J. Berkeyheiser, and R. Wance, “Neutralization of shallow acceptor levels in silicon by atomic hydrogen,” *Physical Review Letters*, vol. 51, no. 24, p. 2224, 1983.

[391] J. Pankove, R. Wance, and J. Berkeyheiser, “Neutralization of acceptors in silicon by atomic hydrogen,” *Applied Physics Letters*, vol. 45, no. 10, pp. 1100–1102, 1984.

[392] N. Johnson, C. Herring, and D. Chadi, “Interstitial hydrogen and neutralization of shallow-donor impurities in single-crystal silicon,” *Physical review letters*, vol. 56, no. 7, p. 769, 1986.

[393] S. T. Pantelides, “Effect of hydrogen on shallow dopants in crystalline silicon,” *Applied physics letters*, vol. 50, no. 15, pp. 995–997, 1987.

[394] B. Pajot, A. Chari, M. Aucouturier, M. Astier, and A. Chantre, “Experimental evidence for boron-hydrogen interaction in boron-doped silicon passivated with hydrogen,” *Solid state communications*, vol. 67, no. 9, pp. 855–858, 1988.

[395] R. Pritchard, M. Ashwin, R. Newman, J. Tucker, E. C. Lightowlers, M. Binns, R. J. Falster, and S. McQuaid, “Vibrational absorption from oxygen-hydrogen (oi-h2) complexes in hydrogenated cz silicon,” in *Materials Science Forum*, vol. 258, pp. 283–288, Trans Tech Publ, 1997.

[396] V. Markevich and M. Suezawa, “Hydrogen–oxygen interaction in silicon at around 50 c,” *J. Appl. Phys.*, vol. 83, no. 6, pp. 2988–2993, 1998.

[397] A. J. Morris, C. J. Pickard, and R. Needs, “Hydrogen/nitrogen/oxygen defect complexes in silicon from computational searches,” *Physical Review B*, vol. 80, no. 14, p. 144112, 2009.

[398] Y. Huang, Y. Ma, R. Job, W. Fahrner, E. Simoen, and C. Claeys, “The lower boundary of the hydrogen concentration required for enhancing oxygen diffusion and thermal donor formation in czochralski silicon,” *Journal of applied physics*, vol. 98, no. 3, p. 033511, 2005.

[399] A. Brown, M. Claybourn, R. Murray, P. Nandhra, R. Newman, and J. Tucker, “Enhanced thermal donor formation in silicon exposed to a hydrogen plasma,” *Semiconductor science and technology*, vol. 3, no. 6, p. 591, 1988.

[400] H. Stein and S. Hahn, “Hydrogen introduction and hydrogen-enhanced thermal donor formation in silicon,” *Journal of applied physics*, vol. 75, no. 7, pp. 3477–3484, 1994.

[401] H. Stein and S. Hahn, “Depth profiles for hydrogen-enhanced thermal donor formation in silicon: Spreading resistance probe measurements,” *Journal of The Electrochemical Society*, vol. 142, no. 4, pp. 1242–1247, 1995.

[402] R. Job, W. Fahrner, N. Kazuchits, and A. Ulyashin, “A two-step low-temperature process for a pn junction formation due to hydrogen enhanced thermal donor formation in p-type czochralski silicon,” in *MRS Proceedings*, vol. 513, p. 337, Cambridge Univ Press, 1998.

[403] A. Ulyashin, A. Ivanov, I. Khorunzhii, R. Job, W. Fahrner, F. Komarov, and A. Kamyshan, “Hydrogen redistribution and enhanced thermal donor formation at post implantation annealing of p-type hydrogen implanted czochralski silicon,” *Materials Science and Engineering: B*, vol. 58, no. 1, pp. 91–94, 1999.

[404] P. Johannesen, J. Byberg, and B. B. Nielsen, “The a center binding a single hydrogen atom in crystalline silicon observed by epr,” *Physica B: Condensed Matter*, vol. 273, pp. 180–183, 1999.

[405] K. B. Nielsen, L. Dobaczewski, K. Goscinski, R. Bendesen, O. Andersen, and B. B. Nielsen, “Deep levels of vacancy-hydrogen centers in silicon studied by laplace dlts,” *Physica B: Condensed Matter*, vol. 273, pp. 167–170, 1999.

[406] J. Bleka, H. Malmbekk, E. Monakhov, B. Svensson, and B. Avset, “Annealing dynamics of irradiation-induced defects in high-purity silicon in the presence of hydrogen,” *Physical Review B*, vol. 85, no. 8, p. 085210, 2012.

[407] A. Endrös, “Charge-state-dependent hydrogen-carbon-related deep donor in crystalline silicon,” *Physical review letters*, vol. 63, no. 1, p. 70, 1989.

[408] A. Endrös, W. Krühler, and J. Grabmaier, “Hydrogen in phosphorus-and carbon-doped crystalline silicon,” *Physica B: Condensed Matter*, vol. 170, no. 1-4, pp. 365–370, 1991.

[409] S. Kirnstoetter, M. Faccinelli, P. Hadley, M. Jelinek, W. Schustereder, J. Laven, and H.-J. Schulze, “H+ implantation profile formation in m: Cz and fz silicon,” in *Ion Implantation Technology (IIT), 2014 20th International Conference on*, pp. 1–4, IEEE, 2014.

[410] J. Panitz, D. Sharp, and C. Hills, “Near-surface microstructural modifications in low energy hydrogen ion bombarded silicon,” *Journal of Vacuum Science & Technology A: Vacuum, Surfaces, and Films*, vol. 3, no. 1, pp. 1–5, 1985.

[411] L. Meda, G. Cerofolini, R. Dierckx, G. Mercurio, M. Servidori, F. Cembali, M. Anderle, R. Canteri, G. Ottaviani, C. Claeys, *et al.*, “Hydrogen implantation into (100) silicon: A study of the released damage,” *Nuclear Instruments and Methods in Physics Research Section B: Beam Interactions with Materials and Atoms*, vol. 39, no. 1-4, pp. 381–385, 1989.

[412] N. Johnson, F. Ponce, R. Street, and R. Nemanich, “Defects in single-crystal silicon induced by hydrogenation,” *Physical Review B*, vol. 35, no. 8, p. 4166, 1987.

[413] S. Muto, S. Takeda, and M. Hirata, “Hydrogen-induced platelets in silicon studied by transmission electron microscopy,” *Philosophical Magazine A*, vol. 72, no. 4, pp. 1057–1074, 1995.

[414] K. Hojou, S. Furuno, K. Kushita, N. Sasajima, and K. Izui, “Eels analysis of sic crystals under hydrogen and helium dual-ion beam irradiation,” *Nuclear Instruments and Methods in Physics Research Section B: Beam Interactions with Materials and Atoms*, vol. 141, no. 1, pp. 148–153, 1998.

[415] H. Assaf and E. Ntsoenzok, “Transfer of thin silicon layers by mev hydrogen implantation,” *Nuclear Instruments and Methods in Physics Research Section B: Beam Interactions with Materials and Atoms*, vol. 240, no. 1, pp. 183–187, 2005.

[416] D. Bisero, F. Corni, S. Frabboni, R. Tonini, G. Ottaviani, and R. Balboni, “Growth kinetics of a displacement field in hydrogen implanted single crystalline silicon,” *Journal of applied physics*, vol. 83, no. 8, pp. 4106–4110, 1998.

[417] L.-J. Huang, Q.-Y. Tong, Y.-L. Chao, T.-H. Lee, T. Martini, and U. Gösele, “Onset of blistering in hydrogen-implanted silicon,” *Applied physics letters*, vol. 74, no. 7, pp. 982–984, 1999.

[418] T. Höchbauer, A. Misra, M. Nastasi, and J. Mayer, “Physical mechanisms behind the ion-cut in hydrogen implanted silicon,” *Journal of applied physics*, vol. 92, no. 5, pp. 2335–2342, 2002.

[419] J. Lee, M. Nastasi, N. D. Theodore, A. Smalley, T. Alford, J. Mayer, M. Cai, and S. Lau, “Effects of hydrogen implantation temperature on ion-cut of silicon,” *Journal of applied physics*, vol. 96, no. 1, pp. 280–288, 2004.

[420] M. Nastasi, T. Höchbauer, J.-K. Lee, A. Misra, J. P. Hirth, M. Ridgway, and T. Lafford, “Nucleation and growth of platelets in hydrogen-ion-implanted silicon,” *Applied Physics Letters*, vol. 86, no. 15, p. 154102, 2005.

[421] W. Düngen, R. Job, Y. Ma, Y. Huang, T. Mueller, W. Fahrner, L. Keller, J. Horstmann, and H. Fiedler, “Thermal evolution of hydrogen related defects in hydrogen implanted czochralski silicon investigated by raman spectroscopy and atomic force microscopy,” *Journal of applied physics*, vol. 100, no. 3, p. 034911, 2006.

[422] L. Shao, Y. Lin, J. Swadener, J.-K. Lee, Q. Jia, Y. Wang, M. Nastasi, P. E. Thompson, N. D. Theodore, T. Alford, *et al.*, “H-induced platelet and crack formation in hydrogenated epitaxial si/ si 0.98 b 0.02/ si structures,” *Applied physics letters*, vol. 88, no. 2, p. 021901, 2006.

[423] Z. Di, Y. Wang, M. Nastasi, F. Rossi, J.-K. Lee, L. Shao, and P. E. Thompson, “Investigation of stress-induced (100) platelet formation and surface exfoliation in plasma hydrogenated si,” *Applied Physics Letters*, vol. 91, no. 24, p. 244101, 2007.

[424] P. Deák, C. R. Ortiz, L. C. Snyder, and J. W. Corbett, "Structure of the (1 1 1) hydrogen platelet in silicon," *Physica B: Condensed Matter*, vol. 170, no. 1-4, pp. 223–226, 1991.

[425] M. Weldon, V. Marsico, Y. Chabal, A. Agarwal, D. Eaglesham, J. Sapjeta, W. Brown, D. C. Jacobson, Y. Caudano, S. Christman, *et al.*, "On the mechanism of the hydrogen-induced exfoliation of silicon," *Journal of Vacuum Science & Technology B: Microelectronics and Nanometer Structures Processing, Measurement, and Phenomena*, vol. 15, no. 4, pp. 1065–1073, 1997.

[426] M. Bruel, B. Aspar, and A.-J. Auberton-Hervé, "Smart-cut: a new silicon on insulator material technology based on hydrogen implantation and wafer bonding," *Japanese journal of applied physics*, vol. 36, no. 3S, p. 1636, 1997.

[427] H. Moriceau, F. Mazen, C. Braley, F. Rieutord, A. Tauzin, and C. Deguet, "Smart cut™: Review on an attractive process for innovative substrate elaboration," *Nuclear Instruments and Methods in Physics Research Section B: Beam Interactions with Materials and Atoms*, vol. 277, pp. 84–92, 2012.

[428] R. Mazur and D. Dickey, "A spreading resistance technique for resistivity measurements on silicon," *Journal of the electrochemical society*, vol. 113, no. 3, pp. 255–259, 1966.

[429] M. Pawlik, "Spreading resistance: A quantitative tool for process control and development," *Journal of Vacuum Science & Technology B: Microelectronics and Nanometer Structures Processing, Measurement, and Phenomena*, vol. 10, no. 1, pp. 388–396, 1992.

[430] S. Kirnstötter, M. Faccinelli, W. Schustereder, J. Laven, H.-J. Schulze, and P. Hadley, "Hydrogen decoration of radiation damage induced defect structures," in *AIP Conference Proceedings*, vol. 1583, pp. 51–55, AIP, 2014.

[431] M. Faccinelli, S. Kirnstoetter, W. Schustereder, J. G. Laven, and P. Hadley, "An ebic and srp study on thermal donors in proton implanted p-type magnetic czochralski silicon," *Phys. Status Solidi C*, vol. 11, no. 11-12, pp. 1583–1588, 2014.

[432] C. G. Van de Walle, "Energies of various configurations of hydrogen in silicon," *Physical Review B*, vol. 49, no. 7, p. 4579, 1994.

[433] K. Chang and D. Chadi, "Theory of hydrogen passivation of shallow-level dopants in crystalline silicon," *Physical review letters*, vol. 60, no. 14, p. 1422, 1988.

[434] J. Zhu, N. Johnson, and C. Herring, "Negative-charge state of hydrogen in silicon," *Physical Review B*, vol. 41, no. 17, p. 12354, 1990.

[435] L. E. Revell and B. E. Williamson, "Why are some reactions slower at higher temperatures?," *Journal of Chemical Education*, vol. 90, no. 8, pp. 1024–1027, 2013.

[436] W. Kaiser, H. Frisch, and H. Reiss, "Mechanism of the formation of donor states in heat-treated silicon," *Physical Review*, vol. 112, no. 5, p. 1546, 1958.

[437] V. Markevich, L. Makarenko, and L. Murin, "Some new features of thermal donor formation in silicon at t< 800 k," *physica status solidi (a)*, vol. 97, no. 2, 1986.

[438] M. Claybourn and R. Newman, "Activation energy for thermal donor formation in silicon," *Applied physics letters*, vol. 51, no. 26, pp. 2197–2199, 1987.

[439] T. Hallberg and J. Lindström, "Activation energies for the formation of oxygen clusters related to the thermal donors in silicon," *Materials Science and Engineering: B*, vol. 36, no. 1-3, pp. 13–15, 1996.

[440] M. Faccinelli, M. Jelinek, T. Wuebben, J. G. Laven, H.-J. Schulze, and P. Hadley, "Simulation of the proton implantation process in silicon," *physica status solidi (c)*, pp. n/a–n/a, 2016.

[441] K. Gill, G. Hall, and B. MacEvoy, "Bulk damage effects in irradiated silicon detectors due to clustered divacancies," *J. Appl. Phys.*, vol. 82, no. 1, pp. 126–136, 1997.

[442] K. Kono, H. Amekura, and N. Kishimoto, "Flux dependent generation rates of radiation-induced defect clustering in n-si under 17 mev proton irradiation," *MRS Online Proceedings Library Archive*, vol. 540, 1998.

[443] M. Kuhnke, E. Fretwurst, and G. Lindstroem, "Defect generation in crystalline silicon irradiated with high energy particles," *Nuclear Instruments and Methods in Physics Research Section B: Beam Interactions with Materials and Atoms*, vol. 186, no. 1-4, pp. 144–151, 2002.

[444] V. Gusakov, "First principle study of the diffusion of oxygen and oxygen complexes in Si, SiGe solid solutions and Si nanocrystals," *Sol. St. Phenom.*, vol. 205, pp. 171–180, 2014.

[445] V. V. Voronkov and R. Falster, "Fast and slow vacancies in silicon," *Sol. St. Phenom.*, vol. 205, pp. 157–162, 2014.

[446] S. Zhao, *Defect reactions and impurity control in silicon.* PhD thesis, Massachusetts Institute of Technology, 1997.

List of Figures

List of Tables

Glossaries

Acronyms

Acronym	Description
CCC	charge carrier concentration
ce	conduction-electron
CV	capacitance-voltage measurement
Cz	silicon grown using the Czochralski method
DFT	density functional theory
DLTS	deep level transient spectroscopy
DR-sim	diffusion-reaction simulation
eh	electron-hole
ENDOR	electron nuclear double resonance
EPR	electron paramagnetic resonance
fcc	face-centered-cubic
FZ	silicon grown using the float zone method
hh	heavy-hole
high E	high energy proton implantation
IR	infra-red
IRR	infra red reflectance
LAOM	localized atomic orbital method
lh	light-hole
low E	low energy proton implantation
m:Cz	silicon grown using the magnetic Czochralski method
mc-CV	minority carrier pulsed capacitance voltage measurement
MD-sim	molecular-dynamics simulation
MNR	Meyer-Neldel rule
NTD	new kind of oxygen related thermal donors generated at higher temperatures
OD-GI	out diffusion and gas ionization
OD-MS	out diffusion and mass spectroscopy

Acronym	Description
ODE	ordinary differential equation
OTD	oxygen related thermal donor
PAS	photo absorption spectroscopy
perm	permeation from gas phase
PTIS	photo thermal ionization spectroscopy
RF	radio frequency
S1	m:Cz-Si, implanted with $5 \times 10^{14}\,\mathrm{H^{+}cm^{-2}}$ at an implantation energy of 2.5 MeV
S2	m:Cz-Si, implanted with $1 \times 10^{15}\,\mathrm{H^{+}cm^{-2}}$ at an implantation energy of 2.5 MeV
S3	m:Cz-Si, implanted with $5 \times 10^{15}\,\mathrm{H^{+}cm^{-2}}$ at an implantation energy of 2.5 MeV
S4	m:Cz-Si, implanted with $1 \times 10^{16}\,\mathrm{H^{+}cm^{-2}}$ at an implantation energy of 2.5 MeV
S5	m:Cz-Si, implanted with $1 \times 10^{14}\,\mathrm{H^{+}cm^{-2}}$ at an implantation energy of 4 MeV
S6	m:Cz-Si, implanted with $1 \times 10^{15}\,\mathrm{H^{+}cm^{-2}}$ at an implantation energy of 4 MeV
S7	m:Cz-Si with lower oxygen concentration, implanted with $1 \times 10^{14}\,\mathrm{H^{+}cm^{-2}}$ at an implantation energy of 2.5 MeV
S8	FZ-Si, implanted with $1 \times 10^{14}\,\mathrm{H^{+}cm^{-2}}$ at an implantation energy of 4 MeV
SIMS	secondary ion mass spectroscopy
so	split-off
SRIM	Stopping Range of Ions in Matter; simulation tool as described in reference [304, 305]
SRP	spreading resistance profiling
STD	shallow thermal donors
TEM	transmission electron microscopy
TRIM	Transport of Ions in Matter; simulation tool, part of the SRIM-software package [304]
H-site	hexagonal lattice site
T-site	tetrahedral lattice site
X-site	split site in the lattice, where two defect share a substitutional position

Variables

Symbol	Description	Unit
A	area	m^2
a_1	lattice constant along x_c	m
a_2	lattice constant along y_c	m
a_3	lattice constant along z_c	m
a_L	lattice parameter	m

Symbol	**Description**	**Unit**
α	auxillary variable for $\frac{D_{\mathrm{X}}\delta t}{\Delta x^2}$	
α_{E_G}	parameter for the calculation of the temperature dependent band gap	JK^{-1}
α_l	lattice angle	$^\circ$
α_μ	parameter describing the temperature dependence of the mobility	
A_{μ_I}	parameter for the calculation of the impurity mobility μ_I	$(\mathrm{cmVs})^{-1}\mathrm{K}^{-\frac{3}{2}}$
$A_{n,n}$	tri-diagonal matrix with $n \times n$ elements	
β_C	auxiliary variable used in the description of the influence of electric charges on the reaction of point defects	
β_{E_G}	parameter for the calculation of the temperature dependent band gap	K
β_l	lattice angle	$^\circ$
β_p	auxiliary variable used in the description of the reaction probability	
B_{μ_I}	parameter for the calculation of the impurity mobility μ_I	$\mathrm{cm}^{-3}\mathrm{K}^{-2}$
CH	defect complex consisting of a carbon and a hydrogen atom	cm^{-3}
$c_{\mathrm{Au},n}$	capture coefficient of electrons in the Auger recombination process	$\mathrm{m}^6\mathrm{s}^{-1}$
$c_{\mathrm{Au},p}$	capture coefficient of holes in the Auger recombination process	$\mathrm{m}^6\mathrm{s}^{-1}$
$c_{\mathrm{B_i}}$	concentration of interstitial boron	cm^{-3}
$c_{\mathrm{B_iH}}$	concentration of $\mathrm{B_iH}$	cm^{-3}
c_{C}	carbon concentration	cm^{-3}
c_{CC}	charge carrier concentration	cm^{-3}
c_{CC}^{sub}	charge carrier concentration in the substrate material	cm^{-3}
$c_{CC}^{\mathrm{sub},0}$	charge carrier concentration in the substrate material before the start of the anneal	cm^{-3}
[H]	hydrogen concentration	cm^{-3}
c_{H}	hydrogen concentration	cm^{-3}
c_{l}	speed of light in vacuum	ms^{-1}
f_{scan}	scan frequency of the proton beam during proton implantation	s^{-1}
C_j^n	one-dimensional array of concentration values $c_{\mathrm{X}}{}_{j+1}^n$ at time j	
C_{j+1}^n	one-dimensional array of concentration values $c_{\mathrm{X}}{}_{j+1}^n$ at time $j+1$	
c_{O}	oxygen concentration	cm^{-3}
[O]	oxygen concentration	cm^{-3}
c_{pulse}	concentration of generated defects during one period of f_{scan}	cm^{-3}
$\left(\frac{c}{d}\right)_{\mathrm{SRIM}}$	defect concentration normalized to the implanted dose as calculated using SRIM	cm^{-3}
c_{V}	total concentration of the silicon vacancy V	cm^{-3}
c_{V^+}	concentration of the positively charged state of the silicon vacancy V	cm^{-3}

Symbol	**Description**	**Unit**
c_{V_2}	total concentration of the silicon divacancy V_2	cm^{-3}
$c_{\mathrm{V}_2^q}$	concentration of the charge state q of the silicon divacancy V_2	cm^{-3}
c_{V^q}	concentration of the charge state q of the silicon vacancy V	cm^{-3}
c_{X}	concentration of X	cm^{-3}
c_{X_0}	concentration of X at the surface of the crystal	cm^{-3}
$c_{\mathrm{X}_\mathrm{A}}$	concentration of the defect X_A	cm^{-3}
$c_{\mathrm{X}_\mathrm{AB}}$	concentration of X_AB	cm^{-3}
$c^G_{\mathrm{X}_\mathrm{A}}$	concentration of defect X_A introduced (H) or generated (V, I) by the proton beam	cm^{-3}
C_{impl}	array containing concentration profiles of defects generated by the proton beam, normalized to the implantation dose	$\mathrm{cm}^{-3}/\mathrm{cm}^{-2}$
$C^{\mathrm{all}}_{\mathrm{X}}$	array containing defect concentration profiles	cm^{-3}
$c_{\mathrm{X}_\mathrm{B}}$	concentration of the defect X_B	cm^{-3}
$c_{\mathrm{X}_\mathrm{C}}$	concentration of the defect X_C	cm^{-3}
c_{X_i}	concentration of X_i	cm^{-3}
c_{X^q}	concentration of X in the charge state q	cm^{-3}
$c_{\mathrm{X}_i^q}$	concentration of X_i in the charge state q	cm^{-3}
D	diffusion constant, diffusivity	$\mathrm{cm}^2\mathrm{s}^{-1}$
d	implantation dose	$\mathrm{H}^+\mathrm{cm}^{-2}$
D_0	Arrhenius parameter, pre-factor for the calculation of the temperature dependent diffusion coefficient D	$\mathrm{cm}^2\mathrm{s}^{-1}$
D_{cc}	charge carrier diffusion constant	$\mathrm{cm}^2\mathrm{s}^{-1}$
ΔC_{diff}	array of profiles containing the change in defect concentration due to diffusion	cm^{-3}
ΔC_{diss}	array of profiles containing the change in defect concentration due to dissociation	cm^{-3}
$\Delta C_{\mathrm{drift}}$	array of profiles containing the change in defect concentration due to ionic drift	cm^{-3}
ΔC_{reac}	array of profiles containing change in defect concentration due to reactions	cm^{-3}
$D(E)$	density of states	$[\mathrm{J}^{-1}\mathrm{m}^{-3}]$
D^{eff}	effective diffusivity	$\mathrm{cm}^2\mathrm{s}^{-1}$
$D^{\mathrm{eff}}_{\mathrm{B}_\mathrm{i}}$	effective diffusivity of the boron interstitial B_i	$\mathrm{cm}^2\mathrm{s}^{-1}$
$D^{\mathrm{eff}}_{\mathrm{C}_\mathrm{i}}$	effective diffusivity of the carbon interstitial C_i	$\mathrm{cm}^2\mathrm{s}^{-1}$
$D^{\mathrm{eff}}_{\mathrm{H}}$	effective diffusivity of hydrogen	$\mathrm{cm}^2\mathrm{s}^{-1}$
$D^{\mathrm{peak}}_{\mathrm{H}}$	effective diffusivity of hydrogen at the implantation peak	$\mathrm{cm}^2\mathrm{s}^{-1}$
$D^{\mathrm{eff}}_{\mathrm{V}}$	effective diffusivity of the silicon vacancy	$\mathrm{cm}^2\mathrm{s}^{-1}$
$D^{\mathrm{eff}}_{\mathrm{X}}$	effective diffusivity of impurity X	$\mathrm{cm}^2\mathrm{s}^{-1}$
ΔE	energy difference	J
ΔE_{AB}	minimum energy required for the reaction $\mathrm{X}_\mathrm{A}+\mathrm{X}_\mathrm{B}\rightarrow\mathrm{X}_\mathrm{AB}$ to occur	J
ΔE_{form}	difference in formation energy	J
ΔG	change in Gibbs free energy	J

Symbol	**Description**	**Unit**
ΔH	enthalpy change	J
$\Delta H_{\mathrm{X_{AB}}}$	difference in the potential energy between $\mathrm{X_A} + \mathrm{X_B}$ and $\mathrm{X_{AB}}$	J
δl_i	jump distance of jump type i	m
ΔS	entropy change	$\mathrm{JK^{-1}}$
Δx	displacement due to ionic drift	cm
d_{fin}	final implantation dose	$\mathrm{H^{+}cm^{-2}}$
D_{MN}	Meyer-Neldel pre-factor	$\mathrm{cm^2s^{-1}}$
D_n	electron diffusion constant	$\mathrm{cm^2s^{-1}}$
Δn	excess electron concentration	$\mathrm{cm^{-3}}$
D_{OH}	diffusion coefficient of the OH-complex	$\mathrm{cm^2s^{-1}}$
D_p	hole diffusion constant	$\mathrm{cm^2s^{-1}}$
Δp	excess hole concentration	$\mathrm{cm^{-3}}$
d_s	distance from surface	m
dt	time interval	s
D_{X}	diffusion constant of impurity X	$\mathrm{cm^2s^{-1}}$
$D_{\mathrm{X_A}}$	diffusion constant of impurity $\mathrm{X_A}$	$\mathrm{cm^2s^{-1}}$
$D_{\mathrm{X_B}}$	diffusion constant of impurity $\mathrm{X_B}$	$\mathrm{cm^2s^{-1}}$
D_{X^q}	diffusion constant of the charge state q of impurity X	$\mathrm{cm^2s^{-1}}$
E	energy	J
E_0	energy at the band minimum or maximum	J
E_A	activation energy for the calculation of the temperature dependent diffusion coefficient D	J
E_a	energy state of acceptor impurity in the band gap	J
E_A^{AB}	activation energy in the Arrhenius equation describing the temperature dependence of the effective reaction rate constant k_r^{AB}	$\mathrm{cm^3s^{-1}}$
$E_{c_{CC}}^{\mathrm{sub}}$	Arrhenius activation energy of the rate of the formation of thermal donors in the substrate material	eV
$E_{A,\mathrm{X}}$	activation energy for the calculation of the temperature dependent diffusion coefficient D_{X}	J
E_b	binding energy	J
$E_{b,\mathrm{X_{AB}}}$	binding energy of the dissociation products of the complex $\mathrm{X_{AB}}$	J
E_C	conduction band energy	J
E_d	energy state of donor impurity in the band gap	J
E_F	Fermi energy	J
E_{max}	maximum of the electric field	$\mathrm{Vcm^{-1}}$
$E_{F,\mathrm{ext}}$	Fermi energy	J
$E_{F,\mathrm{int}}$	Fermi energy	J
$E_{F,n}$	Fermi energy in n-type material	J
E_{form}	formation energy	J
$\Delta E_{\mathrm{form}}^{E_F=0}$	formation energy at the center of the band gap, relative to the formation energy of the neutral charge state of the defect	J

Symbol	**Description**	**Unit**
$\Delta E_{\mathrm{form}}^{E_F=E_V}$	formation energy at the valence band energy at 0 K, relative to the formation energy of the neutral charge state of the defect	J
$E_{\mathrm{form}}^{\mathrm{X}^q}$	formation energy of defect X in the charge state q	J
$E_{F,p}$	Fermi energy in p-type material	J
E_G	band gap energy	J
$E_G(0\,\mathrm{K})$	energy gap at 0 K	J
E_I	energy of interface states	J
$E(\vec{k})$	band structure	J
ϵ	dielectric constant	Fm^{-1}
ϵ_r	relative permittivity	
$E_{q/q+1}$	ionization energy for the ionization of the charge state q to the charge state $q+1$	J
E_T	Energy state of recombination center in the Shockley-Read-Hall recombination process	J
$E_{\mathrm{tot}}(\mathrm{bulk})$	total energy of a super-cell of a perfect crystal	J
$E_{\mathrm{tot}}(\mathrm{X}^q)$	total energy of a super-cell including defect X in the charge state q	J
E_V	valence band energy	J
$\vec{E}$	energy	Vcm^{-1}
E_{X}	energy state of defect X	J
E_{X^q}	energy state of defect X at the charge state q	J
$E_{\mathrm{X}_0^{q+1}}$	ground state of the charge state q+1 of defect X	J
$E_{\mathrm{X}_0^q}$	ground state of the charge state q of defect X	J
$E_{\mathrm{X}_j^q}$	energy state of defect X at the excited state j of the charge state q	J
f_C	auxiliary function describing the influence of electric charges on the reaction of point defects	
f_{d}	attempt frequency of the dissociation process	s^{-1}
$f_{\mathrm{d}}^{\mathrm{AB}}$	attempt frequency of the dissociation process of X_{AB}	s^{-1}
$f(E)$	Fermi function, describes the temperature dependent occupation of energy states	
$f(E)_e$	approximation of the Fermi function for energies close to the conduction band	
$f(E)_h$	approximation of the Fermi function for energies close to the valence band	
Φ	proton flux	$\mathrm{H}^+\mathrm{cm}^{-2}\mathrm{s}^{-1}$
$f_{\mathrm{AB}}^{\mathrm{r}}$	attempt frequency of the reaction of $\mathrm{X}_{\mathrm{A}}+\mathrm{X}_{\mathrm{B}}\rightarrow\mathrm{X}_{\mathrm{AB}}$	s^{-1}
f_v	vibrational frequency of an impurity atom	s^{-1}
G	Gibbs free energy	J
g_a	Degeneracy of the valence band	

Symbol	Description	Unit
γ_{D_0}	geometrical coefficient for the calculation of $D_{0,\mathrm{X}}$, mostly $\gamma_{D_0} = 1$	
Γ_i	jump rate of jump type i	s^{-1}
γ_l	lattice angle	$^\circ$
G_{cc}	generation rate of charge carriers	$\mathrm{cm}^{-3}\mathrm{s}^{-1}$
g_d	Degeneracy of the conduction band	
H	enthalpy	J
I	electrical current or ion current	A
i	index	
I_{pn}	current across a *pn*-junction	A
I_{Schottky}	current across a Schottky-junction	A
$I_{S,pn}$	saturation current of a *pn*-junction	A
$I_{S,\mathrm{Schottky}}$	saturation current of a Schottky-junction	A
j_{diff}	diffusion current	Acm^{-2}
j_n	electron diffusion current	Acm^{-2}
j_p	hole diffusion current	Acm^{-2}
J_{X}	diffusion flux of impurity X	$\mathrm{cm}^{2}\mathrm{s}^{-1}$
k_d^{AB}	dissociation constant of the dissociation of X_{AB} to X_{A} and X_{B}	s^{-1}
$k_d^{\mathrm{A,XX}}$	rate constant of the dissociation of defect X_{A} to X_1 and X_2	$\mathrm{cm}^{-3}\mathrm{s}^{-1}$
$k_d^{\mathrm{B,AX}}$	rate constant of the dissociation of defect X_{B}, forming defect X_{A} and another defect X	$\mathrm{cm}^{-3}\mathrm{s}^{-1}$
k_r^{AB}	rate constant of the second-order reaction $\mathrm{X}_{\mathrm{A}}+\mathrm{X}_{\mathrm{B}}\rightarrow\mathrm{X}_{\mathrm{AB}}$	$\mathrm{cm}^{-3}\mathrm{s}^{-1}$
$k_{r,0}^{\mathrm{AB}}$	pre-factor in the Arrhenius equation describing the temperature dependence of the effective reaction rate constant k_r^{AB}	$\mathrm{cm}^{3}\mathrm{s}^{-1}$
$k_{r,\mathrm{S}}^{\mathrm{AB}}$	reaction constant of the second-order reaction $\mathrm{X}_{\mathrm{A}}+\mathrm{X}_{\mathrm{B}}\rightarrow\mathrm{X}_{\mathrm{AB}}$ after Smoluchowski [43]	$\mathrm{cm}^{3}\mathrm{s}^{-1}$
$k_{r,\mathrm{D}}^{\mathrm{AB}}$	reaction constant of the second-order reaction $\mathrm{X}_{\mathrm{A}}+\mathrm{X}_{\mathrm{B}}\rightarrow\mathrm{X}_{\mathrm{AB}}$ including Coulomb interaction after Debye [46]	$\mathrm{cm}^{3}\mathrm{s}^{-1}$
$k_{r,\mathrm{W}}^{\mathrm{AB}}$	reaction constant of the second-order reaction $\mathrm{X}_{\mathrm{A}}+\mathrm{X}_{\mathrm{B}}\rightarrow\mathrm{X}_{\mathrm{AB}}$ including the reaction probability after Waite [45]	$\mathrm{cm}^{3}\mathrm{s}^{-1}$
$k_r^{\mathrm{B_iH}}$	reaction rate constant of the reaction of an interstitial boron impurity $\mathrm{B_i}$ with hydrogen forming $\mathrm{B_iH}$	$\mathrm{cm}^{3}\mathrm{s}^{-1}$
$k_r^{\mathrm{B_iV}}$	reaction rate constant of the indirect recombination of a vacancy at a boron interstitial $\mathrm{B_i}$ in silicon	$\mathrm{cm}^{3}\mathrm{s}^{-1}$
$k_r^{\mathrm{B_sH}}$	reaction rate constant of the reaction of a substitutional boron impurity $\mathrm{B_s}$ with hydrogen forming $\mathrm{B_sH}$	$\mathrm{cm}^{3}\mathrm{s}^{-1}$
$k_r^{\mathrm{B_sI}}$	reaction rate constant of the reaction of a substitutional boron impurity $\mathrm{B_s}$ with a self-interstitial I in silicon	$\mathrm{cm}^{3}\mathrm{s}^{-1}$

Symbol	Description	Unit
$k_r^{\mathrm{B_sV}}$	reaction rate constant of the reaction of a substitutional boron impurity $\mathrm{B_s}$ with a vacancy V in silicon	$\mathrm{cm^3s^{-1}}$
$k_r^{\mathrm{B_sVI}}$	reaction rate constant of the indirect recombination of a self-interstitial at a boron vacancy complex $\mathrm{B_sV}$ in silicon	$\mathrm{cm^3s^{-1}}$
$k_r^{\mathrm{C_iH}}$	reaction rate constant of the reaction of a carbon interstitial $\mathrm{C_i}$ with hydrogen forming $\mathrm{C_iH}$	$\mathrm{cm^3s^{-1}}$
$k_r^{\mathrm{C_iHO}}$	reaction rate constant of the reaction of $\mathrm{C_iH}$ with oxygen forming $\mathrm{C_iOH}$	$\mathrm{cm^3s^{-1}}$
$k_r^{\mathrm{C_iHOH}}$	reaction rate constant of the reaction of $\mathrm{C_iH}$ with OH	$\mathrm{cm^3s^{-1}}$
$k_r^{\mathrm{C_iO}}$	reaction rate constant of the reaction of a carbon interstitial $\mathrm{C_i}$ with oxygen forming $\mathrm{C_iO}$	$\mathrm{cm^3s^{-1}}$
$k_r^{\mathrm{C_iOHH}}$	reaction rate constant of the reaction of $\mathrm{C_iOH}$ with another hydrogen atom	$\mathrm{cm^3s^{-1}}$
$k_r^{\mathrm{C_iOIH}}$	reaction rate constant of the reaction of $\mathrm{C_iOI}$ with hydrogen	$\mathrm{cm^3s^{-1}}$
$k_r^{\mathrm{C_sI}}$	reaction rate constant of the reaction of a substitutional carbon impurity $\mathrm{C_s}$ with a self-interstitial I in silicon forming $\mathrm{C_i}$	$\mathrm{cm^3s^{-1}}$
k_r^{eff}	effective reaction rate constant	m
$k_r^{\mathrm{HC_iO}}$	reaction rate constant of the reaction of hydrogen with $\mathrm{C_iO}$ forming $\mathrm{C_iOH}$	$\mathrm{cm^3s^{-1}}$
k_r^{HH}	reaction rate constant of the reaction of two hydrogen atoms forming $\mathrm{H_2}$ inside the silicon crystal	$\mathrm{cm^3s^{-1}}$
$k_r^{\mathrm{I_2I}}$	reaction rate constant of the reaction of a di-interstitial and a self-interstitials forming a tri-interstitial $\mathrm{I_3}$	$\mathrm{cm^3s^{-1}}$
$k_r^{\mathrm{I_2I_2}}$	reaction rate constant of the reaction of two di-interstitials forming $\mathrm{I_4}$	$\mathrm{cm^3s^{-1}}$
$k_r^{\mathrm{I_2V}}$	reaction rate constant of the indirect recombination of a di-interstitial and a vacancy forming a single self-interstitial	$\mathrm{cm^3s^{-1}}$
$k_r^{\mathrm{I_2V_2}}$	reaction rate constant of the recombination of a di-interstitial and a divacancy	$\mathrm{cm^3s^{-1}}$ nonumberlist
$k_r^{\mathrm{I_3I}}$	reaction rate constant of the reaction of a tri-interstitial and a self-interstitials forming $\mathrm{I_4}$	$\mathrm{cm^3s^{-1}}$
k_r^{IH}	reaction rate constant of the reaction of a self-interstitial with hydrogen forming IH in silicon	$\mathrm{cm^3s^{-1}}$
k_r^{II}	reaction rate constant of the reaction of two self-interstitials forming a di-interstitial $\mathrm{I_2}$	$\mathrm{cm^3s^{-1}}$
k_r^{IV}	reaction rate constant of the direct recombination of a self-interstitial I and a vacancy V in silicon	$\mathrm{cm^3s^{-1}}$
$k_r^{\mathrm{BC,A}}$	rate constant of the second-order reaction of the defects $\mathrm{X_B}$ and $\mathrm{X_C}$, forming $\mathrm{X_A}$	$\mathrm{cm^{-3}s^{-1}}$
$k_r^{\mathrm{AB,X}}$	rate constant of the second-order reaction of the defects $\mathrm{X_A}$ and $\mathrm{X_B}$, forming X	$\mathrm{cm^{-3}s^{-1}}$

Symbol	**Description**	**Unit**
k_r^{OH}	reaction rate constant of the reaction of interstitial oxygen with hydrogen forming OH inside the silicon crystal	$\mathrm{cm^3s^{-1}}$
$k_r^{\mathrm{OHC_i}}$	reaction rate constant of the reaction of OH with a carbon interstitial $\mathrm{C_i}$ forming $\mathrm{C_iOH}$	$\mathrm{cm^3s^{-1}}$
$k_r^{\mathrm{P_iH}}$	reaction rate constant of the reaction of an interstitial phosphor impurity $\mathrm{P_i}$ with hydrogen forming $\mathrm{P_iH}$	$\mathrm{cm^3s^{-1}}$
$k_r^{\mathrm{P_iV}}$	reaction rate constant of the indirect recombination of a vacancy at a phosphor interstitial $\mathrm{P_i}$ in silicon	$\mathrm{cm^3s^{-1}}$
$k_r^{\mathrm{P_sH}}$	reaction rate constant of the reaction of a substitutional phosphor impurity $\mathrm{P_s}$ with hydrogen forming $\mathrm{P_sH}$	$\mathrm{cm^3s^{-1}}$
$k_r^{\mathrm{P_sI}}$	reaction rate constant of the reaction of a substitutional phosphor impurity $\mathrm{P_s}$ with a self-interstitial I in silicon	$\mathrm{cm^3s^{-1}}$
$k_r^{\mathrm{P_sV}}$	reaction rate constant of the reaction of a substitutional phosphor impurity $\mathrm{P_s}$ with a vacancy V in silicon	$\mathrm{cm^3s^{-1}}$
$k_r^{\mathrm{V_2H}}$	reaction rate constant of the reaction of $\mathrm{V_2}$ with hydrogen	$\mathrm{cm^3s^{-1}}$
$k_r^{\mathrm{V_2I}}$	reaction rate constant of the indirect recombination of a divacancy and a self-interstitial forming a single vacancy	$\mathrm{cm^3s^{-1}}$
$k_r^{\mathrm{V_2OI}}$	reaction rate constant of the recombination of self-interstitials at $\mathrm{V_2O}$ in silicon	$\mathrm{cm^3s^{-1}}$
$k_r^{\mathrm{V_2OV}}$	reaction rate constant of the reaction of $\mathrm{V_2O}$ with another vacancy forming $\mathrm{V_3O}$ in silicon	$\mathrm{cm^3s^{-1}}$
$k_r^{\mathrm{V_2V}}$	reaction rate constant of the reaction of a divacancy and a vacancy forming a trivacancy $\mathrm{V_3}$	$\mathrm{cm^3s^{-1}}$
$k_r^{\mathrm{V_2V_2}}$	reaction rate constant of the reaction of two divacancies forming $\mathrm{V_4}$	$\mathrm{cm^3s^{-1}}$
$k_r^{\mathrm{V_3OI}}$	reaction rate constant of the recombination of self-interstitials at $\mathrm{V_3O}$ in silicon	$\mathrm{cm^3s^{-1}}$
$k_r^{\mathrm{V_3V}}$	reaction rate constant of the reaction of a trivacancy and a vacancy forming $\mathrm{V_4}$	$\mathrm{cm^3s^{-1}}$
k_r^{VH}	reaction rate constant of the reaction of a vacancy with hydrogen forming VH in silicon	$\mathrm{cm^3s^{-1}}$
k_r^{VH2H}	reaction rate constant of the reaction of $\mathrm{VH_2}$ with another hydrogen atom forming $\mathrm{VH_3}$ in silicon	$\mathrm{cm^3s^{-1}}$
k_r^{VHH}	reaction rate constant of the reaction of VH with another hydrogen atom forming $\mathrm{VH_2}$ in silicon	$\mathrm{cm^3s^{-1}}$
k_r^{VO}	reaction rate constant of the reaction of interstitial oxygen with vacancies forming VO in silicon	$\mathrm{cm^3s^{-1}}$
k_r^{VOH}	reaction rate constant of the reaction of VO with hydrogen forming VOH in silicon	$\mathrm{cm^3s^{-1}}$
k_r^{VOHH}	reaction rate constant of the reaction of VOH with another hydrogen atom forming $\mathrm{VOH_2}$ in silicon	$\mathrm{cm^3s^{-1}}$
k_r^{VOI}	reaction rate constant of the recombination of self-interstitials at VO in silicon	$\mathrm{cm^3s^{-1}}$
k_r^{VOV}	reaction rate constant of the reaction of VO with another vacancy forming $\mathrm{V_2O}$ in silicon	$\mathrm{cm^3s^{-1}}$

Symbol	Description	Unit
$k_r^{\mathrm{VP_sI}}$	reaction rate constant of the indirect recombination of a self-interstitial at a phosphor vacancy complex $\mathrm{VP_s}$ in silicon	$\mathrm{cm^3s^{-1}}$
k_r^{VV}	reaction rate constant of the reaction of two vacancies forming a divacancy $\mathrm{V_2}$	$\mathrm{cm^3s^{-1}}$
$\vec{k}$	electron wave vector	
k_x	reciprocal crystal coordinate	
k_y	reciprocal crystal coordinate	
k_z	reciprocal crystal coordinate	
λ	wavelength	$\mathrm{m^-1}$
$L_{D,\mathrm{cc}}$	charge carrier diffusion length	m
L_{D_H}	diffusion length of hydrogen	m
$L_{D,n}$	diffusion length of electrons	m
$L_{D,p}$	diffusion length of holes	m
L_{D_X}	diffusion length of impurity X	m
m	mass	kg
m^*	effective mass of a charge carrier with respect to the electron rest mass m_e	
m^*_{hh}	effective mass of holes in the hh-band	kg
m^*_{ed}	effective mass of electrons in the conduction band for the calculation of $D(E)$	kg
m^*_l	longitudinal effective mass of electrons in the conduction band	kg
m^*_{lh}	effective mass of holes in the lh-band	kg
m^*_{so}	effective mass of holes in the so-band	kg
m^*_t	longitudinal effective mass of electrons in the conduction band	kg
μ	mobility	$\mathrm{cm^2(Vs)^{-1}}$
$\mu_L(300\,\mathrm{K})$	mobility at 300 K	$\mathrm{cm^2(Vs)^{-1}}$
μ_cc	charge carrier mobility	$\mathrm{cm^2(Vs)^{-1}}$
μ_{ccs}	carrier-carrier scattering mobility	$\mathrm{cm^2(Vs)^{-1}}$
μ_e	electron mobility	$\mathrm{cm^2(Vs)^{-1}}$
μ_H	chemical potential of hydrogen	J
μ_h	hole mobility	$\mathrm{cm^2(Vs)^{-1}}$
μ_I	impurity mobility	$\mathrm{cm^2(Vs)^{-1}}$
μ_i	chemical potential of species i	J
μ_k	periodic part of the wavefunction	
μ_L	lattice mobility	$\mathrm{cm^2(Vs)^{-1}}$
μ_r	relative permeability	
μ_X	ion mobility of defect X	$\mathrm{cm^2(Vs)^{-1}}$
μ_X	ion mobility of defect $\mathrm{X_A}$	$\mathrm{cm^2(Vs)^{-1}}$
n	concentration of free electrons in the conduction band	$\mathrm{cm^{-3}}$
$N^\pm$	Concentration of ionized impurities	$\mathrm{cm^{-3}}$
n_0	concentration of electrons at thermodynamic equilibrium	$\mathrm{cm^{-3}}$

Symbol	Description	Unit
n_{SRH}	concentration of electrons occupying trap states in the Shockley-Read-Hall recombination process	cm^{-3}
p_{SRH}	concentration of holes occupying trap states in the Shockley-Read-Hall recombination process	cm^{-3}
N_a	acceptor concentration	cm^{-3}
N_a^-	concentration of ionized acceptors	cm^{-3}
∇	gradient	
N_{band}	effective number of states in an energy band	cm^{-3}
N_C	effective number of states in the conduction band	cm^{-3}
$N_{SO}(300\,\mathrm{K})$	effective number of states in the so-band at 300 K	cm^{-3}
$N_V(300\,\mathrm{K})$	effective number of states in the valence band at 300 K	cm^{-3}
N_{CC}	number of charge carriers per unit area	cm^{-2}
n_{cc}	charge carrier concentration	cm^{-3}
N_{CC}^0	number of charge carriers per unit area before the start of the anneal	cm^{-2}
N_{CC}^{sh}	number of charge carriers per unit area in the shoulder	cm^{-2}
$N_{CC}^{\mathrm{sh},0}$	number of charge carriers in the shoulder of the c_{CC}-profile per unit area before the start of the anneal	cm^{-2}
N_d	donor concentration	cm^{-3}
N_d^+	concentration of ionized donors	cm^{-3}
N_{def}	number of defects	
v_{e}	stoichiometric number of an educt in a defect reaction	
N_{hh}	effective number of states in the hh-band of silicon	cm^{-3}
N_i	number of atoms of type i	
n_i	charge carrier concentration at thermal equilibrium	cm^{-3}
N_{lh}	effective number of states in the lh-band of silicon	cm^{-3}
v_{p}	stoichiometric number of a product in a defect reaction	
n_{p0}	concentration of minority electrons in p-type material at thermodynamic equilibrium	cm^{-3}
N_{so}	effective number of states in the so-band of silicon	cm^{-3}
N_T	concentration of recombination centers	cm^{-3}
N_V	sum of the effective number of states in the lh-band and the hh-band of silicon	cm^{-3}
$N_C(300\,\mathrm{K})$	effective number of states in the conduction band at 300 K	cm^{-3}
N_{X}	implanted dose of X	cm^2
N_x	number of increments in space	
P	probability	
p	concentration of free holes in the valence band	cm^{-3}
p_0	concentration of holes at thermodynamic equilibrium	cm^{-3}
ϕ_b	barrier height of a Schottky junction	J
p_{n0}	concentration of minority holes in n-type material at thermodynamic equilibrium	cm^{-3}
$p_{\mathrm{AB}}^{\mathrm{o}}$	probability, that $\mathrm{X_A}$and $\mathrm{X_B}$ are oriented properly for the reaction to $\mathrm{X_{AB}}$	

Symbol	**Description**	**Unit**
Ψ	wave function	
P_{X^q}	probability that the defect X is in the charge state q_X	
$P_{\mathrm{X}^q_j}$	occupation probability of the energy state $E_{\mathrm{X}^q_j}$	
Q	charge	C
q	charge	C
q^{eff}	effective charge state	
$q^{\mathrm{eff}}_{\mathrm{I}}$	effective charge state of the silicon self-interstitial	
$q^{\mathrm{eff}}_{\mathrm{O}}$	effective charge state of the oxygen interstitial	
$q^{\mathrm{eff}}_{\mathrm{V}}$	effective charge state of the silicon vacancy	
$q^{\mathrm{eff}}_{\mathrm{V}_2}$	effective charge state of the silicon divacancy	
$q^{\mathrm{eff}}_{\mathrm{X}}$	effective charge state of the defect X	
q_X	charge state of defect X	C
Δr	distance parameter in the calculation of the reaction probability	m
R_{Auger}	recombination rate of charge carriers through Auger recombination	$\mathrm{cm}^{-3}\mathrm{s}^{-1}$
$r_{\leftarrow}$	backward reaction rate	$\mathrm{cm}^{-3}\mathrm{s}^{-1}$
r_c	capture radius	m
r_c^0	capture radius for the reaction of neutral defects	m
r_c^{AB}	capture radius for the reaction of $\mathrm{X_A}+\mathrm{X_B}\rightarrow\mathrm{X_{AB}}$	m
R_{cc}	recombination rate of charge carriers	$\mathrm{cm}^{-3}\mathrm{s}^{-1}$
$r^{\mathrm{sub}}_{c_{CC}}$	rate of the formation of thermal donors in the substrate material	$\mathrm{cm}^{-3}\mathrm{s}^{-1}$
$r^{\mathrm{sub},0}_{c_{CC}}$	Arrhenius pre-factor of the rate of the formation of thermal donors in the substrate material	$\mathrm{cm}^{-3}\mathrm{s}^{-1}$
r_c^{eff}	effective capture radius	m
r_d^{AB}	dissociation rate of the dissociation $\mathrm{X_{AB}}-\ >\mathrm{X_A}+\mathrm{X_B}$	$\mathrm{cm}^{-3}\mathrm{s}^{-1}$
R_{direct}	recombination rate of charge carriers through direct band to band recombination	$\mathrm{cm}^{-3}\mathrm{s}^{-1}$
$r_{\rightarrow}$	forward reaction rate	$\mathrm{cm}^{-3}\mathrm{s}^{-1}$
ρ	resistivity	Ω m
R^*	Richardson constant	$\mathrm{A(mK)}^{-2}$
$r_{N_{CC}}$	rate of the change in the number of charge carriers N_{CC}	$\mathrm{cm}^{-2}\mathrm{s}^{-1}$
$r_{N^{\mathrm{sh}}_{CC}}$	rate of the change in the number of charge carriers in the shoulder of the c_{CC}-profile N^{sh}_{CC}	$\mathrm{cm}^{-2}\mathrm{s}^{-1}$
$r_{N^{\mathrm{sh},0}_{CC}}$	Arrhenius pre-factor of the rate of the change in the number of charge carriers in the shoulder of the c_{CC}-profile N^{sh}_{CC}	$\mathrm{cm}^{-2}\mathrm{s}^{-1}$
r_p	projected range od ions in ion implantation	m
r_r^{AB}	reaction rate of the reaction $\mathrm{X_A}+\mathrm{X_B}\rightarrow\mathrm{X_{AB}}$	$\mathrm{cm}^{-3}\mathrm{s}^{-1}$
R_{SRH}	recombination rate of charge carriers through Shockley-Read-Hall recombination	$\mathrm{cm}^{-3}\mathrm{s}^{-1}$
$r_{\mathrm{V_{max}}}$	position of the maximum vacancy concentration	m

Symbol	Description	Unit
S	entropy	JK^{-1}
s_0	surface recombination velocity	$\mathrm{cm\ s}^{-1}$
σ_d	donor formation efficiency	
σ_{r_p}	standard deviation of the projected range	m
$\sigma_{T,n}$	capture cross section of electrons in the Shockley-Read-Hall recombination process	m^2
$\sigma_{T,p}$	capture cross section of holes in the Shockley-Read-Hall recombination process	m^2
s_n	surface recombination velocity of electrons	$\mathrm{cm\ s}^{-1}$
s_p	surface recombination velocity of holes	$\mathrm{cm\ s}^{-1}$
T	temperature	K
t	time	s
τ_Au	charge carrier lifetime from Auger recombination	s
τ_direct	charge carrier lifetime from direct band to band recombination	s
τ_eff	effective charge carrier lifetime	s
$\tau_{h,\mathrm{direct}}$	hole lifetime from direct band to band recombination	s
τ_SRH	charge carrier lifetime from Shockley-Read-Hall recombination	s
$\tau_{\mathrm{SRH},n}$	electron lifetime from Shockley-Read-Hall recombination	s
$\tau_{\mathrm{SRH},p}$	hole lifetime from Shockley-Read-Hall recombination	s
τ_sur	charge carrier lifetime from surface recombination	s
$\tau_{\mathrm{sur},n}$	electron lifetime from surface recombination	s
$\tau_{\mathrm{sur},p}$	electron lifetime from surface recombination	s
T_MN	Meyer-Neldel temperature	K
τ_{sc}	average time between two scattering events	s
t_sim	simulated time	s
V	potential, voltage	V
v	velocity	$\mathrm{cm\ s}^{-1}$
V_b	bias voltage	V
V_{bi}	built-in potential at an electrical junction	V
v_d	drift velocity	$\mathrm{cm\ s}^{-1}$
V_n	potential on the n-type side of an electrical junction	V
V_p	potential on the p-type side of an electrical junction	V
v_{th}	thermal charge carrier velocity	$\mathrm{cm\ s}^{-1}$
$v_{th,n}$	thermal electron velocity	$\mathrm{cm\ s}^{-1}$
$v_{th,p}$	thermal hole velocity	$\mathrm{cm\ s}^{-1}$
W	width of the space charge region (depletion width)	m
x	distance	m
x_0	implantation depth	m
x_c	crystal coordinate	
ξ	auxiliary variable	

Symbol	Description	Unit
ξ_m	magnetic susceptibility	
X_μ	auxiliary variable for the calculation of the mobility of charge carriers in silicon	
x_n	extent of the depletion width at a *pn*-junction into the *n*-type material	m
x_p	extent of the depletion width at a *pn*-junction into the *p*-type material	m
y_c	crystal coordinate	
z_c	crystal coordinate	
Z_{gr}	grand canonical partition function	

Constants

Constant	Description	Value
a_{Si}	lattice constant of silicon	$0.543\,\mathrm{nm}$
$c_{\mathrm{l},0}$	speed of light	$2.9979 \times 10^{8}\,\mathrm{ms}^{-1}$
e	elementary charge	$1.6022 \times 10^{-19}\,\mathrm{C}$
ϵ_0	vacuum permittivity	$8.8542 \times 10^{-12}\,\mathrm{Fm}^{-1}$
E_{SO}	energy difference between the top of the so band and E_V	$0.044\,\mathrm{eV}$
h	Planck constant	$6.6261 \times 10^{-34}\,\mathrm{Js}$
$\hbar$	reduced Planck constant $\hbar = \frac{h}{2\pi}$	$1.0546 \times 10^{-34}\,\mathrm{Js}$
k_B	Boltzmann constant	$1.3806 \times 10^{-23}\,\mathrm{JK}^{-1}$
m_e	electron rest mass	$9.1094 \times 10^{-31}\,\mathrm{kg}$
m_{H^+}	proton rest mass	$1.673 \times 10^{27}\,\mathrm{kg}$
π	Pi	3.14159

Chemicals Defects and Particles

Symbol	Description
B	boron
$\mathrm{B_2H_6}$	diborane
BCI	defect complex consisting of a boron impurity, a carbon impurity and a silicon self-interstitial, structural isomer of $\mathrm{B_iC_s}$
$\mathrm{BCl_3}$	boron trichloride

Symbol	**Description**
β^-	beta particle (high energy electron)
BH	defect complex consisting of one boron and one hydrogen atom
$\mathrm{B_i}$	interstitial boron impurity
$\mathrm{B_{i_2}}$	defect complex consisting of two interstitial boron impurities
$\mathrm{B_{i2}B_s}$	defect complex consisting of two interstitial boron impurities and a substitutional boron impurity
$\mathrm{B_{i_2}B_{s_2}}$	defect complex consisting of two interstitial boron impurities and two substitutional boron impurities
$\mathrm{B_iB_s}$	defect complex consisting of an interstitial boron impurity and a substitutional boron impurity
$\mathrm{B_iB_sH}$	defect complex consisting of an interstitial and a substitutional boron impurity and a hydrogen atom
$\mathrm{B_iC_i}$	defect complex consisting of an interstitial boron impurity and an interstitial carbon impurity
$\mathrm{B_iC_s}$	defect complex consisting of an interstitial boron impurity and a substitutional carbon impurity
$\mathrm{B_iH}$	defect complex of interstitial boron and hydrogen
$\mathrm{B_iH_2}$	defect complex of interstitial boron and two hydrogen atoms
$\mathrm{B_iH_3}$	defect complex of interstitial boron and three hydrogen atoms
$\mathrm{B_iI}$	defect complex consisting of an interstitial boron impurity and a silicon self-interstitial
$\mathrm{B_iI}_n$	group of defect complexes consisting of an interstitial boron impurity and n silicon self-interstitials
$\mathrm{B_{i_m}B_{s_n}}$	defect complexes consisting of m interstitial boron impurities and n substitutional boron impurities
$\mathrm{B_iO}$	defect complex consisting of an interstitial boron impurity and an interstitial oxygen impurity
$\mathrm{B_s}$	substitutional boron impurity
$\mathrm{B_s^-}$	negative charge state of the substitutional boron impurity
$\mathrm{B_{s_2}}$	defect complex consisting of two substitutional boron impurities
$\mathrm{B_{s_3}}$	defect complex consisting of three substitutional boron impurities
$\mathrm{B_sC_i}$	defect complex consisting of an interstitial carbon impurity and a substitutional boron impurity, structural isomer of $\mathrm{B_iC_s}$
$\mathrm{B_sH}$	defect complex of substitutional boron and hydrogen
$\mathrm{B_sI}$	defect complex consisting of a substitutional boron impurity and a silicon self-interstitial
$\mathrm{B_sO}$	defect complex consisting of a substitutional boron impurity and an interstitial oxygen impurity
$\mathrm{B_sO_2}$	defect complex consisting of a substitutional boron impurity and two interstitial oxygen atoms
$\mathrm{B_sV}$	defect complex consisting of a substitutional boron impurity and a silicon vacancy
$\mathrm{B_sV_2}$	defect complex consisting of a substitutional boron impurity and two silicon vacancies

Symbol	Description
C	carbon
CO	carbon monoxide
$\mathrm{C_i}$	interstitial carbon
$\mathrm{C_i^+}$	positive charge state of interstitial carbon
$\mathrm{C_i^-}$	negative charge state of interstitial carbon
$\mathrm{C_i^0}$	neutral charge state of interstitial carbon
$\mathrm{C_iC_s}$	defect complex consisting of an interstitial carbon and a substitutional carbon atom
$\mathrm{C_iC_sH}$	defect complex consisting of an interstitial and a substitutional carbon impurity and a hydrogen atom
$\mathrm{C_iC_sI}$	defect complex consisting of an interstitial carbon, a substitutional carbon atom and a silicon self-interstitial
$\mathrm{C_iC_sI_2}$	defect complex consisting of an interstitial carbon, a substitutional carbon atom and two silicon self-interstitials
$\mathrm{C_iH}$	defect complex consisting of an interstitial carbon impurity and a hydrogen atom
$\mathrm{C_iI}$	defect complex consisting of a carbon interstitial carbon and a self-interstitial
$\mathrm{C_iI}_n$	defect complex consisting of a carbon interstitial carbon and n self-interstitials
$\mathrm{C_iO}$	interstitial carbon-oxygen complex
$\mathrm{C_iO_2H}$	defect complex consisting of a carbon interstitial, two oxygen interstitial and a hydrogen atom
$\mathrm{C_iOH}$	defect complex consisting of a carbon interstitial, an oxygen interstitial and a hydrogen atom
$\mathrm{C_iOH_2}$	defect complex consisting of a carbon interstitial, an oxygen interstitial and two hydrogen atoms
$\mathrm{C_iOI}$	defect complex consisting of a carbon interstitial, an oxygen interstitial and a self-interstitial
$\mathrm{C_iOI_2}$	defect complex consisting of a carbon interstitial, an oxygen interstitial and two self-interstitial
$\mathrm{C_iOIH}$	defect complex consisting of a carbon interstitial, an oxygen interstitial, a self-interstitial and a hydrogen atom
$\mathrm{C_iP_s}$	defect complex consisting of an interstitial carbon and a substitutional phosphorus atom
$\mathrm{C_s}$	substitutional carbon
$\mathrm{C_sH}$	defect complex consisting of an substitutional carbon impurity and a hydrogen atom
$\mathrm{C_sO}$	substitutional carbon-oxygen complex
$\mathrm{C_sO_2}$	defect complex consisting of a substitutional carbon and two oxygen interstitials
$\mathrm{C_sO_3}$	defect complex consisting of a substitutional carbon and three oxygen interstitials
$\mathrm{C_sOH}$	defect complex consisting of a substitutional carbon, an oxygen interstitial and a hydrogen atom
γ	gamma particle
Au	gold

Symbol	Description
H	atomic hydrogen
H^+	positive charge state of atomic hydrogen
H^-	negative charge state of atomic hydrogen
^1H	atomic hydrogen
^2H	deuterium
H_2	molecular hydrogen
H_2^*	molecular hydrogen at a body-centered-anti-bonding position
H_2O	di-hydrogen-oxide, water
H_2^T	molecular hydrogen at a tetragonal interstitial position
^3H	tritium
HCl	hydrochloric acid
HF	hydrofluoric acid
HNO_3	nitric acid
$HSiCl_3$	trichlorosilane
I	silicon self-interstitial
I^+	positive charge state of the silicon self-interstitial I
I^{2+}	double positive charge state of the silicon self-interstitial I
I^-	negative charge state of the silicon self-interstitial I
I^{2-}	double negative charge state of the silicon self-interstitial I
I^0	neutral charge state of the silicon self-interstitial I
I_2	silicon di-interstitial
I_2^{2+}	double positive charge state of the di-interstitial I_2 in silicon
I_2^0	neutral charge state of the di-interstitial I_2 in silicon
I_2H	defect complex consisting of two self-interstitials and a hydrogen atom
I_2O	defect complex consisting of silicon two self-interstitials and one oxygen interstitial
I_2O_2	defect complex consisting of silicon two self-interstitials and two oxygen interstitial
I_2O_3	defect complex consisting of silicon two self-interstitials and three oxygen interstitial
I_3	silicon tri-interstitial
I_3^+	positive charge state of the tri-interstitial I_3 in silicon
I_3^{2+}	double positive charge state of the tri-interstitial I_3 in silicon
I_3^0	neutral charge state of the tri-interstitial I_3 in silicon
I_4	tetra-interstitial defect in silicon
I_5	penta-interstitial defect in silicon
I_6	hexa-interstitial defect in silicon
I_7	interstitial cluster consisting of seven self-interstitials
I_8	octa-interstitial defect in silicon
IH	self-interstitial-hydrogen defect complex
I_2H_2	defect complex consisting of two self-interstitials and two hydrogen atoms
IH_2	defect complex consisting of a self-interstitial and two hydrogen atoms
I_2H_3	defect complex consisting of two self-interstitials and three hydrogen atoms
IH_3	defect complex consisting of a self-interstitial and three hydrogen atoms

Symbol	Description
I_mH_n	group of defect complexes consisting m self-interstitials and n hydrogen atoms
I_nO_m	defect complex consisting of silicon self-interstitials and oxygen interstitials
IO	self-interstitial-oxygen complex
IO_2	self-interstitial-di-oxygen complex
IO_3	defect complex consisting of silicon one self-interstitials and three oxygen interstitial
IX	defect complex of a self-interstitial and some defect complex X
n	neutron
O^0	Neutral charge state of interstitial oxygen in silicon
O_2	oxygen dimer
O_2H_2	defect complex consisting of two oxygen and two hydrogen atoms
OH	oxygen hydrogen defect complex
OH_2	defect complex consisting of an oxygen and two hydrogen atoms
O_nV_m	defect complex consisting of n oxygen interstitials and m vacancies
O	oxygen
P_2VO	defect complex consisting of two phosphor impurities, an oxygen impurity and a vacancy
$^{31}_{15}P$	single stable phosphor isotope with 16 neutrons
Pd	palladium
PCI	defect complex consisting of a substitutional phosphor impurity, a substitutional carbon impurity and a silicon seld interstitial; configurational isomer of P_iC_s
PCl_3	phosphor trichloride
PH	defect complex consisting of one phosphor and one hydrogen atom
PH_3	phosphine
P_i	interstitial phosphor impurity
P_iC_s	defect complex consisting of an interstitial phosphor impurity and a substitutional carbon impurity
P_iH	defect complex consisting of an interstitial phosphor impurity and a hydrogen impurity
P_iI	defect complex consisting of an interstitial phosphor impurity and a silicon self interstitial
P_nV	defect complex consisting of n substitutional phosphor impurities and a lattice vacancy
P_s	substitutional phosphor impurity
P_sC_i	defect complex consisting of a substitutional phosphor impurity and an interstitial carbon impurity; configurational isomer of P_iC_s
P_sH	defect complex of substitutional phosphor and hydrogen
P_sO	defect complex consisting of a substitutional phosphorus impurity and an interstitial oxygen impurity
$^{28}_{14}Si$	stable silicon isotope with 14 neutrons at a natural abundance of ~ 92 %
$^{30}_{14}Si$	stable silicon isotope with 15 neutrons at a natural abundance of ~ 5 %

Symbol	**Description**
${}^{30}_{14}\mathrm{Si}$	stable silicon isotope with 16 neutrons at a natural abundance of ~ 3 %
${}^{31}_{14}\mathrm{Si}$	unstable silicon isotope with 17 neutrons
$\mathrm{Si}_{\mathrm{mono}}$	mono crystalline silicon
SiO_2	quartz
$\mathrm{Si}_{\mathrm{poly}}$	poly crystalline silicon
$\mathrm{Si}_{\mathrm{raw}}$	raw silicon
T_t	transition temperature
V	silicon vacancy
V^{+}	positive charge state of the silicon vacancy V
V^{2+}	double positive charge state of the silicon vacancy V
V^{-}	negative charge state of the silicon vacancy V
V^{2-}	double negative charge state of the silicon vacancy V
V^{0}	ground state or neutral state of the silicon vacancy V
V_2	silicon divacancy
V_2^{+}	positive charge state of the silicon divacancy V_2
V_2^{2+}	double positive charge state of the silicon divacancy V_2
V_2^{-}	negative charge state of the silicon divacancy V_2
V_2^{2-}	double negative charge state of the silicon divacancy V_2
V_2^{0}	ground state or neutral state of the silicon divacancy V_2
$\mathrm{V}_2\mathrm{H}$	defect complex consisting of two vacancies and a hydrogen atom
$\mathrm{V}_2\mathrm{H}_2$	defect complex consisting of two vacancies and two hydrogen atoms
$\mathrm{V}_2\mathrm{H}_3$	defect complex consisting of two vacancies and three hydrogen atoms
$\mathrm{V}_2\mathrm{H}_4$	defect complex consisting of two vacancies and four hydrogen atoms
$\mathrm{V}_2\mathrm{H}_5$	defect complex consisting of two vacancies and five hydrogen atoms
$\mathrm{V}_2\mathrm{H}_6$	defect complex consisting two vacancies and six hydrogen atoms
$\mathrm{V}_2\mathrm{O}$	divacancy-oxygen complex
$\mathrm{V}_2\mathrm{O}_2$	defect complex consisting of two vacancies and two oxygen atoms
$\mathrm{V}_2\mathrm{O}_3$	defect complex consisting of two vacancies and three oxygen atoms
$\mathrm{V}_2\mathrm{OH}$	defect complex consisting of two vacancies, an oxygen and a hydrogen atom
$\mathrm{V}_2\mathrm{P}_{\mathrm{s}}$	defect complex consisting of a substitutional phosphor impurity and two vacancies
V_3	trivacancy
V_3^{+2}	double positive charge state of the tri-vacancy V_3 in silicon
V_3^{2-}	double negative charge state of the tri-vacancy V_3 in silicon
V_3^{0}	neutral charge state of the tri-vacancy V_3 in silicon
$\mathrm{V}_3\mathrm{H}_8$	defect complex consisting three vacancies and six hydrogen atoms
$\mathrm{V}_3\mathrm{O}$	trivacancy-oxygen complex
$\mathrm{V}_3\mathrm{O}_2$	defect complex consisting of three vacancies and two oxygen atoms
$\mathrm{V}_3\mathrm{O}_3$	defect complex consisting of three vacancies and three oxygen atoms
V_4	cluster of four silicon vacancies
V_5	cluster of five silicon vacancies
V_6	cluster of six silicon vacancies
$\mathrm{V}_6\mathrm{H}_{12}$	defect complex consisting six vacancies and twelve hydrogen atoms

Symbol	**Description**
VH	vacancy hydrogen defect complex
VH_2	defect complex consisting of a vacancy and two hydrogen atoms
VH_3	defect complex consisting of a vacancy and three hydrogen atoms
VH_4	defect complex consisting of a vacancy and four hydrogen atoms
VH_5	defect complex consisting of a vacancy and five hydrogen atoms
VH_6	defect complex consisting of a vacancy and six hydrogen atoms
V_mH_n	group of defect complexes consisting m vacancies and n hydrogen atoms
V_mO_n	defect complex consisting of m vacancies and n oxygen interstitials
VO	vacancy-oxygen complex
VO_2	vacancy-di-oxygen complex
VO_3	defect complex consisting of a vacancies and three oxygen atoms
VOH	defect complex consisting of a vacancy, an oxygen and a hydrogen atom
VOH_2	defect complex consisting of a vacancy an oxygen and two hydrogen atoms
VP_s	defect complex consisting of a substitutional phosphor impurity and a vacancy
VP_{s_2}	defect complex consisting of two substitutional phosphor impurities and a vacancy
VX	defect complex of a vacancy and some defect complex X
VX_s	vacancy-impurity complex
X	point-defect or defect complex
X	impurity atom
X^*	activated or transition state of the impurity atom X
X^+	defect X in the charge state $q_X = +1$
X^{2+}	defect X in the charge state $q_X = +2$
X^-	defect X in the charge state $q_X = -1$
X^{2-}	defect X in the charge state $q_X = -2$
X^0	ground state or neutral state of the impurity atom X
X_A	defect X_A
X_{AB}	defect X_{AB}
X_{AB^*}	transition state of the defect X_{AB}
X_B	defect X_B
X_C	defect X_C
X_e	educt in a defect reaction
X_i	interstitial impurity
X_p	product in a defect reaction
X^q	charge state q of the impurity atom X
X^{q+1}	charge state q+1 of the impurity atom X
X_s	substitutional impurity
X_sV	defect complex consisting of a substitutional impurity and a vacancy

A Publication List

M. Faccinelli, S. Kirnstoetter, W. Schustereder, J. G. Laven and P. Hadley "An EBIC and SRP Study of High Temperature Thermal Donors in Proton Implanted p-Type Magnetic Czochralski Silicon", *Physica Status Solidi C*, vol. 11, no. 11-12, pp. 1583-1588, 2014, doi:10.1002/pssc.201400045

M. Faccinelli, M. Jelinek, T. Wuebben, J. G. Laven, H.-J. Schulze and P. Hadley, "Simulation of the proton implantation process in silicon", *Physica Status Solidi C*, vol. 13, no. 10-12, pp. 750-755, 2016, doi: 10.1002/pssc.201600038

S. Kirnstoetter, M. Faccinelli, P. Hadley, R- Job, W. Schustereder, J- G. Laven and H.-J. Schulze "Investigation of Doping Type Conversion and Diffusion Length Extraction of Proton Implanted Silicon by EBIC", *ECS Transcriptions*, vol. 50, no. 5, pp. 115-120, 2013, doi: 10.1149/05005.0115ecst

S. Kirnstoetter, M. Faccinelli, W. Schustereder, J. G. Laven, H.-J. Schulze and P. Hadley "Hydrogen decoration of radiation damage induced defect structures", *AIP Conference Proceedings*, v. 1583, no. 1, pp. 51-55, 2014, doi: 10.1063/1.4865603

S. Kirnstoetter, M. Faccinelli, M. Jelinek, W. Schustereder, J. G. Laven, H.-J. Schulze and P. Hadley "Multiple Proton Implantations into Silicon: A Combined EBIC and SRP Study", *Solid State Phenomena*, vol. 205-206, pp. 311-316, 2014, doi: 10.4028/www.scientific.net/SSP.205-206.311

S. Kirnstoetter, M. Faccinelli, C. Gspan, W. Grogger, M. Jelinek, W. Schustereder, J. G. Laven, H.-J. Schulze and P. Hadley "High dose proton implantations into silicon: a combined EBIC, SRP and TEM study", *Physica Status Solidi C*, vol. 11, no. 11-12, pp. 1545-1550, 2014, doi: 10.1002/pssc.201400051

S. Kirnstoetter, M. Faccinelli, C. Gspan, W. Grogger, M. Jelinek, W. Schustereder, J. G. Laven, H.-J. Schulze and P. Hadley "Depletion of superjunction power MOSFETs visualized by electron beam induced current and voltage contrast measurements", *Physica Status Solidi C*, vol. 11, no. 11-12, pp. 1707-1710, 2014, doi: 10.1002/pssc.201400050

S. Kirnstoetter, M. Faccinelli, P. Hadley, M. Jelinek, W. Schustereder, J. G. Laven and H.-J. Schulze "H^+ implantation profile formation in m:Cz and Fz silicon", *20th International Conference on Ion Implantation Technology (IIT)*, pp. 1-4, 2014, doi: 10.1109/IIT.2014.6940055

A. Kraxner, F. Roger, B. Loeffler, M. Faccinelli, S. Kirnstoetter, R. Minixhofer and P. Hadley “Investigations on CMOS photodiodes using scanning electron microscopy with electron beam induced current measurements”, *Scanning Microscopies 2014*, vol. 9236, pp. 923607, 2014, doi: 10.1117/12.2066124

A. Kraxner, F. Roger, B. Loeffler, M. Faccinelli, E. Fisslthaler, R. Minixhofer and P Hadley “An EBIC Model for TCAD Simulation to Determine the Surface Recombination Rate in Semiconductor Devices”, *IEEE Transactions on eletron devices*, vol. 63, no. 11, pp. 4395-4401, 2016, doi: 10.1109/TED.2016.2606703

B SRP-Measurements of Proton Implanted and Annealed Silicon Samples

B.1 Sample S1: m:Cz-Si, 2.5 MeV, 5×10^{14} $H^{+}cm^{-2}$

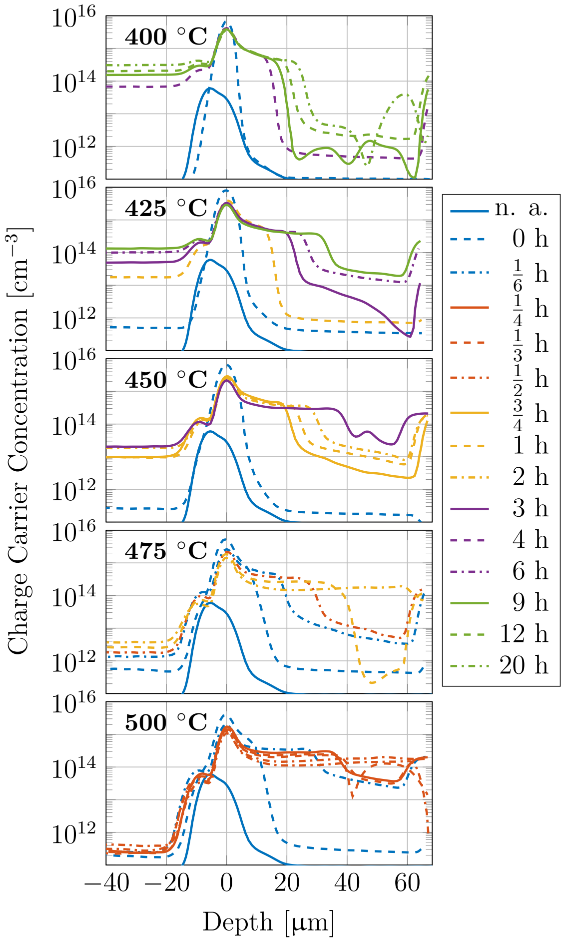

(a) SRP-measurements

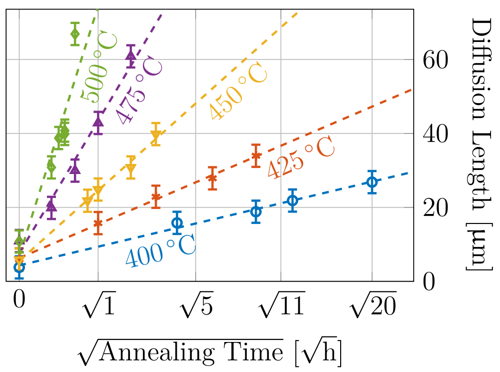

(b) Diffusion length vs. annealing time

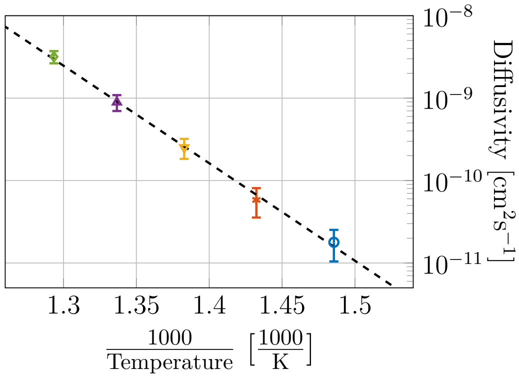

(c) Diffusivity vs. inverse temperature

Figure B.1.1: Measurements and calculations of the hydrogen diffusivity in sample S1.

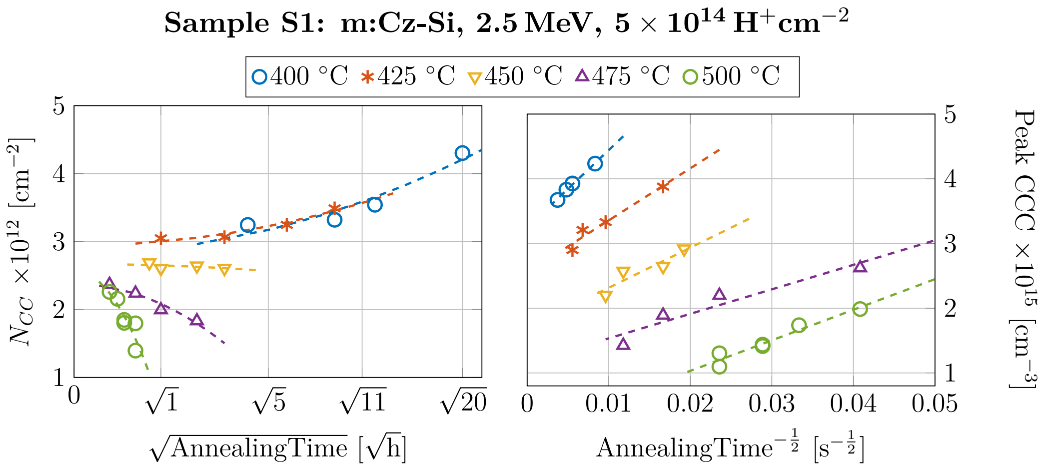

(a) Number of charge carriers in proton implanted region.

(b) CCC at implantation peak.

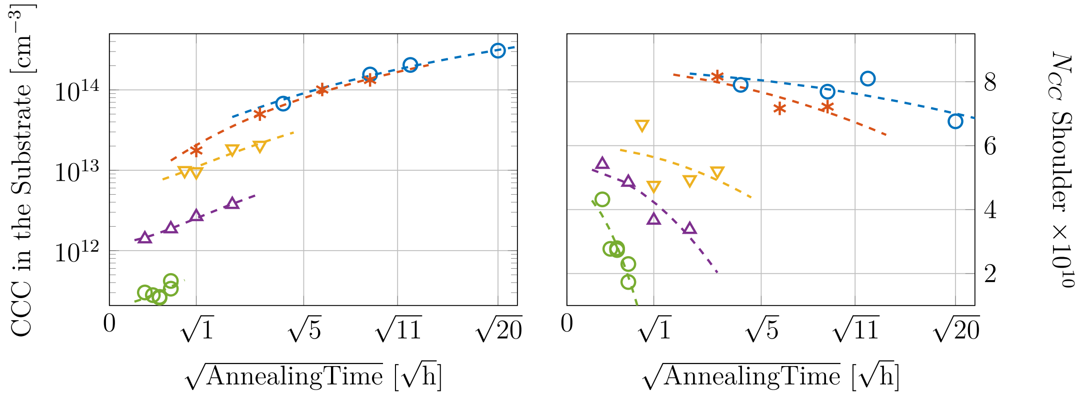

(c) CCC in the substrate material

(d) N_{CC} in the shoulder.

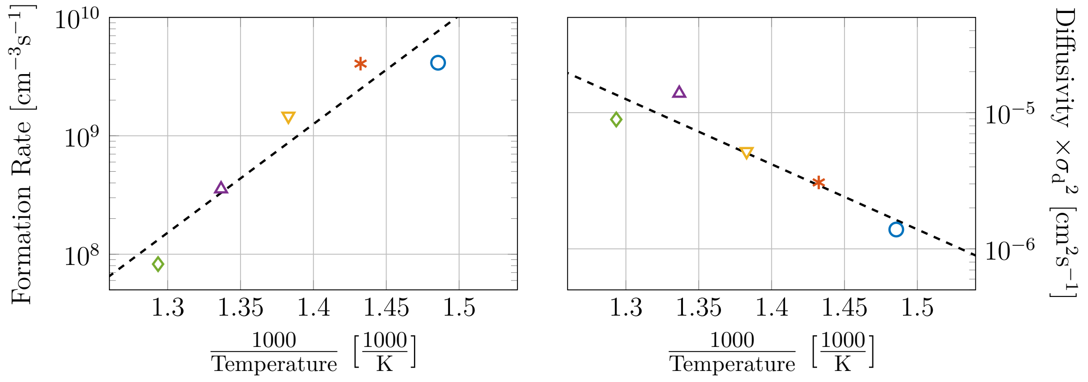

(e) Formation rate of charge carriers in the substrate material

(f) Hydrogen diffusivity at the implantation peak.

Figure B.1.2: CCC in different regions of sample S1 after different anneals.

B.2 Sample S2: m:Cz-Si, 2.5 MeV, 1×10^{15} $H^{+}cm^{-2}$

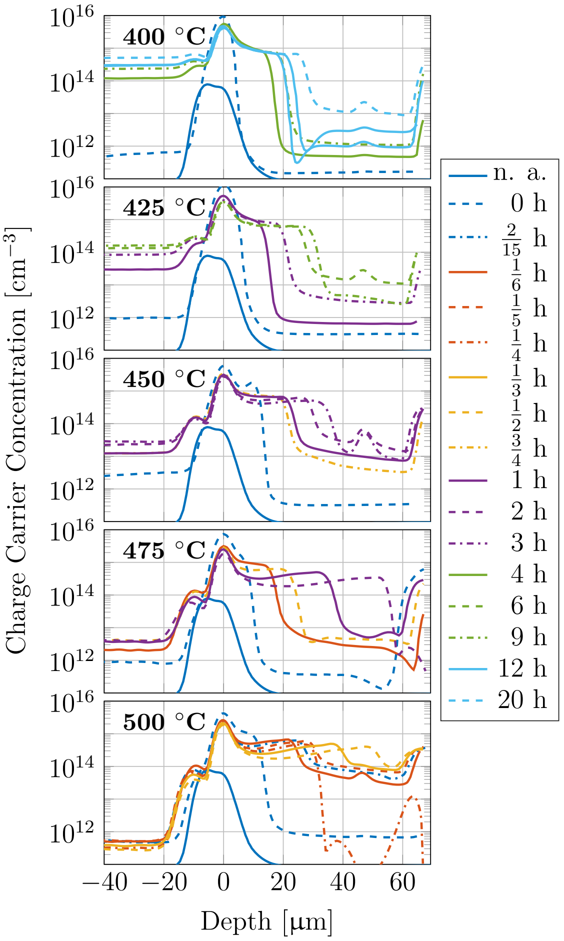

(a) SRP-measurements

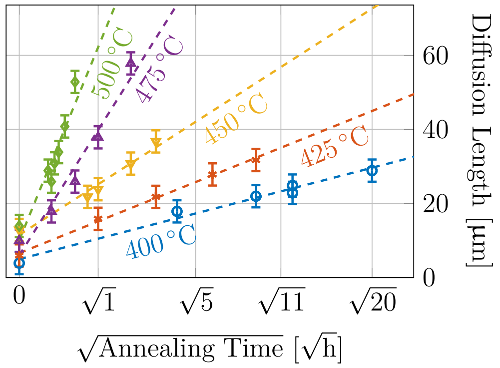

(b) Diffusion length vs. annealing time

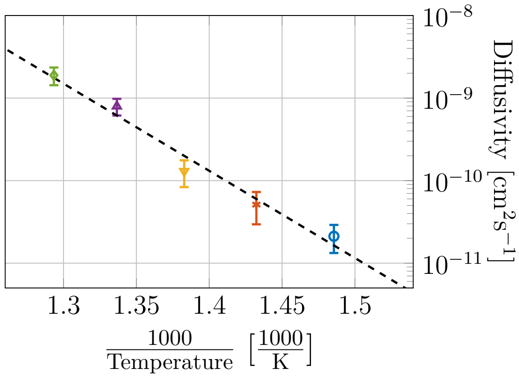

(c) Diffusivity vs. inverse temperature

Figure B.2.1: Measurements and calculations of the hydrogen diffusivity in sample S2.

Sample S2: m:Cz-Si, 2.5 MeV, 1×10^{15} H$^+$cm^{-2}

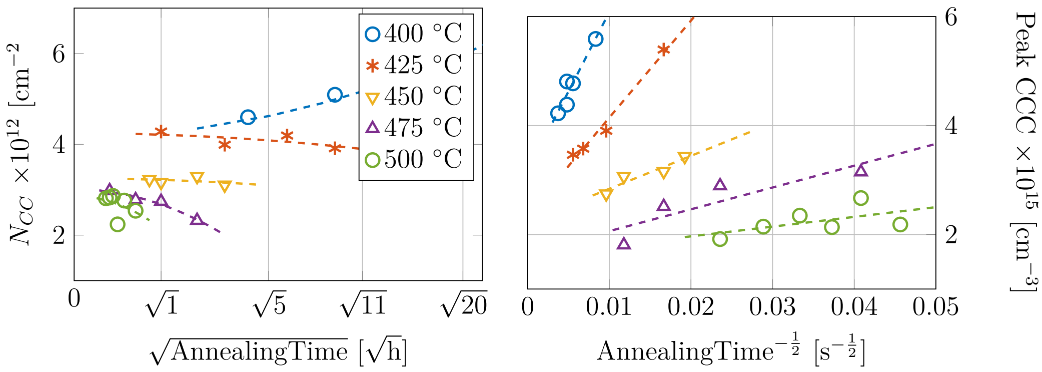

(a) N_{CC} in proton implanted region.

(b) CCC at implantation peak.

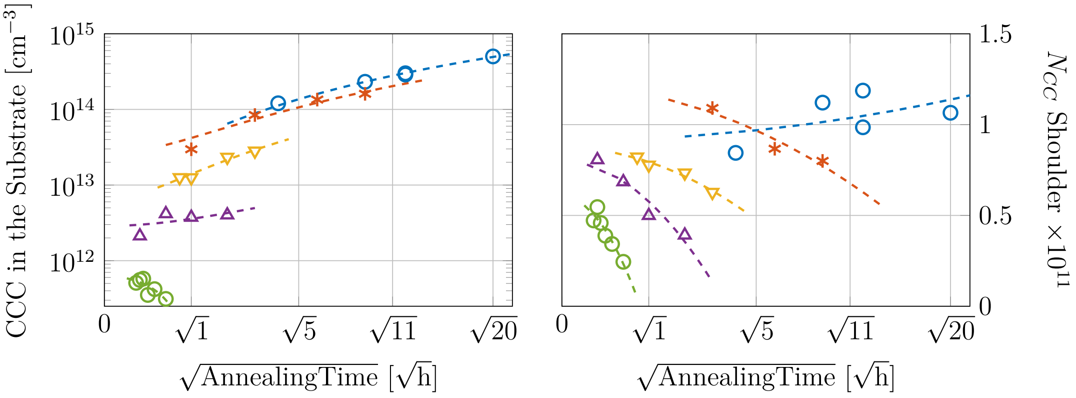

(c) CCC in the substrate material

(d) N_{CC} in the shoulder.

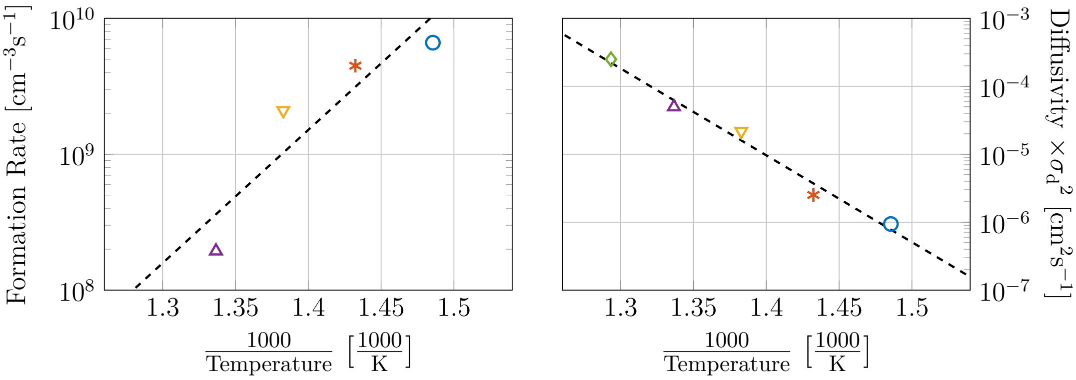

(e) Formation rate of charge carriers in the substrate material

(f) Hydrogen diffusivity at the implantation peak.

Figure B.2.2: CCC in different regions of sample S2 after different anneals.

B.3 Sample S3: m:Cz-Si, 2.5 MeV, 5×10^{15} $\mathrm{H^{+}cm^{-2}}$

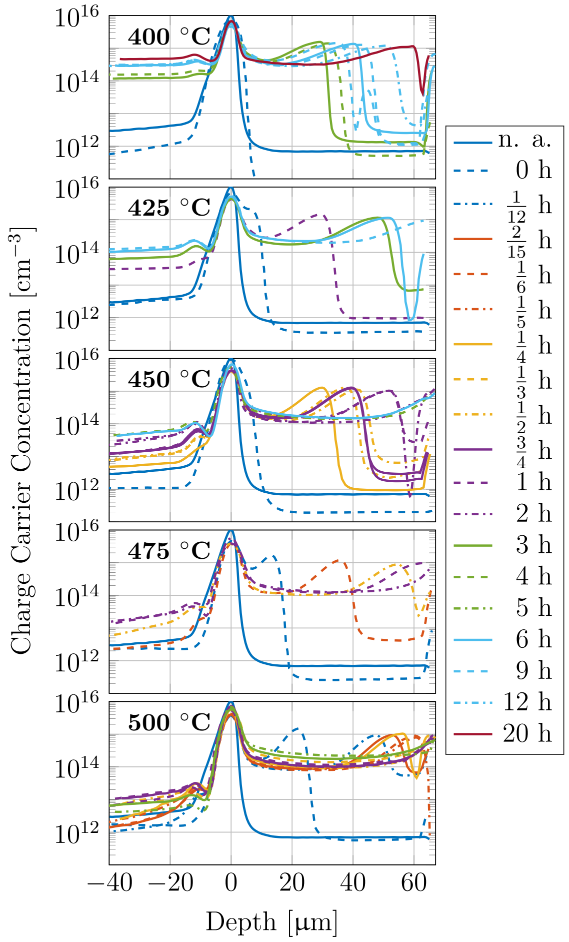

(a) SRP-measurements

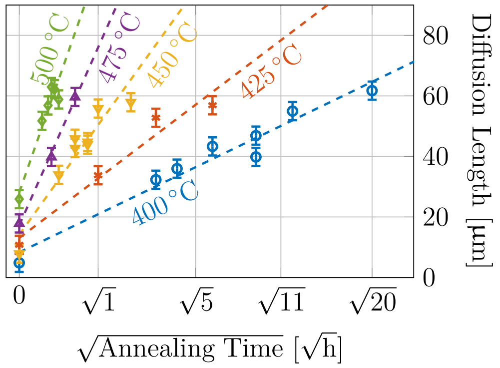

(b) Diffusion length vs. annealing time

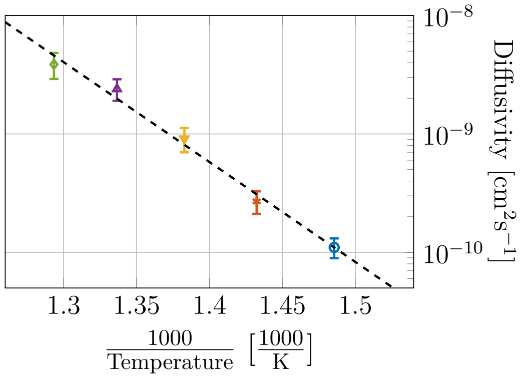

(c) Diffusivity vs. inverse temperature

Figure B.3.1: Measurements and calculations of the hydrogen diffusivity in sample S3.

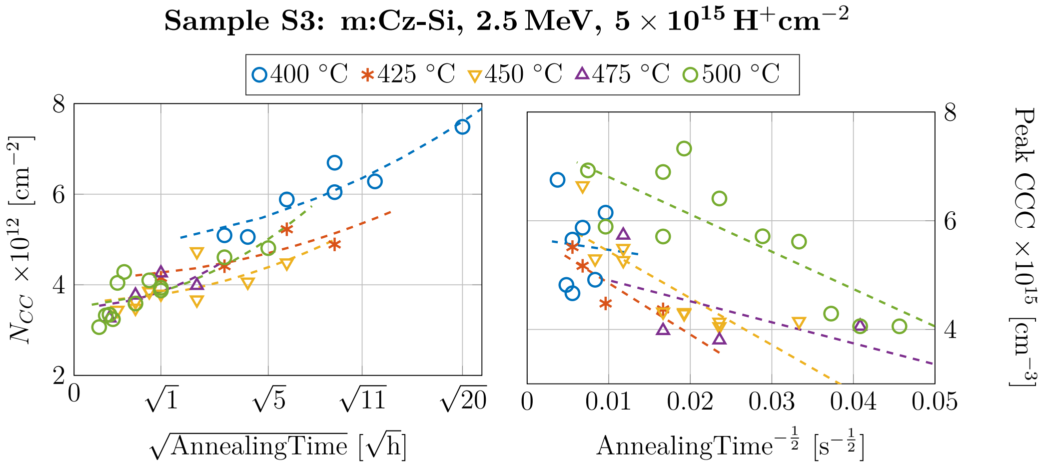

(a) N_{CC} in proton implanted region.

(b) CCC at implantation peak.

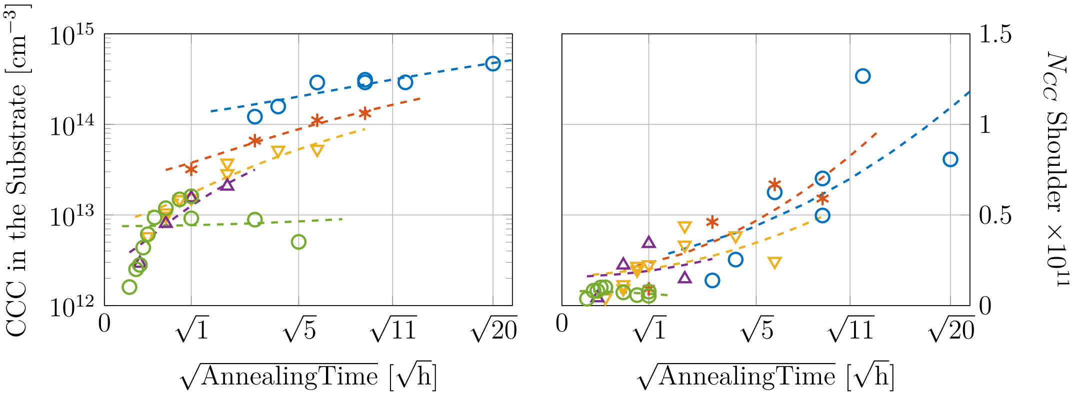

(c) CCC in the substrate material

(d) N_{CC} in the shoulder.

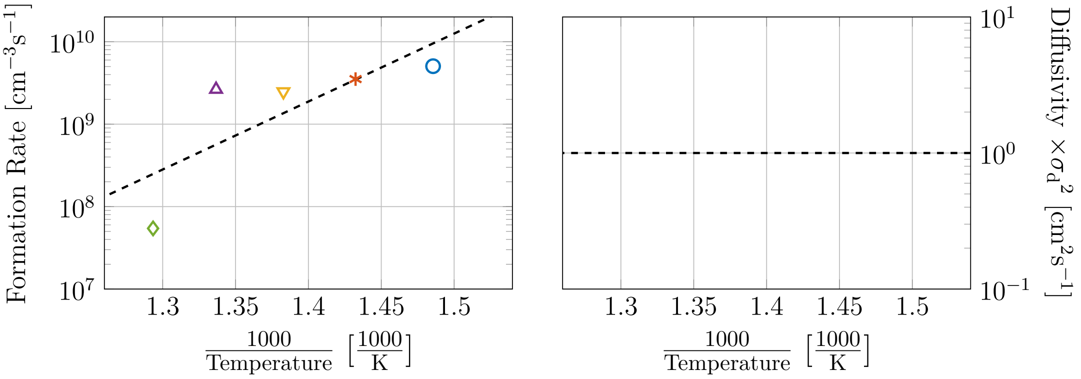

(e) Formation rate of charge carriers in the substrate material

(f) Hydrogen diffusivity at the implantation peak.

Figure B.3.2: CCC in different regions of sample S3 after different anneals.

B.4 Sample S4: m:Cz-Si, 2.5 MeV, $1 \times 10^{16}\,\mathrm{H^+cm^{-2}}$

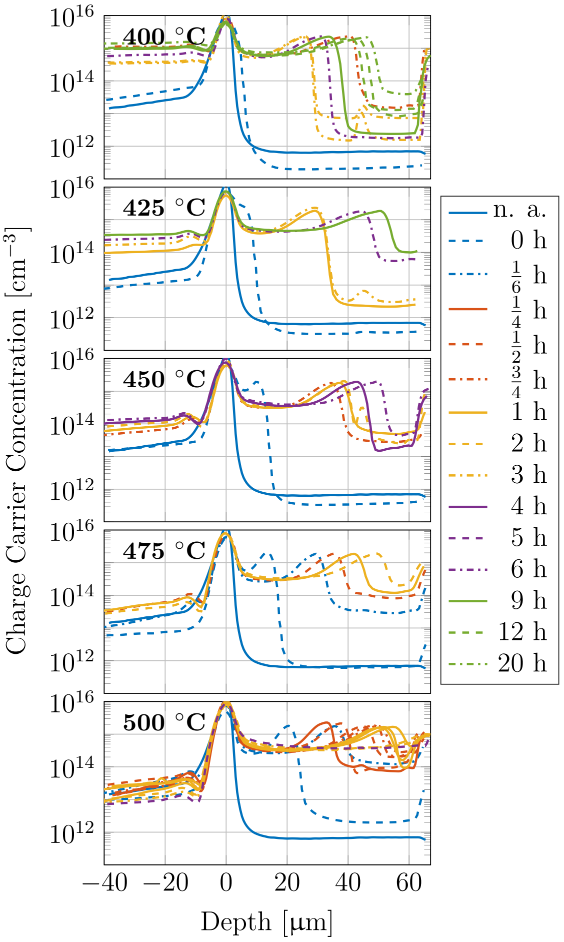

(a) SRP-measurements

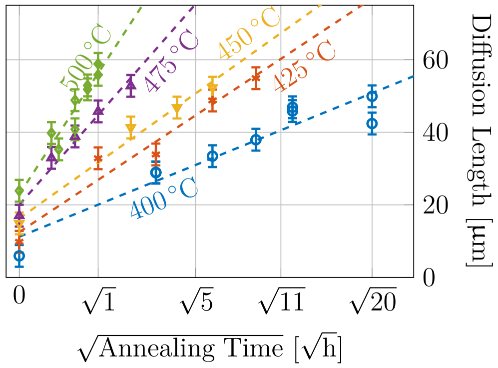

(b) Diffusion length vs. annealing time

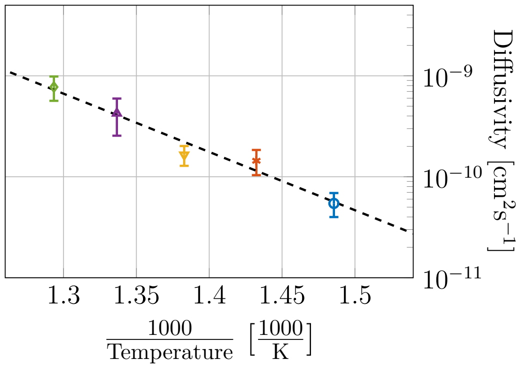

(c) Diffusivity vs. inverse temperature

Figure B.4.1: Measurements and calculations of the hydrogen diffusivity in sample S4.

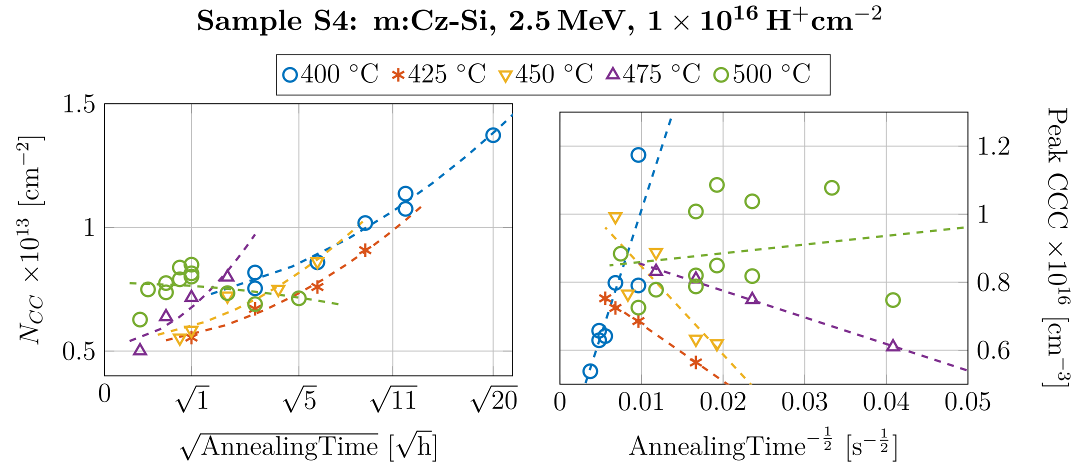

(a) N_{CC} in proton implanted region. **(b)** CCC at implantation peak.

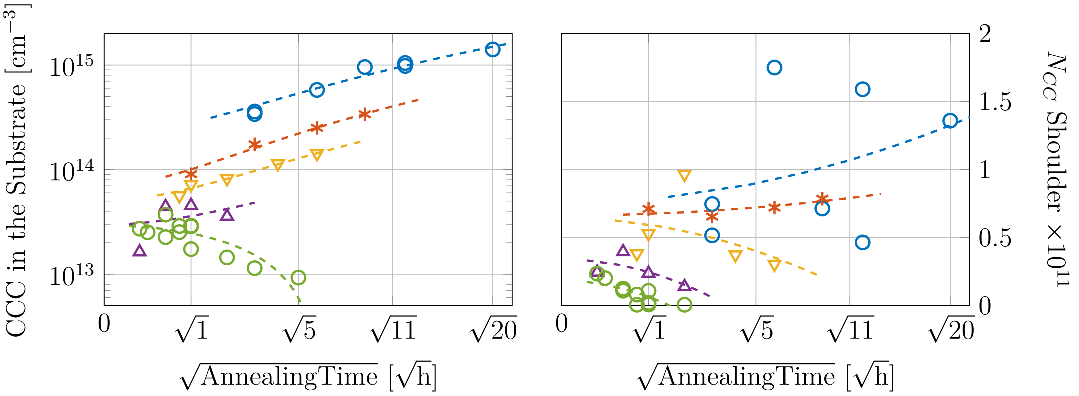

(c) CCC in the substrate material **(d)** N_{CC} in the shoulder.

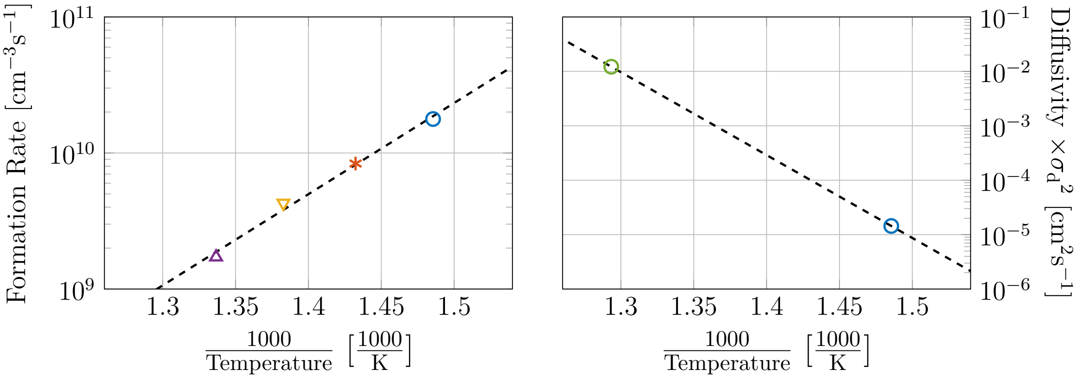

(e) Formation rate of charge carriers in the substrate material **(f)** Hydrogen diffusivity at the implantation peak.

Figure B.4.2: CCC in different regions of sample S4 after different anneals.

B.5 Sample S5: m:Cz-Si, 4 MeV, 1×10^{14} H^{+}cm^{-2}

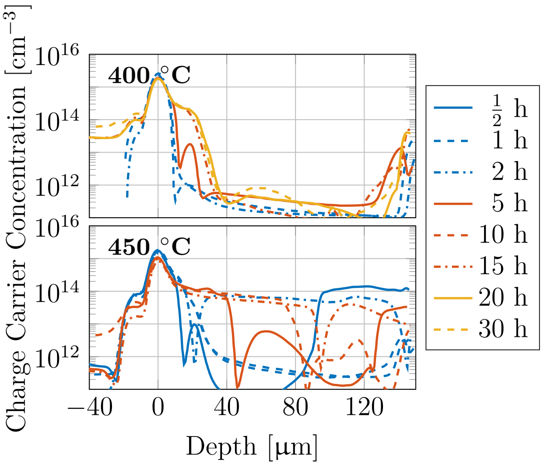

(a) SRP-measurements

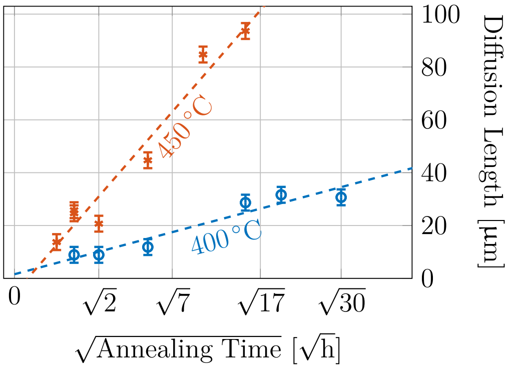

(b) Diffusion length vs. annealing time

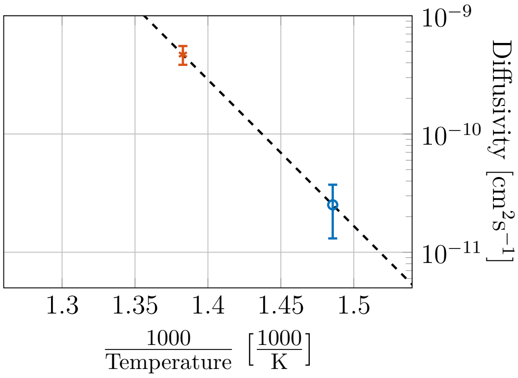

(c) Diffusivity vs. inverse temperature

Figure B.5.1: Measurements and calculations of the hydrogen diffusivity in sample S5.

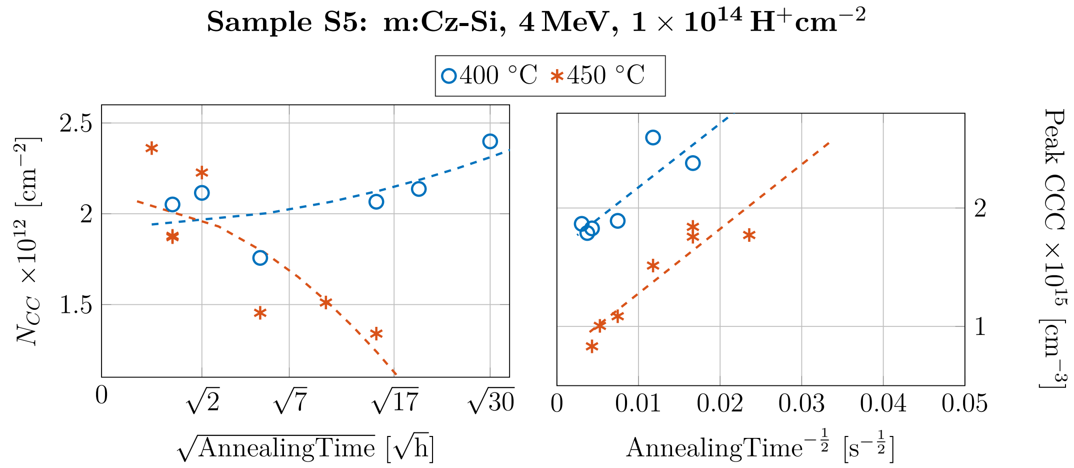

(a) N_{CC} in proton implanted region.

(b) CCC at implantation peak.

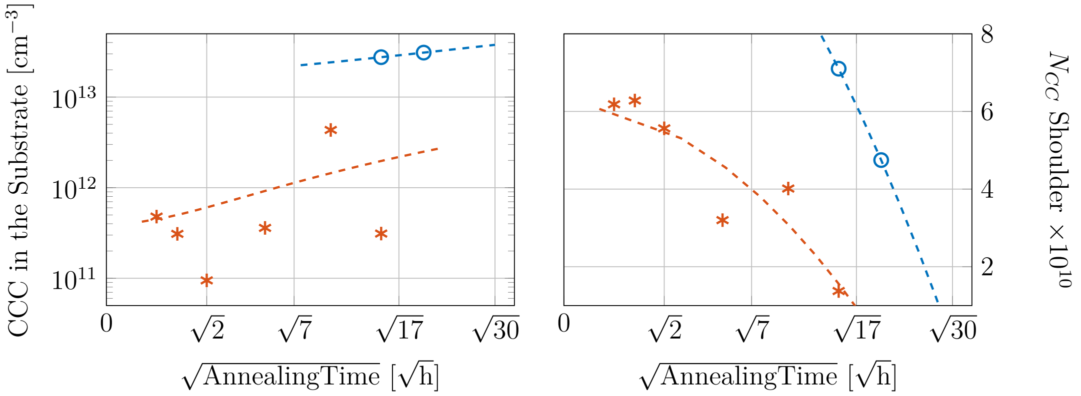

(c) CCC in the substrate material

(d) N_{CC} in the shoulder.

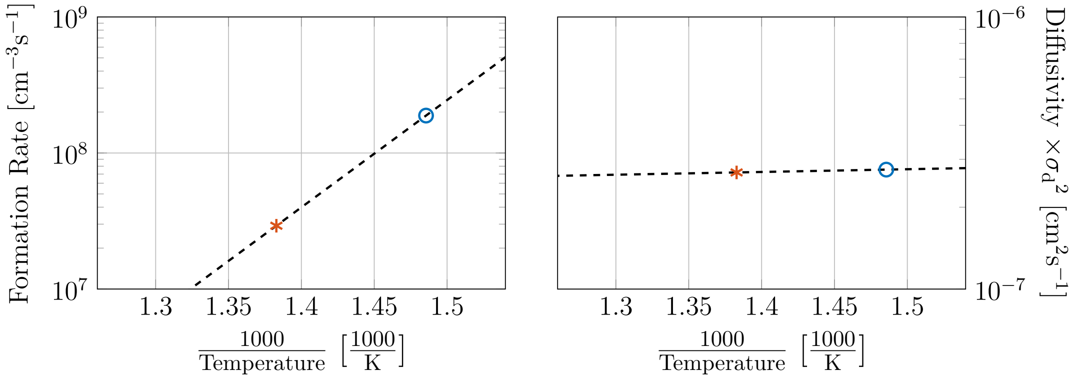

(e) Formation rate of charge carriers in the substrate material

(f) Hydrogen diffusivity at the implantation peak.

Figure B.5.2: CCC in different regions of sample S5 after different anneals.

B.6 Sample S6: m:Cz-Si, 4 MeV, 1×10^{15} H^+cm^{-2}

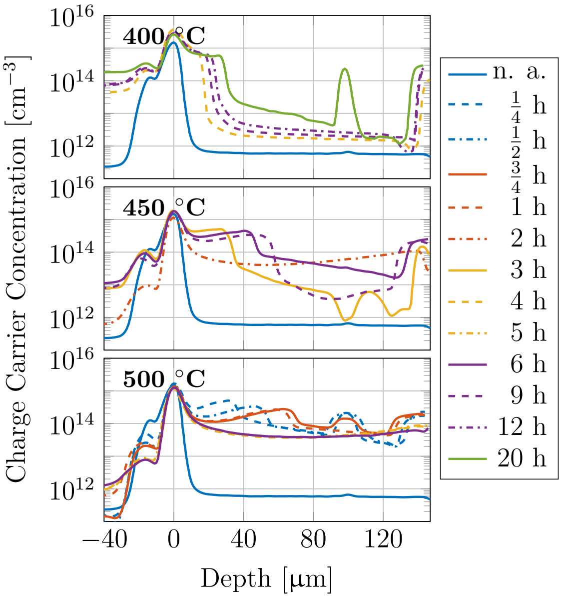

(a) SRP-measurements

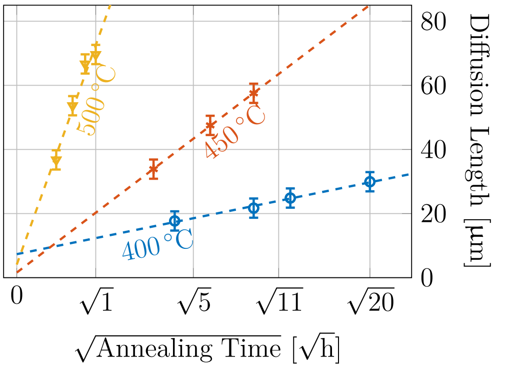

(b) Diffusion length vs. annealing time

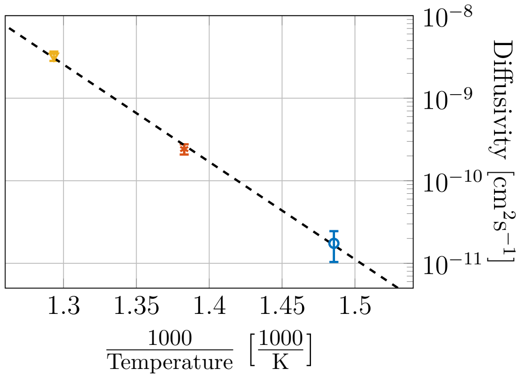

(c) Diffusivity vs. inverse temperature

Figure B.6.1: Measurements and calculations of the hydrogen diffusivity in sample S6.

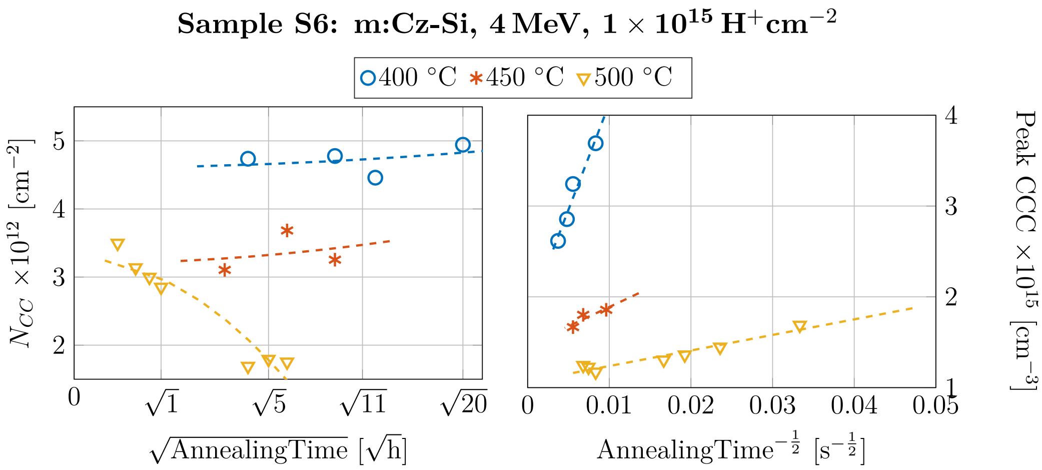

(a) N_{CC} in proton implanted region.

(b) CCC at implantation peak.

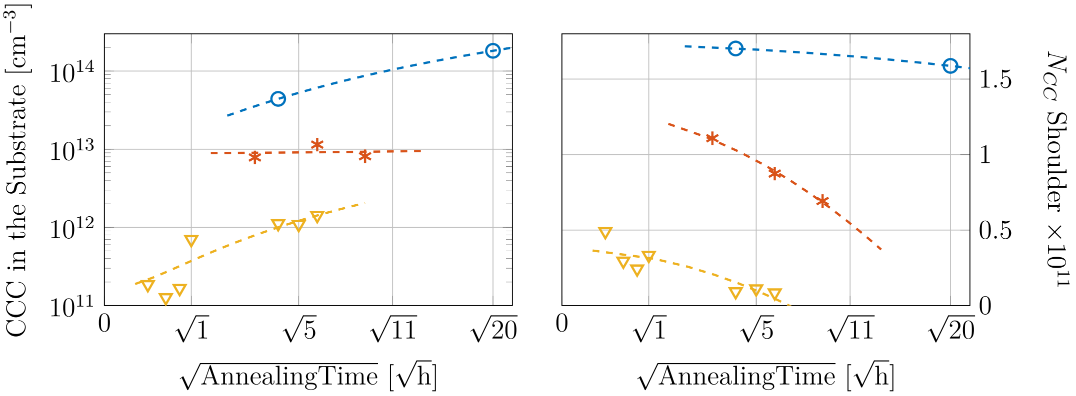

(c) CCC in the substrate material

(d) N_{CC} in the shoulder.

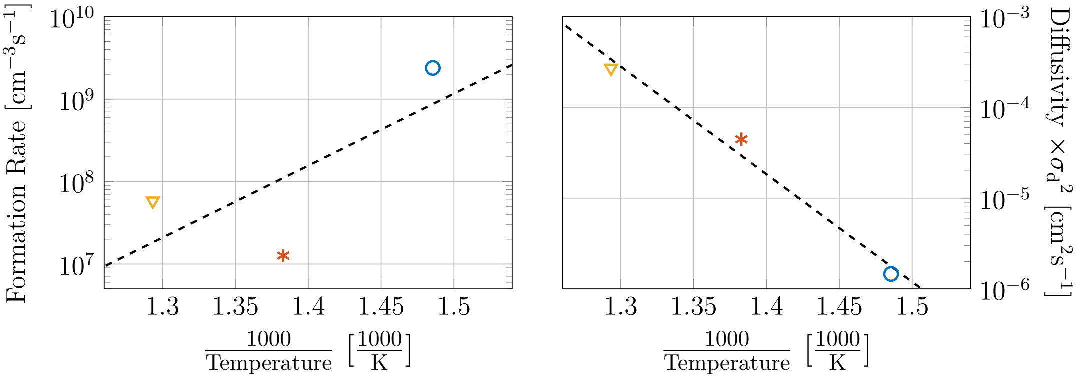

(e) Formation rate of charge carriers in the substrate material

(f) Hydrogen diffusivity at the implantation peak.

Figure B.6.2: CCC in different regions of sample S6 after different anneals.

B.7 Sample S7: Low impurity m:Cz-Si, 2.5 MeV, $1 \times 10^{14}\ \mathrm{H^{+}cm^{-2}}$

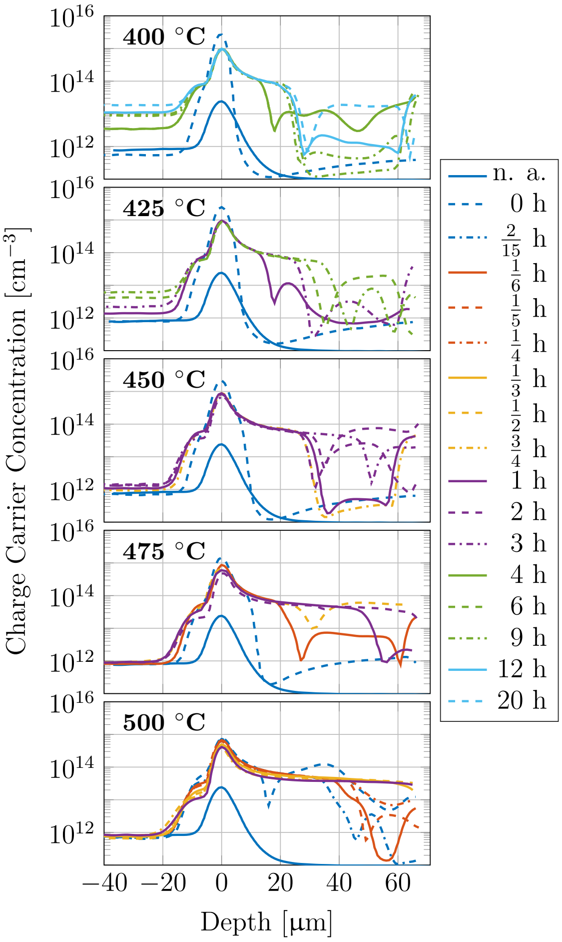

(a) SRP-measurements

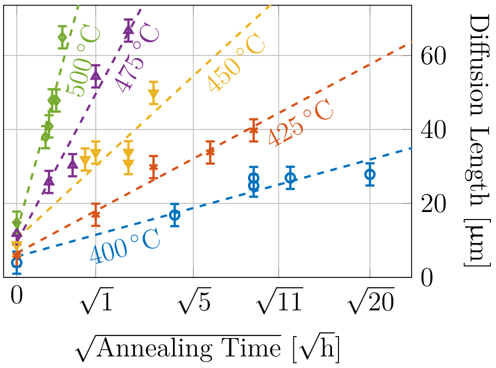

(b) Diffusion length vs. annealing time

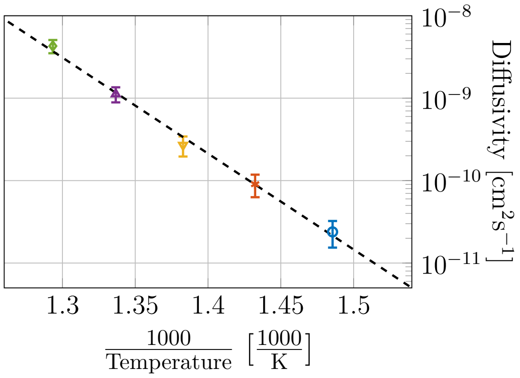

(c) Diffusivity vs. inverse temperature

Figure B.7.1: Measurements and calculations of the hydrogen diffusivity in sample S7.

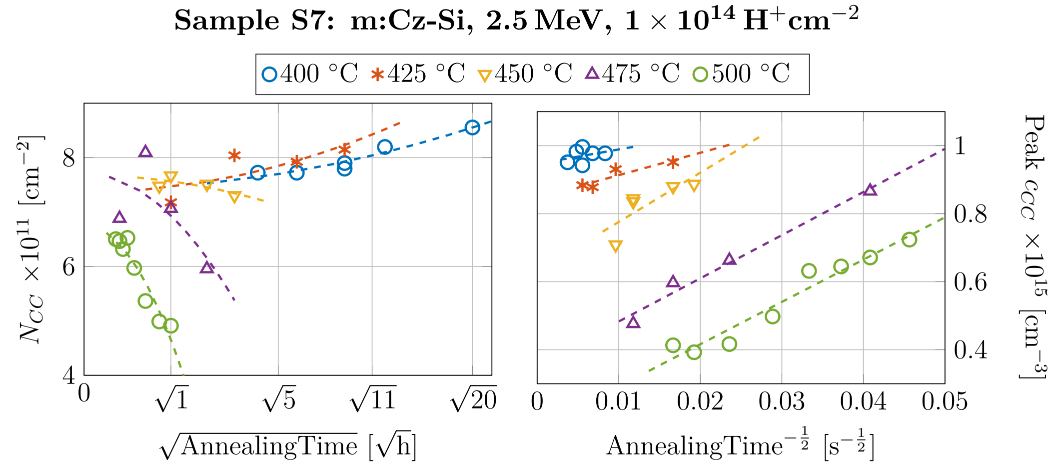

(a) N_{CC} in proton implanted region.

(b) CCC at implantation peak.

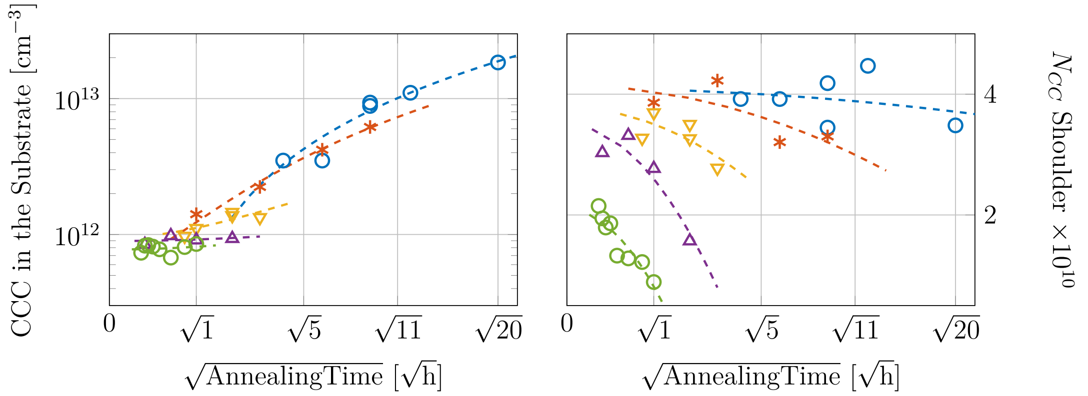

(c) CCC in the substrate material

(d) N_{CC} in the shoulder.

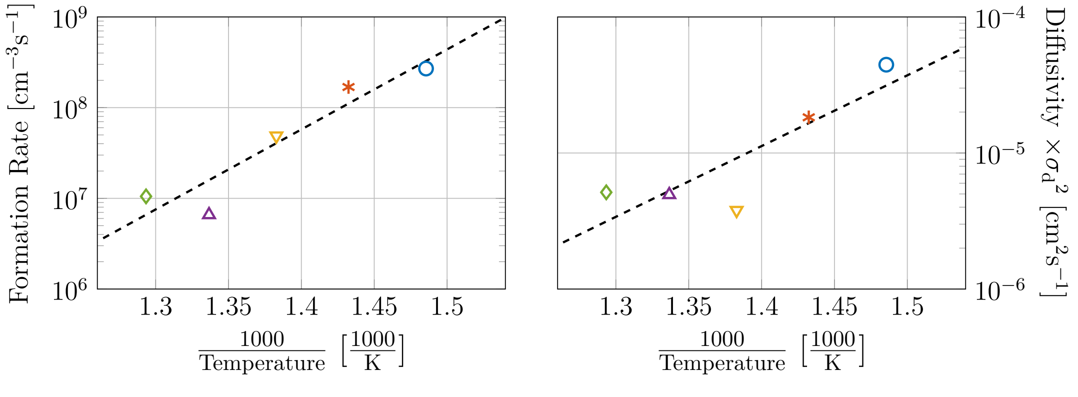

(e) Formation rate of charge carriers in the substrate material

(f) Hydrogen diffusivity at the implantation peak.

Figure B.7.2: CCC in different regions of sample S7 after different anneals.

B.8 Sample S8: FZ-Si, 4 MeV, 1×10^{14} H^{+}cm^{-2}

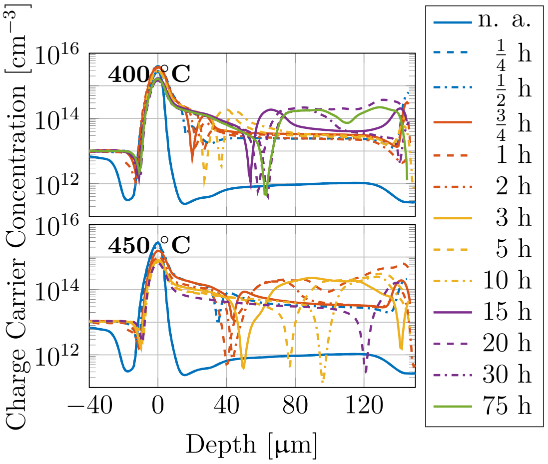

(a) SRP-measurements

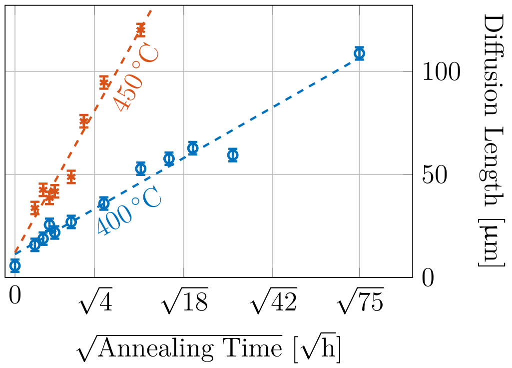

(b) Diffusion length vs. annealing time

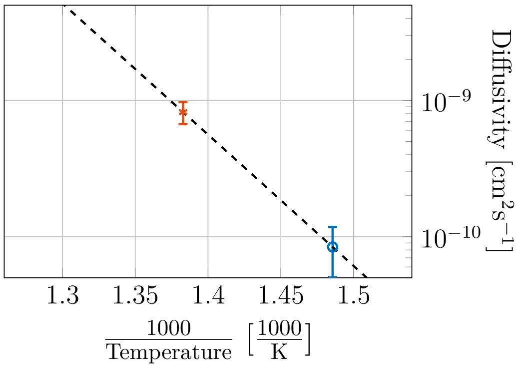

(c) Diffusivity vs. inverse temperature

Figure B.8.1: Measurements and calculations of the hydrogen diffusivity in sample S8.

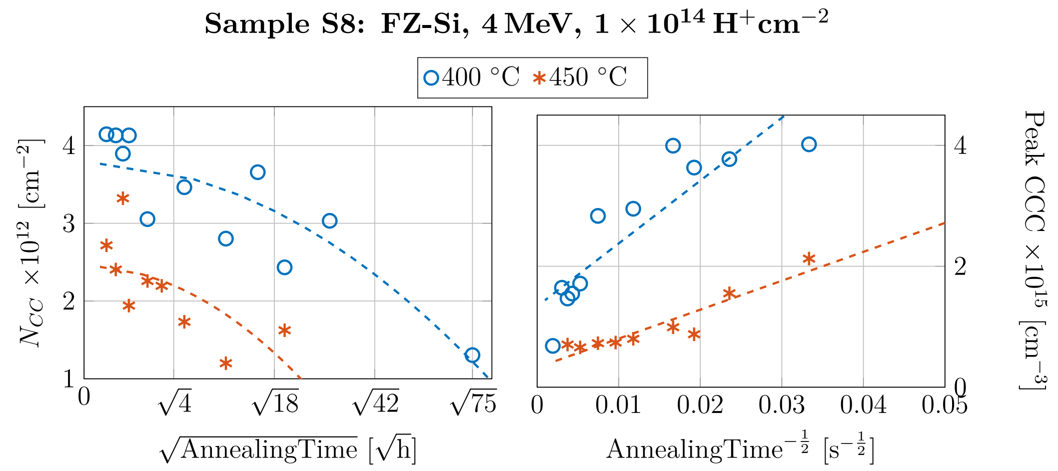

(a) N_{CC} in proton implanted region. **(b)** CCC at implantation peak.

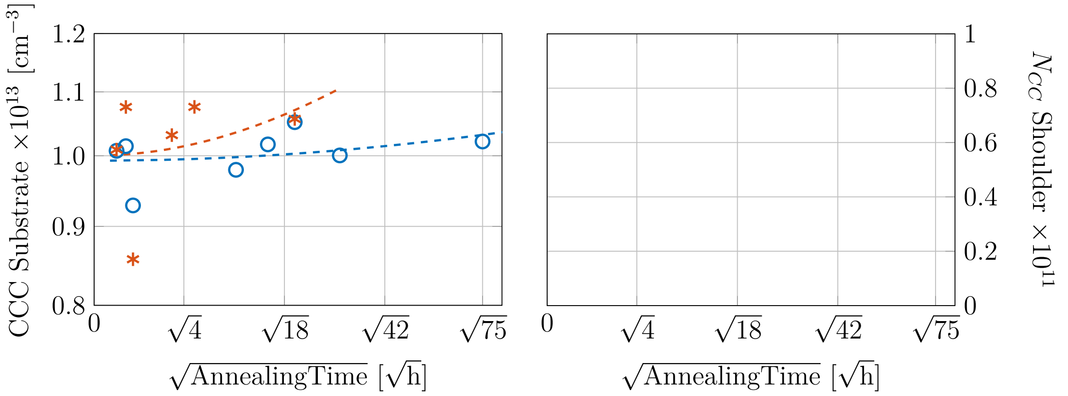

(c) CCC in the substrate material **(d)** N_{CC} in the shoulder.

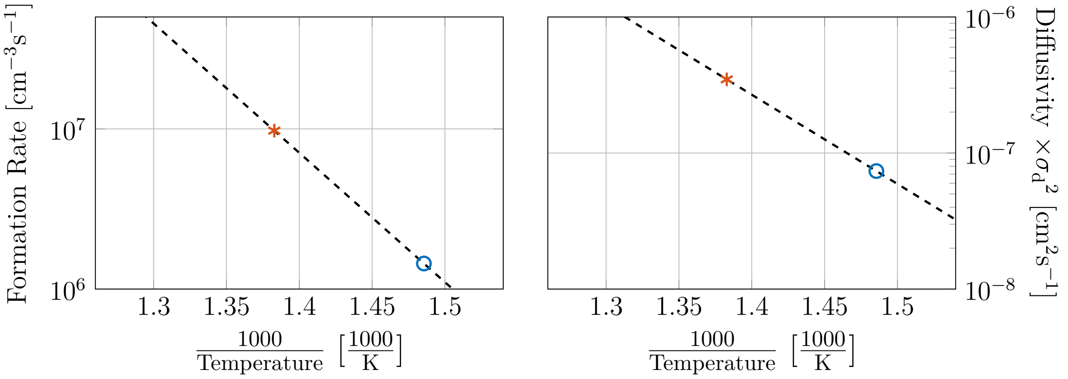

(e) Formation rate of charge carriers in the substrate material **(f)** Hydrogen diffusivity at the implantation peak.

Figure B.8.2: CCC in different regions of sample S8 after different anneals.

C Catalog of the Charge States and the Diffusivity of Selected Defects

This chapter is dedicated to the distribution of the charge states of selected point-defects and defect complexes generated by proton implantation in silicon and to their diffusion. Each defect is described using several figures.

The first figure provides tables listing the formation and ionization energies of the charge states of the defect. Here, $\Delta E_{\text{form}}^{E_F=0}$ is the formation energy of the defect in the middle of the band gap, at a Fermi energy of $0\,\text{eV}$ and $\Delta E_{\text{form}}^{E_F=E_V}$ is the formation energy at the valence band edge at a temperature of $0\,\text{K}$, relative to the formation energy of the neutral charge state of the defect. Some defects appear at different sites in the crystal or show different configurations. In such cases, the formation energies of each (known or calculated) configuration or site of the respective charge states of the defect are given. In another table, the ionization energies of the defect are listed. Here, $E_{q/q+1}$ is the Fermi energy at which the formation energies of two charge states cross and $E_{q/q+1}$-E_V is the energy relative to the valence band energy at $0\,\text{K}$. If an ionization could theoretically be observed, it is written in a bold font. If a defect shows a negative-U system, additional ionizations, where more than one charge carrier is added to or removed from the defect, appear, which are listed as well. The formation energies of the different configurations of each charge state are plotted in sub-figure 1(a) as a function of the Fermi energy within the band gap of silicon. Applying Boltzmann statistics, as described in section 2.2.4, the relative concentration of each charge state of the defect can be calculated at a certain temperature and Fermi energy. In sub-figure 1(b), two-dimensional maps of the relative concentrations of each charge state are plotted as a function of the temperature and of the position of the Fermi energy in the band gap.

In the second figure, the temperature dependence of the relative concentration at different doping concentrations is shown for each charge state. As illustrated in figure 2.9, the Fermi energy itself is a function of the doping concentration and of the temperature. In these plots, the defect concentration is assumed to be much smaller than the doping concentration. Otherwise, the concentration of the non-neutral charge states of the defect have to be included in the calculation of the Fermi energy (see equation 2.83). Sub-figure 2(a) of the second figure of each defect includes one plot of the relative concentrations of all charge states, at different doping concentrations. The doping level increases from intrinsic conditions (N_a=N_d) to a doping concentration of $10^{18}\,\text{cm}^{-3}$. Depending on the temperature, different charge states are dominant, even though the doping concentration stays the same. The temperature at which such a transition appears is measured in DLTS [38]. In sub-figure 2(b) the temperature dependence of the relative concentration at different doping concentrations is plotted separately for each charge state. Even though the data shown here is the same as in sub-figure 2(a), this type of illustration reveals the influence of the doping concentration in a different way.

For mobile defects there is a third figure, illustrating the temperature dependence of their diffusivity. In sub-figure 3(a) the diffusion coefficients of the different charge states are plotted as a function of the inverse temperature. The Arrhenius parameters describing this temperature dependence are listed in the table next to the figure. Often, this list is incomplete and parameters are approximated or copied from other charge states of the same defect. Following equation 2.85, the effective diffusivity D^{eff} of the defect is calculated at different temperatures and Fermi energies. A two-dimensional map of D^{eff} is plotted in sub-figure 3(b), as a function of the position of the Fermi energy in the band gap and of the temperature. This sub-figure also includes the temperature dependence of the Fermi energy at different doping concentrations. Extracting D^{eff} along these lines yields the temperature dependence of D^{eff} at different doping concentrations, which is shown in the sub-figure 3(c). In many cases, the effective diffusivity linearly correlates with the inverse temperature, which again can be described by Arrhenius parameters. For doping concentrations of N_a, N_d=$10^{12}\,\mathrm{cm}^{-3}$, the correlation of D^{eff} with the inverse temperature was fitted in an interval from $0.004\,\mathrm{K}^{-1}$ to $0.003\,\mathrm{K}^{-1}$. For all other doping concentrations a fit interval from $0.0035\,\mathrm{K}^{-1}$ to $0.002\,\mathrm{K}^{-1}$ was used. The extracted Arrhenius parameters describing the temperature correlation of D^{eff} at different doping concentrations are listed in the table in sub-figure 3(c).

C.1 Silicon Vacancy V

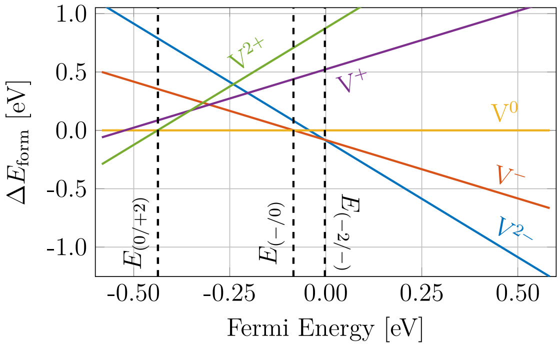

	$\Delta E_{\mathrm{form}}^{E_F=0}$	$\Delta E_{\mathrm{form}}^{E_F=E_V}$
V^{2-}	-0.84	1.08
V^{-}	-0.82	0.50
V^{0}	0.00	0.00
V^{+}	0.52	-0.06
V^{2+}	0.87	-0.29

Trans.	$E_{q/q+1}$	$E_{q/q+1}$-E_V
-2/-	**0.00**	**0.58**
-/0	**-0.08**	**0.50**
0/+	-0.52	0.06
+/+2	-0.35	0.23
0/+2	**-0.44**	**0.15**

Mueller et al. (2003) **bold**: observable transitions

(a) Relative formation energy of each charge state of the silicon vacancy V (based on DFT-simulations by Mueller et al. [54]).

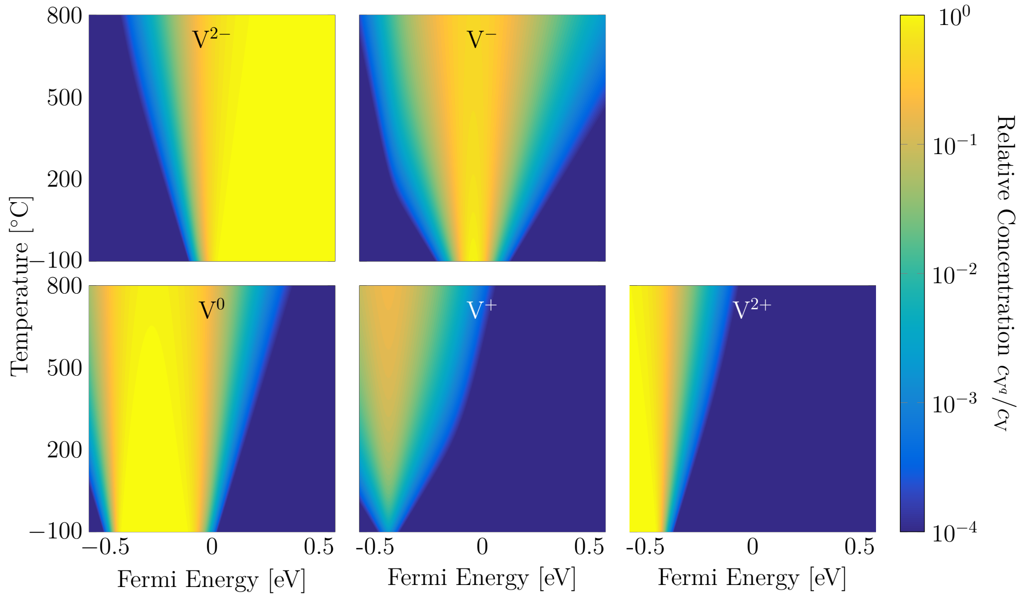

(b) Relative concentration of each charge state of the silicon vacancy V.

Figure C.1.1: Distribution of charge states of the silicon vacancy V. Calculations are based on DFT-simulations by Mueller et al. [54].

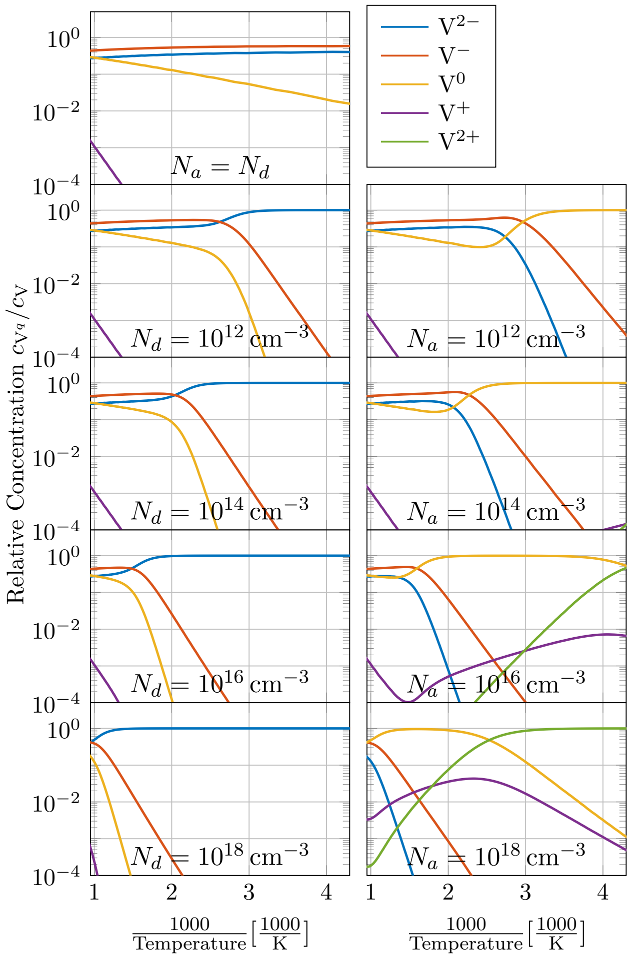

(a) Separate doping concentrations.

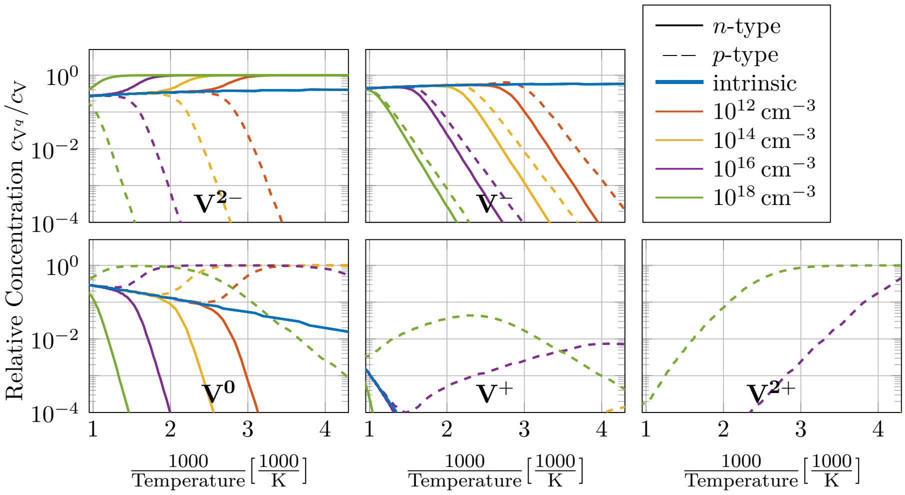

(b) Separate charge states.

Figure C.1.2: Relative concentrations of each charge state of the silicon vacancy.

Diffusivity of the Silicon Vacancy V

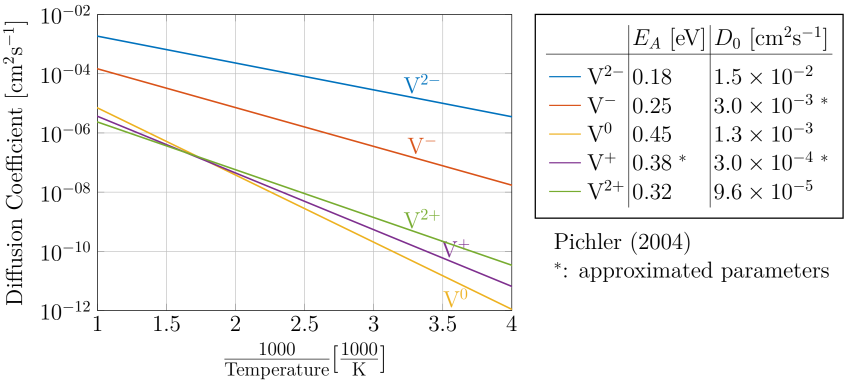

	E_A [eV]	D_0 [cm^{2}s^{-1}]
— V^{2-}	0.18	1.5×10^{-2}
— V^{-}	0.25	3.0×10^{-3} *
— V^{0}	0.45	1.3×10^{-3}
— V^{+}	0.38 *	3.0×10^{-4} *
— V^{2+}	0.32	9.6×10^{-5}

Pichler (2004)

*: approximated parameters

(a) Diffusivity of each charge state of the silicon vacancy (see reference 5).

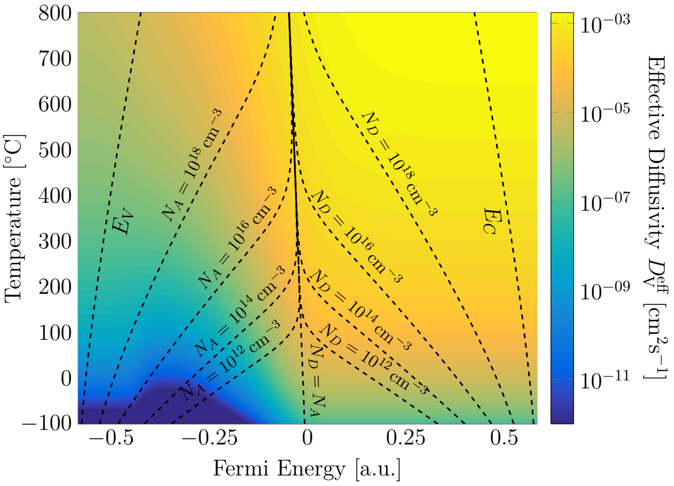

(b) 2D-map of the effective diffusivity of the silicon vacancy.

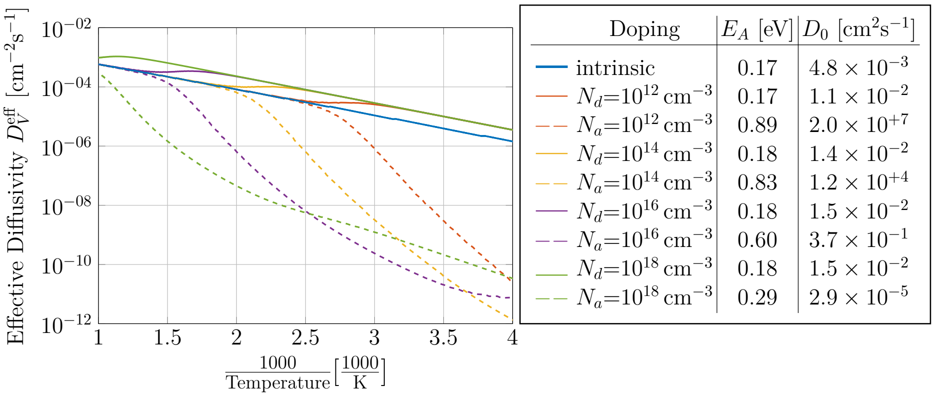

Doping	E_A [eV]	D_0 [cm^{2}s^{-1}]
— intrinsic	0.17	4.8×10^{-3}
— N_d=10^{12} cm^{-3}	0.17	1.1×10^{-2}
– – N_a=10^{12} cm^{-3}	0.89	$2.0 \times 10^{+7}$
— N_d=10^{14} cm^{-3}	0.18	1.4×10^{-2}
– – N_a=10^{14} cm^{-3}	0.83	$1.2 \times 10^{+4}$
— N_d=10^{16} cm^{-3}	0.18	1.5×10^{-2}
– – N_a=10^{16} cm^{-3}	0.60	3.7×10^{-1}
— N_d=10^{18} cm^{-3}	0.18	1.5×10^{-2}
– – N_a=10^{18} cm^{-3}	0.29	2.9×10^{-5}

(c) Temperature dependence of the effective diffusivity of V at selected doping concentrations.

Figure C.1.3: Effective diffusivity of V calculated from Arrhenius parameters published in reference 5

C.2 Silicon Divacancy V_2

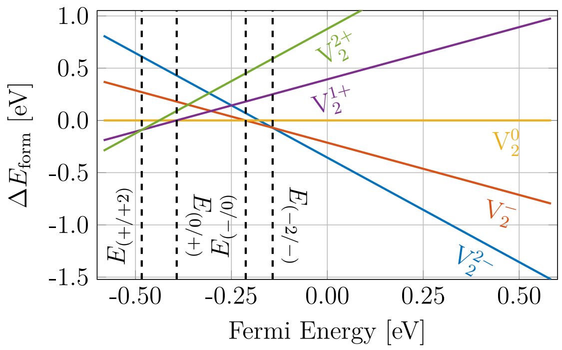

	$\Delta E_{\text{form}}^{E_F=0}$	$\Delta E_{\text{form}}^{E_F=E_V}$
V_2^{2-}	-0.35	0.81
V_2^-	-0.21	0.37
V_2^0	0.00	0.00
V_2^+	0.39	-0.19
V_2^{2+}	0.87	-0.29

Mueller et al. (2003)

Trans.	$E_{q/q+1}$	$E_{q/q+1}$-E_V
-2/-	**-0.14**	**0.44**
-/0	**-0.21**	**0.37**
0/+	**-0.39**	**0.19**
+/+2	**-0.48**	**0.10**

bold: observable transitions

(a) Relative formation energy of each charge state of the silicon divacancy V_2 (based on DFT-simulations by Mueller et al. [54]).

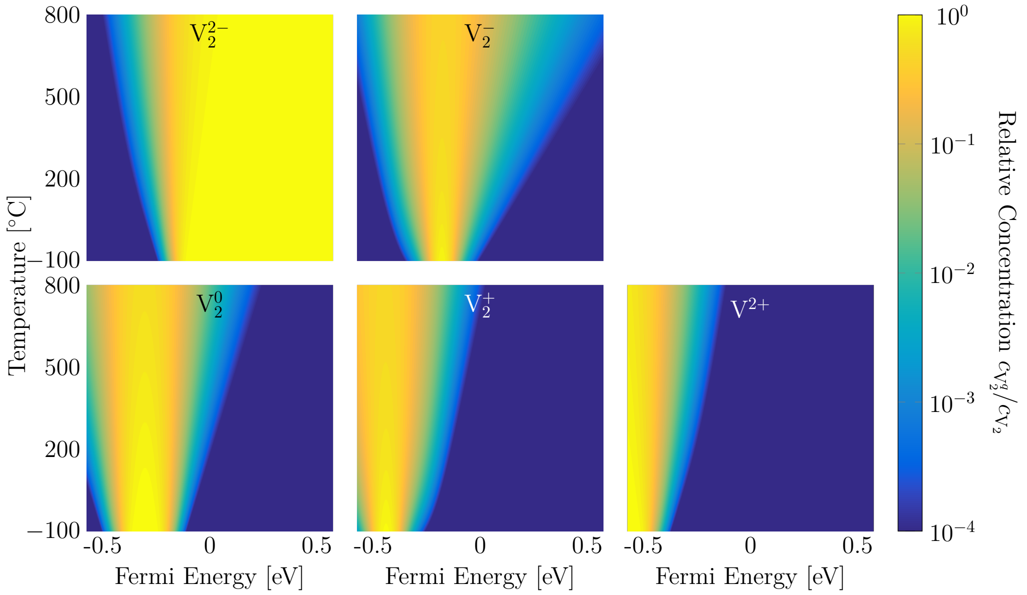

(b) Relative concentration of each charge state of the silicon divacancy V_2.

Figure C.2.1: Distribution of charge states of the divacancy V_2. Calculations are based on DFT-simulations by Mueller et al. [54].

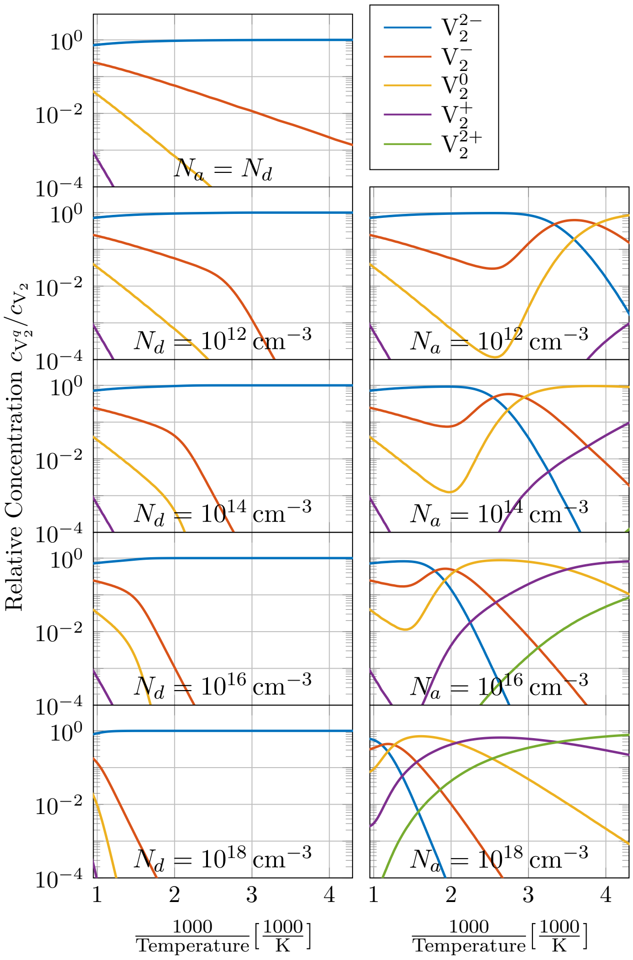

(a) Separate doping concentrations.

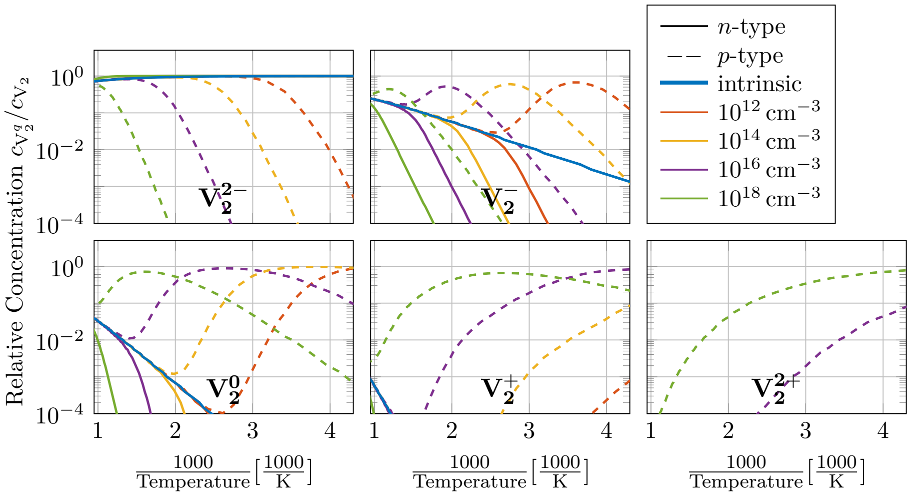

(b) Separate charge states.

Figure C.2.2: Relative concentrations of each charge state of the silicon divacancy.

Diffusivity of the Divacancy V_2

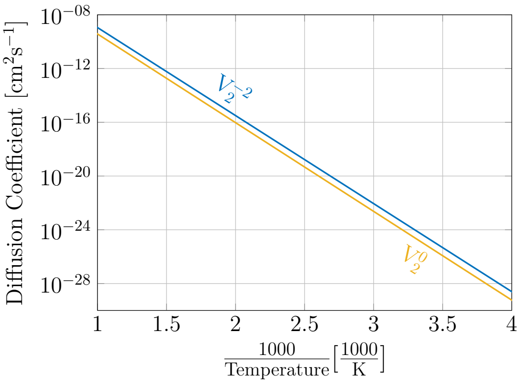

	E_A [eV]	D_0 [cm^2s^{-1}]
— V_2^{2-}	1.30 [a]	4.0×10^{-3} [a]
— V_2^{-}	1.30 *	4.0×10^{-3} *
— V_2^{0}	1.31 [b]	1.5×10^{-3} [b]
— V_2^{+}	1.31 *	1.5×10^{-3} *
— V_2^{2+}	1.31 *	1.5×10^{-3} *

[a]: Mikelsen (2005)
[b]: Ganagona (2014)
*: approximated parameters

(a) Diffusivity of each charge state of the divacancy V_2 (see references 69 and 71).

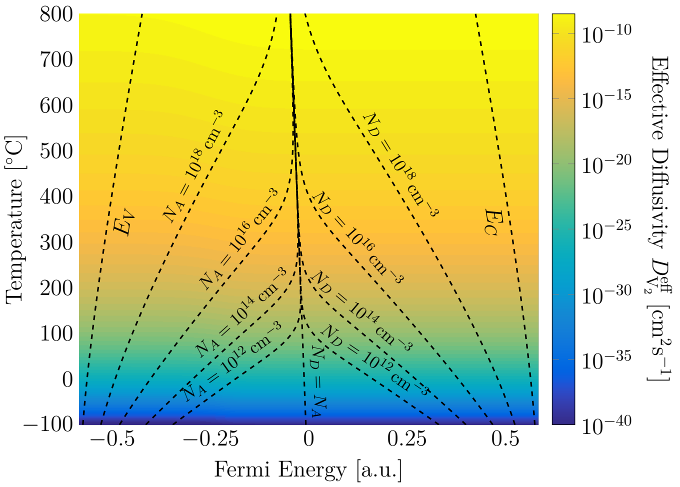

(b) 2D-map of the effective diffusivity of the divacancy.

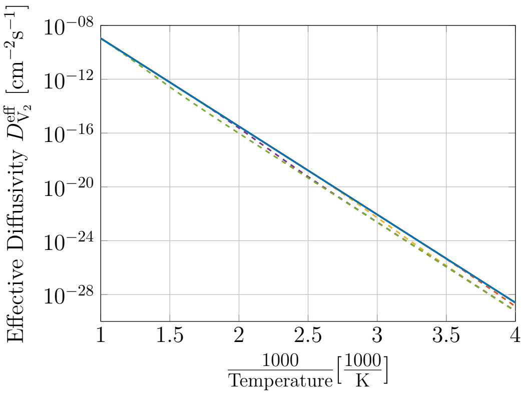

Doping	E_A [eV]	D_0 [cm^2s^{-1}]
— intrinsic	1.30	4.0×10^{-3}
— N_d=10^{12} cm^{-3}	1.30	4.0×10^{-3}
- - N_a=10^{12} cm^{-3}	1.35	2.5×10^{-2}
— N_d=10^{14} cm^{-3}	1.30	4.0×10^{-3}
- - N_a=10^{14} cm^{-3}	1.41	1.2×10^{-1}
— N_d=10^{16} cm^{-3}	1.30	4.0×10^{-3}
- - N_a=10^{16} cm^{-3}	1.36	1.0×10^{-2}
— N_d=10^{18} cm^{-3}	1.30	4.0×10^{-3}
- - N_a=10^{18} cm^{-3}	1.31	2.5×10^{-3}

(c) Temperature dependence of the effective diffusivity of V_2 at selected doping concentrations.

Figure C.2.3: Effective diffusivity of the divacancy V_2 calculated from Arrhenius parameters published in references 69 and 71.

C.3 Silicon Tri-Vacancy V_3

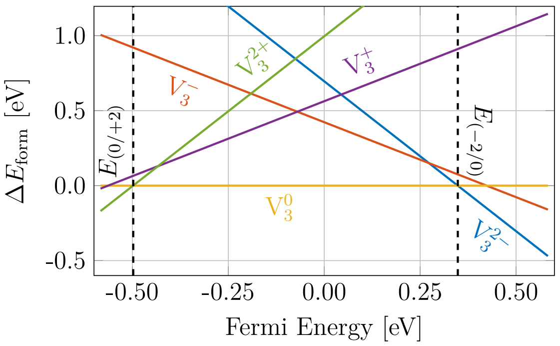

	$\Delta E_{\text{form}}^{E_F=0}$	$\Delta E_{\text{form}}^{E_F=E_V}$
V_3^{2-}	0.70	1.86
V_3^{-}	0.42	1.01
V_3^{0}	0.00	0.00
V_3^{+}	0.56	-0.02
V_3^{2+}	0.99	-0.17

Coutinho et al. (2012)

Trans.	$E_{q/q+1}$	$E_{q/q+1}$-E_V
-2/-	0.27	0.85
-/0	0.43	1.01
0/+	-0.56	0.02
+/+2	-0.43	0.15
-2/0	**-0.50**	**0.09**
0/+2	**0.35**	**0.93**

bold: observable transitions

(a) Relative formation energy of each charge state of the silicon tri-vacancy V_3 (based on DFT-simulations by Coutinho et al. [78]).

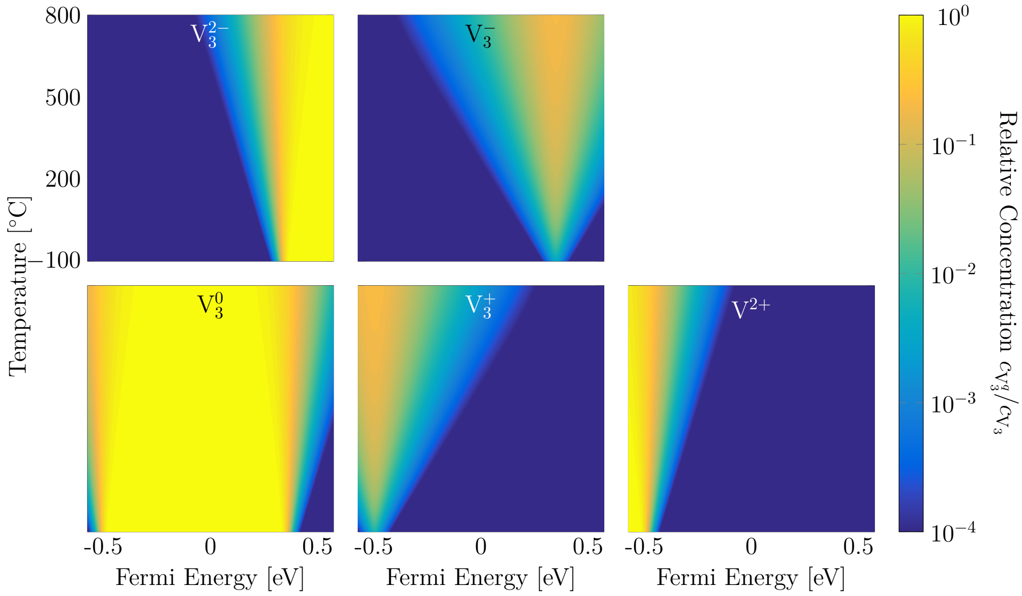

(b) Relative concentration of each charge state of the silicon tri-vacancy V_3.

Figure C.3.1: Distribution of charge states of the tri-vacancy V_3. Calculations are based on DFT-simulations by Coutinho et al. [78].

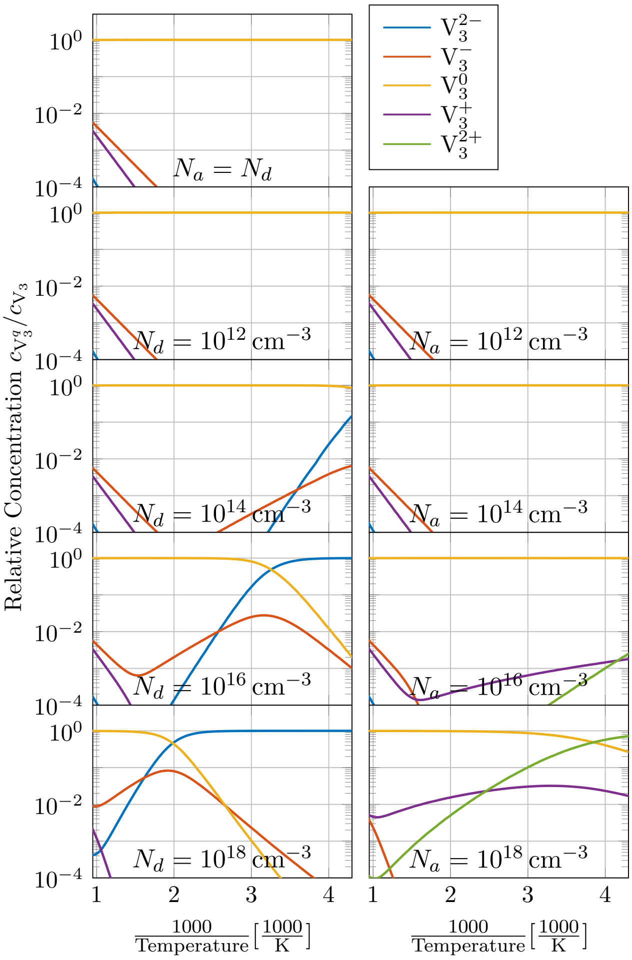

(a) Separate doping concentrations.

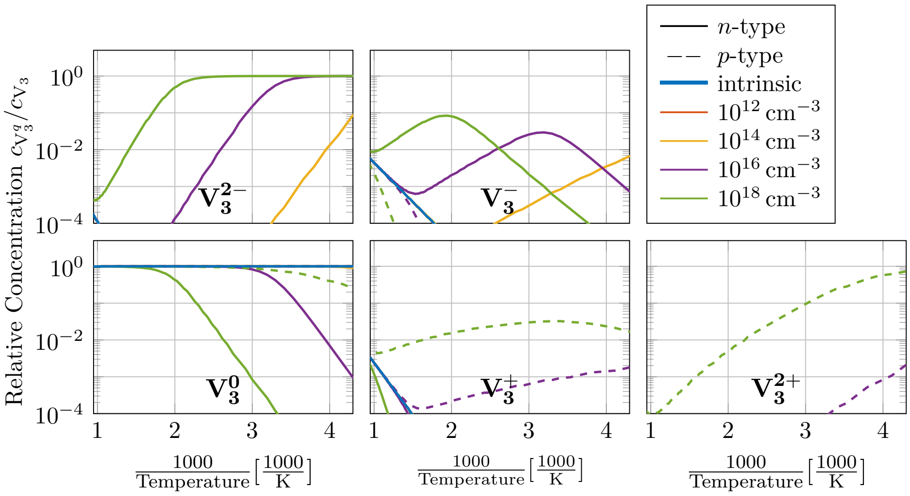

(b) Separate charge states.

Figure C.3.2: Relative concentrations of each charge state of the silicon tri-vacancy.

Diffusivity of the Tri-Vacancy V_3

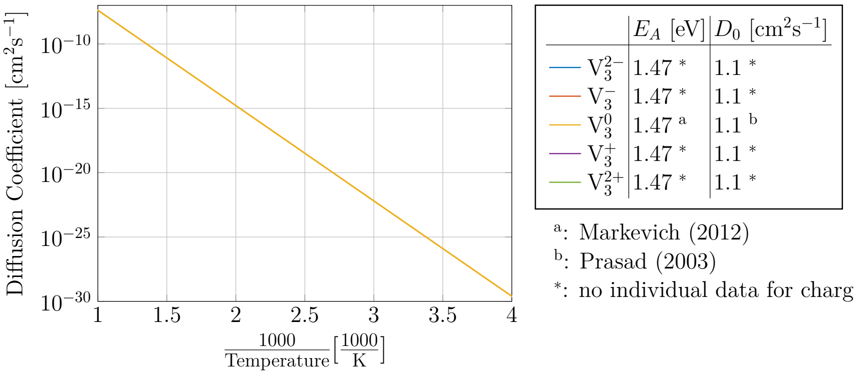

[a]: Markevich (2012)
[b]: Prasad (2003)
*: no individual data for charge states

(a) Diffusivity of each charge state of the tri-vacancy V_3 (see references 69 and 71).

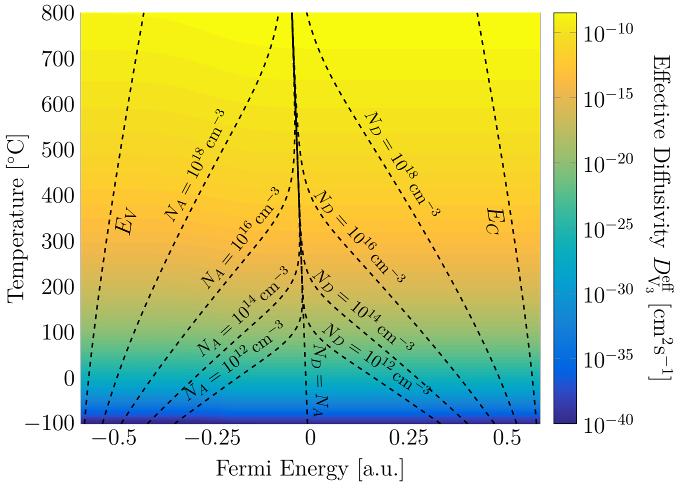

(b) 2D-map of the effective diffusivity of the tri-vacancy.

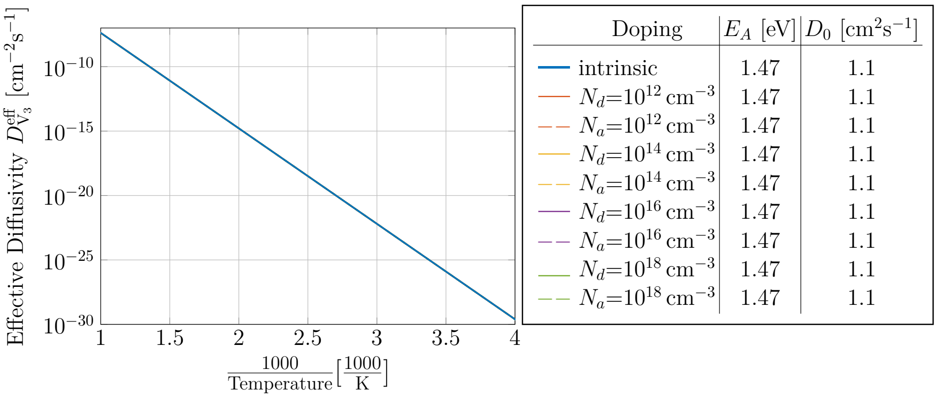

(c) Temperature dependence of the effective diffusivity of V_3 at selected doping concentrations.

Figure C.3.3: Effective diffusivity of V_3 calculated from Arrhenius parameters published in references 69 and 71.

C.4 Silicon Self-Interstitial I

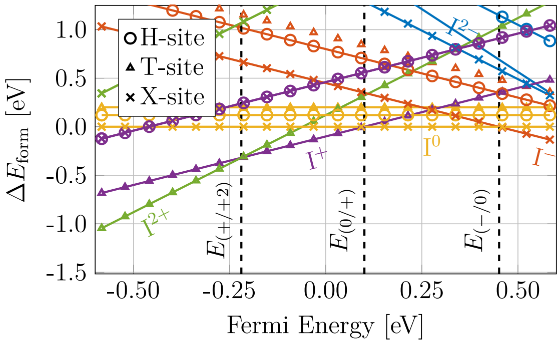

Trans.	$E_{q/q+1}$	$E_{q/q+1}$-E_V
-/0	**0.42**	**1.03**
0/+	**0.10**	**0.68**
+/+2	**-0.22**	**0.36**

bold: observable transitions

	Site	$\Delta E_{\mathrm{form}}^{E_F=0}$	$\Delta E_{\mathrm{form}}^{E_F=E_V}$
I^{2-}	H-Site	2.20	3.37
I^-	H-Site	0.94	1.52
I^0	H-Site	0.20	0.20
I^+	H-Site	-0.10	-0.68
I^{2+}	H-Site	0.12	-1.05

	Site	$\Delta E_{\mathrm{form}}^{E_F=0}$	$\Delta E_{\mathrm{form}}^{E_F=E_V}$
I^{2-}	T-Site	2.05	3.22
I^-	T-Site	0.80	1.38
I^0	T-Site	0.12	0.12
I^+	T-Site	0.46	-0.12
I^{2+}	T-Site	1.51	0.34

	Site	$\Delta E_{\mathrm{form}}^{E_F=0}$	$\Delta E_{\mathrm{form}}^{E_F=E_V}$
I^{2-}	X-Site	1.50	2.66
I^-	X-Site	0.45	1.03
I^0	X-Site	0.00	0.00
I^+	X-Site	0.46	-0.12
I^{2+}	X-Site	1.51	0.34

Lopez et al. (2004)

(a) Relative formation energy of each charge state of the self-interstitial I (based on DFT-simulations by Du et al. [120].

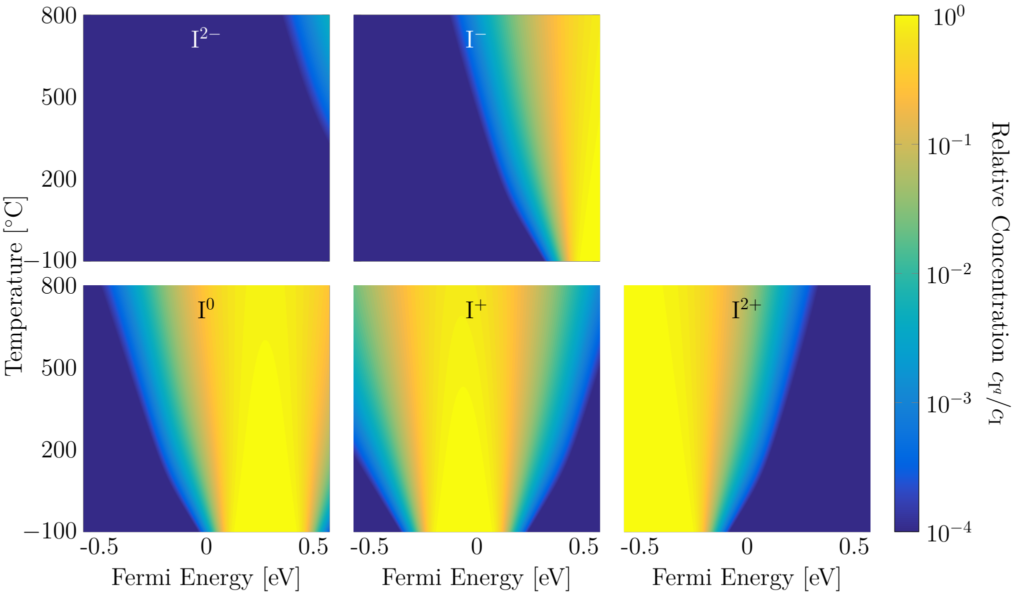

(b) Relative concentration of each charge state of the self-interstitial I.

Figure C.4.1: Distribution of charge states of the self-interstitial I. Calculations are based on DFT-simulations by Du et al. [120].

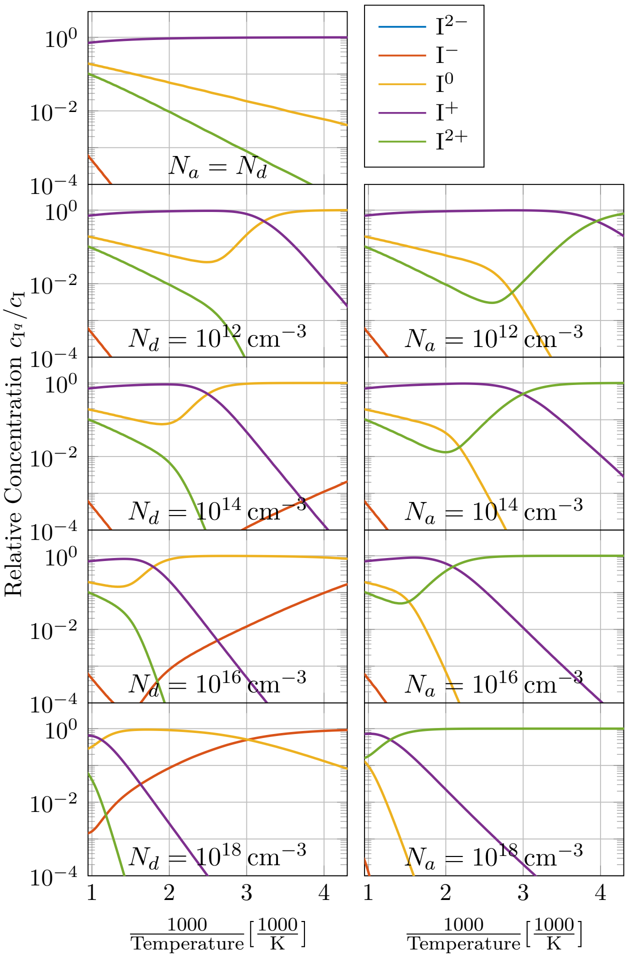

(a) Separate doping concentrations.

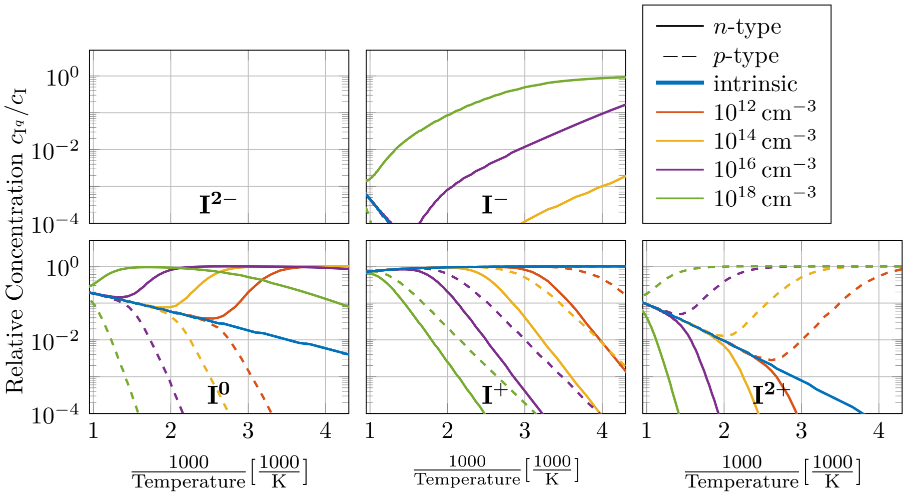

(b) Separate charge states.

Figure C.4.2: Relative concentrations of each charge state of the self-interstitial I.

Diffusivity of the Self-Interstitial I

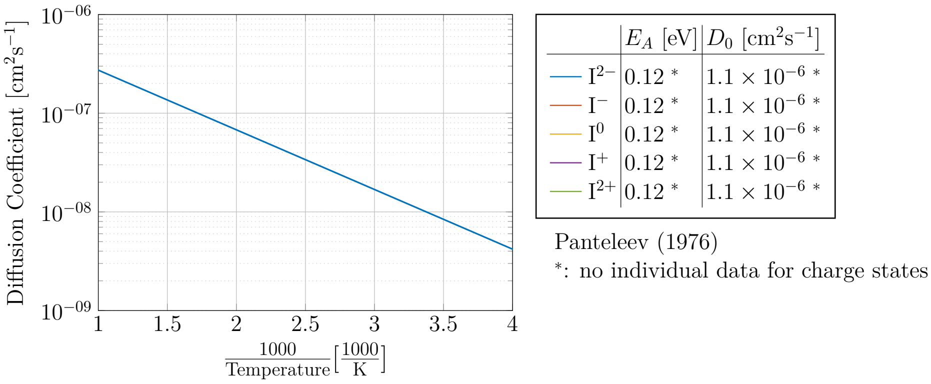

(a) Diffusivity of each charge state of the self-interstitial I (see reference 91).

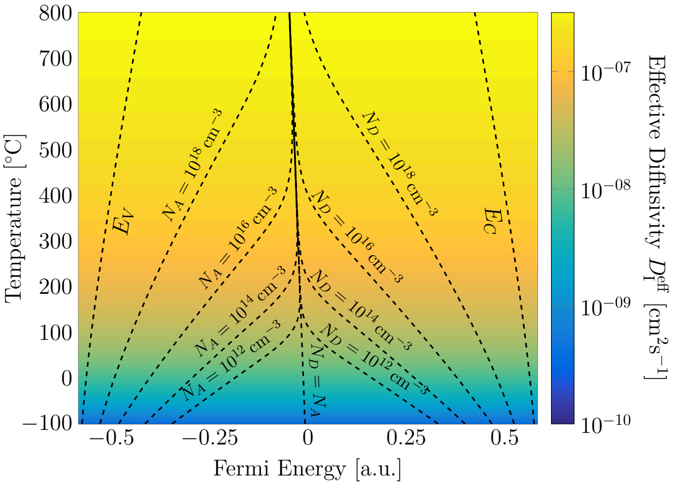

(b) 2D-map of the effective diffusivity of the self-interstitial.

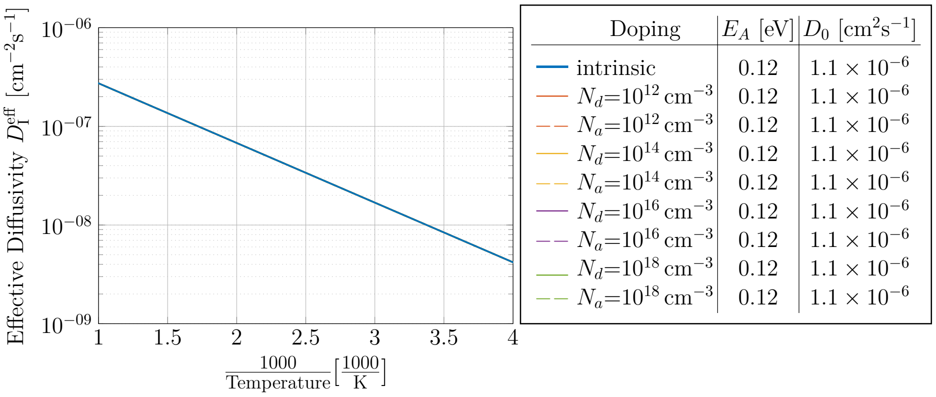

(c) Temperature dependence of the effective diffusivity of I at selected doping concentrations.

Figure C.4.3: Effective diffusivity of the self-interstitial I calculated from Arrhenius parameters published in reference 91.

C.5 Silicon Di-Interstitial I_2

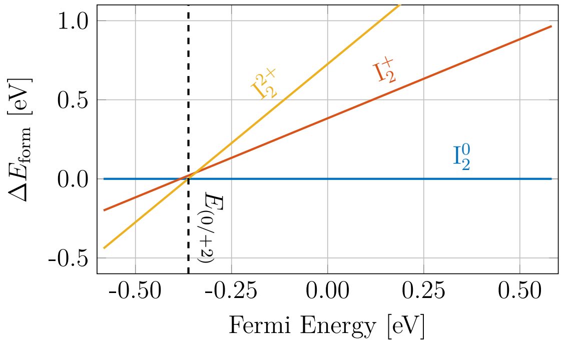

	$\Delta E_{\text{form}}^{E_F=0}$	$\Delta E_{\text{form}}^{E_F=E_V}$
I^0	0.00	0.00
I^+	0.38	-0.20
I^{2+}	0.72	-0.44

Trans.	$E_{q/q+1}$	$E_{q/q+1}$-E_V
0/+	-0.38	0.20
+/+2	-0.34	0.24
0/+2	**-0.36**	**0.22**

Lopez et al. (2004)

bold: observable transitions

(a) Relative formation energy of each charge state of the di-interstitial I_2 (based on DFT-simulations by Lopez et al. [90]).

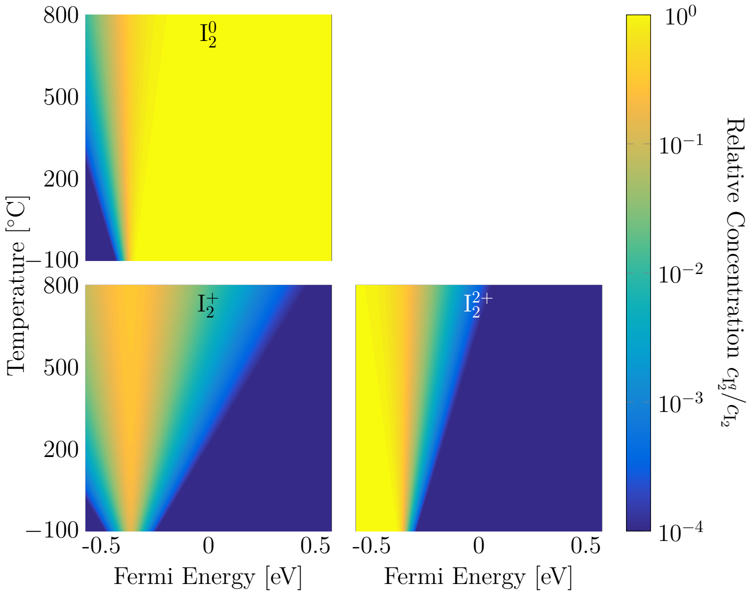

(b) Relative concentration of each charge state of the silicon di-interstitial I_2.

Figure C.5.1: Distribution of charge states of the di-interstitial I_2. Calculations are based on DFT-simulations by Lopez et al. [90].

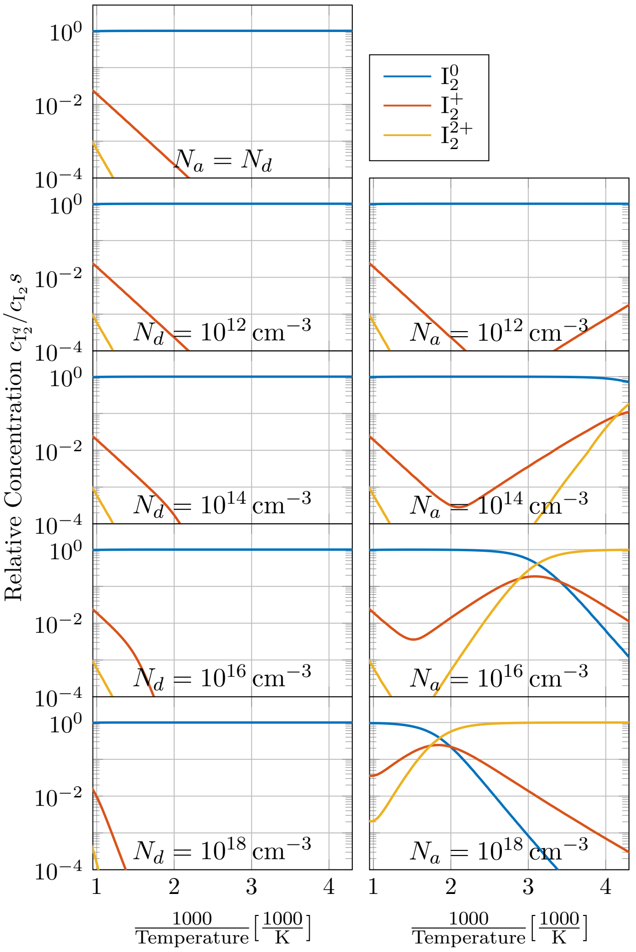

(a) Separate doping concentrations.

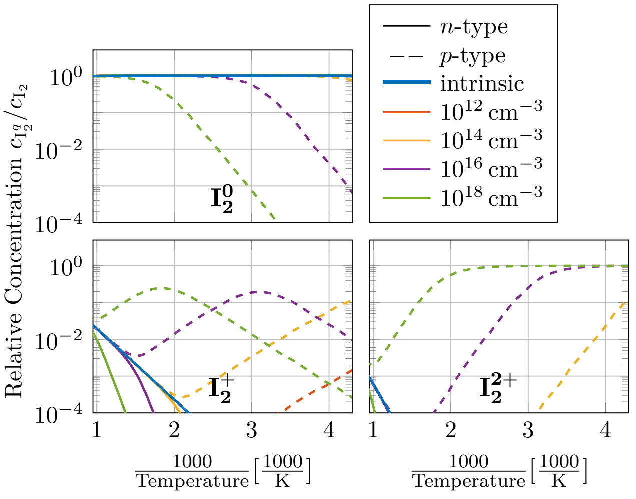

(b) Separate charge states.

Figure C.5.2: Relative concentrations of each charge state of the di-interstitial I_2.

Diffusivity of the Di-Interstitial I$_2$

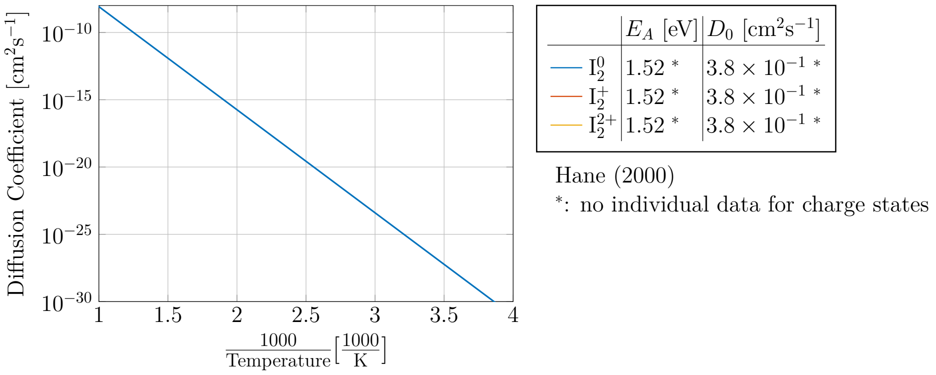

	E_A [eV]	D_0 [cm^{2}s^{-1}]
I_2^0	1.52 *	3.8×10^{-1} *
I_2^+	1.52 *	3.8×10^{-1} *
I_2^{2+}	1.52 *	3.8×10^{-1} *

Hane (2000)

*: no individual data for charge states

(a) Diffusivity of each charge state of the di-interstitial I$_2$ (see reference 92).

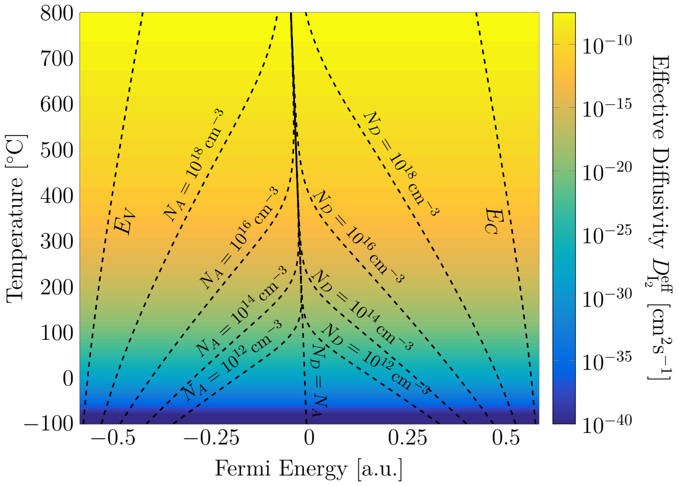

(b) 2D-map of the effective diffusivity of the di-interstitial I$_2$.

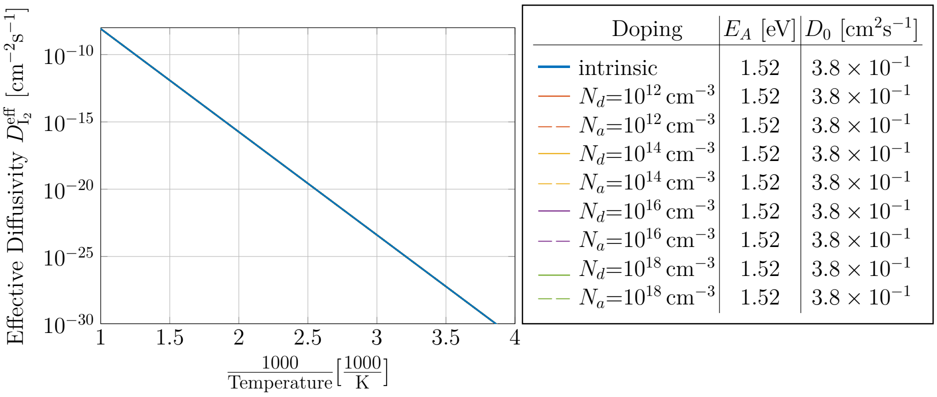

Doping	E_A [eV]	D_0 [cm^{2}s^{-1}]
intrinsic	1.52	3.8×10^{-1}
N_d=10^{12} cm^{-3}	1.52	3.8×10^{-1}
N_a=10^{12} cm^{-3}	1.52	3.8×10^{-1}
N_d=10^{14} cm^{-3}	1.52	3.8×10^{-1}
N_a=10^{14} cm^{-3}	1.52	3.8×10^{-1}
N_d=10^{16} cm^{-3}	1.52	3.8×10^{-1}
N_a=10^{16} cm^{-3}	1.52	3.8×10^{-1}
N_d=10^{18} cm^{-3}	1.52	3.8×10^{-1}
N_a=10^{18} cm^{-3}	1.52	3.8×10^{-1}

(c) Temperature dependence of the effective diffusivity of I$_2$ at selected doping concentrations.

Figure C.5.3: Effective diffusivity of the di-interstitial I$_2$ calculated from Arrhenius parameters published in reference 92.

C.6 Silicon Tri-Interstitial I_3

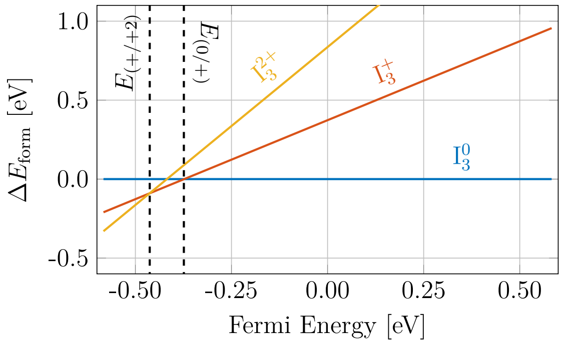

	$\Delta E_{\text{form}}^{E_F=0}$	$\Delta E_{\text{form}}^{E_F=E_V}$
I^0	0.00	0.00
I^+	0.37	-0.21
I^{2+}	0.83	-0.33

Lopez et al. (2004)

Trans.	$E_{q/q+1}$	$E_{q/q+1}$-E_V
0/+	**-0.37**	**0.21**
+/+2	**-0.46**	**0.12**

bold: observable transitions

(a) Relative formation energy of each charge state of the tri-interstitial I_3 (based on DFT-simulations by Lopez et al. [90]).

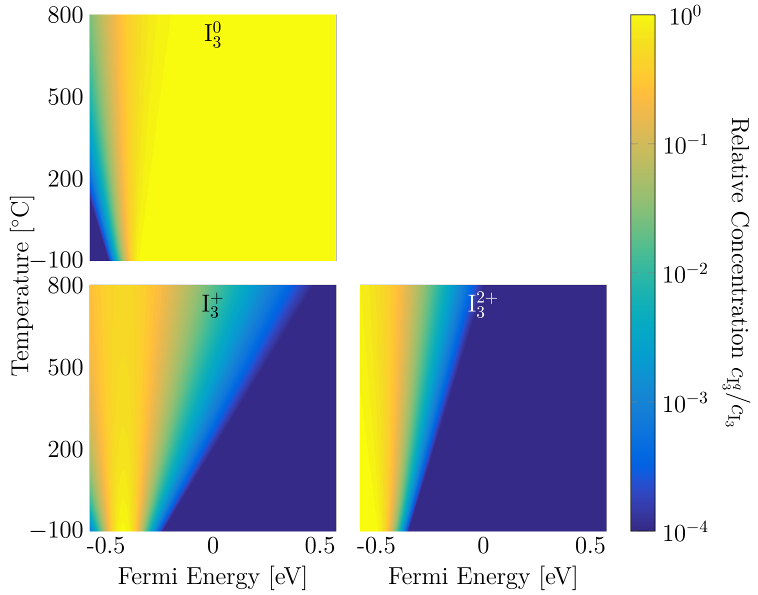

(b) Relative concentration of each charge state of the silicon di-interstitial I_3.

Figure C.6.1: Distribution of charge states of the di-interstitial I_3. Calculations are based on DFT-simulations by Lopez et al. [90].

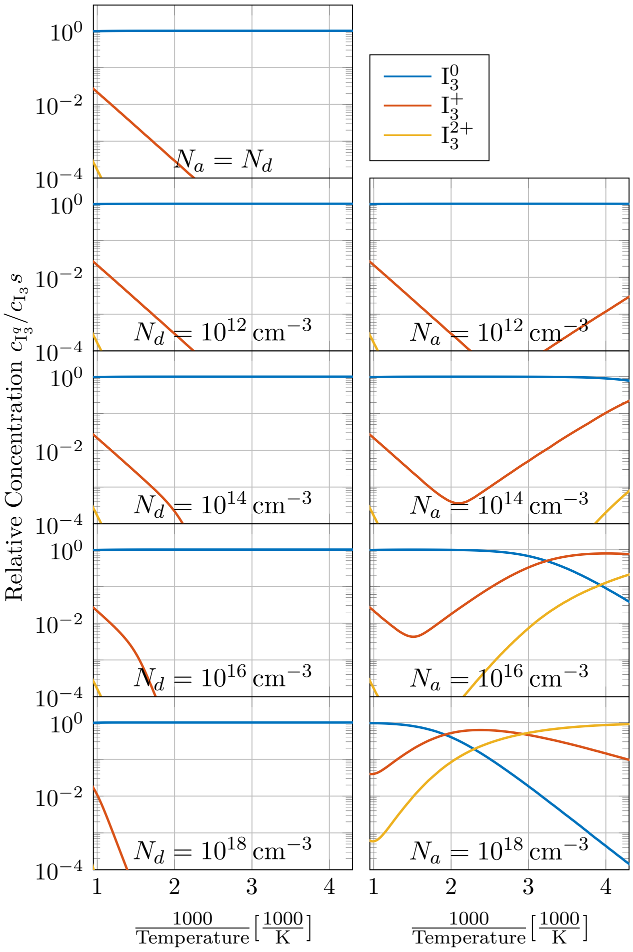

(a) Separate doping concentrations.

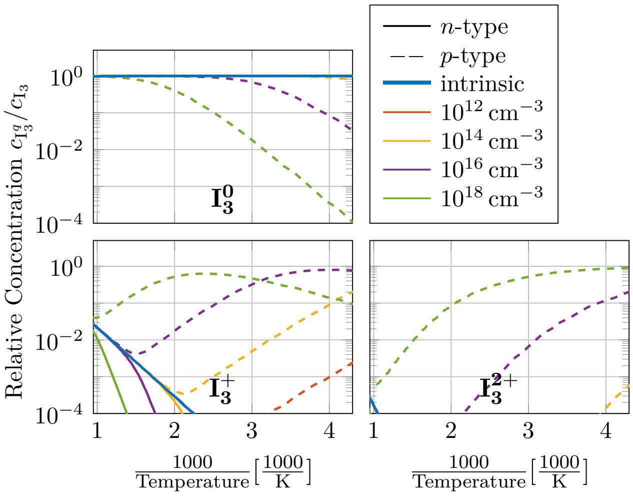

(b) Separate charge states.

Figure C.6.2: Relative concentrations of each charge state of the tri-interstitial I_3.

Diffusivity of the Tri-Interstitial I_3

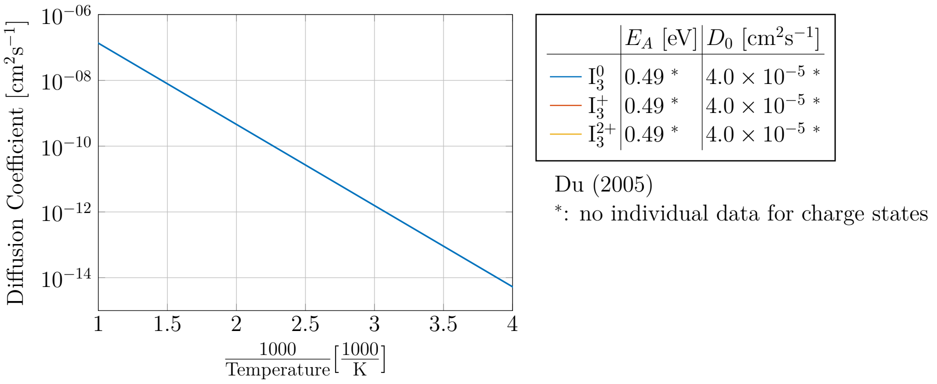

	E_A [eV]	D_0 [cm^{2}s^{-1}]
I_3^0	0.49 *	4.0×10^{-5} *
I_3^+	0.49 *	4.0×10^{-5} *
I_3^{2+}	0.49 *	4.0×10^{-5} *

Du (2005)

*: no individual data for charge states

(a) Diffusivity of each charge state of the tri-interstitial I_3 (see reference 93).

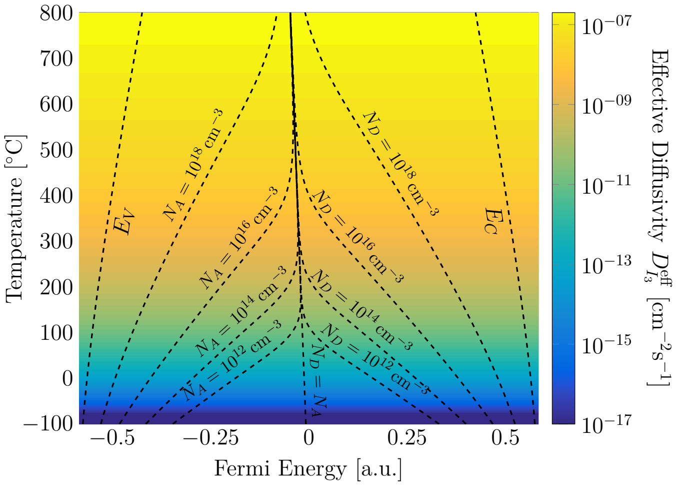

(b) 2D-map of the effective diffusivity of the tri-interstitial I_3.

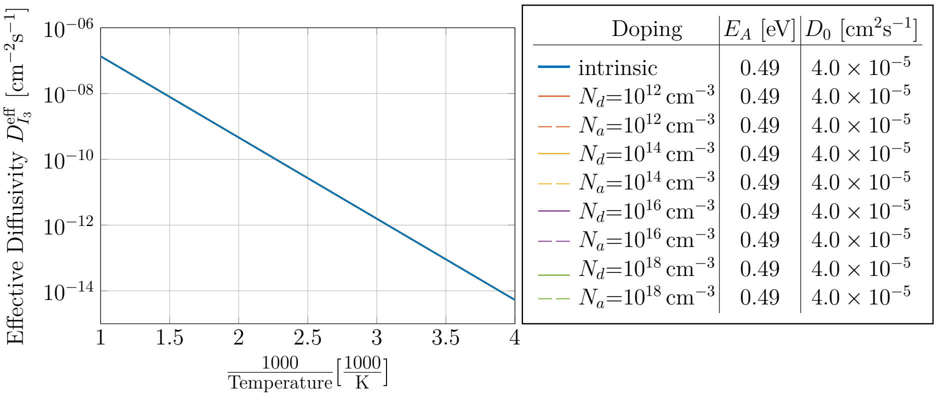

Doping	E_A [eV]	D_0 [cm^{2}s^{-1}]
intrinsic	0.49	4.0×10^{-5}
N_d=10^{12} cm^{-3}	0.49	4.0×10^{-5}
N_a=10^{12} cm^{-3}	0.49	4.0×10^{-5}
N_d=10^{14} cm^{-3}	0.49	4.0×10^{-5}
N_a=10^{14} cm^{-3}	0.49	4.0×10^{-5}
N_d=10^{16} cm^{-3}	0.49	4.0×10^{-5}
N_a=10^{16} cm^{-3}	0.49	4.0×10^{-5}
N_d=10^{18} cm^{-3}	0.49	4.0×10^{-5}
N_a=10^{18} cm^{-3}	0.49	4.0×10^{-5}

(c) Temperature dependence of the effective diffusivity of the tri-interstitial I_3 at selected doping concentrations.

Figure C.6.3: Effective diffusivity of the tri-interstitial I_3 calculated from Arrhenius parameters published in reference 93.

C.7 Interstitial Oxygen O

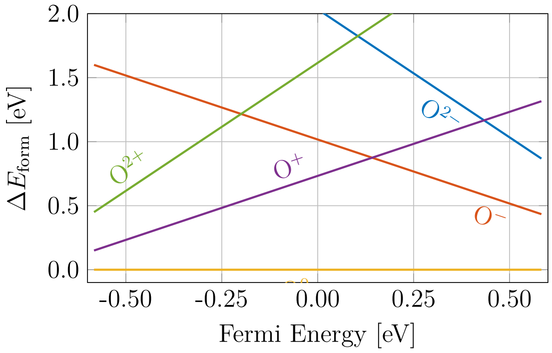

	$\Delta E_{\text{form}}^{E_F=0}$	$\Delta E_{\text{form}}^{E_F=E_V}$
O^{2-}	2.04	3.20
O^{-}	1.02	1.60
O^{0}	0.00	0.00
O^{+}	0.73	0.15
O^{2+}	1.61	0.45

Wang et al. (2013)

Trans.	$E_{q/q+1}$	$E_{q/q+1}$-E_V
-2/-	$> E_C$	$> E_G$
-/0	$> E_C$	$> E_G$
0/+	$< E_V$	< 0
+/+2	$< E_V$	< 0

bold: observable transitions

(a) Relative formation energy of each charge state of the interstitial oxygen impurity O (based on DFT-simulations by Wang et al. [119]).

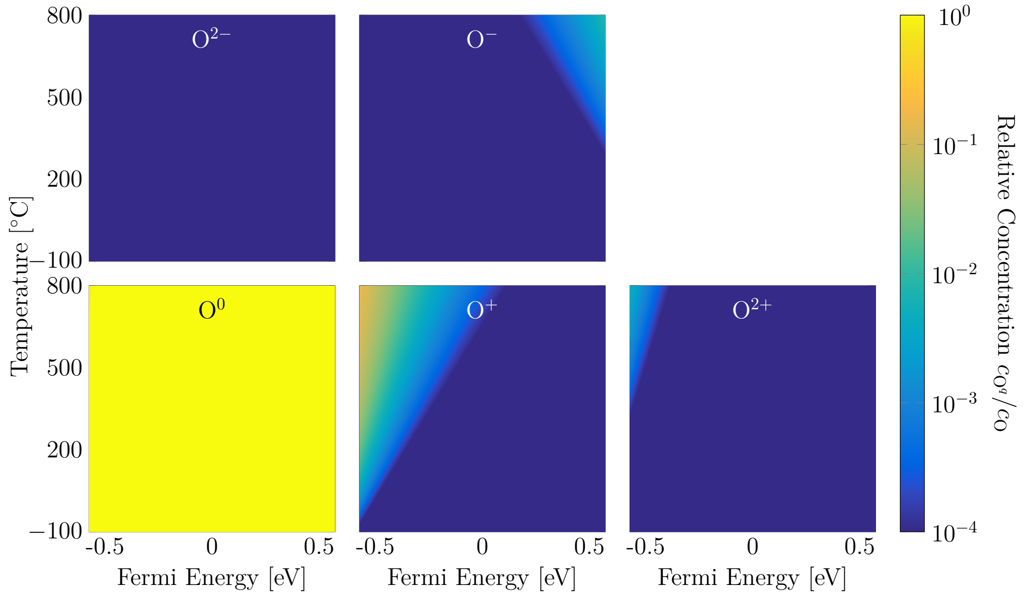

(b) Relative concentration of each charge state of the the interstitial oxygen impurity O.

Figure C.7.1: Distribution of charge states of the interstitial oxygen impurity O. Calculations are based on DFT-simulations by Lopez et al. [119].

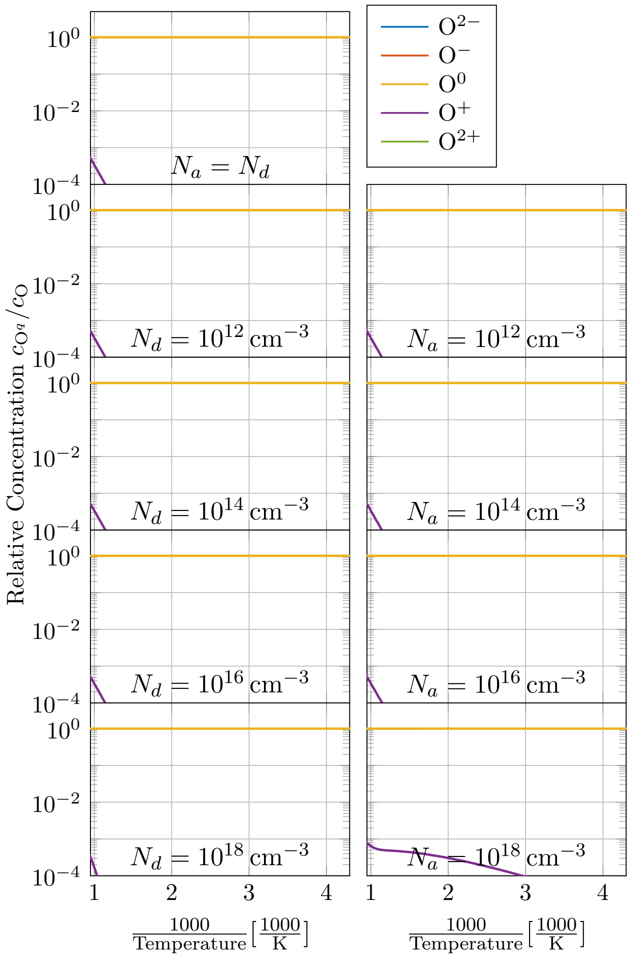

(a) Separate doping concentrations.

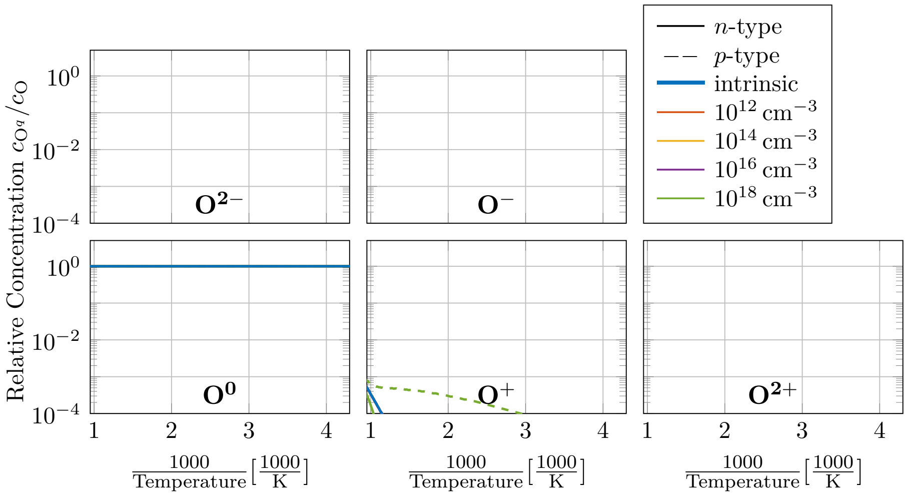

(b) Separate charge states.

Figure C.7.2: Relative concentrations of each charge state of interstitial oxygen O.

Diffusivity of Oxygen O

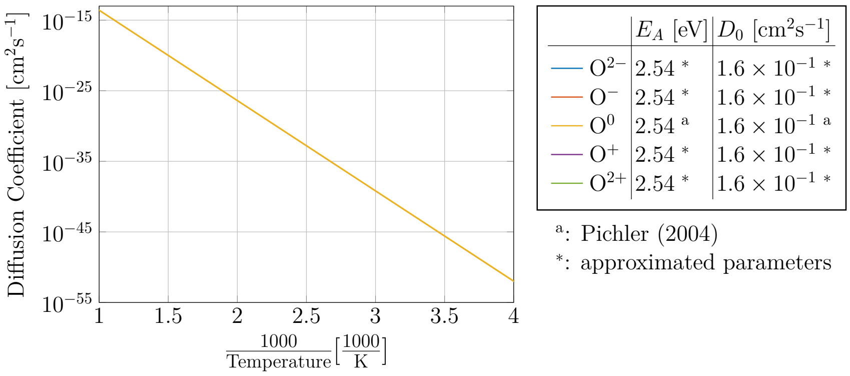

	E_A [eV]	D_0 [cm^{2}s^{-1}]
— O^{2-}	2.54 *	1.6×10^{-1} *
— O^{-}	2.54 *	1.6×10^{-1} *
— O^{0}	2.54 [a]	1.6×10^{-1} [a]
— O^{+}	2.54 *	1.6×10^{-1} *
— O^{2+}	2.54 *	1.6×10^{-1} *

[a]: Pichler (2004)
*: approximated parameters

(a) Diffusivity of each charge state of the interstitial oxygen impurity O (see reference 5).

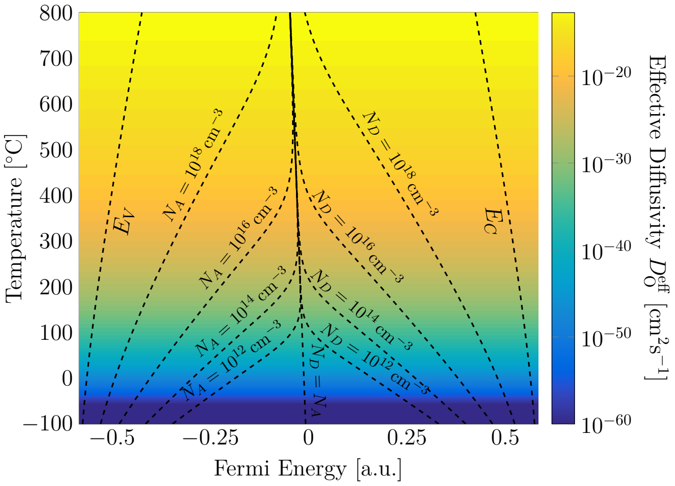

(b) 2D-map of the effective diffusivity of the interstitial oxygen impurity O.

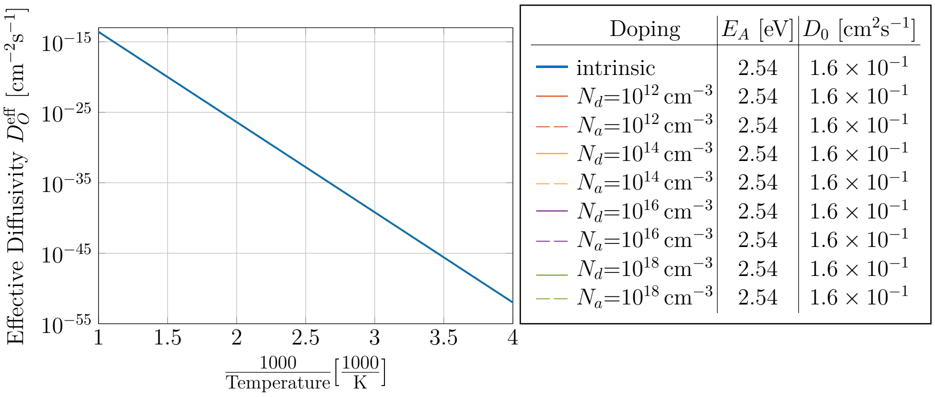

Doping	E_A [eV]	D_0 [cm^{2}s^{-1}]
— intrinsic	2.54	1.6×10^{-1}
— N_d=10^{12} cm^{-3}	2.54	1.6×10^{-1}
– – N_a=10^{12} cm^{-3}	2.54	1.6×10^{-1}
— N_d=10^{14} cm^{-3}	2.54	1.6×10^{-1}
– – N_a=10^{14} cm^{-3}	2.54	1.6×10^{-1}
— N_d=10^{16} cm^{-3}	2.54	1.6×10^{-1}
– – N_a=10^{16} cm^{-3}	2.54	1.6×10^{-1}
— N_d=10^{18} cm^{-3}	2.54	1.6×10^{-1}
– – N_a=10^{18} cm^{-3}	2.54	1.6×10^{-1}

(c) Temperature dependence of the effective diffusivity of O at selected doping concentrations.

Figure C.7.3: Effective diffusivity of interstitial oxygen O calculated from Arrhenius parameters published in reference 5.

C.8 Oxygen DimerO$_2$

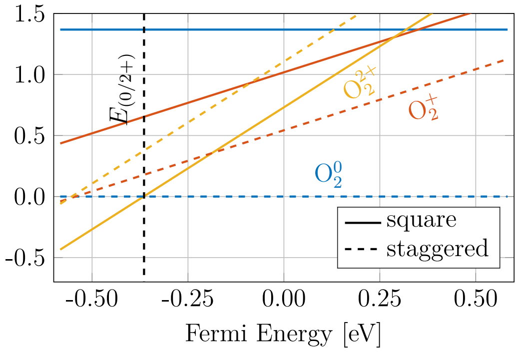

Trans.	$E_{q/q+1}$	$E_{q/q+1}$-E_V
0/+2	**-0.36**	**0.22**

bold: observable transitions

	Configuration	$\Delta E_{\text{form}}^{E_F=0}$	$\Delta E_{\text{form}}^{E_F=E_V}$
O_2^0	square	1.37	1.37
O_2^+	square	1.02	0.44
O_2^{2+}	square	0.73	-0.44

	Configuration	$\Delta E_{\text{form}}^{E_F=0}$	$\Delta E_{\text{form}}^{E_F=E_V}$
O_2^0	staggered	0.00	0.00
O_2^+	staggered	0.54	-0.04
O_2^{2+}	staggered	1.11	-0.06

Du et al. (2006)

(a) Relative formation energy of each charge state of the oxygen-dimer O$_2$ (based on DFT-simulations by Du et al. [120]).

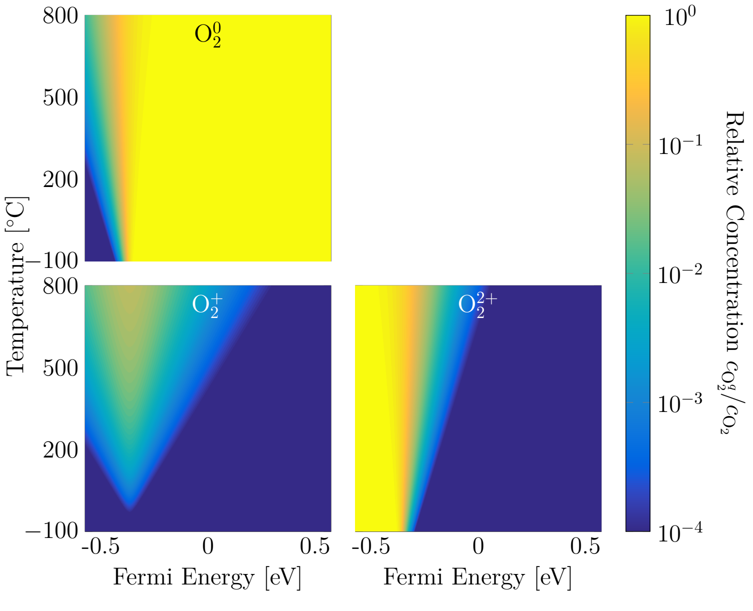

(b) Relative concentration of each charge state of the oxygen-dimer O$_2$.

Figure C.8.1: Distribution of charge states of the oxygen-dimer O$_2$. Calculations are based on DFT-simulations by Du et al. [120].

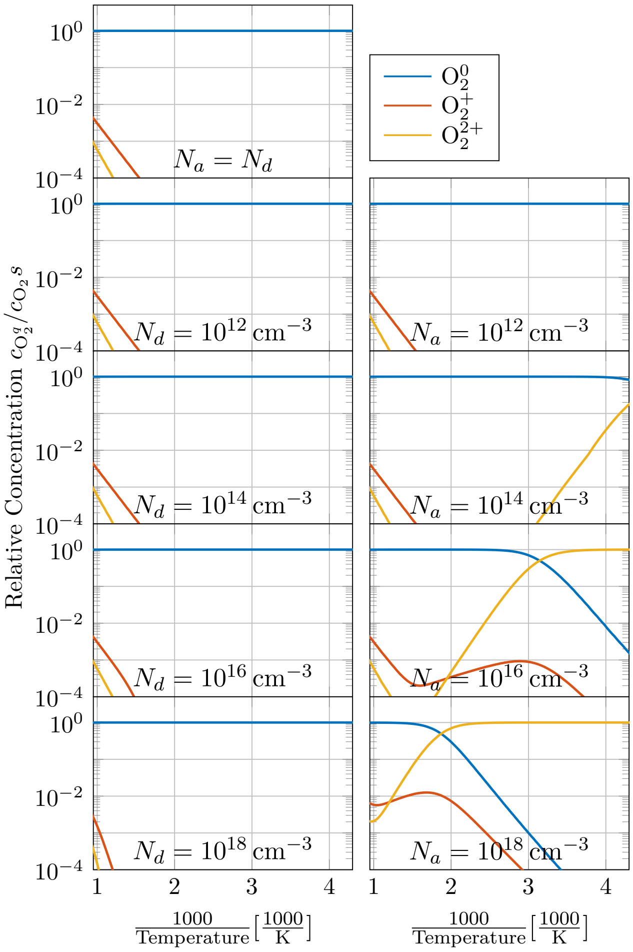

(a) Separate doping concentrations.

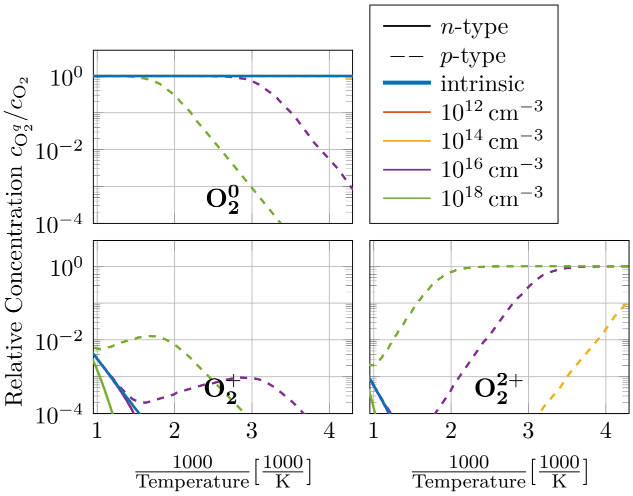

(b) Separate charge states.

Figure C.8.2: Relative concentrations of each charge state of the oxygen-dimer O_2.

Diffusivity of the Oxygen Dimer O_2

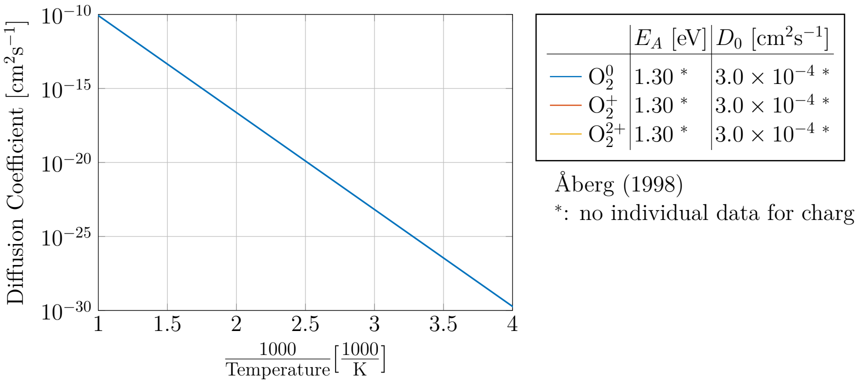

	E_A [eV]	D_0 [cm^2s^{-1}]
O_2^0	1.30 *	3.0×10^{-4} *
O_2^+	1.30 *	3.0×10^{-4} *
O_2^{2+}	1.30 *	3.0×10^{-4} *

Åberg (1998)
*: no individual data for charge states

(a) Diffusivity of each charge state of the oxygen-dimer O_2 (see reference 122).

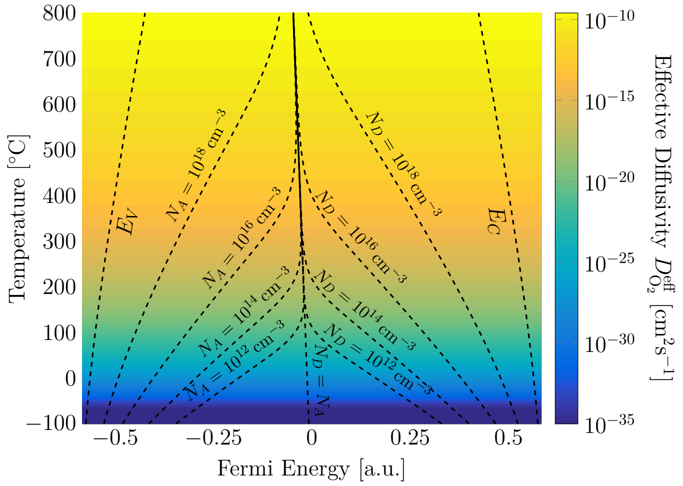

(b) 2D-map of the effective diffusivity of the oxygen-dimer O_2.

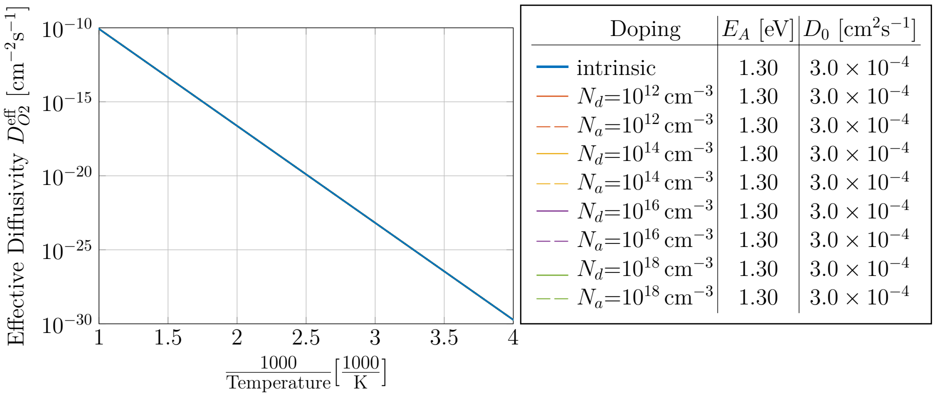

Doping	E_A [eV]	D_0 [cm^2s^{-1}]
intrinsic	1.30	3.0×10^{-4}
N_d=10^{12} cm^{-3}	1.30	3.0×10^{-4}
N_a=10^{12} cm^{-3}	1.30	3.0×10^{-4}
N_d=10^{14} cm^{-3}	1.30	3.0×10^{-4}
N_a=10^{14} cm^{-3}	1.30	3.0×10^{-4}
N_d=10^{16} cm^{-3}	1.30	3.0×10^{-4}
N_a=10^{16} cm^{-3}	1.30	3.0×10^{-4}
N_d=10^{18} cm^{-3}	1.30	3.0×10^{-4}
N_a=10^{18} cm^{-3}	1.30	3.0×10^{-4}

(c) Temperature dependence of the effective diffusivity of O_2 at selected doping concentrations.

Figure C.8.3: Effective diffusivity of the oxygen-dimer O_2 calculated from Arrhenius parameters published in reference 122.

C.9 Vacancy-Oxygen Complex VO

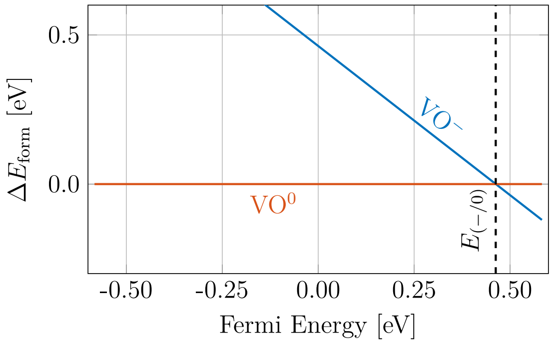

	$\Delta E_{\text{form}}^{E_F=0}$	$\Delta E_{\text{form}}^{E_F=E_V}$
VO^{-}	0.46	1.05
VO^{0}	0.00	0.00

Ferreira-Resende (2000)

Trans.	$E_{q/q+1}$	$E_{q/q+1}$-E_V
-/0	**0.46**	**1.05**

bold: observable transitions

(a) Relative formation energy of each charge state of the VO-complex (based on DFT-simulations by Ferreira-Resende [163]).

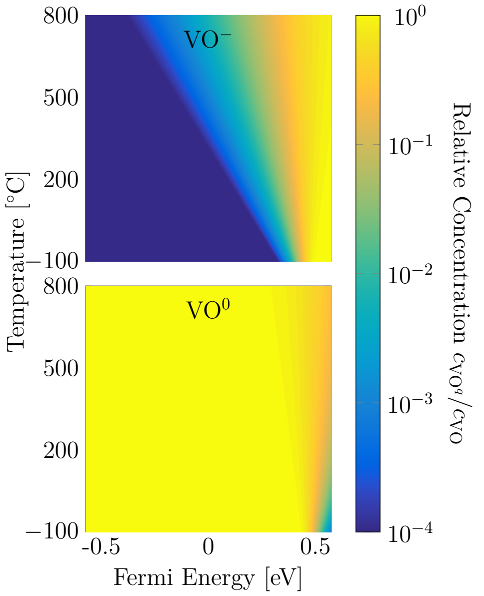

(b) Relative concentration of each charge state of the VO-complex.

Figure C.9.1: Distribution of charge states of the VO-complex. Calculations are based on DFT-simulations by Ferreira-Resende [163].

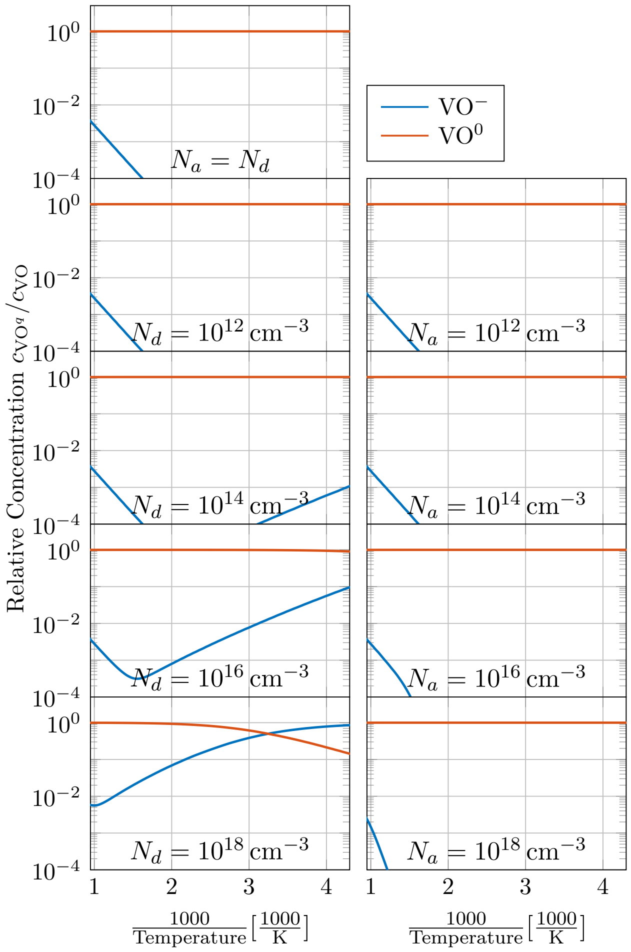

(a) Separate doping concentrations.

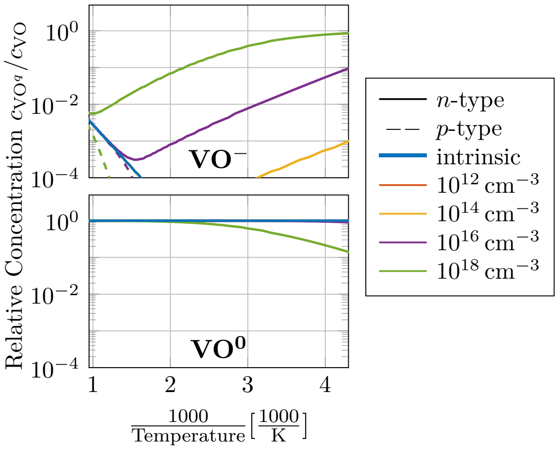

(b) Separate charge states.

Figure C.9.2: Relative concentrations of each charge state of the VO-complex.

Diffusivity of the Vacancy-Oxygen Complex VO

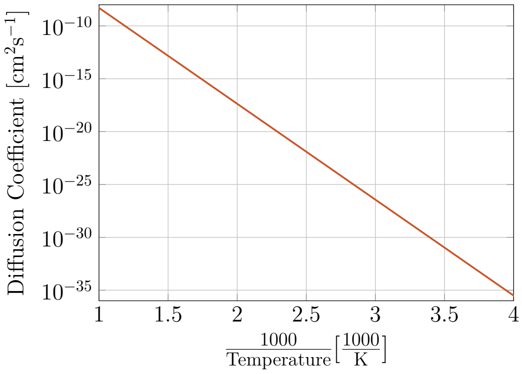

	E_A [eV]	D_0 [$\mathrm{cm^2 s^{-1}}$]
— VO^-	1.80 *	6.0 *
— VO^0	1.80 *	6.0 *

Pellegrino (2001)
*: no individual data for charge states

(a) Diffusivity of each charge state of the VO-complex (see reference 74).

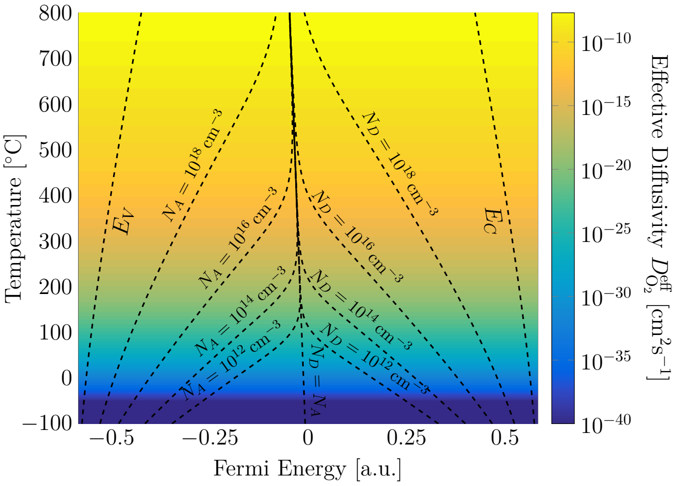

(b) 2D-map of the effective diffusivity of the VO-complex.

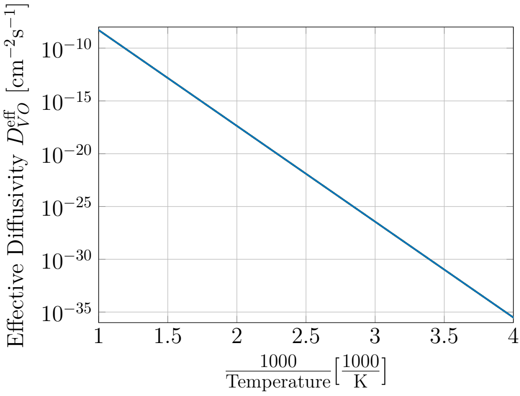

Doping	E_A [eV]	D_0 [$\mathrm{cm^2 s^{-1}}$]
— intrinsic	1.80	6.0
— N_d=$10^{12}\ \mathrm{cm^{-3}}$	1.80	6.0
– – N_a=$10^{12}\ \mathrm{cm^{-3}}$	1.80	6.0
— N_d=$10^{14}\ \mathrm{cm^{-3}}$	1.80	6.0
– – N_a=$10^{14}\ \mathrm{cm^{-3}}$	1.80	6.0
— N_d=$10^{16}\ \mathrm{cm^{-3}}$	1.80	6.0
– – N_a=$10^{16}\ \mathrm{cm^{-3}}$	1.80	6.0
— N_d=$10^{18}\ \mathrm{cm^{-3}}$	1.80	6.0
– – N_a=$10^{18}\ \mathrm{cm^{-3}}$	1.80	6.0

(c) Temperature dependence of the effective diffusivity of VO at selected doping concentrations.

Figure C.9.3: Effective diffusivity of the VO-complex calculated from Arrhenius parameters published in reference 74.

C.10 Divacancy-Oxygen-Complex V_2O

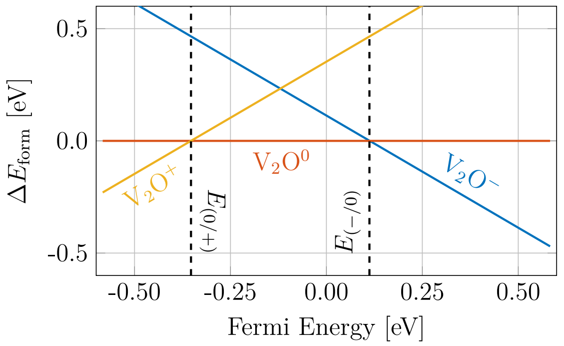

	$\Delta E_{\text{form}}^{E_F=0}$	$\Delta E_{\text{form}}^{E_F=E_V}$
V_2O^-	0.11	0.70
V_2O^0	0.00	0.00
V_2O^+	0.35	-0.23

Ferreira-Resende (2000)

Trans.	$E_{q/q+1}$	$E_{q/q+1}$-E_V
-/0	**0.11**	**0.70**
0/+	**-0.35**	**0.23**

bold: observable transitions

(a) Relative formation energy of each charge state of the divacancy-oxygen complex V_2O (based on DFT-simulations by Ferreira-Resende [163]).

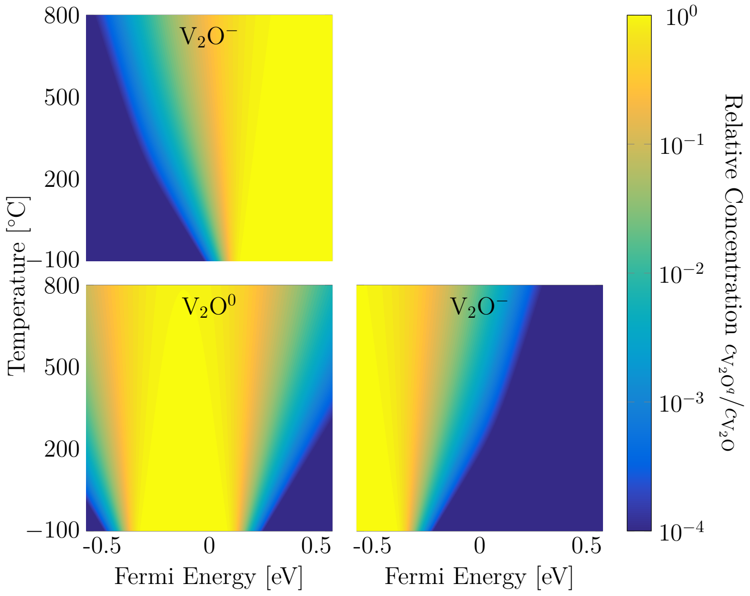

(b) Relative concentration of each charge state of the divacancy-oxygen complex V_2O.

Figure C.10.1: Distribution of charge states of the divacancy-oxygen complex V_2O. Calculations are based on DFT-simulations by Ferreira-Resende [163].

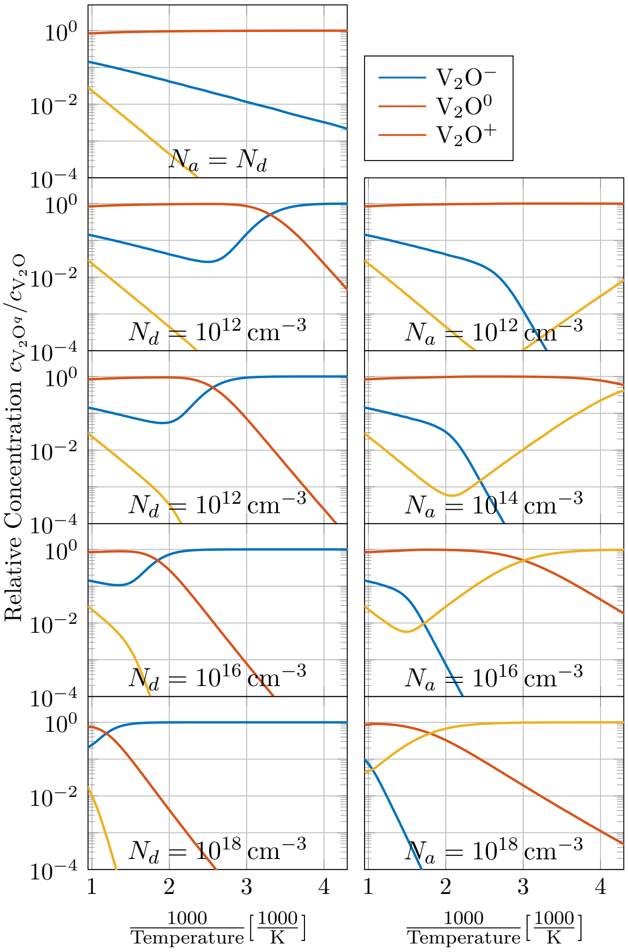

(a) Separate doping concentrations.

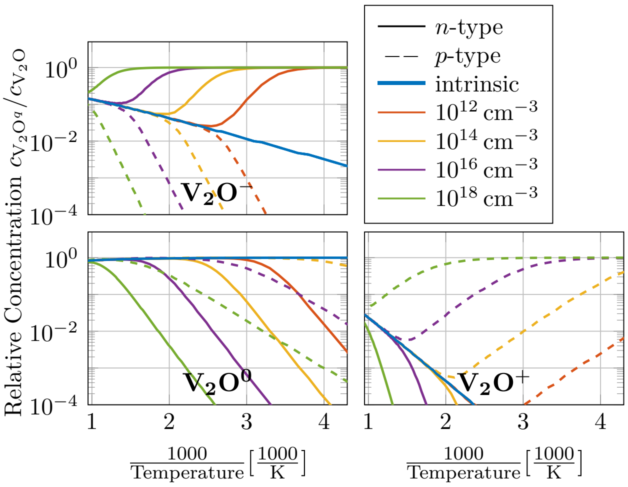

(b) Separate charge states.

Figure C.10.2: Relative concentrations of each charge state of V_2O.

C.11 Tri-Vacancy-Oxygen-Complex V_3O

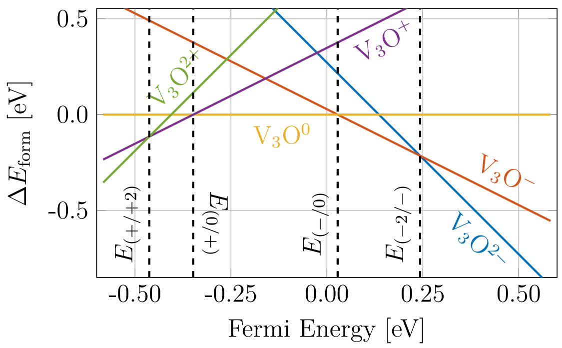

	$\Delta E_{\text{form}}^{E_F=0}$	$\Delta E_{\text{form}}^{E_F=E_V}$
V_3O^{2-}	0.27	0.44
V_3O^{-}	0.03	0.61
V_3O^{0}	0.00	0.00
V_3O^{+}	0.35	-0.23
V_3O^{2+}	0.81	-0.35

Markevich (2011)

Trans.	$E_{q/q+1}$	$E_{q/q+1}$-E_V
-2/-	**0.24**	**0.83**
-/0	**0.03**	**0.61**
0/+	**-0.35**	**0.23**
+/+2	**-0.46**	**0.12**

bold: observable transitions

(a) Relative formation energy of each charge state of the tri-vacancy-oxygen complex V_3O (based on DFT-simulations by Markevich et al. [164]).

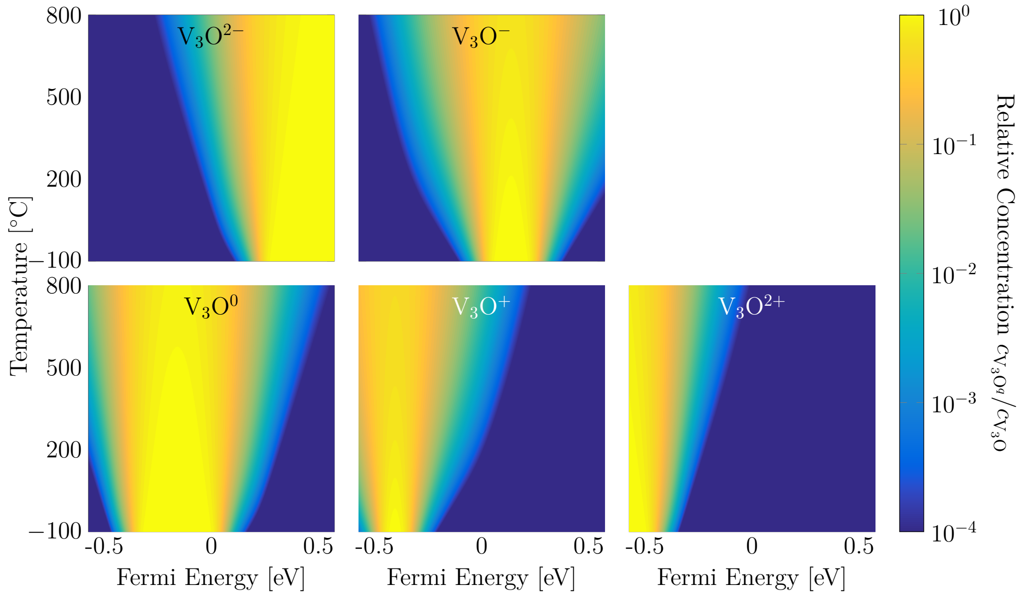

(b) Relative concentration of each charge state of the tri-vacancy-oxygen complex V_3O.

Figure C.11.1: Distribution of charge states of the tri-vacancy-oxygen complex V_3O. Calculations are based on DFT-simulations by Markevich et al. [164].

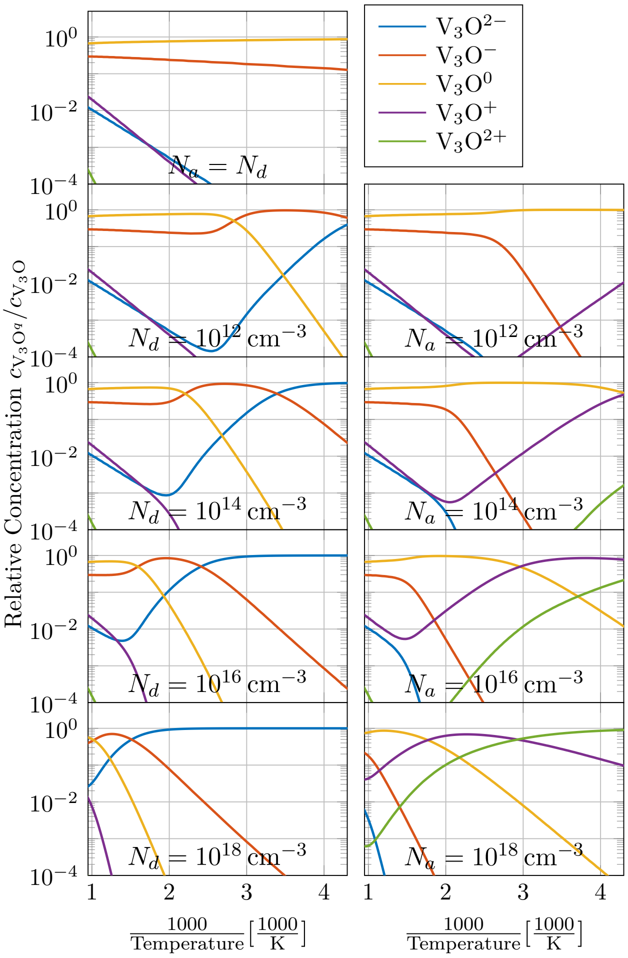

(a) Separate doping concentrations.

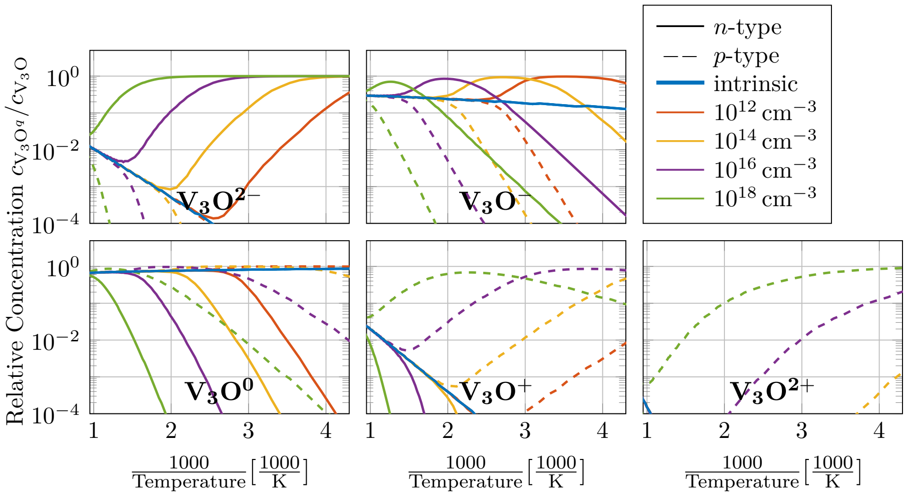

(b) Separate charge states.

Figure C.11.2: Relative concentrations of each charge state of V_3O.

C.12 Substitutional Carbon C_s

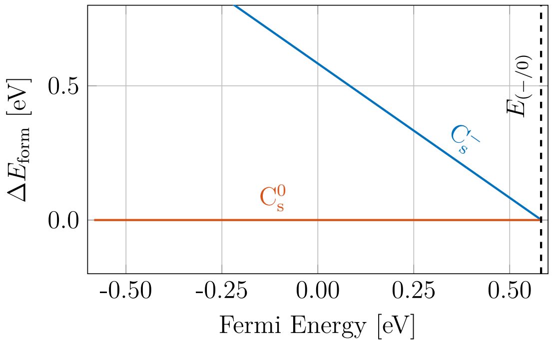

	$\Delta E_{\text{form}}^{E_F=0}$	$\Delta E_{\text{form}}^{E_F=E_V}$
C_s^-	0.58	1.17
C_s^0	0.00	0.00

Windl et al. (1998)

Trans.	$E_{q/q+1}$	$E_{q/q+1}$-E_V
-/0	**0.58**	**1.16**

bold: observable transitions

(a) Relative formation energy of each charge state of substitutional carbon C_s (based on DFT-simulations by Windl et al. [183]).

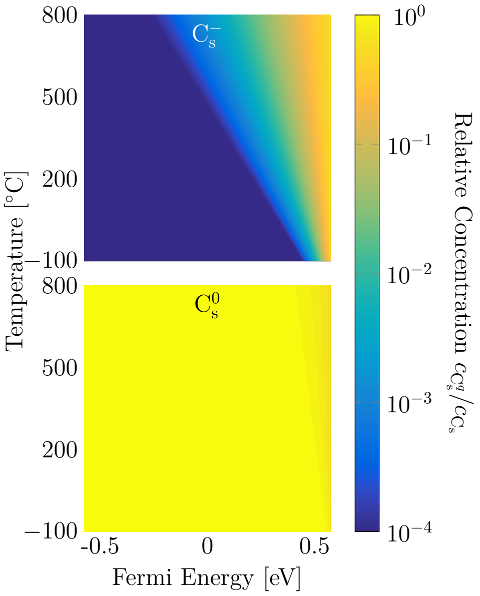

(b) Relative concentration of each charge state of substitutional carbon C_s.

Figure C.12.1: Distribution of charge states of substitutional carbon C_s. Calculations are based on DFT-simulations by Windl et al. [183].

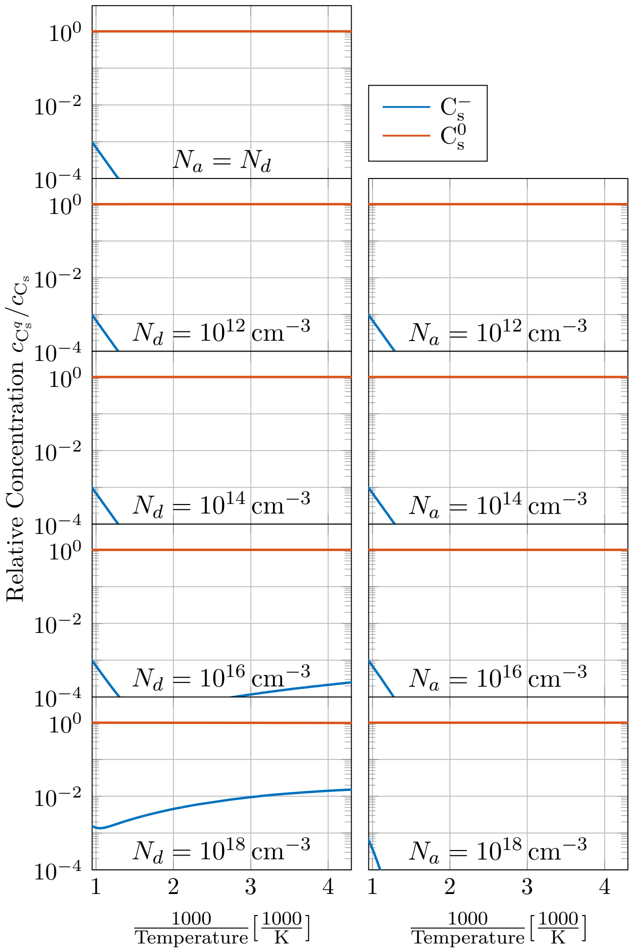

(a) Separate doping concentrations.

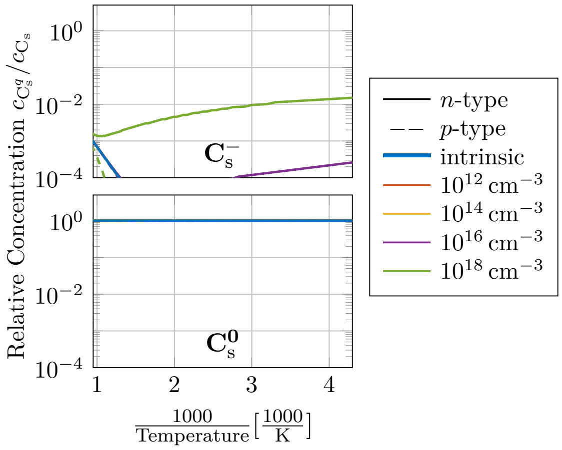

(b) Separate charge states.

Figure C.12.2: Relative concentrations of each charge state of substitutional carbon C_s.

C.13 Interstitial Carbon C_i

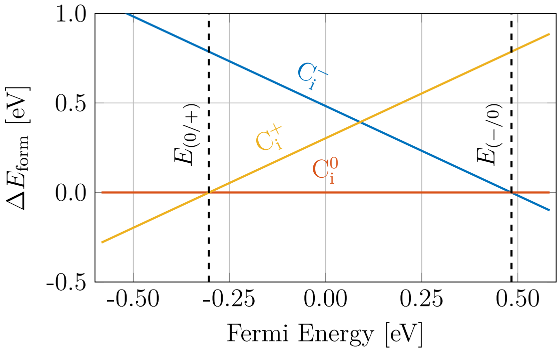

	$\Delta E_{\mathrm{form}}^{E_F=0}$	$\Delta E_{\mathrm{form}}^{E_F=E_V}$
C_i^-	0.48	1.07
C_i^0	0.00	0.00
C_i^+	0.30	-0.08

Ferreira-Resende (2000)

Trans.	$E_{q/q+1}$	$E_{q/q+1}$-E_V
-/0	**0.48**	**1.07**
0/+	**-0.30**	**0.28**

bold: observable transitions

(a) Relative formation energy of each charge state of interstitial carbon C_i (based on DFT-simulations by Ferreira-Resende [163]).

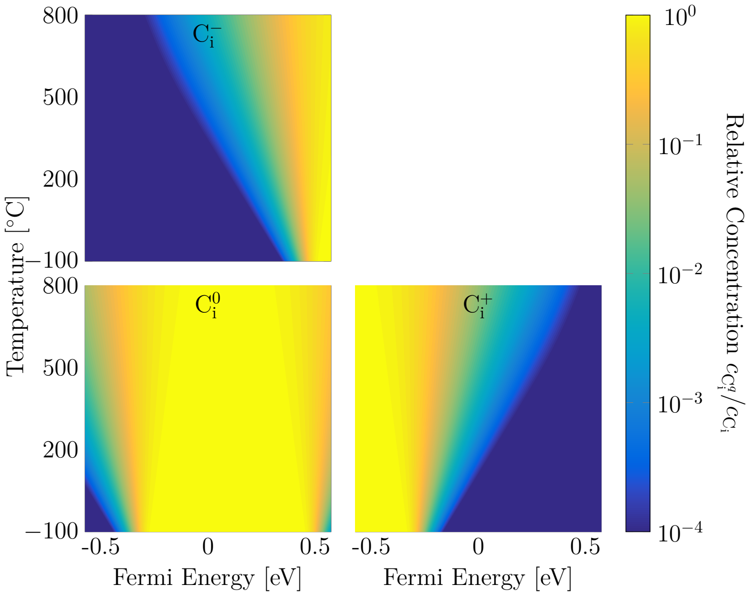

(b) Relative concentration of each charge state of interstitial carbon C_i.

Figure C.13.1: Distribution of charge states of interstitial carbon C_i. Calculations are based on DFT-interstitial by Ferreira-Resende [163].

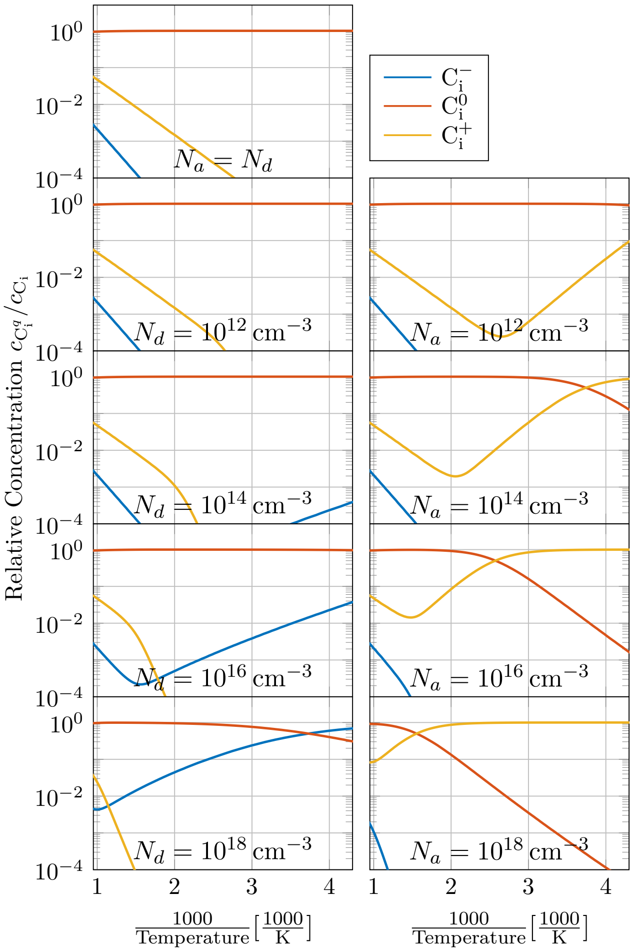

(a) Separate doping concentrations.

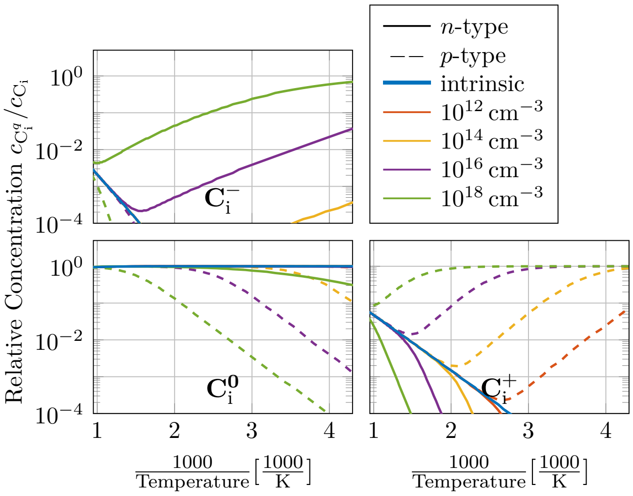

(b) Separate charge states.

Figure C.13.2: Relative concentrations of each charge state of interstitial carbon C_i.

Diffusivity of the Carbon Interstitial C_i

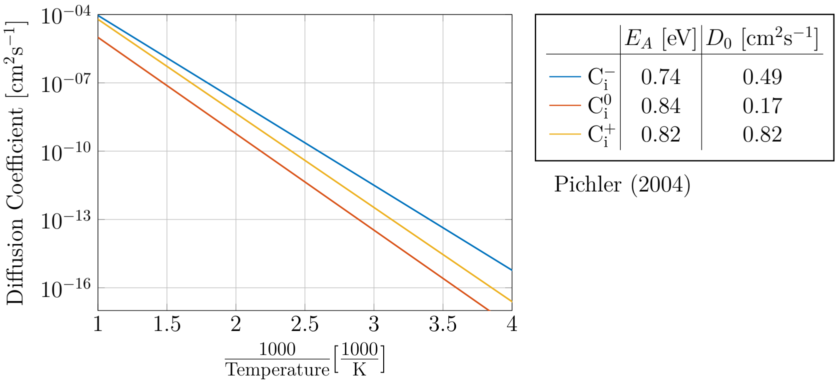

	E_A [eV]	D_0 $[cm^2s^{-1}]$
C_i^-	0.74	0.49
C_i^0	0.84	0.17
C_i^+	0.82	0.82

Pichler (2004)

(a) Diffusivity of each charge state of interstitial carbon C_i (see reference 5).

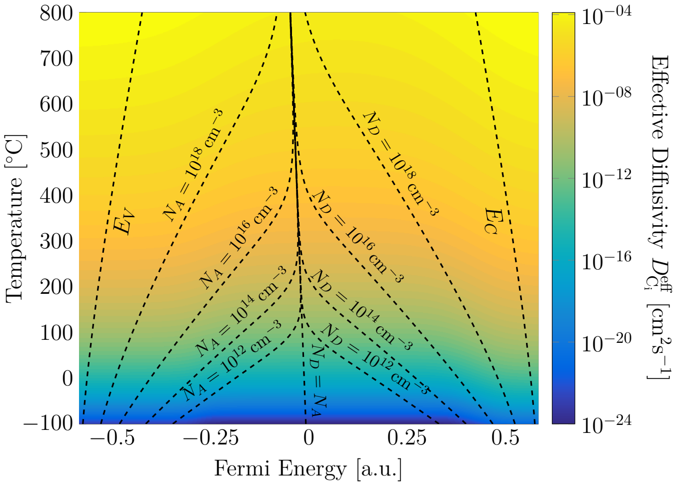

(b) 2D-map of the effective diffusivity of interstitial carbon C_i.

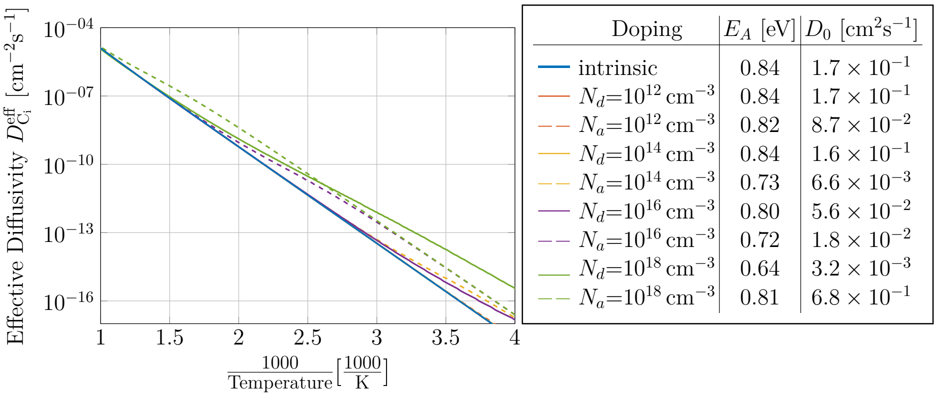

Doping	E_A [eV]	D_0 $[cm^2s^{-1}]$
intrinsic	0.84	1.7×10^{-1}
N_d=10^{12} cm^{-3}	0.84	1.7×10^{-1}
N_a=10^{12} cm^{-3}	0.82	8.7×10^{-2}
N_d=10^{14} cm^{-3}	0.84	1.6×10^{-1}
N_a=10^{14} cm^{-3}	0.73	6.6×10^{-3}
N_d=10^{16} cm^{-3}	0.80	5.6×10^{-2}
N_a=10^{16} cm^{-3}	0.72	1.8×10^{-2}
N_d=10^{18} cm^{-3}	0.64	3.2×10^{-3}
N_a=10^{18} cm^{-3}	0.81	6.8×10^{-1}

(c) Temperature dependence of the effective diffusivity of C_i at selected doping concentrations.

Figure C.13.3: Effective diffusivity of interstitial carbon C_i calculated from Arrhenius parameters published in reference 5.

C.14 Interstitial Carbon-Oxygen-Complex C_iO

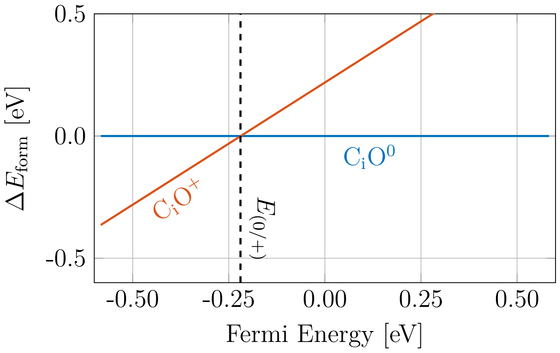

	$\Delta E_{\text{form}}^{E_F=0}$	$\Delta E_{\text{form}}^{E_F=E_V}$
C_iO^0	0.00	0.00
C_iO^+	0.22	-0.36

Coutinho et al. (2001)

Trans.	$E_{q/q+1}$	$E_{q/q+1}$-E_V
0/+	**-0.22**	**0.36**

bold: observable transitions

(a) Relative formation energy of each charge state of the C_iO-complex (based on DFT-simulations by Coutinho et al. [199]).

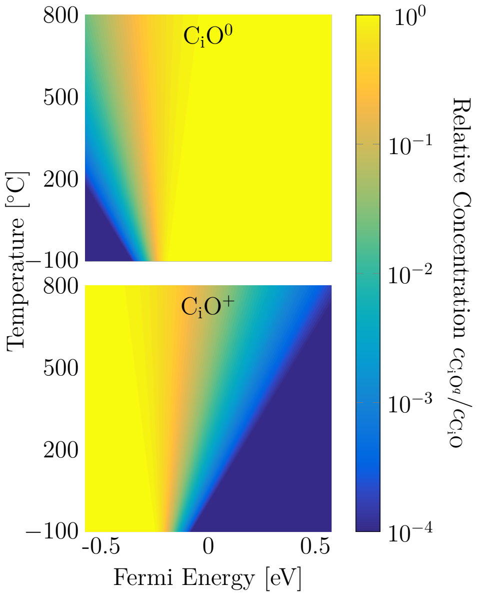

(b) Relative concentration of each charge state of the C_iO-complex.

Figure C.14.1: Distribution of charge states of the C_iO-complex. Calculations are based on DFT-simulations by Coutinho et al. [199].

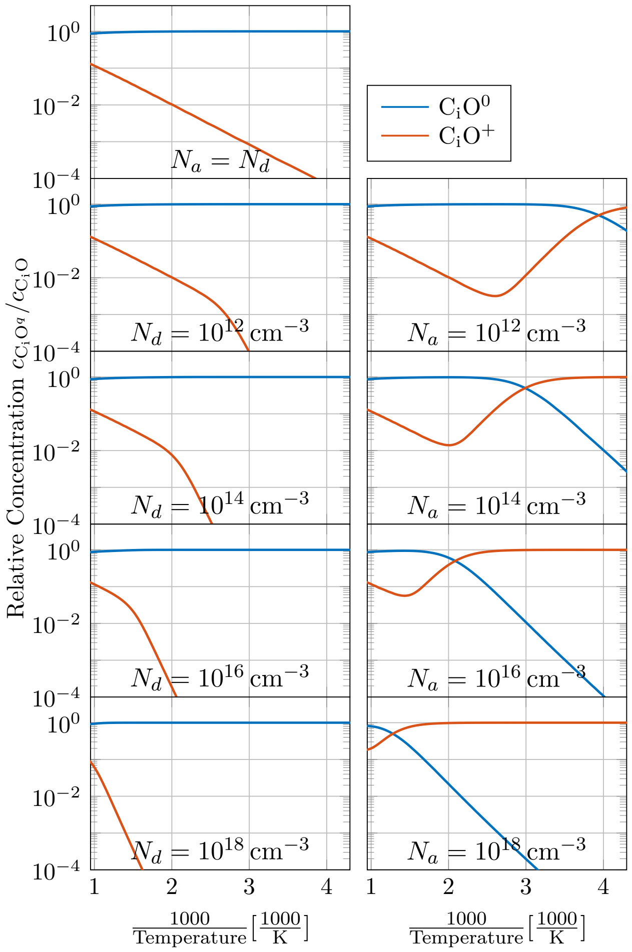

(a) Separate doping concentrations.

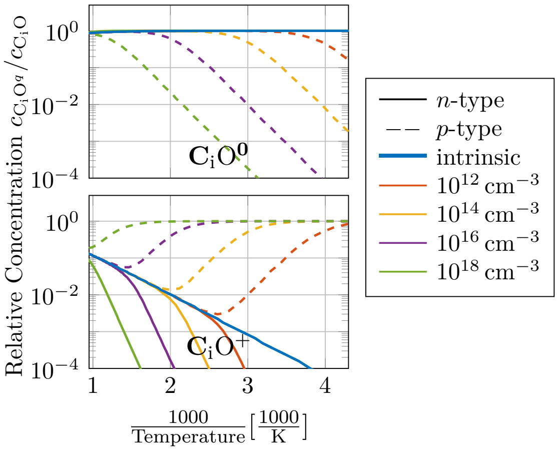

(b) Separate charge states.

Figure C.14.2: Relative concentrations of each charge state of the $\mathrm{C_iO}$-complex.

C.15 C_iOH-Complex

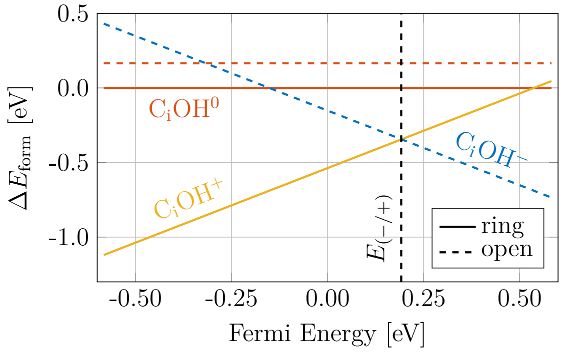

	Configuration	$\Delta E_{\text{form}}^{E_F=0}$	$\Delta E_{\text{form}}^{E_F=E_V}$
C_iOH^0	ring	0.00	0.00
C_iOH^+	ring	-0.54	-1.12
C_iOH^-	open	-0.15	0.43
C_iOH^0	open	0.17	0.17

Trans.	$E_{q/q+1}$	$E_{q/q+1}$-E_V
-/+	**0.19**	**0.77**

bold: observable transitions

Coutinho et al. (2001)

(a) Relative formation energy of each charge state of the C_iOH-complex (based on DFT-simulations by Coutinho et al. [199]).

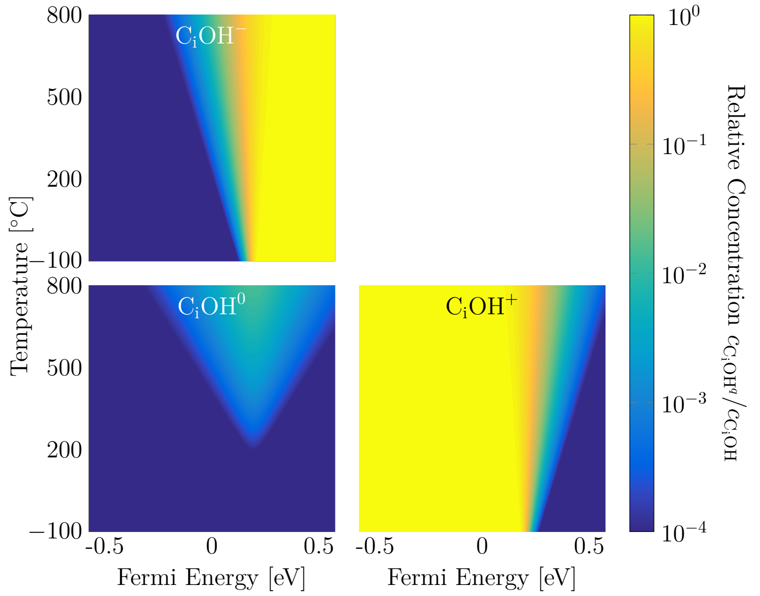

(b) Relative concentration of each charge state of the C_iOH-complex.

Figure C.15.1: Distribution of charge states of the C_iOH-complex. Calculations are based on DFT-simulations by Coutinho et al. [199].

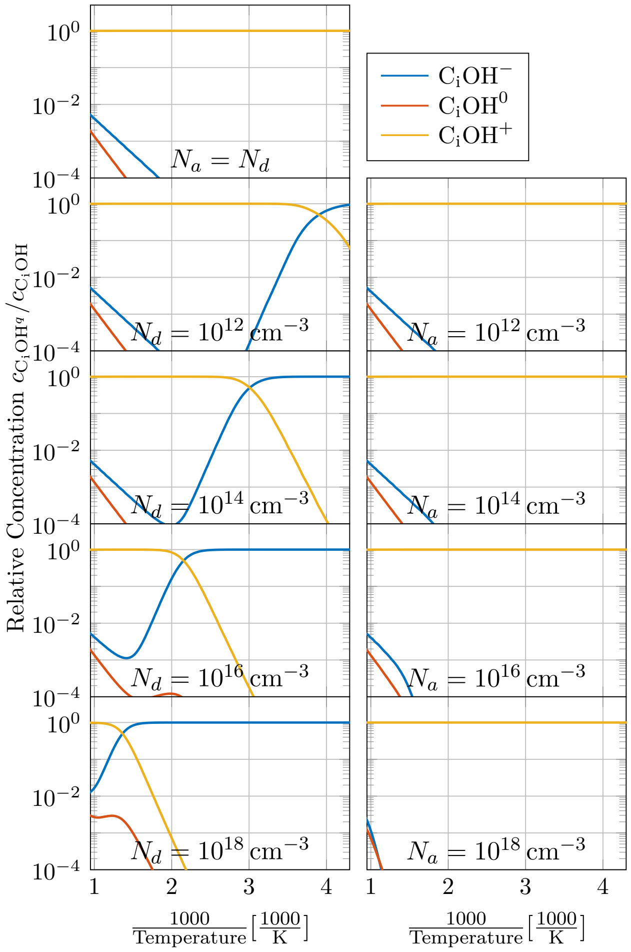

(a) Separate doping concentrations.

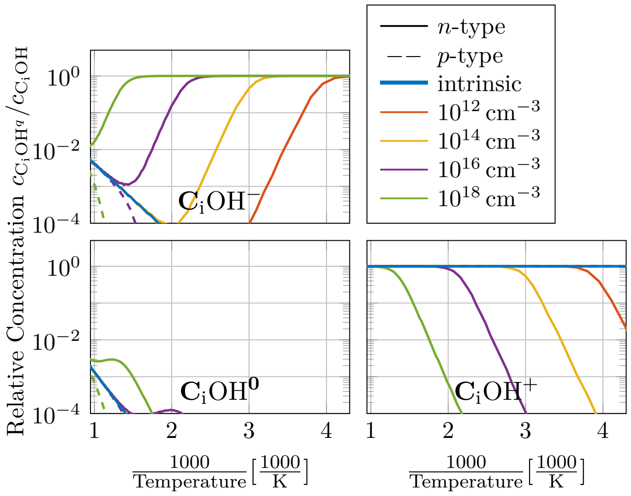

(b) Separate charge states.

Figure C.15.2: Relative concentrations of each charge state of the C_iOH-complex.

C.16 C_iO_2H-Complex

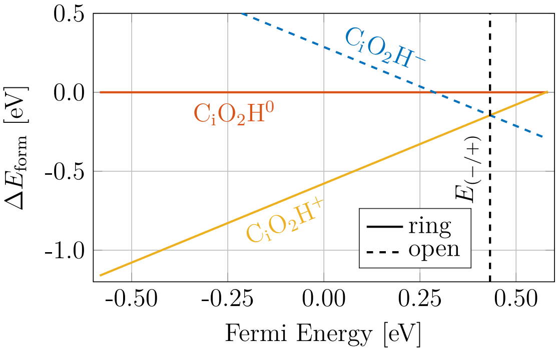

	Configuration	$\Delta E_{\text{form}}^{E_F=0}$	$\Delta E_{\text{form}}^{E_F=E_V}$
$C_iO_2H^0$	ring	0.00	0.00
$C_iO_2H^+$	ring	-0.58	-1.16
$C_iO_2H^-$	open	0.29	0.87
$C_iO_2H^0$	open	0.56	0.56

Coutinho et al. (2001)

Trans.	$E_{q/q+1}$	$E_{q/q+1}$-E_V
-/+	**0.43**	**1.02**

bold: observable transitions

(a) Relative formation energy of each charge state of the C_iO_2H-complex (based on DFT-simulations by Coutinho et al. [199]).

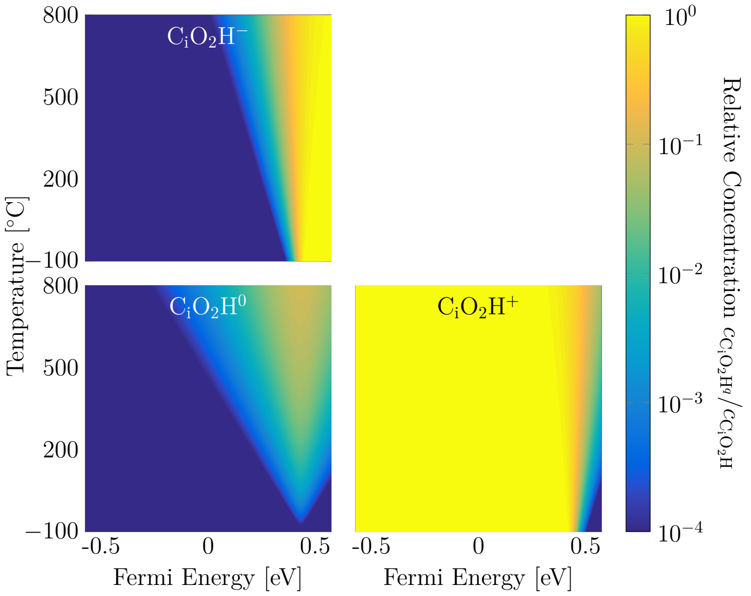

(b) Relative concentration of each charge state of the C_iO_2H-complex.

Figure C.16.1: Distribution of charge states of the C_iO_2H-complex. Calculations are based on DFT-simulations by Coutinho et al. [199].

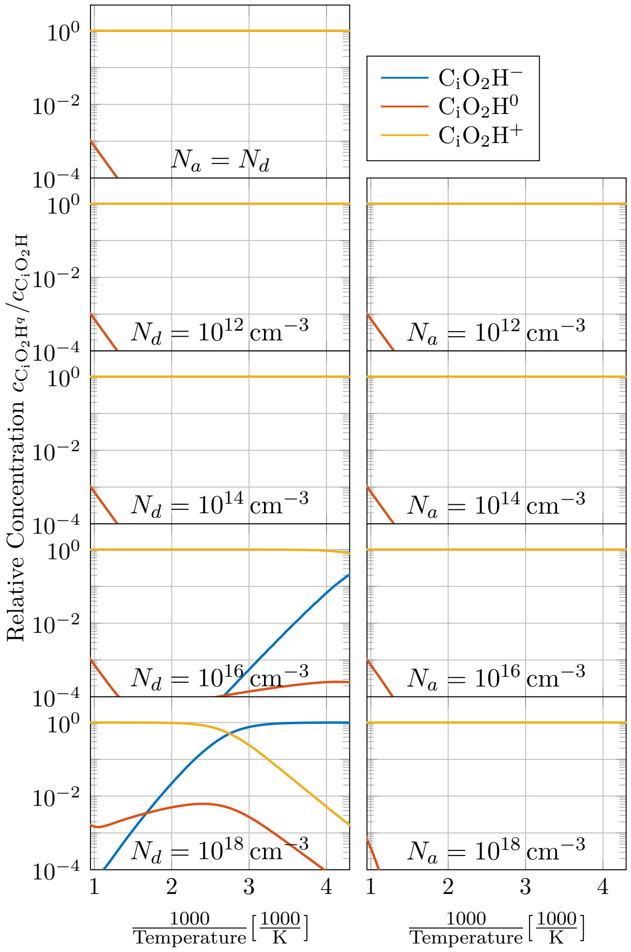

(a) Separate doping concentrations.

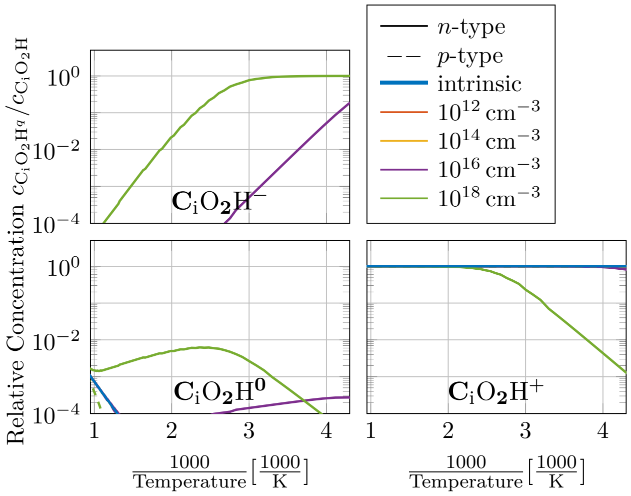

(b) Separate charge states.

Figure C.16.2: Relative concentrations of each charge state of the C_iO_2H-complex.

C.17 C_iI-Complex

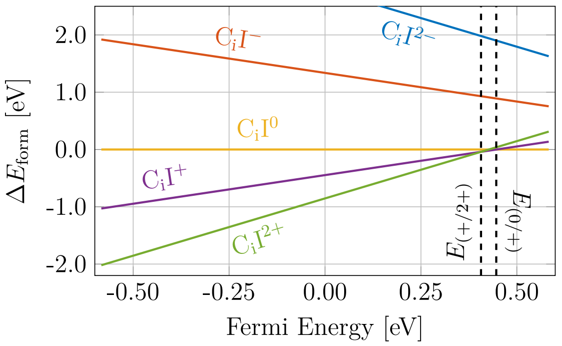

	$\Delta E_{\text{form}}^{E_F=0}$	$\Delta E_{\text{form}}^{E_F=E_V}$
C_iI^{2-}	2.80	3.96
C_iI^-	1.34	1.92
C_iI^0	0.00	0.00
C_iI^+	-0.45	-1.03
C_iI^{2+}	-0.86	-2.02

Wang et al. (2014)

Trans.	$E_{q/q+1}$	$E_{q/q+1}$-E_V
-2/-	$> E_C$	$> E_G$
-/0	$> E_C$	$> E_G$
0/+	**0.45**	**1.03**
+/+2	**0.41**	**0.99**

bold: observable transitions

(a) Relative formation energy of each charge state of the C_iI-complex (based on DFT-simulations by Wang et al. [200]).

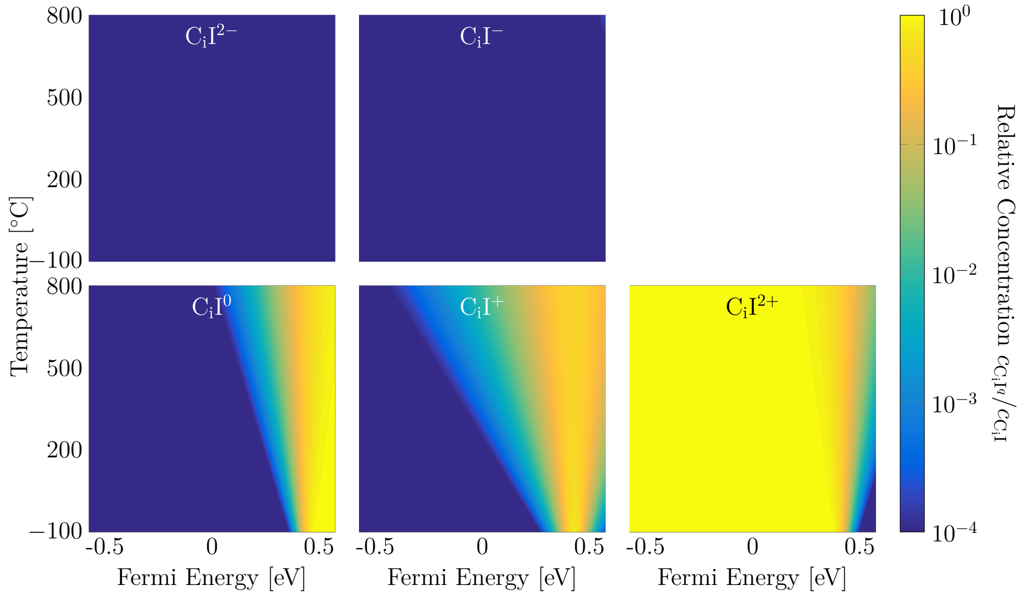

(b) Relative concentration of each charge state of the C_iI-complex.

Figure C.17.1: Distribution of charge states of the C_iI-complex. Calculations are based on DFT-simulations by Wang et al. [200].

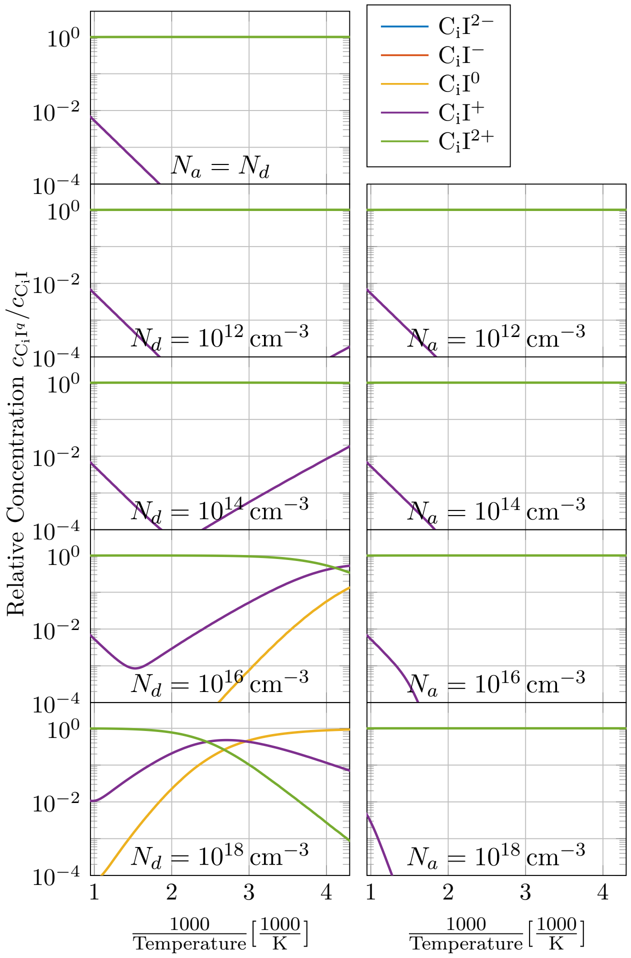

(a) Separate doping concentrations.

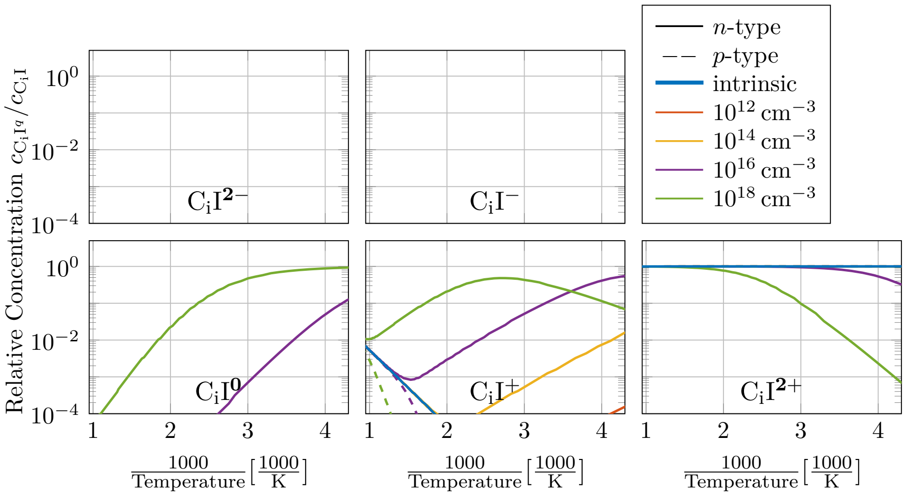

(b) Separate charge states.

Figure C.17.2: Relative concentrations of each charge state of the C_iI-complex.

C.18 C_iOI-Complex

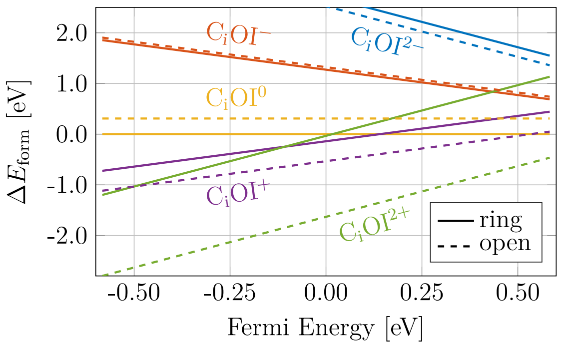

	Configuration	$\Delta E_{\text{form}}^{E_F=0}$	$\Delta E_{\text{form}}^{E_F=E_V}$
C_iOI^{2-}	ring	2.72	3.88
C_iOI^-	ring	1.27	1.85
C_iOI^0	ring	0.00	0.00
C_iOI^+	ring	-0.14	-0.72
C_iOI^{2+}	ring	-0.04	-1.20

	Configuration	$\Delta E_{\text{form}}^{E_F=0}$	$\Delta E_{\text{form}}^{E_F=E_V}$
C_iOI^{2-}	open	2.53	3.69
C_iOI^-	open	1.32	1.91
C_iOI^0	open	0.31	0.31
C_iOI^+	open	-0.53	-1.12
C_iOI^{2+}	open	-1.63	-2.80

Wang et al. (2014)

(a) Relative formation energy of each charge state of the C_iOI-complex (based on DFT-simulations by Wang et al. [200]).

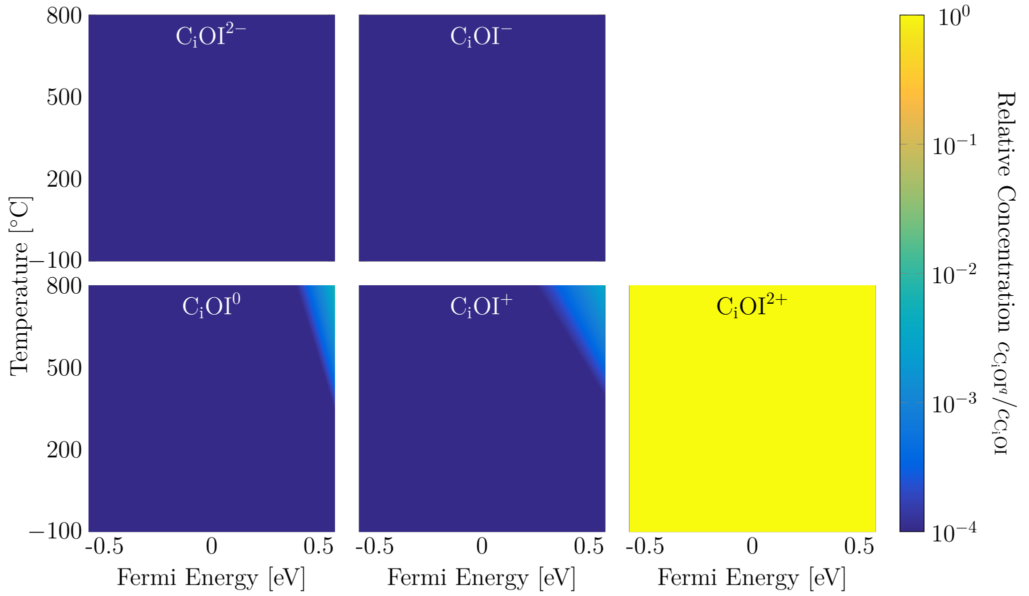

(b) Relative concentration of each charge state of the C_iOI-complex.

Figure C.18.1: Distribution of charge states of the C_iOI-complex. Calculations are based on DFT-simulations by Wang et al. [200].

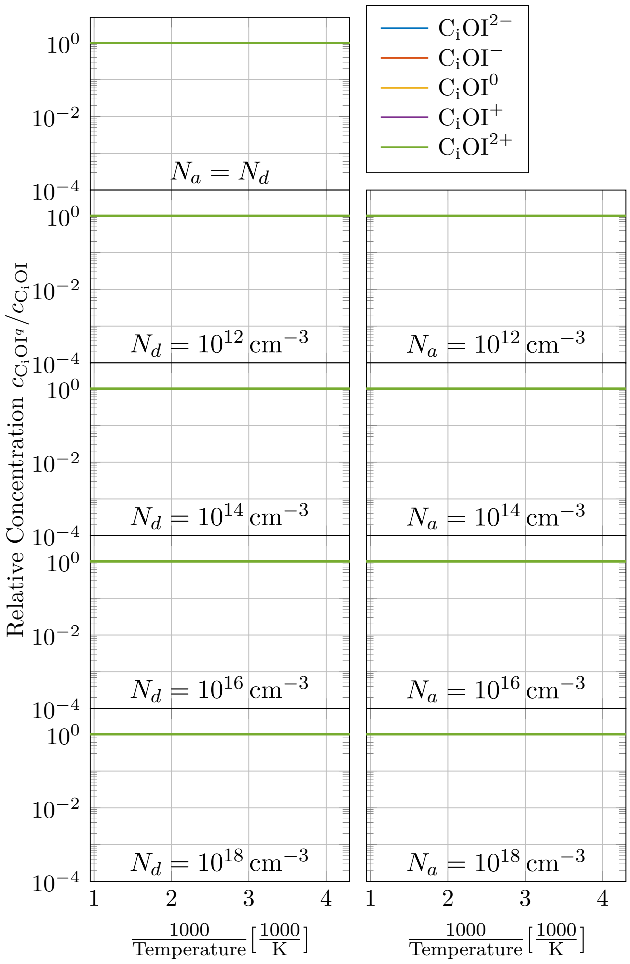

(a) Separate doping concentrations.

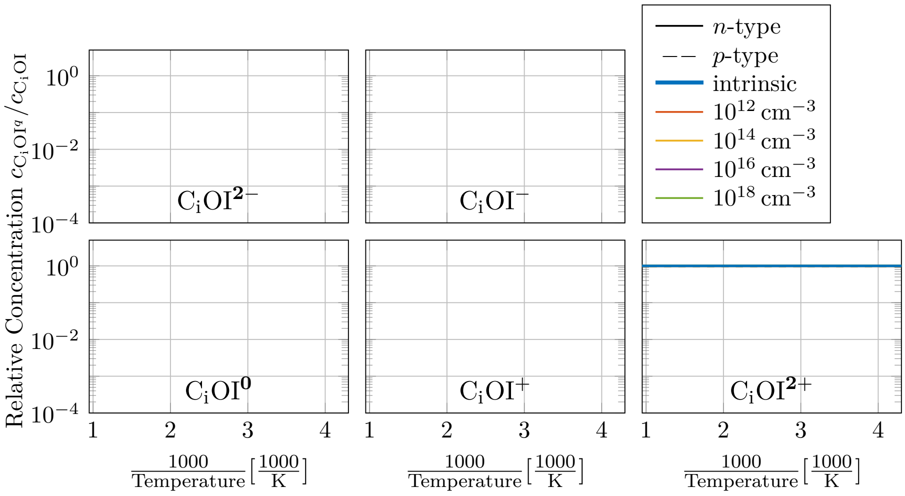

(b) Separate charge states.

Figure C.18.2: Relative concentrations of each charge state of the $\mathrm{C_iOI}$-complex.

C.19 C_iC_s-Complex

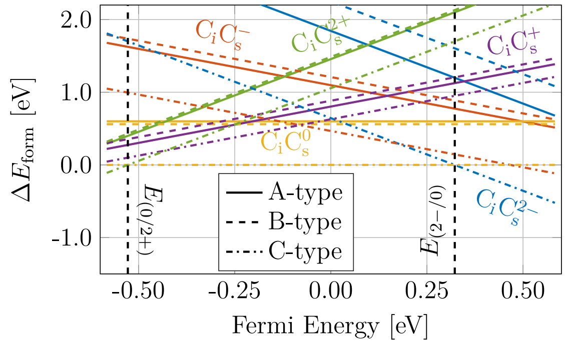

Trans.	$E_{q/q+1}$	$E_{q/q+1}$-E_V
0/2+	**0.10**	**0.68**
2−/0	**-0.22**	**0.36**

bold: observable transitions

	Config.	$\Delta E_{\text{form}}^{E_F=0}$	$\Delta E_{\text{form}}^{E_F=E_V}$
$C_iC_s^{2-}$	A-type	1.85	3.01
$C_iC_s^{-}$	A-type	1.10	1.68
$C_iC_s^{0}$	A-type	0.60	0.60
$C_iC_s^{+}$	A-type	0.80	0.22
$C_iC_s^{2+}$	A-type	1.45	0.29

	Config.	$\Delta E_{\text{form}}^{E_F=0}$	$\Delta E_{\text{form}}^{E_F=E_V}$
$C_iC_s^{2-}$	B-type	2.25	3.42
$C_iC_s^{-}$	B-type	1.21	1.79
$C_iC_s^{0}$	B-type	0.56	0.56
$C_iC_s^{+}$	B-type	0.88	0.30
$C_iC_s^{2+}$	B-type	1.48	0.32

	Config.	$\Delta E_{\text{form}}^{E_F=0}$	$\Delta E_{\text{form}}^{E_F=E_V}$
$C_iC_s^{2-}$	C-type	0.64	1.81
$C_iC_s^{-}$	C-type	0.47	1.05
$C_iC_s^{0}$	C-type	0.00	0.00
$C_iC_s^{+}$	C-type	0.63	0.04
$C_iC_s^{2+}$	C-type	1.05	-0.11

Wang et al. (2014)

(a) Relative formation energy of each charge state of the C_iC_s-complex (based on DFT-simulations by Wang et al. [200]).

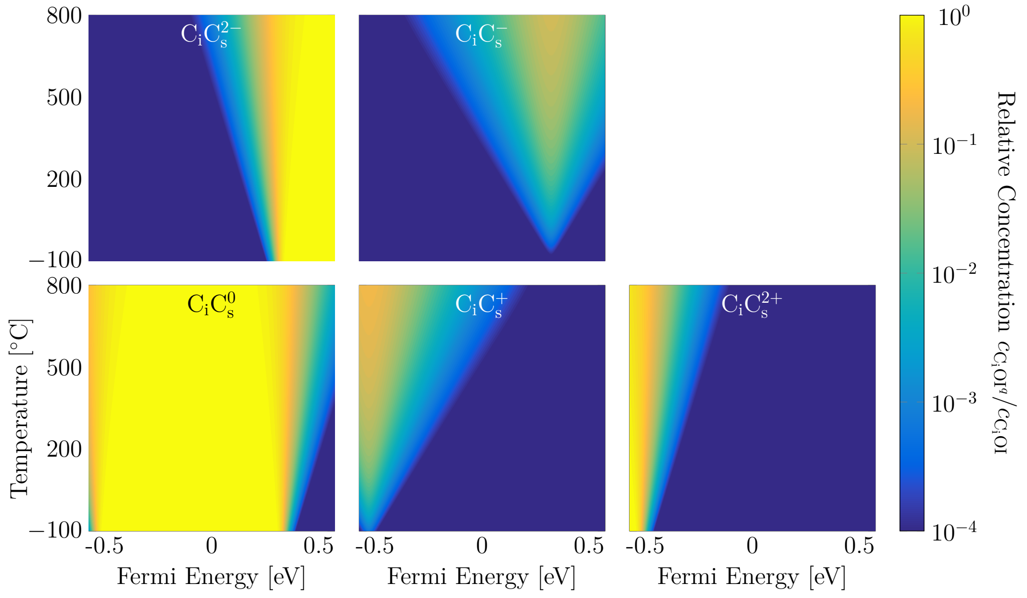

(b) Relative concentration of each charge state of the C_iC_s-complex.

Figure C.19.1: Distribution of charge states of the C_iC_s-complex. Calculations are based on DFT-simulations by Wang et al. [200].

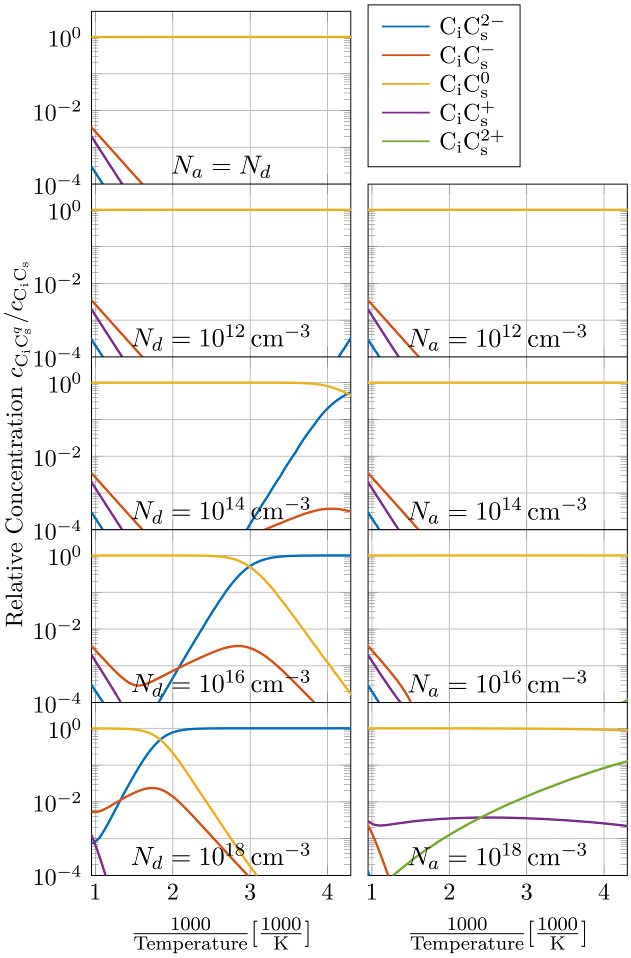

(a) Separate doping concentrations.

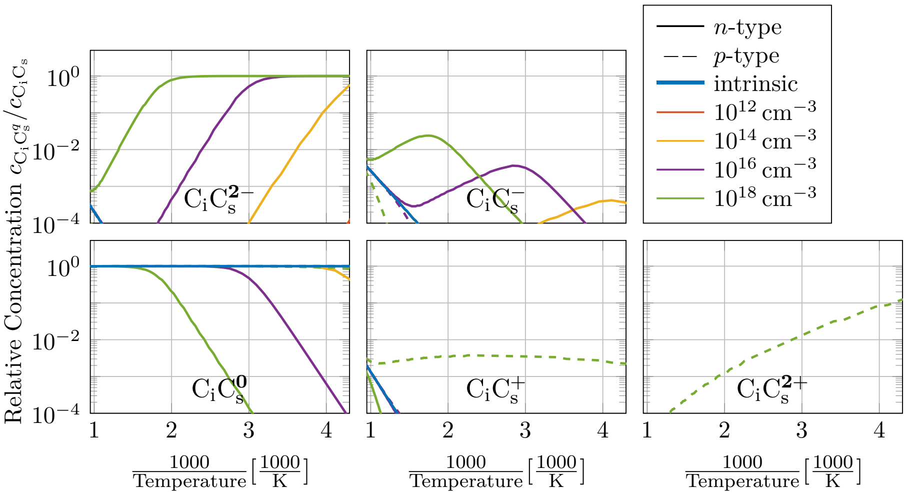

(b) Separate charge states.

Figure C.19.2: Relative concentrations of each charge state of the $\mathrm{C_iC_s}$-complex.

C.20 Substitutional Boron B_s

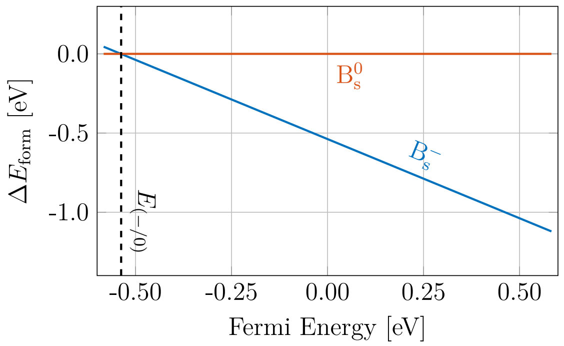

	$\Delta E_{\text{form}}^{E_F=0}$	$\Delta E_{\text{form}}^{E_F=E_V}$
B_s^-	-0.54	0.05
B_s^0	0.00	0.00

Trans.	$E_{q/q+1}$	$E_{q/q+1}$-E_V
-/0	**-0.54**	**0.05**

bold: observable transitions

(a) Relative formation energy of each charge state of substitutional boron B_s (based on an acceptor ionization energy of 0.45 meV).

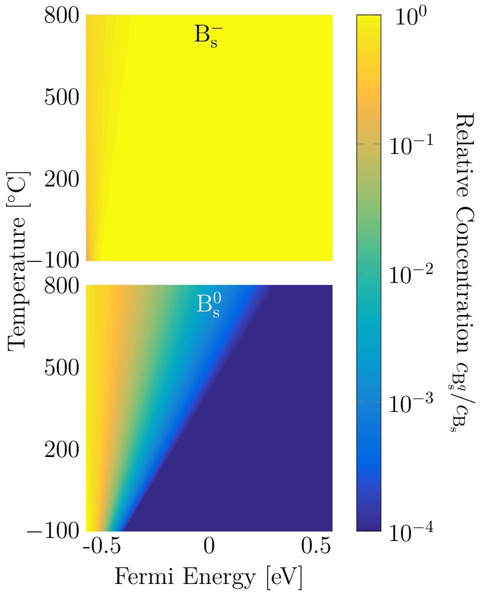

(b) Relative concentration of each charge state of substitutional boron B_s.

Figure C.20.1: Distribution of charge states of substitutional boron B_s. Calculations are based on an acceptor ionization energy of 0.45 meV.

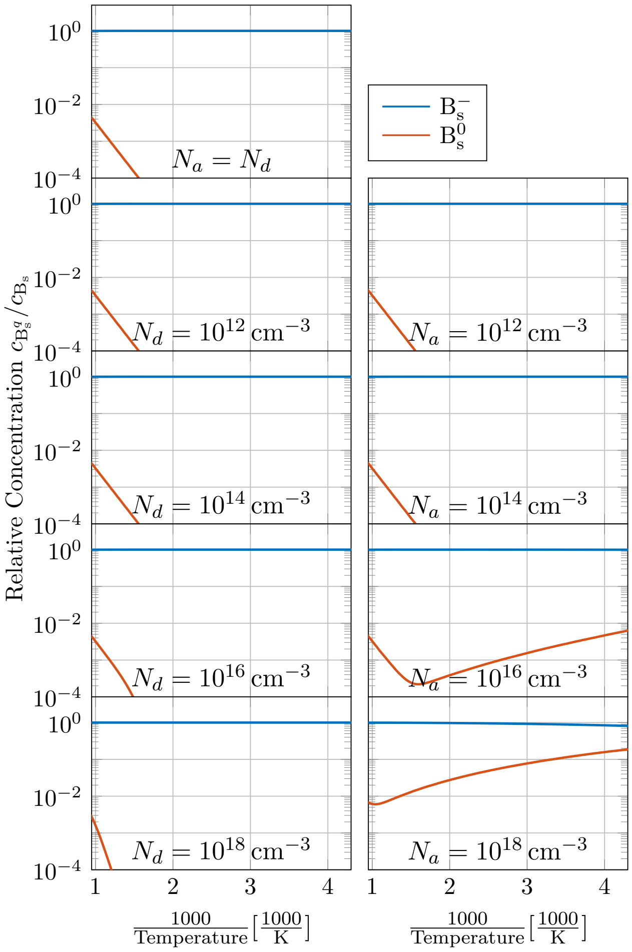

(a) Separate doping concentrations.

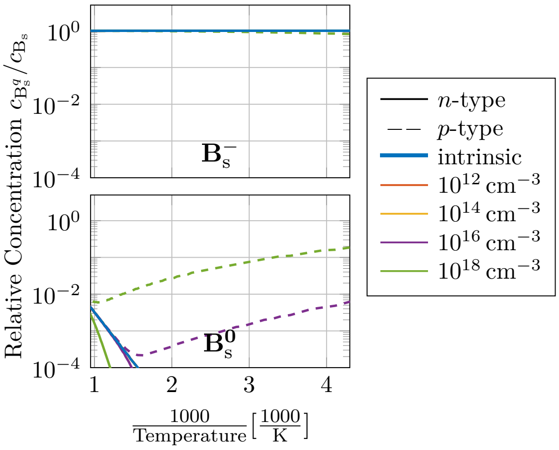

(b) Separate charge states.

Figure C.20.2: Relative concentrations of each charge state of substitutional boron $\mathrm{B_s}$.

C.21 Interstitial Boron B_i

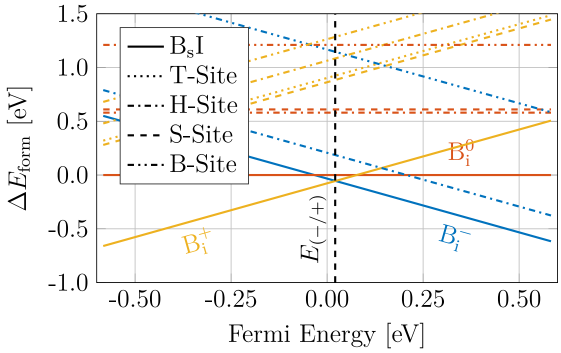

Trans.	$E_{q/q+1}$	$E_{q/q+1}$-E_V
-/+	**0.02**	**0.60**

bold: observable transitions

	Site	$\Delta E_{\mathrm{form}}^{E_F=0}$	$\Delta E_{\mathrm{form}}^{E_F=E_V}$
B_i^-	B_sI	-0.03	0.55
B_i^0	B_sI	0.00	0.00
B_i^+	B_sI	-0.08	-0.66
B_i^+	T-Site	0.90	0.32

	Site	$\Delta E_{\mathrm{form}}^{E_F=0}$	$\Delta E_{\mathrm{form}}^{E_F=E_V}$
B_i^-	H-Site	0.21	0.79
B_i^0	H-Site	0.58	0.58
B_i^+	H-Site	1.06	0.48

Hakala et al. (2000)

	Site	$\Delta E_{\mathrm{form}}^{E_F=0}$	$\Delta E_{\mathrm{form}}^{E_F=E_V}$
B_i^0	S-Site	0.61	0.61
B_i^+	S-Site	0.86	0.28
B_i^-	B-Site	1.17	1.75
B_i^0	B-Site	1.21	1.21
B_i^+	B-Site	1.26	0.68

(a) Relative formation energy of each charge state of interstitial boron B_i (based on DFT-simulations by Hakala et al. [225]).

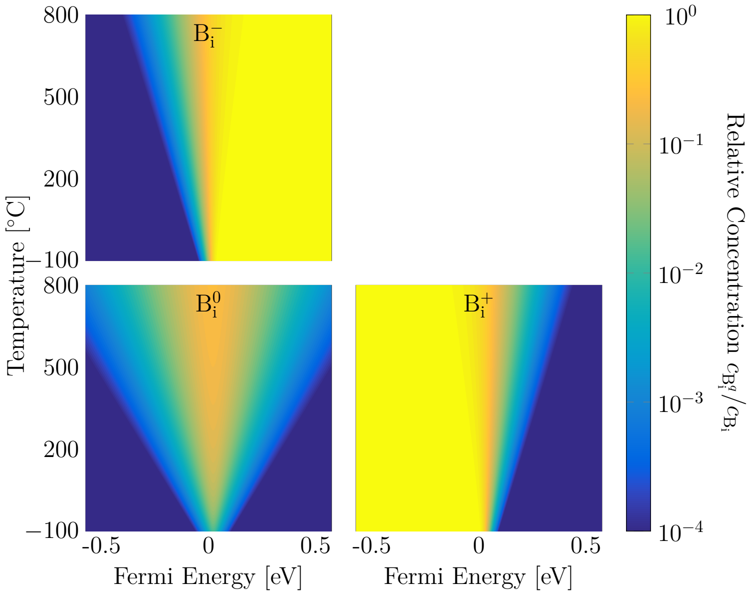

(b) Relative concentration of each charge state of interstitial carbon B_i.

Figure C.21.1: Distribution of charge states of interstitial boron B_i. Calculations are based on DFT-simulations by Hakala et al. [225].

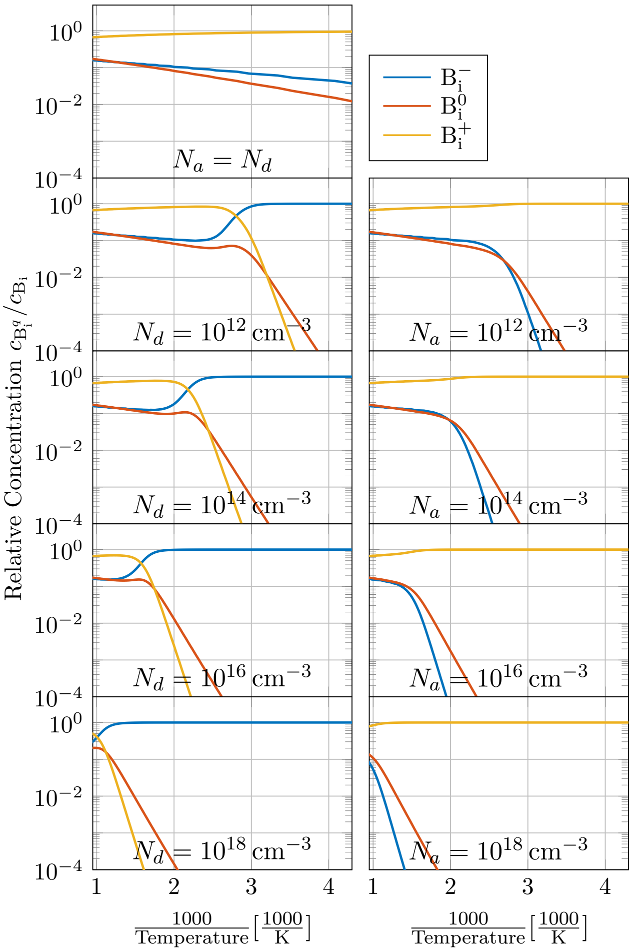

(a) Separate doping concentrations.

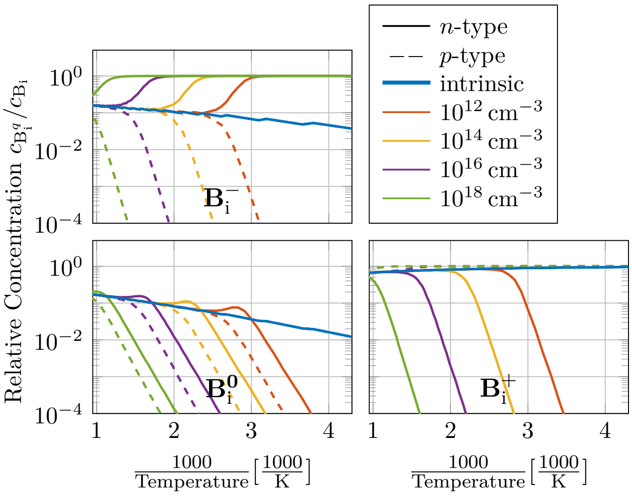

(b) Separate charge states.

Figure C.21.2: Relative concentrations of each charge state of interstitial boron B_i.

Diffusivity of the Boron Interstitial B_i

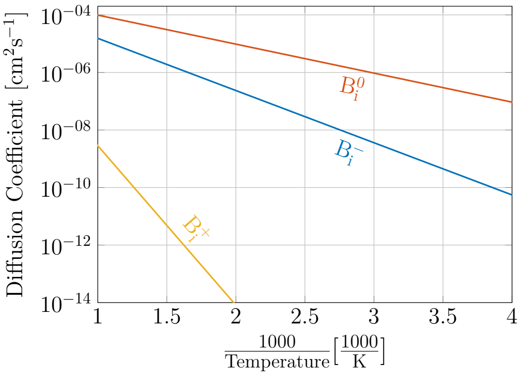

	E_A [eV]	D_0 [cm^{2}s^{-1}]
— $\mathrm{B_i^-}$	0.36	1.0×10^{-3}
— $\mathrm{B_i^0}$	0.20	1.0×10^{-3}
— $\mathrm{B_i^+}$	1.10	1.0×10^{-3}

Martin-Bragado (2005)

(a) Diffusivity of each charge state of interstitial boron $\mathrm{B_i}$ (see reference 236).

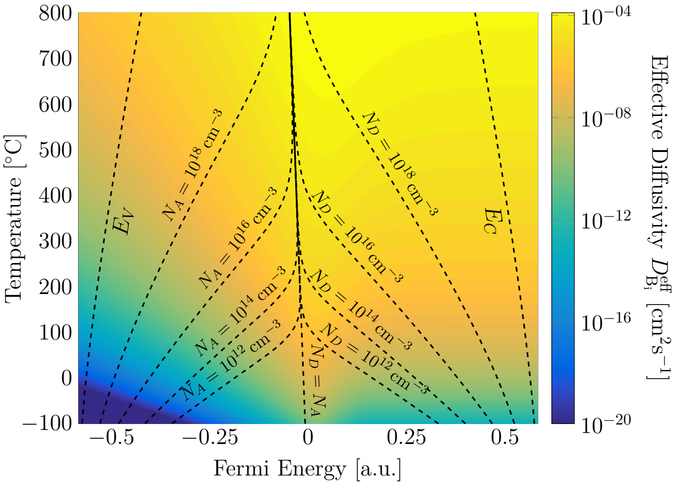

(b) 2D-map of the effective diffusivity of interstitial boron $\mathrm{B_i}$.

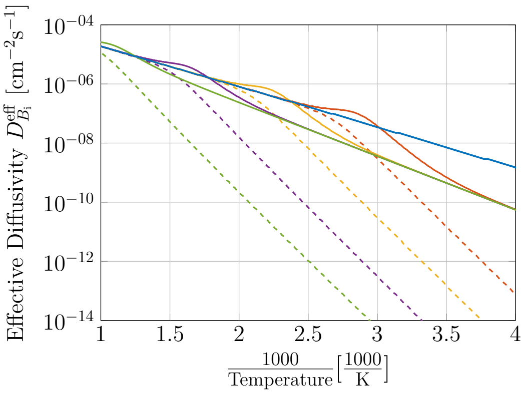

Doping	E_A [eV]	D_0 [cm^{2}s^{-1}]
— intrinsic	0.27	4.5×10^{-5}
— N_d=10^{12} cm^{-3}	0.56	$7.8 \times 10^{+0}$
-- N_a=10^{12} cm^{-3}	0.91	$1.8 \times 10^{+5}$
— N_d=10^{14} cm^{-3}	0.45	2.7×10^{-2}
-- N_a=10^{14} cm^{-3}	0.92	$2.6 \times 10^{+3}$
— N_d=10^{16} cm^{-3}	0.38	1.7×10^{-3}
-- N_a=10^{16} cm^{-3}	0.93	$3.4 \times 10^{+1}$
— N_d=10^{18} cm^{-3}	0.36	1.0×10^{-3}
-- N_a=10^{18} cm^{-3}	0.90	2.5×10^{-1}

(c) Temperature dependence of the effective diffusivity of $\mathrm{B_i}$ at selected doping concentrations.

Figure C.21.3: Effective diffusivity of interstitial boron $\mathrm{B_i}$ calculated from Arrhenius parameters published in reference 236.

C.22 Boron-Vacancy-Complex B_sV

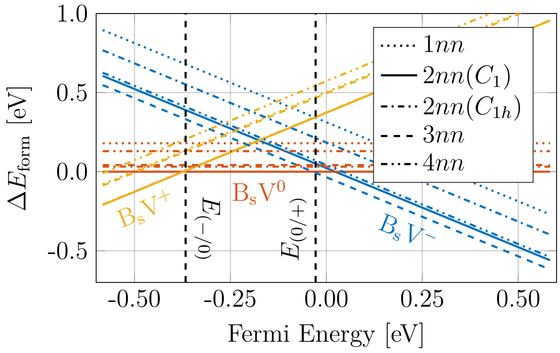

Trans.	$E_{q/q+1}$	$E_{q/q+1}$-E_V
-/0	**-0.03**	**0.55**
0/+	**-0.37**	**0.22**

bold: observable transitions

	Config.	$\Delta E_{\mathrm{form}}^{E_F=0}$	$\Delta E_{\mathrm{form}}^{E_F=E_V}$
B_sV^-	$1nn$	0.31	0.90
B_sV^0	$1nn$	0.18	0.18
B_sV^+	$1nn$	0.50	-0.08
B_sV^-	$2nn(C_1)$	0.02	0.61
B_sV^0	$2nn(C_1)$	0.00	0.00
B_sV^+	$2nn(C_1)$	0.37	-0.21

	Config.	$\Delta E_{\mathrm{form}}^{E_F=0}$	$\Delta E_{\mathrm{form}}^{E_F=E_V}$
B_sV^-	$2nn(C_{1h})$	0.19	0.77
B_sV^0	$2nn(C_{1h})$	0.03	0.03
B_sV^+	$2nn(C_{1h})$	0.37	-0.21

Adey et al. (2005)

	Config.	$\Delta E_{\mathrm{form}}^{E_F=0}$	$\Delta E_{\mathrm{form}}^{E_F=E_V}$
B_sV^-	$3nn$	-0.03	0.55
B_sV^0	$3nn$	0.04	0.04
B_sV^+	$3nn$	0.49	-0.09
B_sV^-	$4nn$	0.04	0.63
B_sV^0	$4nn$	0.13	0.13
B_sV^+	$4nn$	0.57	-0.01

(a) Relative formation energy of each charge state of the boron-vacancy-complex B_sV (based on DFT-simulations by Adey et al. [245]).

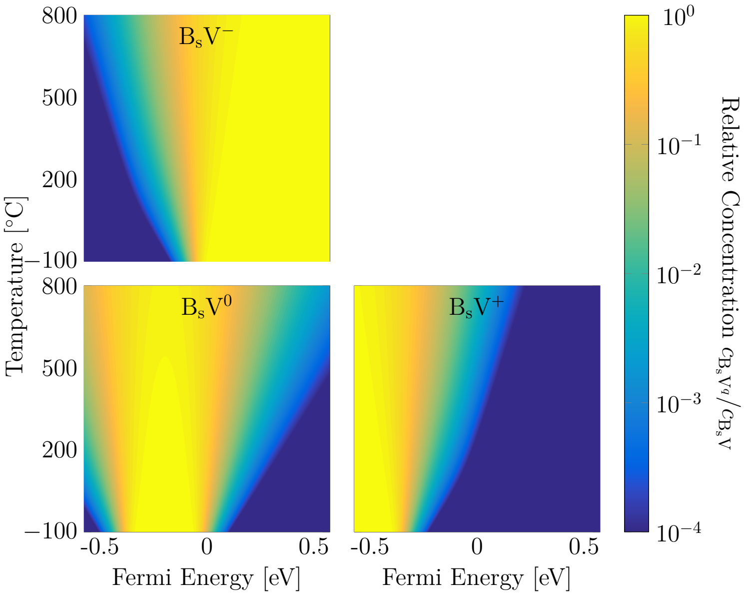

(b) Relative concentration of each charge state of the boron-vacancy-complex B_sV.

Figure C.22.1: Distribution of charge states of the boron-vacancy-complex B_sV. Calculations are based on DFT-simulations by Adey et al. [245].

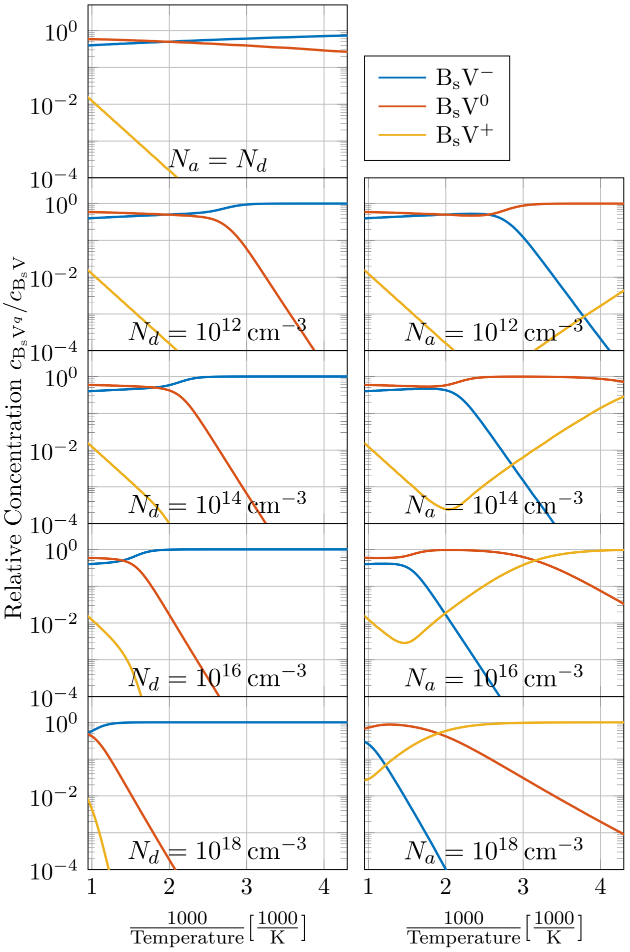

(a) Separate doping concentrations.

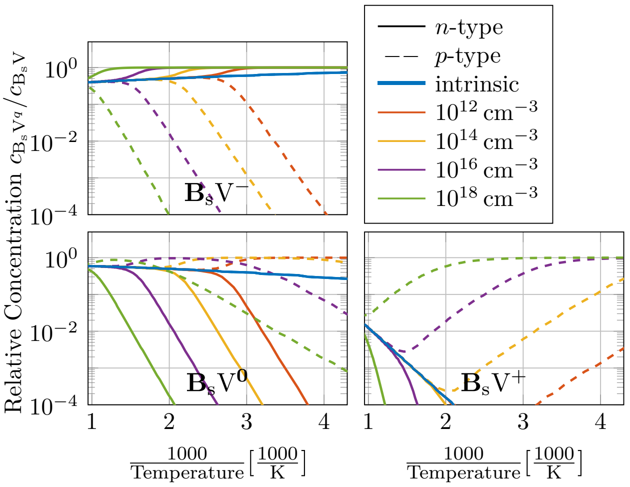

(b) Separate charge states.

Figure C.22.2: Relative concentrations of each charge state of B_sV.

Diffusivity of the Boron-Vacancy-Complex B_sV

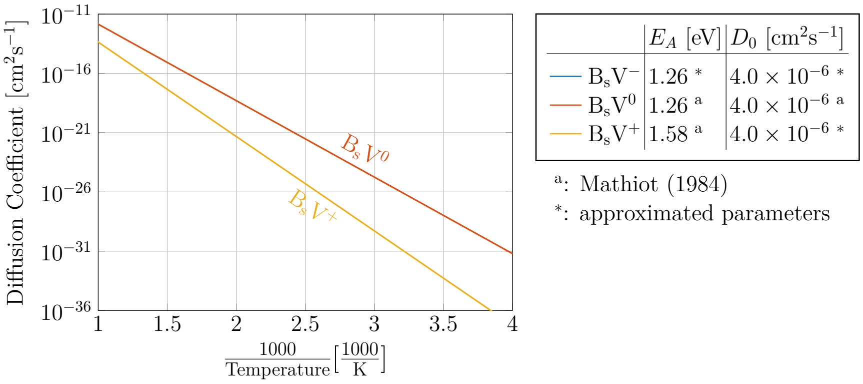

	E_A [eV]	D_0 [cm^{2}s^{-1}]
B_sV^-	1.26 *	4.0×10^{-6} *
B_sV^0	1.26 [a]	4.0×10^{-6} [a]
B_sV^+	1.58 [a]	4.0×10^{-6} *

[a]: Mathiot (1984)

*: approximated parameters

(a) Diffusivity of each charge state of the boron-vacancy-complex B_sV (see reference 238).

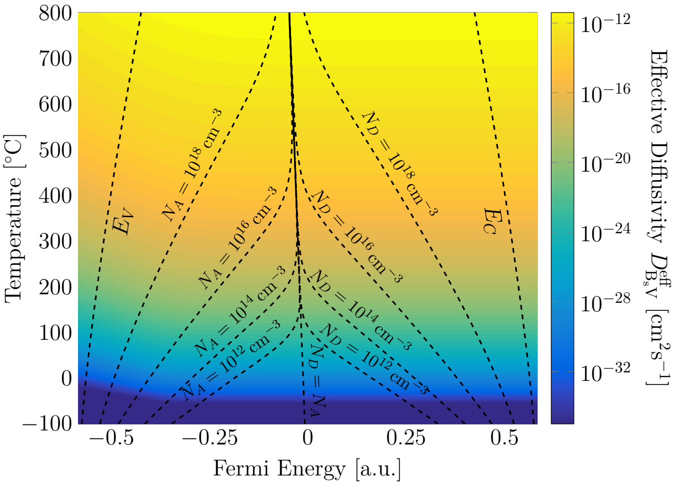

(b) 2D-map of the effective diffusivity of the boron-vacancy-complex B_sV.

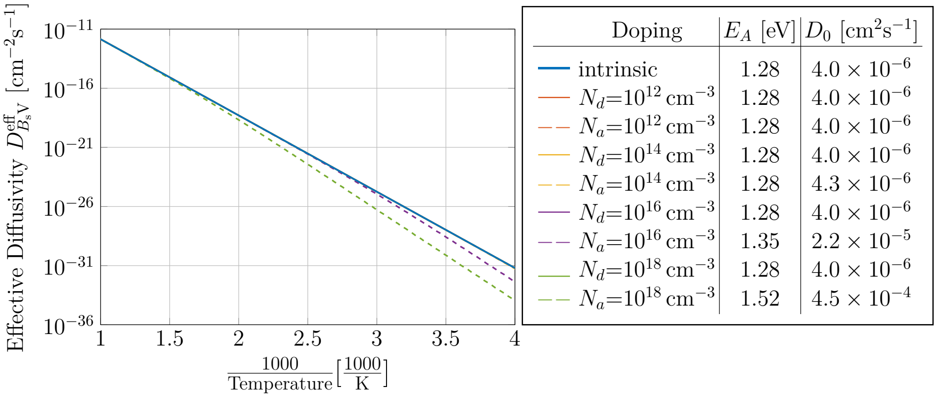

Doping	E_A [eV]	D_0 [cm^{2}s^{-1}]
intrinsic	1.28	4.0×10^{-6}
N_d=10^{12} cm^{-3}	1.28	4.0×10^{-6}
N_a=10^{12} cm^{-3}	1.28	4.0×10^{-6}
N_d=10^{14} cm^{-3}	1.28	4.0×10^{-6}
N_a=10^{14} cm^{-3}	1.28	4.3×10^{-6}
N_d=10^{16} cm^{-3}	1.28	4.0×10^{-6}
N_a=10^{16} cm^{-3}	1.35	2.2×10^{-5}
N_d=10^{18} cm^{-3}	1.28	4.0×10^{-6}
N_a=10^{18} cm^{-3}	1.52	4.5×10^{-4}

(c) Temperature dependence of the effective diffusivity of B_sV at selected doping concentrations.

Figure C.22.3: Effective diffusivity of the boron-vacancy-complex B_sV calculated from Arrhenius parameters published in reference 238.

C.23 Boron-Divacancy-Complex B_sV_2

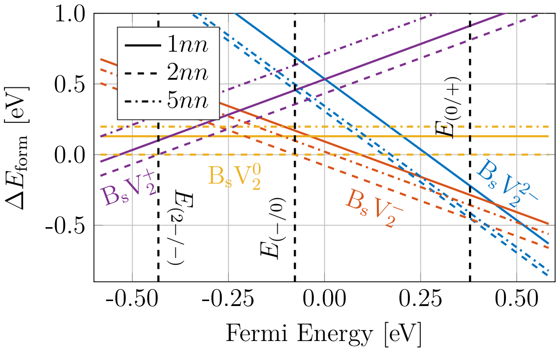

Trans.	$E_{q/q+1}$	$E_{q/q+1}$-E_V
-/2-	**0.38**	**0.96**
-/0	**-0.08**	**0.51**
0/+	**-0.43**	**0.15**

bold: observable transitions

	Config.	$\Delta E_{\text{form}}^{E_F=0}$	$\Delta E_{\text{form}}^{E_F=E_V}$
$B_sV_2^{2-}$	1nn	0.54	1.70
$B_sV_2^-$	1nn	0.09	0.68
$B_sV_2^0$	1nn	0.13	0.13
$B_sV_2^+$	1nn	0.53	-0.05

	Config.	$\Delta E_{\text{form}}^{E_F=0}$	$\Delta E_{\text{form}}^{E_F=E_V}$
$B_sV_2^{2-}$	2nn	0.31	1.47
$B_sV_2^-$	2nn	-0.08	0.51
$B_sV_2^0$	2nn	0.00	0.99
$B_sV_2^+$	2nn	0.43	-0.15

	Config.	$\Delta E_{\text{form}}^{E_F=0}$	$\Delta E_{\text{form}}^{E_F=E_V}$
$B_sV_2^{2-}$	5nn	0.35	1.51
$B_sV_2^-$	5nn	0.02	0.60
$B_sV_2^0$	5nn	0.20	0.20
$B_sV_2^+$	5nn	0.71	0.13

Adey et al. (2005)

(a) Relative formation energy of each charge state of the boron-divacancy-complex B_sV_2 (based on DFT-simulations by Adey et al. [245]).

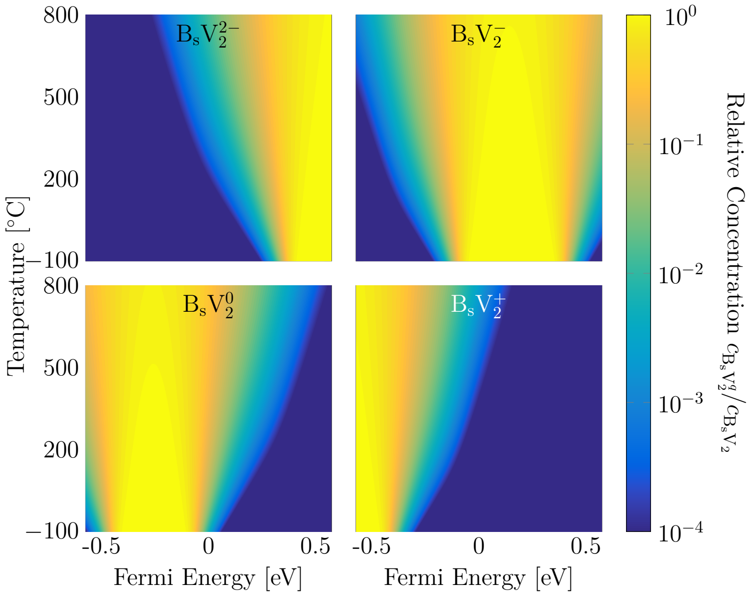

(b) Relative concentration of each charge state of the boron-divacancy-complex B_sV_2.

Figure C.23.1: Distribution of charge states of the boron-divacancy-complex B_sV_2. Calculations are based on DFT-simulations by Adey et al. [245].

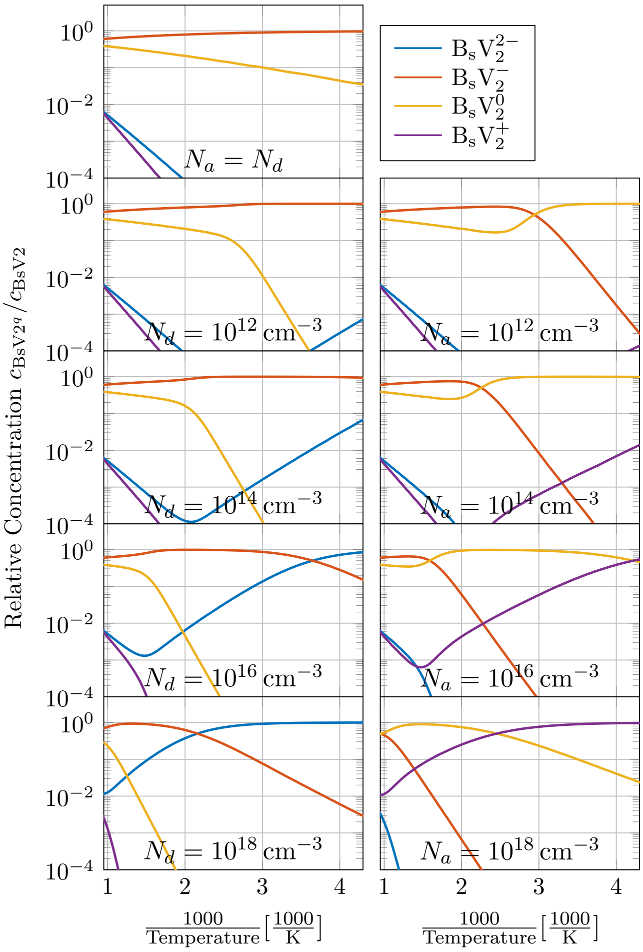

(a) Separate doping concentrations.

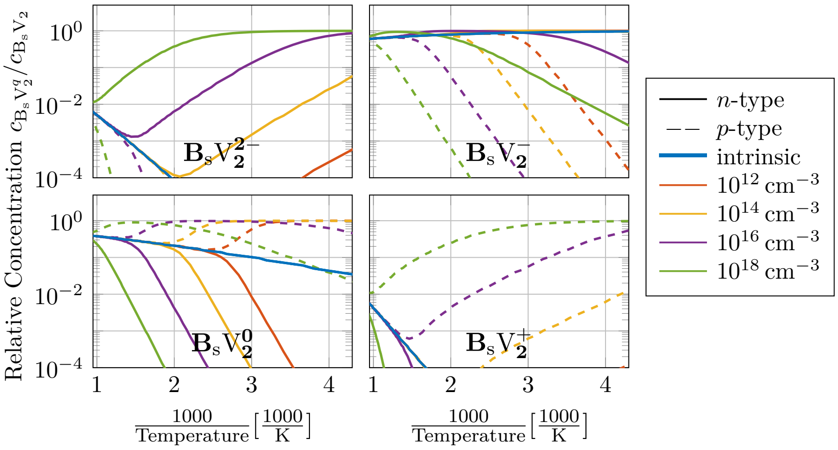

(b) Separate charge states.

Figure C.23.2: Relative concentrations of each charge state of $\mathrm{B_sV_2}$.

C.24 B_iB_s-Complex

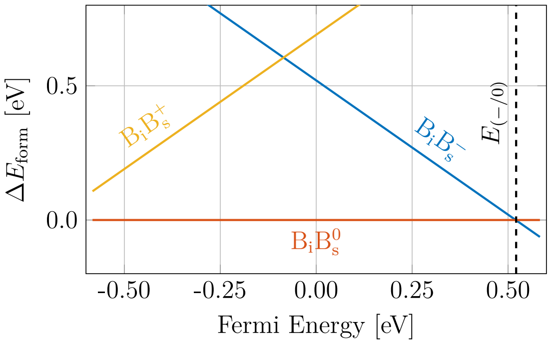

	$\Delta E^{E_F=0}_{\text{form}}$	$\Delta E^{E_F=E_V}_{\text{form}}$
$B_iB_s^-$	0.52	1.10
$B_iB_s^0$	0.00	0.00
$B_iB_s^+$	0.69	0.11

Lenosky, et al. (2000)

Trans.	$E_{q/q+1}$	$E_{q/q+1}$-E_V
-/0	**0.52**	**1.10**
0/+	$< E_V$	< 0

bold: observable transitions

(a) Relative formation energy of each charge state of the B_iB_s-complex (based on DFT-simulations by Lenosky et al. [248]).

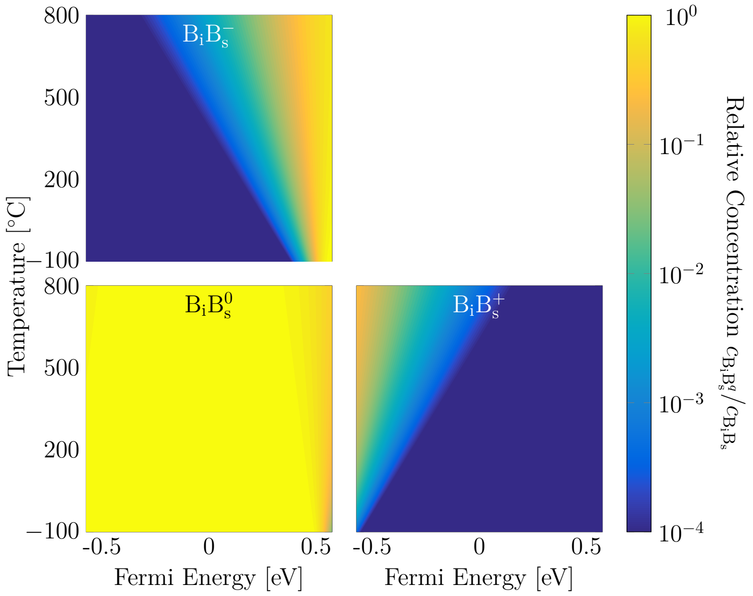

(b) Relative concentration of each charge state of the B_iB_s-complex.

Figure C.24.1: Distribution of charge states of the B_iB_s-complex. Calculations are based on DFT-simulations by Lenosky et al. [248].

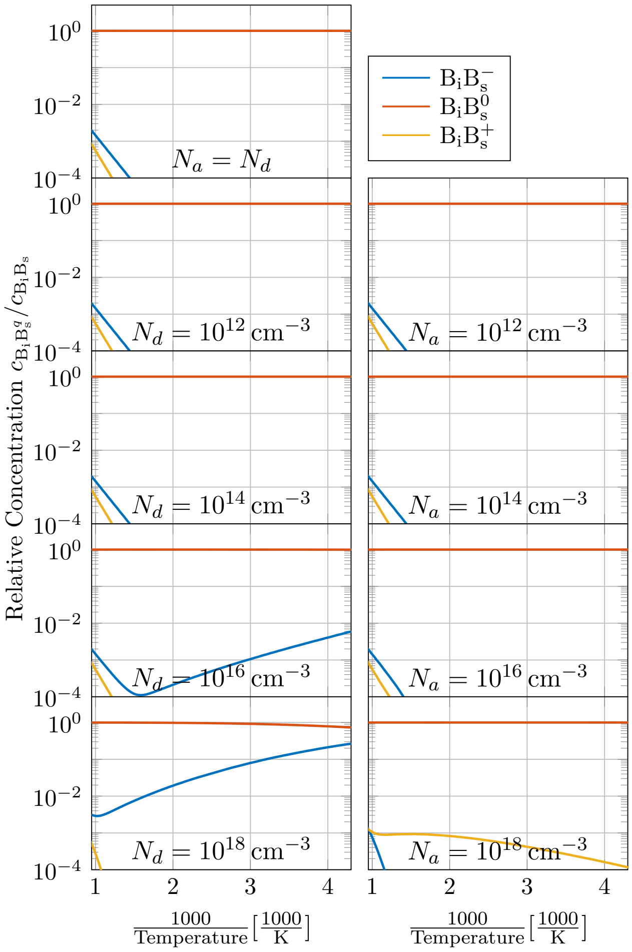

(a) Separate doping concentrations.

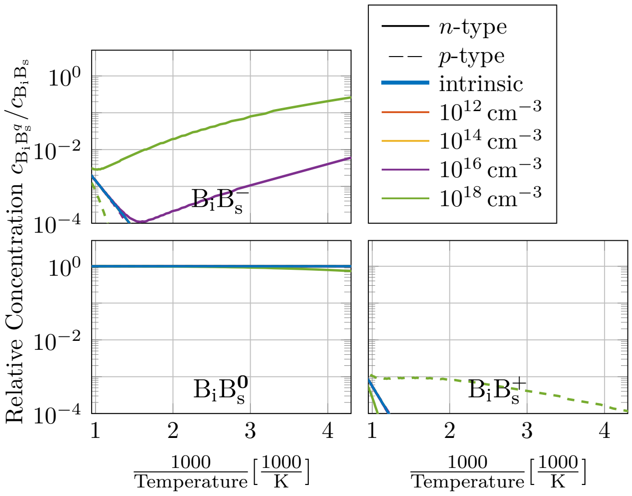

(b) Separate charge states.

Figure C.24.2: Relative concentrations of each charge state of the B_iB_s-complex.

Diffusivity of the B_iB_s-Complex

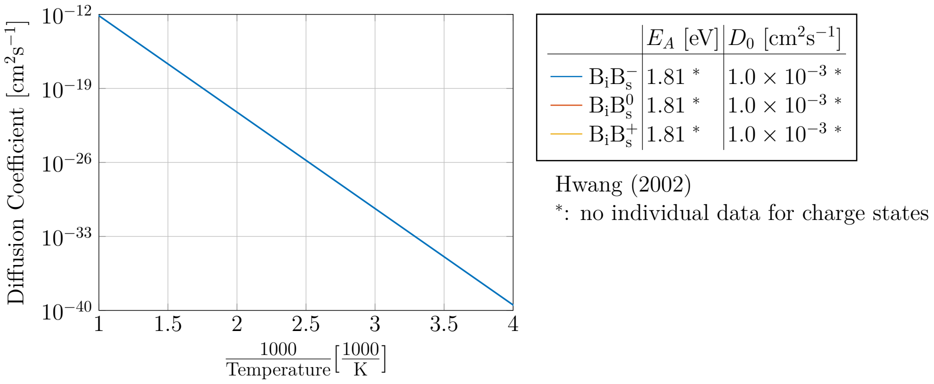

	E_A [eV]	D_0 [cm^2s^{-1}]
$B_iB_s^-$	1.81 *	1.0×10^{-3} *
$B_iB_s^0$	1.81 *	1.0×10^{-3} *
$B_iB_s^+$	1.81 *	1.0×10^{-3} *

(a) Diffusivity of each charge state of the boron-vacancy-complex B_iB_s (see reference 239).

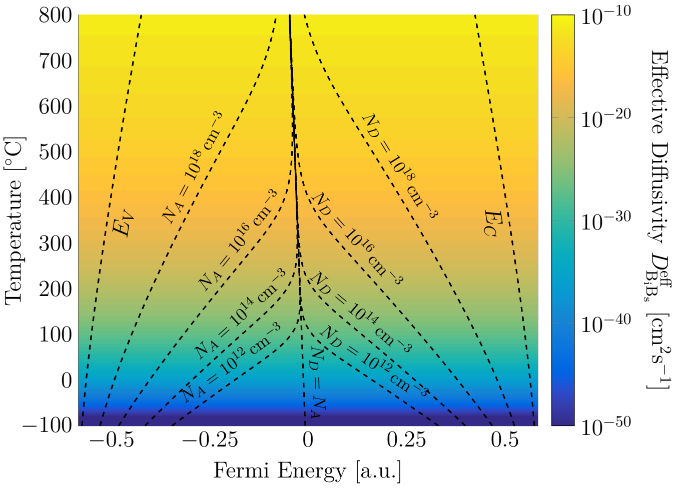

(b) 2D-map of the effective diffusivity of the boron-vacancy-complex B_iB_s.

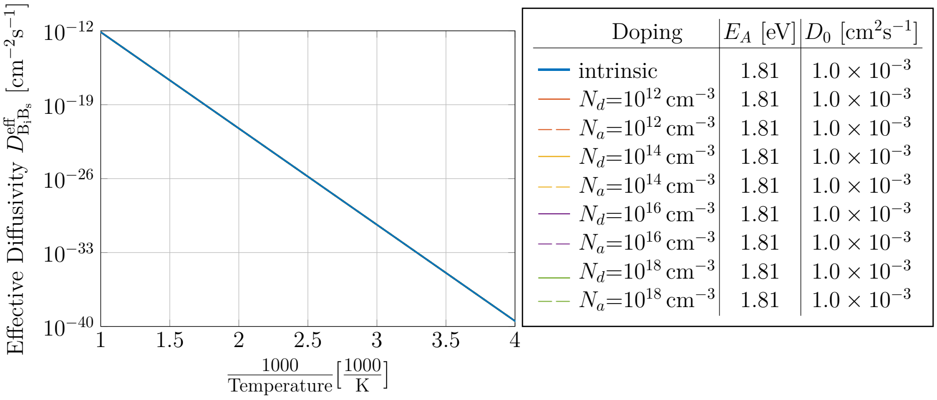

Doping	E_A [eV]	D_0 [cm^2s^{-1}]
intrinsic	1.81	1.0×10^{-3}
N_d=10^{12} cm^{-3}	1.81	1.0×10^{-3}
N_a=10^{12} cm^{-3}	1.81	1.0×10^{-3}
N_d=10^{14} cm^{-3}	1.81	1.0×10^{-3}
N_a=10^{14} cm^{-3}	1.81	1.0×10^{-3}
N_d=10^{16} cm^{-3}	1.81	1.0×10^{-3}
N_a=10^{16} cm^{-3}	1.81	1.0×10^{-3}
N_d=10^{18} cm^{-3}	1.81	1.0×10^{-3}
N_a=10^{18} cm^{-3}	1.81	1.0×10^{-3}

(c) Temperature dependence of the effective diffusivity of B_iB_s at selected doping concentrations.

Figure C.24.3: Effective diffusivity of the boron-vacancy-complex B_iB_s calculated from Arrhenius parameters published in reference 239.

C.25 B_{s_3}-Complex

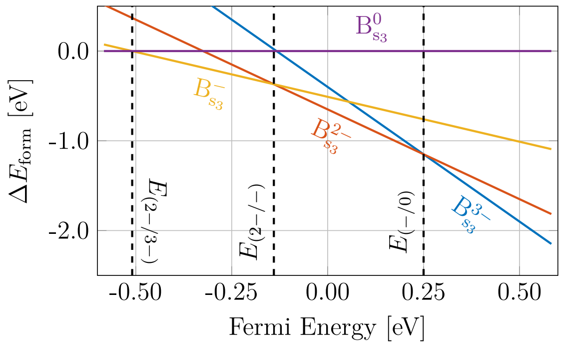

	$\Delta E_{\text{form}}^{E_F=0}$	$\Delta E_{\text{form}}^{E_F=E_V}$
$B_{s_3}^{3-}$	-0.40	1.35
$B_{s_3}^{2-}$	-0.65	0.52
$B_{s_3}^{-}$	-0.51	0.07
$B_{s_3}^{0}$	0.00	0.00

Lenosky, et al. (2000)

Trans.	$E_{q/q+1}$	$E_{q/q+1}$-E_V
3-/2-	0.25	0.83
2-/-	-0.14	0.44
-/0	-0.51	0.07

bold: observable transitions

(a) Relative formation energy of each charge state of the B_{s_3}-complex (based on DFT-simulations by Lenosky et al. [248]).

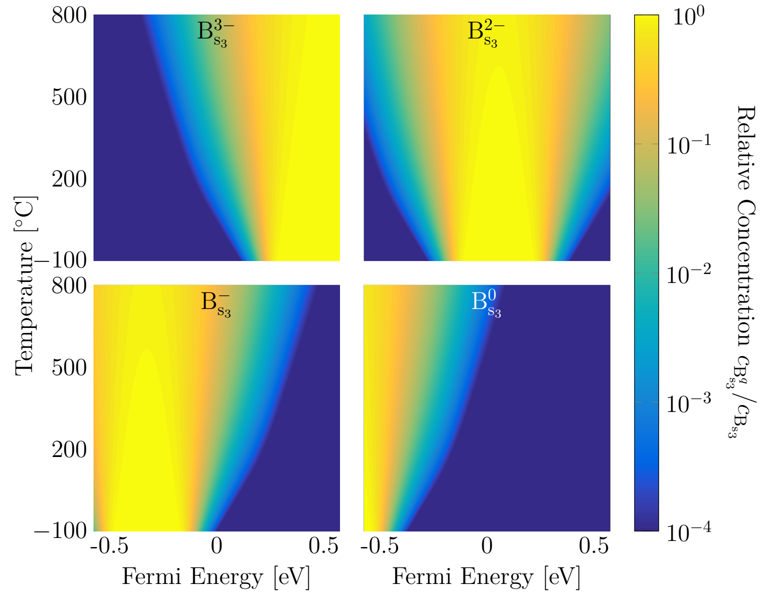

(b) Relative concentration of each charge state of the B_{s_3}-complex.

Figure C.25.1: Distribution of charge states of the B_{s_3}-complex. Calculations are based on DFT-simulations by Lenosky et al. [248].

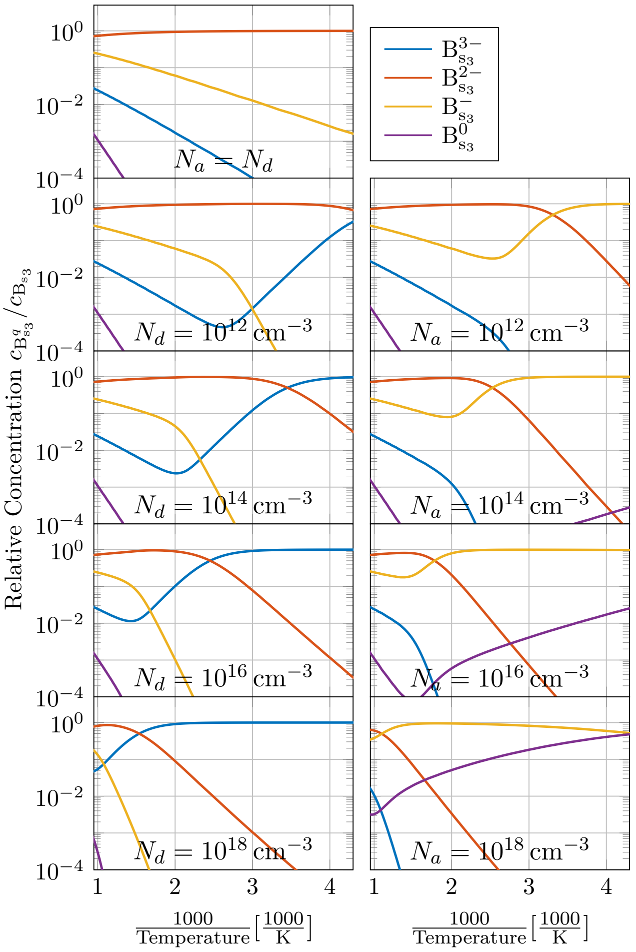

(a) Separate doping concentrations.

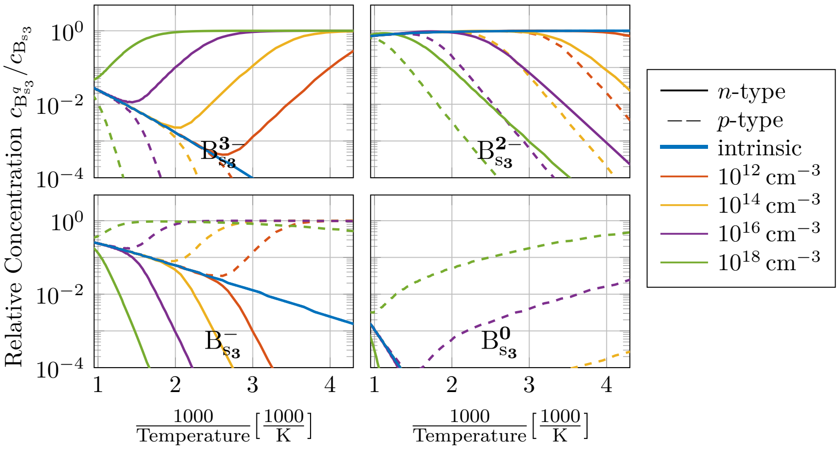

(b) Separate charge states.

Figure C.25.2: Relative concentrations of each charge state of B_{s_3}.

C.26 $B_{i_2}B_{s_2}$-Complex

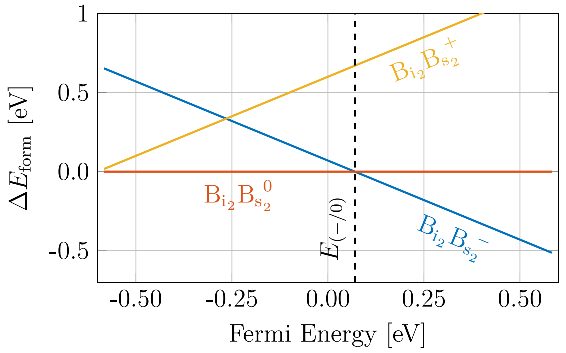

	$\Delta E_{\text{form}}^{E_F=0}$	$\Delta E_{\text{form}}^{E_F=E_V}$
$B_{i_2}B_{s_2}^{-}$	0.07	0.65
$B_{i_2}B_{s_2}^{0}$	0.00	0.00
$B_{i_2}B_{s_2}^{+}$	0.60	0.02

Lenosky, et al. (2000)

Trans.	$E_{q/q+1}$	$E_{q/q+1}$-E_V
-/0	0.07	0.65
0/+	$< E_V$	< 0

bold: observable transitions

(a) Relative formation energy of each charge state of the $B_{i_2}B_{s_2}$-complex (based on DFT-simulations by Lenosky et al. [248]).

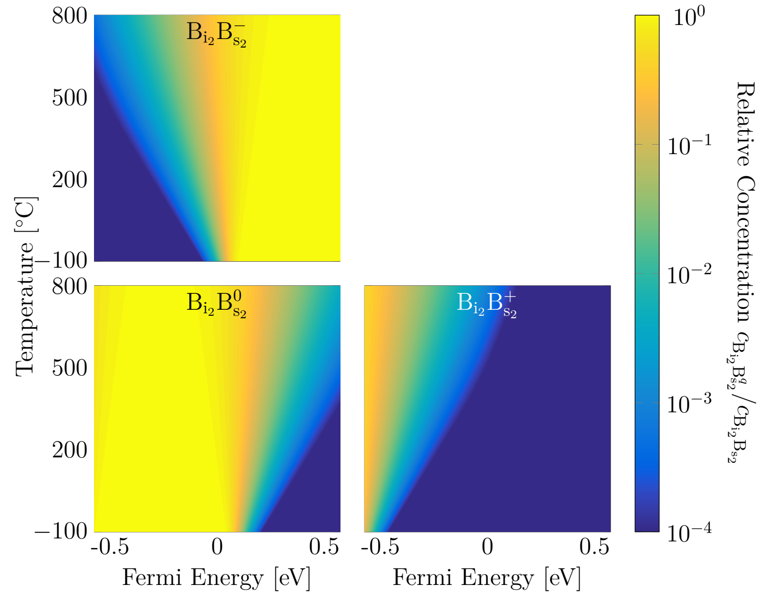

(b) Relative concentration of each charge state of the $B_{i_2}B_{s_2}$-complex.

Figure C.26.1: Distribution of charge states of the $B_{i_2}B_{s_2}$-complex. Calculations are based on DFT-simulations by Lenosky et al. [248].

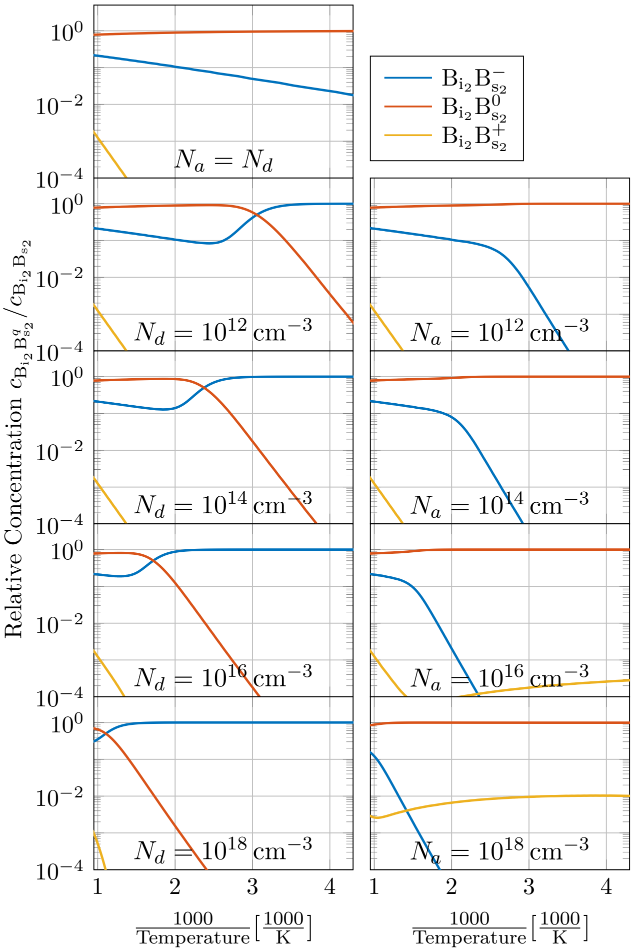

(a) Separate doping concentrations.

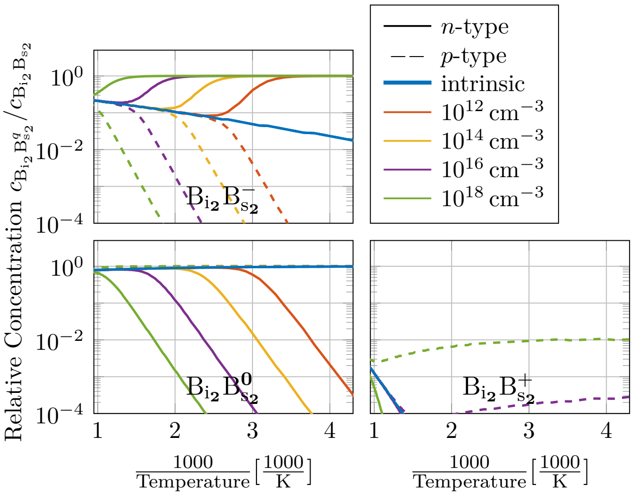

(b) Separate charge states.

Figure C.26.2: Relative concentrations of each charge state of $B_{i_2}B_{s_2}$.

C.27 B_iO-Complex

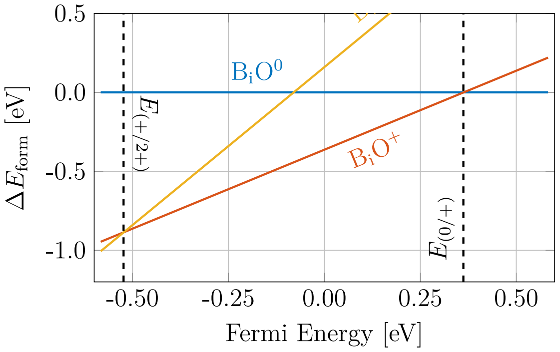

	$\Delta E_{\text{form}}^{E_F=0}$	$\Delta E_{\text{form}}^{E_F=E_V}$
B_iO^0	0.00	0.00
B_iO^+	-0.36	-0.95
B_iO^{2+}	0.16	-1.01

Adey, et al. (2003)

Trans.	$E_{q/q+1}$	$E_{q/q+1}$-E_V
0/+	**0.36**	**0.95**
+/2+	**-0.52**	**0.06**

bold: observable transitions

(a) Relative formation energy of each charge state of the B_iO-complex (based on DFT-simulations by Adey et al. [261]).

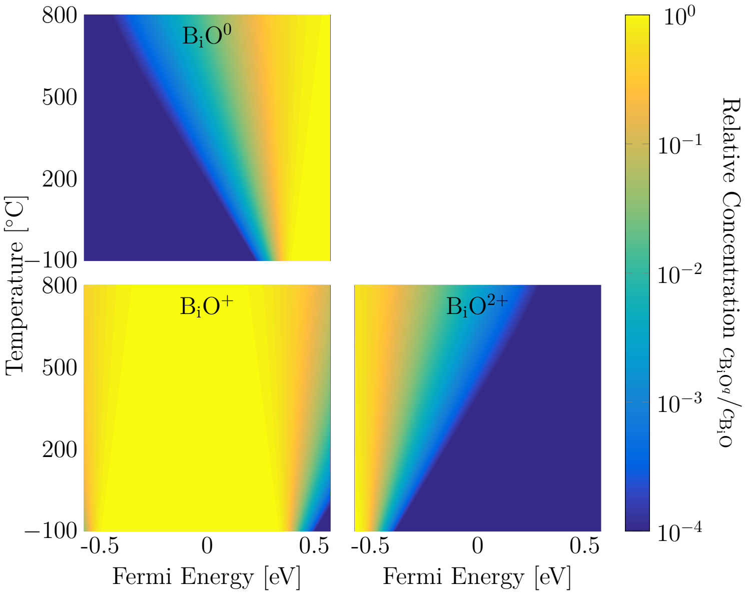

(b) Relative concentration of each charge state of the B_iO-complex.

Figure C.27.1: Distribution of charge states of the B_iO-complex. Calculations are based on DFT-simulations by Adey et al. [261].

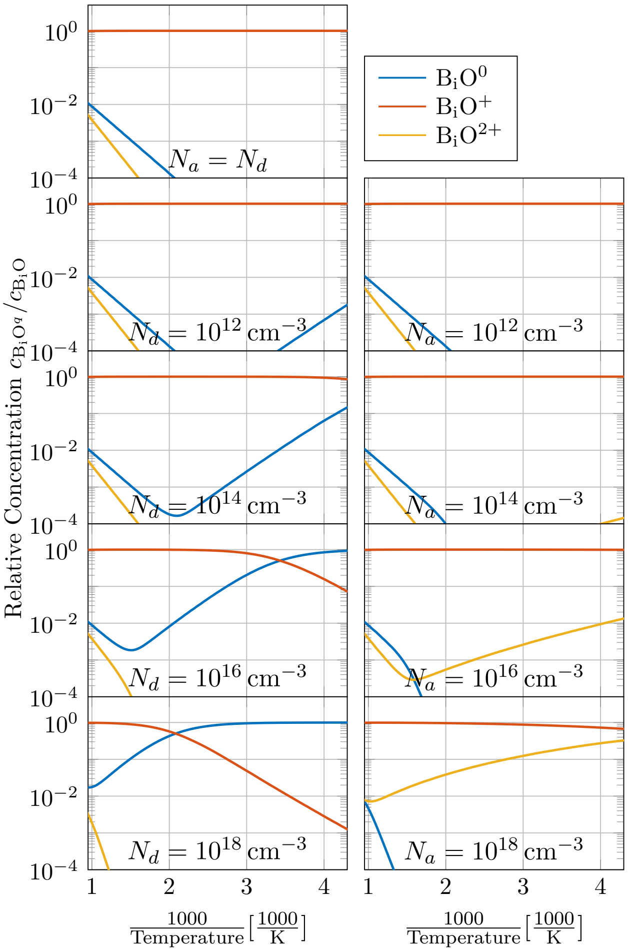

(a) Separate doping concentrations.

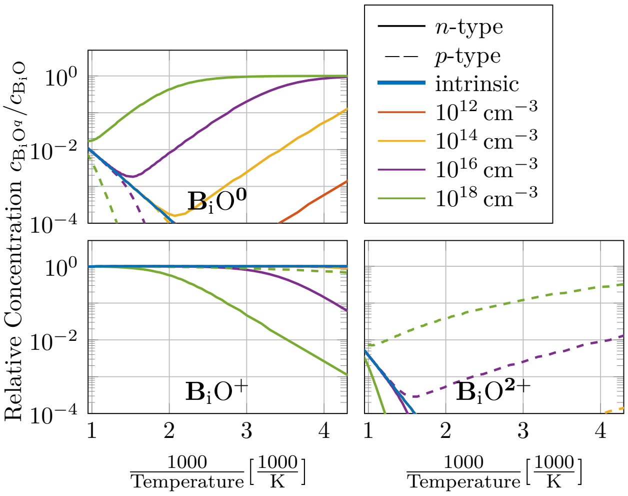

(b) Separate charge states.

Figure C.27.2: Relative concentrations of each charge state of $\mathrm{B_iO}$.

C.28 B_sO_2-Complex

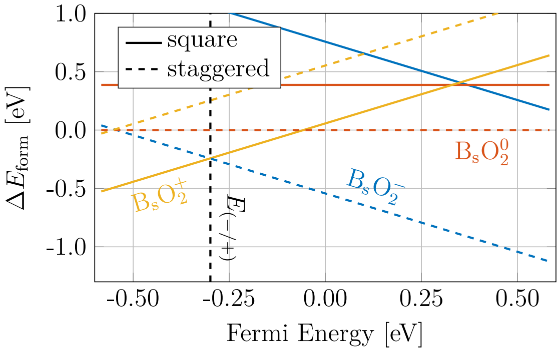

Trans.	$E_{q/q+1}$	$E_{q/q+1}$-E_V
-/+	**-0.30**	**0.28**

bold: observable transitions

	Configuration	$\Delta E_{\mathrm{form}}^{E_F=0}$	$\Delta E_{\mathrm{form}}^{E_F=E_V}$
$B_sO_2^-$	square	0.76	1.34
$B_sO_2^0$	square	0.39	0.39
$B_sO_2^+$	square	0.06	-0.53

	Configuration	$\Delta E_{\mathrm{form}}^{E_F=0}$	$\Delta E_{\mathrm{form}}^{E_F=E_V}$
$B_sO_2^-$	staggered	-0.54	0.04
$B_sO_2^0$	staggered	0.00	0.00
$B_sO_2^+$	staggered	0.55	-0.03

Du et al. (2006)

(a) Relative formation energy of each charge state of the B_sO_2-complex (based on DFT-simulations by Du et al. [245]).

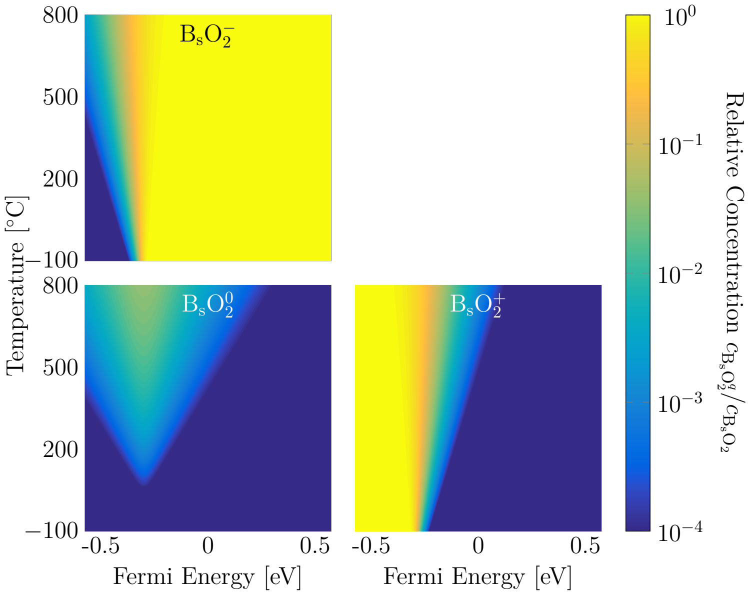

(b) Relative concentration of each charge state of the B_sO_2-complex.

Figure C.28.1: Distribution of charge states of the B_sO_2-complex. Calculations are based on DFT-simulations by Du et al. [245].

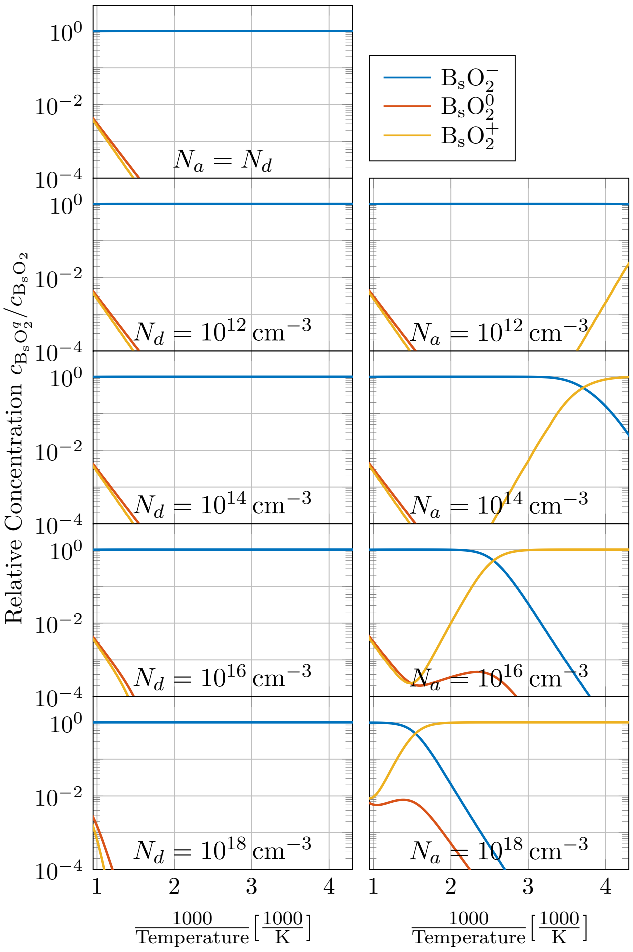

(a) Separate doping concentrations.

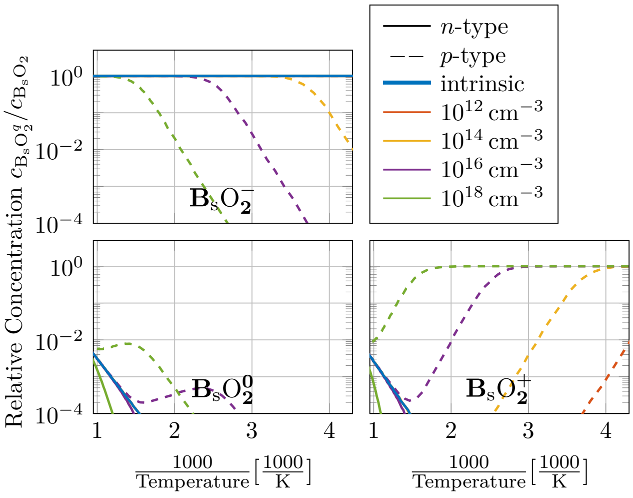

(b) Separate charge states.

Figure C.28.2: Relative concentrations of each charge state of B_sO_2.

C.29 B_iC_s-Complex

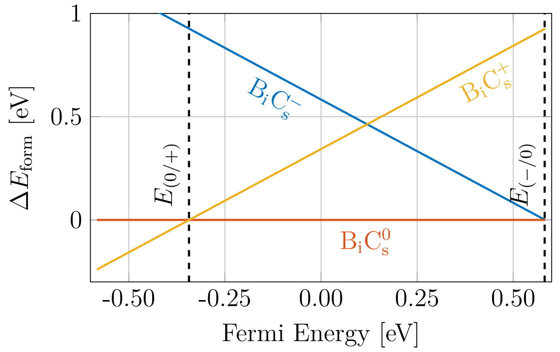

	$\Delta E_{\mathrm{form}}^{E_F=0}$	$\Delta E_{\mathrm{form}}^{E_F=E_V}$
$B_iC_s^-$	0.58	1.17
$B_iC_s^0$	0.00	0.00
$B_iC_s^+$	0.34	-0.24

Trans.	$E_{q/q+1}$	$E_{q/q+1}$-E_V
-/0	**0.58**	**1.16**
0/+	**-0.34**	**0.24**

bold: observable transitions

Adey, et al. (2003)

(a) Relative formation energy of each charge state of the B_iC_s-complex (based on DFT-simulations by Lenosky et al. [248]).

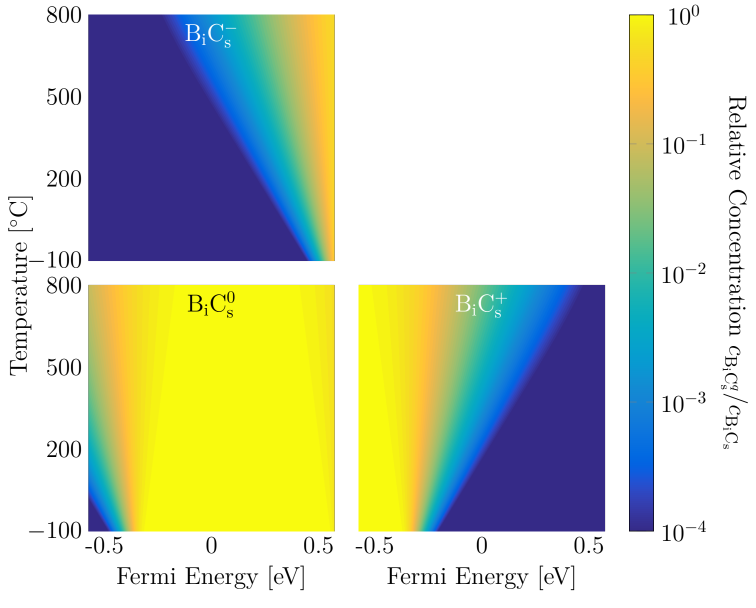

(b) Relative concentration of each charge state of the B_iC_s-complex.

Figure C.29.1: Distribution of charge states of the B_iC_s-complex. Calculations are based on DFT-simulations by Lenosky et al. [248].

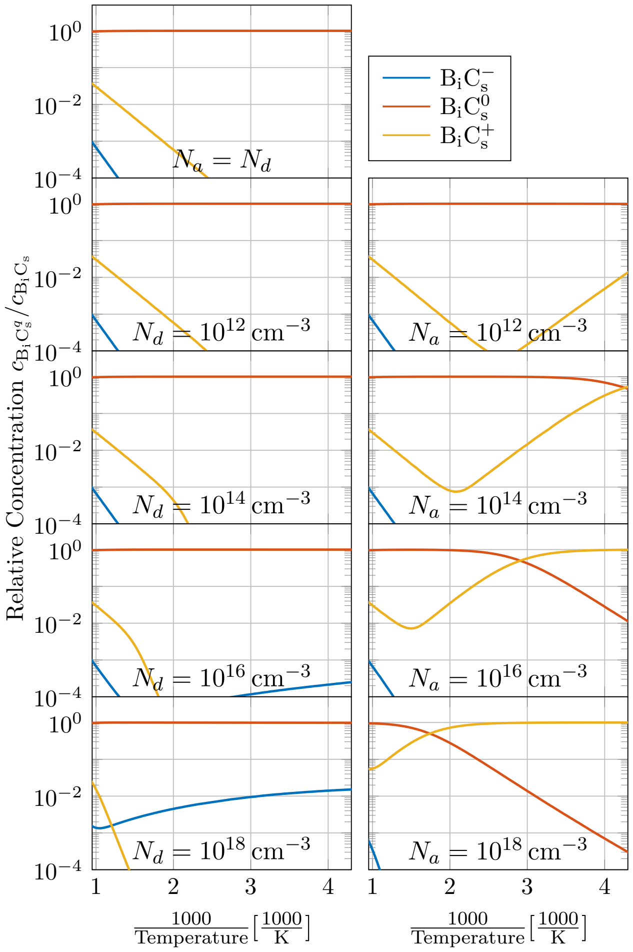

(a) Separate doping concentrations.

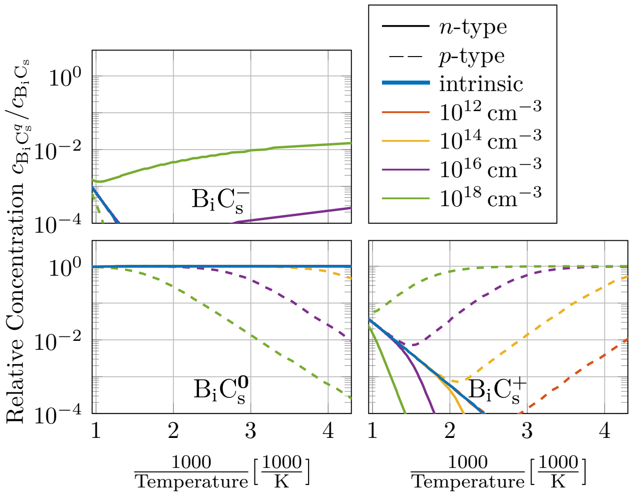

(b) Separate charge states.

Figure C.29.2: Relative concentrations of each charge state of the B_iC_s-complex.

C.30 Substitutional Phosphorus P_s

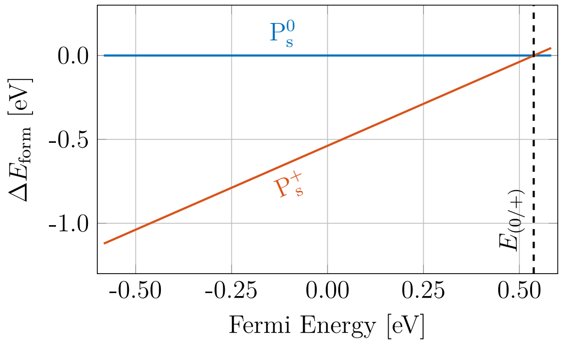

	$\Delta E_{\text{form}}^{E_F=0}$	$\Delta E_{\text{form}}^{E_F=E_V}$
P_s^0	0.00	0.00
P_s^+	-0.54	-1.12

Trans.	$E_{q/q+1}$	$E_{q/q+1}$-E_V
0/+	**0.54**	**1.12**

bold: observable transitions

(a) Relative formation energy of each charge state of substitutional phosphorus P_s (based on a donor ionization energy of 0.45 meV).

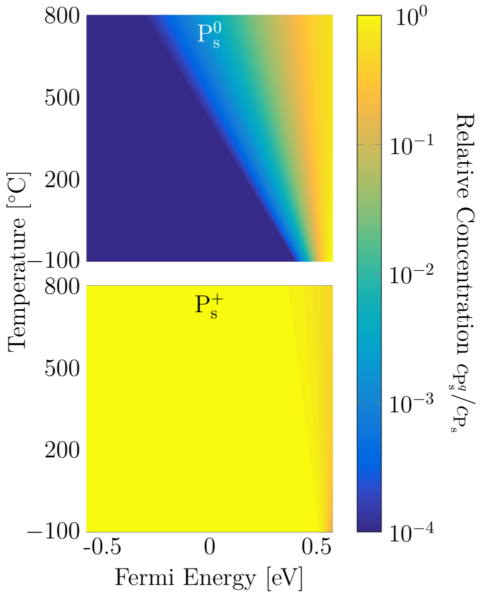

(b) Relative concentration of each charge state of substitutional phosphorus P_s.

Figure C.30.1: Distribution of charge states of substitutional phosphorus P_s. Calculations are based on a donor ionization energy of 0.45 meV.

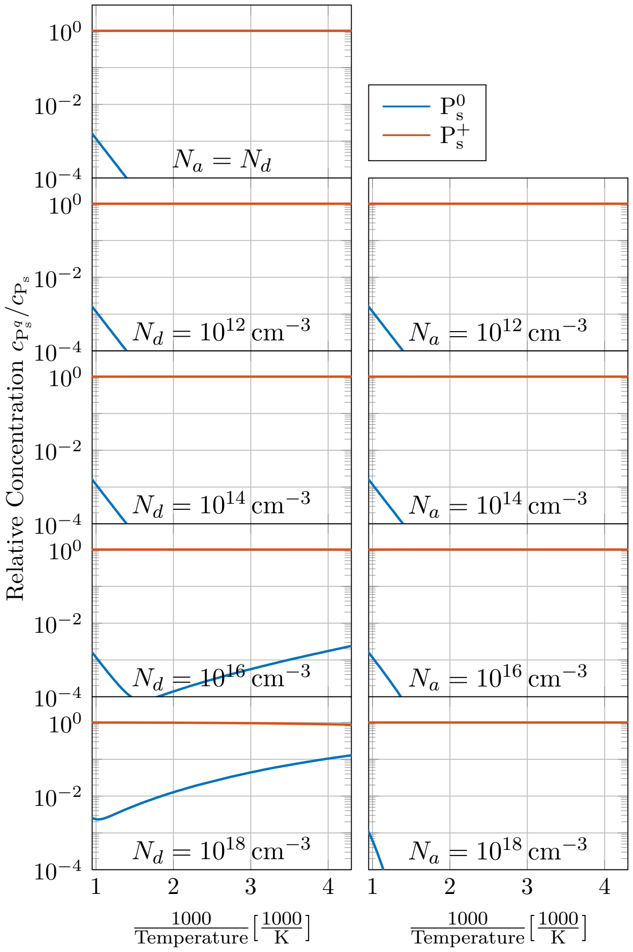

(a) Separate doping concentrations.

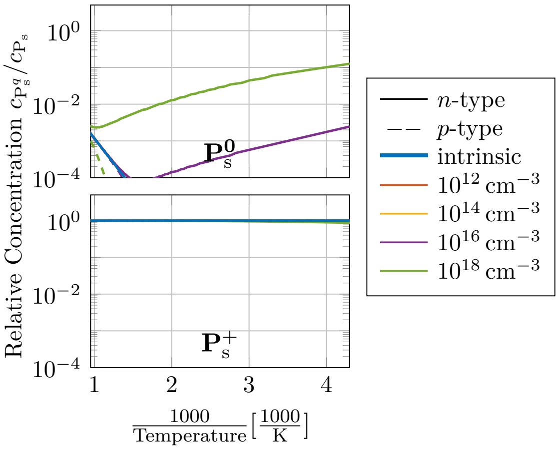

(b) Separate charge states.

Figure C.30.2: Relative concentrations of each charge state of substitutional phosphorus $\mathrm{P_s}$.

C.31 Interstitial Phosphorus P_i

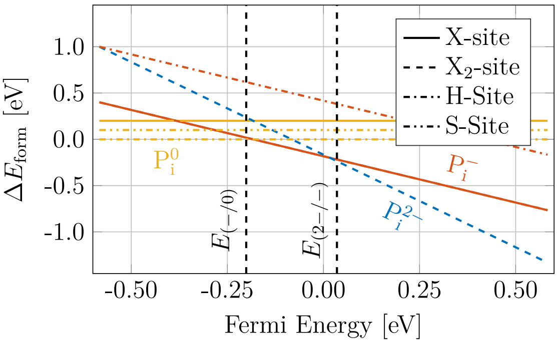

Trans.	$E_{q/q+1}$	$E_{q/q+1}$-E_V
2-/-	**0.03**	**0.61**
-/0	**-0.19**	**0.39**

bold: observable transitions

	Site	$\Delta E_{\text{form}}^{E_F=0}$	$\Delta E_{\text{form}}^{E_F=E_V}$
P_i^-	X-site	-0.18	0.40
P_i^0	X-site	0.20	0.20

	Site	$\Delta E_{\text{form}}^{E_F=0}$	$\Delta E_{\text{form}}^{E_F=E_V}$
P_i^{2-}	X$_2$-site	-0.16	1.00
P_i^-	X$_2$-site	-0.18	0.40

	Site	$\Delta E_{\text{form}}^{E_F=0}$	$\Delta E_{\text{form}}^{E_F=E_V}$
P_i^-	H-site	-0.42	1.00
P_i^0	H-site	0.00	0.00
P_i^0	S-site	0.10	0.10

Liu et al. (2002)

(a) Relative formation energy of each charge state of interstitial phosphorus P_i (based on DFT-simulations by Liu et al. [262]).

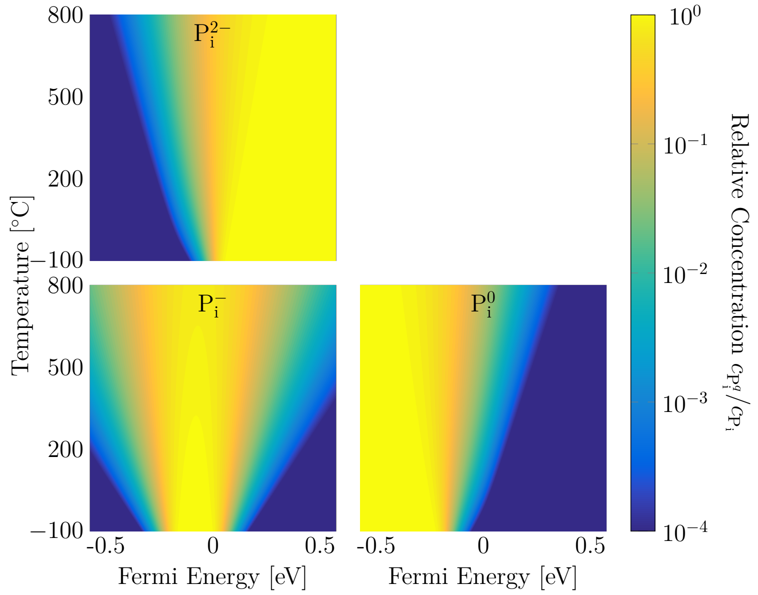

(b) Relative concentration of each charge state of interstitial carbon P_i.

Figure C.31.1: Distribution of charge states of interstitial phosphorus P_i. Calculations are based on DFT-simulations by Liu et al. [262].

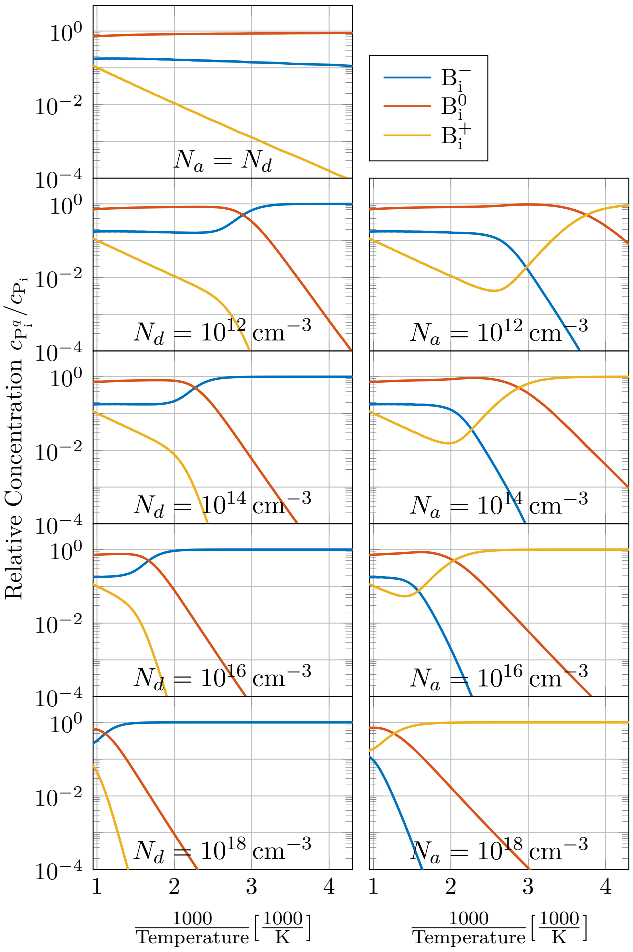

(a) Separate doping concentrations.

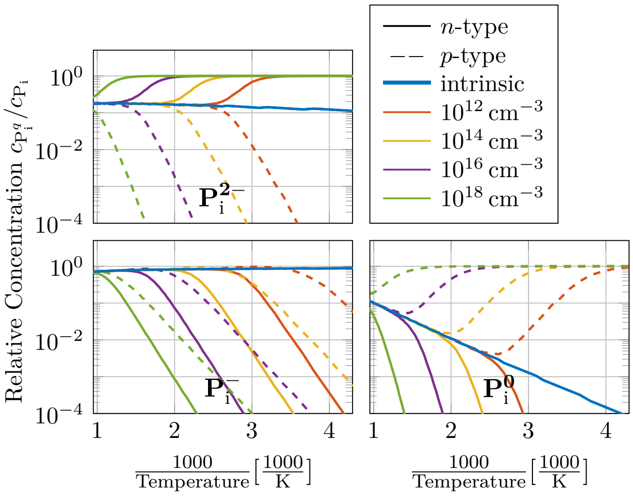

(b) Separate charge states.

Figure C.31.2: Relative concentrations of each charge state of P_i.

Diffusivity of the Phosphorus Interstitial P_i

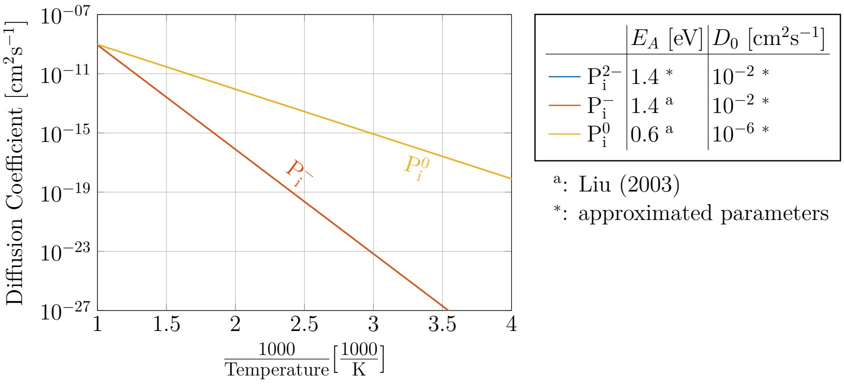

	E_A [eV]	D_0 $[cm^2s^{-1}]$
— P_i^{2-}	1.4 *	10^{-2} *
— P_i^-	1.4 [a]	10^{-2} *
— P_i^0	0.6 [a]	10^{-6} *

[a]: Liu (2003)

*: approximated parameters

(a) Diffusivity of each charge state of interstitial phosphorus P_i (see reference 274).

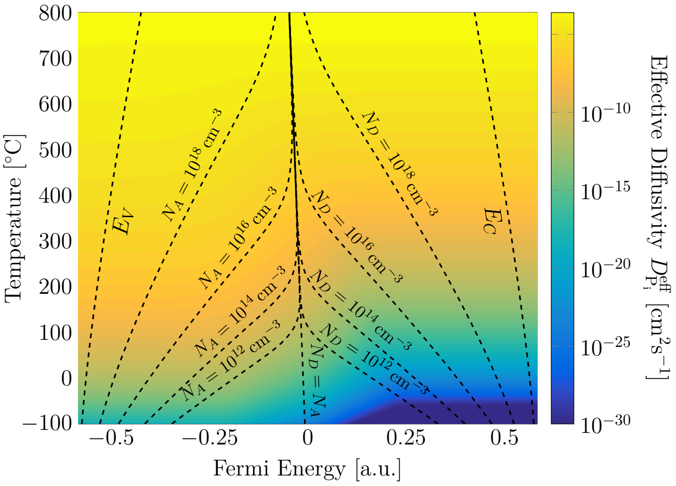

(b) 2D-map of the effective diffusivity of interstitial phosphorus P_i.

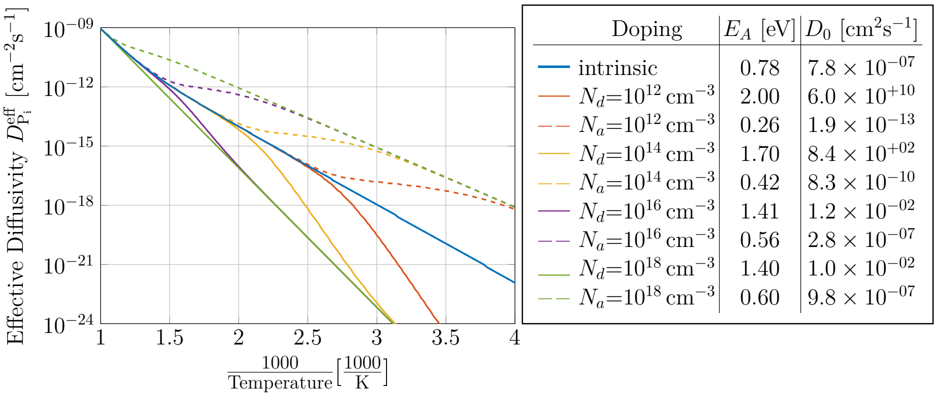

Doping	E_A [eV]	D_0 $[cm^2s^{-1}]$
— intrinsic	0.78	7.8×10^{-07}
— N_d=10^{12} cm^{-3}	2.00	$6.0 \times 10^{+10}$
– – N_a=10^{12} cm^{-3}	0.26	1.9×10^{-13}
— N_d=10^{14} cm^{-3}	1.70	$8.4 \times 10^{+02}$
– – N_a=10^{14} cm^{-3}	0.42	8.3×10^{-10}
— N_d=10^{16} cm^{-3}	1.41	1.2×10^{-02}
– – N_a=10^{16} cm^{-3}	0.56	2.8×10^{-07}
— N_d=10^{18} cm^{-3}	1.40	1.0×10^{-02}
– – N_a=10^{18} cm^{-3}	0.60	9.8×10^{-07}

(c) Temperature dependence of the effective diffusivity of P_i at selected doping concentrations.

Figure C.31.3: Effective diffusivity of interstitial phosphorus P_i calculated from Arrhenius parameters published in reference 274.

C.32 Phosphorus-Vacancy-Pair VP_s

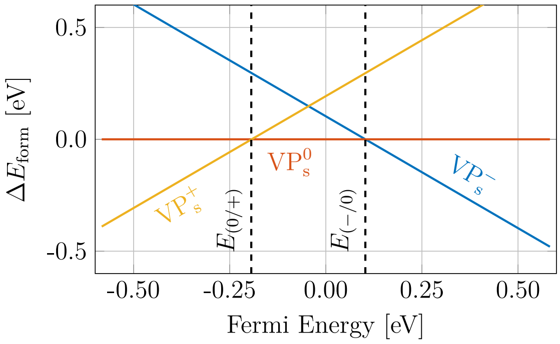

	$\Delta E_\text{form}^{E_F=0}$	$\Delta E_\text{form}^{E_F=E_V}$
VP_s^-	0.10	0.69
VP_s^0	0.00	0.00
VP_s^+	0.19	-0.39

Ferreira-Resende (2000)

Trans.	$E_{q/q+1}$	$E_{q/q+1}$-E_V
-/	**0.10**	**0.69**
0/+	**-0.19**	**0.39**

bold: observable transitions

(a) Relative formation energy of each charge state of VP_s (based on DFT-simulations by Ferreira-Resende [163]).

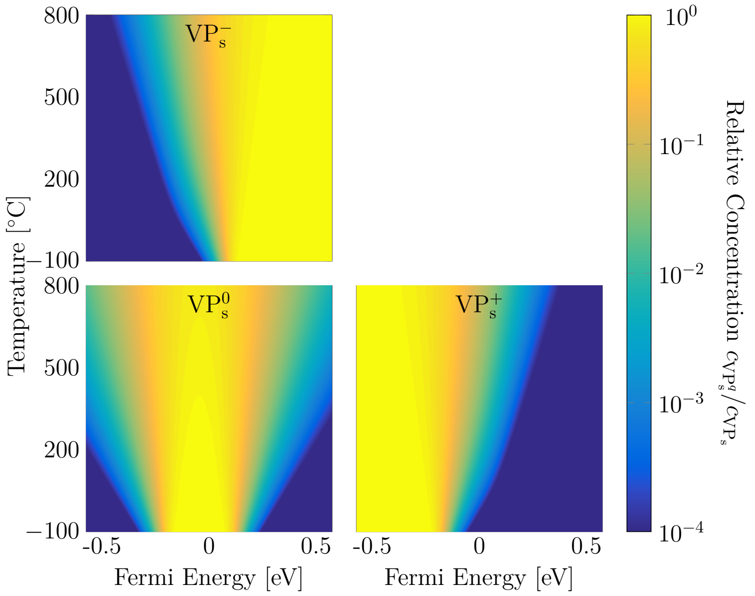

(b) Relative concentration of each charge state of VP_s.

Figure C.32.1: Distribution of charge states of VP_s. Calculations are based on DFT-simulations by Ferreira-Resende [163]

.

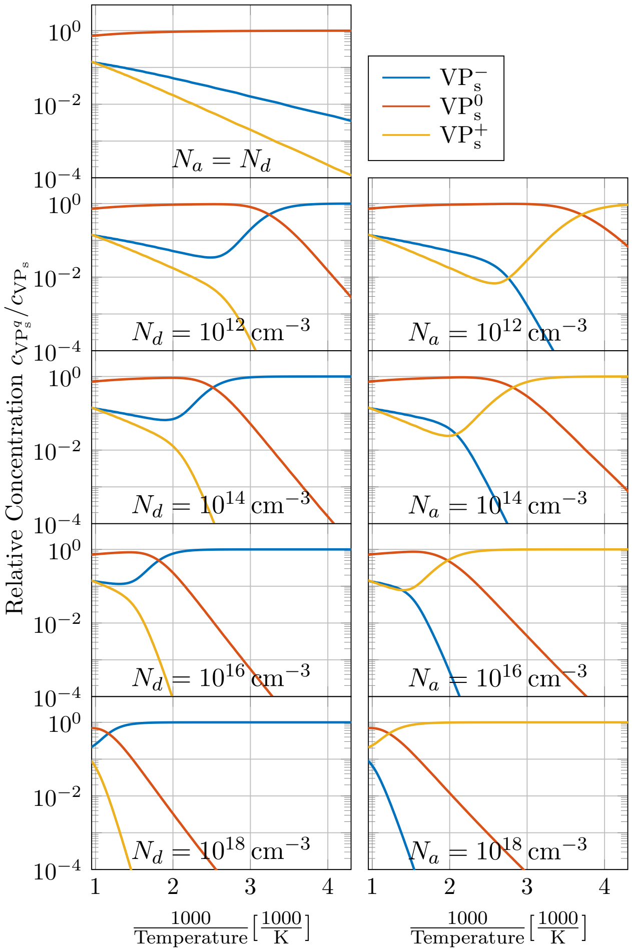

(a) Separate doping concentrations.

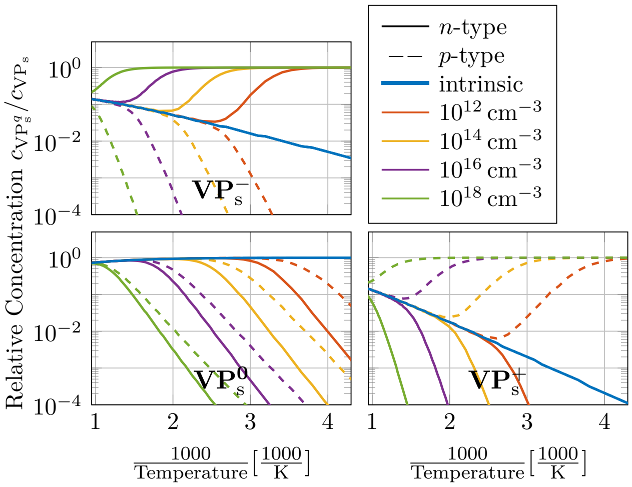

(b) Separate charge states.

Figure C.32.2: Relative concentrations of each charge state of $\mathrm{VP_s}$.

Diffusivity of the Phosphorus Interstitial VP_s

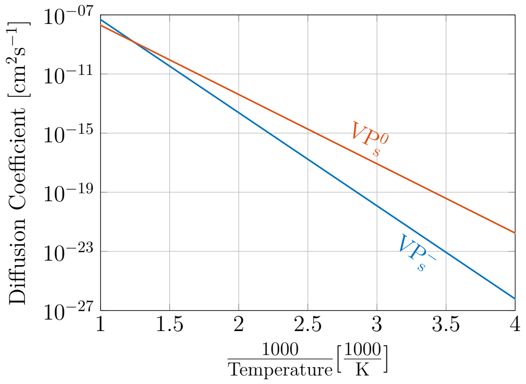

	E_A [eV]	D_0 [cm^{2}s^{-1}]
— VP_s^-	1.25 [a]	$9.6 \times 10^{-2}10^{-2}$ [a]
— VP_s^0	0.93 [a]	$9.7 \times 10^{-2}10^{-4}$ [a]
— VP_s^+	0.93 *	$9.7 \times 10^{-2}10^{-4}$ *

[a]: Pichler (2004)

*: approximated parameters

(a) Diffusivity of each charge state of VP_s (see reference 5).

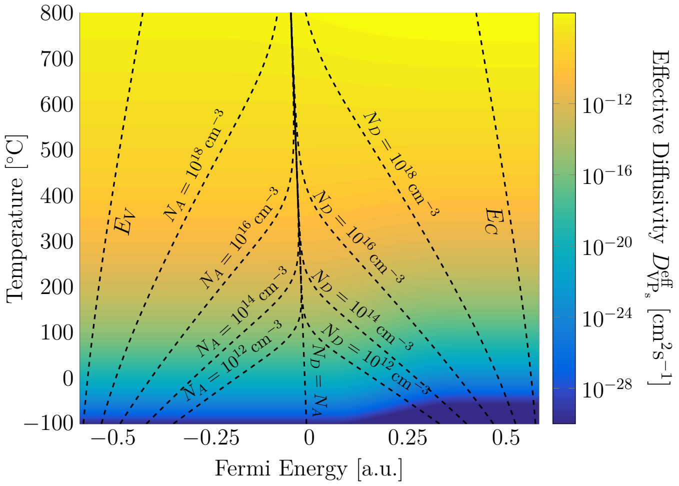

(b) 2D-map of the effective diffusivity of VP_s.

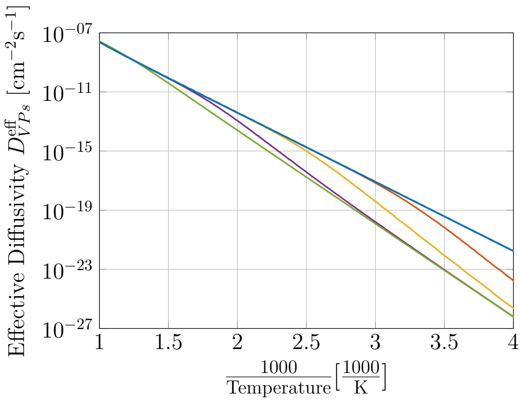

Doping	E_A [eV]	D_0 [cm^{2}s^{-1}]
— intrinsic	0.93	8.9×10^{-4}
— N_d=10^{12} cm^{-3}	1.32	$1.2 \times 10^{+3}$
- - N_a=10^{12} cm^{-3}	0.93	8.9×10^{-4}
— N_d=10^{14} cm^{-3}	1.41	$8.2 \times 10^{+2}$
- - N_a=10^{14} cm^{-3}	0.93	8.9×10^{-4}
— N_d=10^{16} cm^{-3}	1.34	$3.3 \times 10^{+0}$
- - N_a=10^{16} cm^{-3}	0.93	8.9×10^{-4}
— N_d=10^{18} cm^{-3}	1.25	1.1×10^{-1}
- - N_a=10^{18} cm^{-3}	0.93	8.9×10^{-4}

(c) Temperature dependence of the effective diffusivity of VP_s at selected doping concentrations.

Figure C.32.3: Effective diffusivity of VP_s calculated from Arrhenius parameters published in reference 5.

C.33 Interstitial Hydrogen H

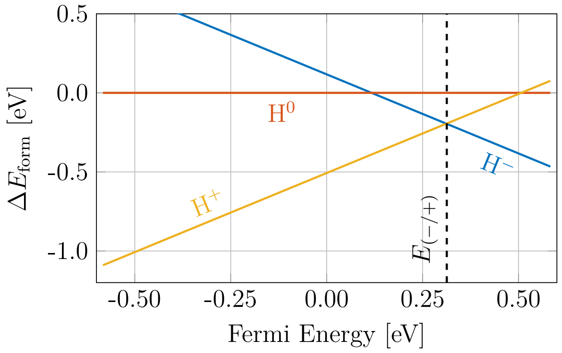

	$\Delta E_{\mathrm{form}}^{E_F=0}$	$\Delta E_{\mathrm{form}}^{E_F=E_V}$
H^-	0.12	0.70
H^0	0.00	0.00
H^+	-0.51	-1.09

Herring et al. (2001)

Trans.	$E_{q/q+1}$	$E_{q/q+1}$-E_V
-/	0.12	0.70
0/+	0.51	1.09
-/+	**0.31**	**0.90**

bold: observable transitions

(a) Relative formation energy of each charge state of hydrogen H (based on DFT-simulations by Herring et al. [327]).

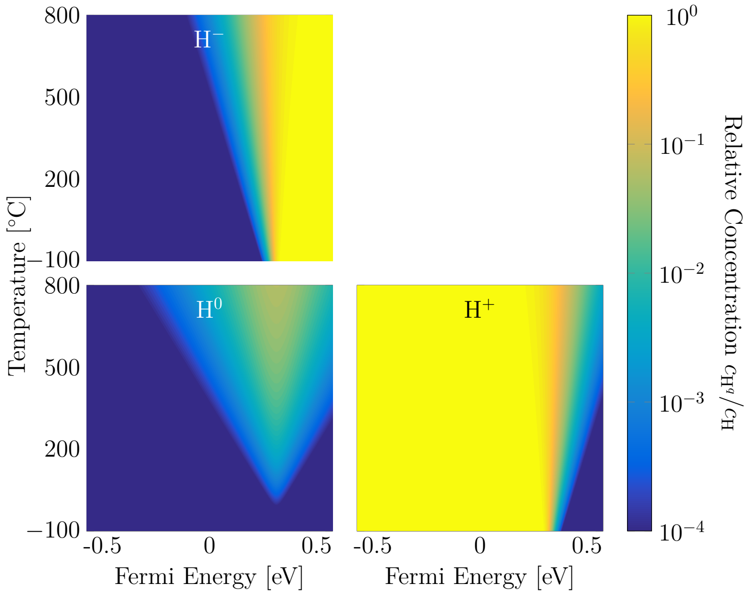

(b) Relative concentration of each charge state of hydrogen H.

Figure C.33.1: Distribution of charge states of hydrogen H. Calculations are based on DFT-simulations by Herring et al. [327]

.

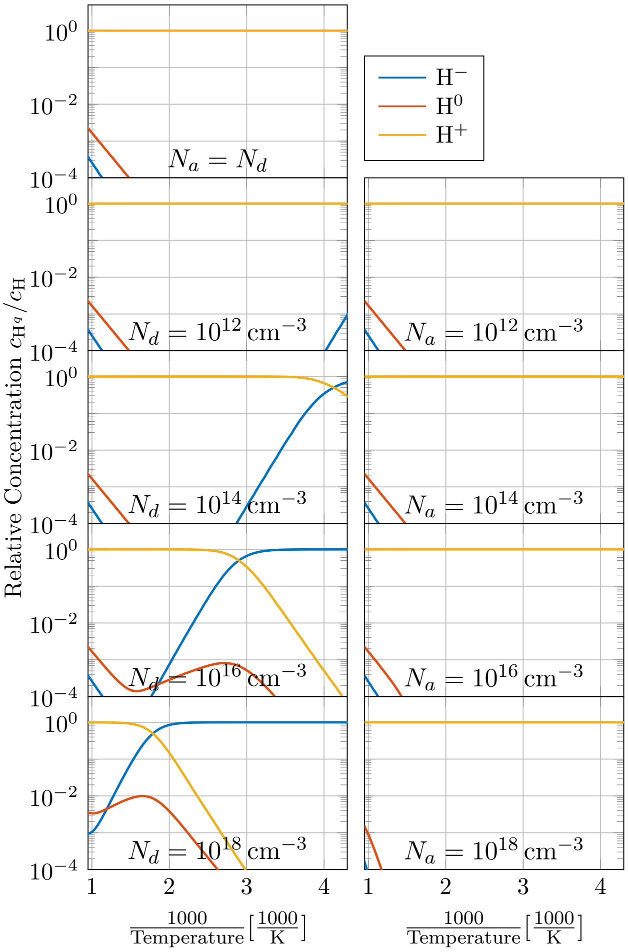

(a) Separate doping concentrations.

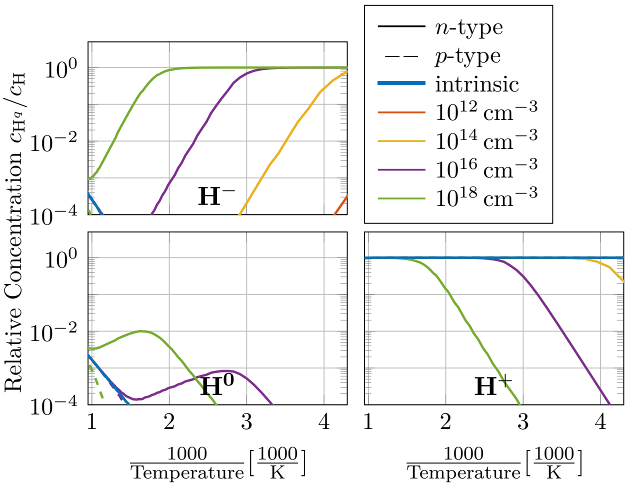

(b) Separate charge states.

Figure C.33.2: Relative concentrations of each charge state of hydrogen H.

Diffusivity of Hydrogen H

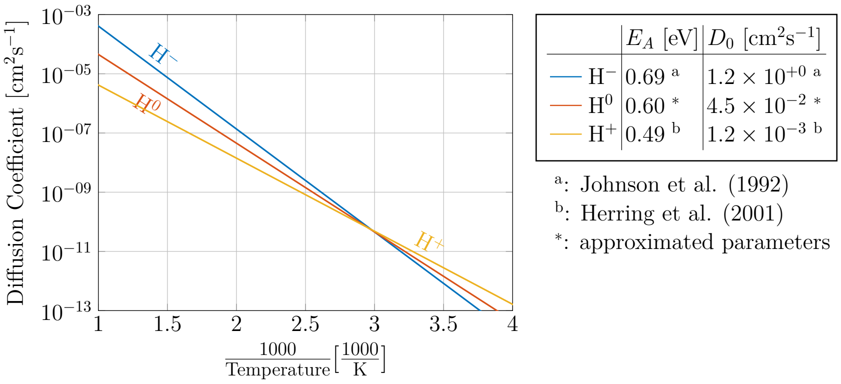

	E_A [eV]	D_0 [cm^{2}s^{-1}]
H^-	0.69 [a]	$1.2 \times 10^{+0}$ [a]
H^0	0.60 *	4.5×10^{-2} *
H^+	0.49 [b]	1.2×10^{-3} [b]

[a]: Johnson et al. (1992)
[b]: Herring et al. (2001)
*: approximated parameters

(a) Diffusivity of each charge state of hydrogen H (see references 327 and 340).

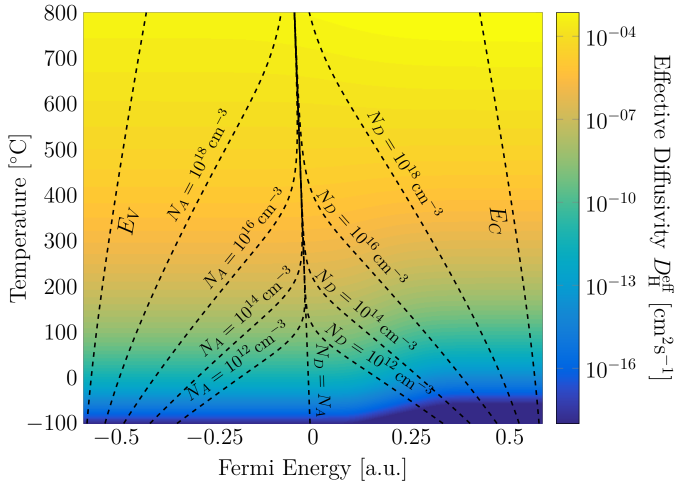

(b) 2D-map of the effective diffusivity of hydrogen H.

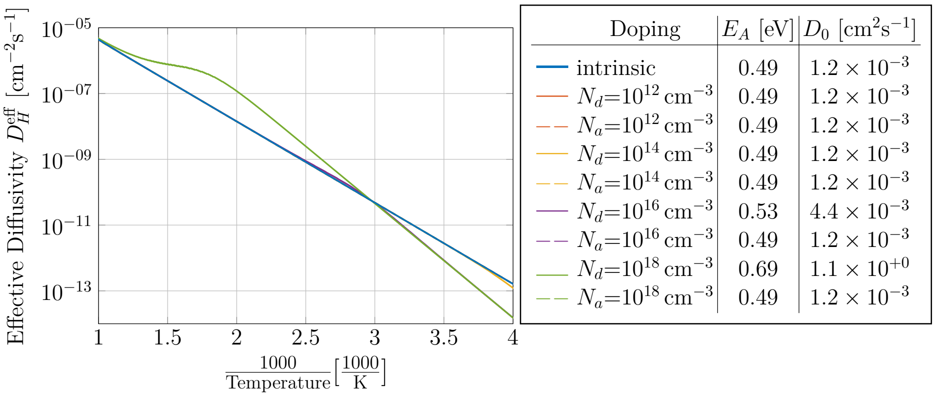

Doping	E_A [eV]	D_0 [cm^{2}s^{-1}]
intrinsic	0.49	1.2×10^{-3}
N_d=10^{12} cm^{-3}	0.49	1.2×10^{-3}
N_a=10^{12} cm^{-3}	0.49	1.2×10^{-3}
N_d=10^{14} cm^{-3}	0.49	1.2×10^{-3}
N_a=10^{14} cm^{-3}	0.49	1.2×10^{-3}
N_d=10^{16} cm^{-3}	0.53	4.4×10^{-3}
N_a=10^{16} cm^{-3}	0.49	1.2×10^{-3}
N_d=10^{18} cm^{-3}	0.69	$1.1 \times 10^{+0}$
N_a=10^{18} cm^{-3}	0.49	1.2×10^{-3}

(c) Temperature dependence of the effective diffusivity of hydrogen H at selected doping concentrations.

Figure C.33.3: Effective diffusivity of hydrogen H calculated from Arrhenius parameters published in references 327 and 340.

C.34 VH-Complex

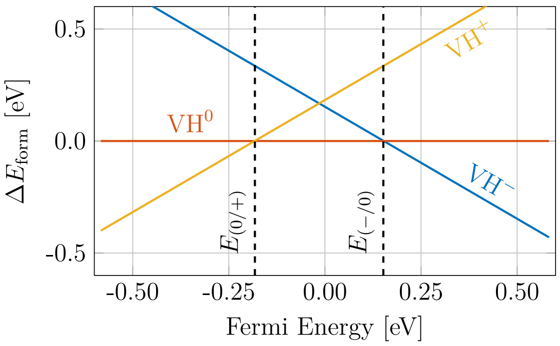

	$\Delta E_{\mathrm{form}}^{E_F=0}$	$\Delta E_{\mathrm{form}}^{E_F=E_V}$
VH$^-$	0.15	0.74
VH^0	0.00	0.00
VH$^+$	0.18	-0.40

Ferreira-Resende (2000)

Trans.	$E_{q/q+1}$	$E_{q/q+1}$-E_V
-/	**0.15**	**0.73**
0/+	**-0.18**	**0.40**

bold: observable transitions

(a) Relative formation energy of each charge state of VH (based on DFT-simulations by Ferreira-Resende [163]).

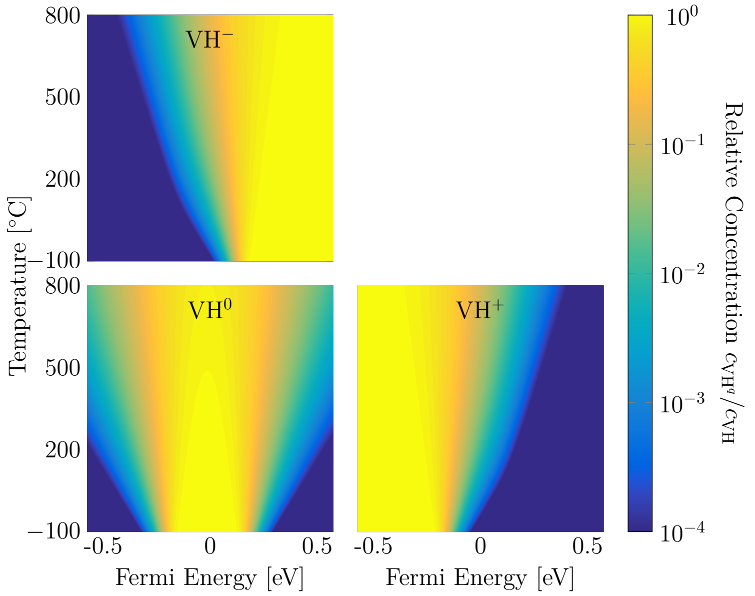

(b) Relative concentration of each charge state of VH.

Figure C.34.1: Distribution of charge states of VH. Calculations are based on DFT-simulations by Ferreira-Resende [163]

.

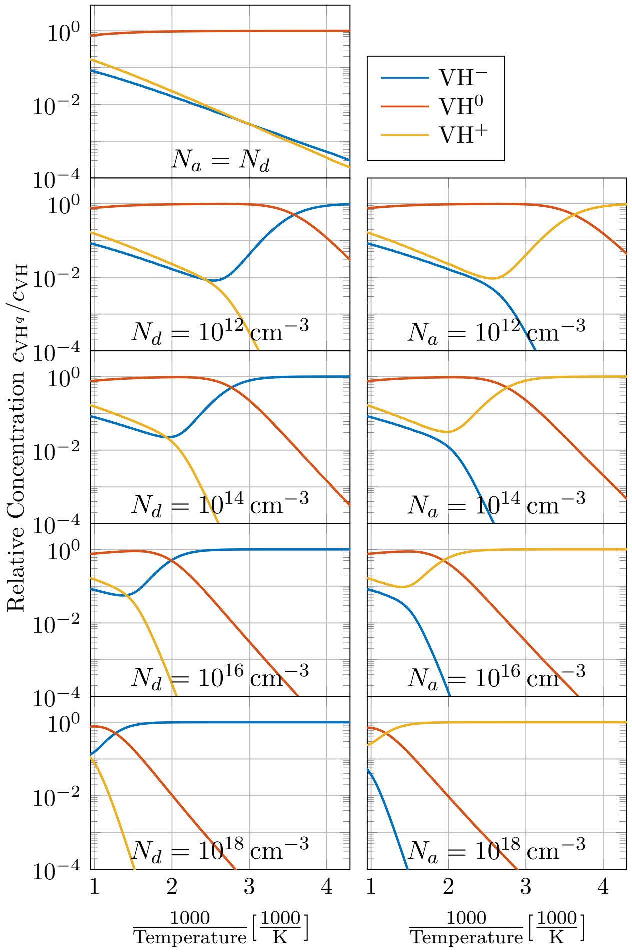

(a) Separate doping concentrations.

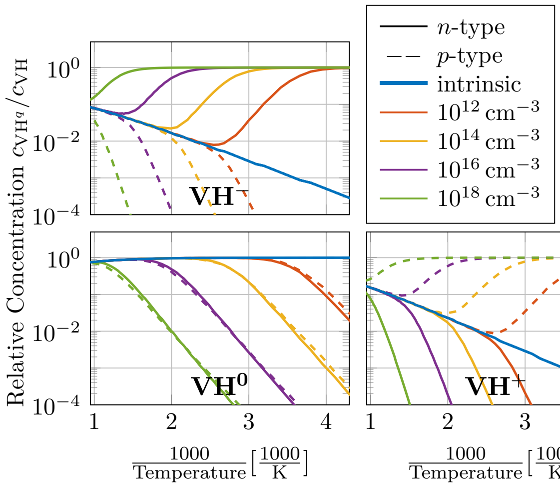

(b) Separate charge states.

Figure C.34.2: Relative concentrations of each charge state of VH.

C.35 VH$_2$-Complex

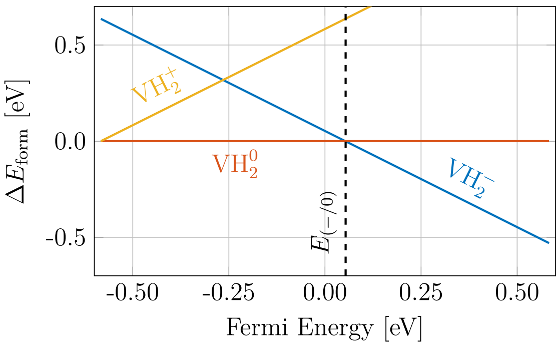

	$\Delta E_{\text{form}}^{E_F=0}$	$\Delta E_{\text{form}}^{E_F=E_V}$
VH_2^-	0.05	0.64
VH_2^0	0.00	0.00
VH_2^+	0.58	0.00

Ferreira-Resende (2000)

Trans.	$E_{q/q+1}$	$E_{q/q+1}$-E_V
-/	**0.05**	**0.64**
0/+	E_V	0

bold: observable transitions

(a) Relative formation energy of each charge state of VH$_2$ (based on DFT-simulations by Ferreira-Resende [163]).

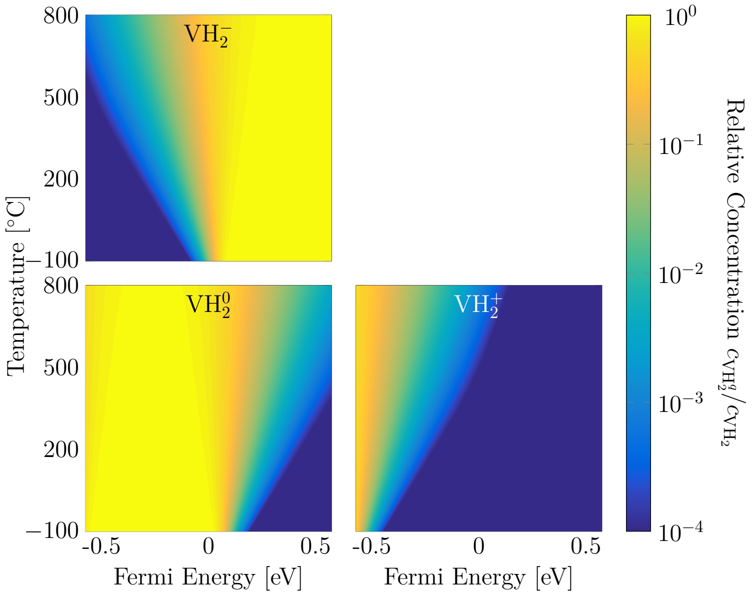

(b) Relative concentration of each charge state of VH$_2$.

Figure C.35.1: Distribution of charge states of VH$_2$. Calculations are based on DFT-simulations by Ferreira-Resende [163]

.

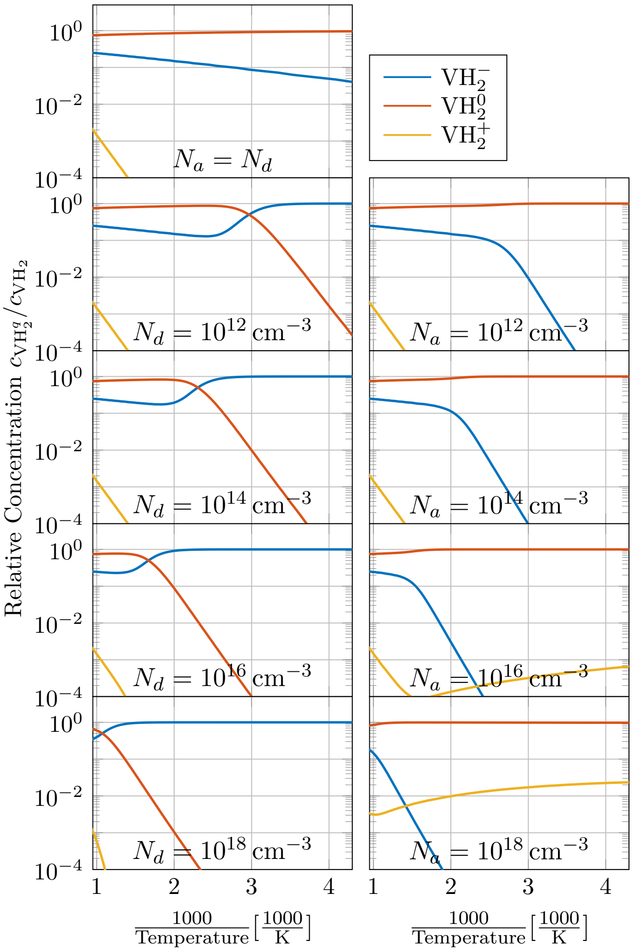

(a) Separate doping concentrations.

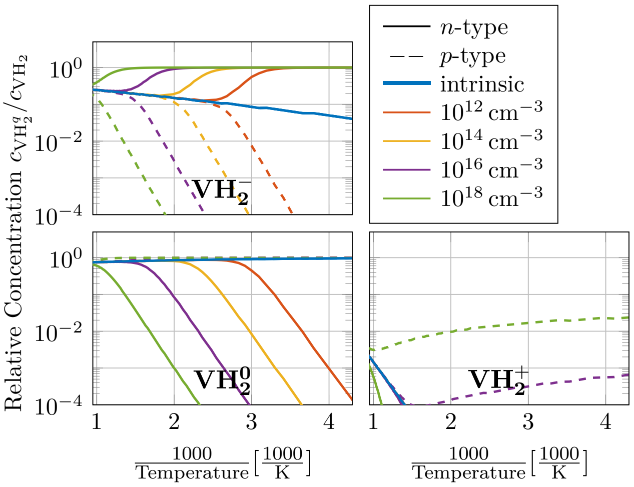

(b) Separate charge states.

Figure C.35.2: Relative concentrations of each charge state of VH_2.

C.36 VH_3-Complex

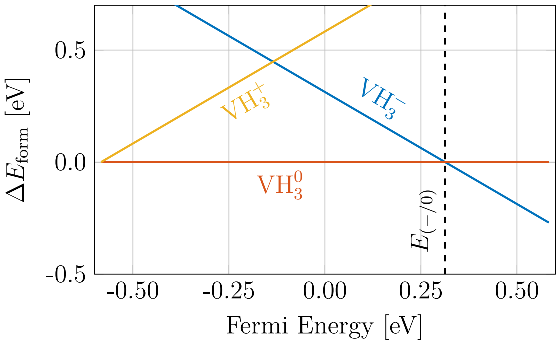

	$\Delta E_{\mathrm{form}}^{E_F=0}$	$\Delta E_{\mathrm{form}}^{E_F=E_V}$
VH_3^-	0.31	0.90
VH_3^0	0.00	0.00
VH_3^+	0.58	0.00

Ferreira-Resende (2000)

Trans.	$E_{q/q+1}$	$E_{q/q+1}$-E_V
-/	**0.31**	**0.90**
0/+	E_V	0

bold: observable transitions

(a) Relative formation energy of each charge state of VH_3 (based on DFT-simulations by Ferreira-Resende [163]).

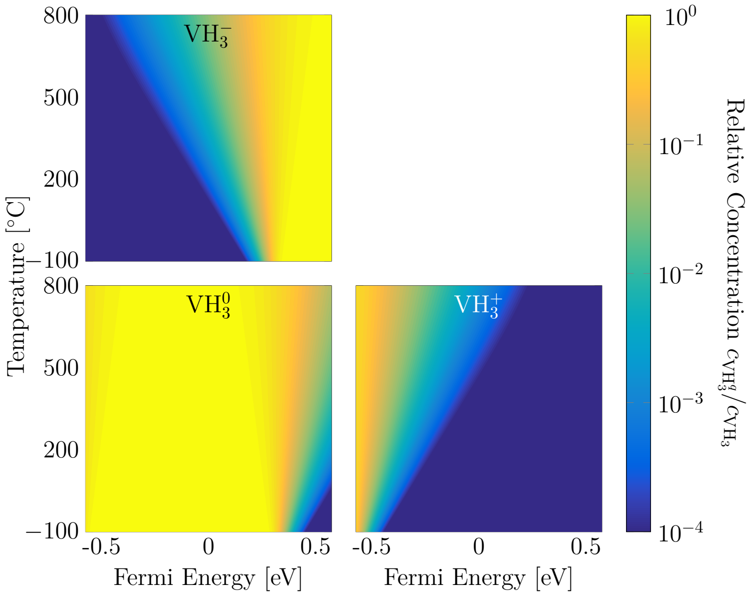

(b) Relative concentration of each charge state of VH_3.

Figure C.36.1: Distribution of charge states of VH_3. Calculations are based on DFT-simulations by Ferreira-Resende [163]

.

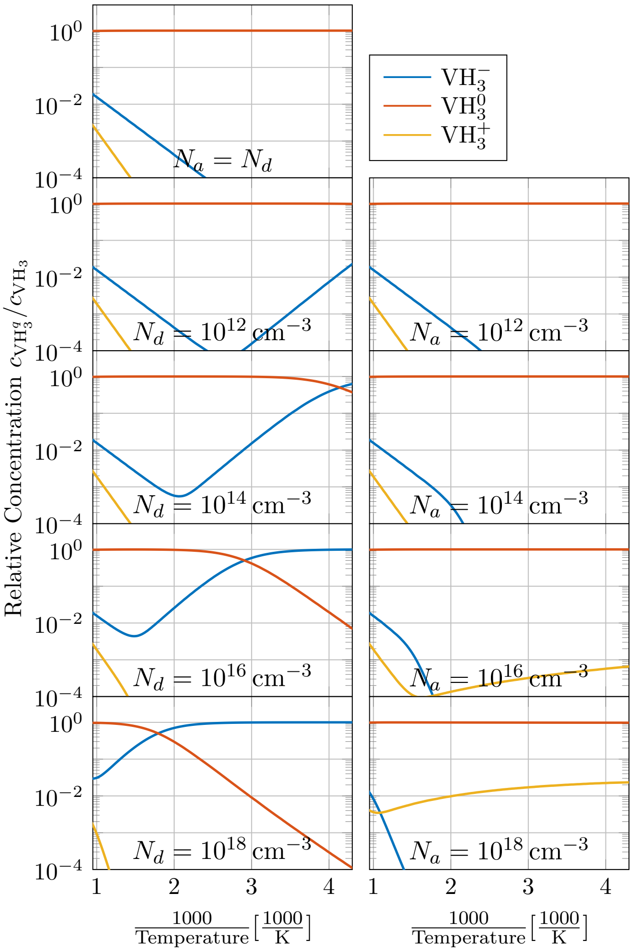

(a) Separate doping concentrations.

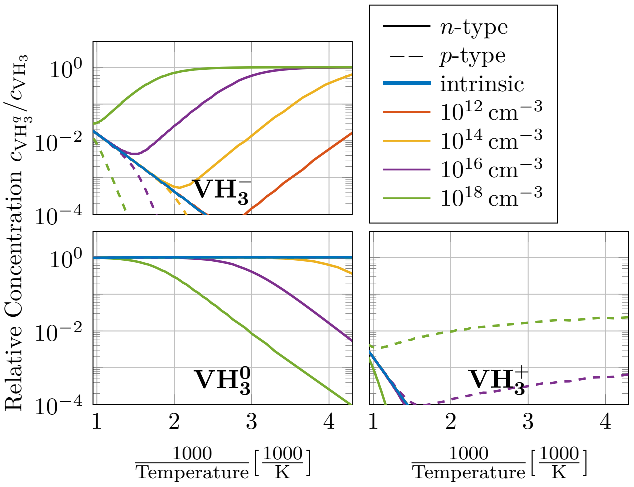

(b) Separate charge states.

Figure C.36.2: Relative concentrations of each charge state of VH_3.

C.37 VOH-Complex

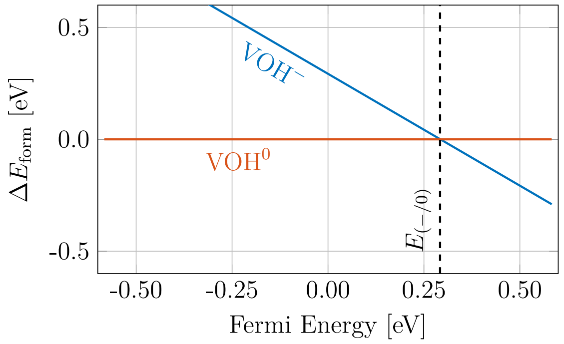

	$\Delta E_{\text{form}}^{E_F=0}$	$\Delta E_{\text{form}}^{E_F=E_V}$
VOH$^-$	0.29	0.88
VOH^0	0.00	0.00

Ferreira-Resende (2000)

Trans.	$E_{q/q+1}$	$E_{q/q+1}$-E_V
-/0	**0.29**	**0.88**

bold: observable transitions

(a) Relative formation energy of each charge state of the VOH-complex (based on DFT-simulations by Ferreira-Resende [163]).

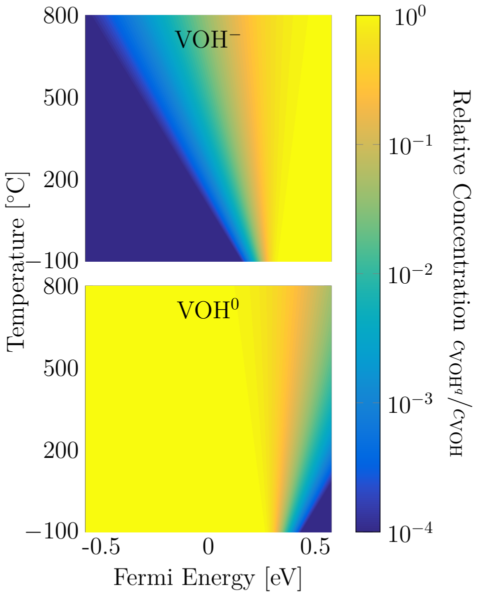

(b) Relative concentration of each charge state of the VOH-complex.

Figure C.37.1: Distribution of charge states of the VOH-complex. Calculations are based on DFT-simulations by Ferreira-Resende [163].

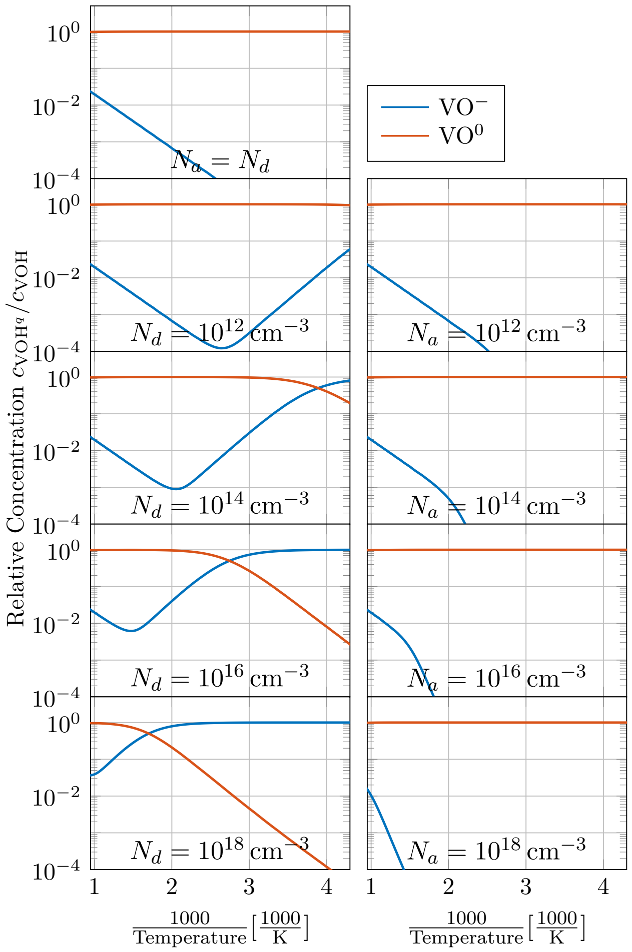

(a) Separate doping concentrations.

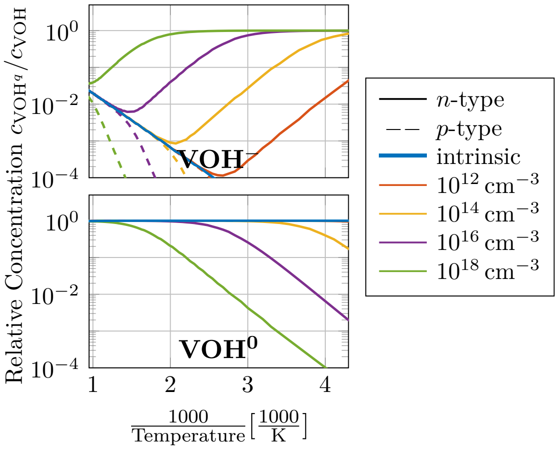

(b) Separate charge states.

Figure C.37.2: Relative concentrations of each charge state of the VOH-complex.

C.38 B_iB_sH-Complex

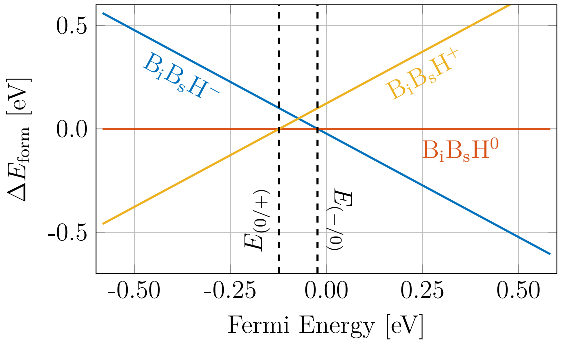

	$\Delta E_{\mathrm{form}}^{E_F=0}$	$\Delta E_{\mathrm{form}}^{E_F=E_V}$
$B_iB_sH^-$	-0.02	0.56
$B_iB_sH^0$	0.00	0.00
$B_iB_sH^+$	0.12	-0.46

Adey et al. (2003)

Trans.	$E_{q/q+1}$	$E_{q/q+1}$-E_V
-/0	**-0.02**	**0.56**
0/+	**-0.12**	**0.46**

bold: observable transitions

(a) Relative formation energy of each charge state of the B_iB_sH-complex (based on DFT-simulations by Adey et al. [253]).

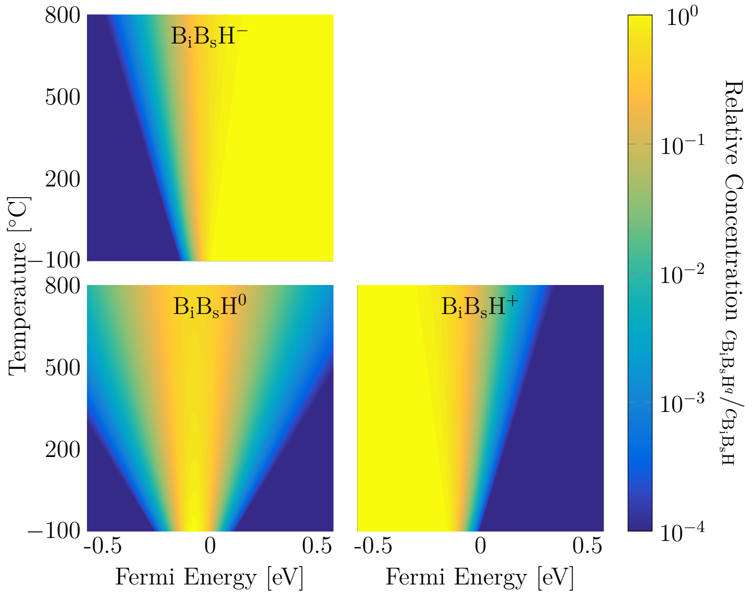

(b) Relative concentration of each charge state of the B_iB_sH-complex.

Figure C.38.1: Distribution of charge states of the B_iB_sH-complex. Calculations are based on DFT-simulations by Adey et al. [253].

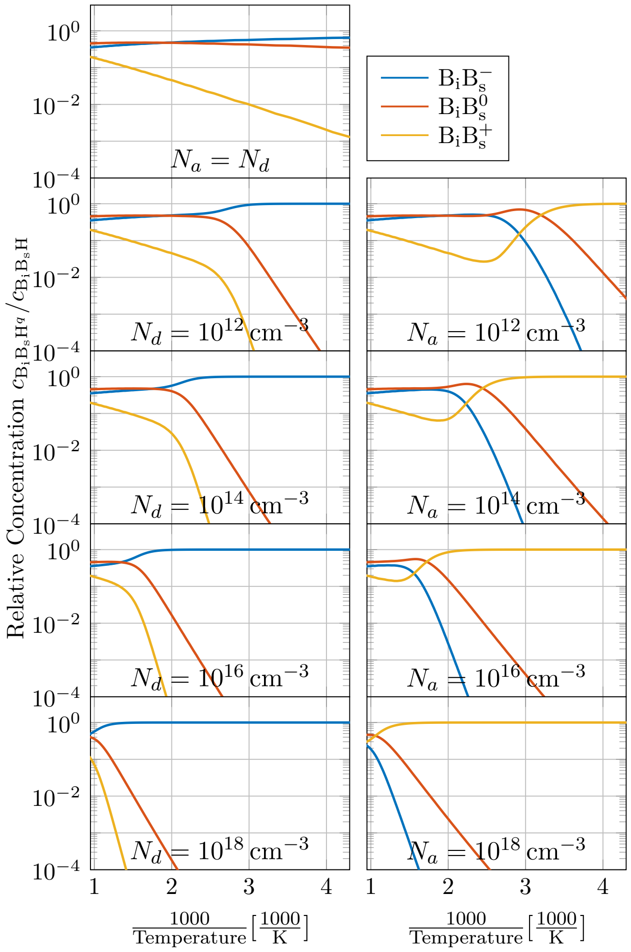

(a) Separate doping concentrations.

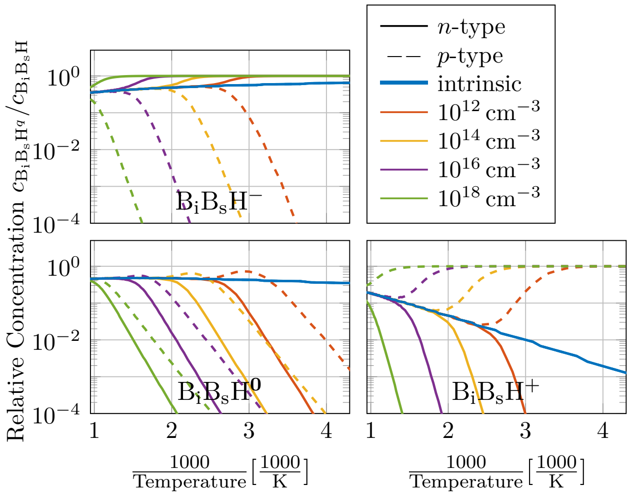

(b) Separate charge states.

Figure C.38.2: Relative concentrations of each charge state of the B_iB_sH-complex.

C.39 C_iC_sH-Complex

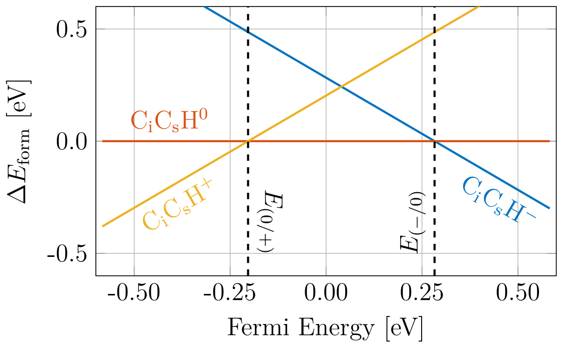

	$\Delta E_{\text{form}}^{E_F=0}$	$\Delta E_{\text{form}}^{E_F=E_V}$
$C_iC_sH^-$	0.28	0.87
$C_iC_sH^0$	0.00	0.00
$C_iC_sH^+$	0.20	-0.38

Ferreira-Resende (2000)

Trans.	$E_{q/q+1}$	$E_{q/q+1}$-E_V
-/0	**0.28**	**0.87**
0/+	**-0.20**	**0.38**

bold: observable transitions

(a) Relative formation energy of each charge state of the C_iC_sH-complex (based on DFT-simulations by Ferreira-Resende [163]).

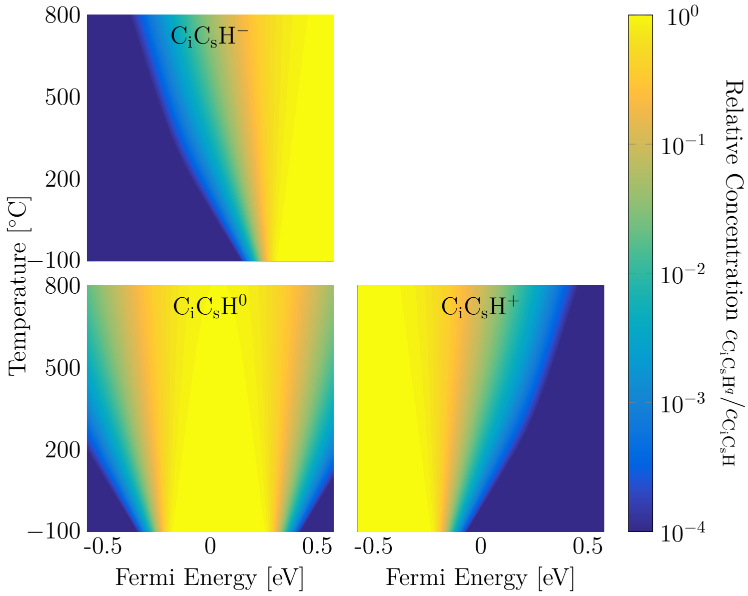

(b) Relative concentration of each charge state of the C_iC_sH-complex.

Figure C.39.1: Distribution of charge states of the C_iC_sH-complex. Calculations are based on DFT-simulations by Ferreira-Resende [163].

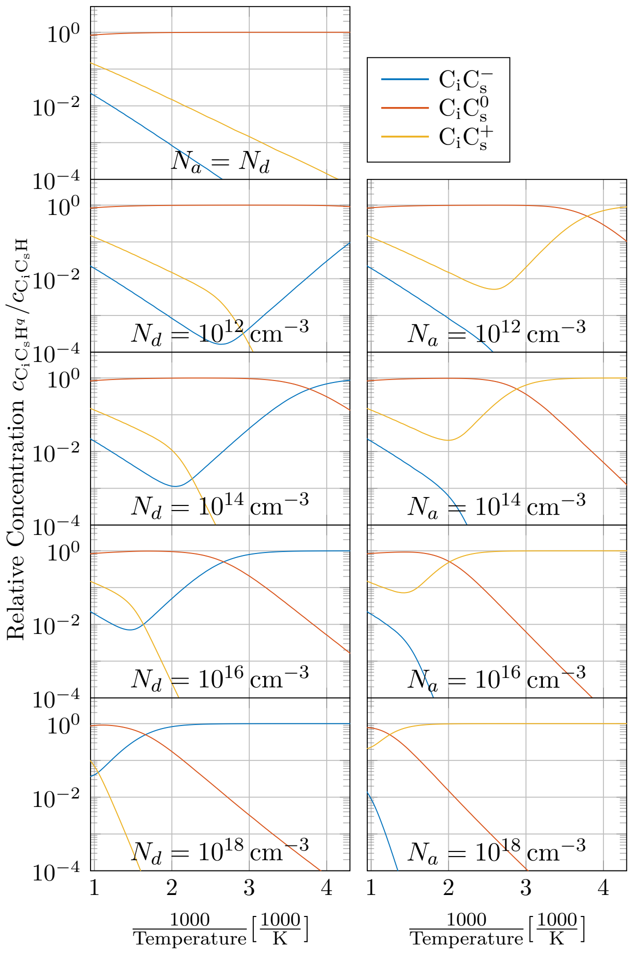

(a) Separate doping concentrations.

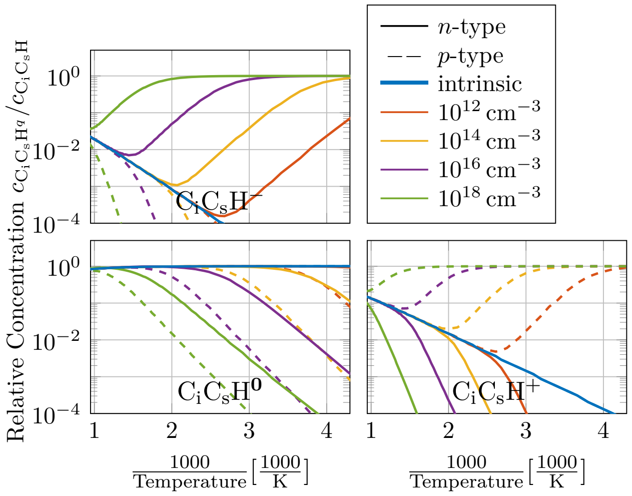

(b) Separate charge states.

Figure C.39.2: Relative concentrations of each charge state of the C_iC_sH-complex.

D Catalog of the Temperature Dependence of the Rate Constants of Selected Reactions

This appendix is a catalog of the temperature dependence of the effective capture radii and the effective rate constants of selected reactions of point defects and defect complexes in proton implanted silicon. The information provided here should help to better estimate which defects might be formed under certain conditions. All reactions treated here are approximated as diffusion limited reactions of second order and the corresponding, effective reaction rate constants k_r^{eff} are calculated as a function of the temperature and of the position of the Fermi energy in the band gap. An introduction to the kinetics of such reactions is found in section 2.2.7.

The dependence of k_r^{eff} on the Fermi energy and on the temperature originates from several contributions: The diffusivities of the reacting educts are temperature dependent (see equation 2.62). Most point defects and defect complexes can be present at different charge states and each charge state is associated with a unique set of Arrhenius parameters. As explained in section 2.2.4, the distribution of different charge states depends on the temperature and on the position of the Fermi energy in the band gap (see equation 2.77). Furthermore, if both reaction partners carry a charge, the effective capture radius of the reaction, and hence, the reaction rate constant will change. This charge dependent interaction is reflected in a change of the Coulomb interaction term f_C (see equation 2.96). If both reactants are of the same charge, they will repel each other, causing a decrease of the reaction rate constant. Reactants of opposite charge will attract each other, resulting in an increase of the reaction rate constant.

For the calculation of the effective capture radius r_c^{eff} all combinations of the different charge states q_1 and q_2 of the two educts $\mathrm{X_A}$ and $\mathrm{X_B}$ have to be taken into account. Each combination is associated with the corresponding Coulomb interaction term $f_C^{q_1,q_2}$. The relative effective capture radius is calculated according to

$$\frac{r_c^{\text{eff}}}{r_c^0}(T, E_F) = \sum_{q_1,q_2} \frac{f_C^{q_1,q_2} c_{\mathrm{X_A^{q_1}}}(T, E_F)\, c_{\mathrm{X_B^{q_2}}}(T, E_F)}{c_{\mathrm{X_A}} c_{\mathrm{X_B}}}, \tag{D.1}$$

where $c_{\mathrm{X_A^q}}/c_{\mathrm{X_A}}$ and $c_{\mathrm{X_B^q}}/c_{\mathrm{X_B}}$ are the relative concentrations of the charge states of the two defects and r_c^0 is the capture radius of two neutral defects, which is here approximated to 2 Å in all reactions. This value has been chosen, as it is used for the capture radii of most reactions discussed by Zhao in reference [446].

The effective reaction rate constant is calculated in a similar way

$$k_r^{\mathrm{AB}}\left(T, E_F\right) = \sum_{q_1, q_2} 4\pi r_c^0 \left(D_{\mathrm{X}_\mathrm{A}^{q_1}}\left(T\right) + D_{\mathrm{X}_\mathrm{B}^{q_2}}\left(T\right)\right) \frac{f_C^{q_1,q_2} c_{\mathrm{X}_\mathrm{A}^{q_1}}\left(T, E_F\right) c_{\mathrm{X}_\mathrm{B}^{q_2}}\left(T, E_F\right)}{c_{\mathrm{X}_\mathrm{A}} c_{\mathrm{X}_\mathrm{B}}}, \tag{D.2}$$

and includes the diffusivities $D_{\mathrm{X}_\mathrm{A}^{q_1}}$ and $D_{\mathrm{X}_\mathrm{B}^{q_2}}$ of each charge state of the reacting defects X_A and X_B. Often, the temperature dependence of the effective reaction rate constant follows Arrhenius' law:

$$k_r^{\mathrm{AB}} = k_{r,0}^{\mathrm{AB}} \exp\left(-\frac{E_A^{\mathrm{AB}}}{k_B T}\right), \tag{D.3}$$

with the pre-factor $k_{r,0}^{\mathrm{AB}}$ and the activation energy E_A^{AB}.

Each reaction listed in this catalog includes figures (**a**-**f**) and a table. The figures **a** and **b** show the formation energies of the charge states of the two reactants within the band gap of silicon. While the transitions between the charge state of the one reactant are indicated by dashed lines, those of the other reactant are illustrated by dotted lines. Figure **c** shows a two-dimensional map of the relative, effective capture radius r_c^{eff} of the reaction, calculated following equation D.1. The dashed lines in figure **c** indicate the temperature dependence of the Fermi energy at different doping concentrations. Figure **d** shows the relative, effective capture radius along these lines, and hence, the temperature dependence of r_c^{eff} at different doping concentrations. Often r_c^{eff} differs for many orders of magnitude between *p*-type and *n*-type material.

Following equation 4.15, and assuming a neutral capture radius r_c^0 of 2 Å, the effective rate constant of the reaction k_r^{eff} is calculated. In figure **e** a two-dimensional map of k_r^{eff}, is illustrated as a function of the position of the Fermi energy in the band gap and of the temperature. Similar to figure **c**, the temperature dependence of the position of the Fermi energy in the band gap at different doping concentrations is indicated by dashed lines. The effective reaction rate constant along these lines, which represents k_r^{eff} at different doping concentrations, is illustrated in figure **f** as a function of the inverse temperature. The temperature correlation of k_r^{eff} can be fitted by an Arrhenius function (see equation D.3). For doping concentrations of N_a,N_d=$10^{12}\,\mathrm{cm}^{-3}$, the temperature correlation of k_r^{eff} was fitted in an interval from $0.004\,\mathrm{K}^{-1}$ to $0.003\,\mathrm{K}^{-1}$. For the other doping concentrations a fit interval from $0.0035\,\mathrm{K}^{-1}$ to $0.002\,\mathrm{K}^{-1}$ was used. The Arrhenius parameters extracted from these fits are listed in the table.

D.1 Kinetics of the Reaction $\mathbf{V} + \mathbf{V} \xrightarrow{k_r^{\mathbf{VV}}} \mathbf{V}_2$

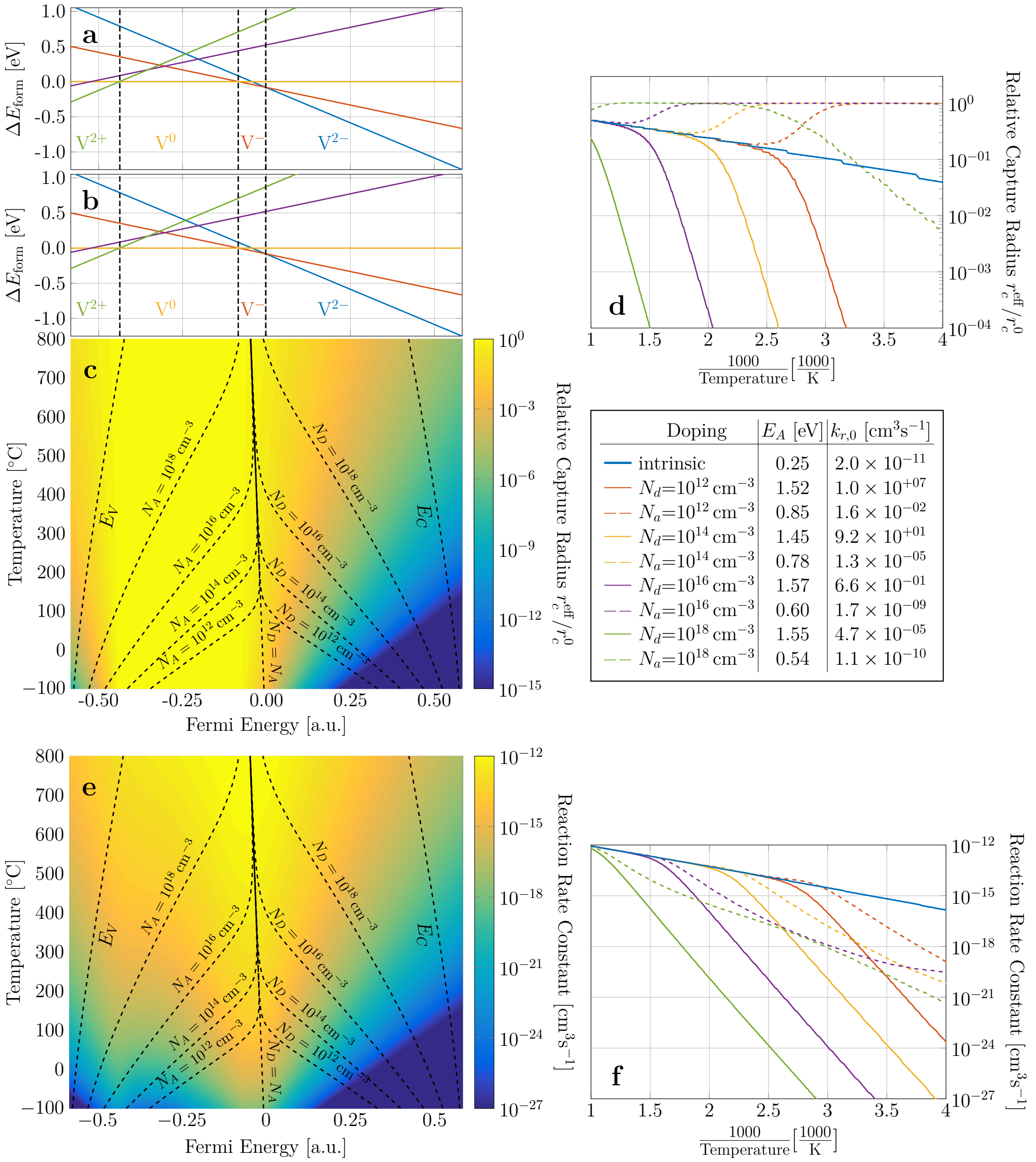

Doping	E_A [eV]	$k_{r,0}$ [cm^{3}s^{-1}]
intrinsic	0.25	2.0×10^{-11}
N_d=10^{12} cm^{-3}	1.52	$1.0 \times 10^{+07}$
N_a=10^{12} cm^{-3}	0.85	1.6×10^{-02}
N_d=10^{14} cm^{-3}	1.45	$9.2 \times 10^{+01}$
N_a=10^{14} cm^{-3}	0.78	1.3×10^{-05}
N_d=10^{16} cm^{-3}	1.57	6.6×10^{-01}
N_a=10^{16} cm^{-3}	0.60	1.7×10^{-09}
N_d=10^{18} cm^{-3}	1.55	4.7×10^{-05}
N_a=10^{18} cm^{-3}	0.54	1.1×10^{-10}

Figure D.1.1: Kinetics of the reaction of two vacancies forming a divacancy V_2.

D.2 Kinetics of the Reaction $V_2 + V \xrightarrow{k_r^{V_2V}} V_3$

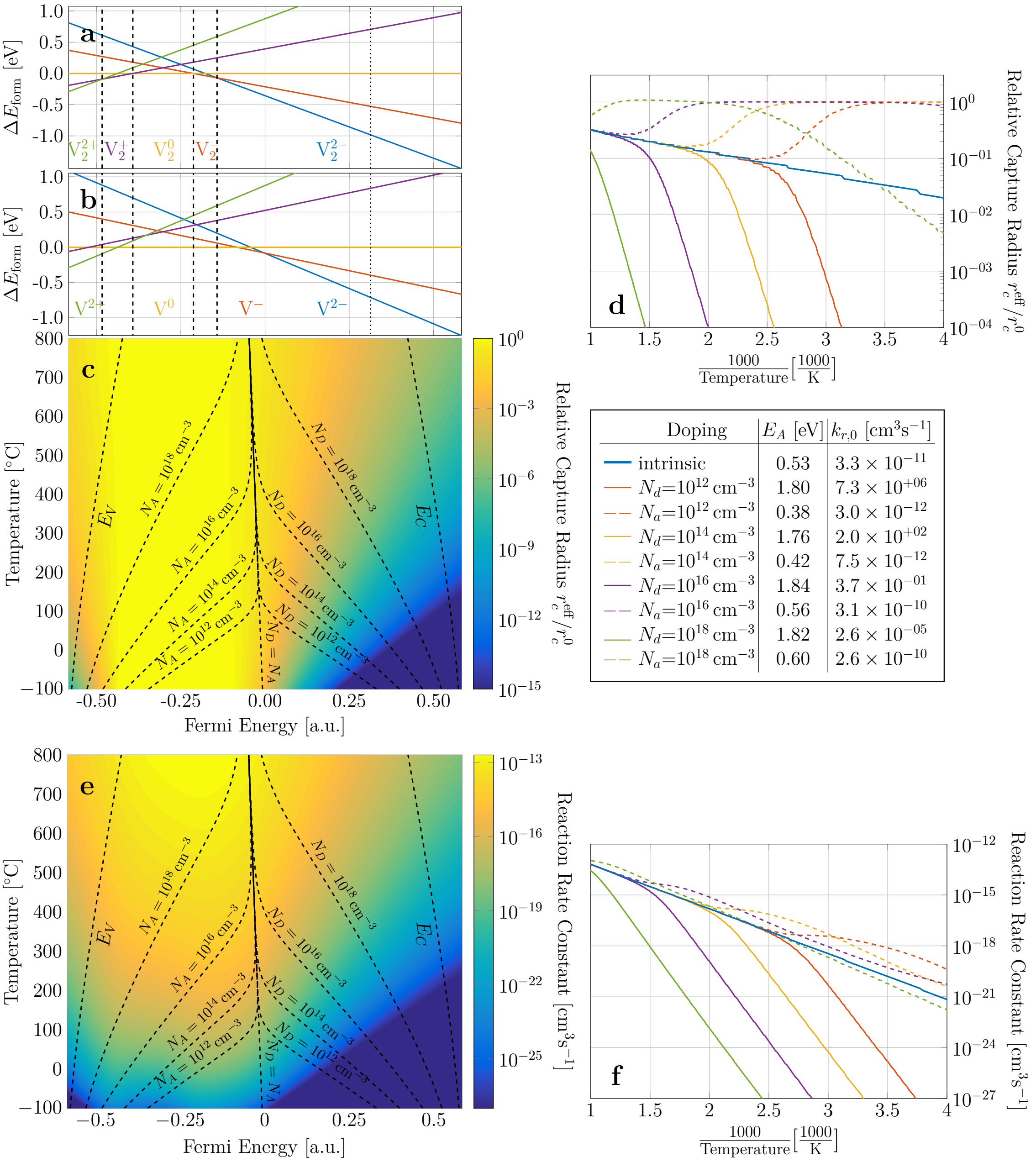

Doping	E_A [eV]	$k_{r,0}$ [cm^{3}s^{-1}]
— intrinsic	0.53	3.3×10^{-11}
— N_d=10^{12} cm^{-3}	1.80	$7.3 \times 10^{+06}$
– – N_a=10^{12} cm^{-3}	0.38	3.0×10^{-12}
— N_d=10^{14} cm^{-3}	1.76	$2.0 \times 10^{+02}$
– – N_a=10^{14} cm^{-3}	0.42	7.5×10^{-12}
— N_d=10^{16} cm^{-3}	1.84	3.7×10^{-01}
– – N_a=10^{16} cm^{-3}	0.56	3.1×10^{-10}
— N_d=10^{18} cm^{-3}	1.82	2.6×10^{-05}
– – N_a=10^{18} cm^{-3}	0.60	2.6×10^{-10}

Figure D.2.1: Kinetics of the reaction of V_2 and V forming V_3.

D.3 Kinetics of the Reaction $V_3 + V \xrightarrow{k_r^{V_3V}} V_4$

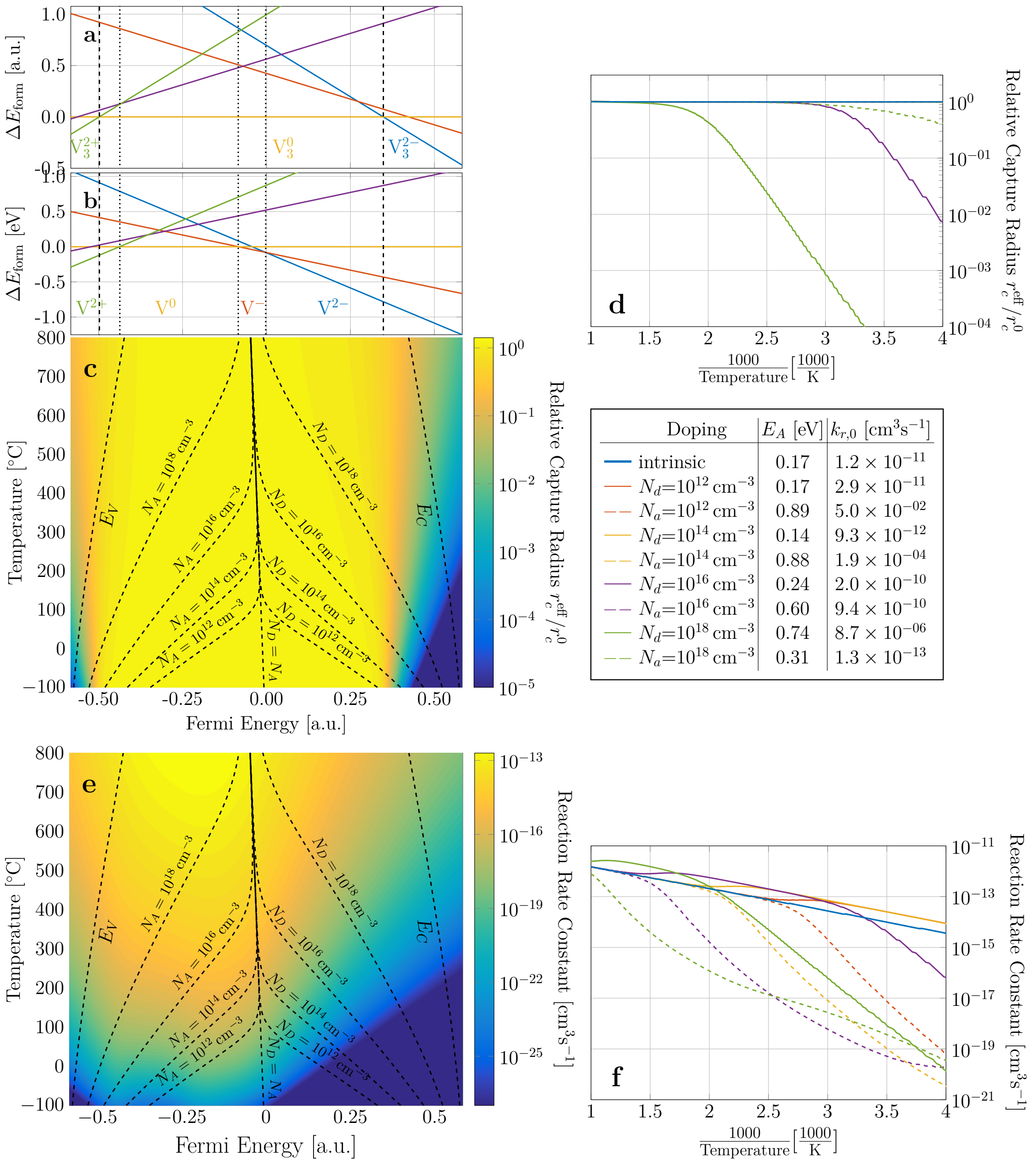

Doping	E_A [eV]	$k_{r,0}$ [cm^{3}s^{-1}]
— intrinsic	0.17	1.2×10^{-11}
— N_d=10^{12} cm^{-3}	0.17	2.9×10^{-11}
– – N_a=10^{12} cm^{-3}	0.89	5.0×10^{-02}
— N_d=10^{14} cm^{-3}	0.14	9.3×10^{-12}
– – N_a=10^{14} cm^{-3}	0.88	1.9×10^{-04}
— N_d=10^{16} cm^{-3}	0.24	2.0×10^{-10}
– – N_a=10^{16} cm^{-3}	0.60	9.4×10^{-10}
— N_d=10^{18} cm^{-3}	0.74	8.7×10^{-06}
– – N_a=10^{18} cm^{-3}	0.31	1.3×10^{-13}

Figure D.3.1: Kinetics of the reaction of V_3 and V forming V_4.

D.4 Kinetics of the Reaction $\mathbf{V}_2 + \mathbf{V}_2 \xrightarrow{k_r^{\mathbf{V}_2\mathbf{V}_2}} \mathbf{V}_4$

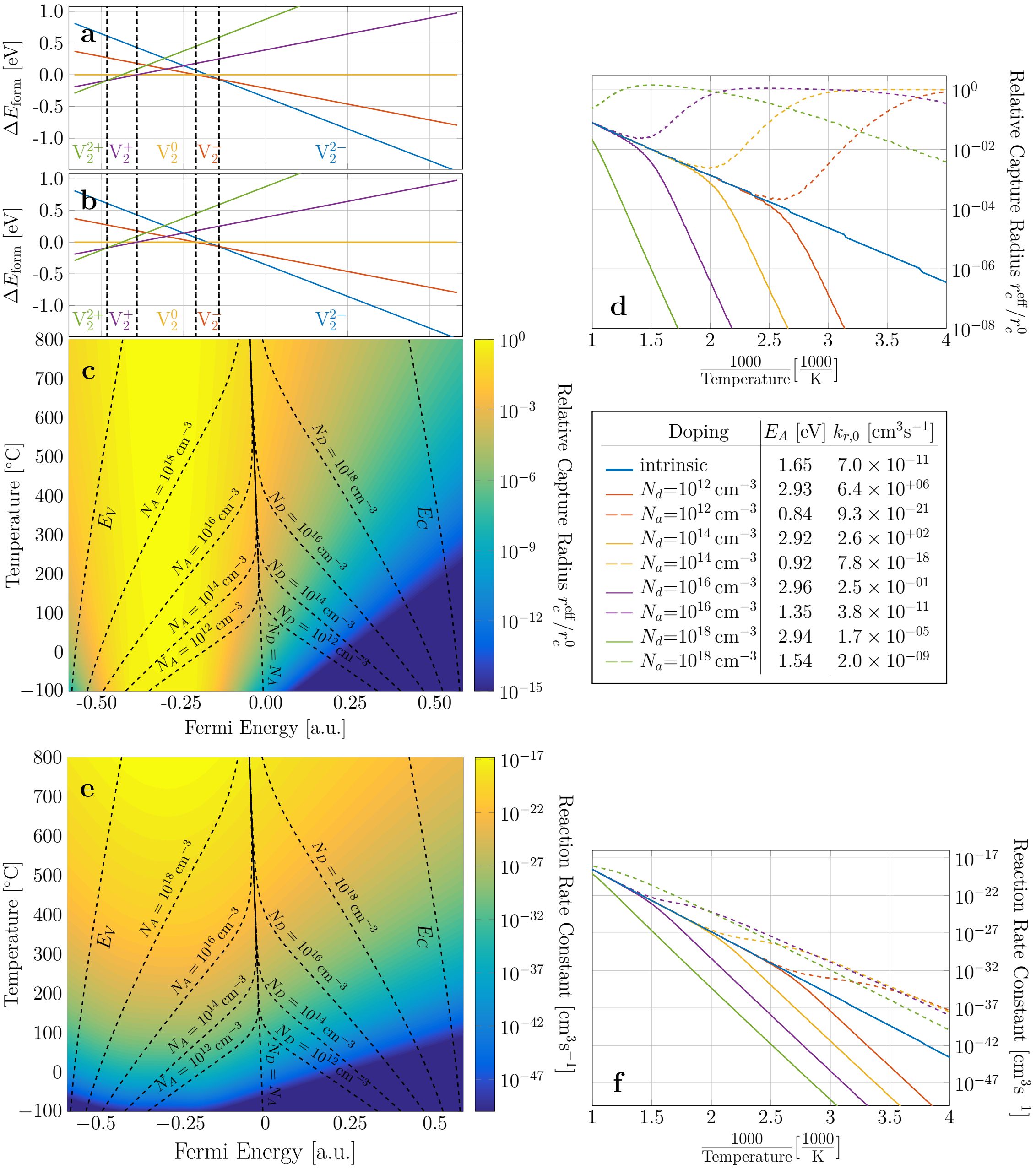

Figure D.4.1: Kinetics of the reaction of two divacancies forming V_4.

D.5 Kinetics of the Reaction $\mathbf{I} + \mathbf{I} \xrightarrow{k_r^{\mathbf{II}}} \mathbf{I}_2$

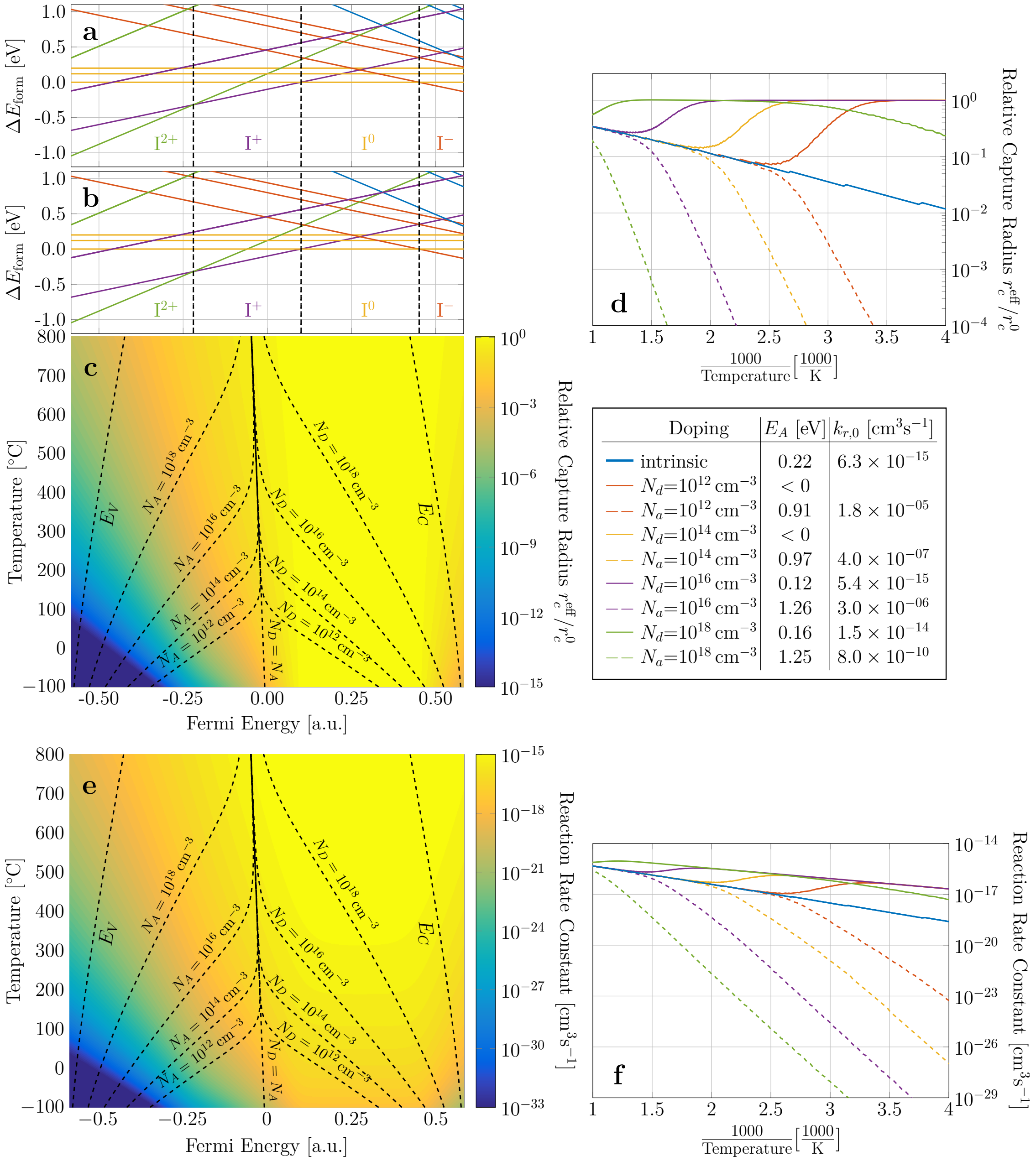

Doping	E_A [eV]	$k_{r,0}$ [cm^{3}s^{-1}]
intrinsic	0.22	6.3×10^{-15}
N_d=10^{12} cm^{-3}	< 0	
N_a=10^{12} cm^{-3}	0.91	1.8×10^{-05}
N_d=10^{14} cm^{-3}	< 0	
N_a=10^{14} cm^{-3}	0.97	4.0×10^{-07}
N_d=10^{16} cm^{-3}	0.12	5.4×10^{-15}
N_a=10^{16} cm^{-3}	1.26	3.0×10^{-06}
N_d=10^{18} cm^{-3}	0.16	1.5×10^{-14}
N_a=10^{18} cm^{-3}	1.25	8.0×10^{-10}

Figure D.5.1: Kinetics of the reaction of two self-interstitials forming I_2.

D.6 Kinetics of the Reaction $\mathbf{I_2 + I \xrightarrow{k_r^{I_2 I}} I_3}$

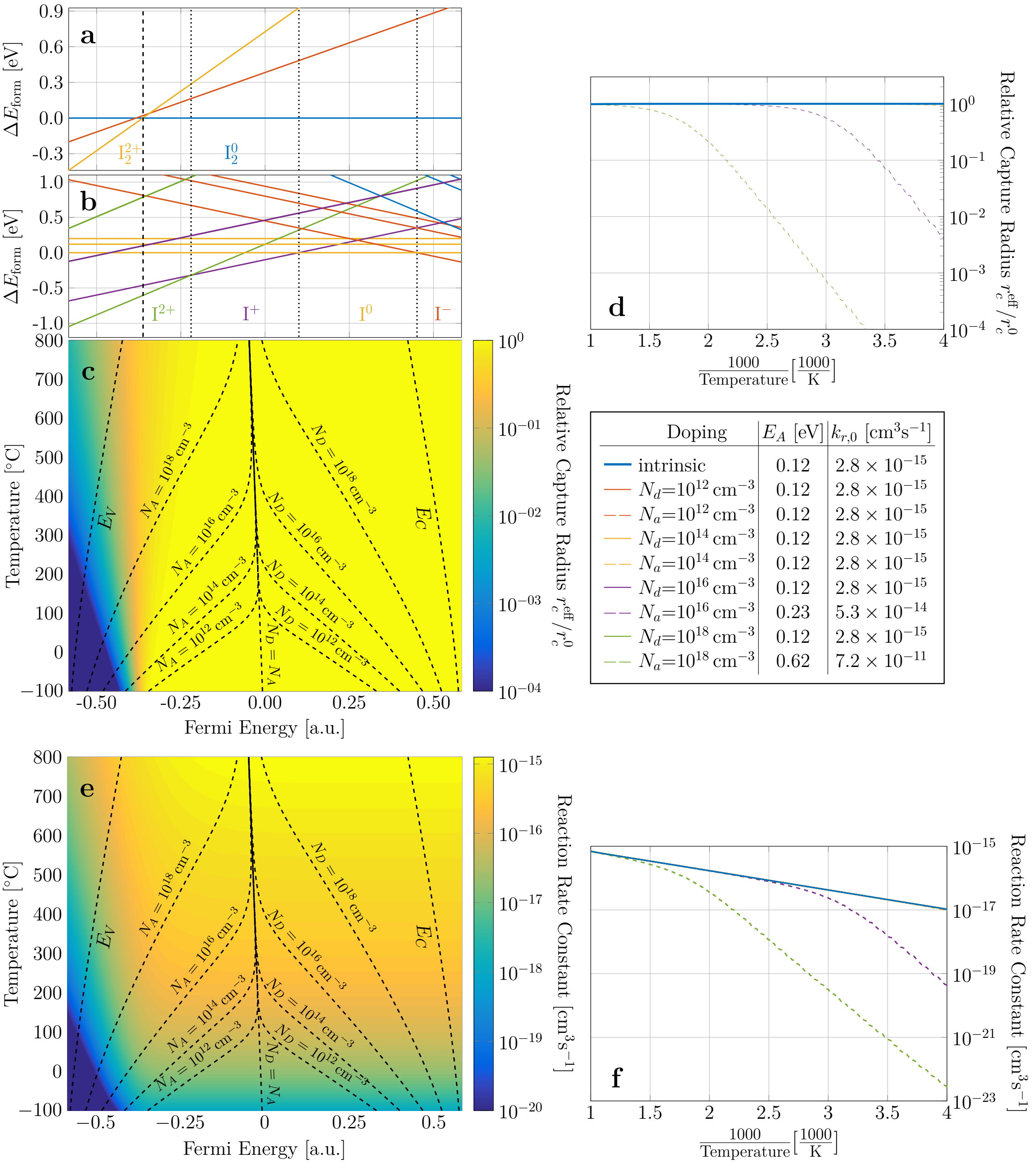

Doping	E_A [eV]	$k_{r,0}$ [cm^{3}s^{-1}]
— intrinsic	0.12	2.8×10^{-15}
— N_d=10^{12} cm^{-3}	0.12	2.8×10^{-15}
– – N_a=10^{12} cm^{-3}	0.12	2.8×10^{-15}
— N_d=10^{14} cm^{-3}	0.12	2.8×10^{-15}
– – N_a=10^{14} cm^{-3}	0.12	2.8×10^{-15}
— N_d=10^{16} cm^{-3}	0.12	2.8×10^{-15}
– – N_a=10^{16} cm^{-3}	0.23	5.3×10^{-14}
— N_d=10^{18} cm^{-3}	0.12	2.8×10^{-15}
– – N_a=10^{18} cm^{-3}	0.62	7.2×10^{-11}

Figure D.6.1: Kinetics of the reaction of I_2 and I forming I_3.

D.7 Kinetics of the Reaction $I_3 + I \xrightarrow{k_r^{I_3 I}} I_4$

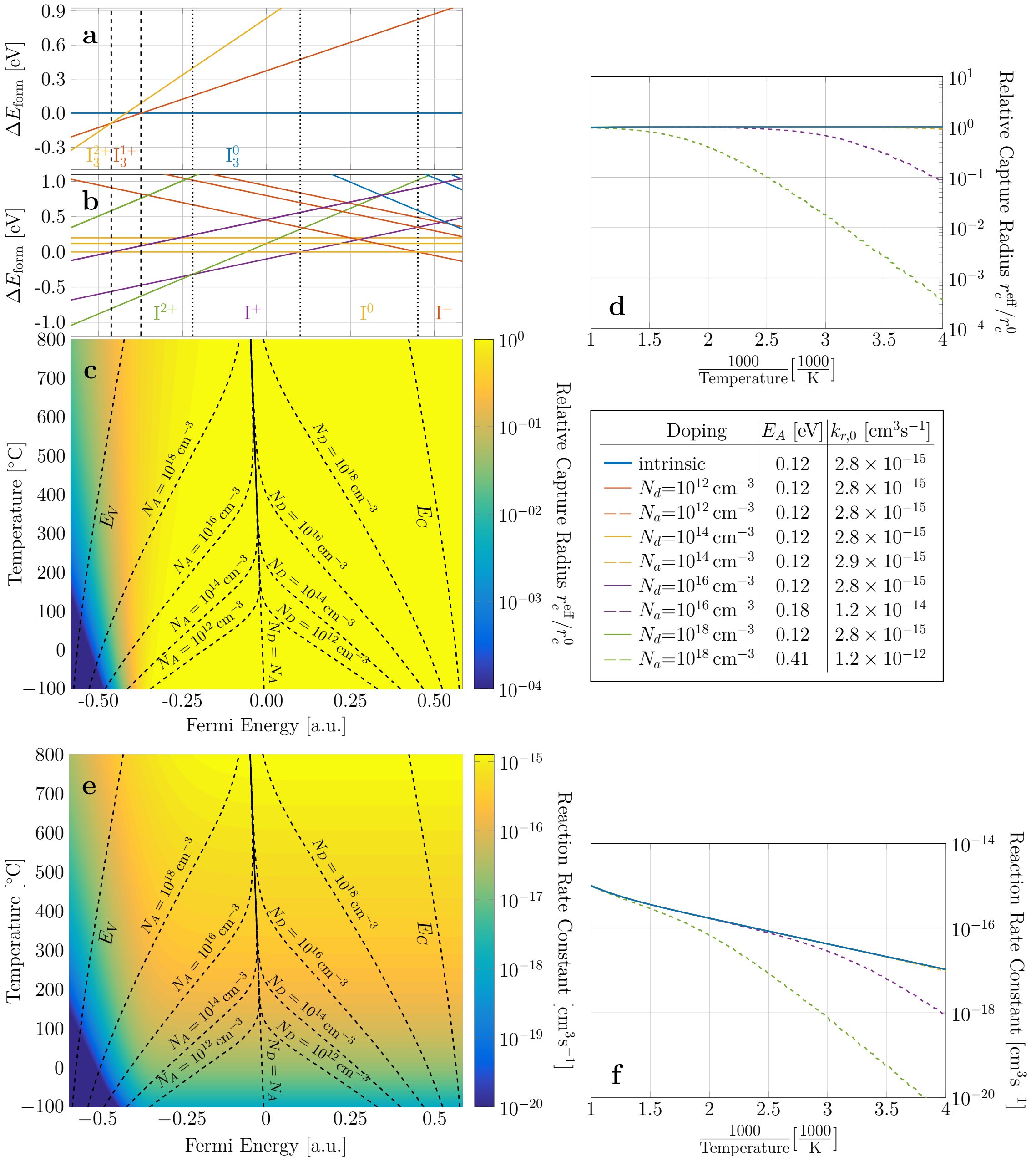

Doping	E_A [eV]	$k_{r,0}$ [cm^{3}s^{-1}]
intrinsic	0.12	2.8×10^{-15}
N_d=10^{12} cm^{-3}	0.12	2.8×10^{-15}
N_a=10^{12} cm^{-3}	0.12	2.8×10^{-15}
N_d=10^{14} cm^{-3}	0.12	2.8×10^{-15}
N_a=10^{14} cm^{-3}	0.12	2.9×10^{-15}
N_d=10^{16} cm^{-3}	0.12	2.8×10^{-15}
N_a=10^{16} cm^{-3}	0.18	1.2×10^{-14}
N_d=10^{18} cm^{-3}	0.12	2.8×10^{-15}
N_a=10^{18} cm^{-3}	0.41	1.2×10^{-12}

Figure D.7.1: Kinetics of the reaction of I_3 and I forming I_4.

D.8 Kinetics of the Reaction $\mathbf{I_2 + I_2 \xrightarrow{k_r^{I_2I_2}} I_4}$

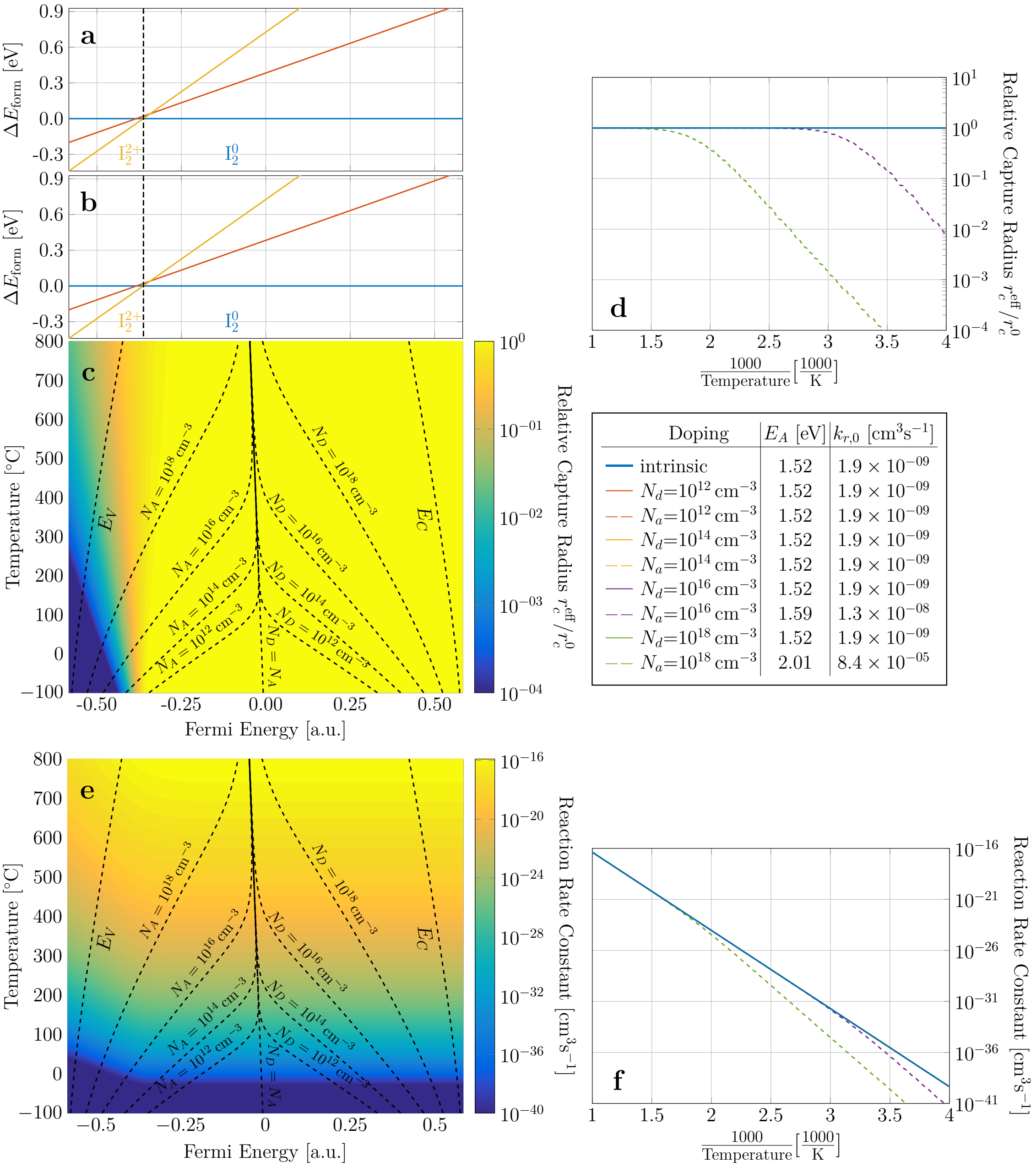

Doping	E_A [eV]	$k_{r,0}$ [cm^{3}s^{-1}]
— intrinsic	1.52	1.9×10^{-09}
— N_d=10^{12} cm^{-3}	1.52	1.9×10^{-09}
– – N_a=10^{12} cm^{-3}	1.52	1.9×10^{-09}
— N_d=10^{14} cm^{-3}	1.52	1.9×10^{-09}
– – N_a=10^{14} cm^{-3}	1.52	1.9×10^{-09}
— N_d=10^{16} cm^{-3}	1.52	1.9×10^{-09}
– – N_a=10^{16} cm^{-3}	1.59	1.3×10^{-08}
— N_d=10^{18} cm^{-3}	1.52	1.9×10^{-09}
– – N_a=10^{18} cm^{-3}	2.01	8.4×10^{-05}

Figure D.8.1: Kinetics of the reaction of two I_2 forming I_4.

D.9 Kinetics of the Reaction $\mathbf{I} + \mathbf{V} \xrightarrow{k_r^{\mathbf{IV}}} 0$

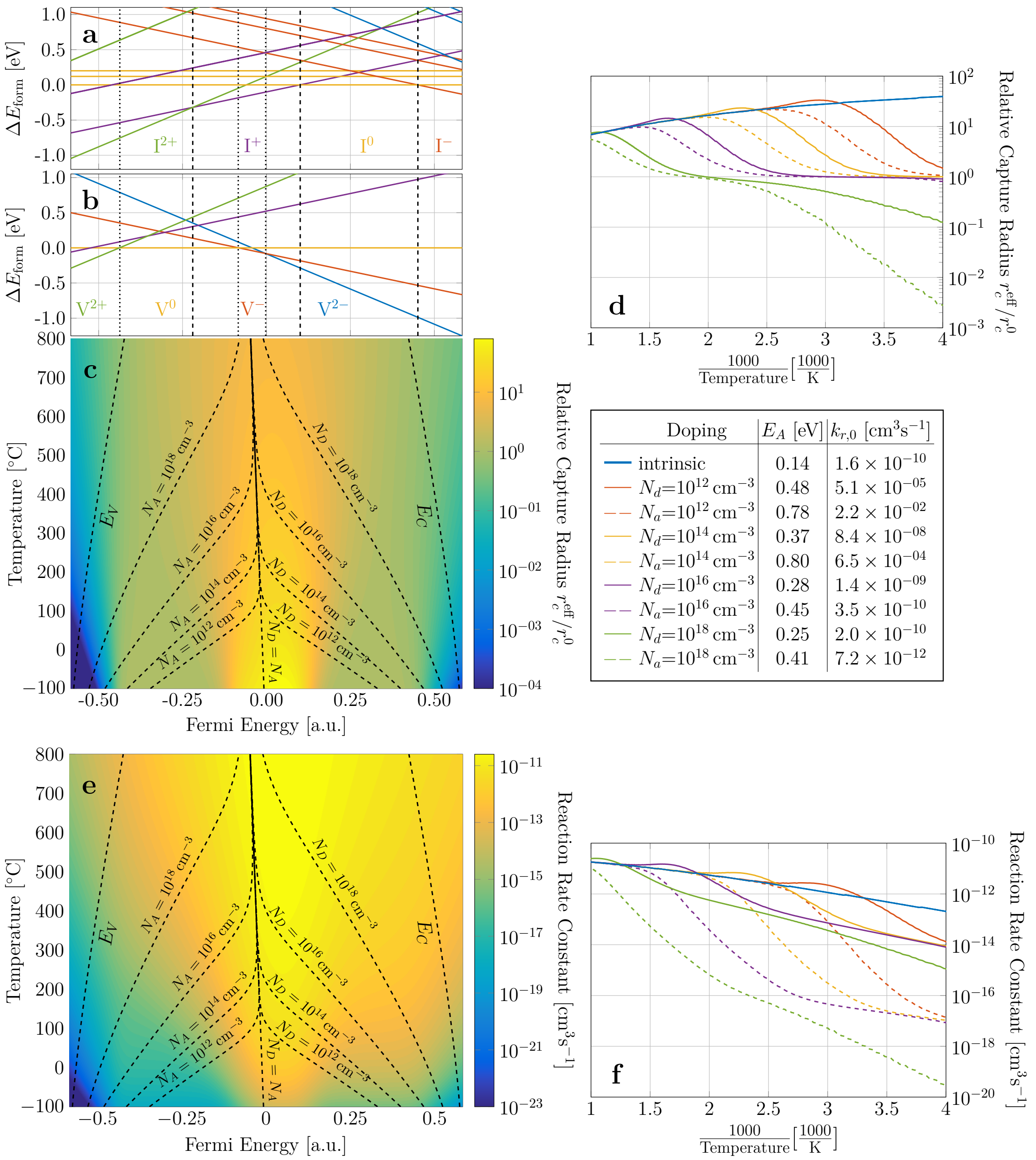

Doping	E_A [eV]	$k_{r,0}$ [cm^{3}s^{-1}]
intrinsic	0.14	1.6×10^{-10}
N_d=10^{12} cm^{-3}	0.48	5.1×10^{-05}
N_a=10^{12} cm^{-3}	0.78	2.2×10^{-02}
N_d=10^{14} cm^{-3}	0.37	8.4×10^{-08}
N_a=10^{14} cm^{-3}	0.80	6.5×10^{-04}
N_d=10^{16} cm^{-3}	0.28	1.4×10^{-09}
N_a=10^{16} cm^{-3}	0.45	3.5×10^{-10}
N_d=10^{18} cm^{-3}	0.25	2.0×10^{-10}
N_a=10^{18} cm^{-3}	0.41	7.2×10^{-12}

Figure D.9.1: Kinetics of the direct recombination of self-interstitials and vacancies.

D.10 Kinetics of the Reaction $V_2 + I \xrightarrow{k_r^{V_2 I}} V$

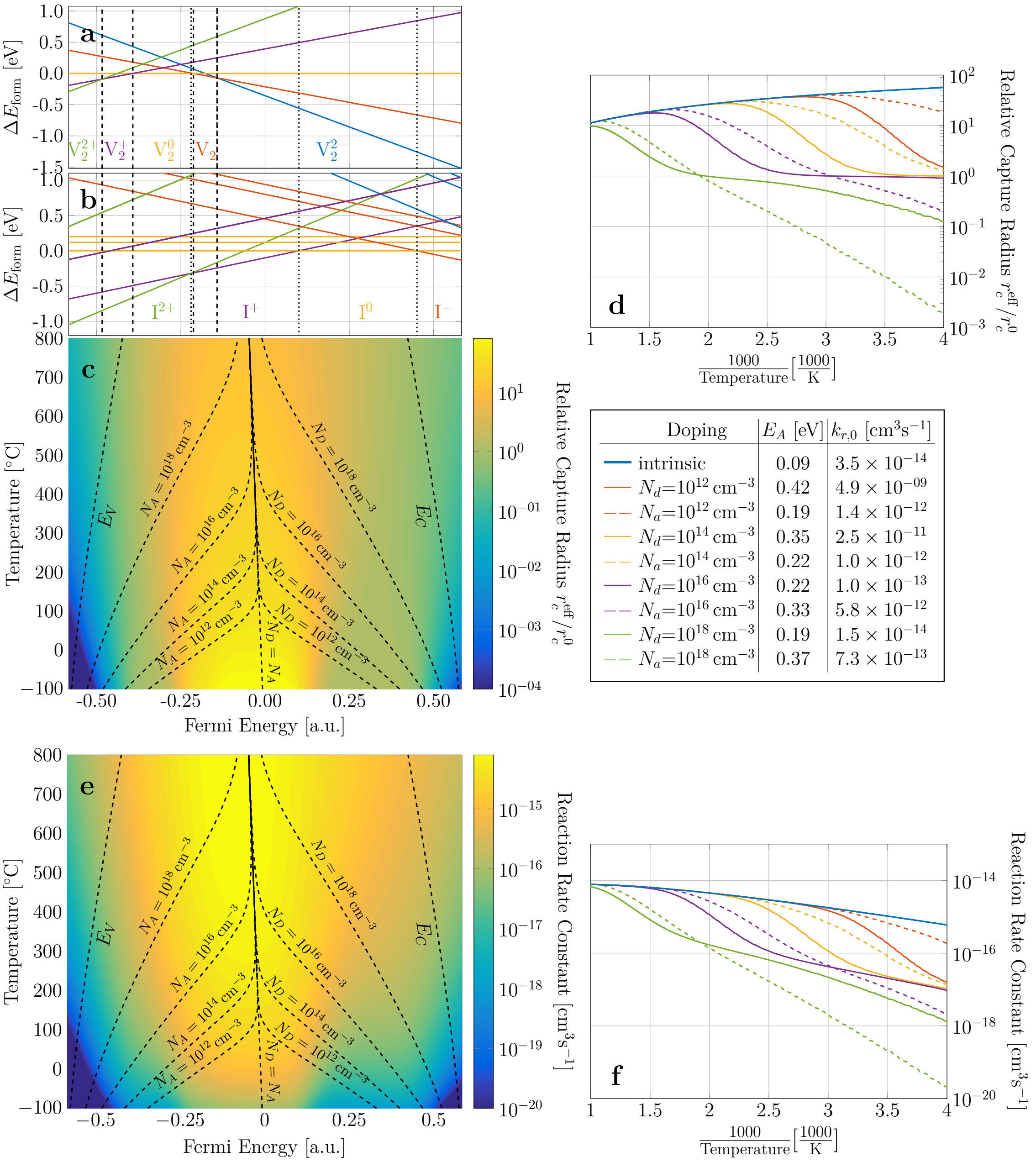

Doping	E_A [eV]	$k_{r,0}$ [cm^{3}s^{-1}]
intrinsic	0.09	3.5×10^{-14}
N_d=10^{12} cm^{-3}	0.42	4.9×10^{-09}
N_a=10^{12} cm^{-3}	0.19	1.4×10^{-12}
N_d=10^{14} cm^{-3}	0.35	2.5×10^{-11}
N_a=10^{14} cm^{-3}	0.22	1.0×10^{-12}
N_d=10^{16} cm^{-3}	0.22	1.0×10^{-13}
N_a=10^{16} cm^{-3}	0.33	5.8×10^{-12}
N_d=10^{18} cm^{-3}	0.19	1.5×10^{-14}
N_a=10^{18} cm^{-3}	0.37	7.3×10^{-13}

Figure D.10.1: Kinetics of the indirect recombination of self-interstitials at V_2.

D.11 Kinetics of the Reaction $I_2 + V \xrightarrow{k_r^{I_2 V}} I$

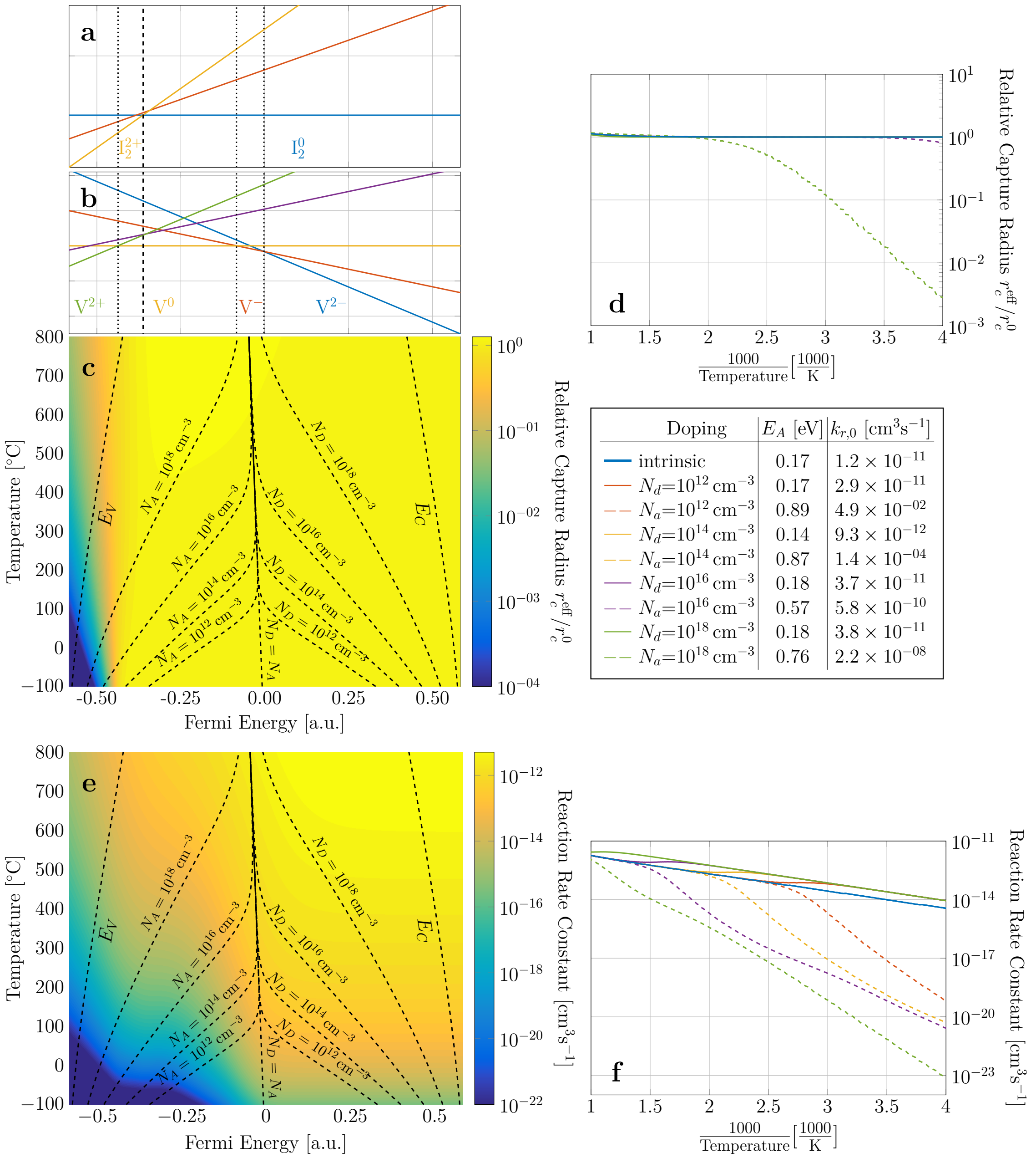

Doping	E_A [eV]	$k_{r,0}$ [cm^{3}s^{-1}]
intrinsic	0.17	1.2×10^{-11}
N_d=10^{12} cm^{-3}	0.17	2.9×10^{-11}
N_a=10^{12} cm^{-3}	0.89	4.9×10^{-02}
N_d=10^{14} cm^{-3}	0.14	9.3×10^{-12}
N_a=10^{14} cm^{-3}	0.87	1.4×10^{-04}
N_d=10^{16} cm^{-3}	0.18	3.7×10^{-11}
N_a=10^{16} cm^{-3}	0.57	5.8×10^{-10}
N_d=10^{18} cm^{-3}	0.18	3.8×10^{-11}
N_a=10^{18} cm^{-3}	0.76	2.2×10^{-08}

Figure D.11.1: Kinetics of the indirect recombination of self-interstitials at V_2.

D.12 Kinetics of the Reaction $I_2 + V_2 \xrightarrow{k_r^{I_2V_2}} 0$

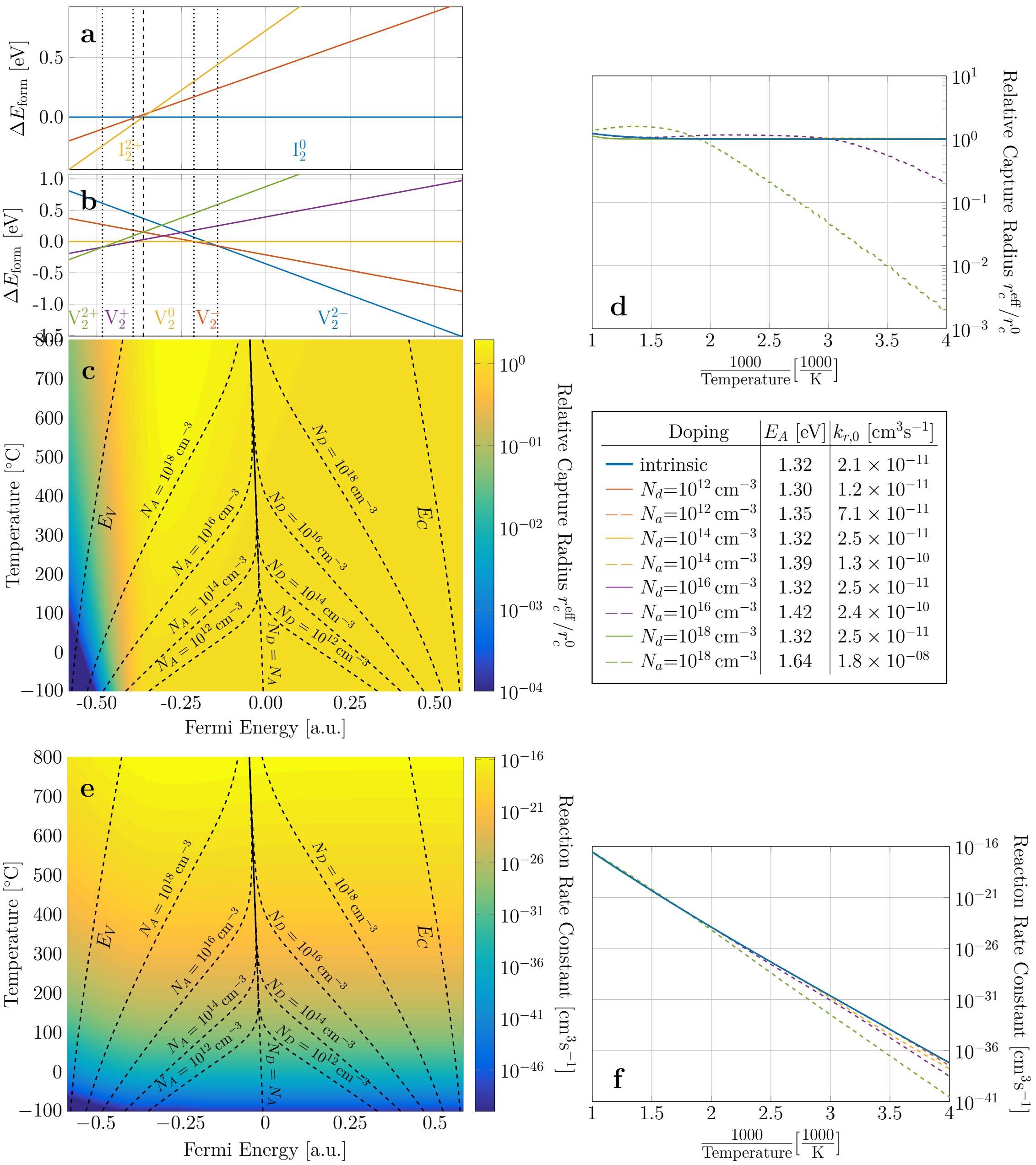

Doping	E_A [eV]	$k_{r,0}$ [cm^{3}s^{-1}]
— intrinsic	1.32	2.1×10^{-11}
— N_d=10^{12} cm^{-3}	1.30	1.2×10^{-11}
– – N_a=10^{12} cm^{-3}	1.35	7.1×10^{-11}
— N_d=10^{14} cm^{-3}	1.32	2.5×10^{-11}
– – N_a=10^{14} cm^{-3}	1.39	1.3×10^{-10}
— N_d=10^{16} cm^{-3}	1.32	2.5×10^{-11}
– – N_a=10^{16} cm^{-3}	1.42	2.4×10^{-10}
— N_d=10^{18} cm^{-3}	1.32	2.5×10^{-11}
– – N_a=10^{18} cm^{-3}	1.64	1.8×10^{-08}

Figure D.12.1: Kinetics of the direct recombination of I_2 and V_2.

D.13 Kinetics of the Reaction $\mathrm{B_s} + \mathrm{I} \xrightarrow{k_r^{\mathrm{B_sI}}} \mathrm{B_i}$

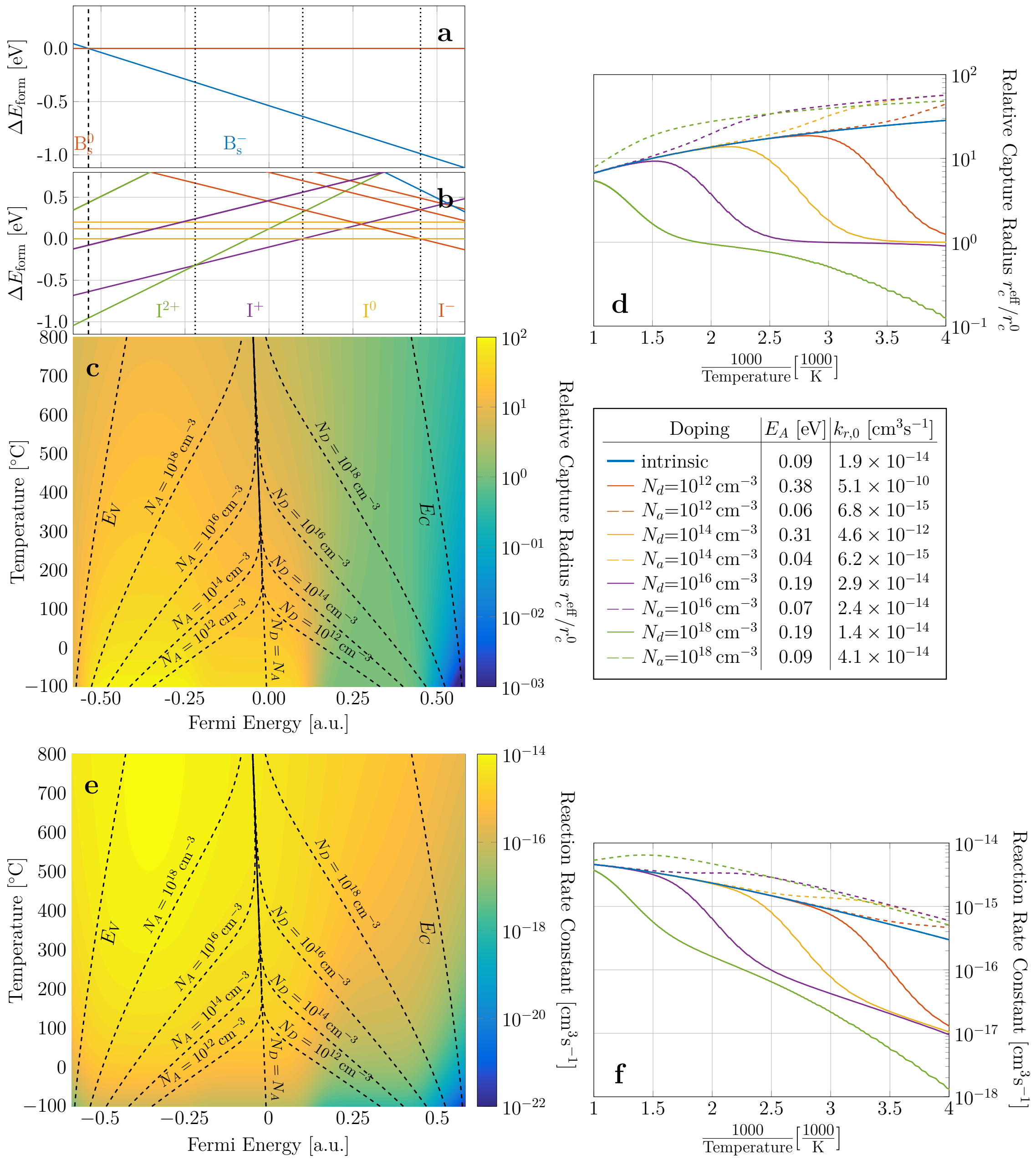

Doping	E_A [eV]	$k_{r,0}$ [cm^{3}s^{-1}]
— intrinsic	0.09	1.9×10^{-14}
— N_d=10^{12} cm^{-3}	0.38	5.1×10^{-10}
– – N_a=10^{12} cm^{-3}	0.06	6.8×10^{-15}
— N_d=10^{14} cm^{-3}	0.31	4.6×10^{-12}
– – N_a=10^{14} cm^{-3}	0.04	6.2×10^{-15}
— N_d=10^{16} cm^{-3}	0.19	2.9×10^{-14}
– – N_a=10^{16} cm^{-3}	0.07	2.4×10^{-14}
— N_d=10^{18} cm^{-3}	0.19	1.4×10^{-14}
– – N_a=10^{18} cm^{-3}	0.09	4.1×10^{-14}

Figure D.13.1: Kinetics of the reaction of $\mathrm{B_s}$ and I forming $\mathrm{B_i}$.

D.14 Kinetics of the Reaction $\mathbf{B_s + V \xrightarrow{k_r^{B_sV}} B_sV}$

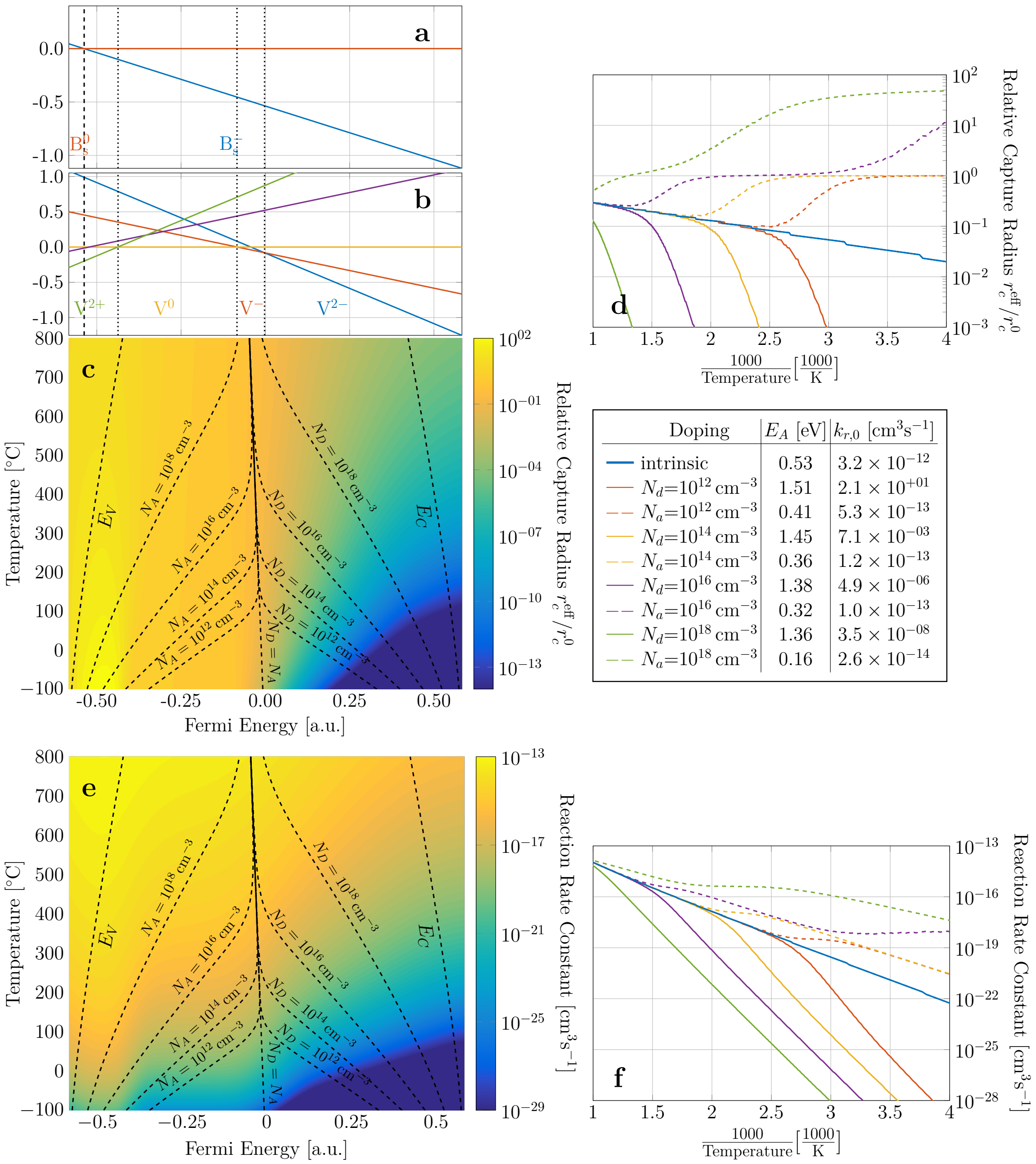

Doping	E_A [eV]	$k_{r,0}$ [cm^{3}s^{-1}]
— intrinsic	0.53	3.2×10^{-12}
— N_d=10^{12} cm^{-3}	1.51	$2.1 \times 10^{+01}$
- - N_a=10^{12} cm^{-3}	0.41	5.3×10^{-13}
— N_d=10^{14} cm^{-3}	1.45	7.1×10^{-03}
- - N_a=10^{14} cm^{-3}	0.36	1.2×10^{-13}
— N_d=10^{16} cm^{-3}	1.38	4.9×10^{-06}
- - N_a=10^{16} cm^{-3}	0.32	1.0×10^{-13}
— N_d=10^{18} cm^{-3}	1.36	3.5×10^{-08}
- - N_a=10^{18} cm^{-3}	0.16	2.6×10^{-14}

Figure D.14.1: Kinetics of the reaction of B_s and V forming B_sV.

D.15 Kinetics of the Reaction $\mathrm{B_sV} + \mathrm{I} \xrightarrow{k_r^{\mathrm{B_sVI}}} \mathrm{B_s}$

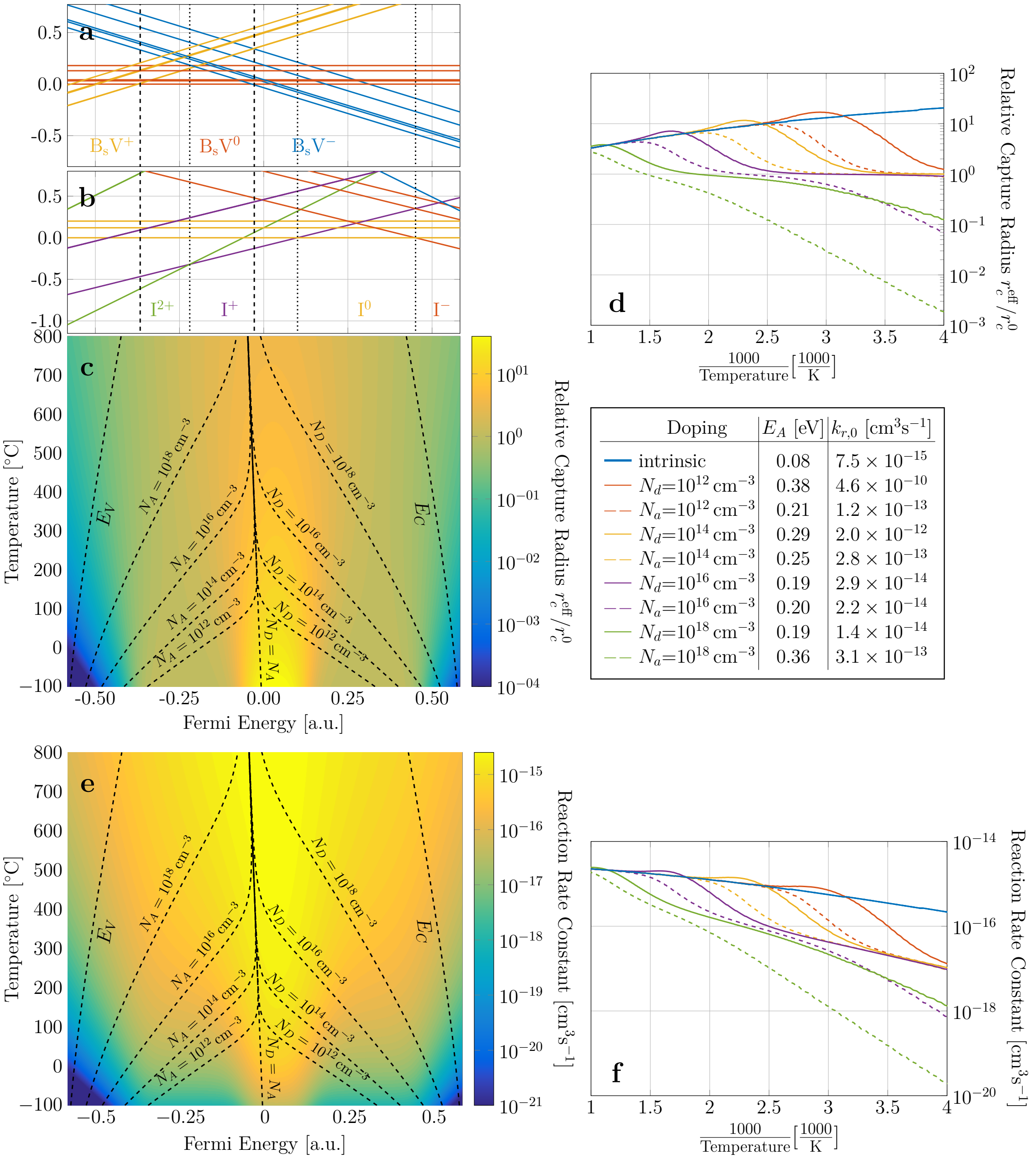

Doping	E_A [eV]	$k_{r,0}$ [cm^{3}s^{-1}]
intrinsic	0.08	7.5×10^{-15}
N_d=10^{12} cm^{-3}	0.38	4.6×10^{-10}
N_a=10^{12} cm^{-3}	0.21	1.2×10^{-13}
N_d=10^{14} cm^{-3}	0.29	2.0×10^{-12}
N_a=10^{14} cm^{-3}	0.25	2.8×10^{-13}
N_d=10^{16} cm^{-3}	0.19	2.9×10^{-14}
N_a=10^{16} cm^{-3}	0.20	2.2×10^{-14}
N_d=10^{18} cm^{-3}	0.19	1.4×10^{-14}
N_a=10^{18} cm^{-3}	0.36	3.1×10^{-13}

Figure D.15.1: Kinetics of the reaction of $\mathrm{B_sV}$ and I forming $\mathrm{B_s}$.

D.16 Kinetics of the Reaction $\mathrm{B_i} + \mathrm{V} \xrightarrow{k_r^{\mathrm{B_iV}}} \mathrm{B_s}$

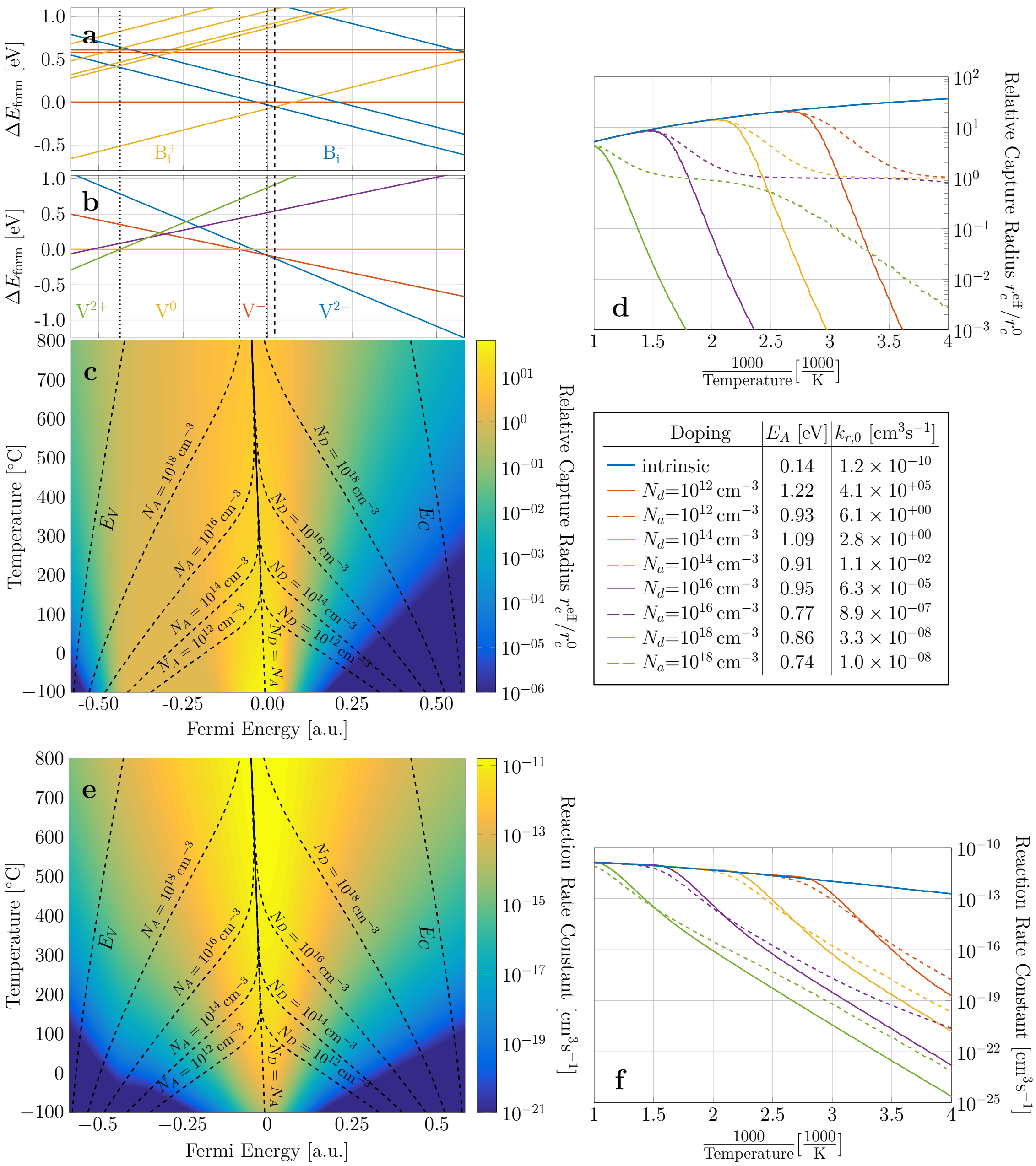

Doping	E_A [eV]	$k_{r,0}$ [cm^{3}s^{-1}]
— intrinsic	0.14	1.2×10^{-10}
— N_d=10^{12} cm^{-3}	1.22	$4.1 \times 10^{+05}$
– – N_a=10^{12} cm^{-3}	0.93	$6.1 \times 10^{+00}$
— N_d=10^{14} cm^{-3}	1.09	$2.8 \times 10^{+00}$
– – N_a=10^{14} cm^{-3}	0.91	1.1×10^{-02}
— N_d=10^{16} cm^{-3}	0.95	6.3×10^{-05}
– – N_a=10^{16} cm^{-3}	0.77	8.9×10^{-07}
— N_d=10^{18} cm^{-3}	0.86	3.3×10^{-08}
– – N_a=10^{18} cm^{-3}	0.74	1.0×10^{-08}

Figure D.16.1: Kinetics of the reaction of $\mathrm{B_i}$ and V forming $\mathrm{B_s}$.

D.17 Kinetics of the Reaction $\mathrm{P_s} + \mathrm{I} \xrightarrow{k_r^{\mathrm{P_s I}}} \mathrm{P_i}$

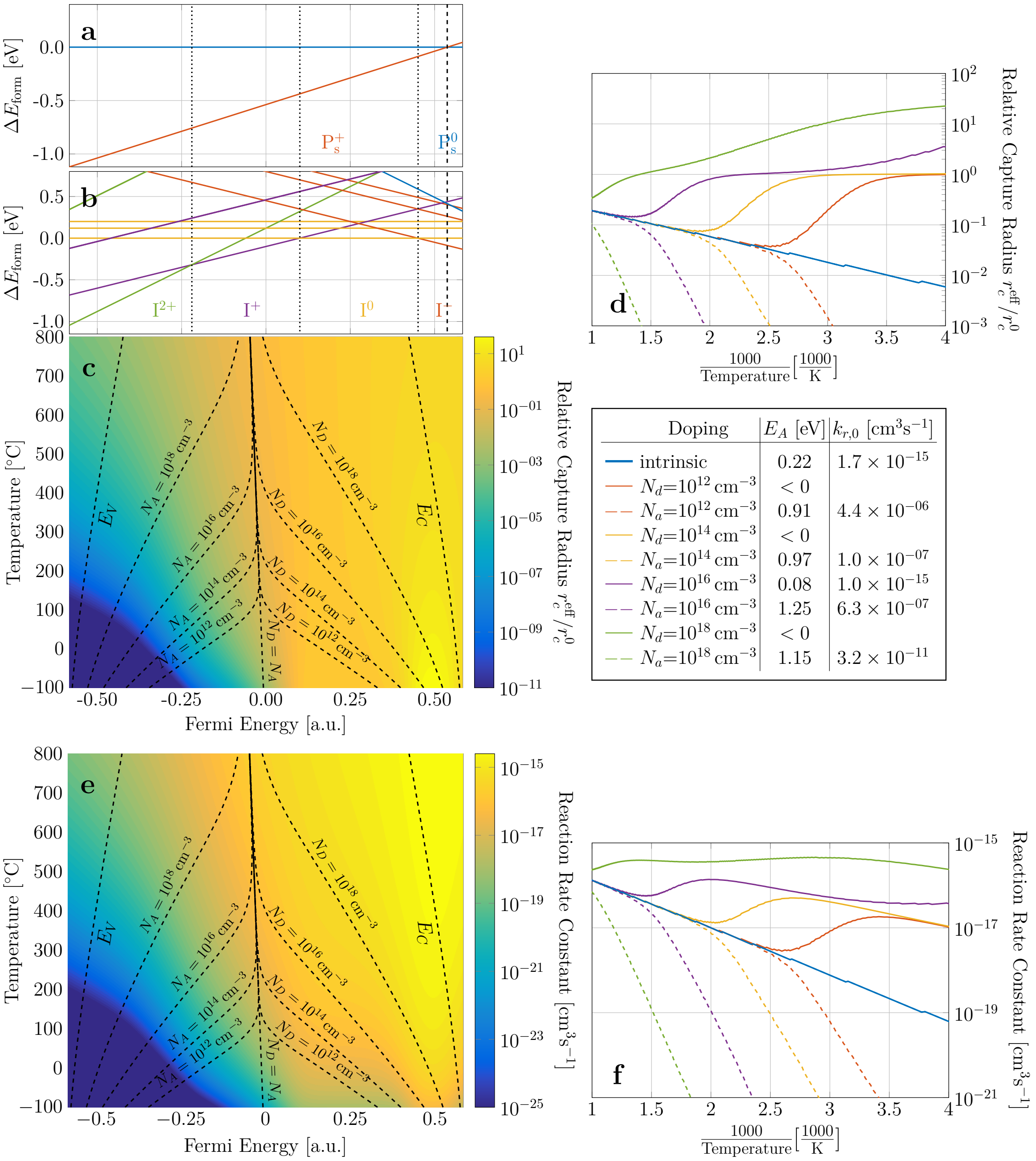

Doping	E_A [eV]	$k_{r,0}$ [cm^{3}s^{-1}]
intrinsic	0.22	1.7×10^{-15}
N_d=10^{12} cm^{-3}	< 0	
N_a=10^{12} cm^{-3}	0.91	4.4×10^{-06}
N_d=10^{14} cm^{-3}	< 0	
N_a=10^{14} cm^{-3}	0.97	1.0×10^{-07}
N_d=10^{16} cm^{-3}	0.08	1.0×10^{-15}
N_a=10^{16} cm^{-3}	1.25	6.3×10^{-07}
N_d=10^{18} cm^{-3}	< 0	
N_a=10^{18} cm^{-3}	1.15	3.2×10^{-11}

Figure D.17.1: Kinetics of the reaction of $\mathrm{P_s}$ and I forming $\mathrm{P_i}$.

D.18 Kinetics of the Reaction $\mathrm{P_s} + \mathrm{V} \xrightarrow{k_r^{\mathrm{P_sV}}} \mathrm{VP_s}$

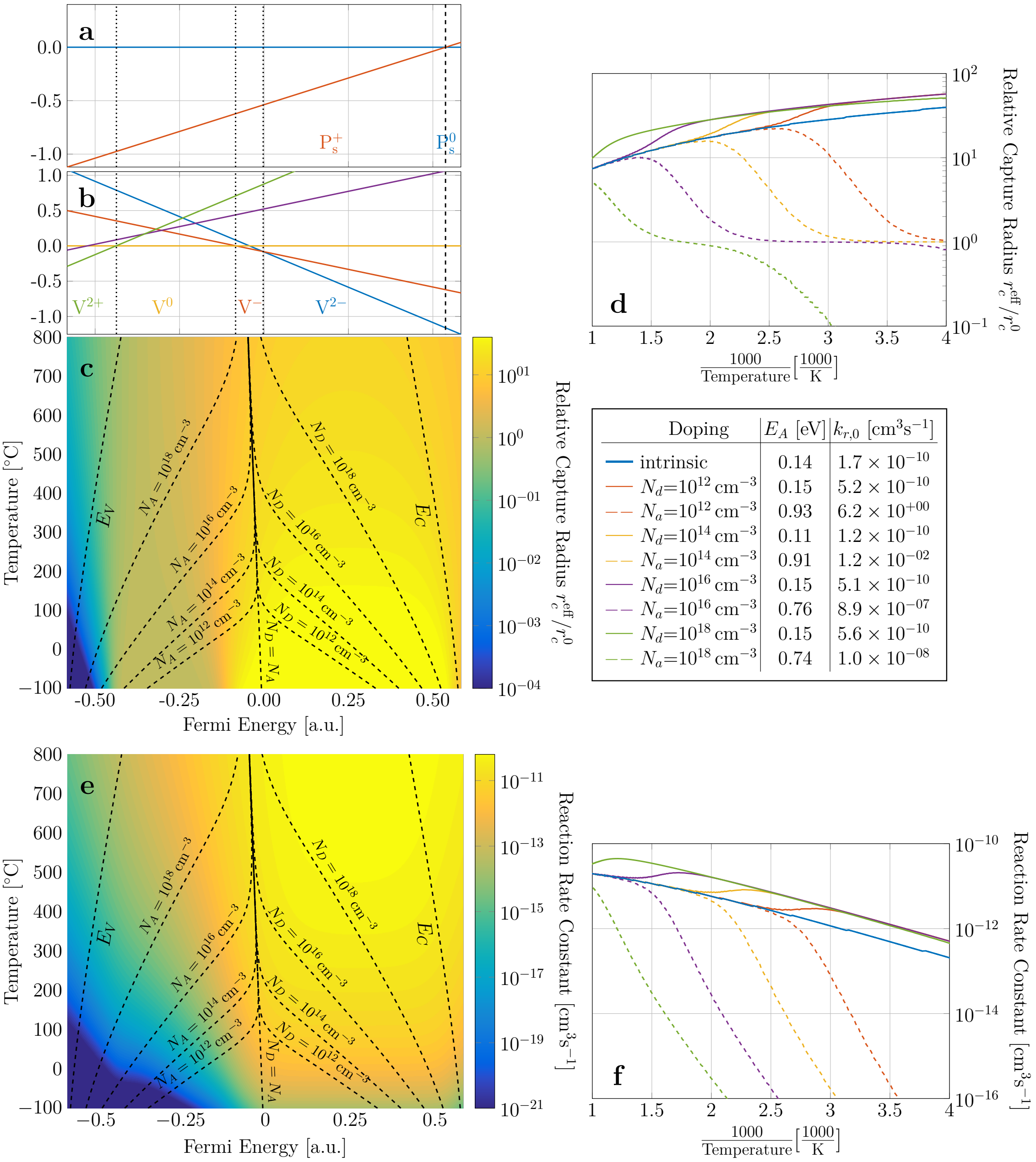

Doping	E_A [eV]	$k_{r,0}$ [cm^{3}s^{-1}]
intrinsic	0.14	1.7×10^{-10}
N_d=10^{12} cm^{-3}	0.15	5.2×10^{-10}
N_a=10^{12} cm^{-3}	0.93	$6.2 \times 10^{+00}$
N_d=10^{14} cm^{-3}	0.11	1.2×10^{-10}
N_a=10^{14} cm^{-3}	0.91	1.2×10^{-02}
N_d=10^{16} cm^{-3}	0.15	5.1×10^{-10}
N_a=10^{16} cm^{-3}	0.76	8.9×10^{-07}
N_d=10^{18} cm^{-3}	0.15	5.6×10^{-10}
N_a=10^{18} cm^{-3}	0.74	1.0×10^{-08}

Figure D.18.1: Kinetics of the reaction of $\mathrm{P_s}$ and V forming $\mathrm{VP_s}$.

D.19 Kinetics of the Reaction $\mathrm{VP_s} + \mathrm{I} \xrightarrow{k_r^{\mathrm{VP_sI}}} \mathrm{P_s}$

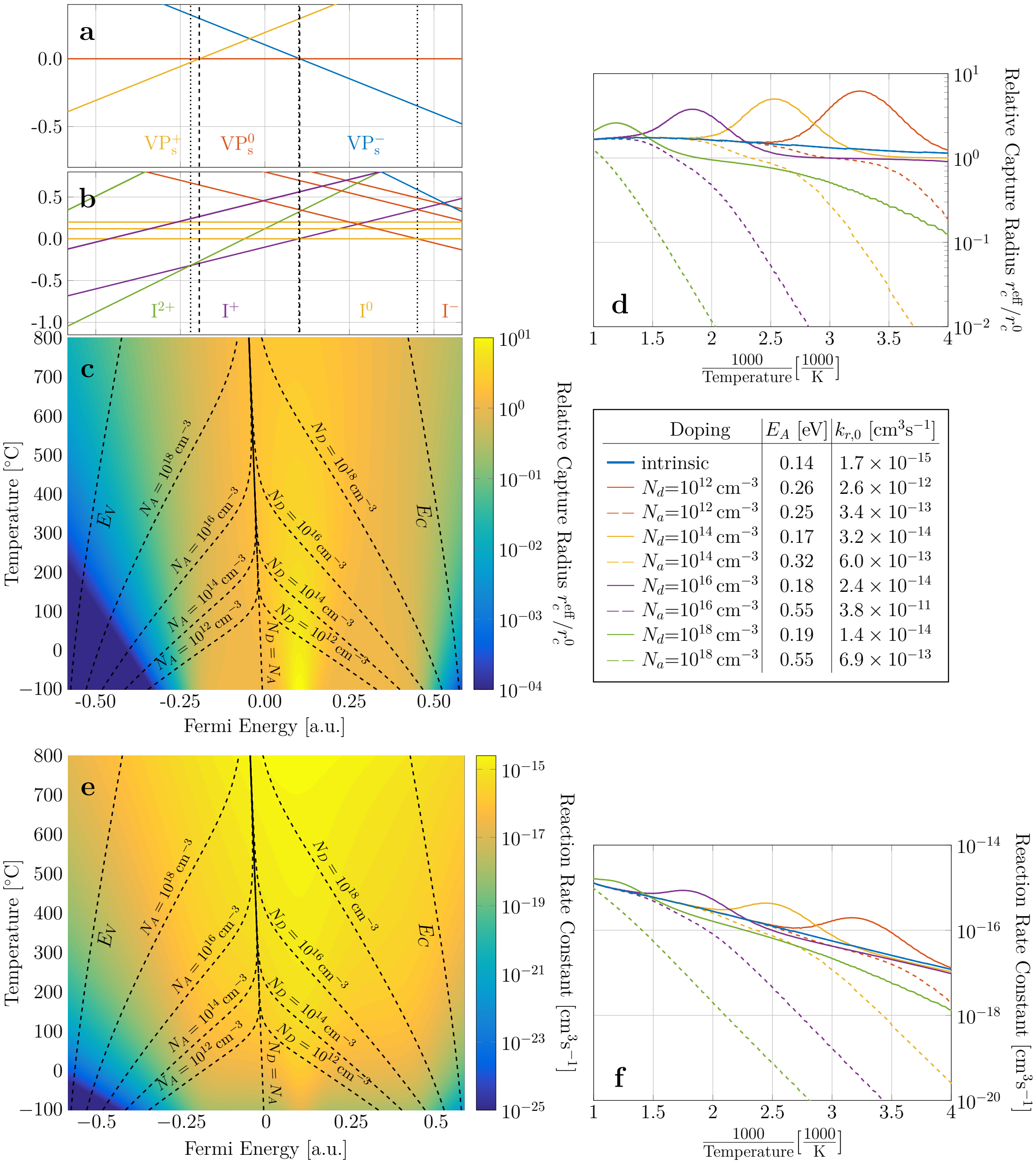

Doping	E_A [eV]	$k_{r,0}$ [cm^{3}s^{-1}]
intrinsic	0.14	1.7×10^{-15}
N_d=10^{12} cm^{-3}	0.26	2.6×10^{-12}
N_a=10^{12} cm^{-3}	0.25	3.4×10^{-13}
N_d=10^{14} cm^{-3}	0.17	3.2×10^{-14}
N_a=10^{14} cm^{-3}	0.32	6.0×10^{-13}
N_d=10^{16} cm^{-3}	0.18	2.4×10^{-14}
N_a=10^{16} cm^{-3}	0.55	3.8×10^{-11}
N_d=10^{18} cm^{-3}	0.19	1.4×10^{-14}
N_a=10^{18} cm^{-3}	0.55	6.9×10^{-13}

Figure D.19.1: Kinetics of the reaction of $\mathrm{VP_s}$ and I forming $\mathrm{P_s}$.

D.20 Kinetics of the Reaction $\mathrm{P_i + V \xrightarrow{k_r^{P_iV}} P_s}$

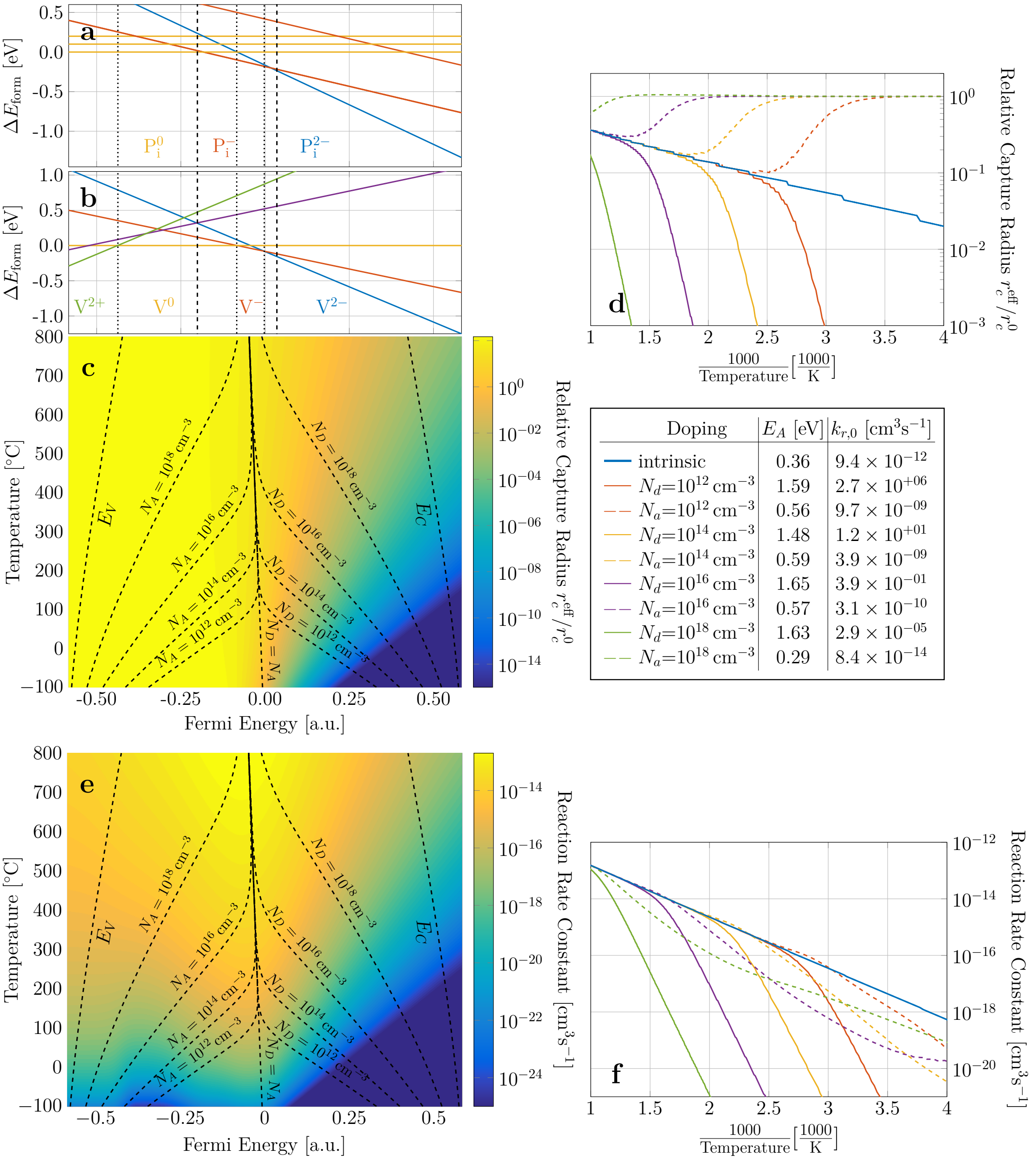

Doping	E_A [eV]	$k_{r,0}$ [cm^{3}s^{-1}]
— intrinsic	0.36	9.4×10^{-12}
— N_d=10^{12} cm^{-3}	1.59	$2.7 \times 10^{+06}$
- - N_a=10^{12} cm^{-3}	0.56	9.7×10^{-09}
— N_d=10^{14} cm^{-3}	1.48	$1.2 \times 10^{+01}$
- - N_a=10^{14} cm^{-3}	0.59	3.9×10^{-09}
— N_d=10^{16} cm^{-3}	1.65	3.9×10^{-01}
- - N_a=10^{16} cm^{-3}	0.57	3.1×10^{-10}
— N_d=10^{18} cm^{-3}	1.63	2.9×10^{-05}
- - N_a=10^{18} cm^{-3}	0.29	8.4×10^{-14}

Figure D.20.1: Kinetics of the reaction of P_i and V forming P_s.

D.21 Kinetics of the Reaction $\mathrm{O} + \mathrm{V} \xrightarrow{k_r^{\mathrm{VO}}} \mathrm{VO}$

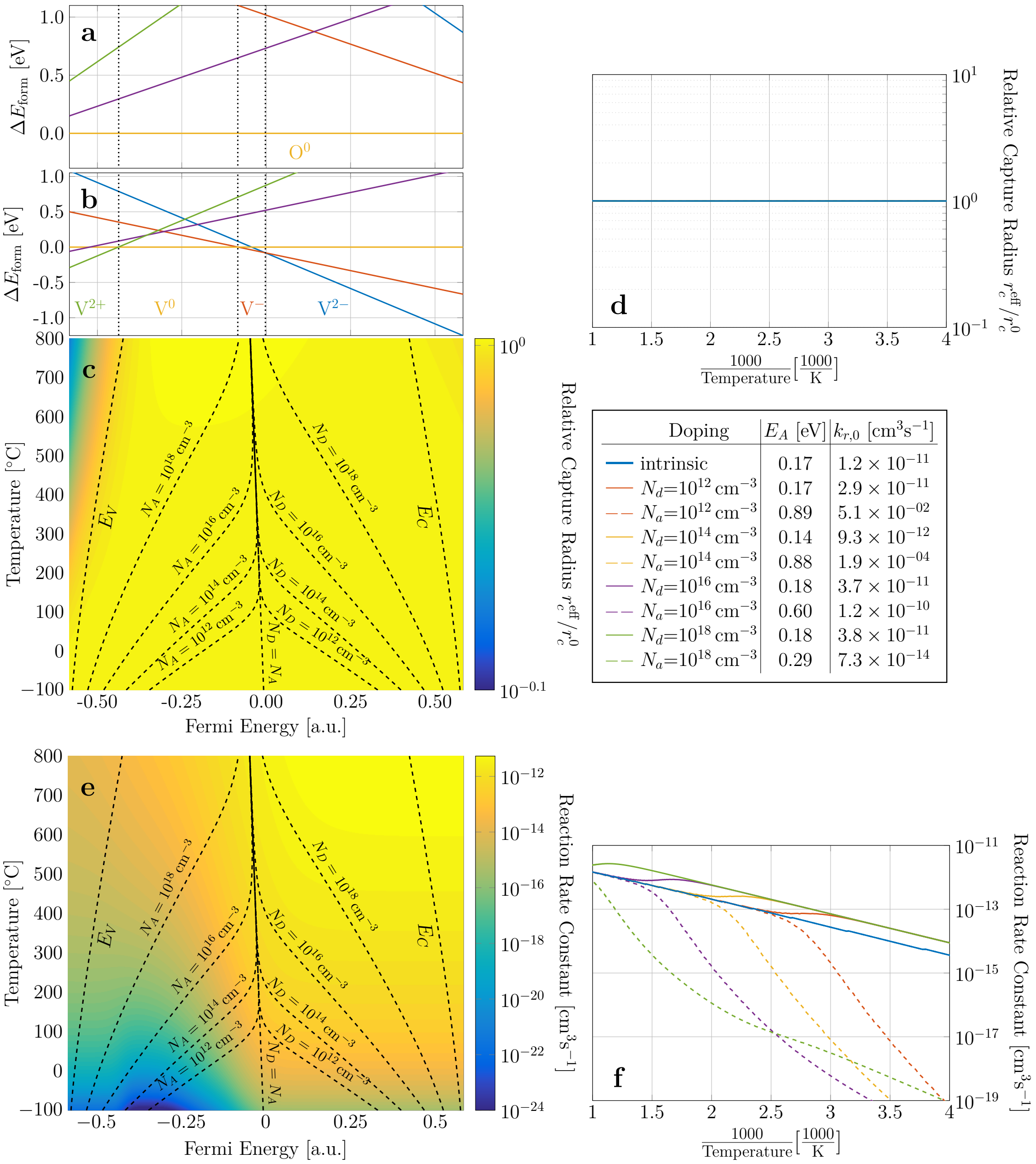

Doping	E_A [eV]	$k_{r,0}$ [cm^{3}s^{-1}]
— intrinsic	0.17	1.2×10^{-11}
— N_d=10^{12} cm^{-3}	0.17	2.9×10^{-11}
– – N_a=10^{12} cm^{-3}	0.89	5.1×10^{-02}
— N_d=10^{14} cm^{-3}	0.14	9.3×10^{-12}
– – N_a=10^{14} cm^{-3}	0.88	1.9×10^{-04}
— N_d=10^{16} cm^{-3}	0.18	3.7×10^{-11}
– – N_a=10^{16} cm^{-3}	0.60	1.2×10^{-10}
— N_d=10^{18} cm^{-3}	0.18	3.8×10^{-11}
– – N_a=10^{18} cm^{-3}	0.29	7.3×10^{-14}

Figure D.21.1: Kinetics of the reaction of oxygen with a vacancy forming VO.

D.22 Kinetics of the Reaction $\mathrm{VO} + \mathrm{V} \xrightarrow{k_r^{\mathrm{VOV}}} \mathrm{V_2O}$

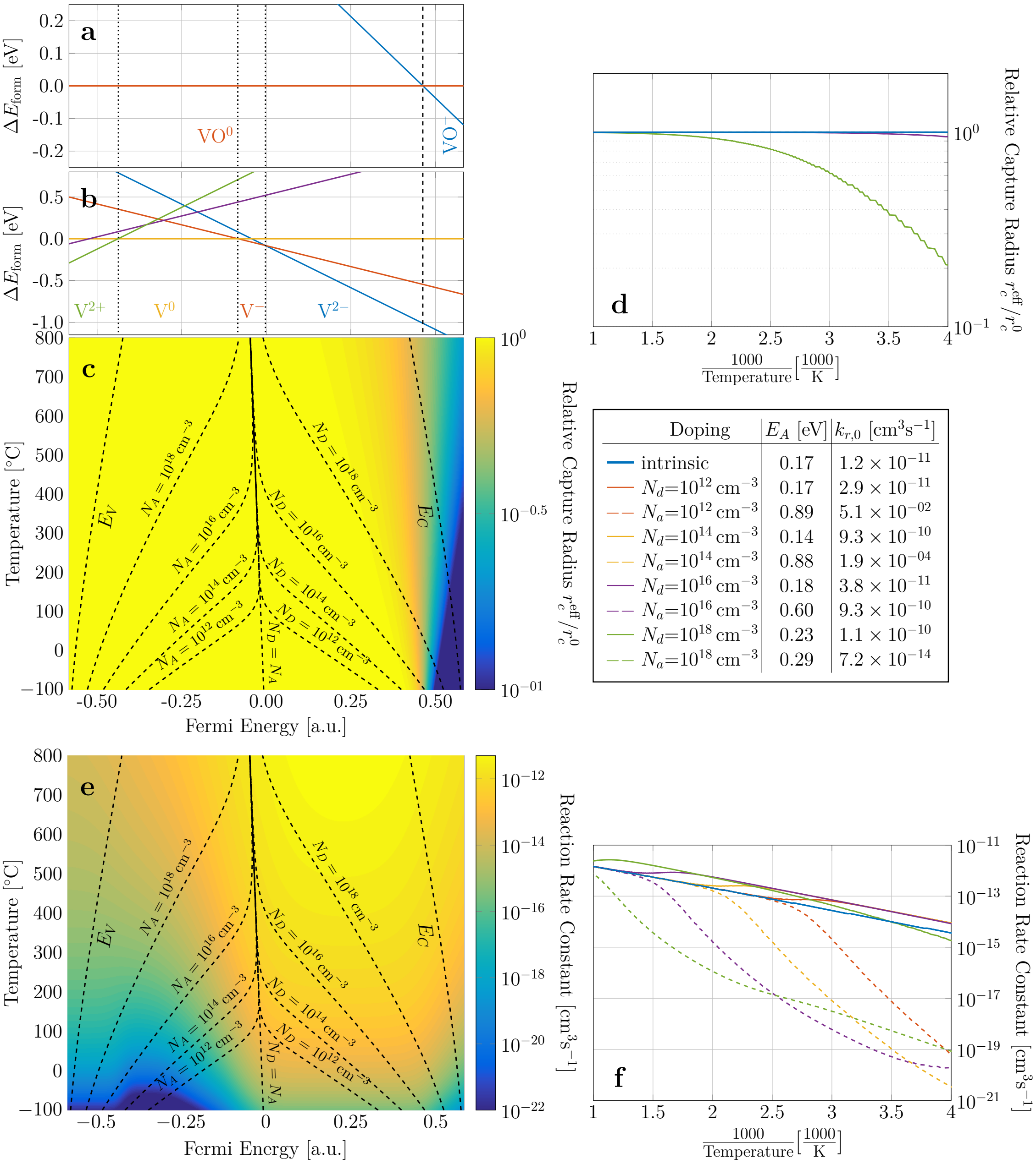

Doping	E_A [eV]	$k_{r,0}$ [cm^{3}s^{-1}]
— intrinsic	0.17	1.2×10^{-11}
— N_d=10^{12} cm^{-3}	0.17	2.9×10^{-11}
– – N_a=10^{12} cm^{-3}	0.89	5.1×10^{-02}
— N_d=10^{14} cm^{-3}	0.14	9.3×10^{-10}
– – N_a=10^{14} cm^{-3}	0.88	1.9×10^{-04}
— N_d=10^{16} cm^{-3}	0.18	3.8×10^{-11}
– – N_a=10^{16} cm^{-3}	0.60	9.3×10^{-10}
— N_d=10^{18} cm^{-3}	0.23	1.1×10^{-10}
– – N_a=10^{18} cm^{-3}	0.29	7.2×10^{-14}

Figure D.22.1: Kinetics of the reaction of VO with another vacancy forming $\mathrm{V_2O}$.

D.23 Kinetics of the Reaction $V_2O + V \xrightarrow{k_r^{V_2OV}} V_3O$

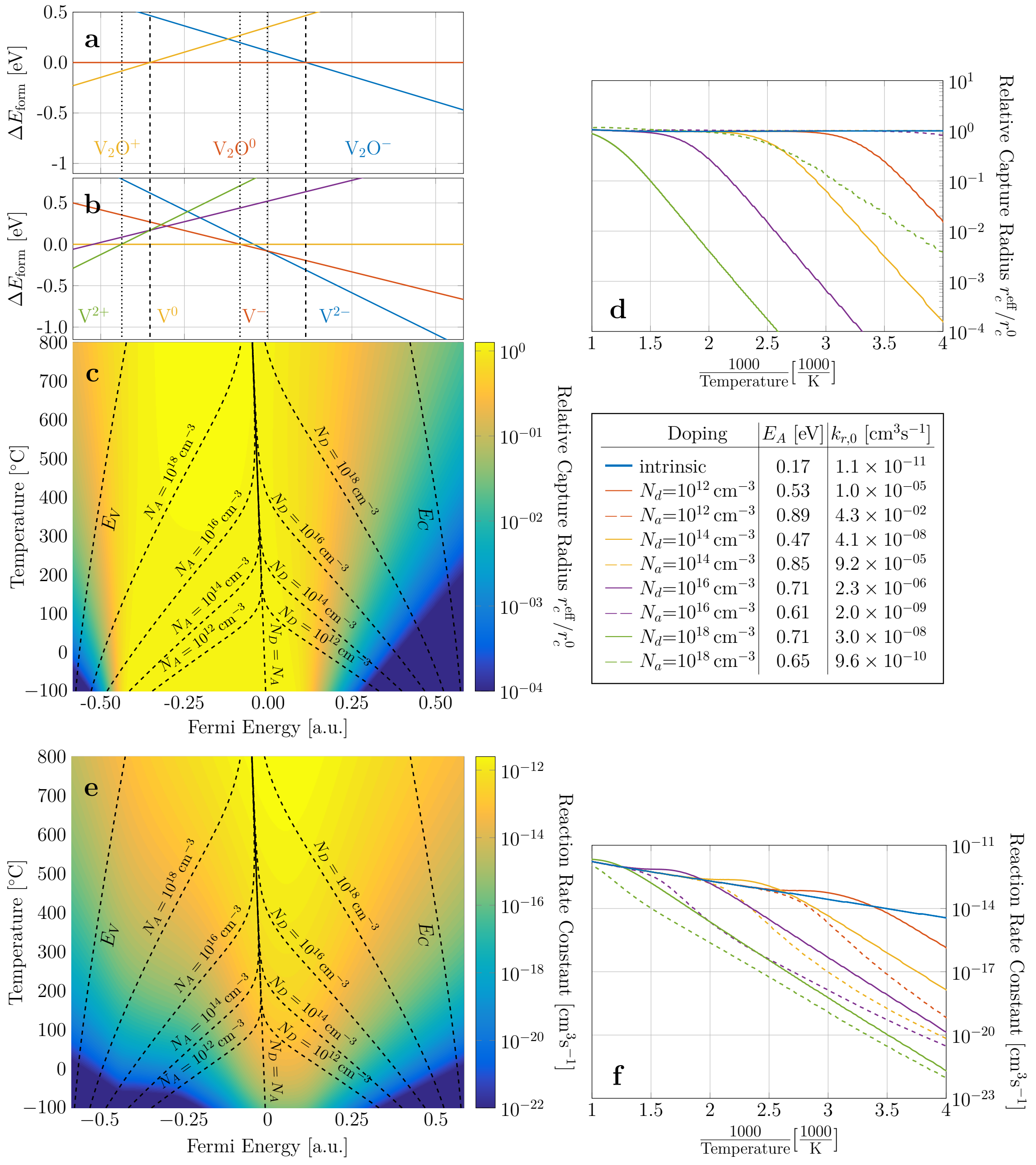

Doping	E_A [eV]	$k_{r,0}$ [cm^{3}s^{-1}]
— intrinsic	0.17	1.1×10^{-11}
— N_d=10^{12} cm^{-3}	0.53	1.0×10^{-05}
– – N_a=10^{12} cm^{-3}	0.89	4.3×10^{-02}
— N_d=10^{14} cm^{-3}	0.47	4.1×10^{-08}
– – N_a=10^{14} cm^{-3}	0.85	9.2×10^{-05}
— N_d=10^{16} cm^{-3}	0.71	2.3×10^{-06}
– – N_a=10^{16} cm^{-3}	0.61	2.0×10^{-09}
— N_d=10^{18} cm^{-3}	0.71	3.0×10^{-08}
– – N_a=10^{18} cm^{-3}	0.65	9.6×10^{-10}

Figure D.23.1: Kinetics of the reaction of V_2O with another vacancy forming V_3O.

D.24 Kinetics of the Reaction VO + I $\xrightarrow{k_r^{\mathrm{VOI}}}$ O

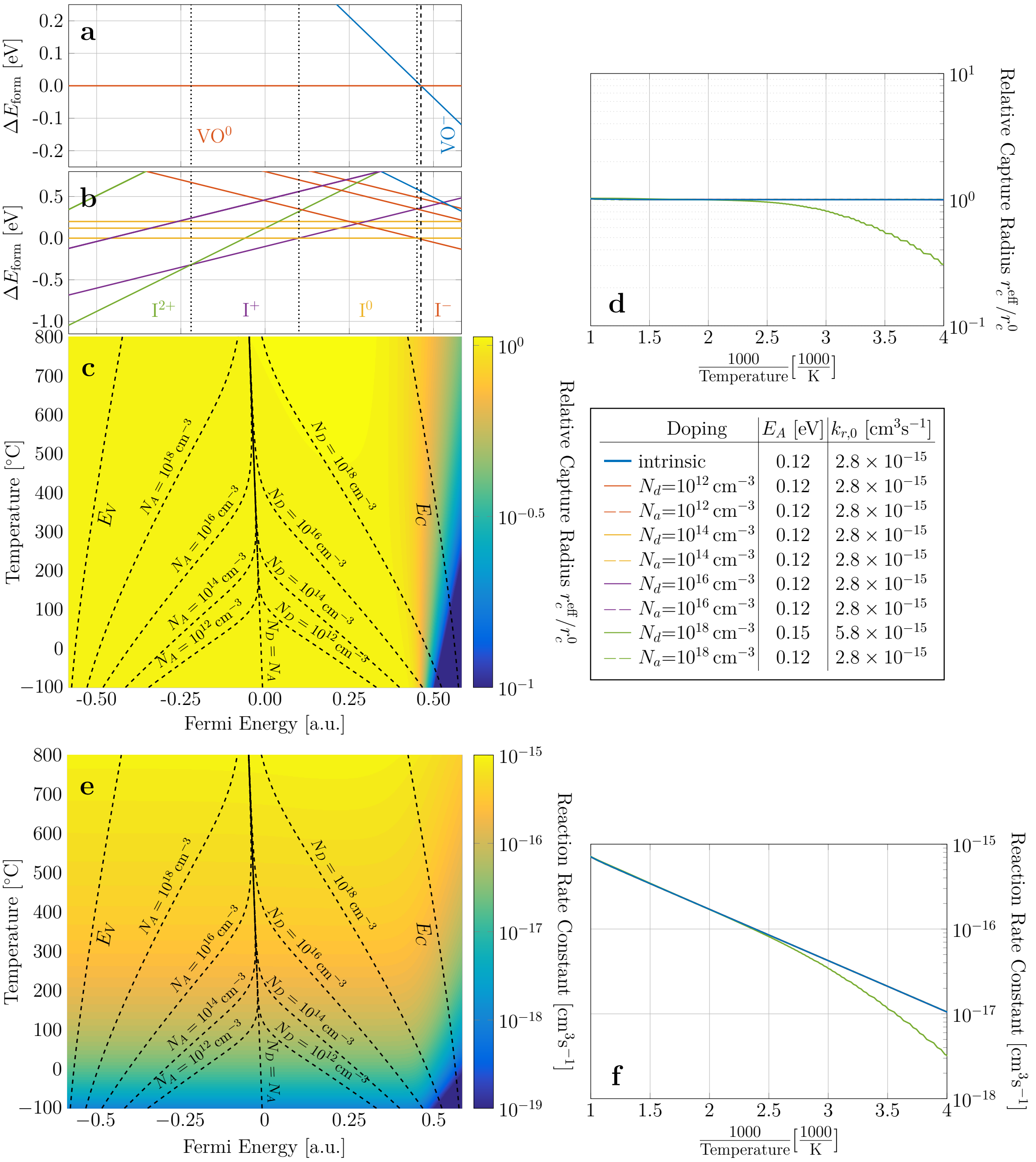

	Doping	E_A [eV]	$k_{r,0}$ [cm^{3}s^{-1}]
—	intrinsic	0.12	2.8×10^{-15}
—	N_d=10^{12} cm^{-3}	0.12	2.8×10^{-15}
--	N_a=10^{12} cm^{-3}	0.12	2.8×10^{-15}
—	N_d=10^{14} cm^{-3}	0.12	2.8×10^{-15}
--	N_a=10^{14} cm^{-3}	0.12	2.8×10^{-15}
—	N_d=10^{16} cm^{-3}	0.12	2.8×10^{-15}
--	N_a=10^{16} cm^{-3}	0.12	2.8×10^{-15}
—	N_d=10^{18} cm^{-3}	0.15	5.8×10^{-15}
--	N_a=10^{18} cm^{-3}	0.12	2.8×10^{-15}

Figure D.24.1: Kinetics of the recombination of self-interstitials at VO.

D.25 Kinetics of the Reaction $\mathbf{V_2O + I \xrightarrow{k_r^{V_2OI}} VO}$

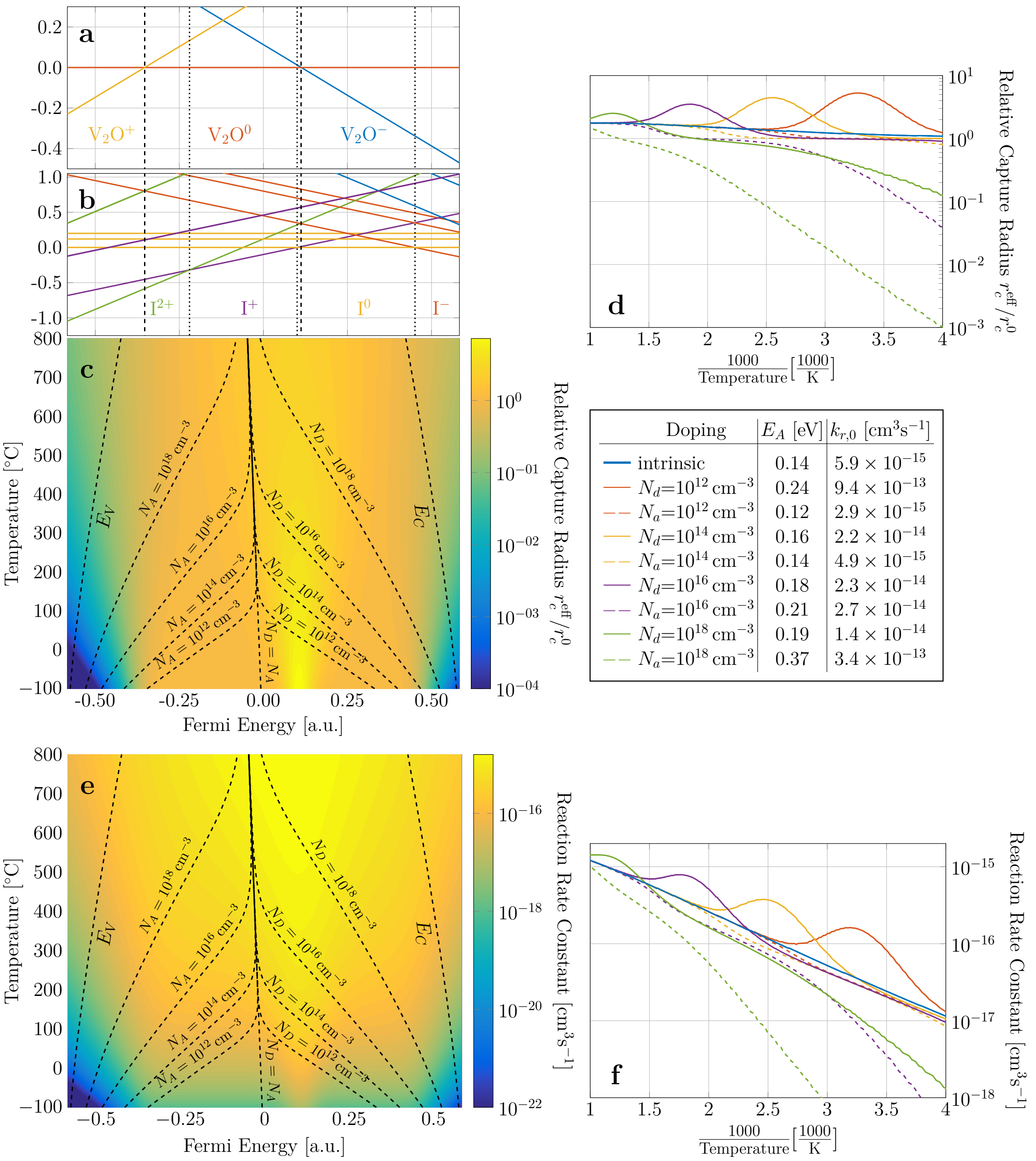

Doping	E_A [eV]	$k_{r,0}$ [cm^{3}s^{-1}]
intrinsic	0.14	5.9×10^{-15}
N_d=10^{12} cm^{-3}	0.24	9.4×10^{-13}
N_a=10^{12} cm^{-3}	0.12	2.9×10^{-15}
N_d=10^{14} cm^{-3}	0.16	2.2×10^{-14}
N_a=10^{14} cm^{-3}	0.14	4.9×10^{-15}
N_d=10^{16} cm^{-3}	0.18	2.3×10^{-14}
N_a=10^{16} cm^{-3}	0.21	2.7×10^{-14}
N_d=10^{18} cm^{-3}	0.19	1.4×10^{-14}
N_a=10^{18} cm^{-3}	0.37	3.4×10^{-13}

Figure D.25.1: Kinetics of the recombination of self-interstitials at V_2O.

D.26 Kinetics of the Reaction $V_3O + I \xrightarrow{k_r^{V_3OI}} VO$

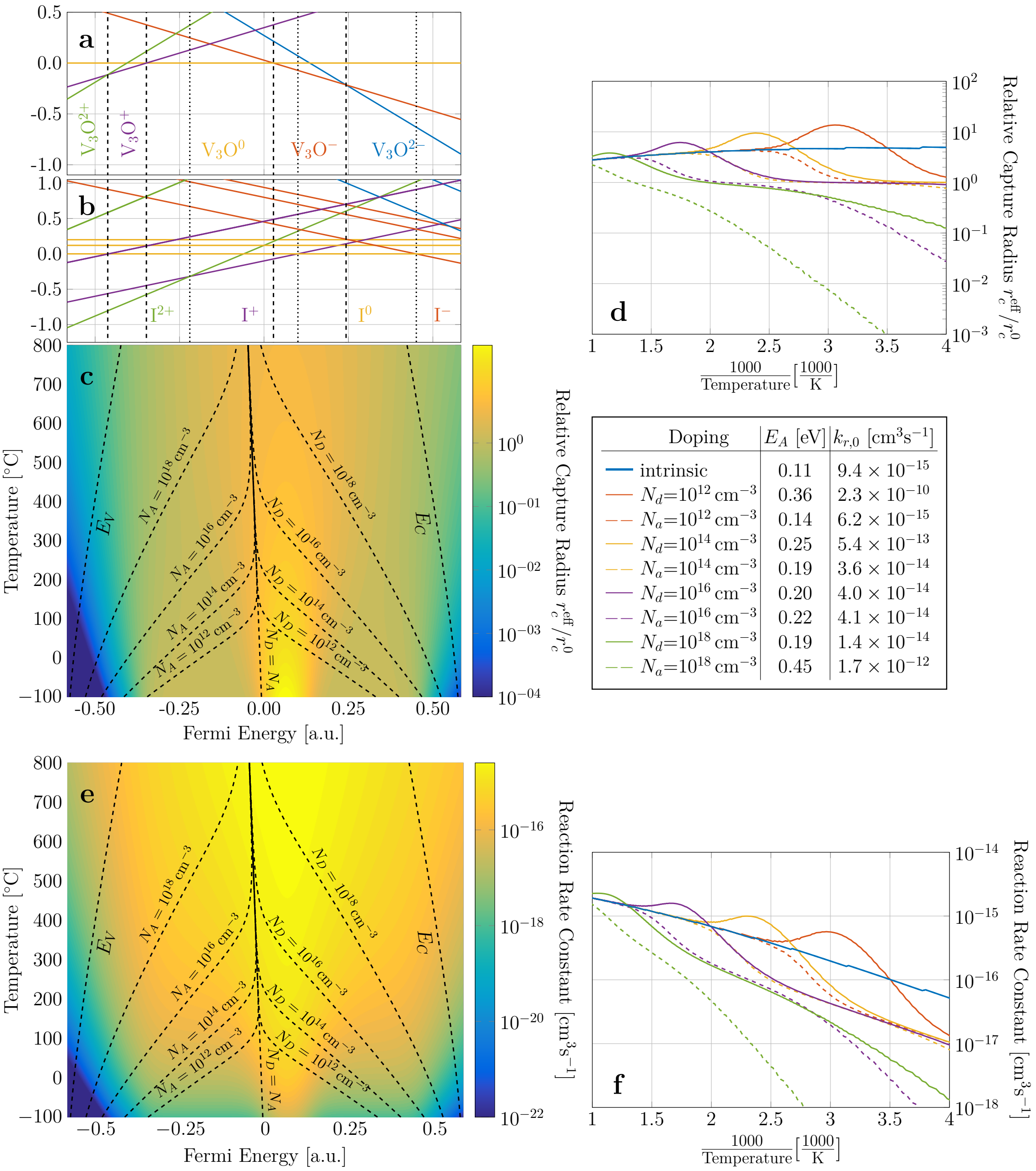

Doping	E_A [eV]	$k_{r,0}$ [cm^{3}s^{-1}]
— intrinsic	0.11	9.4×10^{-15}
— N_d=10^{12} cm^{-3}	0.36	2.3×10^{-10}
– – N_a=10^{12} cm^{-3}	0.14	6.2×10^{-15}
— N_d=10^{14} cm^{-3}	0.25	5.4×10^{-13}
– – N_a=10^{14} cm^{-3}	0.19	3.6×10^{-14}
— N_d=10^{16} cm^{-3}	0.20	4.0×10^{-14}
– – N_a=10^{16} cm^{-3}	0.22	4.1×10^{-14}
— N_d=10^{18} cm^{-3}	0.19	1.4×10^{-14}
– – N_a=10^{18} cm^{-3}	0.45	1.7×10^{-12}

Figure D.26.1: Kinetics of the recombination of self-interstitials at V_3O.

D.27 Kinetics of the Reaction $H + H \xrightarrow{k_r^{HH}} H_2$

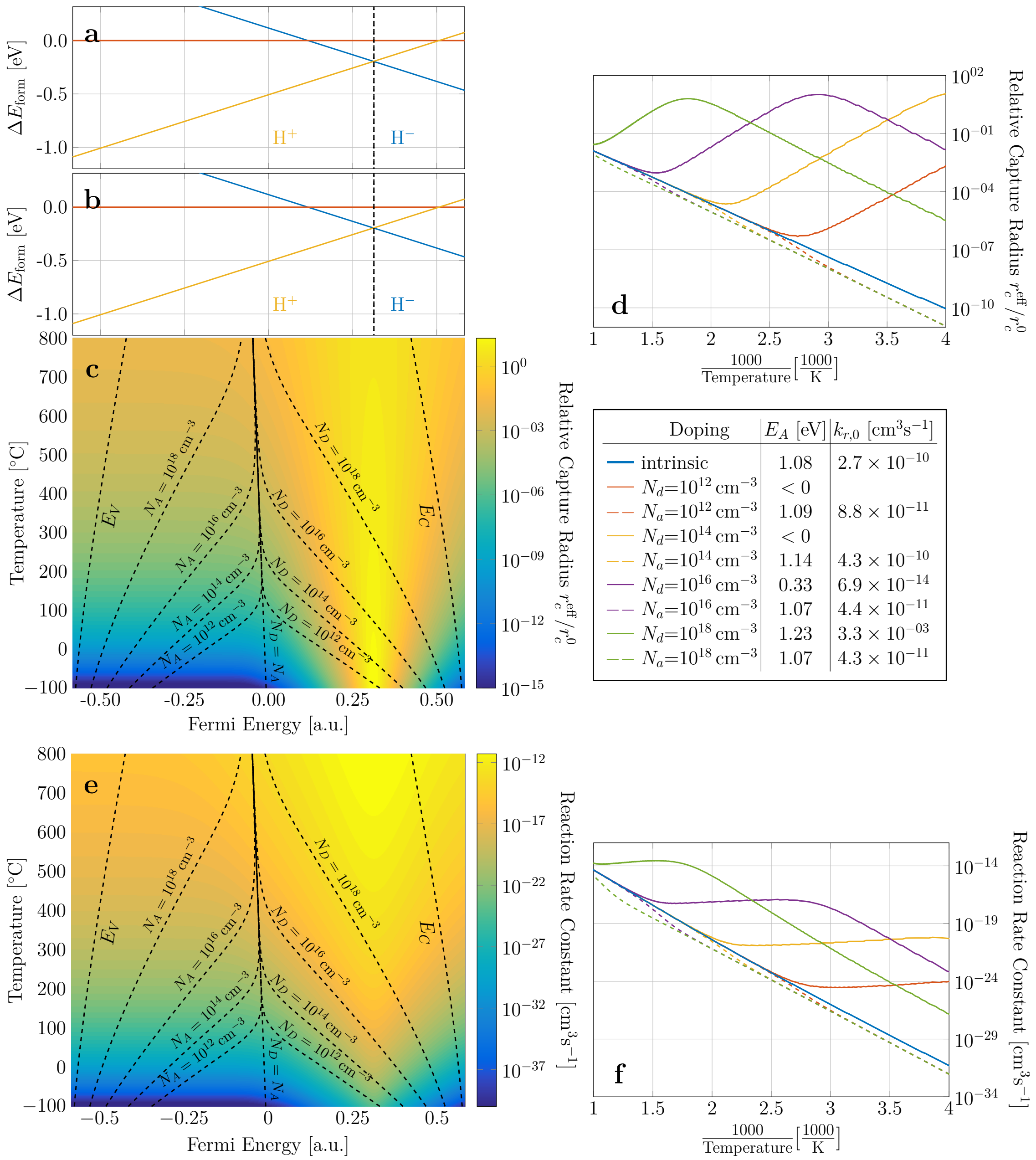

Doping	E_A [eV]	$k_{r,0}$ [cm^{3}s^{-1}]
intrinsic	1.08	2.7×10^{-10}
N_d=10^{12} cm^{-3}	< 0	
N_a=10^{12} cm^{-3}	1.09	8.8×10^{-11}
N_d=10^{14} cm^{-3}	< 0	
N_a=10^{14} cm^{-3}	1.14	4.3×10^{-10}
N_d=10^{16} cm^{-3}	0.33	6.9×10^{-14}
N_a=10^{16} cm^{-3}	1.07	4.4×10^{-11}
N_d=10^{18} cm^{-3}	1.23	3.3×10^{-03}
N_a=10^{18} cm^{-3}	1.07	4.3×10^{-11}

Figure D.27.1: Kinetics of the reaction of a vacancy with hydrogen forming H_2.

D.28 Kinetics of the Reaction $\mathbf{I + H \xrightarrow{k_r^{\mathrm{IH}}} IH}$

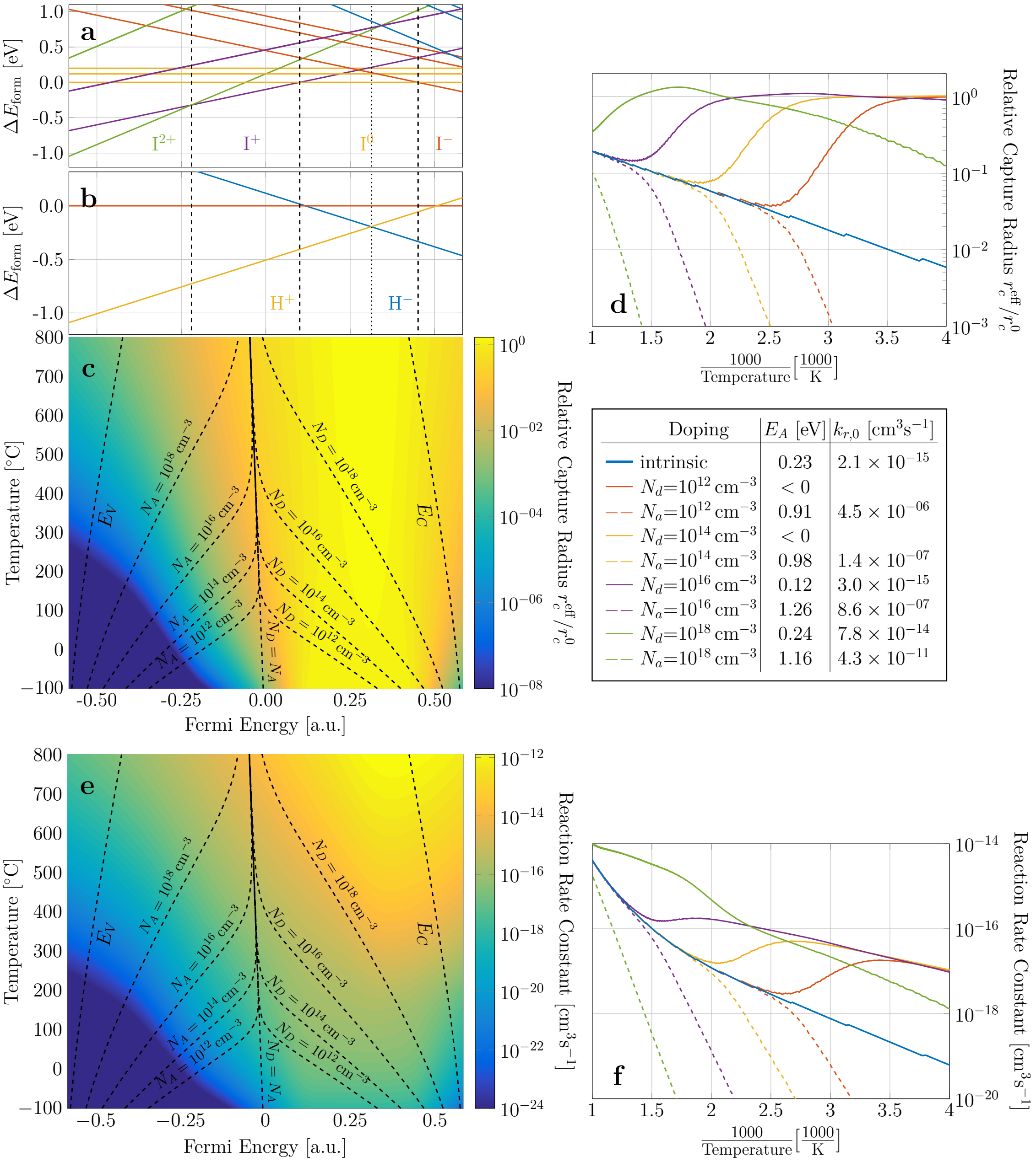

Doping	E_A [eV]	$k_{r,0}$ [cm^{3}s^{-1}]
intrinsic	0.23	2.1×10^{-15}
N_d=10^{12} cm^{-3}	< 0	
N_a=10^{12} cm^{-3}	0.91	4.5×10^{-06}
N_d=10^{14} cm^{-3}	< 0	
N_a=10^{14} cm^{-3}	0.98	1.4×10^{-07}
N_d=10^{16} cm^{-3}	0.12	3.0×10^{-15}
N_a=10^{16} cm^{-3}	1.26	8.6×10^{-07}
N_d=10^{18} cm^{-3}	0.24	7.8×10^{-14}
N_a=10^{18} cm^{-3}	1.16	4.3×10^{-11}

Figure D.28.1: Kinetics of the reaction of a self-interstitials with hydrogen forming IH.

D.29 Kinetics of the Reaction $\mathbf{V + H \xrightarrow{k_r^{\mathrm{VH}}} VH}$

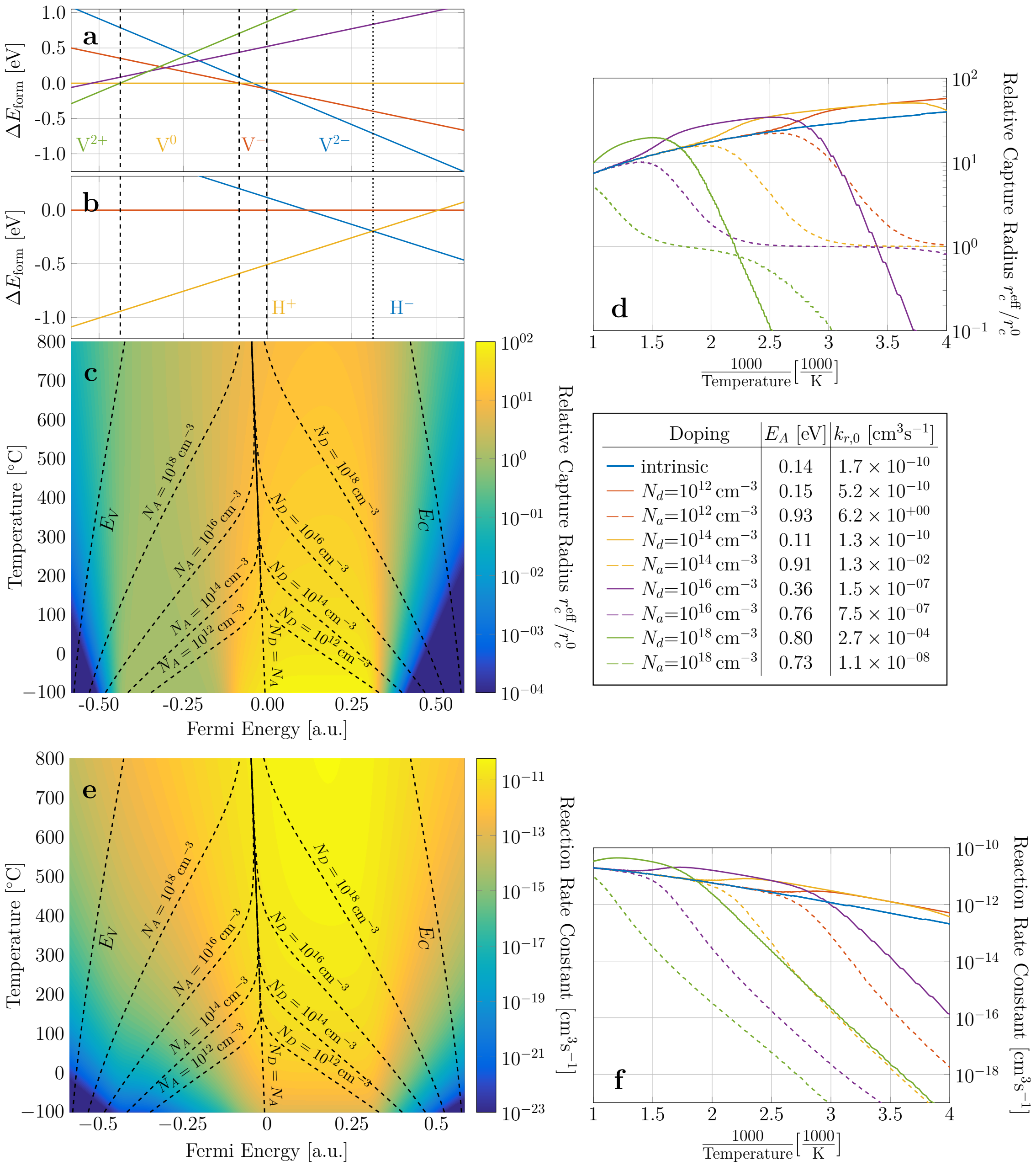

Doping	E_A [eV]	$k_{r,0}$ [cm^{3}s^{-1}]
intrinsic	0.14	1.7×10^{-10}
N_d=10^{12} cm^{-3}	0.15	5.2×10^{-10}
N_a=10^{12} cm^{-3}	0.93	$6.2 \times 10^{+00}$
N_d=10^{14} cm^{-3}	0.11	1.3×10^{-10}
N_a=10^{14} cm^{-3}	0.91	1.3×10^{-02}
N_d=10^{16} cm^{-3}	0.36	1.5×10^{-07}
N_a=10^{16} cm^{-3}	0.76	7.5×10^{-07}
N_d=10^{18} cm^{-3}	0.80	2.7×10^{-04}
N_a=10^{18} cm^{-3}	0.73	1.1×10^{-08}

Figure D.29.1: Kinetics of the reaction of a vacancy with hydrogen forming VH.

D.30 Kinetics of the Reaction $\mathrm{VH} + \mathrm{H} \xrightarrow{k_r^{\mathrm{VHH}}} \mathrm{VH}_2$

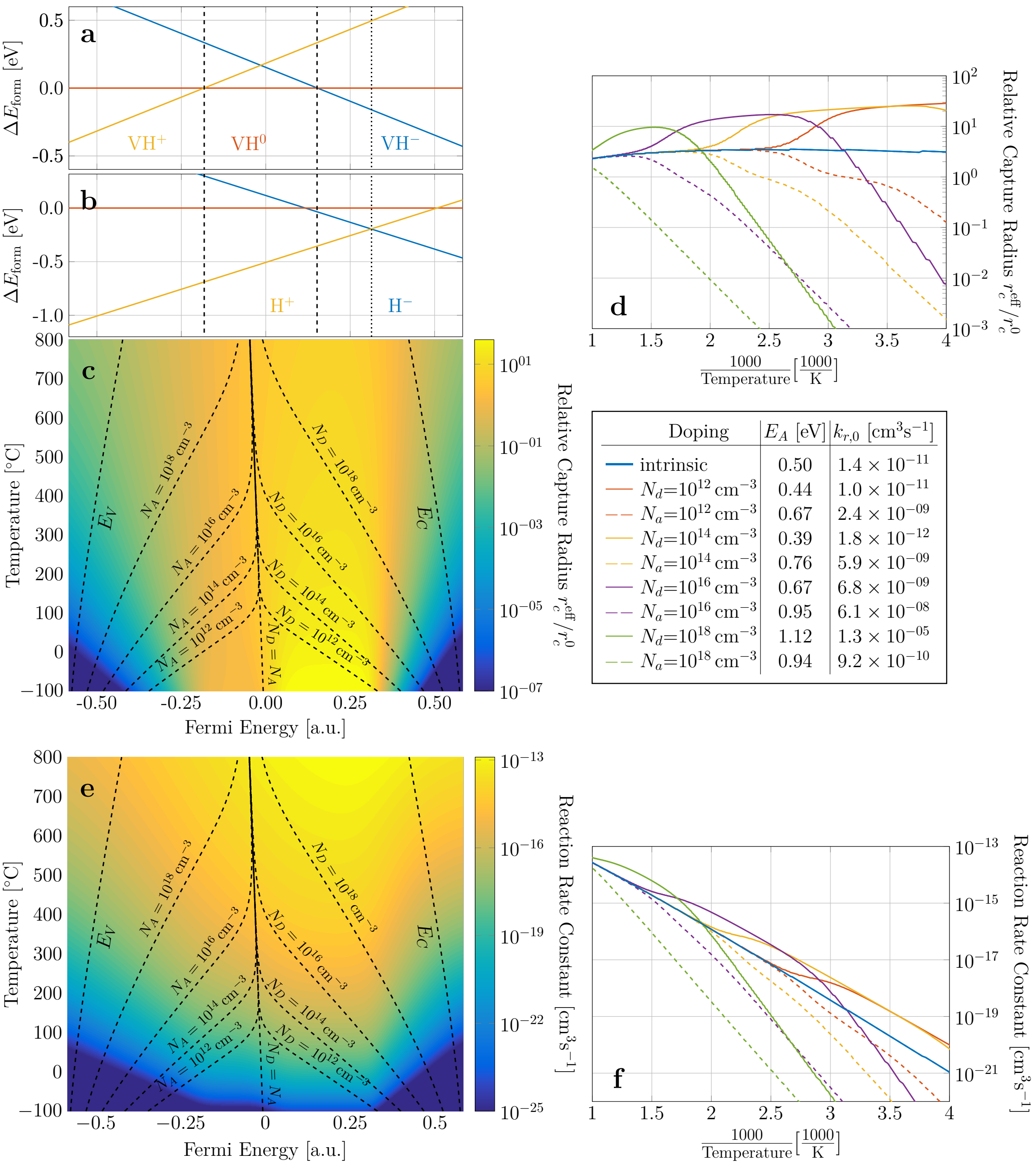

Doping	E_A [eV]	$k_{r,0}$ [cm^{3}s^{-1}]
intrinsic	0.50	1.4×10^{-11}
N_d=10^{12} cm^{-3}	0.44	1.0×10^{-11}
N_a=10^{12} cm^{-3}	0.67	2.4×10^{-09}
N_d=10^{14} cm^{-3}	0.39	1.8×10^{-12}
N_a=10^{14} cm^{-3}	0.76	5.9×10^{-09}
N_d=10^{16} cm^{-3}	0.67	6.8×10^{-09}
N_a=10^{16} cm^{-3}	0.95	6.1×10^{-08}
N_d=10^{18} cm^{-3}	1.12	1.3×10^{-05}
N_a=10^{18} cm^{-3}	0.94	9.2×10^{-10}

Figure D.30.1: Kinetics of the reaction of VH with hydrogen forming VH_2.

D.31 Kinetics of the Reaction $VH_2 + H \xrightarrow{k_r^{\mathrm{VH2H}}} VH_3$

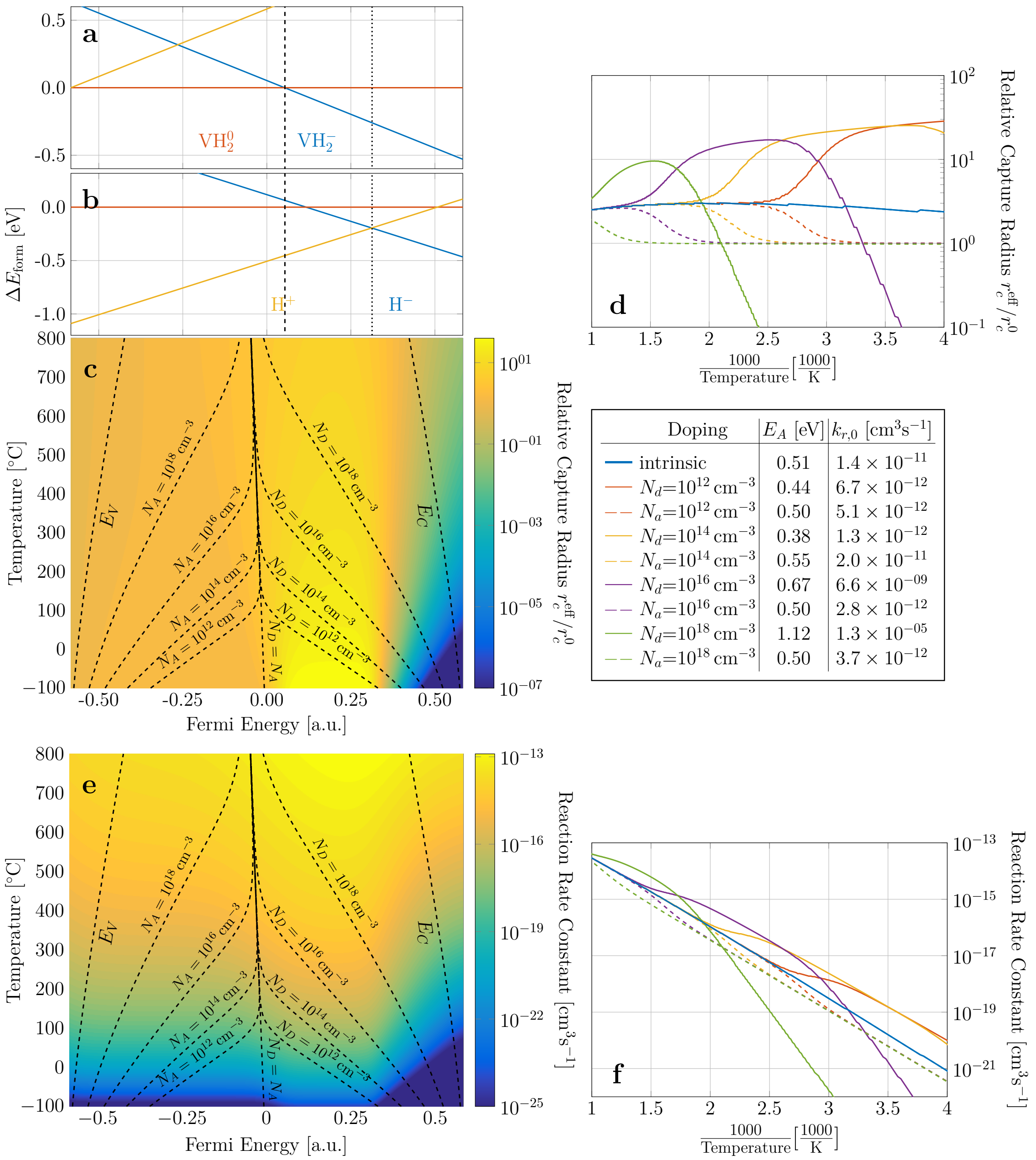

Doping	E_A [eV]	$k_{r,0}$ [cm^{3}s^{-1}]
— intrinsic	0.51	1.4×10^{-11}
— N_d=10^{12} cm^{-3}	0.44	6.7×10^{-12}
-- N_a=10^{12} cm^{-3}	0.50	5.1×10^{-12}
— N_d=10^{14} cm^{-3}	0.38	1.3×10^{-12}
-- N_a=10^{14} cm^{-3}	0.55	2.0×10^{-11}
— N_d=10^{16} cm^{-3}	0.67	6.6×10^{-09}
-- N_a=10^{16} cm^{-3}	0.50	2.8×10^{-12}
— N_d=10^{18} cm^{-3}	1.12	1.3×10^{-05}
-- N_a=10^{18} cm^{-3}	0.50	3.7×10^{-12}

Figure D.31.1: Kinetics of the reaction of VH_2 with hydrogen forming VH_3.

D.32 Kinetics of the Reaction $O + H \xrightarrow{k_r^{\mathrm{OH}}} OH$

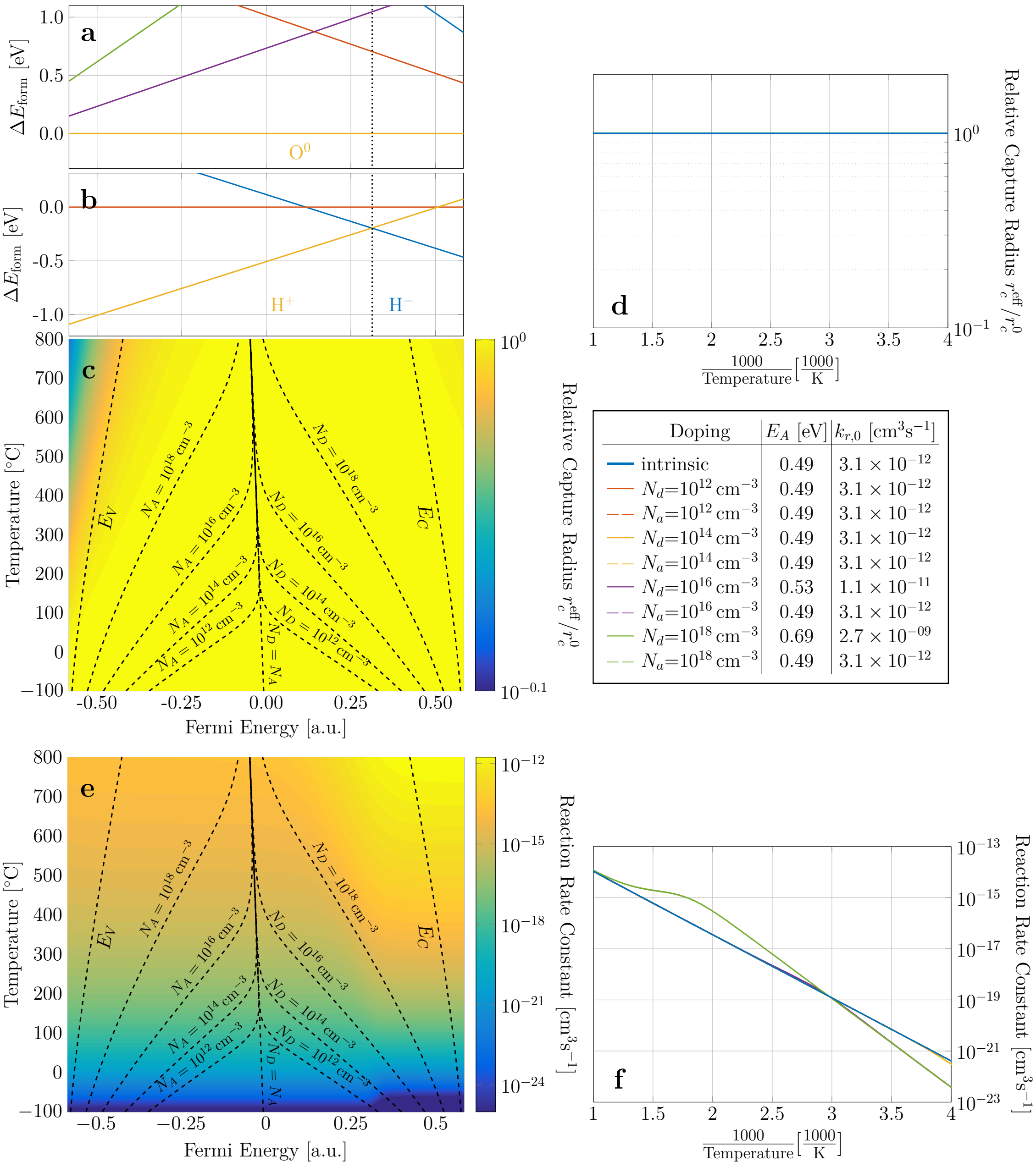

Doping	E_A [eV]	$k_{r,0}$ [cm^{3}s^{-1}]
intrinsic	0.49	3.1×10^{-12}
N_d=10^{12} cm^{-3}	0.49	3.1×10^{-12}
N_a=10^{12} cm^{-3}	0.49	3.1×10^{-12}
N_d=10^{14} cm^{-3}	0.49	3.1×10^{-12}
N_a=10^{14} cm^{-3}	0.49	3.1×10^{-12}
N_d=10^{16} cm^{-3}	0.53	1.1×10^{-11}
N_a=10^{16} cm^{-3}	0.49	3.1×10^{-12}
N_d=10^{18} cm^{-3}	0.69	2.7×10^{-09}
N_a=10^{18} cm^{-3}	0.49	3.1×10^{-12}

Figure D.32.1: Kinetics of the reaction of oxygen with hydrogen forming OH.

D.33 Kinetics of the Reaction VO + H $\xrightarrow{k_r^{\mathrm{VOH}}}$ VOH

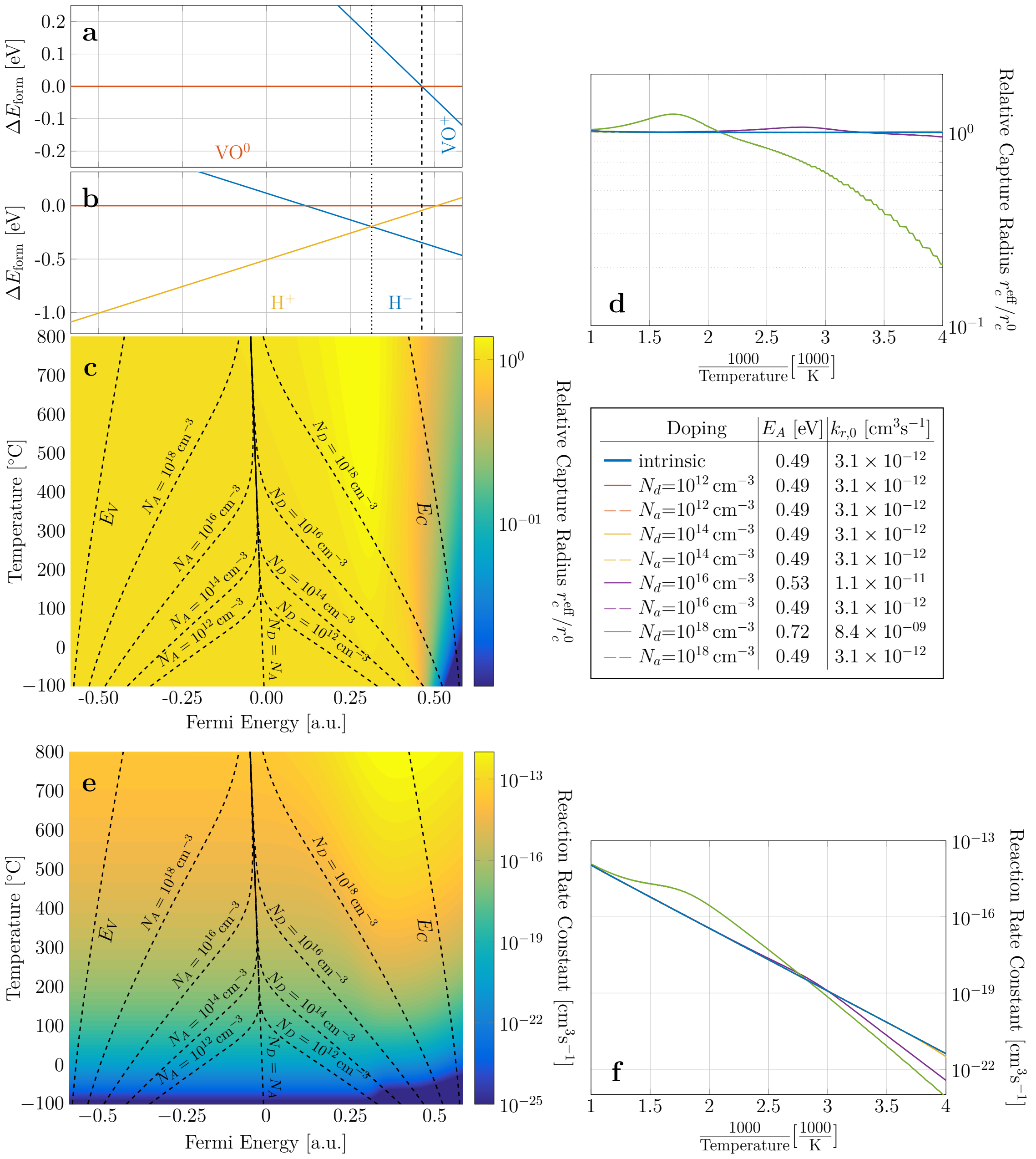

Doping	E_A [eV]	$k_{r,0}$ [cm^{3}s^{-1}]
intrinsic	0.49	3.1×10^{-12}
N_d=10^{12} cm^{-3}	0.49	3.1×10^{-12}
N_a=10^{12} cm^{-3}	0.49	3.1×10^{-12}
N_d=10^{14} cm^{-3}	0.49	3.1×10^{-12}
N_a=10^{14} cm^{-3}	0.49	3.1×10^{-12}
N_d=10^{16} cm^{-3}	0.53	1.1×10^{-11}
N_a=10^{16} cm^{-3}	0.49	3.1×10^{-12}
N_d=10^{18} cm^{-3}	0.72	8.4×10^{-09}
N_a=10^{18} cm^{-3}	0.49	3.1×10^{-12}

Figure D.33.1: Kinetics of the reaction of VO with hydrogen forming VOH.

D.34 Kinetics of the Reaction $\mathrm{VOH} + \mathrm{H} \xrightarrow{k_r^{\mathrm{VOHH}}} \mathrm{VOH_2}$

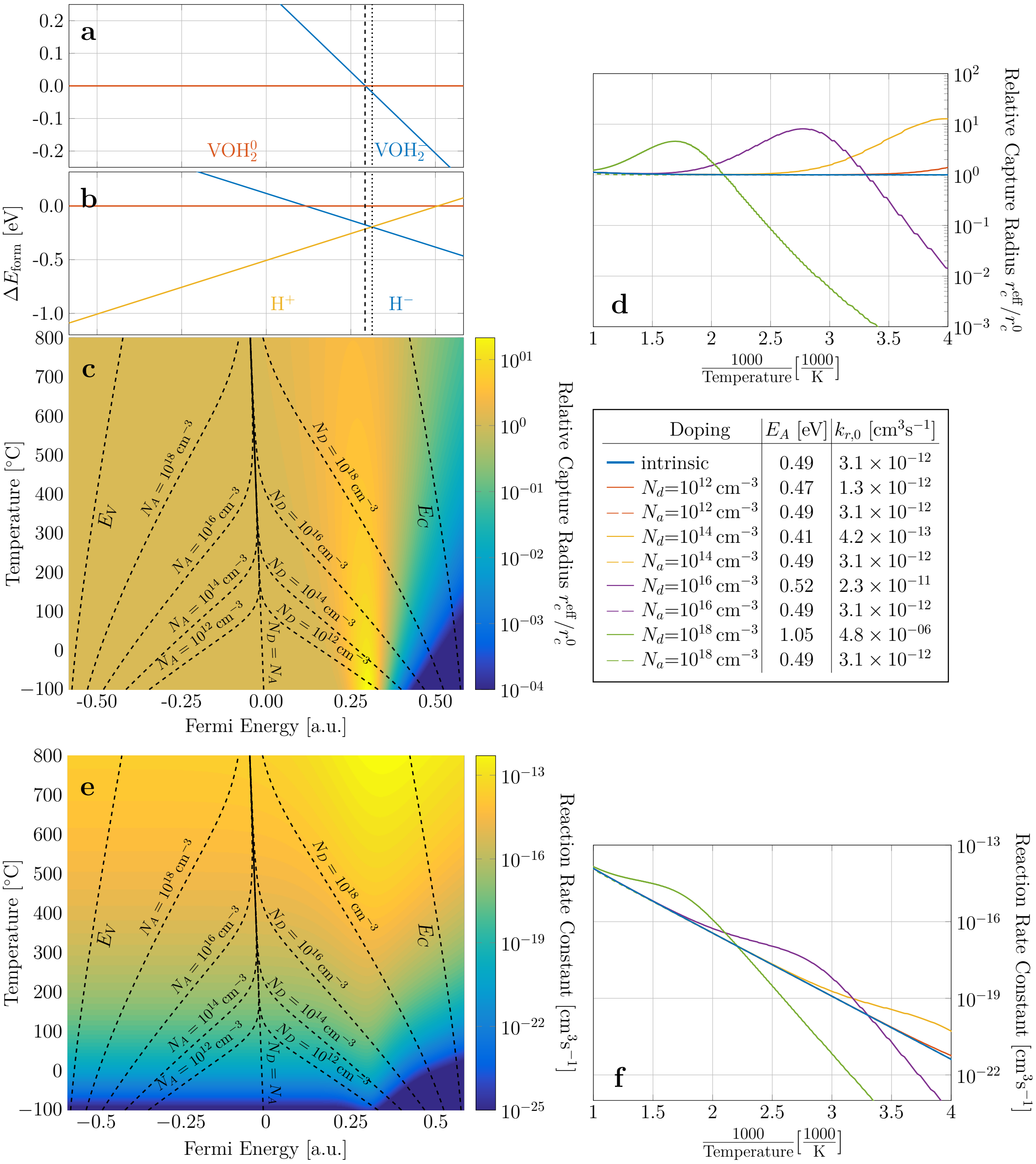

Doping	E_A [eV]	$k_{r,0}$ [cm^{3}s^{-1}]
— intrinsic	0.49	3.1×10^{-12}
— N_d=10^{12} cm^{-3}	0.47	1.3×10^{-12}
– – N_a=10^{12} cm^{-3}	0.49	3.1×10^{-12}
— N_d=10^{14} cm^{-3}	0.41	4.2×10^{-13}
– – N_a=10^{14} cm^{-3}	0.49	3.1×10^{-12}
— N_d=10^{16} cm^{-3}	0.52	2.3×10^{-11}
– – N_a=10^{16} cm^{-3}	0.49	3.1×10^{-12}
— N_d=10^{18} cm^{-3}	1.05	4.8×10^{-06}
– – N_a=10^{18} cm^{-3}	0.49	3.1×10^{-12}

Figure D.34.1: Kinetics of the reaction of VOH with hydrogen forming $\mathrm{VO_2}$.

D.35 Kinetics of the Reaction $\mathrm{B_s} + \mathrm{H} \xrightarrow{k_r^{\mathrm{B_sH}}} \mathrm{B_sH}$

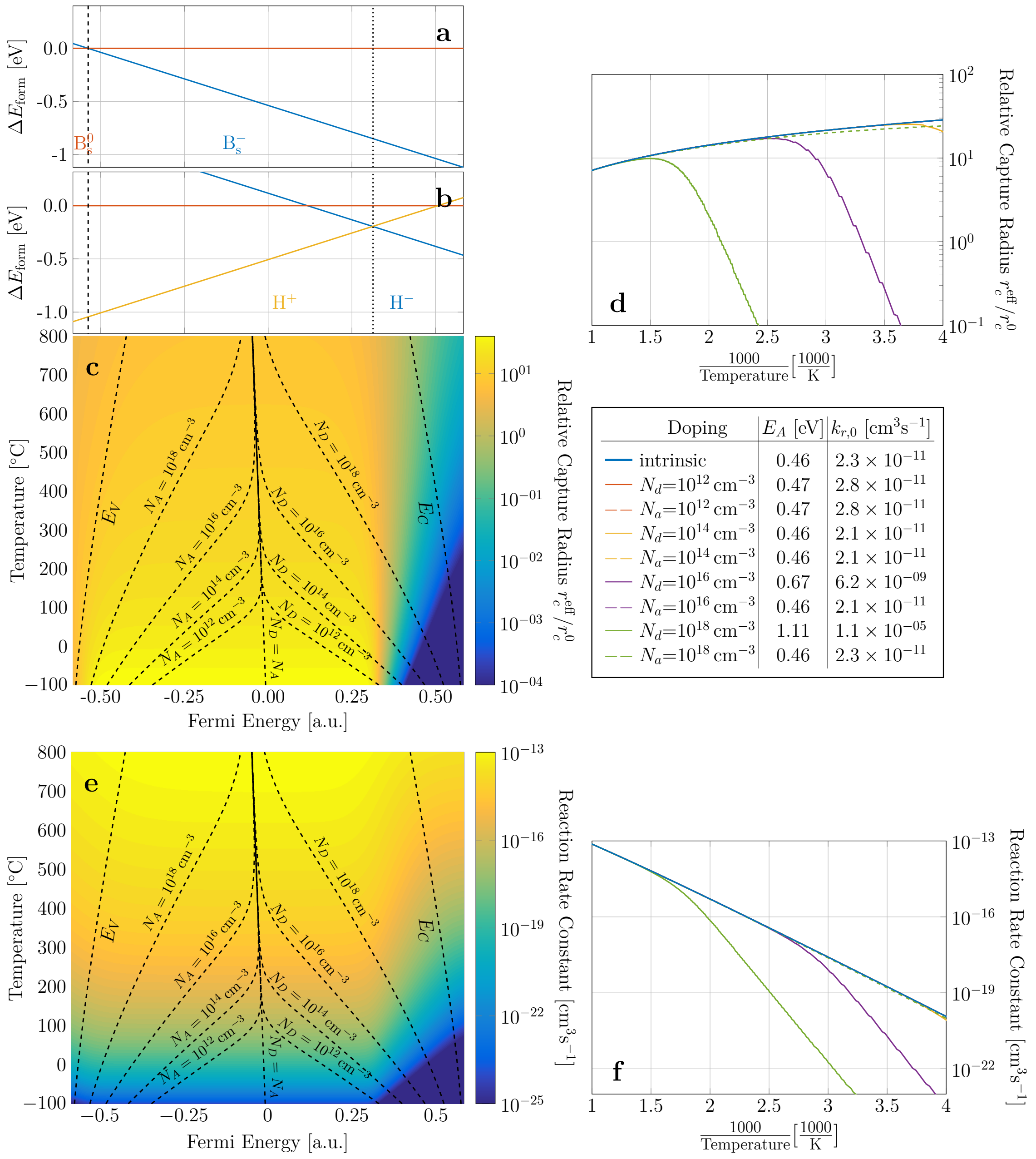

Doping	E_A [eV]	$k_{r,0}$ [cm^{3}s^{-1}]
— intrinsic	0.46	2.3×10^{-11}
— N_d=10^{12} cm^{-3}	0.47	2.8×10^{-11}
- - N_a=10^{12} cm^{-3}	0.47	2.8×10^{-11}
— N_d=10^{14} cm^{-3}	0.46	2.1×10^{-11}
- - N_a=10^{14} cm^{-3}	0.46	2.1×10^{-11}
— N_d=10^{16} cm^{-3}	0.67	6.2×10^{-09}
- - N_a=10^{16} cm^{-3}	0.46	2.1×10^{-11}
— N_d=10^{18} cm^{-3}	1.11	1.1×10^{-05}
- - N_a=10^{18} cm^{-3}	0.46	2.3×10^{-11}

Figure D.35.1: Kinetics of the reaction of $\mathrm{B_s}$ with hydrogen forming $\mathrm{B_sH}$.

D.36 Kinetics of the Reaction $\mathrm{B_i} + \mathrm{H} \xrightarrow{k_r^{\mathrm{B_iH}}} \mathrm{B_iH}$

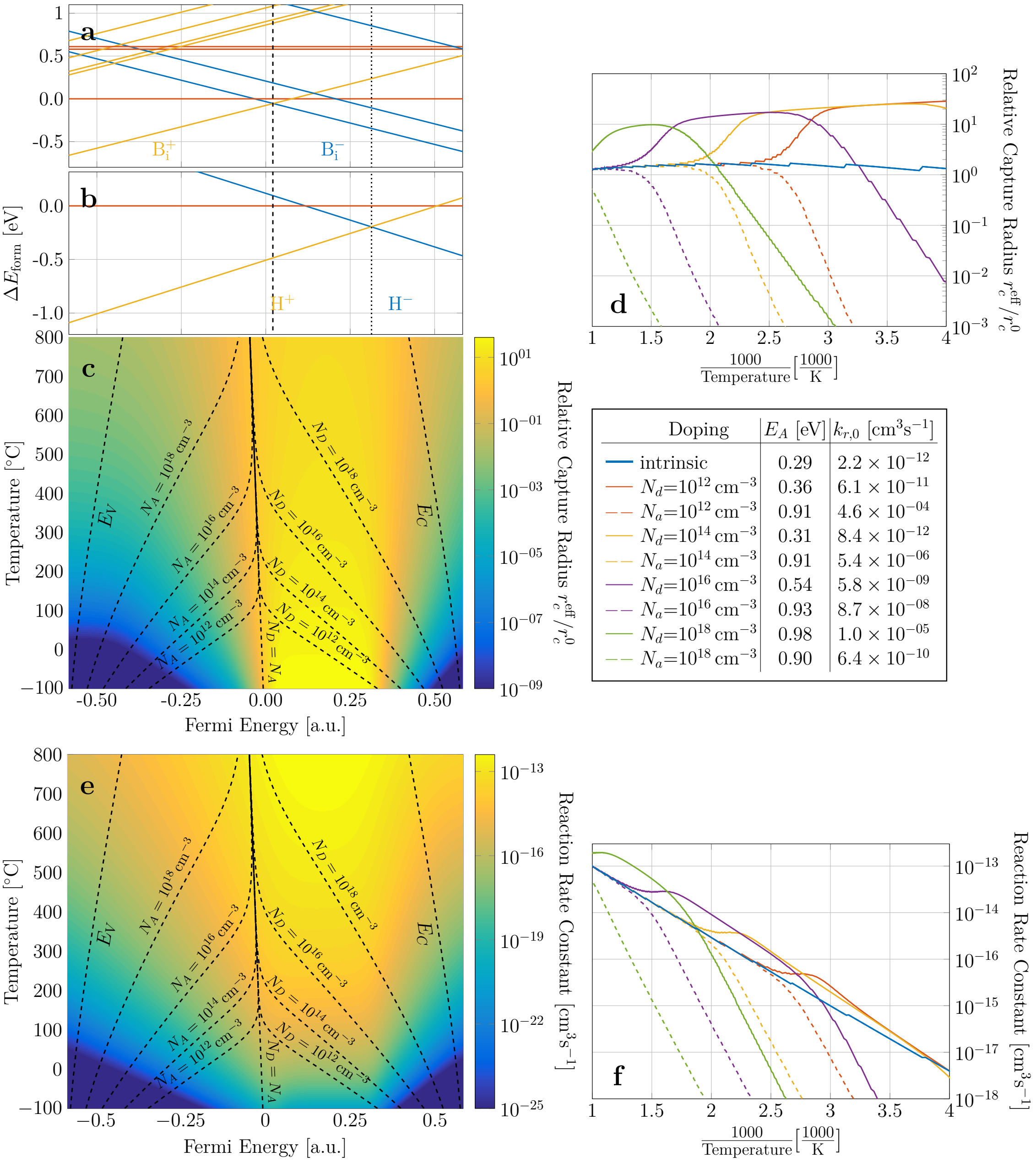

Doping	E_A [eV]	$k_{r,0}$ [cm^{3}s^{-1}]
intrinsic	0.29	2.2×10^{-12}
N_d=10^{12} cm^{-3}	0.36	6.1×10^{-11}
N_a=10^{12} cm^{-3}	0.91	4.6×10^{-04}
N_d=10^{14} cm^{-3}	0.31	8.4×10^{-12}
N_a=10^{14} cm^{-3}	0.91	5.4×10^{-06}
N_d=10^{16} cm^{-3}	0.54	5.8×10^{-09}
N_a=10^{16} cm^{-3}	0.93	8.7×10^{-08}
N_d=10^{18} cm^{-3}	0.98	1.0×10^{-05}
N_a=10^{18} cm^{-3}	0.90	6.4×10^{-10}

Figure D.36.1: Kinetics of the reaction of $\mathrm{B_i}$ with hydrogen forming $\mathrm{B_iH}$.

D.37 Kinetics of the Reaction $P_s + H \xrightarrow{k_r^{P_sH}} P_sH$

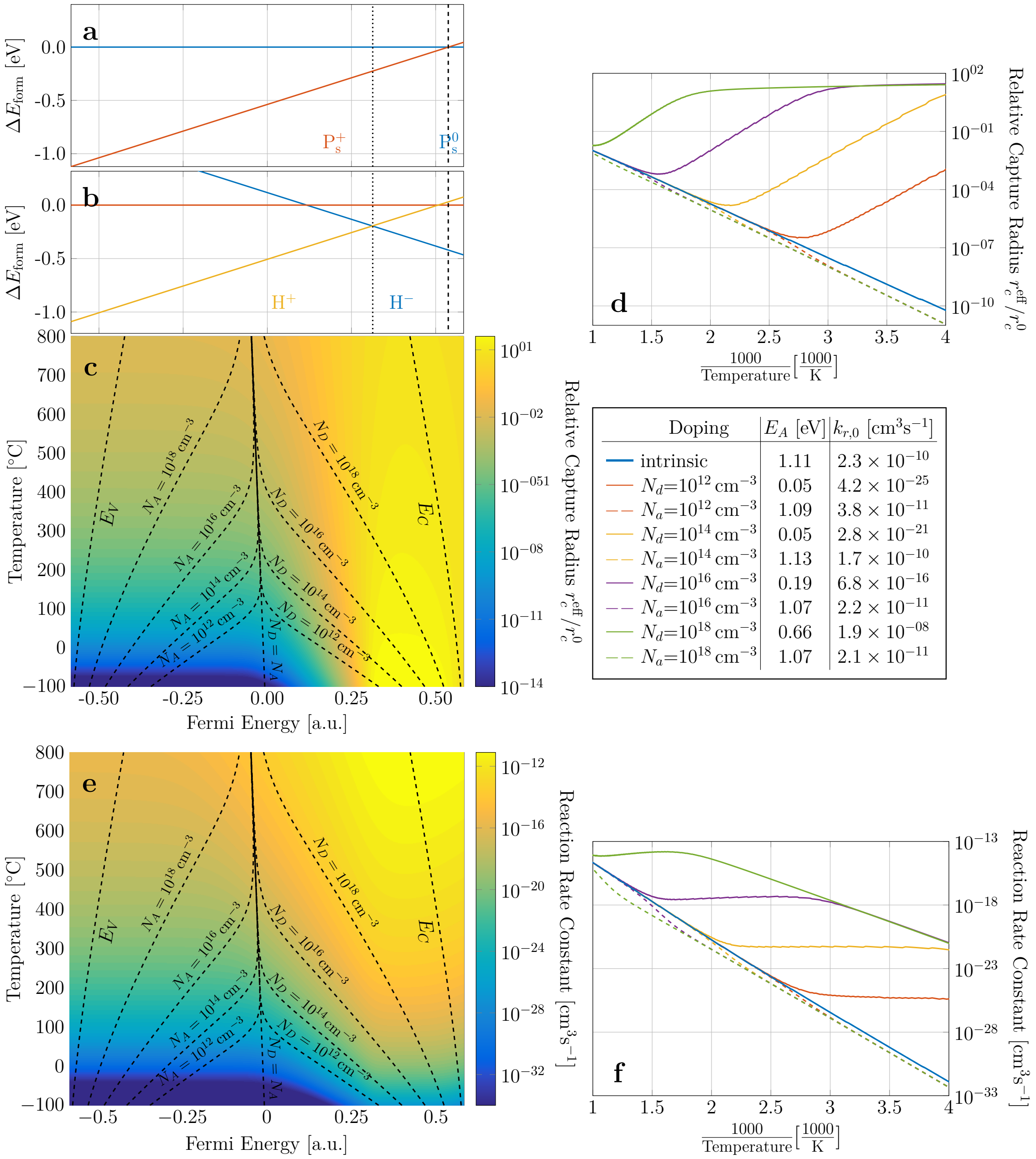

Doping	E_A [eV]	$k_{r,0}$ [cm^{3}s^{-1}]
intrinsic	1.11	2.3×10^{-10}
N_d=10^{12} cm^{-3}	0.05	4.2×10^{-25}
N_a=10^{12} cm^{-3}	1.09	3.8×10^{-11}
N_d=10^{14} cm^{-3}	0.05	2.8×10^{-21}
N_a=10^{14} cm^{-3}	1.13	1.7×10^{-10}
N_d=10^{16} cm^{-3}	0.19	6.8×10^{-16}
N_a=10^{16} cm^{-3}	1.07	2.2×10^{-11}
N_d=10^{18} cm^{-3}	0.66	1.9×10^{-08}
N_a=10^{18} cm^{-3}	1.07	2.1×10^{-11}

Figure D.37.1: Kinetics of the reaction of P_s with hydrogen forming P_sH.

D.38 Kinetics of the Reaction $\mathrm{P_i} + \mathrm{H} \xrightarrow{k_r^{\mathrm{P_iH}}} \mathrm{P_iH}$

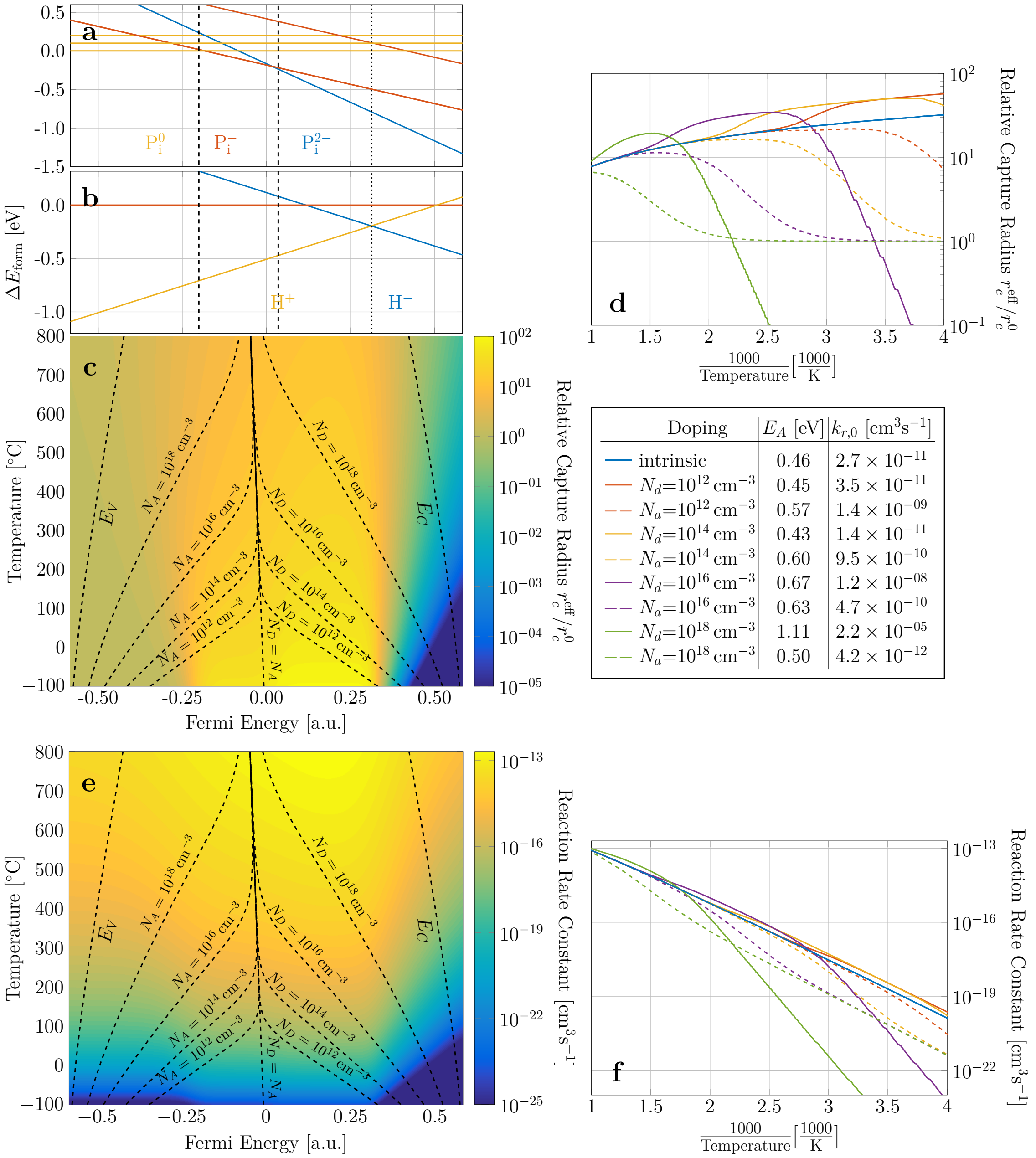

Doping	E_A [eV]	$k_{r,0}$ [cm^{3}s^{-1}]
intrinsic	0.46	2.7×10^{-11}
N_d=10^{12} cm^{-3}	0.45	3.5×10^{-11}
N_a=10^{12} cm^{-3}	0.57	1.4×10^{-09}
N_d=10^{14} cm^{-3}	0.43	1.4×10^{-11}
N_a=10^{14} cm^{-3}	0.60	9.5×10^{-10}
N_d=10^{16} cm^{-3}	0.67	1.2×10^{-08}
N_a=10^{16} cm^{-3}	0.63	4.7×10^{-10}
N_d=10^{18} cm^{-3}	1.11	2.2×10^{-05}
N_a=10^{18} cm^{-3}	0.50	4.2×10^{-12}

Figure D.38.1: Kinetics of the reaction of $\mathrm{P_i}$ with hydrogen forming $\mathrm{P_iH}$.

D.39 Kinetics of the Reaction $\mathrm{C_s} + \mathrm{I} \xrightarrow{k_r^{\mathrm{C_s I}}} \mathrm{C_i}$

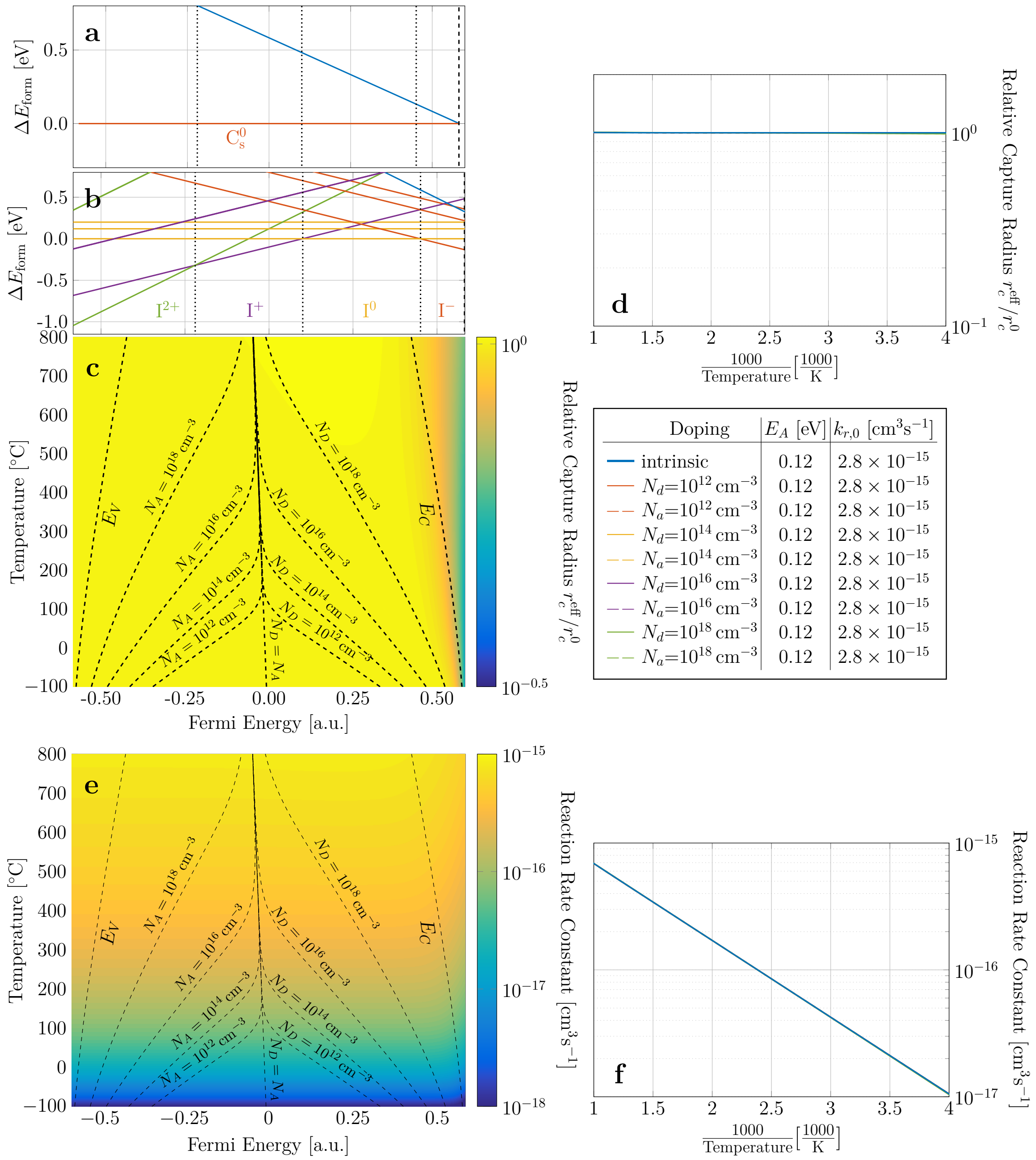

Figure D.39.1: Kinetics of the reaction of $\mathrm{C_s}$ with self-interstitials forming $\mathrm{C_i}$.

D.40 Kinetics of the Reaction $\mathrm{C_i} + \mathrm{H} \xrightarrow{k_r^{\mathrm{C_iH}}} \mathrm{C_iH}$

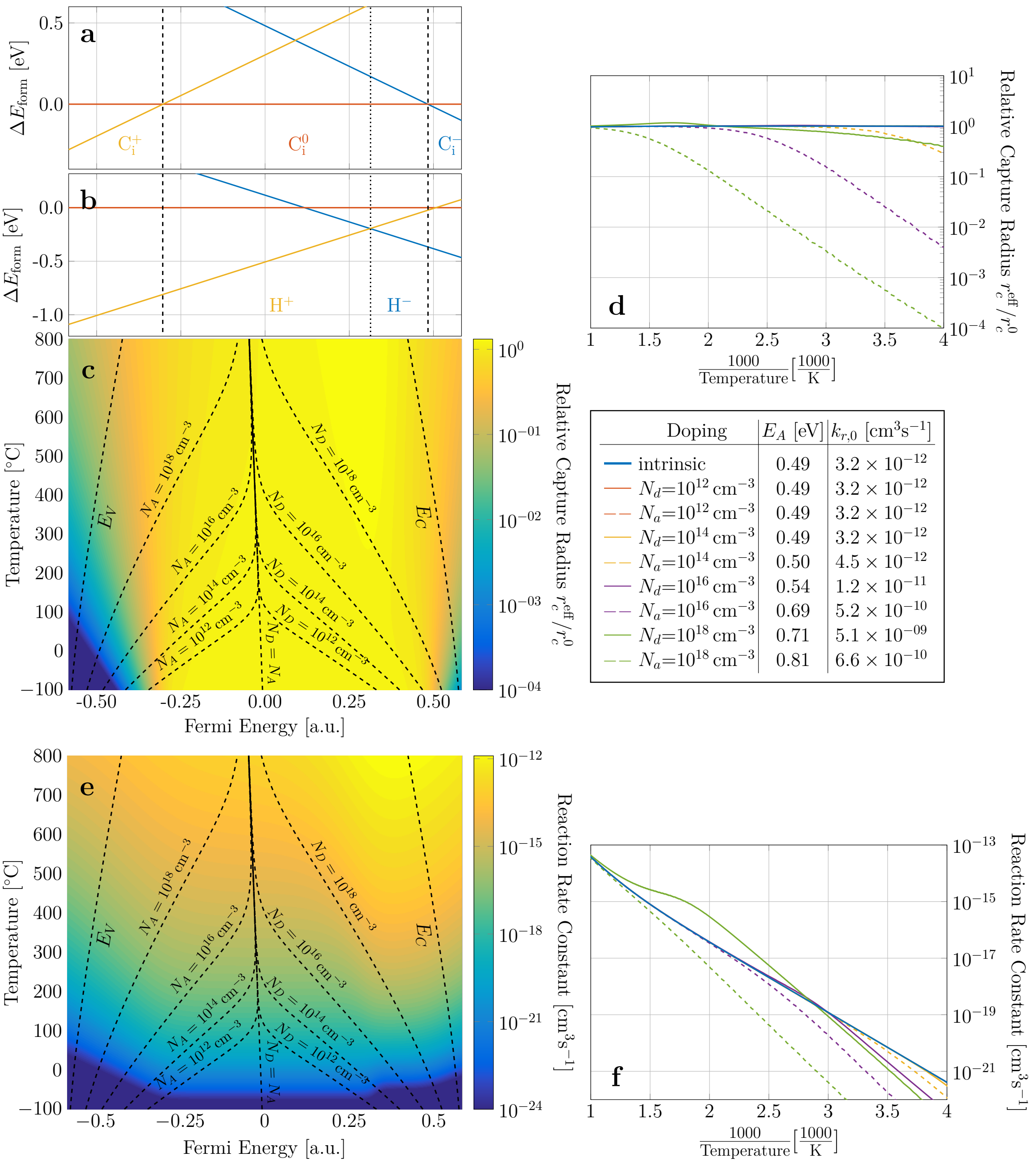

Doping	E_A [eV]	$k_{r,0}$ [cm^{3}s^{-1}]
intrinsic	0.49	3.2×10^{-12}
N_d=10^{12} cm^{-3}	0.49	3.2×10^{-12}
N_a=10^{12} cm^{-3}	0.49	3.2×10^{-12}
N_d=10^{14} cm^{-3}	0.49	3.2×10^{-12}
N_a=10^{14} cm^{-3}	0.50	4.5×10^{-12}
N_d=10^{16} cm^{-3}	0.54	1.2×10^{-11}
N_a=10^{16} cm^{-3}	0.69	5.2×10^{-10}
N_d=10^{18} cm^{-3}	0.71	5.1×10^{-09}
N_a=10^{18} cm^{-3}	0.81	6.6×10^{-10}

Figure D.40.1: Kinetics of the reaction of $\mathrm{C_i}$ with hydrogen forming $\mathrm{C_iH}$.

D.41 Kinetics of the Reaction $C_i + O \xrightarrow{k_r^{C_iO}} C_iO$

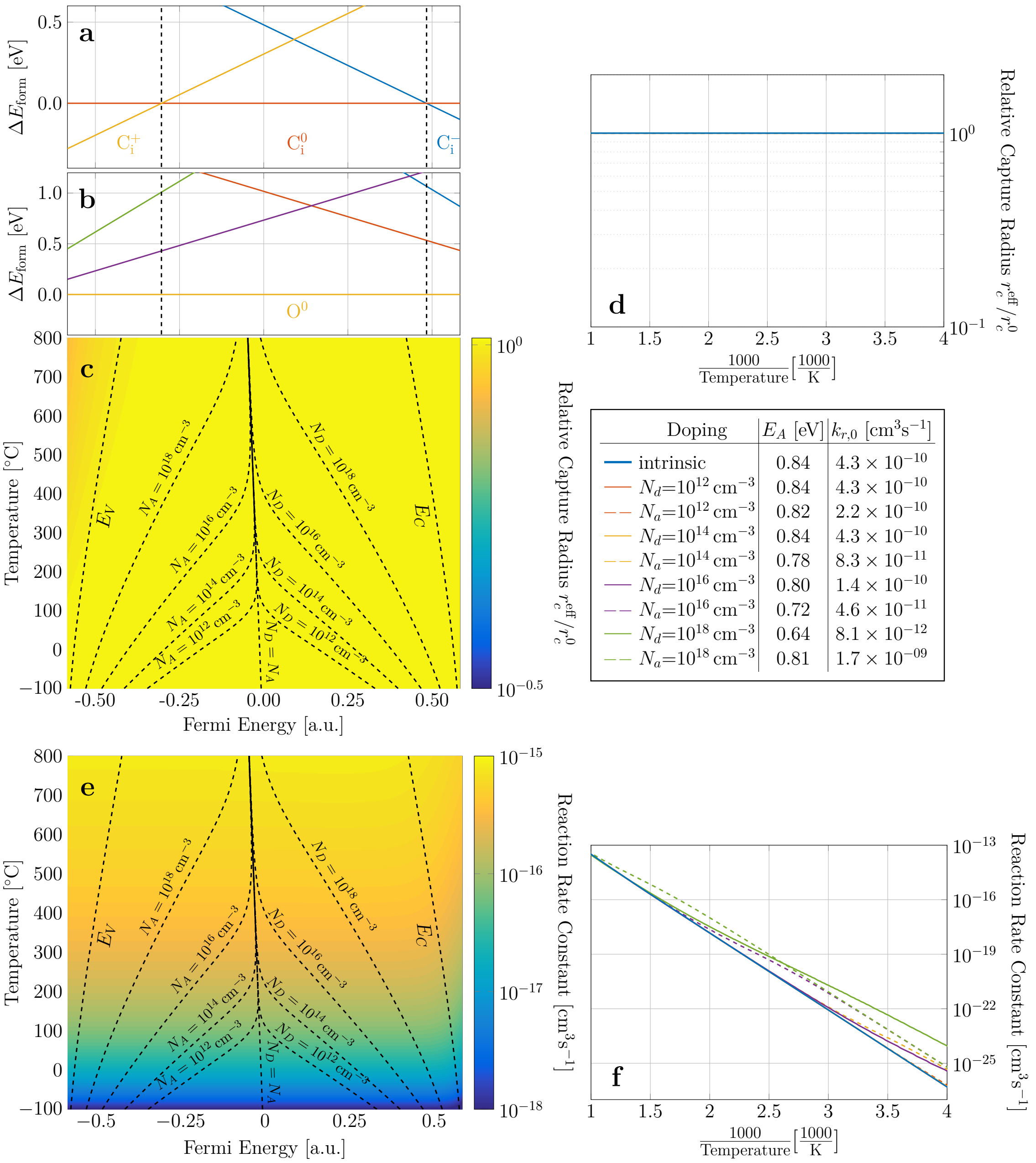

Doping	E_A [eV]	$k_{r,0}$ [cm^{3}s^{-1}]
— intrinsic	0.84	4.3×10^{-10}
— N_d=10^{12} cm^{-3}	0.84	4.3×10^{-10}
- - N_a=10^{12} cm^{-3}	0.82	2.2×10^{-10}
— N_d=10^{14} cm^{-3}	0.84	4.3×10^{-10}
- - N_a=10^{14} cm^{-3}	0.78	8.3×10^{-11}
— N_d=10^{16} cm^{-3}	0.80	1.4×10^{-10}
- - N_a=10^{16} cm^{-3}	0.72	4.6×10^{-11}
— N_d=10^{18} cm^{-3}	0.64	8.1×10^{-12}
- - N_a=10^{18} cm^{-3}	0.81	1.7×10^{-09}

Figure D.41.1: Kinetics of the reaction of C_i with oxygen forming C_iO.

D.42 Kinetics of the Reaction $\mathrm{C_i} + \mathrm{OH} \xrightarrow{k_r^{\mathrm{OHC_i}}} \mathrm{C_iOH}$

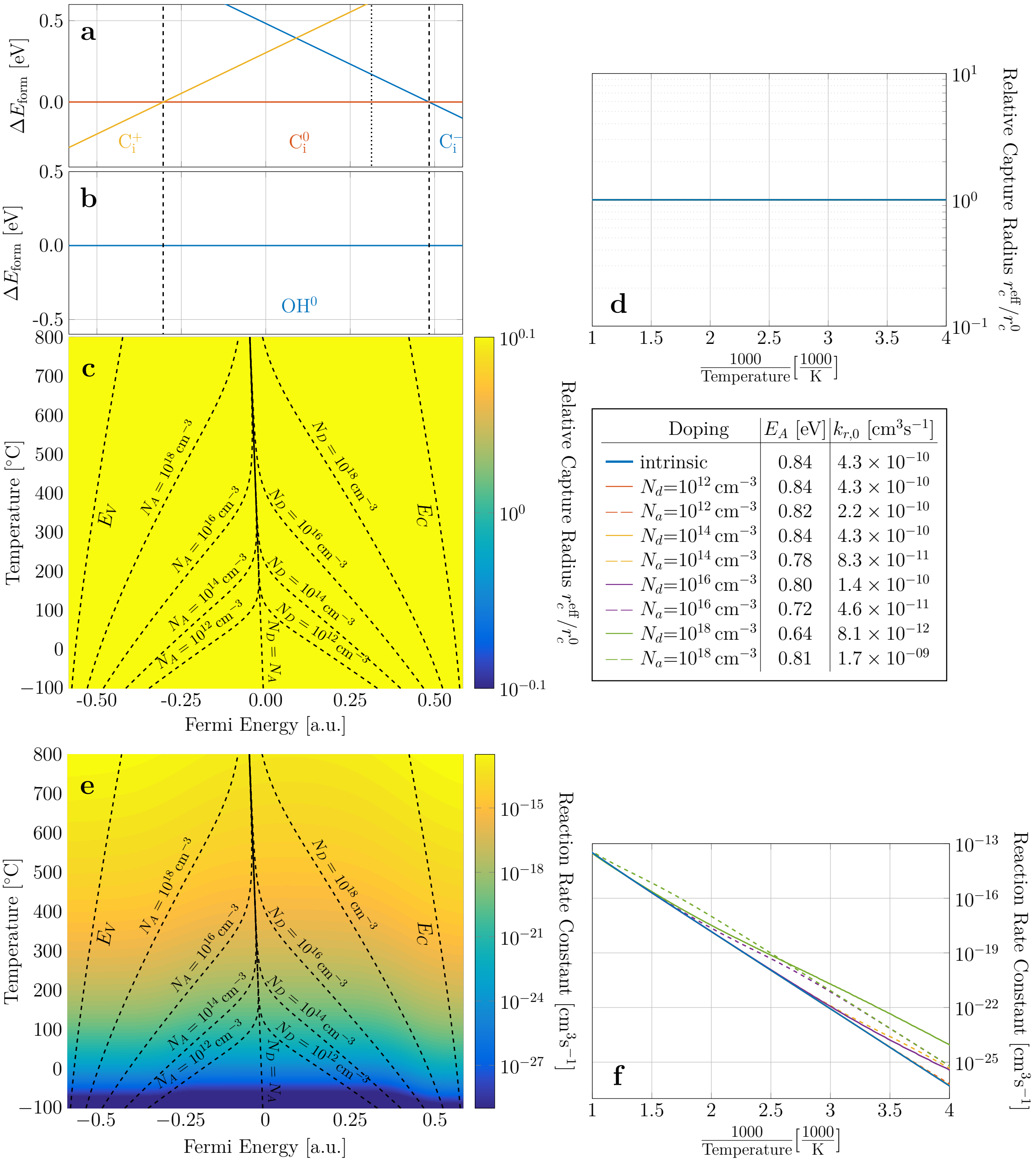

Doping	E_A [eV]	$k_{r,0}$ [cm^{3}s^{-1}]
— intrinsic	0.84	4.3×10^{-10}
— N_d=10^{12} cm^{-3}	0.84	4.3×10^{-10}
- - N_a=10^{12} cm^{-3}	0.82	2.2×10^{-10}
— N_d=10^{14} cm^{-3}	0.84	4.3×10^{-10}
- - N_a=10^{14} cm^{-3}	0.78	8.3×10^{-11}
— N_d=10^{16} cm^{-3}	0.80	1.4×10^{-10}
- - N_a=10^{16} cm^{-3}	0.72	4.6×10^{-11}
— N_d=10^{18} cm^{-3}	0.64	8.1×10^{-12}
- - N_a=10^{18} cm^{-3}	0.81	1.7×10^{-09}

Figure D.42.1: Kinetics of the reaction of $\mathrm{C_i}$ with OH forming $\mathrm{C_iOH}$.

D.43 Kinetics of the Reaction $C_iO + H \xrightarrow{k_r^{HC_iO}} C_iOH$

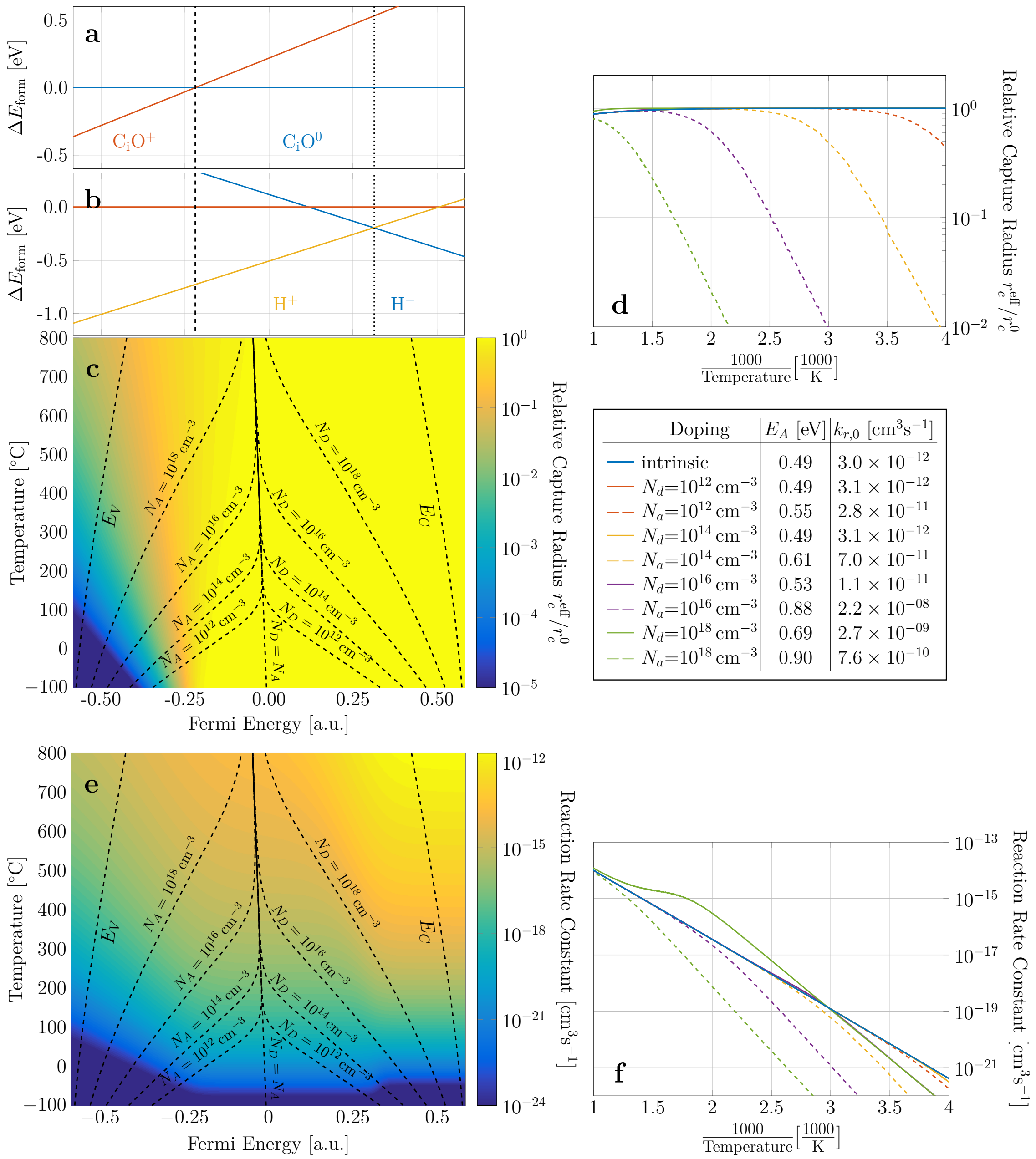

Doping	E_A [eV]	$k_{r,0}$ [cm^{3}s^{-1}]
— intrinsic	0.49	3.0×10^{-12}
— N_d=10^{12} cm^{-3}	0.49	3.1×10^{-12}
– – N_a=10^{12} cm^{-3}	0.55	2.8×10^{-11}
— N_d=10^{14} cm^{-3}	0.49	3.1×10^{-12}
– – N_a=10^{14} cm^{-3}	0.61	7.0×10^{-11}
— N_d=10^{16} cm^{-3}	0.53	1.1×10^{-11}
– – N_a=10^{16} cm^{-3}	0.88	2.2×10^{-08}
— N_d=10^{18} cm^{-3}	0.69	2.7×10^{-09}
– – N_a=10^{18} cm^{-3}	0.90	7.6×10^{-10}

Figure D.43.1: Kinetics of the reaction of C_iO with hydrogen forming C_iOH.

D.44 Kinetics of the Reaction $\mathrm{C_iH + O \xrightarrow{k_r^{C_iHO}} C_iOH}$

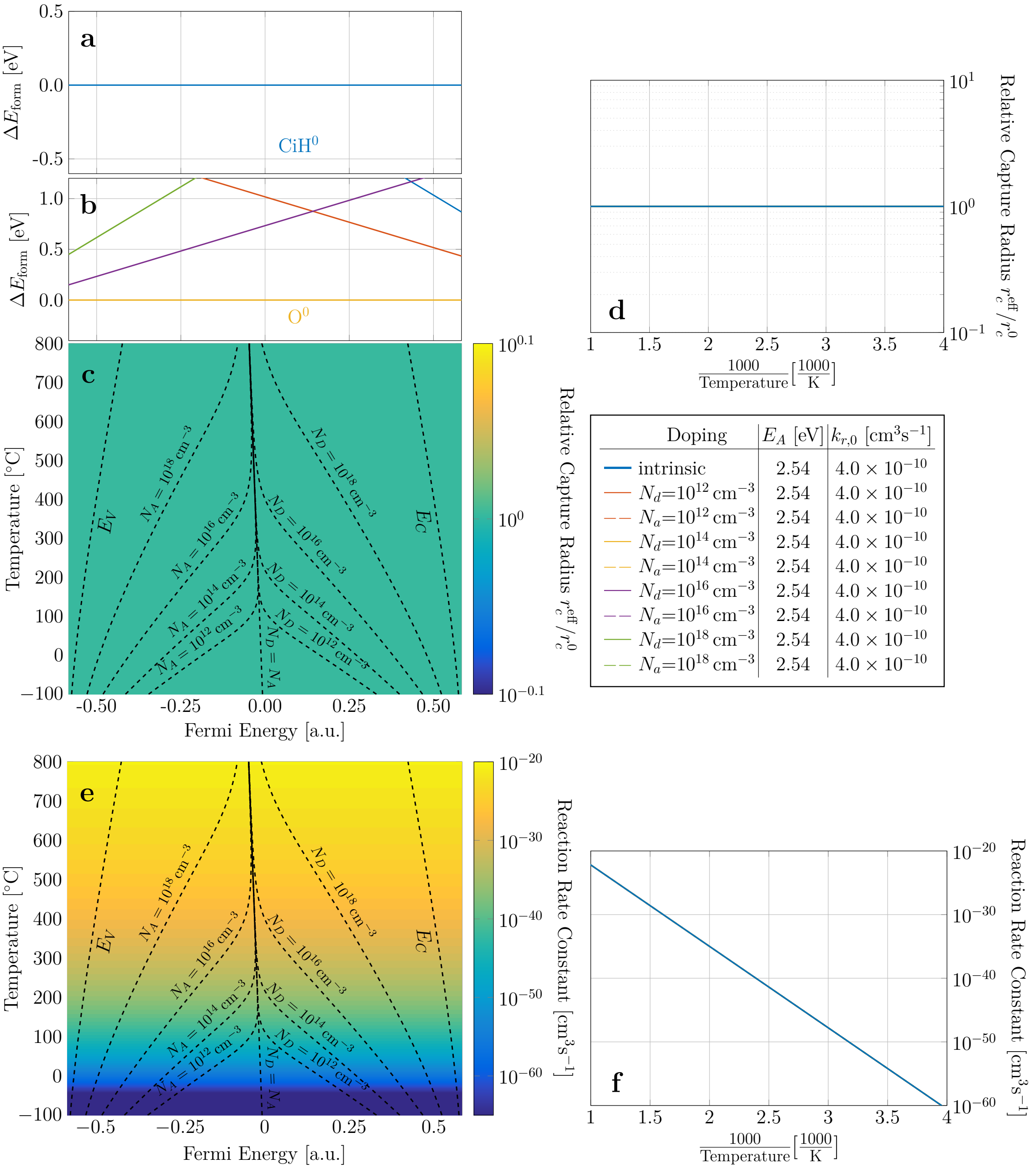

Doping	E_A [eV]	$k_{r,0}$ [cm^{3}s^{-1}]
intrinsic	2.54	4.0×10^{-10}
N_d=10^{12} cm^{-3}	2.54	4.0×10^{-10}
N_a=10^{12} cm^{-3}	2.54	4.0×10^{-10}
N_d=10^{14} cm^{-3}	2.54	4.0×10^{-10}
N_a=10^{14} cm^{-3}	2.54	4.0×10^{-10}
N_d=10^{16} cm^{-3}	2.54	4.0×10^{-10}
N_a=10^{16} cm^{-3}	2.54	4.0×10^{-10}
N_d=10^{18} cm^{-3}	2.54	4.0×10^{-10}
N_a=10^{18} cm^{-3}	2.54	4.0×10^{-10}

Figure D.44.1: Kinetics of the reaction of $\mathrm{C_iH}$ with oxygen forming $\mathrm{C_iOH}$.

D.45 Kinetics of the Reaction $C_iOH + H \xrightarrow{k_r^{C_iOHH}} C_iOH_2$

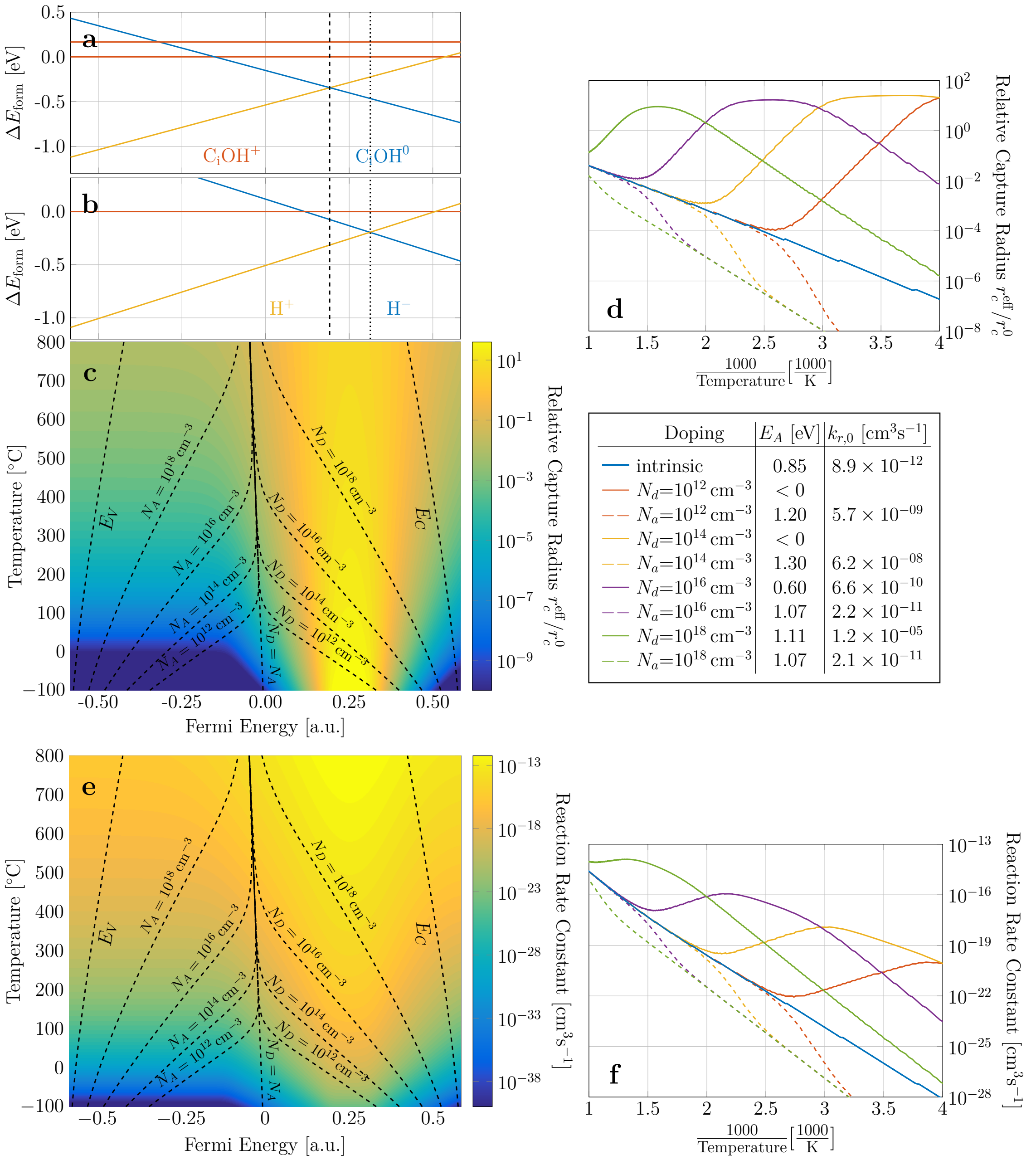

Doping	E_A [eV]	$k_{r,0}$ [cm^{3}s^{-1}]
— intrinsic	0.85	8.9×10^{-12}
— N_d=10^{12} cm^{-3}	< 0	
– – N_a=10^{12} cm^{-3}	1.20	5.7×10^{-09}
— N_d=10^{14} cm^{-3}	< 0	
– – N_a=10^{14} cm^{-3}	1.30	6.2×10^{-08}
— N_d=10^{16} cm^{-3}	0.60	6.6×10^{-10}
– – N_a=10^{16} cm^{-3}	1.07	2.2×10^{-11}
— N_d=10^{18} cm^{-3}	1.11	1.2×10^{-05}
– – N_a=10^{18} cm^{-3}	1.07	2.1×10^{-11}

Figure D.45.1: Kinetics of the reaction of C_iOH with hydrogen forming C_iOH_2.

D.46 Kinetics of the Reaction $C_iH + OH \xrightarrow{k_r^{C_iHOH}} C_iOH_2$

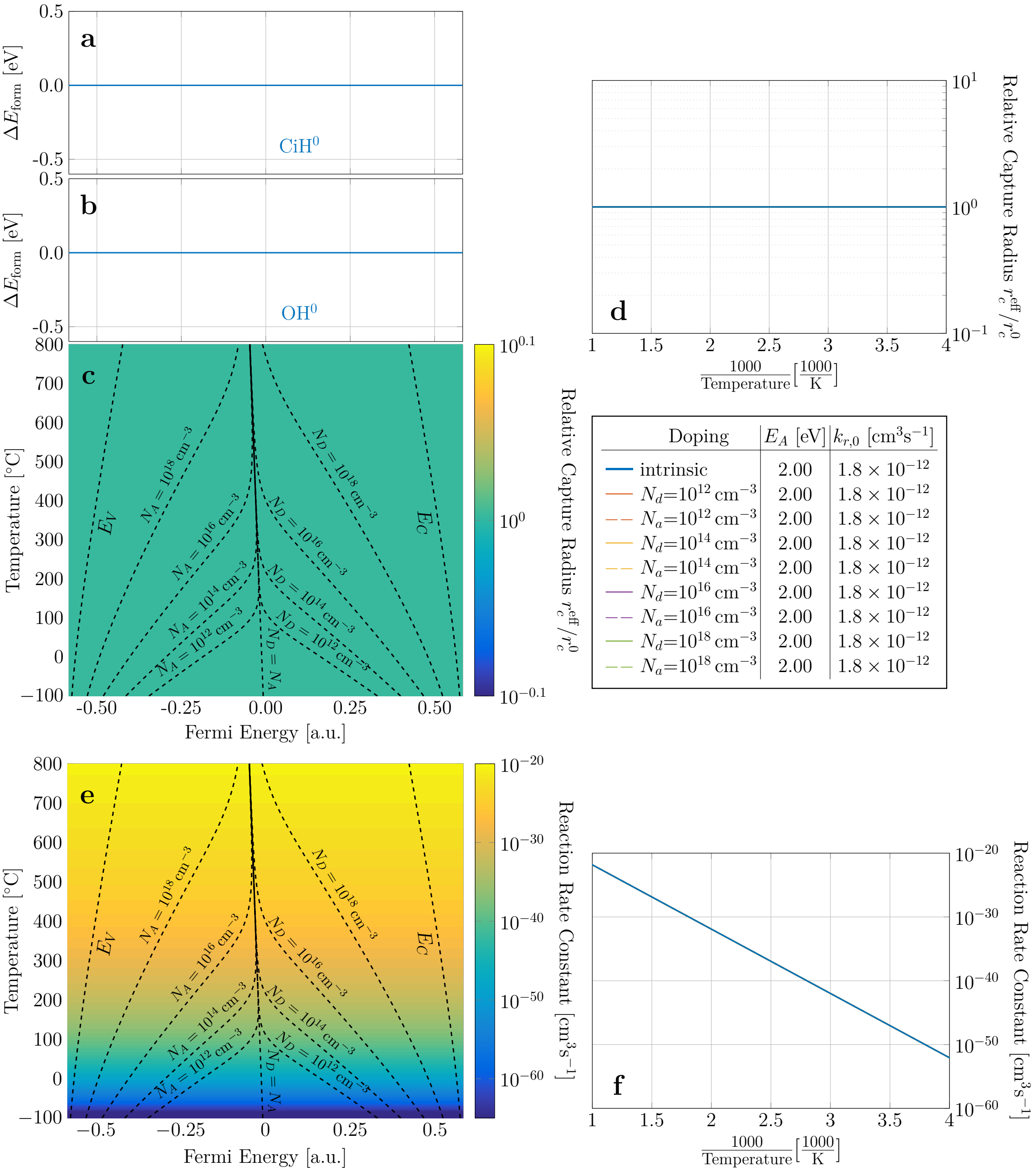

Figure D.46.1: Kinetics of the reaction of C_iH with OH forming C_iOH_2.

D.47 Kinetics of the Reaction $V_2 + H \xrightarrow{k_r^{V_2H}} V_2H$

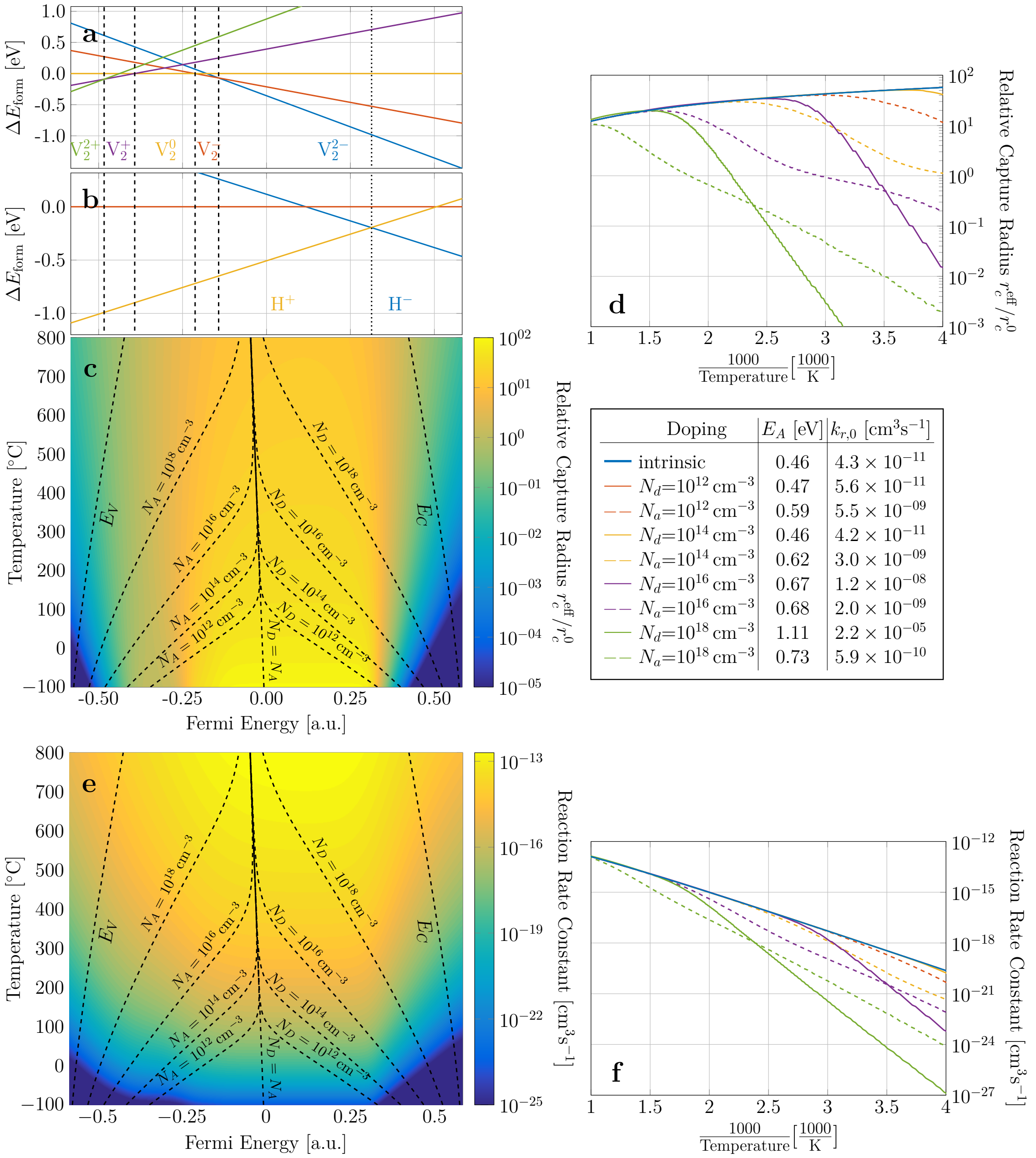

Doping	E_A [eV]	$k_{r,0}$ [cm^{3}s^{-1}]
— intrinsic	0.46	4.3×10^{-11}
— N_d=10^{12} cm^{-3}	0.47	5.6×10^{-11}
– – N_a=10^{12} cm^{-3}	0.59	5.5×10^{-09}
— N_d=10^{14} cm^{-3}	0.46	4.2×10^{-11}
– – N_a=10^{14} cm^{-3}	0.62	3.0×10^{-09}
— N_d=10^{16} cm^{-3}	0.67	1.2×10^{-08}
– – N_a=10^{16} cm^{-3}	0.68	2.0×10^{-09}
— N_d=10^{18} cm^{-3}	1.11	2.2×10^{-05}
– – N_a=10^{18} cm^{-3}	0.73	5.9×10^{-10}

Figure D.47.1: Kinetics of the reaction of C_iH with OH forming V_2H.

D.48 Kinetics of the Reaction $\mathrm{C_iOI} + \mathbf{H} \xrightarrow{k_r^{\mathrm{C_iOIH}}} \mathrm{C_iOIH}$

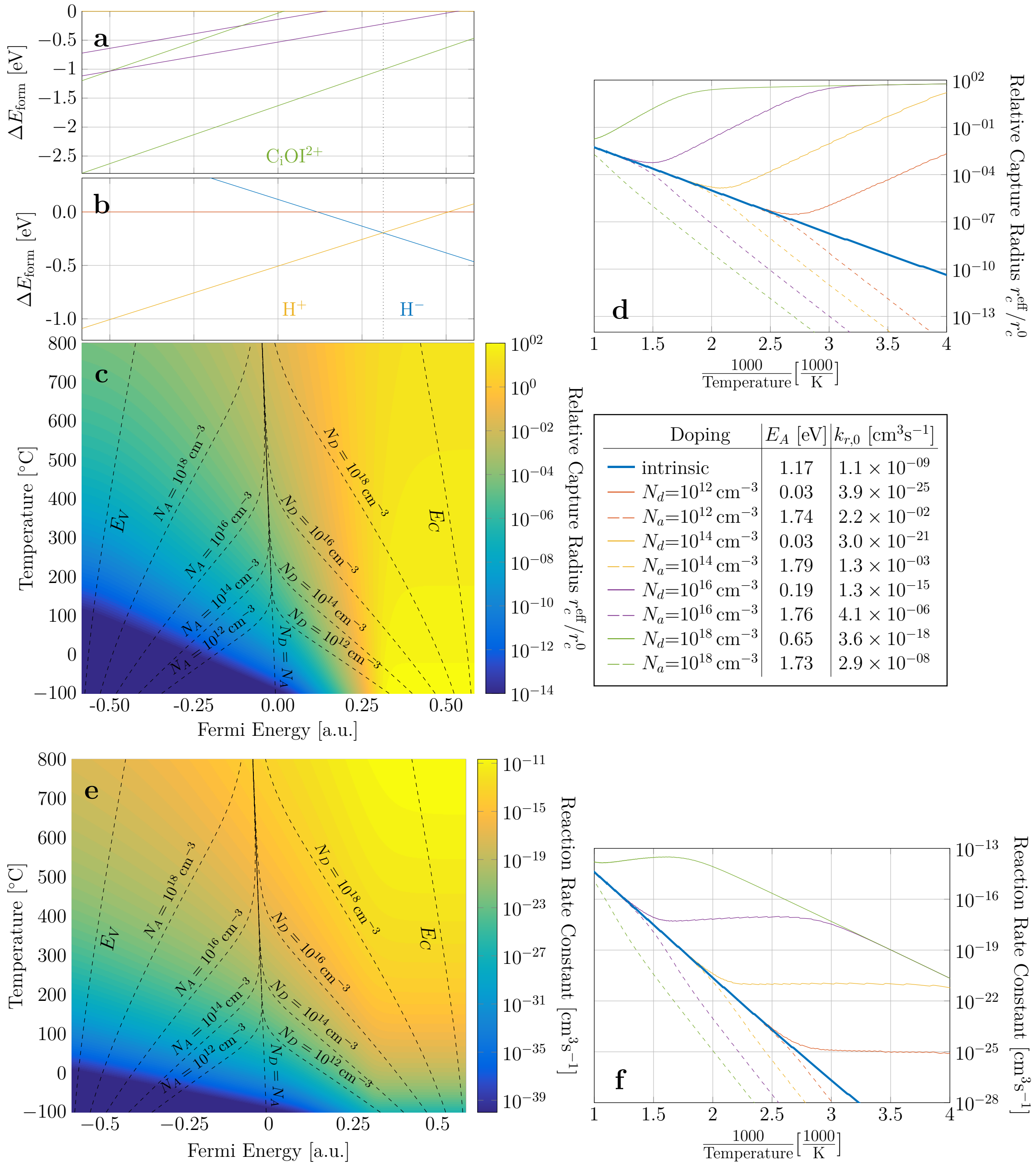

Doping	E_A [eV]	$k_{r,0}$ [cm^{3}s^{-1}]
— intrinsic	1.17	1.1×10^{-09}
— N_d=10^{12} cm^{-3}	0.03	3.9×10^{-25}
- - N_a=10^{12} cm^{-3}	1.74	2.2×10^{-02}
— N_d=10^{14} cm^{-3}	0.03	3.0×10^{-21}
- - N_a=10^{14} cm^{-3}	1.79	1.3×10^{-03}
— N_d=10^{16} cm^{-3}	0.19	1.3×10^{-15}
- - N_a=10^{16} cm^{-3}	1.76	4.1×10^{-06}
— N_d=10^{18} cm^{-3}	0.65	3.6×10^{-18}
- - N_a=10^{18} cm^{-3}	1.73	2.9×10^{-08}

Figure D.48.1: Kinetics of the reaction of $\mathrm{C_iH}$ with OH forming $\mathrm{C_iOIH}$.